

MEASUREMENTS AND MODELING OF NITROGEN OXIDES:
TROPOSPHERIC TRANSFORMATIONS DURING SUMMER AND WINTER
IN POLLUTED REGIONS ACROSS THE U.S.

By

ERIN ELIZABETH MCDUFFIE

B.A., Carleton College, 2013

A thesis submitted to the
Faculty of the Graduate School of the
University of Colorado in partial fulfillment
of the requirement for the degree of
Doctor of Philosophy
Department of Chemistry and Biochemistry

2018

The thesis entitled:
Measurements and Modeling of Nitrogen Oxides:
Tropospheric Transformations During Summer and Winter in Polluted Regions Across the U.S.
written by Erin Elizabeth McDuffie
has been approved for the Department of Chemistry and Biochemistry

Dr. Steven S. Brown

Dr. Joost de Gouw

Date _____

The final copy of this thesis has been examined by the signatories, and we find that both the content and the form meet acceptable presentation standards of scholarly work in the above mentioned discipline.

McDuffie, Erin Elizabeth (Ph.D., Chemistry, Department of Chemistry and Biochemistry)

Measurements and Modeling of Nitrogen Oxides: Tropospheric Transformations During Summer and Winter in Polluted Regions Across the U.S.

Thesis directed by: Dr. Steven S. Brown

Atmospheric reactions of inorganic nitrogen oxides critically influence the composition of the troposphere, the lowest layer of the atmosphere that supports all terrestrial life on Earth. From controlling the global budget and distribution of tropospheric oxidants, to degrading local air quality through the production of ozone (O_3) and secondary particulate matter (PM), understanding the underlying chemistry of reactive nitrogen oxides is vital to both improving our predictive capabilities of global tropospheric chemistry and to developing effective mitigation strategies in regions with persistently poor air quality. Despite decades of research into their chemical mechanisms, significant uncertainties remain in the seasonally dependent lifetime and distribution of nitrogen oxides. Key remaining questions include: 1) the sensitivity of photochemical pollutant production to location-specific emission sectors, 2) factors influencing nocturnal inter-conversion processes, which involve multiphase reactions, and 3) the quantitative contribution of these heterogeneous reactions to wintertime air pollution.

In this thesis, I address these questions using observational and modeling-based analyses of data collected during three U.S. field campaigns in summer 2014 and the winters of 2015 and 2017. I first present observations from summer 2014 and results from an observationally-constrained, photochemical box model. This study was the first to quantify the contribution of oil and natural gas emissions to local O_3 pollution in the Colorado Front Range, a region that has been out of compliance with national air quality standards for O_3 since 2008. I next present the first

wintertime aircraft determinations of aerosol uptake coefficients of dinitrogen pentoxide (N_2O_5) and production yields of nitryl chloride (ClNO_2). These parameters were derived from a custom, iterative, inorganic nocturnal nitrogen chemistry box model, fit to aircraft observations collected over the U.S. east coast in 2015. Field-determinations of these parameters are further compared to laboratory-based parameterizations to evaluate the current representation of these processes in global models. Lastly, I present results from the first aircraft observations in Salt Lake Valley, Utah. Observations and box model simulations are combined to assess the contribution of heterogeneous reactive nitrogen chemistry to wintertime PM formation in this region, which frequently violates PM air quality standards during wintertime pollution events.

Acknowledgements

There are many who I need to thank for the experiences that have shaped both the scientist and person I am today, making the work in this dissertation possible.

I would like to first acknowledge my undergraduate experiences at Carleton College that provided valuable lessons about work-life balance. I would also like to thank the entire Carleton Chemistry Department for the rigor, support, and intellectually-stimulating environment that prepared me for independent research. Specifically, I owe a debt of gratitude to my undergraduate advisor, Deborah Gross, who introduced me to the field of atmospheric chemistry and whose support, passion, and expectations always motivated me to attain the highest level.

Second, this dissertation has only been possible with the support and guidance of my graduate research advisor, Steve Brown. Steve, thank you for taking a chance on a first year graduate student who emailed you out of the blue looking for an advisor. Working with you has shaped the trajectory of my career and provided opportunities I never could have imagined. Your enthusiasm and scientific curiosity are truly inspiring and I can only hope, one day, to become a scientist of your caliber and expertise.

To Dorothy, Carrie, Rob, and Bill for serving as mentor figures for me throughout the last four years. From Dorothy who was always willing to provide valuable guidance and career advice, to Rob's ever-willingness to provide a helping hand and reminders not to take things so seriously, my graduate school experience would not have been the same without all of you. The same can be said for Bill, who requires a special thanks. Without Bill, I would not know a fraction of what I do about machining, electronics, instrument operation, or electric motorcycles. Bill's commitment to our lab and to CSD has truly made the group what it is today. His knowledge, skills, and most

importantly, personality will be missed and I am grateful for the opportunity to have worked so closely with him.

I would like to thank everyone in CSD for their open door policies and willingness to help answer my questions, no matter how big or small. I hope to work again in an environment with this level of expertise and productivity. I would also like to thank NOAA, Trop Chem, and CIRES financial support that has allowed me to attend scientific conferences and meetings. My attendance and presentations at these and other events have helped foster my science communication skills and provided unique opportunities to develop professional contacts. Also, to those who don't get thanked enough, thank you Rick, Gabi, Jenny, and Ken for providing countless hours of computing support during field campaigns and modeling work, and for always staying calm during my many computer crises.

To my cohort of graduate students, from the flood of IGOR assignments to the actual flood, together we survived the first year of graduate school. I will remember that time with a mixture of relief and fondness for the strong comradery.

Finally, to my family and friends outside of work who have provided unwavering support and understanding throughout this challenging and exhilarating time. You have kept me moving in a forward direction, provided, at times, much-needed breaks, and have ultimately enabled me to achieve this dissertation.

Acknowledgements for specific Chapters are as follows.

Chapter 3

Much of the work this Chapter was supported by NOAA's Atmospheric Chemistry, Carbon Cycle, and Climate Program. I would like to thank my co-authors who have provided data and

support to this analysis: Pete Edwards, Jessica Gilman, Brian Lerner, Bill Dubé, Michael Trainer, Dan Wolfe, Wayne Angevine, Joost de Gouw, Eric Williams, Alex Tevlin, Jen Murphy, Emily Fischer, Stu McKeen, Tom Ryerson, Jeff Peischl, John Holloway, Ken Aikin, Andy Langford, Christoph Senff, Raul Alvarez II, Sam Hall, Kirk Ullmann, Kathy Lantz, and Steve Brown. I would like to especially thank Betsy Weatherhead for her contribution to the statistical analysis. Also Patrick Reddy for insightful comments and discussion during preparation and Frank Flocke and Gabriele Pfister for FRAPPÉ campaign organization.

Chapters 4 and 5

I again thank my co-authors for the support and data they provided to this analysis: Dorothy Fibiger, Bill Dubé, Felipe Lopez-Hilfiker, Ben Lee, Joel Thornton, Viral Shah, Lyatt Jaeglé, Hongyu Guo, Rodney Weber, Mike Reeves, Andy Weinheimer, Jason Schroder, Pedro Campuzano-Jost, Jose Jimenez, Jack Dibb, Patrick Veres, Carly Ebben, Tamara Sparks, Paul Wooldridge, Ron Cohen, Becky Hornbrook, Eric Apel, Teresa Campos, Samuel Hall, Kirk Ullmann, and Steve Brown. Much of the work in this Chapter was supported by NOAA's Atmospheric Chemistry Carbon Cycle, and Climate Program. I would also like to acknowledge personal funding from the CIRES Graduate Research Fellowship, which supported me during the second half of these analyses. I would also like to thank Jim Roberts for his insights and the NSF-NCAR Research Aircraft Facility staff.

Chapter 6

I would like to thank the NOAA AOC Twin Otter support staff Rob Miletic and Pilots J. C. Clark and Rob Mitchell for their flexibility, professionalism, enthusiasm, and excellence in flight photography. Also thank you to my co-authors Dorothy Fibiger, Carrie Womack, Bill Dube, Ale Franchin, Ann Middlebrook, Lexie Goldberger, Ben Lee, Joel Thornton, Alex Moravek, Jen

Murphy, Munkh Bassandorj, and Steve Brown. I would also like to acknowledge support for the UWFPS campaign from the Utah Department of Environmental Quality and the NOAA Atmospheric Chemistry, Climate and Carbon Cycle (AC4) Program.

Contents

Chapter 1 : Introduction.....	1
<i>1.1 Atmospheric Chemistry of Inorganic Nitrogen Oxides</i>	<i>1</i>
1.1.1 Summer Dominant, Daytime Chemical Reactions and Products	2
1.1.2 Winter Dominant, Nocturnal Heterogeneous Reactions and Products	5
<i>1.2 Research Approach: Ambient Observations and Chemical Box Modeling.....</i>	<i>10</i>
<i>1.3 Thesis Overview</i>	<i>11</i>
Chapter 2 : Research Methods	14
2.1 Introduction.....	14
2.2 Instrumentation for Nitrogen Oxides and Ozone	14
2.2.1 Cavity Ring Down Spectroscopy – Applied to ARNOLD and NOxCaRD Instruments	16
2.2.2 NO ₃ and N ₂ O ₅ Measurements.....	18
2.2.2.1 Measurement Interferences and Corrections	19
2.2.2.2 Instrument Zero.....	21
2.2.2.3 Calibrations.....	22
2.2.2.3.1 N ₂ O ₅ Calibration.....	22
2.2.2.3.1.1 N ₂ O ₅ Calibration Sources.....	24
2.2.2.3.2 NO ₃ Calibration	26
2.2.2.4 Accuracy and Detection Limits.....	26
2.2.3 ARNOLD and NOxCaRD NO, NO ₂ , NO _y , and O ₃ Measurements.....	27
2.2.3.1 Measurement Interferences and Corrections	29
2.2.3.2 Instrument Zero Procedure	30
2.2.3.3 NO _y Heater.....	30
2.2.3.4 NO ₂ Calibration.....	32
2.2.3.5 Accuracy and Detection Limits.....	33
2.2.4 Instrument Hardware and Software Overview	34
2.3 Field Campaigns and Associated Measurements.....	36
2.3.1 FRAPPÉ 2014.....	36
2.3.1.1 Campaign Overview.....	36

2.3.1.2 BAO Tower and PISA Carriage.....	37
2.3.1.3 Instrumentation	38
2.3.2 WINTER 2015.....	39
2.3.2.1 Campaign Overview.....	39
2.3.2.2 Instrumentation	40
2.3.3 UWFPS 2017	44
2.3.3.1 Campaign Overview.....	44
2.3.3.2 Instrumentation	44
2.3.4 Auxiliary Campaigns and Measurements.....	46
2.3.4.1 SONNE 2012	46
2.3.4.2 CalNEX 2010.....	47
2.4 <i>Chemical Box Models</i>	47
2.4.1 DSMACC and MCM	48
2.4.1.1 Model Overview.....	49
2.4.1.2 Chemical Constraints and Model VOC Scenarios.....	50
2.4.1.2.1 Base Case Scenario (Case 1).....	50
2.4.1.2.2 VOC Scenarios 2 and 3.....	56
2.4.1.3 Photolysis Rates	58
2.4.1.4 Physical Loss	59
2.4.1.5 Sensitivity Studies.....	61
2.4.1.6 DSMACC Updates from McDuffie et al., 2016	62
2.4.2 Box Model for Nocturnal N ₂ O ₅ Uptake and ClNO ₂ Production	62
2.4.2.1 Overview and Set-Up	63
2.4.2.2 Model Mechanism.....	66
2.4.2.3 Simulation Duration and Start Time Determination	74
2.4.2.4 Model Fit Parameters for WINTER Flights	77
2.4.2.5 Limitations and Filters for WINTER Simulations.....	78
2.4.2.6 Limitations for UWFPS Campaign.....	80
2.4.2.7 Sensitivity Study Results for WINTER Simulations	80
2.4.2.7.1 Aerosol Surface Area.....	82
2.4.2.7.2 CRDS vs TD-LIF NO ₂ Observations.....	83
2.4.2.7.3 CRDS vs CL O ₃ Observations.....	84
2.4.2.7.4 CRDS vs CIMS N ₂ O ₅ Measurements	84
2.4.2.7.5 CIMS ClNO ₂ Measurements	85

2.4.2.7.6 CRDS vs CL NO _y	86
2.4.2.7.7 AMS vs PILS-IC Nitrate.....	86
2.4.2.7.8 Simulation Duration & Start Time	87
2.4.2.7.9 Photolysis Frequencies.....	90
2.4.2.7.10 NO ₃ Reactivity.....	91
2.4.2.7.11 Ocean Surface Deposition.....	94
2.4.2.7.12 Dilution over the Ocean	97
2.5 Conclusions.....	98
Chapter 3 : Influence of oil and gas emissions on summertime ozone in the Colorado Northern Front Range.....	101
3.1 Introduction.....	102
3.2 Experimental Analysis Methods.....	107
3.2.1 Measurements and Field Campaigns	107
3.2.2 Ozone Production Efficiency.....	108
3.2.2.1 OPE Derivation – Data Coverage	109
3.2.2.2 OPE Derivation - Time Interval.....	110
3.2.2.3 OPE Derivation - Fit Intercept Filter.....	111
3.2.3 Box Model - Overview and Set-Up	112
3.3 Results and Discussion	115
3.3.1 Observed chemical composition and wind patterns.....	115
3.3.2 VOC OH Reactivity – 2012	116
3.3.3 Ozone Production Efficiency – 2014.....	117
3.3.3.1 NFR Emission Sector OPEs	119
3.3.3.1.1 OPE as a Function of Wind Direction	119
3.3.3.1.2 OPE as a function of Chemical Tracers.....	122
3.3.3.2 Uncertainty in OPE Analysis	123
3.3.4 Box Model Simulations – Maximum Photochemical O ₃	126
3.3.4.1 NO _x Sensitivity	127
3.3.4.2 O&NG Influence.....	128
3.3.4.3 Biogenic Influence	133
3.3.4.4 Model Ozone Production Efficiency.....	134
3.3.4.5 Model Sensitivity Studies	135
3.3.4.6 Model Chemical Mechanism Comparison	138
3.4 Conclusions and Future Work	141

Chapter 4 : Heterogeneous N₂O₅ uptake during winter: Aircraft measurements during the 2015 WINTER campaign and critical evaluation of current parameterizations..... 144

4.1 Introduction..... 145

4.2 Methods..... 149

 4.2.1 WINTER Campaign and Measurements..... 149

 4.2.2 Iterative Box Model 153

 4.2.2.1 Model Description..... 153

 4.2.2.2 Model Filter, Limitations, and Sensitivity Studies..... 156

4.3 Results..... 157

 4.3.1 Box Model Results..... 157

 4.3.2 Comparison to the Steady State Approximation 165

4.4 Discussion..... 167

 4.4.1 Model Mechanism Background..... 167

 4.4.2 Dependence of $\gamma(\text{N}_2\text{O}_5)$ on Controlling Variables..... 169

 4.4.2.1 Ambient Temperature..... 170

 4.4.2.2 Relative Humidity/Aerosol Liquid Water 172

 4.4.2.3 The Nitrate Effect..... 175

 4.4.2.4 Aerosol Nitrate/Chloride 178

 4.4.2.5 Aerosol pH..... 179

 4.4.2.6 Aerosol Organic Content..... 180

 4.4.2.7 Aerosol Size 183

 4.4.2.8 Trends Summary 184

 4.4.3 Parameterization of $\gamma(\text{N}_2\text{O}_5)$ 186

 4.4.3.1 Previous $\gamma(\text{N}_2\text{O}_5)$ Parameterizations..... 186

 4.4.3.2 Comparison of Box Model Results to Laboratory-Derived
 Parameterizations 187

 4.4.3.3 Empirical Parameterization..... 199

4.5 Summary, Conclusions, and Future Directions 200

Chapter 5 : ClNO₂ yields from aircraft measurements during the 2015 WINTER campaign and critical evaluation of current parameterizations..... 203

5.1 Introduction..... 204

5.2 Methods..... 207

 5.2.1 Measurement Campaign and Box Model..... 207

 5.2.2 Box Model Limitations, Uncertainties, and Sensitivity Studies..... 209

5.3 Results..... 211

5.3.1 Box Model Analysis.....	211
5.3.2 Comparison to Multiple Definitions of $\phi(\text{ClNO}_2)$	215
5.4 Discussion – Evaluation of Current $\phi(\text{ClNO}_2)$ Parameterizations.....	219
5.4.1 Parameterization Background.....	219
5.4.2 Box Model – Parameterization Comparison.....	220
5.4.3 Sources of Parametrization-Box Model Differences.....	224
5.4.3.1 Observed Trends/Water Dependence.....	224
5.4.3.2 Additional Aqueous Competition Reactions.....	230
5.4.3.3 Direct ClNO_2 loss.....	235
5.5 Conclusions and Future Work.....	238
Chapter 6 : Evaluating the contribution of nocturnal heterogenous reactive nitrogen chemistry to particulate matter formation during winter pollution events in Northern Utah.....	242
6.1 Introduction.....	243
6.2 Methods.....	248
6.2.1 UWFPS Campaign Overview and Instrumentation.....	248
6.2.2 Box Model.....	249
6.3 Results and Discussions.....	252
6.3.1 $\text{PM}_{2.5}$ in Salt Lake Valley – Winter 2017.....	252
6.3.2 Limiting and Excess Reagents for NH_4NO_3 Aerosol.....	253
6.3.2.1 Method #1: Molar Ratios of Oxidized to Reduced Nitrogen.....	254
6.3.2.2 Method #2 - ISORROPIA Model Sensitivity Studies.....	255
6.3.3 Nitrate Production via Heterogeneous Reactive Nitrogen Chemistry.....	260
6.3.3.1 Nitrate Radical Production Rates.....	261
6.3.3.2 Modeled Uptake Coefficients and Production Yields.....	263
6.3.3.3 Modeled Nitrate Production Rates and Fractional Contribution of Heterogeneous Chemistry to Total NH_4NO_3 Aerosol.....	268
6.4 Conclusions and Future Work.....	270
Chapter 7 : Summary and Conclusions.....	272
Bibliography.....	278
Glossary of Terms.....	309
Appendix A.....	312
Appendix B.....	316
Appendix C.....	325

Tables

Table 2.1. Model treatment, OH rate constant (298 K), and O&NG contribution factors for SONNE Chemical Observations.....	52
Table 2.2. Statistics for 10 secondary compounds	61
Table 2.3. Box Model Chemical Mechanism.....	66
Table 2.4. NO ₃ + VOC Reactions and Rate Equations.....	68
Table 2.5. Measured k_{VOC} by flight. All units are in s ⁻¹	69
Table 2.6. Estimation method of k_{VOC} for WINTER flights without TOGA and/or PICARRO measurements.....	69
Table 2.7. Instrument Measurement used as Fit Parameters for each WINTER flight	78
Table 2.8. Sensitivity study results for box model derived median WINTER $\gamma(N_2O_5)$ and $\phi(ClNO_2)$ values.....	81
Table 3.1 Summary of BAO chemical and physical observations used in this analysis	108
Table 3.2. VOC Scenario Statistics by non-methane VOC class ^a	114
Table 3.3. Maximum Simulated Photochemical O ₃ for three VOC scenarios.	130
Table 3.4. Box-Model Sensitivity Study Results ^a	136
Table 4.1. Summary of WINTER observations used in the Box Model analysis	150
Table 4.2. Summary of $\gamma(N_2O_5)$ Trend Analyses	186
Table 5.1. Correlations between $\phi(ClNO_2)$ parameterization-box model differences and aerosol composition factors. Correlation coefficients and trend signs are provided for parameterized values calculated with AMS (a) and PILS (b) particle chloride measurements. Data are for all box model results. N = 2884 for AMS parameterization, N = 3141 for PILS parameterization. All results are statistically significant.....	225
Table 6.1. Aircraft measurements used in this analysis	249

Figures

Figure 1.1. Schematic of the day-night cycle of inorganic reactive nitrogen chemistry. Boundary layer dynamics are illustrated by dashed lines.....	1
Figure 1.2. Example curves illustrating the sensitivity of daily photochemical O ₃ production (ppbv) sensitivities to changes in NO _x (x-axis, arbitrary units) and VOC (three curves) concentrations. The light gray curve represents O ₃ production as a function of NO _x at a normalized VOC concentration of 1. The dark gray and black curves represent the daily maximum O ₃ as function of NO _x with higher concentrations of VOCs or more reactive (i.e. with OH) mixtures.....	4
Figure 1.3. Image of pollution event in Salt Lake Valley during winter 2017, illustrating layer capping from warm, high pressure systems aloft.....	9
Figure 2.1. Schematic of 6-channel ARNOLD Instrument for the simultaneous 2 Hz detection of (A) N ₂ O ₅ and (B) NO ₃ by direct detection of NO ₃ and of (C) NO _y , (D) O ₃ , (E) NO ₂ , and (F) NO by direct detection of NO ₂	15
Figure 2.2. Generalized schematic of CRDS.....	16
Figure 2.3. Convolution of literature absorption cross-section spectrum for NO ₃ at 298K and diode laser profile. Literature $\sigma_{NO_3} = 4.56 - 0.00787 * T * 1 \times 10^{-17} \text{cm}^2$	19
Figure 2.4. N ₂ O ₅ calibration scheme for ARNOLD CRD instrument. (Left) example calibration from the UWFPS campaign using the gas-phase N ₂ O ₅ calibration source. The transmission and thermal conversion efficiencies were 99.0%. (Right) example calibration from WINTER aircraft campaign using the solid-phase N ₂ O ₅ source. Transmission and thermal conversion efficiencies were 99.2%.....	23
Figure 2.5. Gas-Phase N ₂ O ₅ calibration source. (Left) front and back panels, (right) top-down view. Specific components are labeled for clarity.....	25
Figure 2.6. Literature NO ₂ absorption cross section (Vandaele et al., 1998) (gray), cross section convolution with OBIS laser profile (black), and laser wavelengths measured with the NOxCaRD spectrometer (Ocean Optics USB4000) (red), calibrated against literature mercury absorption lines (Sansonetti et al., 1996).....	27
Figure 2.7. (a) Temperature profiles of two NO _y heaters used in the Brown Lab since 2014. Both heaters were set to 650°C and flow rates of 1.4 slpm (standard liters per minute, at 273 K and 1 atm). Differences in temperature profiles result from the specific construction of each heater. (b) Reproduced from Wild et al. (2014), shows the small interference expected from NH ₃ under conditions of low (< 100 ppbv) O ₃ concentration. Heater #1 was used to conduct the calibration curves shown in panel b.	31

Figure 2.8. Example NO₂ calibration procedure. (a) raw time series of τ (as measured by ARNOLD) during a 7 step calibration procedure. (b) α plotted against measured [NO₂]. Markers represent each calibration step and the fit line slopes are σ_{NO_2}/RL for each cavity. (c) pressure dependent calibration factors for each cavity. Each point is the slope from a single-pressure calibration, as shown in panel b. Linear fits to these data are used with measurement of cavity pressures to calculate σ_{NO_2}/RL and ambient mixing ratios during aircraft campaigns.33

Figure 2.9. (a) BAO Tower with labels highlighting the PISA carriage, 10 m monitoring station, one of the ground-site trailers, and 300 m total tower height. (b) Simultaneous sampling during FRAPPÉ of instruments in the PISA carriage and on the NASA P-3B aircraft. (c) ARNOLD CRDS instrument installed in the PISA carriage.....38

Figure 2.10. ARNOLD Instrument installed in the C-130 aircraft (inset photo) during WINTER. Various instrument components are labeled.....40

Figure 2.11. NSF/NCAR C-130 aircraft instrument payload during the WINTER campaign.....42

Figure 2.12. Reproduced from final UWFPS report (UWFPS Science Team, 2018). (Left) Image of instrumentation mounted inside the Twin Otter aircraft, taken from the rear, facing forward. (Right) Image of Twin Otter with arrows indicating instrument inlet locations on the side (UHSAS, AMS, I-TOF-CIMS), nose (met probe), and top (QC-TLDAS, NOxCARD) of the aircraft.45

Figure 2.13. Diel averages of observed and modeled (case 1) chemical constraints (VOCs measured by Jessica Gilman and Brian Lerner, NO_x measured by Pete Edwards). $\Sigma(n\text{-Pentane}) = \Sigma(n\text{-Pentane} + 1,1\text{-Dimethylcyclopentane})$, $\Sigma(n\text{-Hexane}) = \Sigma(n\text{-Hexane} + Cyclopentane + Methylcyclopentane)$, $\Sigma(n\text{-Octane}) = \Sigma(n\text{-Octane} + 1\text{-Ethyl-1-Methylcyclohexane})$, $\Sigma(n\text{-Nonane}) = \Sigma(n\text{-Nonane} + 1,1,3\text{-Trimethylcyclohexane} + Methylcyclohexane)$, $\Sigma(n\text{-Decane}) = \Sigma(n\text{-Decane} + Ethylcyclohexane + Trans\text{-}1,2\text{-dimethylcyclohexane} + Cis\text{-}1,3\text{-Dimethylcyclohexane} + Trans\text{-}1,3\text{-Dimethylcyclohexane})$, $\Sigma(\beta\text{-Pinene}) = \Sigma(\beta\text{-Pinene} + 3\text{-Carene})$ 54

Figure 2.14. O&NG fraction of observed non-methane VOCs as a function of normalized carbon mixing ratio and VOC OH Reactivity. Note: Aldehydes and ketones were initialized with base case mixing ratios (assuming O&NG VOC Fraction = 0) and calculated by DSMACC in all simulations. The aldehyde and ketone O&NG fractions (OHR: 19%, ppbC: 13%) were derived from a comparison of the base case VOC scenario (Case 1) with the removed O&NG scenario (Case 2) at 2012 observed NO_x mixing ratios (VOC scenarios derived from work by Jessica Gilman).58

Figure 2.15. Total photolysis frequencies of (left) $j(NO_2)$ and (right) $j(O^1D)$. Observed values (dashed) (measured by Samuel Hall), scaled TUV values (solid), and un-scaled TUV (black). All DSMACC model simulations in this analysis are scaled to 2014 (solid blue) photolysis profiles. The presence of high thunderstorm activity in 2014 is evident by the difference in shape between the afternoon $j(NO_2)$ observations and TUV profile, which assumes clear sky conditions.59

Figure 2.16. Diel profiles of nine secondary non-methane VOCs during SONNE (measured by Jessica Gilman). Black: 30-minute diel average observations ± 1 standard deviation, Red: Case 1 model output for simulations run with observed NO_x mixing ratios and a dilution rate of constant of $1.11 \times 10^{-4} \text{ s}^{-1}$ 61

Figure 2.17. (a-d) Box model iterative steps for an example point off-shore of South Carolina during flight RF04. The air was calculated to be older than the time since sunset and the simulation start time was set to 1.3 hours prior to sunset (as indicated by the gray/yellow shading). Black traces are individual, iterative model simulations while red traces show the derived simulation that simultaneously predicts measured mixing ratios (red diamonds) within designated thresholds as described in the main text. For this point, the derived $\gamma(\text{N}_2\text{O}_5)$ was 0.021 and $\phi(\text{ClNO}_2)$ was 22.7%. (e-f) Correlations of model-derived initial O_3 (e) and NO_x (f) mixing ratios at sunset (sunset start points only (N = 2003)) against observed mixing ratios, colored by simulation duration. Red lines are reference lines with slopes of 1 and 4..... 65

Figure 2.18. Comparison of box-model derived $k_{\text{N}_2\text{O}_5}$ and calculated k_{Homo} as a function of ambient water vapor for WINTER..... 72

Figure 2.19. Measured photolysis rates for all day-into-night WINTER flights. Red lines: Exponential fits used to calculate photolysis rates for the iterative box model..... 73

Figure 2.20. Photolysis profiles of $j(\text{NO}_3)$ of the $\gamma(\text{N}_2\text{O}_5)$ analysis in Chapter 4. (a) Measured and calculated $j(\text{NO}_3)$ for the CalNEX Campaign. (b) WINTER photolysis rates calculated with CalNEX multivariate fit to $j(\text{NO}_2)$ and SZA. Red line: Exponential fit used to determine the photolysis rates for the iterative box model..... 73

Figure 2.21. Comparison of $j(\text{NO}_3)$ and $j(\text{ClNO}_2)$ values used in the $\gamma(\text{N}_2\text{O}_5)$ (Chapter 4) and $\phi(\text{ClNO}_2)$ (Chapter 5) analyses. The left column shows the $j(\text{NO}_3)$ values derived from CalNEX measurements and original $j(\text{ClNO}_2)$ values. The right column shows the $j(\text{NO}_3)$ values calculated from a re-analysis of WINTER measurements and updated $j(\text{ClNO}_2)$ 74

Figure 2.22. Time series of daytime steady state N_2O_5 mixing ratios (red) and CRDS (black) and I-TOF-CIMS (gray) observations for two example WINTER flights. Vertical lines represent the time of divergence as calculated from CRDS (black) and I-TOF-CIMS (gray) observations. 75

Figure 2.23. Histogram of box model $\gamma(\text{N}_2\text{O}_5)$ sensitivities to (a) uncertainties in dry aerosol surface area density as described in text and (b) wet aerosol SA density calculated from the E-AIM derived growth factor, assuming pure NH_4NO_3 aerosol. 82

Figure 2.24. (a) Correlation between TD-LIF and CRDS NO_2 Observations (10-second average). Data were filtered to include nocturnal measurements below 1500 mAGL. Dashed line represents the 1:1 correlation. Solid black line is the 2-sided regression fit. Histogram of base case box model (b) $\gamma(\text{N}_2\text{O}_5)$ and (c) $\phi(\text{ClNO}_2)$ results and those calculated with $\pm 10\%$ changes in NO_2 83

Figure 2.25. (a) Correlation between CL and CRDS O₃ Observations (10-second averages). Data were filtered to include nocturnal measurements below 1500 mAGL. Dashed line represents the 1:1 correlation. Solid black line is the 2-sided regression fit. Histogram of base case box model (b) $\gamma(\text{N}_2\text{O}_5)$ and (c) $\phi(\text{ClNO}_2)$ results and those calculated with $\pm 5\%$ changes in O₃. 84

Figure 2.26. (a) Correlation between I-TOF CIMS and CRDS N₂O₅ Observations (10-second averages). Data were filtered to include nocturnal measurements below 1500 m AGL. Dashed line: 1:1 correlation. Solid black line: 2-sided regression fit. Histogram of base case box model (b) $\gamma(\text{N}_2\text{O}_5)$ and (c) $\phi(\text{ClNO}_2)$ results and those calculated with I-TOF CIMS N₂O₅ observations. 85

Figure 2.27. Histogram of base case $\phi(\text{ClNO}_2)$ results and those calculated with $\pm 30\%$ ClNO₂. 85

Figure 2.28. Correlation between CL and CRDS NO_y Observations (10-second averages). Data were filtered to include nocturnal measurements below 1500 m AGL. Dashed line represents the 1:1 correlation. Solid black line is the 2-sided regression fit. 86

Figure 2.29. Correlation between PILS-IC and AMS Particle Nitrate Observations. AMS measurements were averaged to the PILS collection time (~1.5 minutes) for this comparison only. Data were filtered to include nocturnal measurements below 1500 mAGL. Dashed line represents the 1:1 correlation. Solid black line is the 2-sided regression fit. 87

Figure 2.30. Histogram of base case box model (a) $\gamma(\text{N}_2\text{O}_5)$ and (b) $\phi(\text{ClNO}_2)$ results and those calculated with a pre-sunset start time of 0 and 1.75 hours..... 88

Figure 2.31. Histogram of base case box model (a) $\gamma(\text{N}_2\text{O}_5)$ and (b) $\phi(\text{ClNO}_2)$ results and those calculated with the oldest possible and youngest reasonable air ages. 90

Figure 2.32. Histogram of base case box model (a) $\gamma(\text{N}_2\text{O}_5)$ and (b) $\phi(\text{ClNO}_2)$ values and those calculated with $\pm 40\%$ changes in photolysis frequencies. 90

Figure 2.33. Histogram of base case box model (a) $\gamma(\text{N}_2\text{O}_5)$ and (b) $\phi(\text{ClNO}_2)$ results and those calculated with $\pm 10\%$ changes in k_{NO_3} 91

Figure 2.34. Percent change in $\gamma(\text{N}_2\text{O}_5)$ and $\phi(\text{ClNO}_2)$ when accounting for N₂O₅ ocean surface deposition. Yellow points highlight values where the deposition rate constant, calculated from the exchange flux in Kim et al. (2014), was larger than the loss derived from the iterative box model..... 95

Figure 2.35. Parameterized values of $\phi(\text{ClNO}_2)$ calculated from Bertram and Thornton (2009) with PILS (top row) and AMS (bottom row) particle chloride (pCl) measurements vs. box model results. (left) original results; (middle) box model results re-calculated with N₂O₅ surface deposition (-1.66 m s⁻¹ exchange velocity); (right) box model results re-calculated with N₂O₅ and ClNO₂ (-0.55 m s⁻¹ exchange velocity) deposition. Data with pCl >

instrument LODs are in bold. Medians ($pCI > LOD$ points) of each comparison are shown by the square points in each panel.....96

Figure 2.36. Model sensitivity to dilution over the ocean. Map shows the percent change in $\gamma(N_2O_5)$ and $\phi(ClNO_2)$ relative to base case. Histograms show the $\gamma(N_2O_5)$ and $\phi(ClNO_2)$ distributions in the base case scenarios (black bars) and sensitivity studies (colored bars).98

Figure 3.1. Elevation map of the Northern Front Range (NFR) region of Colorado showing the O_3 nonattainment area, Weld County (dashed lines), major roads, rivers, urban regions, power plants (scaled by relative NO_x emissions), large agricultural facilities (feedlots sized by animal capacity), and active O&NG wells ((Colorado Oil and Gas Conservation Commission (COGCC), 1/2016)). The red diamond indicates the location of the BAO measurement site..... 104

Figure 3.2. O_3 time series, 16 July – 15 August 2014. (Grey) Surface O_3 measured at BAO; (Black) O_3 data coverage for 305 OPEs as measured by CRDS; (Red) O_3 data coverage for 80 OPEs as measured by CRDS; Dashed) EPA 2008 (75 ppbv) and 2015 (70 ppbv) 8-hour O_3 air quality standards (NAAQS); (Green) Maximum Daily 8-hr Average (MDA8). 110

Figure 3.3. (Top) Time series for 8 August 2014 (12 pm - 6 pm MDT); (bottom) O_x/NO_z correlation for 1-minute averaged data on 8 August 2014, colored by observed CH_4/CO ratio; (black points) example 15-minute period used to derive individual OPEs..... 111

Figure 3.4. Histogram and Gaussian fit of 381 OPEs (point filter applied)..... 112

Figure 3.5. Diel average of non-methane VOC and NO_x model constraints (SONNE measurements). VOCs (left axis) are given in VOC OH reactivity, NO_x and O_3 (right axes) are given in mixing ratio. Bar height is the average VOC OHR colored by the fractional VOC class contribution every 60-minutes. Average VOC class contributions are calculated from the sum of averaged (24-hour) individual VOCs. VOC OHR does not include contributions from HCHO, CO, or CH_4 . Aldehydes and ketones shown here were not used as model constraints but instead used to derive the dilution rate constant..... 113

Figure 3.6. (a) Histogram of July-August 2012 and 2014 wind direction measured at BAO (100 m); (b) Median mixing ratios of chemical tracers averaged between 2012 and 2014 campaign years, normalized to mixing ratios in the western wind sector to illustrate relative sector-to-sector differences on the same scale for all species. CO and CH_4 plotted as normalized enhancements above observed 2012 and 2014 backgrounds. All data filtered for wind speeds > 2.5 m/s. Binned wind directions are north: $315^\circ-45^\circ$, east: $45^\circ-135^\circ$, south: $135^\circ-225^\circ$, and west: $225^\circ-315^\circ$ 115

Figure 3.7. (left) Observed O_x/NO_z correlation for 16 July – 15 August 2014 (12 pm – 6 pm MDT, $N = 8268$), colored by observed wind direction; (right) Example O_x/NO_z correlation during one, 15-minute time interval. This OPE meets the point number (> 11), intercept (56.7 ± 9.3 ppbv), and $r^2 (> 0.5)$ filter requirements discussed in text..... 118

Figure 3.8. 80 individual OPEs with high ($r^2 > 0.5$) O_x/NO_z correlation plotted radially as a function of wind direction, colored by NE (0-90°, blue) and SE (90-180°, red) wind sectors.

Box and whisker plots show median OPE for each wind sector (SE: 5.1 ppbv/ppbv, NE: 4.9 ppbv/ppbv) and range between the 10 th and 90 th percentiles.....	120
Figure 3.9. Average ($\pm 1\sigma^*$) observational OPEs in northeast and southeast wind sectors as derived from winds observed at BAO (solid) and FLEXPART model simulations (dashed).	121
Figure 3.10. 80 individual OPEs with high ($r^2 > 0.5$) O _x /NO _z correlation as a function of simple chemical tracers. CH ₄ and CO mixing ratios are the enhancements above background. Correlation coefficients (r^2) for all species suggest no statistically significant trend (95% confidence level) in OPE with tracers.	122
Figure 3.11. Base Case Simulated O ₃ . Observed diel average (red) and base-case simulated (black dashed) mixing ratios. Difference between observed and modeled maxima is -0.3%.	126
Figure 3.12. NO _x sensitivity of maximum photochemical O ₃ in the base case simulation. 11 simulations are shown with SONNE (2012) observed NO _x mixing ratios, represented by a scaling factor of 1, scaled from 0 to 5. Pie chart insert represents the 24-hour average fractional contribution of non-methane VOCs to OH Reactivity.	127
Figure 3.13. NO _x sensitivity of simulated maximum photochemical O ₃ mixing ratios for three VOC scenarios. Asterisk indicates a difference of 17.4% between observed VOC base case (Case 1) and VOC scenario with O&NG VOCs removed (Case 2) at SONNE (2012) observed NO _x mixing ratios. Pie chart inserts illustrate the 24-hour average non-methane VOC OHR (s ⁻¹) and carbon mixing ratio (ppbC) of each VOC scenario (VOC scenarios derived from work by Jessica Gilman). Distributions do not include CH ₄ , CO, or HCHO.	129
Figure 3.14. NO _x sensitivity curves for three VOC scenarios. In contrast to Figure 3.13, the third VOC scenario has O&NG VOCs reduced by half instead of completely removed. The red line and symbols provide example locations to the north and south of BAO with different O&NG and NO _x mixing ratios that experience the same photochemical O ₃ enhancement as that at BAO.	133
Figure 3.15. Same format as Figure 3.13 but instead showing three additional simulations where isoprene constraints have been multiplied by 3 (dashed lines).....	134
Figure 3.16. NO _x sensitivity of maximum photochemical O ₃ with $\pm 25\%$ adjusted photolysis rates. (Black) Original case 1 NO _x sensitivity curve; (red shading) Photochemical O ₃ at each NO _x scaling factor with $\pm 25\%$ original photolysis rates.	137
Figure 3.17. Maximum O ₃ sensitivity to O&NG VOCs with photolysis rates scaled by $\pm 25\%$. (Solid Bars) case 1 maximum photochemical O ₃ (at observed SONNE NO _x mixing ratios); (dashed bars) case 2 maximum photochemical O ₃ (at observed SONNE NO _x mixing ratios).	138

Figure 3.18. Diel average ozone observed (red line) compared to simulated with explicit (dotted black line) and lumped (dash-dot black line) VOC mechanisms.	140
Figure 3.19. NO _x sensitivity of simulated maximum photochemical ozone mixing ratios for three VOC scenarios. As in Figure 3.13, colors represent the VOC scenarios (black – observed VOCs, green – doubled O&G VOCs, blue – zero O&G OVCs). Solid lines are the updated MCM results, and the dotted lines are the CB6r3 results.	140
Figure 4.1. Schematic of the N ₂ O ₅ chemical system. Black arrows indicate reactions that do not require sunlight, red arrows show photochemical reactions.	146
Figure 4.2. Uptake schematic highlighting the relation between the chemical mechanism and resistor model framework in terms of each mechanistic step (R4.1-R4.6) and its associated conductance (Γ).	147
Figure 4.3. Hygroscopic Diameter Growth Factors for <1μm diameter aerosol. (Red circles) derived for WINTER, used for base case calculations; (red dashed line) derived for WINTER, assuming pure NH ₄ NO ₃ aerosol (calculated from E-AIM by Viral Shah); (black, gray lines) reported in Brown et al. (2009) and Wagner et al. (2013), respectively. Surface area growth factors are the square of diameter growth factors.	152
Figure 4.4. (a) Map of WINTER flight tracks of the NSF/NCAR C-130 in the Eastern U.S., colored to show day and night (as defined by SZA > 90°) flight periods, which represented 42 and 58% of the data, respectively. The aircraft was based at NASA Langley in coastal Virginia and executed 13 flights of approximately 8 hours duration between 3 February – 13 March 2015. (b) Flight tracks colored by γ(N ₂ O ₅), derived from the box model analysis. (c) Histogram of box model results.	158
Figure 4.5. Histogram of base case results comparing the distributions of γ(N ₂ O ₅) values derived over the U.S. main land (green) and Atlantic ocean (blue).	159
Figure 4.6. WINTER γ(N ₂ O ₅) results listed by flight, with shaded regions indicating error estimates for each determination.	160
Figure 4.7. Example time-series from three different WINTER research flights illustrating the variability of γ(N ₂ O ₅), N ₂ O ₅ , and aerosol liquid water content (LWC) (calculated by Hongyu Guo from ISORROPIA) within and between different air parcels sampled.	160
Figure 4.8. Comparison of WINTER γ(N ₂ O ₅) values derived from the box model and GEOS-Chem simulations (60 second averages). Map shows the WINTER flight tracks, colored by the percent difference in box model and GEOS-Chem results (from Viral Shah). Percent difference = (GEOS-Chem-box model)/box model)*100. Histogram insert shows the distributions of both.	162
Figure 4.9. Previous field determinations of γ(N ₂ O ₅) in comparison to OH, O ₃ , and NO _x sensitivities in GEOS-Chem, data courtesy of Mat Evans (Macintyre & Evans, 2010). N represents the number of points in each study, if reported. ^a Approximate range, exact	

values not reported. ^bRange not reported. ^cAverage not reported, diamond represents the median, Minimum and maximum values not reported, 25th and 75th percentiles shown instead. ^dAverage and median not reported, diamond represents the most frequent value. Vertical lines in the lower panels show the value of $\gamma(\text{N}_2\text{O}_5)$, NO_x , O_3 , and OH are most sensitive to in the northern hemisphere (red) and globally (blue). 164

Figure 4.10. Comparison of iterative box model and steady state approximation. (a) Comparison of WINTER $\gamma(\text{N}_2\text{O}_5)$ values, colored by simulation duration; (b) comparison of WINTER N_2O_5 lifetimes, colored by percent difference between box model and steady state predicted $\gamma(\text{N}_2\text{O}_5)$ values; (c) histogram comparing box model results to those derived by the steady state approximation. 167

Figure 4.11. Model-derived $\gamma(\text{N}_2\text{O}_5)$ and observed ambient variables listed by flight. Box and whisker plots show 10-90th and 25-75th percentiles, with median (bar) and average (star) values. Pie charts represent the average distribution of submicron aerosol composition as measured by the AMS with corresponding median surface area (including water) listed above. To account for the presence of sea salt, aerosol chloride was measured by the PILS-IC, with an average contribution ranging from 0.1-1.2% for all night flights. AMS measurements were unavailable on RF05 as well as subsequently calculated pH and liquid water. Data shown are only for points with simultaneous $\gamma(\text{N}_2\text{O}_5)$ observations, the number of which are given under each flight label. Inorganic water component and pH were calculated with ISORROPIA by Hongyu Guo, as described in Guo et al. (2016) 170

Figure 4.12. Variation of $\gamma(\text{N}_2\text{O}_5)$ with ambient observed temperature. Box and whisker plots show 10th to 90th (bars), and 25th to 75th (boxes) percentiles, and median values. The histogram shows the distribution of observed temperatures. The red line shows the linear fit to all of the data points (green) with fit results listed in the box. 171

Figure 4.13. Comparison of the temperature dependence of $\gamma(\text{N}_2\text{O}_5)$ with literature laboratory results for inorganic aerosol. Gray dots/red line WINTER results from Figure 4.12. Laboratory measurements for H_2SO_4 (diamonds) (Hallquist et al., 2000), $(\text{NH}_4)_2\text{SO}_4$ (orange circles) and NH_4HSO_4 (triangles) (Griffiths & Cox, 2009), NaNO_3 (squares) (Hallquist et al., 2003), pure water (blue circles) (George et al., 1994; Schweitzer et al., 1998), and 1M NaCl (George et al., 1994). 172

Figure 4.14. (a) WINTER $\gamma(\text{N}_2\text{O}_5)$ with relative humidity, (b) aerosol water molarity (inorganic component calculated from ISORROPIA by Hongyu Guo) (M), and (c) aerosol water liquid content (water mass fraction). Box and whisker plots, histogram, and fit lines as in Figure 4.12. 174

Figure 4.15. Comparison of the $\gamma(\text{N}_2\text{O}_5)$ RH dependence with literature laboratory results for inorganic aerosol. Gray dots/red line are WINTER results from Figure 4.14a. Laboratory measurements for H_2SO_4 (diamonds) (Hallquist et al., 2000; Hu & Abbatt, 1997; Kane et al., 2001; Mozurkewich & Calvert, 1988), $(\text{NH}_4)_2\text{SO}_4$ (hourglasses) (Badger et al., 2006; Hallquist et al., 2003; Hu & Abbatt, 1997; Kane et al., 2001), NH_4HSO_4 (diamonds) (Bertram & Thornton, 2009; Folkers et al., 2003; Griffiths & Cox, 2009; Hallquist et al., 2003; Kane et al., 2001; Sohn, 1998), NaHSO_4 (squares) (Mentel et al., 1999;

Mozurkewich & Calvert, 1988), NaNO_3 (triangles) (Hallquist et al., 2003; Wahner et al., 1998b), NH_4NO_3 (circles) (Folkers, 2001), and NaCl and synthetic sea salt (hexagons) (Behnke et al., 1997; Behnke et al., 1991; McNeill et al., 2006; Stewart et al., 2004; Thornton & Abbatt, 2005). 175

Figure 4.16. (a) WINTER $\gamma(\text{N}_2\text{O}_5)$ with aerosol nitrate mass fraction, including contribution from aerosol water (inorganic component from ISORROPIA simulations by Hongyu Guo); (b) WINTER $\gamma(\text{N}_2\text{O}_5)$ with aerosol $\text{H}_2\text{O}:\text{NO}_3^-$ molar ratio, colored by ambient temperature. The shaded region represents the range of previous laboratory determinations of $\gamma(\text{N}_2\text{O}_5)$ on pure water droplets over the range of 262-277 K (George et al., 1994), 264-275 K (Schweitzer et al., 1998), and 271-282 K (Van Doren et al., 1990). Box and whisker plots, histograms, and fit lines as in preceding figures. 177

Figure 4.17. (a) WINTER $\gamma(\text{N}_2\text{O}_5)$ with aerosol chloride molarity (derived from PILS-IC measurements), colored by aerosol water molarity (inorganic component calculated by Hongyu Guo from ISORROPIA); (b) WINTER $\gamma(\text{N}_2\text{O}_5)$ with aerosol $\text{Cl}^-:\text{NO}_3^-$ molar ratio. The gray shaded region represents the range of previous laboratory determinations of $\gamma(\text{N}_2\text{O}_5)$ on pure water droplets. Box and whisker plots, histograms, and fit lines as in preceding figures. 179

Figure 4.18. (a) WINTER $\gamma(\text{N}_2\text{O}_5)$ with aerosol pH (inorganic component calculated by Hongyu Guo from ISORROPIA). Box and whisker plot, histogram, and fit line as in preceding figures. Dashed line is linear regression fit to data between pH -2 to 1 to separate the influence from nitrate suppression at pH >1. (b) Correlation of measured aerosol nitrate dry mass fraction and pH for points with concurrent $\gamma(\text{N}_2\text{O}_5)$ values, colored by aerosol water molarity. 180

Figure 4.19. WINTER $\gamma(\text{N}_2\text{O}_5)$ with (a) aerosol organic dry mass fraction, (b), organic wet mass fraction (including water, inorganic component calculated by Hongyu Guo from ISORROPIA), (c) aerosol $\text{Org}:\text{SO}_4^{2-}$ mass ratio, and (d) O:C ratio. All aerosol data were collected by the AMS. Box and whisker plots, histograms, and fit lines as in preceding figures. 183

Figure 4.20. Comparisons between parameterized and model-derived $\gamma(\text{N}_2\text{O}_5)$ values. Correlation coefficient, RMSE (root-mean-square-error), and point number are provided on each plot. Red lines indicate the 1:1 line. Black squares represent median values. Dashed lines represent the range of values within factors of ± 2 and ± 10 188

Figure 4.21. Supplemental comparisons between $\gamma(\text{N}_2\text{O}_5)$ parameterizations and box-model results. Same format as Figure 4.20. 190

Figure 4.22. Comparison of 14 literature and empirical parameterizations relative to WINTER $\gamma(\text{N}_2\text{O}_5)$ results. Comparisons are given in terms of their root-mean-square-error (upper panel) and median percent difference (lower panel). Comparisons are listed in order of decreasing RMSE within each group of parameterization type (inorganic only, combined inorganic and organic, and empirical). Parameterizations that incorporated BT09 are shown with (dark gray) and without (light gray) the contribution from chloride. 194

- Figure 4.23. WINTER Aerosol O:C vs. Relative humidity. Liquid phase separations are expected to occur below the separation relative humidity line (SRH: red line) as parameterized by Bertram et al. (2011). Graph is colored by model-derived $\gamma(\text{N}_2\text{O}_5)$ values..... 196
- Figure 4.24. (a) AMS mass factor ratio: f_{44} to f_{43} . The black and green lines represent the boundaries defined in Ng et al. (2010). Gray points show all AMS nighttime data ($\text{SZA} > 90^\circ$). Points with corresponding derived $\gamma(\text{N}_2\text{O}_5)$ values are overlaid on top and colored by $\gamma(\text{N}_2\text{O}_5)$. (b) AMS mass factor ratio: $f_{\text{CO}_2^+}$ to $f_{\text{C}_5\text{H}_6\text{O}^+}$. Dashed line represents the urban background and biomass burning (BB) ratio and black line represents the ratio for monoterpene-influenced SOA as presented in Hu et al. (2015). Gray points show all AMS nighttime data ($\text{SZA} > 90^\circ$). Points with corresponding derived $\gamma(\text{N}_2\text{O}_5)$ values are overlaid on top and colored by $\gamma(\text{N}_2\text{O}_5)$ 198
- Figure 5.1. WINTER $\phi(\text{ClNO}_2)$ box model results. (a) flight tracks colored by night ($\text{SZA} > 90^\circ$) and daytime ($\text{SZA} < 90^\circ$) flights; (b) flight tracks colored by box-model derived $\phi(\text{ClNO}_2)$ values; (c) histogram of box model $\phi(\text{ClNO}_2)$ results..... 211
- Figure 5.2. Histogram of ClNO_2 yields for data sampled over the ocean (blue) and over land (green). The ocean-land boundary was defined as the geographic boundary of the U.S. east coast..... 212
- Figure 5.3. Times series of box model $\phi(\text{ClNO}_2)$ values (black dots) and associated errors (gray shading). 213
- Figure 5.4. Map of all reported field-derived $\phi(\text{ClNO}_2)$ values. The geographic location of each study is shown by a diamond, colored by reported (or calculated) average or median $\phi(\text{ClNO}_2)$. All 3425 values from Figure 5.1 are shown. Graph inserts show the reported range and median or average of each study, if reported. Data from Mielke et al. (2013); Mielke et al. (2016); Osthoff et al. (2008); Phillips et al. (2016); Riedel et al. (2013); Tham et al. (2016); Thornton et al. (2010); Wagner et al. (2013); Wagner et al. (2012); Wang, X. et al. (2017); Wang, Z. et al. (2017)..... 214
- Figure 5.5. (left) Box and whisker plots comparing four derivation methods for $\phi(\text{ClNO}_2)$. Bars: 10th, 50th, and 90th percentiles; boxes: 25th to 75th percentiles; stars: average. Parameterized $\phi(\text{ClNO}_2)$ calculated with (4a) AMS particle chloride and (4b) PILS particle chloride. (Right) Median values of each method (diamond) and absolute errors in medians (whiskers). 215
- Figure 5.6. Correlation of observed ClNO_2 against total soluble nitrate ($\text{HNO}_3(\text{g}) + \text{NO}_3^-(\text{p})$). Gray points correspond to all WINTER data where the box model derived values for $\phi(\text{ClNO}_2)$. Red points represent example correlations ($r^2 > 0.5$) derived using Method 2..... 217
- Figure 5.7. $\phi(\text{ClNO}_2)$ as a function of WINTER aerosol chloride to water molar ratio, calculated from (a) AMS and (b) PILS particle chloride measurements. Laboratory-based parameterizations are shown by gray lines and WINTER box model results shown by blue markers. Data with particle chloride measurements above reported detections limits for

lines represent the total absolute upper and lower error limits of the Bertram and Thornton parameterization..... 221

Figure 5.8. Base case (gray) and highest (red) and lowest (blue) estimated box model $\phi(\text{ClNO}_2)$ values, plotted against WINTER $\text{Cl}^-:\text{H}_2\text{O}$ molar ratio. Black curve represented the $\phi(\text{ClNO}_2)$ values predicted by the Bertram and Thornton (2009) parameterization. Grady curve are the parameterization error upper and lower limits. Squares represent the median $\phi(\text{ClNO}_2)$ value of each set of modeled WINTER $\phi(\text{ClNO}_2)$ values ($\text{pCl} > \text{LOD}$ points only), plotted at the median $\text{Cl}^-:\text{H}_2\text{O}$ molar ratio. 223

Figure 5.9. Difference between $\phi(\text{ClNO}_2)$ parameterization and box model results for WINTER, calculated using AMS (a) and PILS (b) particle chloride against aerosol water (inorganic water component calculated by Hongyu Guo from ISORROPIA). Data above chloride detection limits shown in black points with the fit line slopes by solid lines. All data are shown in gray points with fit line slopes by dashed lines. 226

Figure 5.10. (a) Parameterized WINTER $\phi(\text{ClNO}_2)$ values (with AMS chloride) against aerosol water (inorganic component from ISORROPIA calculated by Hongyu Guo); (b) Parameterized WINTER $\phi(\text{ClNO}_2)$ values (with PILS chloride) against aerosol water. In both a and b, points above instrument LODs in black, all data in gray. Correlation fits in solid and dashed lines, respectively. (c) Box model derived WINTER $\phi(\text{ClNO}_2)$ values with aerosol water. Points colored by flight number according to legend. 227

Figure 5.11. Aerosol O:C ratio (from the AMS) vs. the ambient relative humidity. Black line is the parameterized RH where liquid-liquid organic coatings are predicted (separation relative humidity (SRH)) following Bertram et al. (2011). Data below the SRH are predicted to have liquid-liquid separations. Data are colored by difference between parameterized $\phi(\text{ClNO}_2)$ values (Bertram & Thornton, 2009) and those predicted by the box model. 230

Figure 5.12. Correlation of $(\phi(\text{ClNO}_2)^{-1} - 1) * [\text{Cl}^-]/[\text{H}_2\text{O}]$ product from E5.6 against aerosol $\text{SO}_4^{2-}:\text{H}_2\text{O}$ molar ratio in (a) and (b) and $\text{Org}:\text{H}_2\text{O}$ molar ratio in (c) and (d), calculated using AMS and PILS chloride measurements. Points with $\text{pCl} > \text{LOD}$ are in dark gray. Red lines are the linear fits with fit equations provided in each figure. From E5.6, slopes are the $k_{5.14}/k_{5.12}$ ratio and intercepts are the $k_{5.11}/k_{5.12}$ ratio. Dashed lines represent the same fits, holding the intercept constant at 0.002 (from Bertram & Thornton, 2009). Organic molarity calculated by applying a constant molecular weight of 120 g mol^{-1} to AMS organic mass concentration measurements. Larger y-values correspond to smaller values of box model $\phi(\text{ClNO}_2)$ 233

Figure 6.1. Left) Elevation Map of Utah’s Wasatch Front Range (Utah State in insert), with the Great Salt Lake (north) and Utah Lake (south) shown in blue, and county borders in black. U.S. EPA designated non-attainment areas (NAA) for $\text{PM}_{2.5}$ are shown in red. From north to south these include the Logan NAA: “Moderate” status, Salt Lake City NAA: “Serious” status, and Provo NAA: “Serious” status. UWFPS flight tracks are shown in pink. Purple markers indicate the locations of major cities, including Logan in Cache Valley, Salt Lake City in Salt Lake Valley, and Provo in Utah Valley. The location of missed approaches

conducted with the TO are shown in dark pink circles. The Hawthorne measurement site in Salt Lake Valley is labeled as HW. Right) Zoomed in view of Salt Lake Valley with flight data for this analysis highlighted in green. 244

Figure 6.2. Time series of total PM_{2.5} mass ($\mu\text{g m}^{-3}$) (1-hr and 24-hr averages) for the 2016-2017 winter, measured at the Hawthorne (HW) UDAQ site in Salt Lake Valley. The 24-hour EPA national ambient air quality standard for PM_{2.5} ($35 \mu\text{g m}^{-3}$) is shown by the dashed gray line. Gray shading indicates days when the TO aircraft was flying as part of the UWFPS campaign. Average aerosol mass fractions, measured by the AMS aboard the TO are given in pie charts for each measurement period. Aerosol components by color are nitrate (blue), ammonium (gold), sulfate (red), non-refractory chloride (pink), and organics (green). 253

Figure 6.3. Time series of calculated nitrogen ratios (10s average) for pollution events in SLV (top) and concurrent PM_{2.5} mass (24-hour average) measured at the HW ground-site (bottom). Individual nitrogen ratios are colored by the aircraft altitude (mAGL), yellow and gray shading indicate times of day and night. 255

Figure 6.4. Reproduced from UWFPS Report (UWFPS Science Team, 2018). Comparison between measurements (x-axis) and model results (y-axis) of the phase partitioning of ammonium (yellow), nitrates (blue) and chloride (pink) for all TO flights. left column) Input total ammonium, nitrate, and chloride (gas + aerosol). Center column) model-observation comparison of gas-phase concentrations, right column) model-observation comparison of particle-phase concentrations. 258

Figure 6.5. Comparison between base case model results (x-axis) and simulations with a 50% reduction in total nitrate (y-axis), for SLV only (run by Alessandro Franchin). (a) Total aerosol mass from the base case and sensitivity test simulations compared to observed total aerosol mass; (b) Changes in gas-phase (left column) and particle phase (right column) for ammonium, nitrate, and chloride relative to base case simulations. 259

Figure 6.6. Comparison between base case model results (x-axis) and simulations with a 50% reduction in total ammonium (y-axis), for SLV only (run by Alessandro Franchin). Panels a and b are in the same format as Figure 6.5. 260

Figure 6.7. Twin Otter vertical profiles (mAGL) of total PM_{2.5} (measured by the AMS), P_{NO_3} (calculated from ambient temperature and NO_xCaRD measurements of NO₂ and O₃ (1Hz)), NO₂, and O₃ (measured by NO_xCaRD) during pollution events in SLV. Circles are the median at each altitude bin and bars represent the 25th-75th percentile range. Light blue squares in (a) and (b) and squares in (c) are the median values measured and calculated (from 1 hour averages of PM_{2.5}, NO₂, O₃, and temperature (reported by Munkh Bassandorj)) at the HW ground site during concurrent nights with TO flights. Dark blue squares in (a) and (b) are the average nighttime values (8 pm – 7 am local time) from 27 January – 4 February. Bars for each represent the 25th-75th percentile range. 262

Figure 6.8. Time series PM_{2.5} (24-hour average) (bottom) and P_{NO_3} (top) calculated from hourly NO₂, O₃, and temperature measurements at the Hawthorne ground-site (reported by Munkh

Bassandorj). Day and night are shown by the yellow and gray shading. TO flight periods are shown by the red shading.....263

Figure 6.9. (a) Histograms of $\gamma(\text{N}_2\text{O}_5)$ determinations from SLV during pollution events (green) and WINTER campaign results (dashed bars); (b) histograms of $\phi(\text{ClNO}_2)$ determinations from SLV during pollution events (blue) and WINTER campaign results (dashed bars). Medians are provided in each plot.265

Figure 6.10. Methods comparison for $\gamma(\text{N}_2\text{O}_5)$ values during SLV pollution events. Solid circles show the comparison between steady state (y-axis) and box model (x-axis) derived values, colored by model simulation duration (i.e. time since sunset+1.3 hrs). The 2-sided fit has a slope of 1.07 ± 0.01 (black line). Open circles show the comparison between parametrized values (from Bertram and Thornton (2009)) (y-axis) and box model (x-axis) results. Dashed line is the 1:1 correlation.....266

Figure 6.11. Simulation of nocturnal chemistry from sunset to sunrise of a representative air parcel sampled over SLV on 28 January 2017. Model derived $\gamma(\text{N}_2\text{O}_5)$ and $\phi(\text{ClNO}_2)$ values for this point were 0.05 and 0.21, respectively. Modeled nocturnal nitrate (blue) is the absolute amount calculated by the model from nocturnal chemistry. Pre-existing nitrate (yellow) represents the nitrate present at sunset from the previous day and is calculated as the difference between total measured nitrate from the aircraft (red diamond) and the model calculated value at the time of aircraft measurement (vertical black line). Assuming pre-existing nitrate is constant overnight (i.e. no deposition or dilution), the fractional contribution of nocturnal nitrate is calculated as the ratio of modeled nitrate to total nitrate (pre-existing + modeled) at sunrise (simulation hour 14).268

List of Publications

First Author Peer-Reviewed Publications:

4. McDuffie, E. E., Fibiger, D. L., Womack, C., Dubé, W. P., Franchin, A., Middlebrook, A., Goldberger, L., Lee, B. H., Thornton, J. A., Moravek, A., Murphy, J., Bassandorj, M., & Brown, S. S. Evaluating the contribution of nocturnal heterogeneous reactive nitrogen chemistry to particulate matter formation during wintertime pollution events in Northern Utah. *Atmospheric Chemistry and Physics – In Preparation*
3. McDuffie, E. E., Fibiger, D. L., Dubé, W. P., Lopez-Hilfiker, F., Lee, B., Thornton, J. A., Guo, H., Weber, R. J., Shah, V., Jaeglé, L., Reeves, M., Weinheimer, A., Schroder, J. C., Campuzano-Jost, P., Jimenez, J. L., Dibb, J. E., Veres, P., Ebben, C., Sparks, T., Wooldridge, P. J., Cohen, R. C., Hornbrook, R., Apel, E., Campos, T., Hall, S., Ullmann, K., & Brown, S. S. ClNO₂ yields from aircraft measurements during the 2015 WINTER campaign and critical evaluation of current parameterizations. *Journal of Geophysical Research: Atmospheres – In Preparation*
2. McDuffie, E. E., Fibiger, D. L., Dubé, W. P., Lopez-Hilfiker, F., Lee, B., Thornton, J. A., Guo, H., Weber, R. J., Shah, V., Jaeglé, L., Reeves, M., Weinheimer, A., Schroder, J. C., Campuzano-Jost, P., Jimenez, J. L., Dibb, J. E., Veres, P., Ebben, C., Sparks, T., Wooldridge, P. J., Cohen, R. C., Hornbrook, R., Apel, E., Campos, T., Hall, S., Ullmann, K., & Brown, S. S. (2018). Heterogeneous N₂O₅ uptake during winter: Aircraft measurements during the 2015 WINTER campaign and critical evaluation of current parameterizations. *Journal of Geophysical Research: Atmospheres*. <https://doi.org/10.1002/2018JD028336>
1. McDuffie, E. E., Edwards, P. M., Gilman, J. B., Lerner, B. M., Dubé, W. P., Trainer, M., Wolfe, D. E., Angevine, W. M., deGouw, J., Williams, E. J., Tevlin, A. G., Murphy, J. G., Fischer, E. V., McKeen, S., Ryerson, T. B., Peischl, J., Holloway, J. S., Aikin, K., Langford, A. O., Senff, C. J., Alvarez, R. J., Hall, S. R., Ullmann, K., Lantz, K. O., & Brown, S. S. (2016). Influence of oil and gas emissions on summertime ozone in the Colorado Northern Front Range. *Journal of Geophysical Research: Atmospheres*, 121(14), 8712-8729. <https://doi.org/10.1002/2016jd025265>

Co-Author Peer-Reviewed Publications:

11. Kenagy, H. S., Sparks, T. L., Ebben, C. J., Wooldridge, P. J., Lopez-Hilfiker, F. D., Lee, B., H., Thornton, J. A., **McDuffie, E. E.**, Fibiger, D. L., Brown, S. S., Montzka, D. D., Weinheimer, A. J., Schroder, J. C., Campuzano-Jost, P., Day, D. A., Jimenez, J., Dibb, J. E., Apel, E. C., Shah, V., Jaeglé, L., & Cohen, R. C. (2018). NO_x Lifetime and NO_y Partitioning During WINTER. *Journal of Geophysical Research: Atmospheres – Submitted*

10. Salmon, O. E., Shepson, P. B., Ren, X., He, H., Dickerson, R. R., Stirm, B. H., Brown, S. S., Fibiger, D. L., **McDuffie, E. E.**, Campos, T. L., Gurney, K. R., & Thornton, J. A. (2018). Top-down estimates of NO_x and CO emissions from Washington, D.C.-Baltimore During WINTER. *Journal of Geophysical Research: Atmospheres* – Submitted
9. Schroder, J. C., Campuzano-Jost, P., Day, D. A., Shah, V., Larson, K., Sommers, J. M., Sullivan, A. P., Campos, T., Reeves, J. M., Hills, A., Hornbrook, R., Blake, N., Scheuer, E., Guo, H., **McDuffie, E. E.**, Fibiger, D. L., Hayes, P. L., Weber, R. J., Dibb, J. E., Apel, E., Jaeglé, L., Brown, S. S., Thornton, J. A., & Jimenez, J. L. (2018). Sources and secondary production of organic aerosols in the Northeastern U.S. during WINTER. *Journal of Geophysical Research: Atmospheres* – Submitted
8. Lee, B. H., Lopez-Hilfiker, F. D., Veres, P. R., **McDuffie, E. E.**, Fibiger, D. L., Sparks, T. L., Ebben, C. J., Green, J. R., Schroder, J. C., Campuzano-Jost, P., Iyer, S., D'Ambro, E. L., Schobesberger, S., Brown, S. S., Wooldridge, P. J., Cohen, R. C., Bililign, S., Jimenez, J. L., Kurtén, T., Weinheimer, A. J., Jaeglé, L., & Thornton, J. A. (2018). Flight deployment of a high-resolution time-of-flight chemical ionization mass spectrometer: Observations of reactive halogen and nitrogen oxide species. *Journal of Geophysical Research: Atmospheres* – Submitted
7. Mattila, J. M., Brophy, P., Kirkland, J., Hall, S., Ullmann, K., Fischer, E. V., Brown, S., **McDuffie, E.**, Tevlin, A., & Farmer, D. K. (2018). Tropospheric sources and sinks of gas-phase acids in the Colorado Front Range, *Atmospheric Chemistry and Physics Discussions, in review*. <https://doi.org/10.5194/acp-2018-326>
6. Fibiger, D. L., **McDuffie, E. E.**, Dubé, W. P., Aikin, K. C., Lopez-Hilfiker, F. D., Lee, B. H., Green, J. R., Fiddler, M. N., Holloway, J. S., Ebben, C., Sparks, T. L., Wooldridge, P., Weinheimer, A. J., Montzka, D. D., Apel, E. C., Hornbrook, R. S., Hills, A. J., Blake, N. J., DiGangi, J. P., Wolfe, G. M., Bililign, S., Cohen, R. C., Thornton, J. A., & Brown, S. S. (2018). Wintertime overnight NO_x removal in a southeastern United States coal-fired power plant plume: A model for understanding winter NO_x processing and its implications. *Journal of Geophysical Research: Atmospheres*, 123, 1412–1425. <https://doi.org/10.1002/2017JD027768>
5. Tevlin, A. G., Li, Y., Collett, J. L., **McDuffie, E. E.**, Fischer, E. V., & Murphy, J. G. (2017). Tall tower vertical profiles and diurnal trends of ammonia in the Colorado Front Range. *Journal of Geophysical Research: Atmospheres*, 122, 12468-12487. <https://doi.org/10.1002/2017JD026534>
4. Zaragoza, J., Callahan, S., **McDuffie, E. E.**, Kirkland, J., Brophy, P., Durrett, L., Farmer, D. K., Zhou, Y., Sive, B., Flocke, F., Pfister, G., Knote, C., Tevlin, A., Murphy, J., & Fischer, E. V. (2017). Observations of acyl peroxy nitrates during the Front Range Air Pollution and Photochemistry Experiment (FRAPPÉ). *Journal of Geophysical Research: Atmospheres*, 122, 12416-12432. <https://doi.org/10.1002/2017JD027337>
3. Wang, L., Newchurch, M. J., Alvarez Ii, R. J., Berkoff, T. A., Brown, S. S., Carrion, W., De Young, R. J., Johnson, B. J., Ganoe, R., Gronoff, G., Kirgis, G., Kuang, S., Langford, A. O.,

- Leblanc, T., **McDuffie, E. E.**, McGee, T. J., Pliutau, D., Senff, C. J., Sullivan, J. T., Sumnicht, G., Twigg, L. W., & Weinheimer, A. J. (2017). Quantifying TOLNet ozone lidar accuracy during the 2014 DISCOVER-AQ and FRAPPÉ campaigns. *Atmospheric Measurement Techniques*, *10*(10), 3865-3876. <https://doi.org/10.5194/amt-10-3865-2017>
2. Baier, B. C., Brune, W. H., Miller, D. O., Blake, D., Long, R., Wisthaler, A., Cantrell, C., Fried, A., Heikes, B., Brown, S., **McDuffie, E.**, Flocke, F., Apel, E., Kaser, L., & Weinheimer, A. (2017). Higher measured than modeled ozone production at increased NO_x levels in the Colorado Front Range. *Atmospheric Chemistry and Physics*, *17*(18), 11273-11292. <https://doi.org/10.5194/acp-17-11273-2017>
 1. Brown, S. S., An, H.-J., Lee, M., Park, J.-H., Lee, S.-D., Fibiger, D., **McDuffie, E.**, Dubé, W., Wagner, N. L., & Min, K.-E. (2017). Cavity enhanced spectroscopy for measurement of nitrogen oxides in the anthropocene: Results from the Seoul Tower during MAPS 2015. *Faraday Discussions*. <https://doi.org/10.1039/C7FD00001D>

Co-Authored Scientific Assessment Reports for U.S. State Agencies:

2. Utah Winter Fine Particulate Study Science Team (2018). Utah Winter Fine Particulate Study, Final Report to the Utah Department of Environmental Quality. [Available at: <https://deq.utah.gov/legacy/programs/air-quality/research/projects/northern-ut-air-pollution/winter-fine-particulate-aircraft-study.htm>].
1. Ramboll Environ. (2017). Science Synthesis Report: Atmospheric Impacts of Oil and Gas Development in Texas. Final Report to the Texas Commission on Environmental Quality. [Available at: https://www.tceq.texas.gov/assets/public/implementation/air/am/contracts/reports/oth/58216632516-20170629-enviroilgas_impact_aq_synthesis.pdf].

Chapter 1: Introduction

1.1 Atmospheric Chemistry of Inorganic Nitrogen Oxides

Atmospheric chemical transformations of inorganic nitrogen oxides (also referred to here as reactive nitrogen) are shown in Figure 1.1. These reactions control the oxidative capacity of the troposphere and contribute products that degrade local air quality in urban regions around the world. While this chemistry has been studied extensively, uncertainties remain surrounding factors that influence the rate and products of these reactions in specific locations and seasons. Addressing these uncertainties is key to both improving atmospheric modeling capabilities and to developing effective mitigation strategies for regions non-compliant with air quality standards.

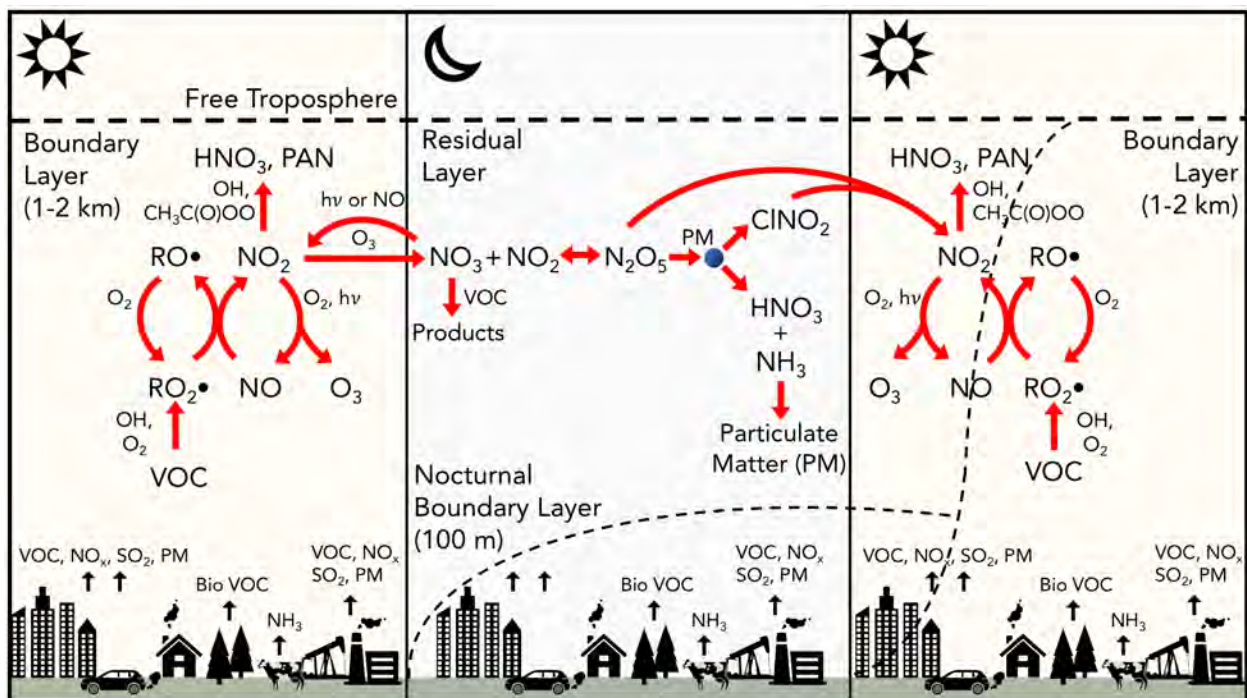


Figure 1.1. Schematic of the day-night cycle of inorganic reactive nitrogen chemistry. Boundary layer dynamics are illustrated by dashed lines.

1.1.1 Summer Dominant, Daytime Chemical Reactions and Products

Daytime chemical reactions are shown in the left and right panels of Figure 1.1. Daytime inorganic reactive nitrogen chemistry in polluted regions involves the reaction of nitric oxide (NO), emitted from combustion and natural sources, with peroxy radicals that are intermediates in the oxidation of volatile organic compounds (VOCs), emitted from a variety of anthropogenic and biogenic sources. In low VOC environments, NO mainly reacts with ozone (O₃) to form NO₂ (not shown). The NO + RO₂• (i.e. peroxy radical) reaction in Figure 1.1 will lead to the formation of an organic nitrate molecule (RONO₂, NO_x reservoir species, not shown in Figure 1.1), or produce both an NO₂ molecule and an RO• (or HO•) radical that can recycle to RO₂• (or HO₂•). The branching ratio between these two pathways is VOC-dependent with saturated hydrocarbons typically leading to small fractions of organic nitrates relative to NO₂.

Once formed, the NO₂ molecule can react further to form acyl peroxy nitrates (APN = NO_x reservoir species) (formation of peroxyacetyl nitrate (PAN) from NO₂ + CH₃C(O)OO illustrated in Figure 1.1), react with OH to form nitric acid (HNO₃ = NO_x sink), or photolyze in the presence of oxygen (O₂) to generate an O₃ molecule and reform NO (Chameides, 1978; Crutzen, 1970). Reaction of NO with O₃ and subsequent NO₂ photolysis is a null cycle, whereas reaction of NO with peroxy radicals leads to catalytic production of O₃. This chemistry occurs throughout the well-mixed daytime boundary layer (typically 1-2 km in depth) and the catalytic O₃ production cycle is largely driven by the sunlight-initiated, hydroxyl radical (OH) formation mechanism that initiates VOC oxidation cycles and peroxy radical formation. Longer days, warmer temperatures, and larger OH concentrations (from increased concentrations of ozone and water vapor) make these reactions dominant during the summer season, relative to nocturnal reactions.

These photochemical nitrogen oxide reactions are the only known chemical source of O₃ in the troposphere (Chameides, 1978; Crutzen, 1970). Ozone is the third most potent greenhouse gas behind carbon dioxide (CO₂) and methane (CH₄) (IPCC, 2014), has been linked to increased mortality rates (e.g. Bell et al., 2006), and has been estimated to cause over 10 billion dollars in annual crop losses (e.g. Avnery et al., 2011). Due to its health and environmental threat, O₃ has been designated a criteria pollutant by the U.S. EPA with a current standard set not to exceed 70 parts per billion by volume (ppbv) for the annual 4th highest, maximum daily 8 hour average mixing ratio, averaged over three consecutive years (US EPA, 2017).

Ozone production under warm, summertime conditions has been extensively studied. Relatively few studies, however, have quantified the contribution of certain VOC sources, such as oil and natural gas activities (O&NG), to O₃ production during summer (e.g. Kemball-Cook et al., 2010; Rodriguez et al., 2009). Quantification of such sources is particularly important for regions like Colorado that are currently noncompliant with federal O₃ standards and consequently required to develop O₃ mitigation strategies (Colorado Department of Public Health and Environment (CDPHE), 2018).

Quantifying the contribution of specific emission sources to O₃ is complex, largely due to the non-linear response of O₃ production to changes in VOC and NO_x emissions. For example, photochemical O₃ production can be “NO_x limited” (VOC or radical saturated), where O₃ production is relatively insensitive to changes in VOC emissions relative NO_x (Figure 1.2). Production can also be “VOC or radical limited” (NO_x saturated) where increases in VOC emissions cause increases in O₃. Under these conditions, increasing NO_x will lead to decreases in O₃, as shown in the example O₃ sensitivity curve in Figure 1.2. This decreasing O₃ trend results from increased radical (and subsequent O₃) suppression from the NO₂ + OH termination reaction,

which dominates at high NO_x concentrations. The magnitude of O_3 production and whether it is NO_x or VOC/radical limited in a given location is, therefore, dependent on the emissions of NO_x relative to the amount and types of VOCs emitted (Figure 1.2). The type of VOC, in addition to the absolute amount, is important as each compound has a different OH-reaction rate constant (Atkinson & Arey, 2003) and efficiency for resupplying radicals through propagation reactions. The types and amounts of VOCs also vary with season, location, and emission sector (Finlayson-Pitts & Pitts, 2000). As a result, the development of effective O_3 pollution mitigation strategies requires that the O_3 NO_x/VOC sensitivity regime be characterized and the dominant emission sectors identified for each location in question. These determinations frequently require long-term or targeted observational records (e.g. Abeleira & Farmer, 2017) and/or sensitivity studies with computational models (e.g. Edwards et al., 2014; Kemball-Cook et al., 2010).

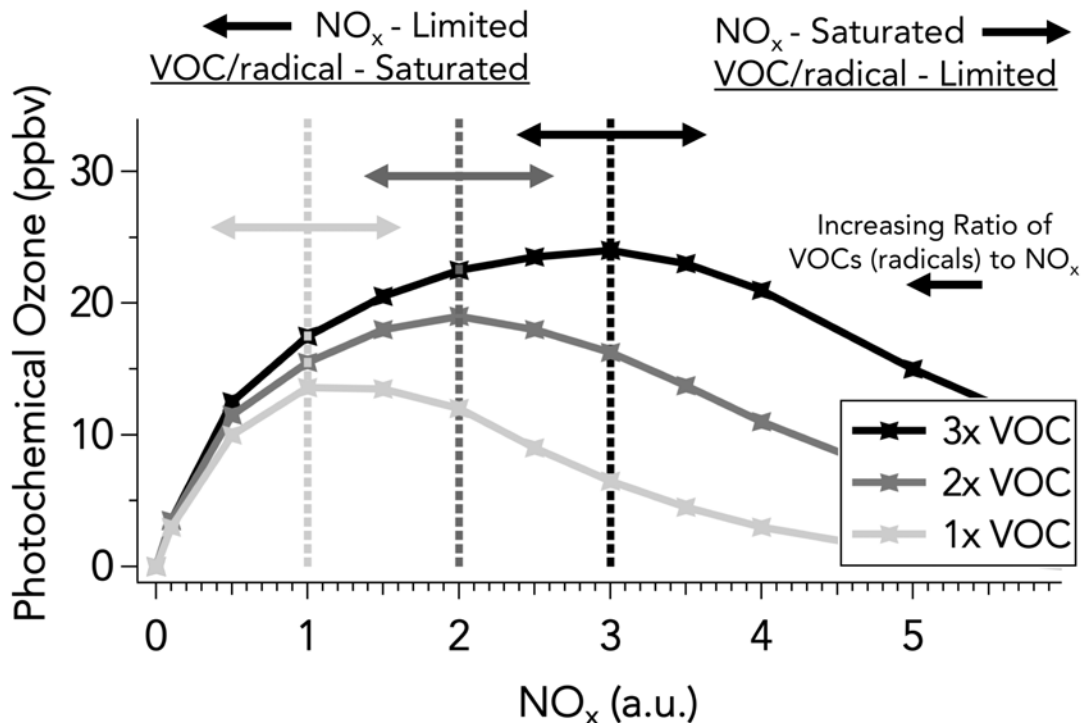


Figure 1.2. Example curves illustrating the sensitivity of daily photochemical O_3 production (ppbv) sensitivities to changes in NO_x (x-axis, arbitrary units) and VOC (three curves) concentrations. The light gray curve represents O_3 production as a function of NO_x at a normalized VOC concentration of 1. The dark gray and black curves represent the daily maximum O_3 as function of NO_x with higher concentrations of VOCs or more reactive (i.e. with OH) mixtures.

1.1.2 Winter Dominant, Nocturnal Heterogeneous Reactions and Products

In contrast to summer photochemistry, nocturnal reactions of tropospheric nitrogen oxides, which dominate during long and cold winter nights, have not been as extensively studied. There remain questions regarding the influence of nighttime nitrogen oxide chemical cycles on the lifetime and global distribution of O_3 and OH , as well as the contribution of this chemistry to wintertime particulate matter pollution. These uncertainties have persisted in part because the relevant atmospheric chemistry occurs largely at night in the residual layer (RL) where it is removed from the surface, and in part because it involves multiphase processes (Figure 1.1) with parameters that are not directly observable and must be derived from additional measurements. Previous observations during summer have shown regional variability in these processes, but wintertime data have been relatively limited, though the number of winter-focused studies has been increasing in the U.S., Europe, and China.

Inorganic reactive nitrogen reactions that occur largely at night are shown in the center panel of Figure 1.1. This chemistry has been reviewed previously by Brown and Stutz (2012). Once the sun sets, the sunlight driven oxidation of VOCs stops and the nitrate radical (NO_3) starts to build from the oxidation of NO_2 by O_3 . NO_3 formation does occur during the day but mixing ratios typically remain < 1 pptv as both photolysis and reaction with NO cause it to efficiently reform NO_2 (Figure 1.1). Once formed, NO_3 will either react with VOCs to form a variety of products, including organic nitrogen, or react with a second NO_2 molecule to form an equilibrium with dinitrogen pentoxide (N_2O_5). Similarly to NO_3 , N_2O_5 is only found in small (< 10 pptv) mixing ratios during the day (Brown et al., 2005) due to limited daytime concentrations of NO_3 and the photochemical and thermal instability of N_2O_5 at warmer temperatures (e.g. 40 s and > 10 minute lifetime at 290 and 270 K, respectively).

The nocturnal fate of N_2O_5 has important consequences for the net balance between wintertime O_3 production and destruction due to NO_x emissions (Evans & Jacob, 2005; Macintyre & Evans, 2010), the NO_x budget and distribution (Macintyre & Evans, 2010; Tie et al., 2003), particulate matter formation (e.g. Pusede et al., 2016; Watson & Chow, 2002), and tropospheric halogen activation (Simpson et al., 2015 and references therein), which can further impact radical and O_3 budgets (Sarwar et al., 2014; Sherwen et al., 2017). Due to strong vertical gradients in nocturnal O_3/NO_x ratios, enhanced in part by stratification of the nocturnal boundary layer (NBL) and RL (Stull, 1988), N_2O_5 produced in the RL and upper NBL will either persist throughout the night, or react heterogeneously with aerosol to form nitric acid (HNO_3) and/or nitryl chloride (ClNO_2). Upon sunrise, as illustrated by the transition between the middle and right panels of Figure 1.1, increased N_2O_5 thermal dissociation and subsequent NO_3 photolysis will serve to reform NO_2 , which can contribute to NO_x regeneration and O_3 production downwind of initial emission sources. Photo-labile ClNO_2 will dissociate to form NO_2 and a chlorine radical ($\text{Cl}\bullet$), the latter of which can oxidize VOCs and further contribute to O_3 formation (e.g. Simpson et al., 2015). In contrast, HNO_3 is typically considered a net sink of tropospheric NO_x as its main atmospheric removal pathway is by dry deposition. In the presence of emissions of ammonia (NH_3), however, HNO_3 can additionally lead to the formation of ammonium nitrate (NH_4NO_3) aerosol (e.g. Mozurkewich, 1993). The importance of these reactions to NO_x and oxidant budgets is greater during the winter season due to longer nights that allow more time for heterogeneous processes to occur, colder temperatures that favor N_2O_5 in its equilibrium with NO_3 , and lower biogenic VOC emissions, which often constitute the largest source of nocturnal NO_3 -VOC loss (e.g. Aldener et al., 2006; Brown & Stutz, 2012).

The partitioning between N_2O_5 , HNO_3 and ClNO_2 is an active area of research and is dependent on multiple factors, which during winter are dominated by the efficiency of N_2O_5 uptake onto aerosol (defined as $\gamma(\text{N}_2\text{O}_5)$) and the production yield of ClNO_2 relative to HNO_3 (defined as $\phi(\text{ClNO}_2)$). Gas-aerosol exchange involves a series of complex steps, driven by competing kinetic and thermodynamic processes. As reviewed by Kolb et al. (2002) and Pöschl et al. (2007), these processes are simplified to the term γ , which is defined as the probability a gas will be taken up onto an aerosol surface upon collision. For N_2O_5 , derived $\gamma(\text{N}_2\text{O}_5)$ values typically range from 1×10^{-4} to 0.1 in the troposphere (Riedel et al., 2012a; Wagner et al., 2013) and are dependent on aerosol composition (e.g. Anttila et al., 2006; Bertram & Thornton, 2009; Bertram et al., 2009b; Thornton et al., 2003). The formation of ClNO_2 is relatively less complex, thought only to depend on the presence of aerosol-phase chloride relative to water. The yield of ClNO_2 is defined as a value between 0 (2 HNO_3 produced per N_2O_5 lost) and 1 (1 ClNO_2 + 1 HNO_3 produced per N_2O_5 lost), the full range of which has been observed in the ambient atmosphere (e.g. Phillips et al., 2016; Wagner et al., 2013). Both $\gamma(\text{N}_2\text{O}_5)$ and $\phi(\text{ClNO}_2)$ have been determined from laboratory studies of heterogeneous reactions on model substrates, but the degree to which these laboratory studies represent actual atmospheric complexity must be tested against field measurements of nighttime reactive nitrogen partitioning from gas and aerosol phase observations.

N_2O_5 uptake and the subsequent formation of HNO_3 was first incorporated into global models 25 years ago with a constant $\gamma(\text{N}_2\text{O}_5)$ value of 0.1 (Dentener & Crutzen, 1993). As discussed in Chapters 4 and 5, current models now implement parameterized values of $\gamma(\text{N}_2\text{O}_5)$ and $\phi(\text{ClNO}_2)$ based on aerosol composition, with model predictions highly sensitive to these parameters. For example, sensitivity studies with the GEOS-Chem global model (Macintyre & Evans, 2010), showed that northern hemisphere predictions of O_3 , NO_x , and the OH radical

changed by up to 40%, depending on $\gamma(\text{N}_2\text{O}_5)$, within the range of 1×10^{-5} and 1. These simulations did not consider the formation of ClNO_2 but did illustrate that the sensitivity of these tropospheric constituents to $\gamma(\text{N}_2\text{O}_5)$ was largest in the range of $\sim 1 \times 10^{-3}$ to 0.5 and decreased at both the lowest values where N_2O_5 becomes non-reactive with aerosol and the largest values where conversion to HNO_3 and ClNO_2 becomes limited by the gas-phase formation rates of NO_3 and N_2O_5 .

The subsequent production of ClNO_2 was first evaluated in 3D models much more recently (e.g. Simon 2009) and also has important consequences for regional and global tropospheric composition. Over the last 10 years, multiple 3D and box modeling efforts have shown that ClNO_2 production from N_2O_5 heterogeneous chemistry contributes to enhanced VOC oxidation due to the higher reactivity of $\text{Cl}\cdot$ than $\text{OH}\cdot$ with alkanes and alkenes, subsequent ozone production, and particle formation (e.g. Sherwen et al., 2017). The first 3D modeling study to assess the impact of ClNO_2 production on oxidants in the Northern Hemisphere found that ClNO_2 formation, predicted by parameterized $\phi(\text{ClNO}_2)$ values, increased wintertime tropospheric O_3 by as much as 10% over North America (Sarwar et al., 2014).

Despite the global importance of this chemistry and recent work on this topic (reviewed by Chang et al. (2011)), there remain uncertainties regarding the parameterizations of both $\gamma(\text{N}_2\text{O}_5)$ and $\phi(\text{ClNO}_2)$ that are currently implemented in global models. These composition-dependent parameterizations have been developed from laboratory-based experiments of N_2O_5 uptake on inorganic and single-component organic aerosol (e.g. Anttila et al., 2006; Bertram & Thornton, 2009). Discrepancies exist between these parameterized values and those derived from field-observations, which could result from inaccurate dependencies on factors already incorporated into parameterizations, incorrect identification of controlling factors, or comparisons to a relative small number of field data sets (< 30), typically collected under a narrow range of environmental

conditions at single surface locations. Field-laboratory reconciliation and subsequent model improvement will, therefore, require a combination of laboratory studies on complex aerosol mixtures as well as aircraft field studies to derive regional scale $\gamma(\text{N}_2\text{O}_5)$ and $\phi(\text{ClNO}_2)$ values from ambient RL observations.

Lastly, the contribution of heterogeneously produced HNO_3 to NH_4NO_3 aerosol formation is potentially important for wintertime air quality in the western U.S. (e.g. Pusede et al., 2016; Watson & Chow, 2002). For example, Northern Utah, including Salt Lake Valley (SLV), experiences high pressure meteorological systems during winter that trap colder air near the surface (Figure 1.3) and cause regional accumulation. These events can last between 1 to 18 days (Whiteman et al., 2014). During these events, the SLV has historically experienced the worst air pollution in the U.S., with levels of fine particulate matter less than 2.5 μm in diameter ($\text{PM}_{2.5}$), exceeding national air quality standards. $\text{PM}_{2.5}$ reduces visibility and specifically in SLV, has been linked to increased hospitalizations and risk of cardiac events during pollution episodes (Beard et al., 2012; Pope et al., 2006; Pope et al., 2015). The SLV region has been non-compliant with national standards since 2009, which are currently set at 35 $\mu\text{g m}^{-3}$ for 98th percentile, 24-hour average concentrations, averaged over three years (US EPA, 2016).



Figure 1.3. Image of pollution event in Salt Lake Valley during winter 2017, illustrating layer capping from warm, high pressure systems aloft.

Previous studies have shown that NH_4NO_3 constitutes the largest fraction of $\text{PM}_{2.5}$ mass during these pollution events in SLV (e.g. Baasandorj et al., 2017; Kelly et al., 2013), yet the contribution from heterogeneous nocturnal chemistry remains unknown. While ground based observations have suggested that NH_4NO_3 formation in this region is limited by the availability of gas-phase HNO_3 , effective mitigation will require identification of the primary atmospheric source of HNO_3 (e.g. day or night NO_x oxidation), currently limited by a lack RL observations.

1.2 Research Approach: Ambient Observations and Chemical Box Modeling

Addressing current uncertainties in the contribution of emission sources to summertime O_3 production, regional-scale wintertime N_2O_5 partitioning, and the impact of heterogeneous chemistry on wintertime PM formation will require two steps. The first is to collect additional observations of nitrogen oxides and their reaction products in polluted regions during the summer and winter seasons. Reactive nitrogen oxides shown in Figure 1.1 are highly variable in space and time, have relatively short lifetimes (especially true for NO_3 and N_2O_5), and are typically found in small mixing ratios ranging from ~50-100 ppbv (for O_3) to 10s of pptv (NO_3). The need for in situ, real time, high precision measurements of these species has led to the development of an instrument, described in Chapter 2, that simultaneously measures NO , NO_2 , O_3 , NO_3 , and N_2O_5 using the detection technique of cavity ring down spectroscopy (e.g. Fuchs et al., 2009; Wagner et al., 2011; Washenfelder et al., 2011a; Wild et al., 2014). This instrument does not measure ClNO_2 , but more recent advancements in iodide adduct chemistry, coupled with chemical ionization mass spectrometry (Kercher et al., 2009; Osthoff et al., 2008) has provided an in situ, fast time response ClNO_2 measurement, as well as measurements for N_2O_5 and HNO_3 . Simultaneous detection of these key species across regional scales is the first step to addressing uncertainties described above.

The second step is to couple ambient observations with simple, computational box models for targeted analyses. In contrast to chemical transport models (CTMs), which simulate emissions, atmospheric chemistry, transport, and processes such as atmosphere-land exchange, box models can provide simple alternatives when developed for specific applications. CTMs are computationally expensive and require chemical mechanisms that “lump” species of similar reactivity and/or structure. In contrast, box model simplicity allows them to be chemically explicit, important for investigating non-linear processes such as VOC degradation and the associated photochemical O₃ production. This efficiency also allows for repeated iterations that can be used to conduct studies of O₃ production sensitivity to changes in emissions, or to derive non-measured heterogeneous parameters from iterative fits to observations.

1.3 Thesis Overview

In this thesis, results from summer and winter field campaigns have been combined with two chemical box models to address key uncertainties in the day/night chemical transformation of inorganic nitrogen oxides, both regionally and in specific locations. The chapters are as follows:

Chapter 2. Research Methods

In Chapter 2, I describe the analytical methods used in this thesis. These include: 1) two cavity ring down instruments used for primary data collection, 2) field campaigns in which these instruments were deployed, as well as additional relevant instrumentation, and 3) background information, set-up details, and sensitivity studies of two box models that were used as major components of each analysis in Chapters 3-6.

Chapter 3. Influence of oil and gas emissions on summertime ozone in the Colorado Northern Front Range

The Front Range Air Pollution and Photochemistry Experiment (FRAPPÉ) was conducted at multiple sites across the Colorado Northern Front Range in summer 2014. This region is currently out of compliance with national air quality standards for O₃ during summer. Based at the Boulder Atmospheric Observatory, centered between the Denver urban area to the south and intensive oil and natural gas extraction activities to the north, observational analyses in combination with an observationally-constrained box model provide the first quantitative estimates of the contribution of O&NG activities to local O₃ production in the Front Range. Additional analyses include an assessment of the contribution of O&NG activities to observed VOC concentration, OH reactivity, and ozone production efficiency, an estimated contribution from biogenic VOCs, as well as an evaluation of O₃ production differences between chemically-explicit and “lumped” mechanisms to assess the chemistry employed in CTMs.

Chapter 4. Heterogeneous N₂O₅ uptake during winter: Aircraft measurements during the 2015 WINTER campaign and critical evaluation of current parameterizations

The Wintertime INvestigation of Transport, Emissions, and Reactivity (WINTER) aircraft campaign conducted both day and night flights over the eastern U.S. during February and March 2015. In this Chapter, I discuss the derivation of N₂O₅ uptake coefficients ($\gamma(\text{N}_2\text{O}_5)$) from a custom box model that iteratively fits to observations of NO₂, O₃, N₂O₅, and ClNO₂. These are the first $\gamma(\text{N}_2\text{O}_5)$ values reported from aircraft during the winter and span a range of 4 orders of magnitude. These regional scale values are compared to ambient observations of temperature, relative humidity, and aerosol composition to assess factors that may be important in driving the variability in uptake efficiency. These values are further evaluated against those predicted by current

laboratory-based parameterization to provide a critical assessment of the applicability of each to WINTER conditions. Lastly, these results are used to derive the first, empirical, field-based parameterization for $\gamma(\text{N}_2\text{O}_5)$.

Chapter 5. ClNO₂ yields from aircraft measurements during the 2015 WINTER campaign and critical evaluations of current parameterizations

In this Chapter, the model described in Chapters 2 and 4 is extended to predict ClNO₂ yields during the 2015 aircraft WINTER campaign. These are the first reported $\phi(\text{ClNO}_2)$ values from aircraft observations. Box model results are compared to values predicted by additional observationally-based methods, as well as current laboratory-based parameterizations. This comparison evaluates the current understanding of ClNO₂ yields on ambient aerosol and helps identify research needs on this topic.

Chapter 6. Evaluating the Contribution of Nocturnal Heterogeneous Reactive Nitrogen Chemistry to Particulate Matter Formation during Wintertime pollution events in Northern Utah

The Utah Wintertime Fine Particulate Study conducted aircraft flights over the most densely populated region of Utah, including Salt Lake Valley (SLV). This region is currently out of compliance with national air quality standards for PM_{2.5} during winter. In this Chapter, the box model used for analyses in Chapters 4 and 5 is applied to data collected during UWFPS night flights to derive $\gamma(\text{N}_2\text{O}_5)$ and $\phi(\text{ClNO}_2)$ values for this region. In combination with additional observational analyses and forward-integrated box model simulations, I discuss the role of heterogeneous chemistry to HNO₃ and NH₄NO₃ aerosol formation in SLV.

Chapter 7. Summary and Conclusions

Chapter 2: Research Methods

2.1 Introduction

The first part of this chapter provides a detailed description of the reactive nitrogen oxide and ozone instruments used in this work. The second section provides descriptions of the field campaigns in which these instruments were deployed. Analyses in this thesis are based on data collected during the 2014 Colorado Front Range Air Pollution and Photochemistry Experiment (FRAPPÉ), the 2015 Wintertime Investigation of Transport, Emissions, and Reactivity (WINTER) aircraft campaign over the eastern U.S., and the 2017 Utah Winter Fine Particulate Study (UWFPS) aircraft campaign based out of Salt Lake City, Utah. Locations, sampling platforms, and auxiliary measurements are described. Information is also provided about measurements from additional campaigns that aided in both the observational and computational analyses presented here. The final section provides detailed descriptions of the two computational box models adapted and developed for this work. In addition to model overview, set-up, and chemical constraint details, model sensitivity studies are presented for the custom nocturnal box model, developed to simulate nocturnal inorganic reactive nitrogen chemistry in the wintertime residual layer.

2.2 Instrumentation for Nitrogen Oxides and Ozone

Two primary instruments were used to collect data for the analyses in Chapters 3 – 6. Both instruments are based on the principle of cavity ring down spectroscopy (CRD or CRDS), the theory of which is described in further detail below. The first instrument is the Airborne Ring-

down Nitrogen Oxide Laser-based Detector, or ARNOLD. ARNOLD consists of six, high-finesse optical cavities that provide simultaneous in-situ measurements of N_2O_5 , NO_3 , NO , NO_2 , NO_y , and O_3 at a frequency of 2 Hz (Figure 2.1). Both NO_3 and NO_2 are measured directly in channels B and E, respectively. Additional measurement of N_2O_5 (Figure 2.1A) is achieved by thermal decomposition of N_2O_5 to NO_3 prior to sampling (following R2.1), followed by subtraction of the ambient NO_3 measurement (Figure 2.1B). Likewise, O_3 and NO are measured (Figure 2.1D and F) by chemical conversion to NO_2 with additions of NO and O_3 , respectively (following R2.2), followed by subtraction of the ambient NO_2 measurement (Figure 2.1E). Lastly, total oxidized reactive nitrogen ($\text{NO}_y = \text{NO} + \text{NO}_2 + \text{NO}_3 + 2\text{N}_2\text{O}_5 + \text{ClNO}_2 + \text{HO}_2\text{NO}_2 + \text{HNO}_3 + \text{PAN} + \text{organic nitrates} + \text{aerosol nitrates} \dots$) is measured as NO_2 following thermal conversion in a quartz heater held at 650°C (Figure 2.1C).

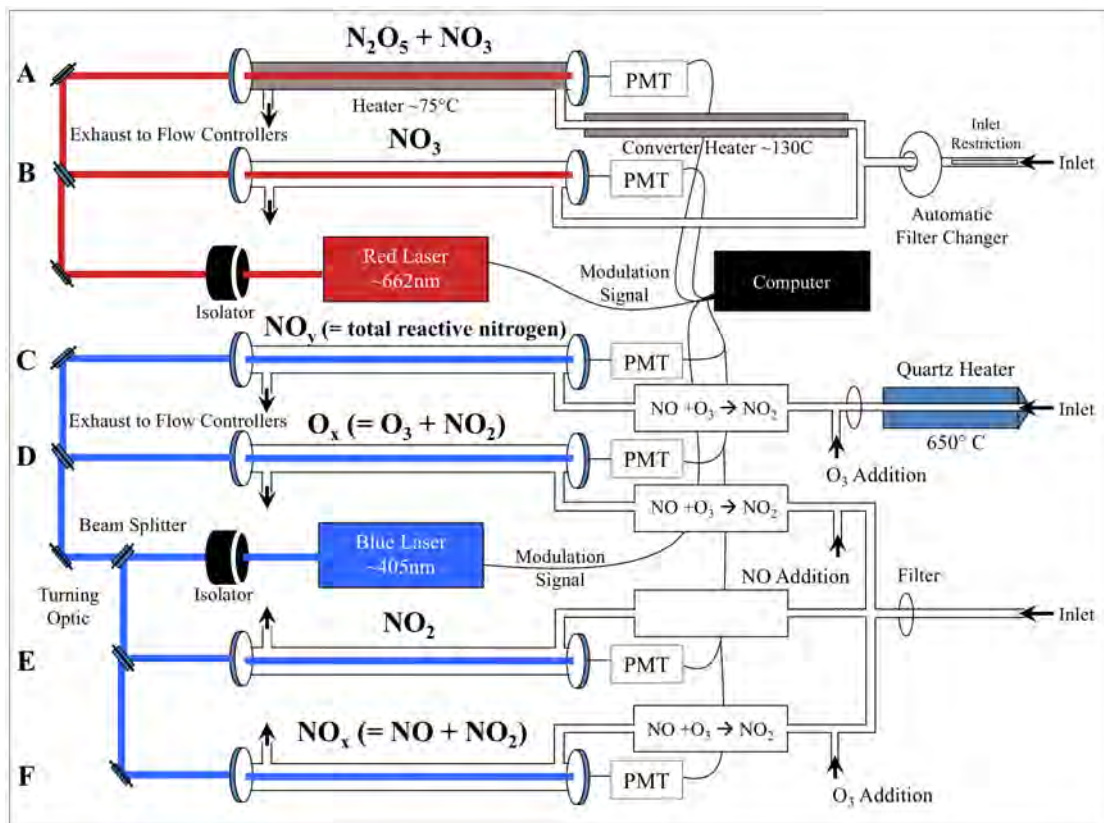
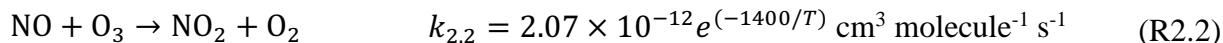
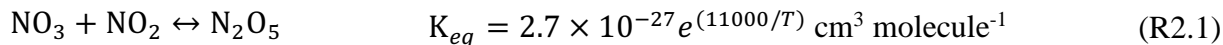


Figure 2.1. Schematic of 6-channel ARNOLD Instrument for the simultaneous 2 Hz detection of (A) N_2O_5 and (B) NO_3 by direct detection of NO_3 and of (C) NO_y , (D) O_3 , (E) NO_2 , and (F) NO by direct detection of NO_2 .



The second instrument, Nitrogen Oxides by Cavity Ring Down, or NOxCaRD, is identical in principle to the ARNOLD measurements of NO, NO₂, NO_y, and O₃. An overview of the operating principles of both instruments is provided in the following sections, focused on ARNOLD. More detailed information about both instruments has been published elsewhere (Dubé et al., 2006; Fuchs et al., 2009; Fuchs et al., 2008; Wagner et al., 2011; Washenfelder et al., 2011a; Wild et al., 2014; Womack et al., 2016).

2.2.1 Cavity Ring Down Spectroscopy – Applied to ARNOLD and NOxCaRD Instruments

The reactive nitrogen and ozone compounds measured by ARNOLD and NOxCaRD are typically present in polluted regions at levels as low as a few parts per trillion (pptv) up to 100 parts per billion (ppbv) and, therefore, require sensitive techniques for their detection. Both ARNOLD and NOxCaRD use the technique of Cavity Ring Down Spectroscopy (CRDS), a sensitive form of direct absorption spectroscopy, which couples a laser beam to a high-finesse cavity (i.e. stable optical resonator with high-reflectivity mirrors) for the sensitive, absolute measurement of trace-compounds (Figure 2.2).

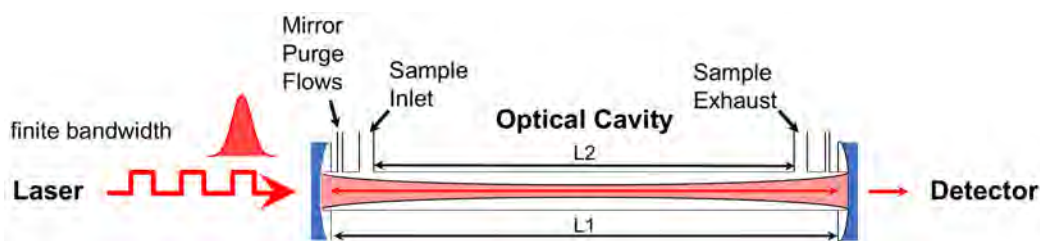


Figure 2.2. Generalized schematic of CRDS.

Here, both ARNOLD and NOxCaRD utilize multimode CRDS, in which the output of each continuous wave diode laser (Coherent, OBIS 660 LX and 405 LX models) passively couples to several thousand modes of each cavity (50 – 100 cm in length), achieved as the laser beam widths

exceed (0.5 nm full width half max) the cavity free spectral range (~ 150 MHz) (E2.1). Lasers in both instruments are typically operated at 100 mW output power, modulated with digital TTL signals (< 2 ns rise and fall time), and are optically isolated from each cavity to prevent damage from light backscatter (shown in Figure 2.1).

$$FSR \approx \frac{c}{2 * Cavity\ Length} \quad (2.1)$$

Unlike direct absorption spectroscopy, the laser signal in CRDS is modulated on and off. When the laser is modulated off, absorption time constants are measured as the time that light transmitted through the back mirror exponentially decays to e^{-1} of its starting intensity (collected here by photomultiplier tube (PMT) detectors (Hamamatsu HC120-05M) with colored glass/bandpass filters to remove stray light). The concentration of the target compound [X] is then derived in Equation E2.2 from speed of light (c), absorption cross section of the target absorber (σ), the ratio (R_L) of the cavity length (Figure 2.2, L1) to the length where the target absorber is present (Figure 2.2, L2), and the absorption time constants, measured with (τ) and without (τ_o) the target absorber. The expression in E2.2 applies to the simple case of a single absorber and α is the optical extinction coefficient (units of inverse length). More detailed expressions to account for non-target absorbers either through explicit corrections or by including them in τ_o are given in following sections.

$$[X]\sigma = \alpha = \frac{R_L}{c} \left(\frac{1}{\tau} - \frac{1}{\tau_o} \right) \quad (2.2)$$

Advantages over direct absorption spectroscopy include the insensitivity of τ to light source fluctuations, as well as the long path lengths that are attained from high-finesse cavities (here, ~ 10 to ≥ 100 km). Being an absolute measurement, the accuracy of CRDS depends only on the accuracy of σ (an inherent molecular, not instrumental property), knowledge of interferences from additional absorption and scattering processes (discussed below), and R_L . The value of R_L in

ARNOLD and NOxCaRD is greater than 1 due to the addition of zero air near each mirror (25 sccm) that is used to maintain cleanliness. For the N₂O₅ and NO₃ measurements, R_L is taken to be the physical distance between mirror purge additions relative to mirror distance ($R_L = 1.21$). For the measurements of NO, NO₃, O₃, and NO_y (from both ARNOLD and NOxCaRD), σ_{NO_2}/R_L is derived during the calibration procedure, described below.

Extensive details about CRD fundamentals and applications to atmospheric studies has been reviewed previously by Brown (2003). The reader is directed to this source and its references for additional CRDS details not provided in the overview here. The remaining sections provide more detailed information about specific operating and calibration procedures for the ARNOLD and NOxCaRD instruments.

2.2.2 NO₃ and N₂O₅ Measurements

Utilizing direct NO₃ absorption near its peak at 662 nm (Figure 2.3, left), the ARNOLD instrument directly measures NO₃ in channel B, while simultaneously measuring the sum of N₂O₅ and NO₃ after thermal dissociation in channel A (Figure 2.1). Both channels share a common Teflon inlet with 1.6 mm inner diameter (ID) flow restriction, used to reduce cavity pressure and minimize wall loss and light scattering (discussed below). After passing through a Teflon filter (details below), inlet flow is then split between the two channels, controlled downstream by individual mass flow controllers, typically set to maintain constant volumetric flows of 9 liters per minute (LPM) for the N₂O₅ channel and 14 LPM for NO₃. After the inlet split, a ~ 40 cm long, 130° C heater initiates thermal dissociation of N₂O₅ immediately prior to entering channel A. The channel A cavity is then held at 75° C to maintain thermal dissociation, while channel B is temperature controlled, if necessary, at the ambient inlet temperature to avoid sampling N₂O₅. The set temperature of the heater is based on the residence time of the air in the heater (i.e. flow rate)

and is empirically determined as a function of flow rate using a calibration source of N_2O_5 (for example, see Fuchs et al. (2008)).

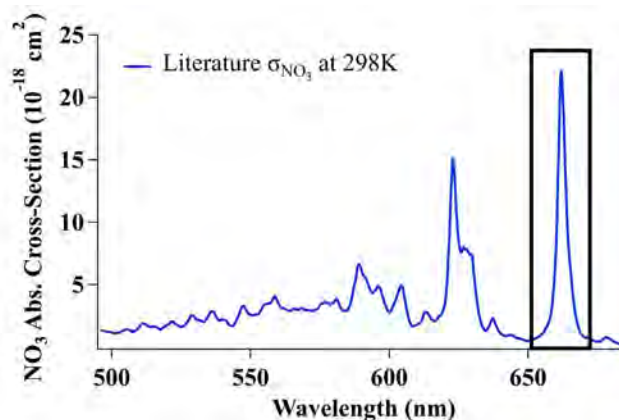


Figure 2.3. Convolution of literature absorption cross-section spectrum for NO_3 at 298K and diode laser profile. Literature $\sigma_{NO_3} = (4.56 - 0.00787 * T) * 1 \times 10^{-17} [cm^2]$

Absolute concentrations of NO_3 and N_2O_5 are then calculated from the measured total absorption time constants in each channel using E2.2, with background time constants from the zeroing procedure (described below), and the temperature-dependent NO_3 absorption cross section from Osthoff et al. (2007) and Yokelson et al. (1994) (Figure 2.3). Measurement of total absorption at 662 nm, however, is not entirely specific to NO_3 . The measured time constants for NO_3 and N_2O_5 , therefore, require additional corrections during data reduction (i.e. post-processing) to account for interferences from additional absorbers and light loss from Rayleigh and Mie scattering, discussed next.

2.2.2.1 Measurement Interferences and Corrections

The presence of ambient concentrations of NO_2 and O_3 that do not vary linearly between zero measurements cause absorption interferences at 662nm in channels A and B. While both compounds have absorption cross sections ~ 4 orders of magnitude smaller than NO_3 , their ambient concentrations are typically ~ 3 orders of magnitude larger. Both τ and τ_0 are corrected for this additional absorption signal during the data reduction process using equation E2.3. In E2.3, a value

of R_L has been previously derived in the laboratory from sampling constant concentrations of NO_2 with and without mirror purge flows. Simultaneous ambient measurements of NO_2 and O_3 from channels D and E (details below) are then used with literature absorption cross sections of NO_2 (3.9×10^{-21}) (Vandaele et al., 1998) and O_3 ($2.02 \times 10^{-21} \text{ cm}^2$) (Burkholder & Talukdar, 2012) to calculate $\sigma_{\text{O}_3}[\text{O}_3]$ and $\sigma_{\text{NO}_2}[\text{NO}_2]$ in E2.3.

$$\tau \text{ or } \tau_0 = \left(\frac{1}{\tau_{\text{measured}}} - \frac{c(\sigma_{\text{O}_3}[\text{O}_3] + \sigma_{\text{NO}_2}[\text{NO}_2] + \sigma_{\text{H}_2\text{O}}[\text{H}_2\text{O}])}{R_L} - \frac{cN\sigma_{\text{RS}}}{1} \right)^{-1} \quad (2.3)$$

The measured time constants may also be corrected for the absorption of water, which has distinct absorption lines in this region. In practice, however, such corrections have not been implemented because they have been found unnecessary. For example, this correction was calculated to only account for 0.02% of the total N_2O_5 signal during the WINTER campaign (relevant to Chapter 4 and Chapter 5).

The final term in E2.3 is used to correct the measured time constant for additional light loss from Rayleigh (or gas-phase) scattering. Due to the highly-reflective mirrors (5 ppm total loss) and relatively small absorption contributions from NO_2 , O_3 , and H_2O , Rayleigh scattering is the largest interfering source of light loss in channels A and B. The light loss associated with Rayleigh scattering has been minimized by reducing the pressure in each cavity through a flow restriction (1.6 mm ID) at the front of the common inlet (Figure 2.1). Increased volumetric flow at reduced pressure also decreases the cell residence time and thus potential NO_3 wall losses. It also reduces the water vapor concentrations. The somewhat reduced scattering signal is corrected during the data reduction process using E2.3. For ground-based measurements at constant pressure, the term σ_{RS} may be calculated from the atmospheric composition-weighted cross sections of N_2 , Ar, and O_2 , but this correction is unnecessary since Rayleigh scattering does not vary between zeros and is therefore accounted for in the zero scheme. For aircraft sampling, the cell pressure is

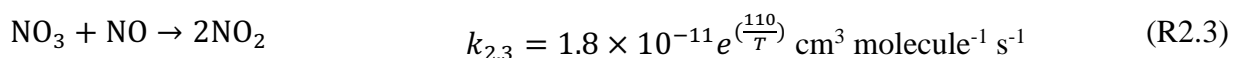
proportional to the ambient pressure outside of the aircraft at different altitudes. In this case, and effective σ_{RS} is calculated from the slope of τ_0^{-1} vs. the air number density (molec. cm^{-3}) in each cavity during instrument zeros (described below). Additional corrections for Mie (or aerosol-phase) scattering are not required as aerosol are filtered from the sample flow by a Teflon filter (2 μm pore size, 25 μm thickness), housed in an automatic filter changer, described in Dubé et al. (2006). During field operation, the filter is automatically changed every 1-3 hours to minimize NO_3 loss due to accumulation of reactive material on the filter surfaces (Dorn et al., 2013; Fuchs et al., 2008).

After concentrations in channels A and B have been calculated in E2.2 from the corrected values of τ and τ_0 from E2.3, three final corrections are applied. These account for: 1) possible decreases in NO_3 concentration in plumes of high ambient NO_2 concentrations (calculated from measured NO_2 concentrations and the R2.1 forward reaction rate constant), 2) dilution from the mirror purge flows, and 3) inlet transmission efficiencies of NO_3 and N_2O_5 (discussed in the calibration section).

2.2.2.2 Instrument Zero

In order to monitor changes in the background time constant, τ_0 , channels A and B employ an automatic chemical zeroing procedure that is specific to NO_3 . During instrument zeros, a 30 standard $\text{cm}^3 \text{ minute}^{-1}$ (sccm) addition of 100 ppm NO in N_2 is added upstream of the common inlet restriction. This addition has been designed to convert 99.9% of ambient NO_3 to NO_2 (following reaction R2.3) while simultaneously minimizing changes in NO_2 absorption between the instrument zero and ambient sampling. The instrument is typically zeroed for 30s every 2-10 minutes, depending on the sampling platform. The zeroing frequency is automatically increased during periods of large and/or rapid changes in cavity pressure that are associated with aircraft ascents and descents that cause large changes in τ_0 due to Rayleigh scattering. In addition to the

corrections discussed above, measured τ_0 is corrected during the data reduction process for the variation in the optical extinction signal from O_3 and NO_2 that occurs between NO zeros and that cannot be corrected by linear interpolation between zeros. A correction is also applied, if necessary, for the additional signal from the NO_2 impurity present in the NO cylinder. For typical NO_2 impurity levels in the NO cylinder from the supplier (typically $\sim 0.2\%$ for 100 ppm NO), the extinction signal from the NO_2 impurity is below the instrument limit of detection, but in practice there is often a larger mixing ratio of NO_2 due to contamination in the NO deliver system. At the nominal operating cavity pressures (~ 350 mbar), and with highly reflective dielectric mirrors of 99.9995% (or 5 ppm loss), the background time constants (τ_0) for channels A and B are typically between 350 and 460 μs , corresponding to pathlengths of $\sim 100 - 140$ km.



2.2.2.3 Calibrations

While CRD, in principle, is a direct absorption detection method, the instrument response for NO_3 and N_2O_5 must be calibrated to account for inlet transmission efficiencies, which are the largest sources of uncertainty in the NO_3 measurement (Dubé et al., 2006). The N_2O_5 measurement must also be calibrated for its thermal dissociation efficiency in the 130°C heater and subsequent NO_3 wall loss. Calibration methods for both NO_3 and N_2O_5 have been described previously in Fuchs et al. (2008), and are overviewed here.

2.2.2.3.1 N_2O_5 Calibration

The N_2O_5 calibration scheme is shown in Figure 2.4, designed to quantify the inlet transmission and thermal conversion efficiencies of N_2O_5 in channel A. Calibration is achieved offline by measuring the channel response to a constant N_2O_5 addition, relative to the simultaneous response of NO_2 on Channel E (separately calibrated as discussed in Section 2.2.3.4). During the

FRAPPÉ and WINTER field campaigns, calibrations were conducted with a solid source of N_2O_5 (Figure 2.4, right). Calibrations during the UWFPS study were conducted and with a newly-built gas-phase source (discussed below, Figure 2.4, left), which was used with ARNOLD to assist with calibrations of the University of Washington’s iodide chemical ionization mass spectrometer. The N_2O_5 calibration procedure can be conducted manually or with an automatic LabVIEW procedure, with the goal incorporating automatic calibrations into future ambient sampling procedures, similar to current automatic procedures for instrument zeros and filter changes. For all campaigns discussed in this thesis, averaged N_2O_5 calibrations resulted in required corrections of $\leq 5\%$ (i.e. 95% transmission + conversion efficiencies) to N_2O_5 mixing ratios.

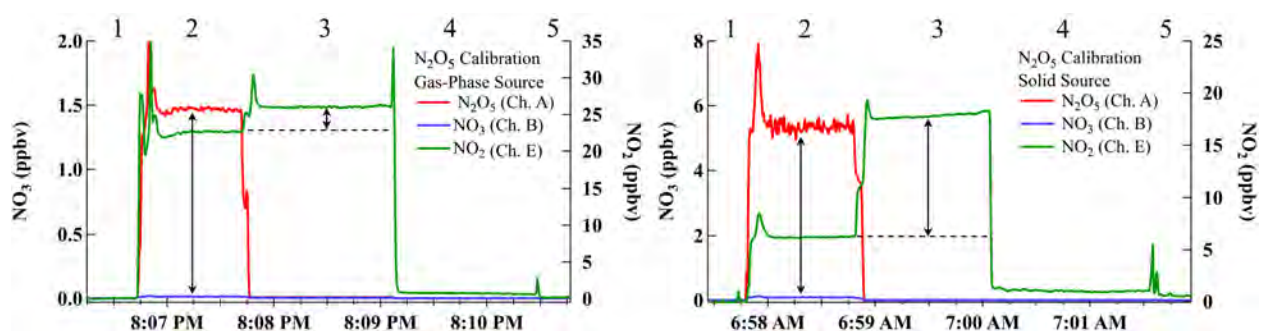


Figure 2.4. N_2O_5 calibration scheme for ARNOLD CRD instrument. (Left) example calibration from the UWFPS campaign using the gas-phase N_2O_5 calibration source. The transmission and thermal conversion efficiencies were 99.0%. (Right) example calibration from WINTER aircraft campaign using the solid-phase N_2O_5 source. Transmission and thermal conversion efficiencies were 99.2%.

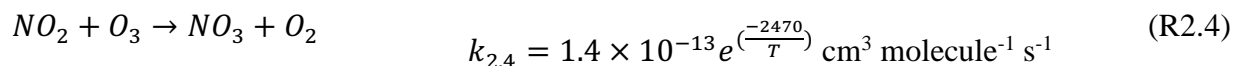
The first of five calibration steps for N_2O_5 establishes the instrument background by zeroing measurements of both N_2O_5 and NO_2 . The second steps adds a small flow of N_2O_5 to the tip of the inlet in an overflow of zero air. During this step, the measured NO_2 is from the background NO_2 mixing ratio of the N_2O_5 calibration source. Step three maintains the addition of N_2O_5 while adding a flow of 100 ppm NO (same as NO_3 zero procedure). Since NO converts each NO_3 to $2*NO_2$ molecules (R2.3), the change in NO_2 relative to step two corresponds to the sum of the background from the N_2O_5 source, NO_2 impurity in the NO tank, and twice the mixing ratio of

the calibration N_2O_5 source. Step four removes the flow of N_2O_5 to measure the cylinder NO_2 impurity. Step five conducts a second instrument zero to measure any baseline drift during the calibration procedure. The measured N_2O_5 and NO_2 mixing ratios from each step are then used to calculate the inlet transmission and conversion efficiencies following E2.4. This calibration procedure can be conducted in parallel (common inlet split between channels A and E), but was exclusively run in series (output of channel A connected to input of channel E) during the UWFPS and WINTER campaigns to eliminate uncertainties in the conversion efficiency of a second heater, required for a parallel calibration.

$$T_{e_{N_2O_5}} = 100 * \frac{[N_2O_5]_{Step\ 2}}{0.5 * ([NO_2]_{Step\ 3} - [NO_2]_{Step\ 2} - ([NO_2]_{Step\ 4} - [NO_2]_{Step\ 5}))} \quad (2.4)$$

2.2.2.3.1.1 N_2O_5 Calibration Sources

Averaged calibration results are independent of the specific N_2O_5 calibration source used, though each has its advantages and challenges. The solid-phase N_2O_5 has been used more frequently for instrument calibrations, but must be synthesized (procedure adapted from Davidson et al. (1978) and Bertram et al. (2009a)) and kept in a dry ice/2-propanol bath to maintain a constant temperature of $-78^\circ C$. The solid source is advantageous as it has a relatively small background of NO_2 , but is subject to contamination and instability in its output (as shown by the drifting NO_2 signal in step 3 of Figure 2.4, right). Motivated by the difficulty of maintaining solid source purity in the field, I, with help from Dorothy Fibiger and Bill Dubé, built a second, gas-phase N_2O_5 calibration source, based on reactions R2.4 and R2.1, pictured in Figure 2.5.



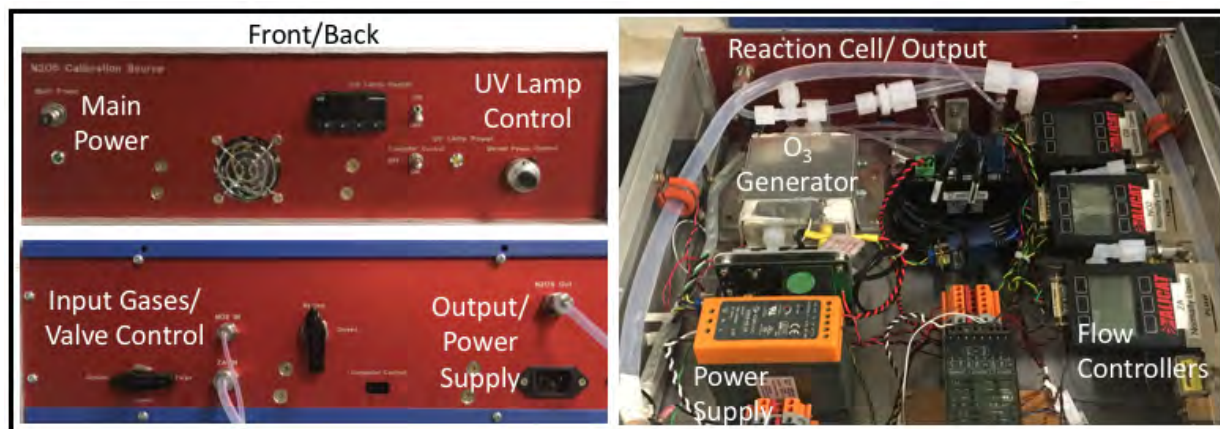


Figure 2.5. Gas-Phase N_2O_5 calibration source. (Left) front and back panels, (right) top-down view. Specific components are labeled for clarity.

This gas-phase source is designed to mix a 10 sccm flow of O_3 with 5 sccm of excess NO_2 (46.2 ppm NO_2 in air from Scott Marin) to form N_2O_5 . The limiting reagent, O_3 , is generated in a homebuilt reaction cell that illuminates a volume of zero air with a UV penray lamp, heated to 60°C to maintain constant output. The O_3 concentration (and subsequent N_2O_5) can be adjusted with a potentiometer on the front of the source, with output ranging from 200-700 ppbv of O_3 in a flow of 10 sccm. Flows of NO_2 and O_3 are then combined in ~ 1.5 m reaction cell (0.476 cm ID), designed to allow for 99.9% conversion of O_3 to N_2O_5 . Immediately prior to output, the sample flow is combined with a dilution flow that serves to carry the addition to the instrument. All flow rates are adjustable with three individual, normally open flow controllers (Alicat, models MC-10SLPM-D-DB15B-NO and MC-50SCCM-D-DB15B-NO). The only required inputs are additions of NO_2 and zero air, and a power supply of 120 V. During field deployment, the small flows of required zero air and NO_2 allow for continuous generation of N_2O_5 that only needs to be combined with a larger carrier flow during calibrations. All components of the calibration source are shown in Figure 2.5, housed in a 16" aircraft rackmount box (Buckeye Shapeforms, model DII-52-4-16RM), that will allow for future incorporation into aircraft instrumentation racks. When

not in use, a valve system has been designed to allow for a continuous flow of zero air to flush the lines and flow controllers, or to seal the reaction cell from ambient air.

Secondary output from this source includes nitric acid (formed on humid surfaces), which does not interfere with the ARNOLD instrument calibration. The main disadvantage of this system for ARNOLD calibrations is the large background of NO₂, which requires a small correction to account for possible N₂O₅ reformation after thermal dissociation (R2.1), and results in larger NO₂ concentrations and a smaller ΔNO₂ between calibration steps two and three (Figure 2.4).

2.2.2.3.2 NO₃ Calibration

The transmission efficiency of NO₃ through channels A and B must also be determined in order to account for loss of ambient NO₃ on Teflon walls and aerosol filter. Both efficiencies are calculated in channels A ($T_{eNO_3}^{heated}$) and B (T_{eNO_3}) using the same five step calibration method as for the N₂O₅ calibrations in E2.4. The same N₂O₅ source as described above is also used for the NO₃ calibration, but run through a heater prior to addition to the instrument inlet. Using this method, NO₃ transmission efficiencies are typically ~80% and accounted for in the final calculation of ambient N₂O₅ and NO₃ mixing ratios following Equations E2.5 and E2.6.

$$[N_2O_5]_{ambient} = \frac{[N_2O_5 + NO_3]_{measured} - T_{eNO_3}^{heated} * [NO_3]_{ambient}}{T_{eN_2O_5}} \quad (2.5)$$

$$[NO_3]_{ambient} = \frac{[NO_3]_{measured}}{T_{eNO_3}} \quad (2.6)$$

2.2.2.4 Accuracy and Detection Limits

As described, the N₂O₅ and NO₃ measurement detection limits are typically better than 2 pptv (2σ, 1s), but vary by campaign and are dependent on factors such as laser temperature (i.e. wavelength), cavity mirror/laser alignment, and mirror cleanliness. The measurement accuracies for both species are subject to uncertainties in the temperature dependence of σ_{NO₃} (~5%), exact

value of R_L (~3%), and variation between individual transmission efficiency calibrations (~6.5%). Campaign-specific instrument detection limits and accuracies are provided in Section 2.3.

2.2.3 ARNOLD and NOxCaRD NO, NO₂, NO_y, and O₃ Measurements

As overviewed above, both the ARNOLD and NOxCaRD instruments measure NO, NO₂, NO_y, and O₃ in four additional cavities (Figure 2.1, C-F). All species are measured by direct absorption of NO₂ at 405 nm after chemical conversion (except NO₂). Each measurement has been individually described in detail in previous literature (Fuchs et al., 2009; Washenfelder et al., 2011a; Wild et al., 2014). Absolute concentrations of NO₂ in ARNOLD channels C-F are calculated in E2.2 using the σ_{NO_2}/R_L ratio derived from the calibration procedure (described below). To maximize sensitivity to NO₂, the nominal 405 nm laser (OBIS 405 LX), is typically held at ~18.5°C and is temperature-tuned for maximum overlap with a local feature in the NO₂ absorption cross section (Figure 2.6). The remaining sections describe details specific to the ARNOLD instrument, but are largely the same for the NOxCaRD instrument.

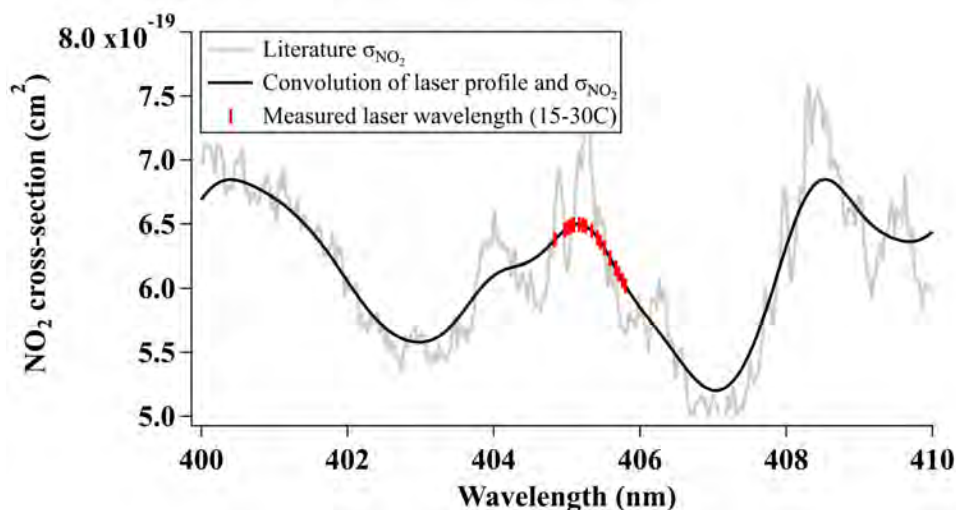


Figure 2.6. Literature NO₂ absorption cross section (Vandaele et al., 1998) (gray), cross section convolution with OBIS laser profile (black), and laser wavelengths measured with the NOxCaRD spectrometer (Ocean Optics USB4000) (red), calibrated against literature mercury absorption lines (Sansonetti et al., 1996).

ARNOLD channels D-F share a common 0.198 cm ID Teflon inlet. The inlet for channel C (NO_y) is a 63 cm long quartz tube (0.39 inner diameter), wrapped in Nichrome wire, heated to a set temperature of 650°C, and insulated with fiberglass in a metal housing (discussed below). Flow through each cavity is controlled downstream by individual mass flow controllers, typically set to volumetric flows of 2.7 LPM to maintain constant residence time during pressure changes (e.g. aircraft altitude changes).

The common inlet is run through a 1 μm Teflon filter in a commercial PFA Teflon mount (Savillex) to remove aerosol and minimize Mie scattering in each cavity. The filter pore size is smaller than the 2 μm filters used on the channel A/B inlet as the 405 nm channels have an increased sensitivity to scattering from smaller particles. Loss of NO , NO_2 and O_3 on these filters is negligible even after accumulation of aerosol particles on the filter. Filters are therefore, only changed as a precaution once per day or after each research flight. The NO_y inlet flow is run through a separate filter downstream of the quartz heater (Parker Balston, model 9933-05-AQ). This filter has been chosen to minimize the filter volume (0.01L) to reduce differences in sample residence times between channel C and the 3 \times -faster common inlet of channels D-F.

Downstream of the filter, the common inlet is split between three reaction cells (44.6 cm^3 volume) immediately prior to entering each cavity (Figure 2.1). Here, small additions of O_3 (12 sccm) and NO (25 sccm) are added to facilitate quantitative conversion of NO and O_3 to NO_2 . Flow rates of these additions have been calculated based on the residence time of the reaction cell (calculated as a function of channel flow rate and volume) and chosen to ensure 99.9% conversion, while minimizing additional NO_2 to N_2O_5 conversion through reaction with excess O_3 (R2.4, R2.1). The NO_y channel also has a reaction cell of the same volume to allow for any necessary conversion of NO to NO_2 with an addition of excess O_3 (12 sccm). The O_3 addition ($\sim 1 \times 10^{14}$ molec. cm^{-3}) used on channels C and F is generated through UV photolysis of a small O_2 flow

around a Mercury lamp (UVP 90-0004-01), while NO on channel D is added directly from a Scott Marin cylinder (2 part per thousand (ppth) in N₂). Prior to addition, the NO flow is run through a FeSO₄ scrubber intended to convert NO₂ to NO to minimize background NO₂ from the cylinder and its regulator. As all additions are added continuously, including during instrument zeros (details below), the background NO₂ serves to reduce the detection limit on the O₃ channel by reducing both τ and τ_0 . This NO₂ background is a constant between the signal and the zero measurement however, and does not require a correction.

2.2.3.1 Measurement Interferences and Corrections

With Mie scattering from aerosol particles effectively eliminated by Teflon filters, time constants measured at 405 nm only require corrections to account for Rayleigh scattering, following E2.7. Additional corrections for interfering absorbers are not required as σ_{O_3} is 4 orders of magnitude smaller than σ_{NO_2} at 405 nm and there is no known absorption due to water vapor at this wavelength that is greater than its Rayleigh scattering efficiency. Similar to channels A and B, σ_{RS} for ground based campaigns may be calculated from the atmospheric composition-weighted cross sections of Ar, N₂, and O₂ (although the procedure is not strictly necessary), and from the slope of τ_0^{-1} vs. air number density during zeros in aircraft measurements. Time constants (τ_0 and τ) are also corrected in E2.7 for changes in Rayleigh scattering associated with changes in water vapor concentration between zeros and ambient sampling, calculated from cavity RH and the difference between σ_{RS} and σ_{H_2O} ($= -5 \times 10^{-27}$, Fuchs et al. (2009)).

$$\tau \text{ or } \tau_0 = \left(\frac{1}{\tau_{measured}} - \frac{cN\sigma_{RS}}{1} - \frac{cN_{H_2O}(\sigma_{H_2O} - \sigma_{RS})}{R_L} \right)^{-1} \quad (2.7)$$

After concentrations are calculated in E2.2 from corrected time constants in E2.7, final corrections are applied to account for: 1) possible decreases in NO_x and NO_y channels from conversion of NO₂ to NO₃/N₂O₅ in excess O₃, 2) possible decreases in O₃ and NO_x channels due

to non-complete chemical conversion (calculated from reaction rate equations and reaction cell residence times), and 3) dilution in all channels from mirror purge and addition flows. Unlike NO_3 , NO_2 is transmitted efficiently through Teflon and does not require inlet transmission efficiency calibrations. Similarly, the thermal conversion efficiency of NO_y in the quartz heater does not require routine calibration after initial construction and calibration of the heater (Section 2.2.3.3). These measurements, however, do require routine calibration of σ_{NO_2}/R_L , discussed below.

2.2.3.2 Instrument Zero Procedure

The background time constants (τ_0) for the four 405 nm channels on ARNOLD and NOxCARD are measured simultaneously by an addition of zero air to the front of the inlets, set to overflow the combined total inlet flow. While the zero air addition is at the front of the common inlet (Channels D-F), it is placed directly after the quartz heater for channel C in order to avoid the use of non-heated fittings and thus minimize nitric acid loss prior to the heater. All channels are zeroed for 30 s, every 5-10 minutes, depending on the sampling platform. Same as for channels A and B, the zeroing frequency is automatically increased if cavity pressures undergo rapid changes, typically caused by aircraft altitude changes. With highly reflective mirrors of 99.9965% (or 35 ppm total loss) the background time constants for these four channels, run at ambient pressure, are typically between 25 and 40 μs , corresponding to pathlengths of $\sim 7.5 - 12$ km.

2.2.3.3 NO_y Heater

As previously mentioned and shown in Figure 2.1, a heated quartz tube is placed at the front of the NO_y inlet to quantitatively, thermally dissociate higher oxides of reactive nitrogen to NO_2 and NO (subsequently converted to NO_2 in excess O_3). This method, along with heater calibration results, have been described in detail by Womack et al. (2016) and Wild et al. (2014). As discussed in Wild et al. (2014), the heater set point temperature of 650°C has been chosen to

quantitatively dissociate many known components of NO_y (Figure 2.7b). This temperature, however, does not allow for 100% conversion of HONO (typically a small component of NO_y) but does include quantitative conversion of ammonium nitrate aerosol, provided it enters the inlet (Womack et al., 2016), which has not been designed for efficient aerosol collection. It is also necessary to heat the quartz inlet to the tip to ensure quantitative collection of nitric acid.

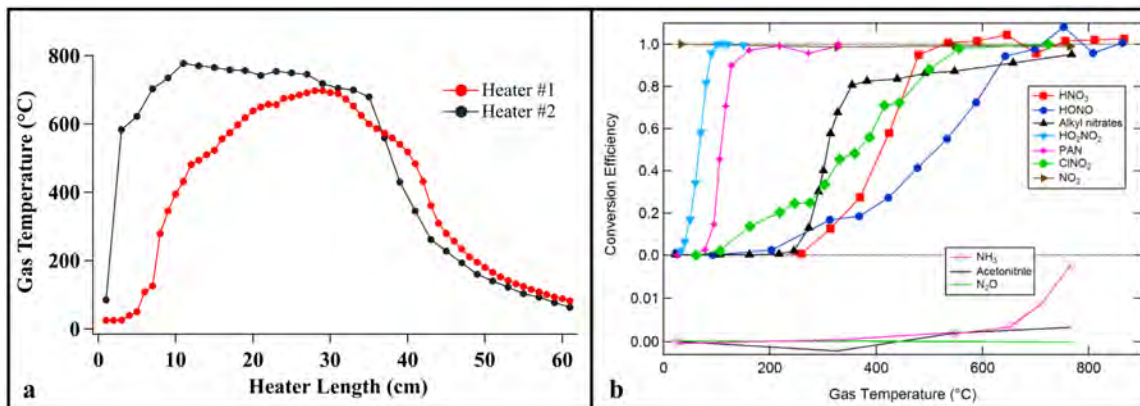


Figure 2.7. (a) Temperature profiles of two NO_y heaters used in the Brown Lab since 2014. Both heaters were set to 650°C and flow rates of 1.4 slpm (standard liters per minute, at 273 K and 1 atm). Differences in temperature profiles result from the specific construction of each heater. (b) Reproduced from Wild et al. (2014), shows the small interference expected from NH_3 under conditions of low (< 100 ppbv) O_3 concentration. Heater #1 was used to conduct the calibration curves shown in panel b.

While the accuracy of this method was determined to be $\sim 10\%$ (Wild et al., 2014), Womack et al. (2016) additionally noted that the operation (i.e. flow rate) and design of individual heaters (i.e. Nichrome wire wrap density and temperature controller placement) will produce unique internal temperature profiles (Figure 2.7a) that require calibration with various NO_y species to determine appropriate set point temperatures. Since initial construction, the Brown group has utilized three different NO_y heaters that were most recently calibrated in summer 2016. During this time, Womack et al. (2016) also discovered additional uncertainties and potential interferences from the conversion of NH_3 in the presence of high levels of O_3 . This conversion (up to 12% NH_3 in 100 ppbv O_3) could lead to NO_y interferences in locations with large agricultural emissions and high ambient O_3 concentrations. As further described in Womack (2016), and consistent with

previous literature describing other NO_y converters (e.g., Fahey (1985)), conversion of NH_3 is apparently suppressed in ambient air containing water vapor through a mechanism that remains uncertain and poorly defined. This potential interference, as it pertains to the FRAPPÉ campaign, is discussed in Section 3.3.3.2.

2.2.3.4 NO_2 Calibration

Calibration of the response of each optical cavity is required as σ_{NO_2}/R_L may be slightly different for each and can change as a function of pressure (e.g. aircraft altitude). It is also sensitive to changes in laser spectral shape and center wavelength, although these factors do not lead to differences in response between different optical cavities. Maximum differences are observed to be 1-2%, although individual channel to channel differences are often smaller. The ratio of σ_{NO_2}/R_L is routinely calibrated during field-deployments using standard additions of NO_2 , generated by quantitative conversion of known O_3 concentrations (generated and measured by commercial instrument) with excess NO (2 ppth). The NO_2 calibration ‘cart’ used for these calibrations is field-portable and operates independent of all instruments. Mounted on the cart is a calibrated TECO 2B commercial O_3 monitor and a rack mount box that houses the required mass flow controllers and chemical reaction cell. The cart also holds a small NO cylinder (2 ppth) with a dedicated regulator.

Typical calibrations use five standard NO_2 additions of 1-200 ppbv (Figure 2.8a) to derive σ_{NO_2}/R_L from plots of α (E2.2) against NO_2 concentration, which is directly proportional to the O_3 concentration measured by the commercial instrument (Figure 2.8b). The background time constant (τ_0) is calculated as the average during the first and final steps (Figure 2.8, Steps 1 and 7) when the instrument is zeroed by addition of zero air. An example calibration procedure from the WINTER campaign is shown in the first panel of Figure 2.8. Standard additions of NO_2 are

generated by adjusting the UV lamp power of the O₃ generator. For ground-based measurements, the slope of each channel in Figure 2.8b is used to calculate ambient measured mixing ratios in each channel in E2.2. The pressure sensitivity of σ_{NO_2}/R_L requires a final calibration step for aircraft measurements, shown in Figure 2.8c. In this step, the entire calibration procedure in Figure 2.8a and b must be repeated under a range of pressures (using different length inlet restrictions) to derive the pressure-dependent calibration equation for each channel, used with measured cavity pressures to calculate σ_{NO_2}/R_L in E2.2 during periods of ambient aircraft sampling.

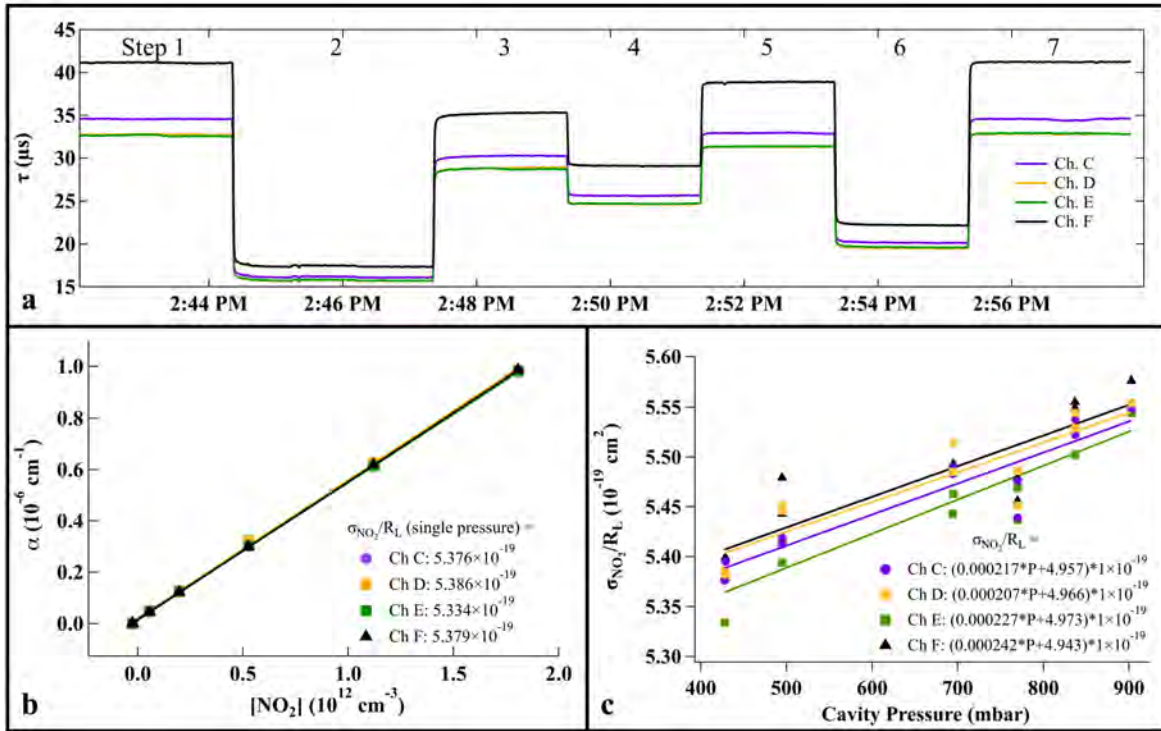


Figure 2.8. Example NO₂ calibration procedure. (a) raw time series of τ (as measured by ARNOLD) during a 7 step calibration procedure. (b) α plotted against measured $[\text{NO}_2]$. Markers represent each calibration step and the fit line slopes are σ_{NO_2}/R_L for each cavity. (c) pressure dependent calibration factors for each cavity. Each point is the slope from a single-pressure calibration, as shown in panel b. Linear fits to these data are used with measurement of cavity pressures to calculate σ_{NO_2}/R_L and ambient mixing ratios during aircraft campaigns.

2.2.3.5 Accuracy and Detection Limits

During the field campaigns described in this thesis, the NO₂, NO, O₃, and NO_y measurements had detection limits ≤ 150 pptv (larger for O₃, depending on NO₂ impurity in the

NO addition), which are campaign dependent and derived from the precision of τ_0 measurements during ambient sampling at high altitudes or during zeros. Previously reported instrument performance during both laboratory and field studies has been as good as 20 pptv (Fuchs 2009, Wild 2014). For NO, NO₂, and O₃, the measurement uncertainties are dominated by uncertainty in the effective NO₂ absorption cross section, which is directly related to the calibration procedure and commercial O₃ instrument ($\leq 3\%$). An additional uncertainty of 1% is associated with uncertainties in the sample dilution from additions of O₃ and NO. The 12% accuracy of NO_y has been previously determined by Wild et al. (2014), and is based on in-field comparisons to other NO_y instruments. The uncertainty is consistent with estimated uncertainties in the thermal conversion efficiencies of NO_y components ($\sim 10\%$), in addition to cross-section calibrations. Campaign-specific detection limits and accuracies are presented in Section 2.3.

2.2.4 Instrument Hardware and Software Overview

Instrument power supplies in addition to mass flow controllers, valves, and their associated measurement computing boards (NI USB-1208FS, USB-TC) are all housed below the optical table/carbon fiber cage system (Wild et al., 2014) and (if required) communicate with the PC rack mount computer via USB. Both ARNOLD and NOxCaRD instruments are operated using custom LabVIEW software (programs hereafter referred to as ‘VIs’), primarily written by Hendrik Fuchs and Nick Wagner. This code has been updated and modified for work in this thesis on an ‘as-needed’ basis. For example, prior to the WINTER campaign, I updated control of the automatic filter changer to a USB stepper motor (Allmotion, USB Stepper Stick) that allows for fast and reliable control of the filter changer via a custom subVI.

The instrument computer houses two (one, NOxCaRD) digital oscilloscope cards (National Instruments PCI-6132) that digitally modulate (TTL signals) the 662 nm laser at 250 Hz and the 405nm laser at 2 kHz. Different modulation rates account for differences in light decay times

between channels A/B and C-F (i.e. $\sim 300 \mu\text{s}$ vs. $\sim 25 \mu\text{s}$). The timing of the pulse chain is set and controlled in a custom LabVIEW data acquisition subVI using frequency and duty cycle parameters. Signals are sent from the PCI card to the laser remote via co-axial cables with BNC-SMB connectors to ensure sharp and clean signals. Individual ring down traces collected by PMTs are then digitalized and transferred over the PCI bus to the computer where they are co-added in batches of 100. The custom DAQ subVI fits the co-added traces to a single exponential decay. In theory, instrument data acquisition rates are limited only by the laser modulation rate, but are here limited to sampling rates of 2 Hz due to computer overhead and current structure of the main VI.

The main LabView VI for ARNOLD (also adapted for NOxCARD) has a single sequence structure with three main frames that control operation of the instrument. The first frame initializes communication with instrument hardware, turns on lasers, and sets default values (read from instrument configuration file, or saved during previous operation). The second frame has additional sub-sequence structures that repeatedly loop until the user specifies instrument shutdown, in which the program progresses to the third frame where hardware communication channels are closed, inlet and addition flows are turned off, and lasers are shut down. The second frame includes all major components of the instrument including data acquisition, ring down trace fitting, mixing ratio calculation and display, data saving and file writing, flow rate and valve control, temperature and pressure monitoring, and instrument zeroing sequences, which can be initialized automatically at a set time interval or manually by the user. Combined, these processes limit the data acquisition rate since the ring down trace fitting, display, and hardware communication must all happen before the DAQ VI can be called in the next loop. Total acquisition speed can therefore be increased above 2 Hz by implementing a different code structure, such as a producer-consumer framework. I have begun implementing this framework by relocating LabVIEW-laser communication procedures (used to monitor laser power, current, and

head temperature) outside of the main sequence structure where they can supply data to the main structure at their native rates (1-2 seconds), without slowing the acquisition speed. In addition to these changes, I have also added more extensive error handling in many of the subVIs to more easily identify and track errors upon start-up and during operation.

Once started and warmed-up, the ARNOLD and NOxCaRD instruments can be set to automatic sampling modes for in-field operation with minimal maintenance outside of regular calibration. Discussed in further chapters are deployments of ARNOLD in the FRAPPÉ and WINTER campaigns and NOxCaRD in the UWFPS study.

2.3 Field Campaigns and Associated Measurements

2.3.1 FRAPPÉ 2014

2.3.1.1 Campaign Overview

In July-August 2014 the National Science Foundation (NSF) Front Range Air Pollution and Photochemistry Experiment (FRAPPÉ) and the final phase of the NASA (National Aeronautics and Space Administration) Deriving Information on Surface Conditions from Column and Vertically Resolved Observations Relevant to Air Quality (DISCOVER-AQ) field campaigns conducted aircraft, mobile, and ground-based measurements at over 15 locations across the Colorado Front Range. Both campaigns were designed with the goal of better understanding the sources contributing to elevated summertime O₃ concentrations as well as improving the capability of future satellites to monitor regional air quality around the world. Flights with the NSF/ National Center for Atmospheric Research (NCAR) C-130 aircraft conducted aerial surveys while the NASA P-3B aircraft conducted repeats of a single flight pattern, which included a spiral (1,000-15,000 ft) directly over the Boulder Atmospheric Observatory (BAO) tower (Figure 2.9b). These flights overlapped in time with measurements used in this work, which were collected at the BAO site between 16 July and 15 August 2014 and included surface and vertically resolved

observations. FRAPPÉ data are available at <http://www-air.larc.nasa.gov>, <http://www.esrl.noaa.gov/psd/technology/bao/>, and <http://www.esrl.noaa.gov/gmd/dv/data/?category=Ozone&site=BAO>.

2.3.1.2 BAO Tower and PISA Carriage

The Boulder Atmospheric Observatory (BAO: [40.05°N, 105.01°W] (Kaimal & Gaynor, 1983) was an atmospheric research facility located in the southwest corner of Weld County, roughly 35 km north of Denver, 25 km east of Boulder, and 1584 meters above sea level (mASL). Most notable for its tall (300 m) tower, the site was closed in 2016 and the tower demolished in late 2017 after nearly 40 years of hosting field-campaigns and providing continuous chemical and meteorological measurements.

During FRAPPÉ, an external carriage mounted on the southwest side of the tower provided a platform for vertically resolved chemical measurements (Figure 2.9). The instrument carriage, known as the Profiling Instrument Shelter with Amenities (PISA) (Brown et al., 2013), held an instrument payload of roughly 900 kilograms, was operated remotely via a wireless link to the ground, and was powered by an electric drive motor with emissions that did not influence on-board chemical or physical measurements. Use of PISA to conducted vertical profiles (0-290 m in 10 minutes) during previous campaigns demonstrated the ability of this sampling platform to capture concentration gradients from local boundary layer dynamics and aid in the characterization of chemistry in stratified nocturnal layers (Wagner et al., 2013).

The PISA was operated during FRAPPÉ in both stationary and vertical profiling modes. When profiling, the carriage was manually set to ascend or descend continuously, or in discrete steps (~50 to 100 m). Over the course of the campaign, vertical profiles were conducted at least once during all times of day (morning, afternoon, evening, and overnight). Data from both operation modes were used in the Chapter 3 analysis but were filtered for altitudes < 1 mAGL to

avoid artifacts when the carriage was sitting on the ground. Instruments not installed in the PISA during FRAPPÉ were housed in a series of ground-based trailers (e.g. Figure 2.9). Additionally, south-facing stationary platforms (booms) at 10, 100, and 300 m along the tower provided meteorological measurements of temperature, relative humidity, wind speed, and wind direction throughout the campaign.

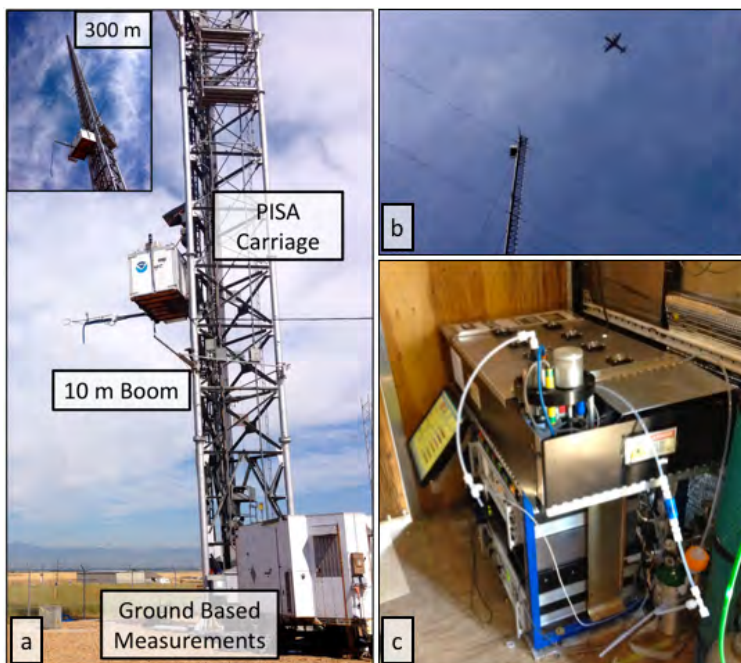


Figure 2.9. (a) BAO Tower with labels highlighting the PISA carriage, 10 m monitoring station, one of the ground-site trailers, and 300 m total tower height. (b) Simultaneous sampling during FRAPPÉ of instruments in the PISA carriage and on the NASA P-3B aircraft. (c) ARNOLD CRDS instrument installed in the PISA carriage.

2.3.1.3 Instrumentation

Measurements from the PISA, used in the Chapter 3 analysis, included CH_4 and CO from a commercial CRD instrument (Picarro, model 2401) (operated by Emily Fischer) (Chen et al., 2013; Crosson, 2008), gas-phase ammonia (NH_3) from a quantum-cascade laser instrument (QC-TILDAS) (operated by Alex Tevlin, Jennifer Murphy) (McManus et al., 2008), and NO , NO_2 , NO_y , O_3 , N_2O_5 , and NO_3 from the ARNOLD CRDS instrument described in Section 2.2. The accuracy and detection limits of NO_x , NO_2 , and O_3 in 2014 were $< 5\%$ and < 50 pptv, respectively.

The NO_y channel had a limit of detection < 200 pptv and an accuracy of 12% (Wild et al., 2014). Conversion of NO_y in a 650 °C quartz oven may have also suffered interference from the unintended conversion of a small fraction (~6%) of NH₃ in the presence of O₃ (Womack et al., 2016) (Section 2.2.3.3). The NO_y data were not corrected and the associated uncertainty was estimated based on co-located NH₃ and O₃ measurements (Section 3.3.3.2). All ARNOLD measurements were collected through three separate downward facing inlets, mounted on the underside of the PISA carriage.

In addition to carriage instruments, O₃ LIDAR (NOAA TOPAZ) (Alvarez et al., 2011; Langford et al., 2015) measurements were made at a ground site ~0.5 km south of the main tower (collected by Andrew Langford, Raul Alvarez II, Christoph Senff) and j(NO₂) photolysis frequencies (NCAR filter radiometer (Shetter et al., 2003)) were measured from a trailer parked at the tower base (operated by Samuel Hall, Kirk Ullmann). Lastly, spectral surface albedo measurements derived from a visible (415-1625 nm) Multi-Filter Rotating Shadowband Radiometer (MFRSR) (Harrison et al., 1994; Michalsky & Hodges, 2013), were made from a NOAA Surface and Radiation Budget Monitoring (SURFRAD) mobile lab (Augustine et al., 2000) parked at BAO for the duration of the campaign (operated by Kathy Lantz). A summary the measurements used in Chapter 3 analysis is provided in Table 3.1.

2.3.2 WINTER 2015

2.3.2.1 Campaign Overview

The Wintertime INvestigation of Transport, Emissions, and Reactivity (WINTER) campaign conducted 13 research flights with the NSF/NCAR C-130 between 3 February and 13 March 2015 over the eastern U.S.. Based out of Langley, VA, these flights were designed to probe current uncertainties in wintertime emissions and chemical transformations that occur in polluted regions during both day and night. Instruments relevant to the analyses of wintertime

heterogeneous reactive nitrogen chemistry (Chapter 4 and 5) are discussed below. All data from the WINTER campaign are available at http://data.eol.ucar.edu/master_list/?project=WINTER.

2.3.2.2 Instrumentation

On-board the C-130 aircraft, NO, NO₂, O₃, NO_y, and N₂O₅ were measured with the NOAA custom-built ARNOLD instrument discussed in Section 2.2 (Figure 2.10). The accuracy and detection limits during WINTER were better than 4% and 95 pptv (1s, 1σ) for NO₂, NO_x, and O₃, 12% and 90 pptv (1s, 1σ) for NO_y, and 12% and 4.5 pptv (1s, 1σ) for N₂O₅.

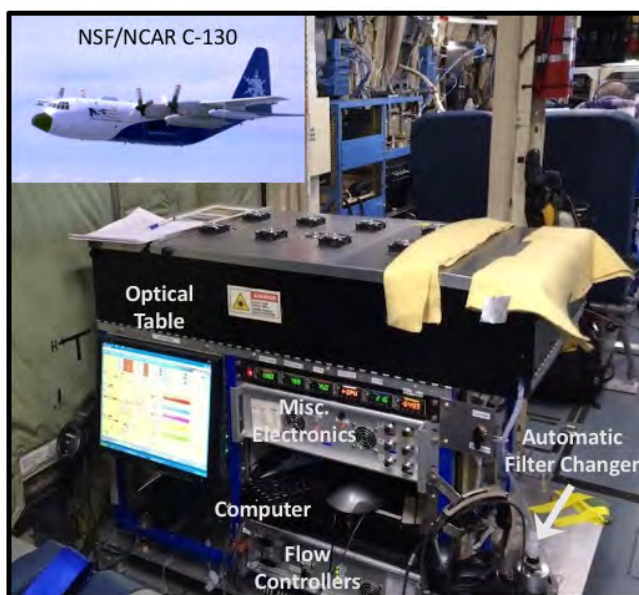


Figure 2.10. ARNOLD Instrument installed in the C-130 aircraft (inset photo) during WINTER. Various instrument components are labeled.

Additional instruments are shown in Figure 2.11. Briefly, NO, NO_y, and O₃ were additionally measured with the NCAR Chemiluminescence Detector (CL) (Weinheimer et al., 1994) (operated by Andrew Weinheimer) with accuracies better than 5% for O₃ and NO and 20% for NO_y. NO₂ was additionally measured by the University of California Berkeley Thermal Dissociation – Laser Induced Fluorescence Instrument (TD-LIF) (Day et al., 2002) (operated by Tamara Sparks, Carly Ebben, Paul Wooldridge, Ronald Cohen) with 10% accuracy and a 20 pptv detection limit. N₂O₅, ClNO₂, and other acidic gases were measured by two High Resolution,

Time-of-Flight Chemical Ionization Mass Spectrometers (Iodide and Acetate ionization TOF CIMS) from the University of Washington, described previously by Lee et al. (2014) (operated by Felipe Lopez-Hilfiker, Benn Lee, Joel Thornton, and Patrick Veres). The accuracy and detection limits for the N_2O_5 and ClNO_2 measured with the I-TOF-CIMS were typically $< 30\%$ and 0.6 pptv respectively. A full suite of 54 speciated VOCs were measured in grab samples concentrated for 35 seconds every two minutes with the NCAR Trace Organic Gas Analyzer (TOGA) (Apel et al., 2015), operated by Eric Apel, Nicola Blake, Alan Hills, and Rebecca Hornbrook. Accuracies were compound dependent and typically below 30% , but as large as 50% for some alkyl nitrates, butene, and substituted aromatics. Aerosol composition for submicron particles was measured by the University of Colorado Boulder High-Resolution Time-of-Flight Aerosol Mass Spectrometer (AMS) (DeCarlo et al., 2006), operated by Pedro Campuzano-Jost, Jason Schroder, and Jose Jimenez. Sampling details specific to the WINTER campaign are described in Guo et al. (2016) and (Schroder et al., submitted, 2018). Detection limits were flight and compound dependent, typically between $0.012 - 0.474 \mu\text{g sm}^{-3}$, and always $< 1.2 \mu\text{g sm}^{-3}$. In addition to the CU-Boulder AMS, submicron particle anion composition was measured by the Georgia Institute of Technology, Particle Into Liquid Sampler (PILS) as described by Guo et al. (2016) (operated by Amy Sullivan, Rodney Weber, analyzed by Hongyu Guo). The PILS can efficiently measure soluble refractory species (i.e. NaCl , NaNO_3 , $\text{Ca}(\text{NO}_3)_2$, $\text{Mg}(\text{NO}_3)_2$, MgSO_4 , KCl , KNO_3 , and K_2SO_4) while the AMS cannot. Therefore, the high-precision, 1 Hz AMS measurements were primarily used in Chapter 4 (N_2O_5 uptake coefficient analysis) while both PILS and AMS measurements of particle phase chloride were used in Chapter 5 (ClNO_2 production analysis, further details in Chapter 5). Particles $< 4 \mu\text{m}$ in diameter were additionally collected in flight with a filter-sampling system every $\sim 5-7$ minutes, later analyzed offline for water-soluble ions by ion

chromatography, as described previously (Dibb et al., 1999; Dibb et al., 2000) (operated by Jack Dibb). These data were not used in analyses here for reasons described in Chapters 4 and 5.

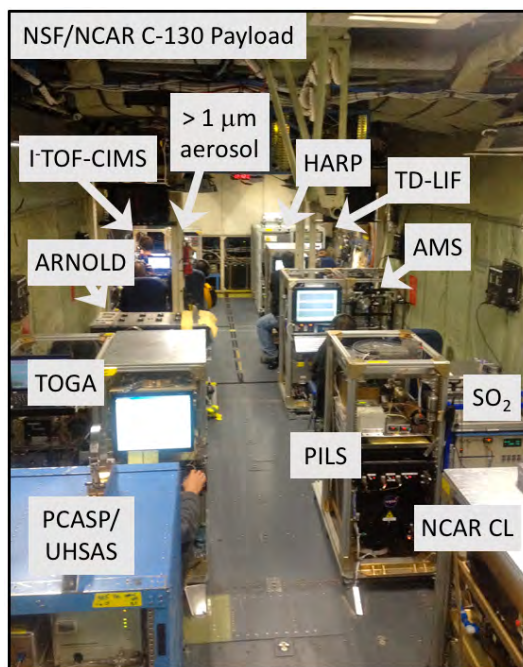


Figure 2.11. NSF/NCAR C-130 aircraft instrument payload during the WINTER campaign

Photolysis frequencies were calculated from spectrally resolved actinic flux density measurements from the High-performance Instrumented Airborne Platform for Environmental Research (HIAPER) Airborne Radiation Package – Actinic Flux (HARP-AF) instrument (Shetter et al., 2003; Shetter & Müller, 1999), operated by Samuel Hall and Kirk Ullmann. Photolysis frequency uncertainties at high sun are driven by a combination of instrument and molecular uncertainties in the cross-section and quantum yields for each molecule. Representative 1σ uncertainties in photolysis frequencies are $\pm 12\%$ and $\pm 25\%$ for $j(\text{NO}_2)$ and $j(\text{O}^1\text{D})$, respectively. However, the low sun angles in this study exacerbate optical angular response biases, resulting in uncertainties ramping to as high as $\pm 40\%$ at sunset.

Dry aerosol surface area densities were measured aboard the C-130 with two NCAR aerosol optical counters, operated by NCAR research staff and analyzed by J. Michael Reeves.

The NCAR Ultra-High Sensitivity Aerosol Spectrometer (UHSAS) and the Passive Cavity Aerosol Spectrometer Probe (PCASP), both manufactured by Droplet Measurement Technologies (DMT) Inc., are particle spectrometers based on optical scattering of laser light. The UHSAS sizes individual particles in the diameter range 0.06 to 1.0 μm with 99 channels, while the PCASP covers 0.1 to 3.0 μm in 30 channels. Both probes utilize aerodynamic focusing of the aerosol sample stream to provide nearly 100% counting efficiency.

Lastly, total dry surface area densities (used to calculate N_2O_5 uptake coefficients in Chapter 4) were calculated from the sum of these submicron (PCASP or UHSAS) and 1-3 μm (PCASP) particle measurements. Data coverage during WINTER was better for the PCASP than the UHSAS instrument. In instances where the UHSAS was unavailable, the PCASP measurements were used for <1 μm particles after applying a scaling factor of 1.216 (the median UHSAS/PCASP ratio during the entire WINTER campaign). Main sources of uncertainty in these optical particle spectrometers were from the range of refractive indices encountered in ambient aerosol and the dependence of number concentration on sample flow rate. For both probes, the combined uncertainty in total measured dry surface area was 34%. To account for the reduced resolution of PCASP measurements, an additional uncertainty of 23% (2σ from a Gaussian fit to UHSAS/PCASP campaign ratio (60s-averaged) histogram) was added in quadrature for a total uncertainty of 41% in <1 μm PCASP measurements. Despite these large uncertainties, the magnitude is similar to those reported in previous field studies (e.g. Brown et al., 2009; Morgan et al., 2015; Phillips et al., 2016; Wagner et al., 2013), suggesting a commonality in the level of uncertainty among field-derivations of N_2O_5 uptake coefficients (discussed in Chapter 4).

2.3.3 UWFPS 2017

2.3.3.1 Campaign Overview

The Utah Winter Fine Particulate Study (UWFPS) included both aircraft and ground-based measurements throughout Salt Lake, Cache, and Utah Valleys during January and February 2017 (Figure 6.1). A total of 23 research flights were conducted during both day and night with the NOAA Twin Otter aircraft, equipped with aerosol and gas-phase instrumentation to probe the regional sources and formation mechanisms of particulate matter less than 2.5 μm in diameter ($\text{PM}_{2.5}$), responsible for regional wintertime air pollution. The Twin Otter is a flexible measurement platform, used to collect spatially resolved measurements in shallow (< 1000 ft / 300 m AGL) boundary layers within these mountainous basins. Instrumentation used in Chapter 6 is discussed below. All data from the UWFPS campaign are available at <https://www.esrl.noaa.gov/csd/groups/csd7/measurements/2017uwfps/>.

2.3.3.2 Instrumentation

The Twin Otter payload (Figure 2.12) included measurements of NO_x , NO_2 , NO_y , and O_3 (1 Hz sample frequency) from the NO_xCaRD instrument described in Section 2.2, gas-phase NH_3 (1 Hz sample frequency) with an Aerodyne mid infrared absorption instrument (QC-TDLAS) from the University of Toronto (measured by Alexander Moravek and Jennifer Murphy) (Ellis et al., 2010), N_2O_5 , HNO_3 , and ClNO_2 (1 Hz sample frequency) with the University of Washington I-TOF-CIMS (operated by Lexie Goldberger, Ben Lee, and Joel Thornton) (Lee et al., 2014; Lee et al., submitted, 2018), non-refractory sub-micron aerosol composition (sample every ~ 10 s) from the NOAA Aerosol Mass Spectrometer (AMS) (operated by Alessandro Franchin and Ann Middlebrook) (Bahreini et al., 2009; Middlebrook et al., 2012), aerosol size (sample every ~ 3 s) with a commercial (DMT) UHSAS (operated by Alessandro Franchin) (Brock et al., 2011), and ambient temperature and pressure (1 Hz sample frequency) from a commercial (Avantech)

meteorological probe. Accuracies were typically better than 5% for NO_x , NO_2 , and O_3 and 12% for NO_y , but increased during periods of rapid altitude change. Detection limits were also altitude dependent due to pressure-induced changes in the Rayleigh scattering cross section that could not be fully corrected during post-processing. Average detection limits for AMS-measured aerosol composition were 0.04, 0.09, 0.33, 0.03, and $0.07 \mu\text{g m}^{-3}$ for particulate nitrate, ammonium, organics, sulfate, and chloride, respectively with uncertainties of $\sim 20\%$ for all species. Gas-phase NH_3 was measured with a detection limit of 450 pptv ($1s\ 3\sigma$) and variable accuracy, dependent on aircraft altitude and laser temperature drift. Accuracy and detection limits for N_2O_5 , ClNO_2 , and HNO_3 were similar to those reported from the same instrument deployed during WINTER (≤ 0.6 pptv ($1s\ 1\sigma$), 30%). The accuracy of the commercial UHSAS instrument is also expected to be similar to that used during WINTER ($\sim 34\%$). A summary of aircraft instrumentation is provided in Table 6.1.

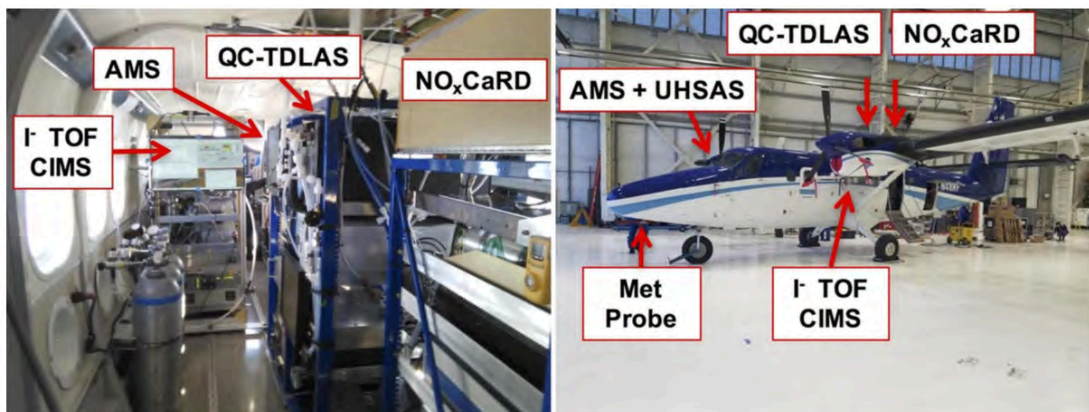


Figure 2.12. Reproduced from final UWFPS report (UWFPS Science Team, 2018). (Left) Image of instrumentation mounted inside the Twin Otter aircraft, taken from the rear, facing forward. (Right) Image of Twin Otter with arrows indicating instrument inlet locations on the side (UHSAS, AMS, I-TOF-CIMS), nose (met probe), and top (QC-TDLAS, NO_xCaRD) of the aircraft.

2.3.4 Auxiliary Campaigns and Measurements

2.3.4.1 SONNE 2012

The Summer Ozone Near Natural gas Emissions (SONNE) field campaign was conducted at BAO between 27 July and 12 August 2012. Data from this campaign were used to supplement the measurements collected during the FRAPPÉ campaign as described further below in Section 2.4.1.1 and in Chapter 3. Chemical measurements were acquired via inlets mounted 8 meters above ground level (mAGL) on a walkup tower ~10 m south of the main tower. Continuous in-situ measurements of a full suite of C₂-C₁₀ hydrocarbons, C₂-C₄ oxygenated VOCs, aromatics, C₂-C₃ alkyl nitrates, and dimethyl sulfide (DMS) were collected via a custom-built, two-channel gas chromatograph-mass spectrometer (GC-MS) by Jessica Gilman and Brian Lerner (Gilman et al., 2010). Samples were acquired (5 minutes) and analyzed (25 minutes) on a repeating cycle every 30 minutes. The accuracy and detection limits were compound dependent but less than 25% and 10 parts per trillion by volume (pptv), respectively (Gilman et al., 2010). NO and NO₂ were measured by the ARNOLD instrument, operated by Pete Edwards and Bill Dubé (Section 2.2). The accuracy and limit of detection for both species was < 5% and < 30 pptv, respectively. O₃ was measured via UV absorbance by a commercial instrument (Thermo Environmental Instruments, Inc., Model 49c), operated by Eric Williams. Methane (CH₄) was measured via CRD spectroscopy using a wavelength-scanned CRD instrument (Picarro, model 1301-m), operated by Jeff Peischl (Peischl et al., 2012). Carbon monoxide (CO) was measured by a vacuum ultraviolet fluorescence instrument (Gerbig et al., 1999), operated by John Holloway. All chemical measurements were collected at a 1 Hz time resolution and averaged to the GC-MS acquisition period of 5 minutes every half hour. SONNE data are available at <http://esrl.noaa.gov/csd>.

2.3.4.2 CalNEX 2010

The California NEXus campaign was conducted during May and June 2010 and included aircraft, ground, and ship-based sampling platforms throughout southern CA (Ryerson et al., 2013). Photolysis rates calculated from spectral actinic flux measurements collected by Harald Stark (Stark et al., 2007) aboard the NOAA WP-3D aircraft were used to estimate $j(\text{NO}_3)$ photolysis rates in Chapter 4 as described in Section 2.4.2.3. Additional VOC and CO data (Borbon et al., 2013) collected by John Holloway, Jessica Gilman, Joost de Gouw, and William Kuster from the ground site in Pasadena, CA were used to estimate the required scaling factor for acetylene measurements during the SONNE campaign, used in Chapter 3 (see Section 2.4.1.1). CalNEX data are available at <http://esrl.noaa.gov/csd>.

2.4 Chemical Box Models

Two zero-dimension box models were developed/adapted for the work presented in Chapters 3 - 6. Each is introduced and described in this section with details specific to each analysis provided in the relevant chapters. Briefly, box models integrate a detailed set of chemical rate equations and include observational constraints for species concentrations, with transport represented by simple first-order dilution terms. Box models are much simpler than 3-D chemical transport models (CTM) such as WRF-Chem and GEOS-Chem that include quantitative emissions and transport schemes. Box models advantages include independence from uncertainties in emission inventories, as well as increased computational efficiency that allows for both the incorporation of near-explicit chemical mechanisms and iterative computation, beneficial for chemical sensitivity studies (Chapter 3) and the derivation of non-measured parameters (Chapters 4-6). For the number of advantages, however, are a similar number of disadvantages, the balance of which will depend on the desired application. For example, box models simulations of field environments are constrained to single locations with limited transport and/or require short

simulation times, due to their simplified parameterizations of production and loss processes. Additionally, simulations must be constrained by chemical and physical observations and cannot represent the spatial heterogeneity in regional emission sources or vertical/horizontal distributions in chemical species. Despite these limitations, box models were the ideal tool for analyses presented in this thesis, which: 1) use a series of sensitivity simulations to identify the role of specific VOCs to the chemical production of O₃ in a well-mixed environment in the Colorado Front Range (Chapter 3), 2) iterate simulations of nocturnal chemistry in the residual layer (largely removed from emissions and loss processes) to derive non-measured parameters related to heterogeneous chemistry (Chapters 4 and 5), and 3) forward integrate observationally-informed simulations to estimate the chemical production of NH₄NO₃ in the residual layer and the contribution of heterogeneous chemistry to air pollution in Salt Lake Valley, Utah (Chapter 6). Details of each model are described next.

2.4.1 DSMACC and MCM

The Dynamically Simple Model for Atmospheric Chemistry (DSMACC), previously described by Emmerson and Evans (2009), is a box model that has been designed to help improve the understanding of the chemical composition of the troposphere. DSMACC (written in Fortran, requires Linux/Unix operating system) most commonly utilizes the Master Chemical Mechanism (MCM) (Jenkin et al., 2015) for its chemistry scheme and the NCAR Tropospheric Ultraviolet and Visible Radiation Model (TUV v5.2) (Madronich et al., 1998) for photolysis rates. The Kinetic PreProcessor (KPP) software (Sandu & Sander, 2006) is additionally used to automatically generate a series of ordinary differential equations (written in Fortran90 code) from the original chemical reaction and rate constant data downloaded from the MCM website. Originally written to address a variety of concerns ranging from ambient radical budgets (Edwards et al., 2013) to upper tropospheric NO_x partitioning (Henderson et al., 2011), DSMACC source-code is freely

available online and designed for user-flexibility. With DSMACC, the user can easily change the chemical mechanism, adjust photolysis rate calculations, and choose to run simulations in either free-running or constrained mode. Due to this flexibility and prior use in the Brown research group (e.g. Edwards et al., 2014), DSMACC was used for the box model analysis presented in Chapter 3. The following sections describe details about the specific chemical mechanism and model set-up used in this work. Much of this work has been updated/reproduced from McDuffie et al. (2016).

2.4.1.1 Model Overview

In this work, DSMACC was used to assess the impact of oil and gas VOC and NO_x emissions on local O₃ formation chemistry in the Colorado Northern Front Range (Chapter 3). To this end, DSMACC simulations were initialized at 8 am MDT and forward integrated for 24-hours with a 10 minute time step, while using the Master Chemical Mechanism (MCM v3.3.1) for the chemistry scheme. The MCM is a near-explicit chemical mechanism representing the gas-phase tropospheric degradation of VOCs (Jenkin et al., 2015). The MCM uses laboratory kinetic and product data for measured reactions and structure-activity relationships (SARs) for unknown parameters. The subset of chemistry used here includes a complete inorganic mechanism and degradation scheme for 50 primary VOCs, with a total of 4002 species and 15555 reactions.

To represent the NFR as a photochemical box, simulations were initialized with, and constrained every 30 minutes to, SONNE (Section 2.3.4.1) diel average observations of temperature, pressure, and mixing ratios of CO, CH₄, 42 non-methane VOCs (shown in Figure 2.13), and water vapor (derived from 10 m relative humidity measurements). Simulations were constrained to 2012 data only due to lack of speciated VOC measurements in 2014. For comparison, both temperature and observed O₃ mixing ratios were higher in 2012 than 2014 with differences in maximum diel averages (27 July – 12 August, 2012 and 2014) of 1° C and 1.8 ppbv, respectively. DSMACC simulations were additionally constrained to SONNE diel average

observations of total NO_x, which was partitioned by the model into its components (NO and NO₂) every 10 minutes assuming photo-stationary state, using $j(\text{NO}_2)$, temperature, and O₃. A dilution rate constant was also applied to all 4002 model compounds (as described in Section 2.4.1.4) to simulate average vertical transport and loss from the box.

2.4.1.2 Chemical Constraints and Model VOC Scenarios

Three VOC scenarios were developed to 1) simulate average photochemical O₃ production at BAO (Case 1) and 2) to quantify the contribution from regional O&NG VOC emissions by conducting simulations without O&NG VOCs (Case 2) and with their concentrations doubled (Case 3). For each case, 42 VOCs in the model mechanism were constrained as described above to set concentrations every 30 minutes. VOC scenarios are described in the following sections and summarized in Table 3.2.

2.4.1.2.1 Base Case Scenario (Case 1)

Base (Case 1) simulations were constrained to observed diel-average VOC concentrations. The VOC data from 2012, however, included some compounds not explicitly represented in the MCM, including 3 cyclo-pentanes, 7 cyclo-hexanes, and 1 monoterpene. To incorporate these measurements into model simulations, these species were lumped with alkanes and monoterpenes in the mechanism according to their OH-rate constants calculated with SAR principles and formulas (Atkinson, 1987) (see Table 2.1). Relative to the SONNE average diel observations, this method of VOC lumping increased the total mixing ratio of carbon (ppbC) in the simulated base case simulation by < 0.3% and total VOC OH-reactivity (defined in Section 3.3.2) by < 0.4% (24-hour average). In contrast to these compounds, the GC-MS also measured as lumped pairs, the M- and P- isomers of Xylene and 3- and 4- isomers of 1-Ethyl-X-methylbenzene, which are individually represented in the MCM. An average value of each measured pair was used to

initialize and constrain each pair as individual compounds, which influenced the simulated maximum O₃ mixing ratio by less than 0.028 ppbv or 0.04%.

Formaldehyde (HCHO) was not measured by the GC-MS but is also required to accurately initialize model simulations of O₃ production. HCHO is important to consider as its photolysis leads to primary radical production that influences the formation of O₃ (Edwards et al., 2014; Edwards et al., 2013). The sources of HCHO are predominantly secondary from the oxidation of a variety of VOCs (Fried et al., 2003) but may also have primary sources, such as incomplete combustion in motor vehicles (Altshuller, 1993; Anderson et al., 1996; Olaguer et al., 2009). Here HCHO was derived from observations of HCHO and acetaldehyde (CH₃CHO) made from the C-130 aircraft in the lowest 3 km (AGL) over the Northern Front Range during FRAPPÉ, measured using the NCAR Trace Organic Gas Analyzer (TOGA) (operated by Rebecca Hornbrook and Eric Apel) (Apel et al., 2015). A 2-sided regression fit to these data resulted in a 1.4 ± 0.1 ppbv/ppbv slope that was applied to observed 2012 SONNE CH₃CHO. In all simulations, HCHO was initialized at the first time step but not constrained further due to its dominant secondary production pathways.

Lastly, acetylene (C₂H₂) measurements during SONNE were a factor of ~2 lower than expected based on acetylene/CO emission ratios in urban areas (Borbon et al., 2013) and the acetylene/benzene ratio measured by the same GC-MS at BAO in winter 2011 (Gilman et al., 2013). This observed, but unknown low bias, was accounted for by calculating acetylene based on its correlation with CO during the 2010 CalNEX (Section 2.3.4.2) campaign in Pasadena, California (Borbon et al., 2013).

Each compound used to constrain base case simulations are listed in Table 2.1, along with their model treatment, OH reaction rate constants, and O&NG contribution factors (described

below). Comparisons between the observed and base case-model mixing ratios are also provided in Figure 2.13 to confirm that Case 1 simulations were appropriately constrained to observations.

Table 2.1. Model treatment, OH rate constant (298 K), and O&NG contribution factors for SONNE Chemical Observations

Compound	OH Rate Constant ($\times 10^{-12}$) ^a	Model Treatment	O&NG Factors (%) ^d
NO	9 ^b	Constrained to SONNE diel average of PSS mixing ratio, derived from measured NO _x	0 ^e
NO ₂	10 ^b	Constrained to SONNE diel average of PSS mixing ratio, derived from measured NO _x	0 ^e
O ₃	0.073 ^b	Initialized + Model Calculated	-
<i>Alkanes</i>			
Methane	0.0064	Constrained to SONNE observed diel average	75 ^f
Ethane	0.248	Constrained to SONNE observed diel average	72
Propane	1.09	Constrained to SONNE observed diel average	90
n-Butane	2.36	Constrained to SONNE observed diel average	95
iso-Butane	2.12	Constrained to SONNE observed diel average	93
n-Pentane	3.8	Constrained to SONNE observed diel average	96
iso-Pentane	3.6	Constrained to SONNE observed diel average	95
n-Hexane	5.2	Constrained to SONNE observed diel average	78
2-Methylpentane	5.2	Constrained to SONNE observed diel average	71
n-Heptane	6.76	Constrained to SONNE observed diel average	73
n-Octane	8.11	Constrained to SONNE observed diel average	63
n-Nonane	9.7	Constrained to SONNE observed diel average	46
n-Decane	11	Constrained to SONNE observed diel average	33
<i>Cycloalkanes</i>			
Cyclopentane	4.97	Lumped as n-Hexane	100
Methylcyclopentane	5.6 ^c	Lumped as n-Hexane	68
1,1-Dimethylcyclopentane	3.9 ^c	Lumped as n-Pentane	0 ^e
Cyclohexane	6.97	Constrained to SONNE observed diel average	67
Methylcyclohexane	9.64	Lumped as n-Nonane	72
Ethylcyclohexane	12 ^c	Lumped as n-Decane	49
Trans-1,2-Dimethylcyclohexane	11.8 ^c	Lumped as n-Decane	57
Cis-1,3-Dimethylcyclohexane	11.8 ^c	Lumped as n-Decane	57
Trans-1,3-Dimethylcyclohexane	11.8 ^c	Lumped as n-Decane	57
1,1,3-Trimethylcyclohexane	9.1 ^c	Lumped as n-Nonane	0 ^e
1-Ethyl-1-Methylcyclohexane	8.8 ^c	Lumped as n-Octane	0 ^e

Table 2.1 Continued

Aromatics			
Benzene	1.21	Constrained to SONNE observed diel average	32
Toluene	5.63	Constrained to SONNE observed diel average	31
Σ(m-,p-Xylene)	18.7	Constrained to SONNE observed diel average, 50% split between m- and p- isomers	23
o-Xylene	13.6	Constrained to SONNE observed diel average	20
Ethyl Benzene	7	Constrained to SONNE observed diel average	15
n-Propyl Benzene	5.8	Constrained to SONNE observed diel average	6.6
iso-Propyl Benzene	6.3	Constrained to SONNE observed diel average	17
1-Ethyl-2-methylbenzene	11.9	Constrained to SONNE observed diel average	0
1,3,5-Trimethylbenzene	56.7	Constrained to SONNE observed diel average	9.5
1,2,3-Trimethylbenzene	32.7	Constrained to SONNE observed diel average	0
1,2,4-Trimethylbenzene	32.5	Constrained to SONNE observed diel average	1.5
Σ(1-Ethyl-3,4-methylbenzene)	15.2	Constrained to SONNE observed diel average, 50% split between 3- and 4-methyl isomers	3.9
Styrene	58	Constrained to SONNE observed diel average	0
Alkenes and Alkynes			
Ethyne (Acetylene)	0.88	Constrained to SONNE observed diel average *2.65	0
Ethene	8.52	Constrained to SONNE observed diel average	8.6
Propene	26.3	Constrained to SONNE observed diel average	1.8
1-Butene	31.4	Constrained to SONNE observed diel average	0 ^e
1,3-Butadiene	66.6	Constrained to SONNE observed diel average	0 ^e
Aldehydes and Ketones			
Acetone	0.175	Initialized + Model Calculated	0 (13 ^g)
2-Butanone (Methyl Ethyl Ketone)	1.1	Initialized + Model Calculated	0 (33 ^g)
Acetaldehyde	15	Initialized + Model Calculated	0 (26 ^g)
Propanal	19.1	Initialized + Model Calculated	0 (28 ^g)
Butanal	23.7	Initialized + Model Calculated	0 (20 ^g)
2-Propenal (Acrolein)	20	Initialized + Model Calculated	0 ^e (6 ^g)
Formaldehyde	9.37	Initialized + Model Calculated	0 ^e
Alcohols			
Methanol	0.895	Constrained to SONNE observed diel average	0
Ethanol	3.2	Constrained to SONNE observed diel average	0
Biogenics			
Isoprene	100	Constrained to SONNE observed diel average	0
Methyl Vinyl Ketone	20	Constrained to SONNE observed diel average	0
Methacrolein	28.6	Constrained to SONNE observed diel average	0
α-Pinene	52.5	Constrained to SONNE observed diel average	0 ^e
β-Pinene	78.8	Constrained to SONNE observed diel average	0
3-Carene	88	Lumped as β-Pinene	0 ^e
Limonene	164	Constrained to SONNE observed diel average	0 ^e
Dimethyl Sulfide	4.84	Constrained to SONNE observed diel average	0
Alkyl Nitrates			
Ethyl Nitrate	0.18	Initialized + Model Calculated	0 ^e (29 ^g)
n-Propyl Nitrate	0.58	Initialized + Model Calculated	0 ^e (33 ^g)
iso-Propyl Nitrate	0.29	Initialized + Model Calculated	0 ^e (41 ^g)

^aunits are cm³ molecule⁻¹ s⁻¹; from literature (Atkinson, 2003; Atkinson & Aschmann, 1984; Atkinson & Arey, 2003), ^bcalculated by MCM, ^ccalculated with SAR principles and formulas found in Atkinson (1987), ^dreproduced from Gilman et al. (2013), ^enot reported in Gilman et al. (2013), assuming no O&NG influence, ^freproduced from Pétron et al. (2014), ^gModel-calculated difference between observed and removed O&NG VOC scenarios. Initialized with Case 1 mixing ratios, assuming no O&NG influence.

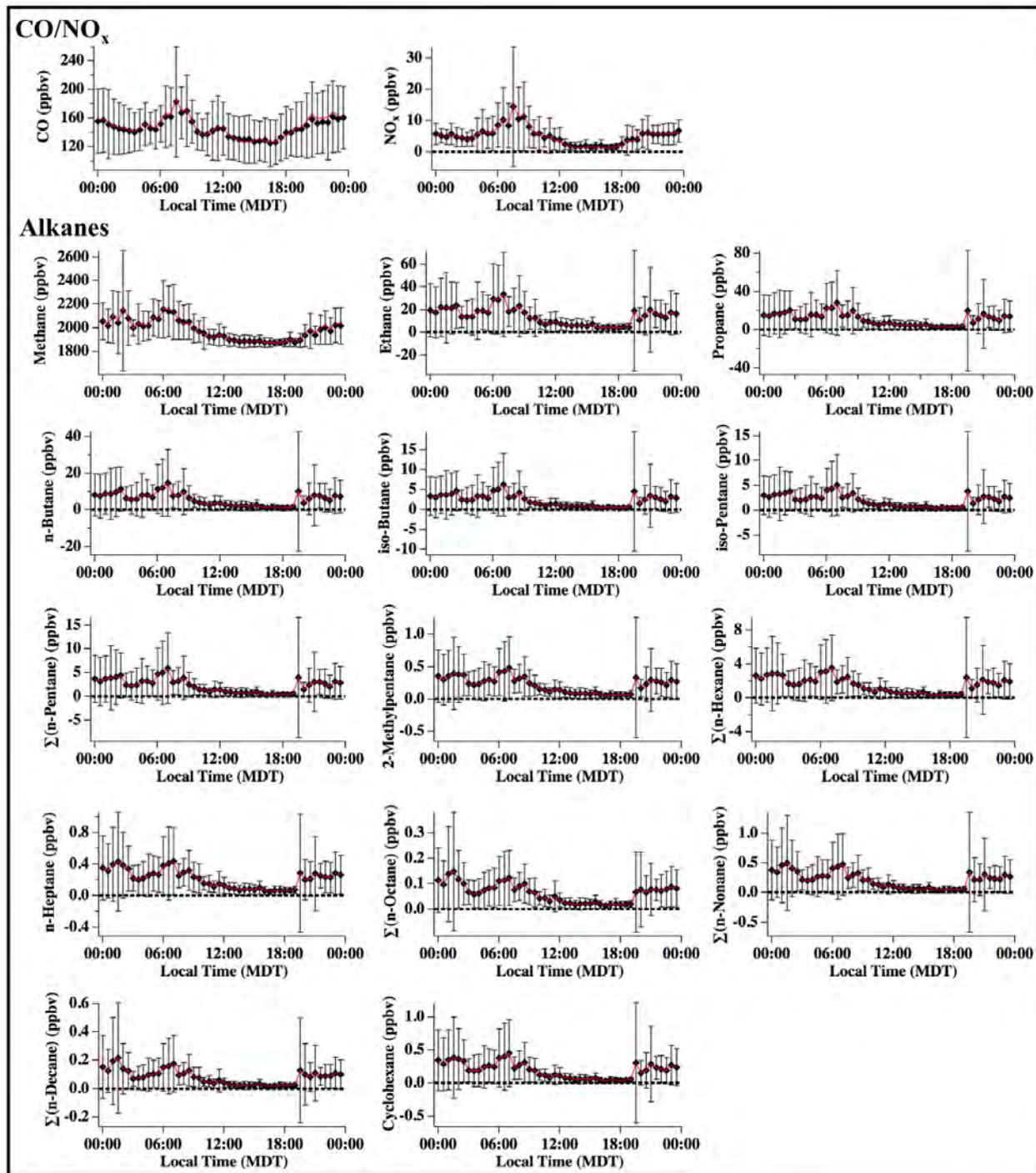


Figure 2.13. Diel averages of observed and modeled (case 1) chemical constraints (VOCs measured by Jessica Gilman and Brian Lerner, NO_x measured by Pete Edwards). $\Sigma(n\text{-Pentane}) = \Sigma(\text{n-Pentane} + 1,1\text{-Dimethylcyclopentane})$, $\Sigma(n\text{-Hexane}) = \Sigma(\text{n-Hexane} + \text{Cyclopentane} + \text{Methylcyclopentane})$, $\Sigma(n\text{-Octane}) = \Sigma(\text{n-Octane} + 1\text{-Ethyl-1-Methylcyclohexane})$, $\Sigma(n\text{-Nonane}) = \Sigma(\text{n-Nonane} + 1,1,3\text{-Trimethylcyclohexane} + \text{Methylcyclohexane})$, $\Sigma(n\text{-Decane}) = \Sigma(\text{n-Decane} + \text{Ethylcyclohexane} + \text{Trans-1,2-dimethylcyclohexane} + \text{Cis-1,3-Dimethylcyclohexane} + \text{Trans-1,3-Dimethylcyclohexane})$, $\Sigma(\beta\text{-Pinene}) = \Sigma(\beta\text{-Pinene} + 3\text{-Carene})$

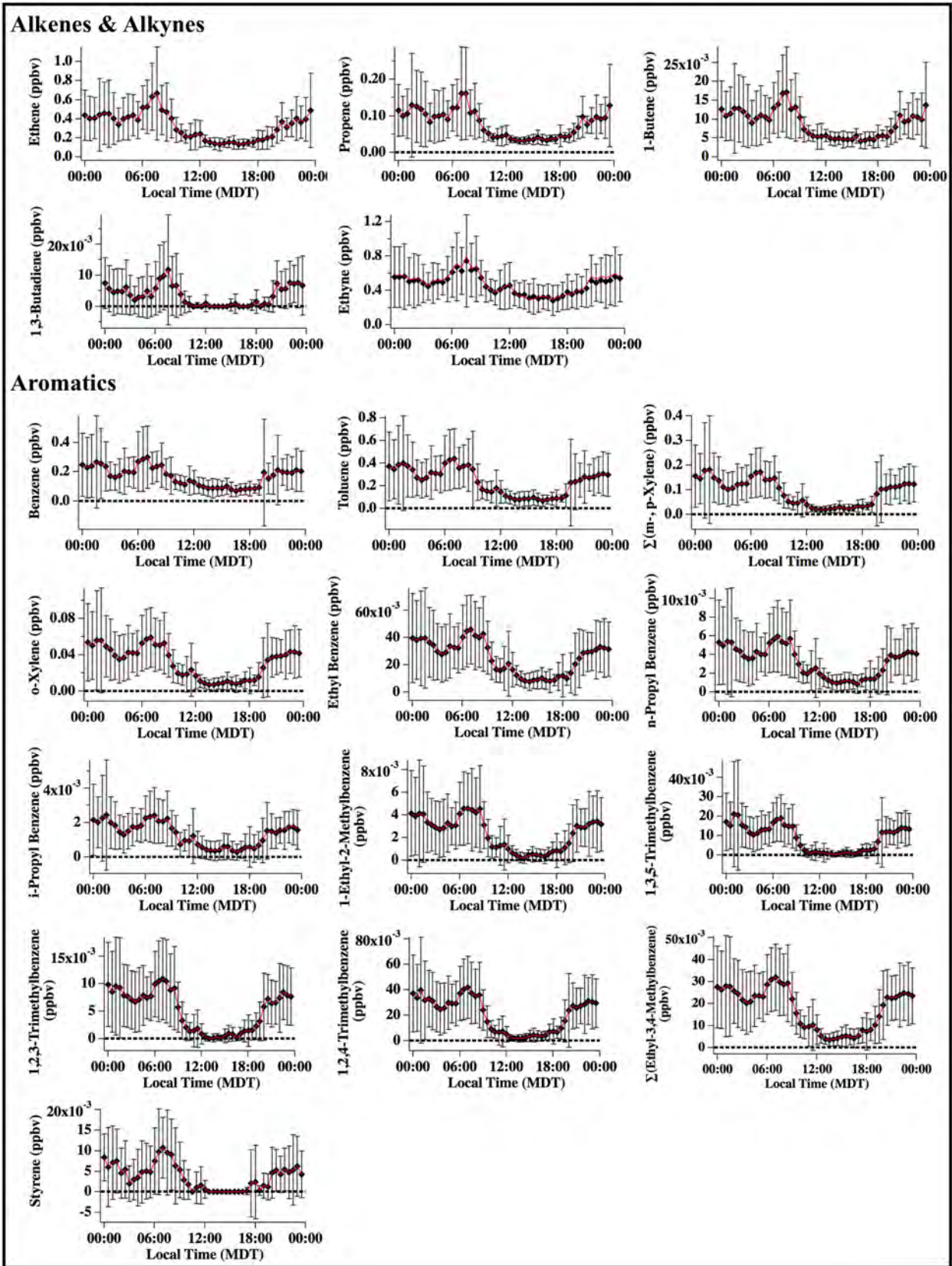


Figure 2.13. Continued

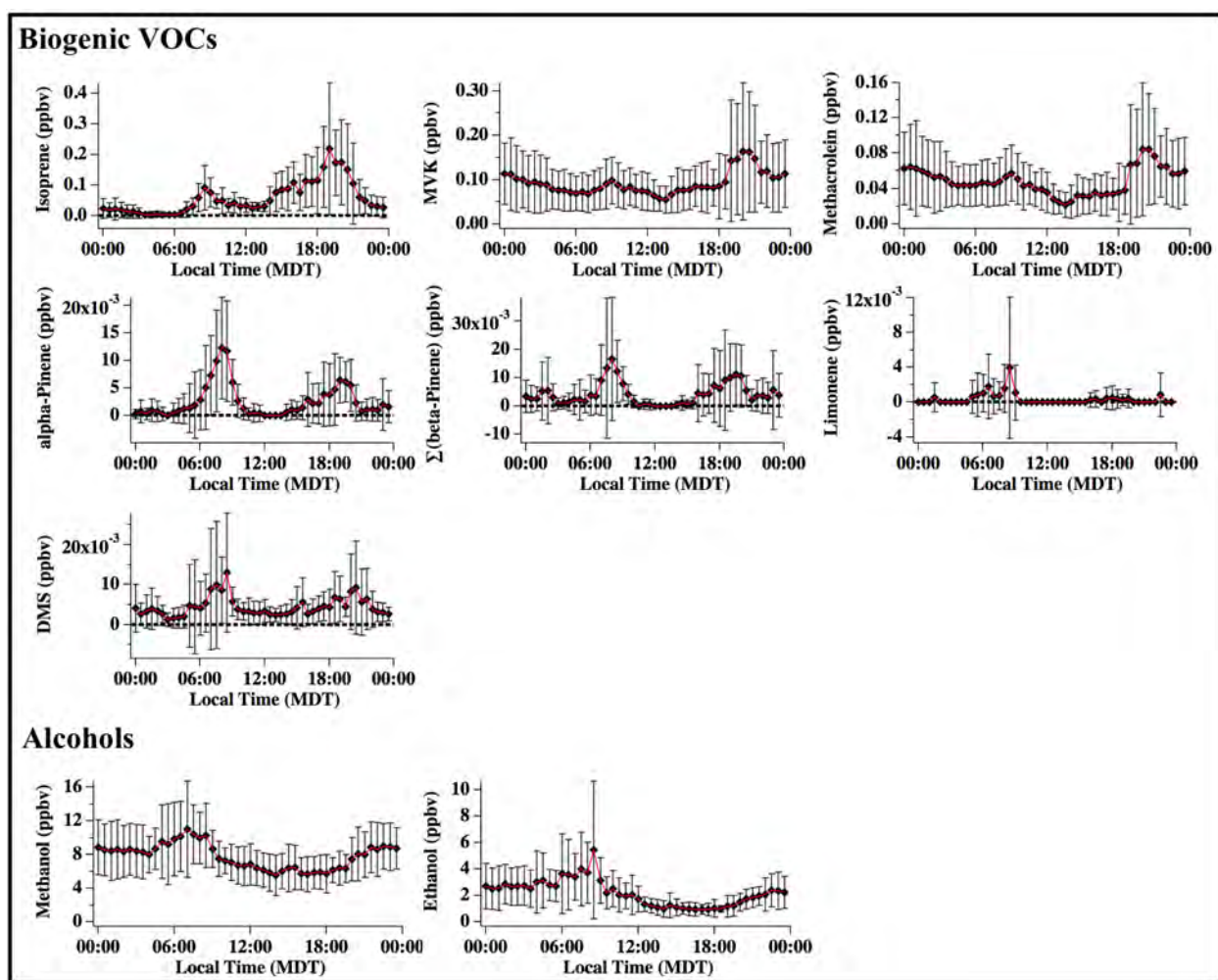


Figure 2.13. Continued

2.4.1.2.2 VOC Scenarios 2 and 3

The Case 2 VOC scenario was designed to represent the average chemical composition at BAO without primary O&NG VOCs. Similarly, the Case 3 VOC scenario was designed to represent the average BAO chemical composition with double the contribution of primary O&NG VOCs. To derive these VOC scenarios, speciated fractions of primary VOCs emitted from O&NG activity (derived by Gilman et al. (2013)) were either subtracted (for Case 2) or added (for Case 3) to base case diel average observations. For example, propane was reduced by 90% between Cases 1 and 2, as 90% of observed propane at BAO was attributed to O&NG emissions (Gilman et al., 2013).

Table 2.1 provides a full list of O&NG contribution factors for each chemical compound. Gilman et al. (2013) previously derived these factors for all non-methane VOCs by using a multivariate regression with O&NG (propane) and urban (acetylene) tracers measured at BAO during winter 2011. Oxygenated VOCs were not tightly correlated with either tracer during that analysis and were not assigned an O&NG factor by Gilman et al. (2013). In this analysis, the O&NG factors for these compounds were set to 0%, resulting in a conservative (lower limit) estimate for the attributed O&NG fraction of observed VOCs. In addition, 3 cycloalkanes, 2 alkenes, 1 aldehyde, 3 biogenic VOCs, and 3 alkyl nitrates measured during SONNE were not reported by Gilman et al. (2013) and were also assigned an O&NG contribution of 0%. The cycloalkanes likely have an O&NG source but minimally impact simulated O₃ due to their small mixing ratios (< 0.03 ppbv) and non-explicit representation in the MCM (discussed above). For all additional species measured but not explicitly represented in the MCM, factors were applied to each individual compound prior to lumping. As illustrated in Figure 2.14, primary O&NG emissions contributed to the majority of alkane OH reactivity (87%) and carbon mixing ratio (86%), but < 25% to all other VOC classes. For CH₄, Pétron et al. (2014) quantified the O&NG contribution in the Wattenberg Gas Field as 75% using a combination of aircraft CH₄ observations and a regional bottom-up emission inventory (derived from literature emission factors, Colorado State inventory data, and EPA reported facility-level emission estimates). Here, 75% was applied to the observed average diel profile of enhanced CH₄ (minus campaign background of 1814 ppbv).

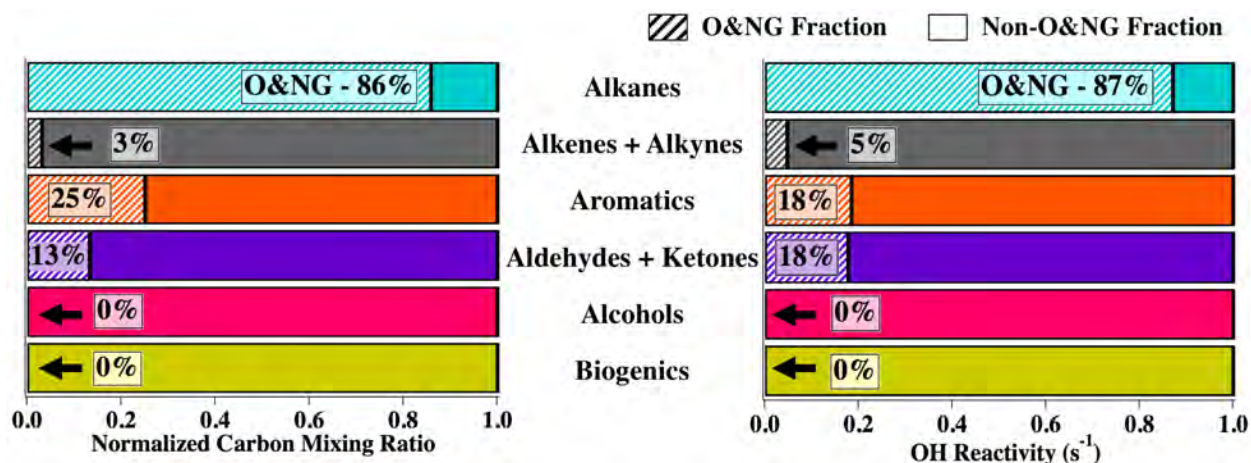


Figure 2.14. O&NG fraction of observed non-methane VOCs as a function of normalized carbon mixing ratio and VOC OH Reactivity. Note: Aldehydes and ketones were initialized with base case mixing ratios (assuming O&NG VOC Fraction = 0) and calculated by DSMACC in all simulations. The aldehyde and ketone O&NG fractions (OHR: 19%, ppbC: 13%) were derived from a comparison of the base case VOC scenario (Case 1) with the removed O&NG scenario (Case 2) at 2012 observed NO_x mixing ratios (VOC scenarios derived from work by Jessica Gilman).

2.4.1.3 Photolysis Rates

Photolysis rates in DSMACC are calculated by TUV using inputs for latitude, longitude, and Julian day to calculate solar zenith angle, as well as temperature, pressure altitude, total O₃ column, and albedo. The temperature input was constrained to the diel average profile of 10 m tower temperatures and altitude pressure was constrained to diel surface observations at the BAO site. A total O₃ column of 297.00 Dobson Units (DU) was derived from averaged OMI satellite data over the BAO site for July and August 2014. A broadband albedo measurement (0.28-0.735 μ m) of 0.067 was calculated from the average of literature values in the UV (< 0.415 μ m) reported over grassland (Feister & Grewe, 1995) and measurements in the visible (.415 μ m-.725 μ m) from a Multi-Filter Rotating Shadowband radiometer (Harrison et al., 1994; Michalsky & Hodges, 2013).

In all DSMACC simulations, TUV-calculated photolysis rates were scaled to observations of $j(\text{NO}_2)$, except for $j(\text{O}^1\text{D})$. Total $j(\text{NO}_2)$ and $j(\text{O}^1\text{D})$ photolysis rates (downwelling + upwelling

frequencies) were derived from comparisons of available 2014 downwelling $j(\text{NO}_2)$ (measured by Samuel Hall) to observations of $j(\text{NO}_2)$ and $j(\text{O}^1\text{D})$ made with a calibrated diffuse filter radiometer at BAO between 31 July and 9 August 2007, collected by Harald Stark. A diel average profile of total 2014 $j(\text{NO}_2)$ (Figure 2.15, left, dashed) was calculated from the ratio of the 2007 diel average profiles of downwelling and total $j(\text{NO}_2)$. A diel average profile of total 2014 $j(\text{O}^1\text{D})$ (Figure 2.15, right, dashed) was calculated by applying the 2007/2014 ratio of diel averaged downwelling $j(\text{NO}_2)$ to the 2007 diel averaged profile of total $j(\text{O}^1\text{D})$. DSMACC photolysis rates were scaled to match 2014-scaled TUV profiles (Figure 2.15, solid blue), which resulted in raw-TUV scaling factors of 1 for O_3 and 0.80 for all remaining photolysis reactions.

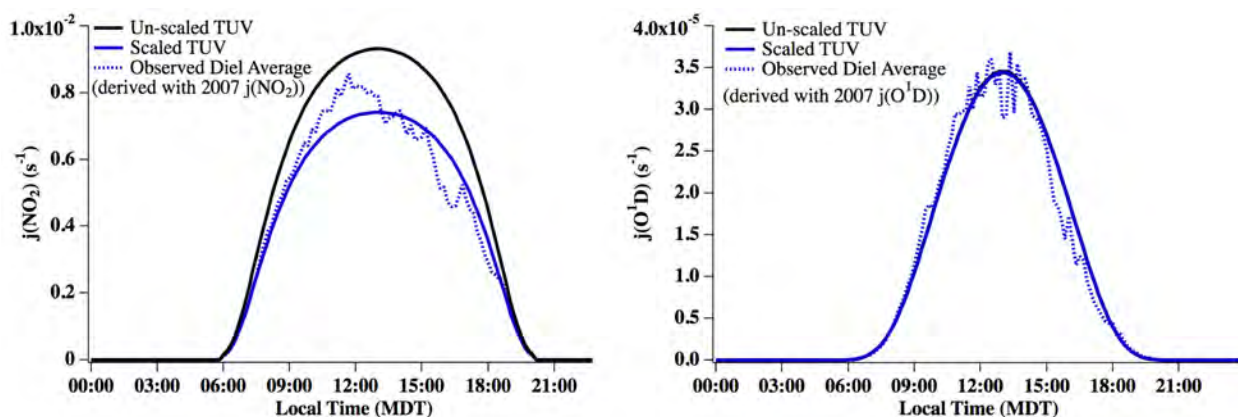


Figure 2.15. Total photolysis frequencies of (left) $j(\text{NO}_2)$ and (right) $j(\text{O}^1\text{D})$. Observed values (dashed) (measured by Samuel Hall), scaled TUV values (solid), and un-scaled TUV (black). All DSMACC model simulations in this analysis are scaled to 2014 (solid blue) photolysis profiles. The presence of high thunderstorm activity in 2014 is evident by the difference in shape between the afternoon $j(\text{NO}_2)$ observations and TUV profile, which assumes clear sky conditions.

2.4.1.4 Physical Loss

First order rate constants were used to simulate all non-chemical loss in the model from dilution and to a lesser extent, surface deposition. The MCM is inherently a gas phase chemical mechanism and no heterogeneous loss to aerosol surface was included. Dry deposition rates were included for O_3 ($k = 3.5 \times 10^{-6} \text{ s}^{-1}$) and HNO_3 ($k = 2.2 \times 10^{-5} \text{ s}^{-1}$), calculated from accepted literature

deposition velocities (O_3 : 0.8 cm/s, HNO_3 : 5 cm/s) (Finlayson-Pitts & Pitts, 2000) assuming a boundary layer height of 2.3 km.

An additional loss term, applied to all 4002 modeled compounds, was used to represent boundary layer dynamics in this zero-dimension framework. The work in this thesis focused on the production of O_3 in a single 24-hour simulation (O_3 production period typically 8 am - 3 pm MDT) (see Figure 3.11) and used one first-order rate constant to represent atmospheric dilution and mixing from the daily vertical expansion of the atmospheric boundary layer (typically 8 am - 12 pm MDT). Actual boundary layer growth varies day to day and this single dilution parameter can only capture its variation in an average sense. The dilution rate was varied to produce the best fit to 10 secondary products (O_3 , 6 oxygenated VOCs, 3 alkyl nitrates) between the hours of 11 am and 3 pm MDT (± 2 hours from solar noon). The dilution term is the only adjustable model parameter, and the fit produces a value of $1.11 \times 10^{-4} \text{ s}^{-1}$ (dilution time: ~ 2.5 hrs), with a resulting model-to-observation average deviation of -12.6% across all 10 secondary species (Table 2.2).

Background mixing ratios of these 10 compounds were added to the model at the same rate of dilution to account for entrainment and mixing with the residual layer during morning boundary layer growth. Background O_3 (58 ppbv) was calculated from campaign-averaged (FRAPPÉ) O_3 LIDAR data at altitudes between 500 m and 2 km during the morning hours of 8 am - 11 am MDT. This average represents the background O_3 mixing ratio of the lower free troposphere, as the boundary layer is typically less than 500 mAGL between 8-11 am MDT. Backgrounds of the remaining nine photochemically produced VOCs (Table 2.2) were derived from nighttime (12 am - 3 am MDT) averages of their average diel profiles. Comparisons of diel average observations ($\pm 1\sigma$) to simulated mixing ratios of the nine secondary VOCs for base (Case 1) simulations are shown in Figure 2.16.

Table 2.2. Statistics for 10 secondary compounds

Compound	Average Relative Deviation ((Model – Obs.) / Obs.) (%) ^a	Background Mixing Ratio ($\pm 1\sigma$) ^b
O ₃	-0.05	58 \pm 6 ppbv
Acetone	+13.7	2.174 \pm 0.0398 ppbv
Acetaldehyde	+18.0	605.8 \pm 19.3 pptv
Methyl Ethyl Ketone	-2.6	234.9 \pm 6.6 pptv
Propanal	-25.0	171.5 \pm 6.4 pptv
2-Propenal (Acrolein)	-30.9	54.7 \pm 3.3 pptv
Butanal	-38.4	35.8 \pm 1.6 pptv
iso-Propyl Nitrate	-17.0	8.5 \pm 0.7 pptv
Ethyl Nitrate	-6.9	3.8 \pm 1.1 pptv
n-Propyl Nitrate	-37.4	1.1 \pm 0.5 pptv

^aAverage relative deviation during 11 am - 3 pm MDT

^bDerived from 12 am - 3 am MDT diel averages. Background O₃ was derived from LIDAR measurements as described above

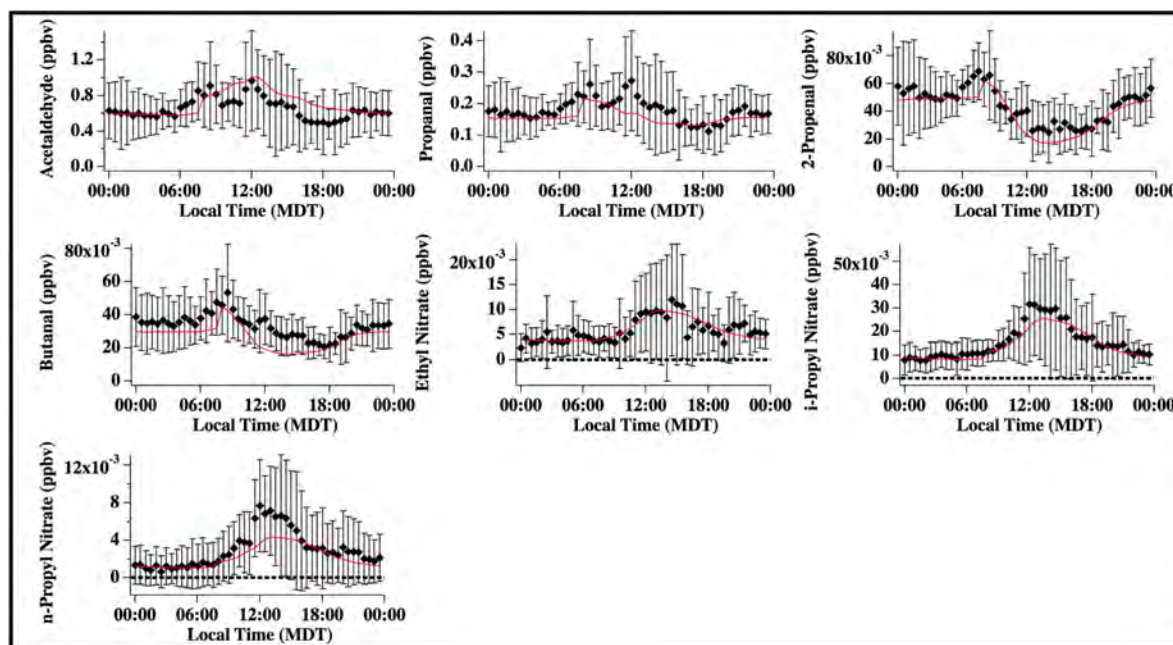


Figure 2.16. Diel profiles of nine secondary non-methane VOCs during SONNE (measured by Jessica Gilman). Black: 30-minute diel average observations ± 1 standard deviation, Red: Case 1 model output for simulations run with observed NO_x mixing ratios and a dilution rate of constant of $1.11 \times 10^{-4} \text{ s}^{-1}$.

2.4.1.5 Sensitivity Studies

To test the sensitivity of photochemical O₃ production to uncertainties in the model set-up and constraints described above, a series of 12 simulations were conducted. These simulations tested the change in base (Case 1) modeled maximum 24-hour photochemical O₃ to $\pm 10\%$ changes

in photolysis rates, albedo, temperature, background O₃, methane, and deposition rates. Results of these and additional tests conducted with Case 2 and 3 VOC constraint scenarios are discussed in Section 3.3.4.5 in terms of the impacts on Chapter 3 results.

2.4.1.6 DSMACC Updates from McDuffie et al., 2016

In the original simulations published in McDuffie et al. (2016), the DSMACC model calculated ambient number density concentrations from initial inputs of temperature (constrained to 2012 BAO tower 10 m diel profile) and pressure (constant 830 mbar) at 8am MDT. This single value was applied at each time step of the model (every 10 min) to calculate rate constants and VOC constraint concentrations from reported mixing ratios (described above). To more accurately capture diel changes in rate constants and VOC concentrations, DSMACC was updated to calculate ambient number density at each 10 minute time step throughout the entire 24 -hour simulation. All DSMACC results presented in this thesis are from simulations with this update. Many of these updated simulations have also been reported in Ramboll Environ (2017).

2.4.2 Box Model for Nocturnal N₂O₅ Uptake and ClNO₂ Production

For analyses presented in Chapters 4-6, I have developed a zero-dimensional box model for use in IGOR Pro, that simulates the nocturnal chemical evolution of an air parcel and iteratively fits to chemical observations of NO₂, O₃, N₂O₅, and ClNO₂ to quantitatively derive the N₂O₅ uptake coefficient and yield of ClNO₂. The original version of this model is described in Wagner et al. (2013), and was originally developed to simulate wintertime nocturnal chemistry at the BAO tower in Colorado. The model has been significantly altered here for use with aircraft data from the WINTER and UWFPS campaigns. Model set-up details and sensitivity study results are provided in this chapter with model results and discussions of additional model limitations presented in Chapters 4 - 6. The IGOR Pro code for this model can be found online at the NOAA Chemical

Sciences Division Website at: <https://www.esrl.noaa.gov/csd/groups/csd7/measurements/2015winter/pubs/>. The majority of content in this section has been adapted from the main text and supplemental information of McDuffie et al. (2018): Heterogeneous N₂O₅ uptake during winter: Aircraft measurements during the 2015 WINTER campaign and critical evaluation of current parameterizations, and McDuffie et al, (2018) *in Prep*: ClNO₂ yields from aircraft measurements during the 2015 WINTER campaign and critical evaluation of current parameterizations.

2.4.2.1 Overview and Set-Up

The original model described in Wagner et al. (2013) has been adapted here to simulate the nocturnal chemical evolution of an air parcel in the residual layer (RL), assuming constant temperature and relative humidity, from the onset of nocturnal chemistry (1.3 hours prior to sunset or time of NO_x emission, described below), until the time of aircraft measurement. Nighttime data were defined as periods of time with solar zenith angle (SZA) greater than 90°, calculated from aircraft GPS location and time.

This model follows three main iterative steps (Figure 2.17), fitting final simulated mixing ratios to observations of NO₂, O₃, N₂O₅, and ClNO₂ to derive the first-order loss rate coefficient of N₂O₅ ($k_{N_2O_5} = k_{2.5} + k_{2.6} [s^{-1}]$) and production rate coefficient of ClNO₂ ($k_{ClNO_2} = k_{2.6} [s^{-1}]$), as the numeric solutions to a series of initialized, first-order differential equations. For WINTER analyses, these equations represent the 14 chemical reactions and 15 species shown in Table 2.3, chosen to represent the simplest set of reactions that accurately describe the inorganic chemistry of nitrogen oxides and ozone in the wintertime RL.

As shown in Figure 2.17, the first step initializes $k_{N_2O_5}$ with a value of $1 \times 10^{-4} s^{-1}$, k_{ClNO_2} with a value of $0 s^{-1}$ and holds each constant while iteratively adjusting the initial concentrations of NO₂ (or NO) and O₃ until the final simulated mixing ratios are within 0.5% of the observed

values. The correlations and color scales in panels e and f of Figure 2.17 show that initial concentrations of NO_x and O_3 at sunset, derived from the WINTER campaign (y-axis), have a similar level of variability as the final observed mixing ratios (x-axis) and that changes between initial and final concentrations are strongly dependent on the simulation duration (as expected). Combined, panels a, b, e, and f show that both species slowly decrease at night with reductions in mixing ratios from sunset until measurement typically less than a factor of 4 for NO_x and always less than 30% for O_3 . The second model step holds these derived-initial concentrations constant while iteratively adjusting $k_{\text{N}_2\text{O}_5}$ until the simulated N_2O_5 mixing ratio is within 1% of the aircraft observations. Steps 1 and 2 are repeated until NO_2 , O_3 , and N_2O_5 simultaneously meet their respective fit criteria (i.e. 0.5% for O_3 and NO_2 and 1% for N_2O_5). The third step holds all derived parameters constant while iteratively adjusting k_{ClNO_2} until the final simulated mixing ratio of ClNO_2 is within 1% of observations. For WINTER and UWFPS, this process was repeated with a 10-second resolution during all flights with $\text{SZA} > 90^\circ$. Although most chemical measurements were collected at a 1-Hz resolution, data were averaged to 10-seconds to improve the model's computational efficiency and reduce scatter in the $\gamma(\text{N}_2\text{O}_5)$ and $\phi(\text{ClNO}_2)$ products, while maintaining their spatial resolution of $\sim 1\text{-}10$ km. Due to the multiple measurements of nitrogen oxides, O_3 , and aerosol nitrate during WINTER, instrument-specific observations used as fit parameters varied by flight and are listed in Table 2.7. Correlation plots of all overlapping measurements (see Section 2.4.2.7) indicate agreement to within 12% for all species.

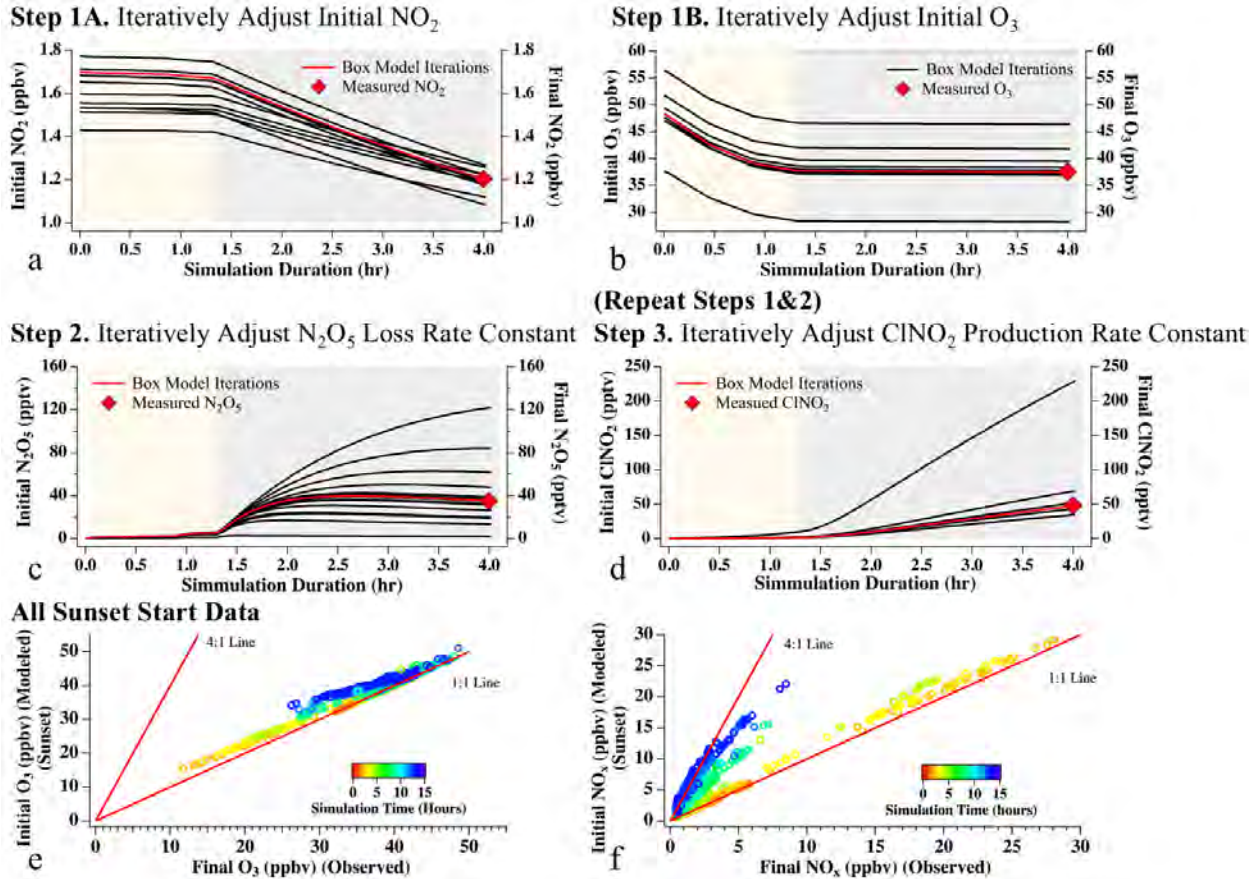


Figure 2.17. (a-d) Box model iterative steps for an example point off-shore of South Carolina during flight RF04. The air was calculated to be older than the time since sunset and the simulation start time was set to 1.3 hours prior to sunset (as indicated by the gray/yellow shading). Black traces are individual, iterative model simulations while red traces show the derived simulation that simultaneously predicts measured mixing ratios (red diamonds) within designated thresholds as described in the main text. For this point, the derived $\gamma(\text{N}_2\text{O}_5)$ was 0.021 and $\phi(\text{ClNO}_2)$ was 22.7%. (e-f) Correlations of model-derived initial O_3 (e) and NO_x (f) mixing ratios at sunset (sunset start points only ($N = 2003$)) against observed mixing ratios, colored by simulation duration. Red lines are reference lines with slopes of 1 and 4.

Model-derived values for $k_{\text{N}_2\text{O}_5}$ and k_{ClNO_2} were then used in Equations E4.5 and E4.6, with aircraft observations of aerosol surface area density (SA) ($< 3\mu\text{m}$ diameter) and the mean molecular speed of N_2O_5 (c) to calculate $\gamma(\text{N}_2\text{O}_5)$ and $\phi(\text{ClNO}_2)$ for every 10 second period. Additional model details, limitations, and sensitivity studies are provided in the following sections.

2.4.2.2 Model Mechanism

As noted above, the chemical mechanism implemented in this model consists of 14 chemical reactions and 15 compounds. This limited set of reactions is sufficient to provide an accurate representations of inorganic reactive nitrogen chemistry in the wintertime residual layer. A discussion of mechanism details and uncertainties is provided below.

Table 2.3. Box Model Chemical Mechanism

	Reactants	Products	Rate Coefficient Expression	Reference/Source
R2.4	NO ₂ + O ₃	→ NO ₃ + O ₂	$k_{2.4} = 1.4 \times 10^{-13} e^{(-2470/Temp)}$ [cm ³ molecule ⁻¹ s ⁻¹]	IUPAC 2012
R2.1f	NO ₃ + NO ₂	→ N ₂ O ₅	$k_{2.1f} = (k_0/k_\infty) * F / (k_0 + k_\infty)$ [cm ³ molecule ⁻¹ s ⁻¹] ^a	IUPAC 2012
R2.1r	N ₂ O ₅	→ NO ₃ + NO ₂	$k_{2.1r} = (k_0/k_\infty) * F / (k_0 + k_\infty)$ [cm ³ molecule ⁻¹ s ⁻¹] ^b	IUPAC 2012
R2.5	N ₂ O ₅ + aerosol	→ 2 HNO ₃	$k_{2.5} = k_{HNO_3}$ [s ⁻¹]	Model Derived
R2.6	N ₂ O ₅ + aerosol	→ HNO ₃ + ClNO ₂	$k_{2.6} = k_{ClNO_2}$ [s ⁻¹]	Model Derived
R2.7	NO ₃ + VOC	→ Products	$k_{2.7} = k_{VOC}$ [s ⁻¹]	Measured ^c
R2.8	NO ₃ + HO ₂	→ NO ₂ + OH + O ₂	$k_{2.8} = k_{HO_2} = 1.2 \times 10^{-4}$ [s ⁻¹]	(Stone et al., 2014) ^c
R2.3	NO ₃ + NO	→ 2 NO ₂	$k_{2.3} = 1.80 \times 10^{-11} e^{(110/Temp)}$ [cm ³ molecule ⁻¹ s ⁻¹]	IUPAC 2008
R2.2	NO + O ₃	→ NO ₂ + O ₂	$k_{2.2} = 2.07 \times 10^{-12} e^{(-1400/Temp)}$ [cm ³ molecule ⁻¹ s ⁻¹]	IUPAC 2013
R2.9	O ₃ + hv	→ O + O ₂	$k_{2.9} = j(O^1D)$	Measured
R2.1	NO ₂ + hv	→ NO + O	$k_{2.10} = j(NO_2)$	Measured
0				
R2.1	NO ₃ + hv	→ NO ₂ + O	$k_{2.11} = j(NO_3)$	Calculated ^c
1				
R2.1	N ₂ O ₅ + hv	→ NO ₂ + NO ₃	$k_{2.12} = j(N_2O_5)$	Measured
2				
R2.1	ClNO ₂ + hv	→ Cl + NO ₂	$k_{2.13} = j(ClNO_2)$	Measured
3				

^a $k_0 = 3.6 \times 10^{-30} * M * (Temp/300)^{-4.1}$, $k_\infty = 1.9 \times 10^{-12} * (Temp/300)^{0.2}$, $KR = k_0/k_\infty$, $NC = 0.75 - 1.27 * \log_{10}(0.35)$, $F = 10^{(\log_{10}(0.35)/(1 + \log_{10}(KR/NC)^2))}$, $M = \text{Pressure [mbar]} \times 1 \times 10^{-4} / (k_b * Temp)$

^b $k_0 = 1.3 \times 10^{-3} * M * (Temp/300)^{-3.5} e^{(-11000/Temp)}$, $k_\infty = 9.7 \times 10^{14} * (Temp/300)^{0.1} e^{(-11080/Temp)}$, $KR = k_0/k_\infty$, $NC = 0.75 - 1.27 * \log_{10}(0.35)$, $F = 10^{(\log_{10}(0.35)/(1 + \log_{10}(KR/NC)^2))}$

^cDescribed in this section

As noted in previous studies, large uncertainties in mechanisms of nocturnal chemistry arise from uncertainties in NO₃ loss reactions (e.g. Phillips et al., 2016; Wagner et al., 2011). In the absence of photochemical radical production, NO₃ serves as one of the primary nocturnal tropospheric oxidants for volatile organic compounds (VOCs). NO₃ also reacts with RO₂ and HO₂ radicals, which can contribute to nocturnal NO_x recycling (Vaughan et al., 2006). In this analysis, NO₃-VOC oxidation reactions were lumped and treated as a net NO_x sink (R2.7) with a rate

constant ($k_{VOC} = k_{2.7} [s^{-1}]$), defined in the WINTER analysis as the sum of speciated VOC concentrations, multiplied by their individual NO_3 -VOC reaction rate constants (Table 2.4). For each WINTER flight, k_{VOC} was calculated for every 10 second period using TOGA VOC and PICARRO methane (CH_4) and CO observations aboard the C-130 aircraft. The 35-second TOGA measurements were interpolated and expanded to match the 1-Hz resolution of NO_2 , O_3 , N_2O_5 , and $ClNO_2$ gas-phase measurements. Methane and CO were measured and reported at 1-Hz. Observations below the instrumental detection limits were set to zero for the k_{VOC} calculation. For WINTER flights with available measurements, the average k_{VOC} ranged from 1.3×10^{-4} to $4.6 \times 10^{-4} s^{-1}$ for data below 1000 mAGL (Table 2.5) with a combined average contribution of 30% from CH_4 and CO. The rate constant for the $NO_3 + CO$ reaction in Table 2.4 was reduced to a value of $4.9 \times 10^{-20} cm^3 molec^{-1} s^{-1}$ (*personal communication, A. R. Ravishankara*) for the simulations of $\phi(ClNO_2)$, presented in Chapter 5. This reduction had a minimal influence on the resulting data products with $\ll 1\%$ change in both $\gamma(N_2O_5)$ and $\phi(ClNO_2)$ in the updated simulations.

Table 2.4. NO₃ + VOC Reactions and Rate Equations

VOC	A Factor (10 ⁻¹⁴ cm ³ s ⁻¹)	B Factor	Reference
Alkanes			
CH ₄	0.0001	0	(Atkinson & Arey, 2003)
Propane	0.007	0	(Atkinson & Arey, 2003)
<i>iso</i> -Butane	305	3060	(Atkinson & Arey, 2003)
<i>n</i> -Butane	276	3279	(Atkinson & Arey, 2003)
<i>iso</i> -Pentane	299	2927	(Atkinson & Arey, 2003)
<i>n</i> -Pentane	0.0087	0	(Atkinson & Arey, 2003)
2-Methyl Pentane	0.018	0	(Atkinson & Arey, 2003)
3-Methyl Pentane	0.022	0	(Atkinson & Arey, 2003)
<i>n</i> -Hexane	0.011	0	(Atkinson & Arey, 2003)
<i>n</i> -Heptane	0.015	0	(Atkinson & Arey, 2003)
Alkenes			
∑(<i>iso</i> , 1-Butene)	31.4 ^a	938	(Atkinson & Arey, 2003)
Aromatics			
Benzene	0.003	0	(Atkinson & Arey, 2003)
Toluene	0.007	0	(Atkinson & Arey, 2003)
∑(Ethylbenzene, m, p-Xylene)	0.045 ^b	0	(Atkinson & Arey, 2003)
<i>o</i> -Xylene	0.041	0	(Atkinson & Arey, 2003)
1,2,4-Trimethylbenzene	0.18	0	(Atkinson & Arey, 2003)
1,2,3-Trimethylbenzene	0.19	0	(Atkinson & Arey, 2003)
Biogenics			
Isoprene	315	450	(Atkinson & Arey, 2003)
MVK	0.06	0	(Atkinson & Arey, 2003)
MACR	0.34	0	(Atkinson & Arey, 2003)
α-pinene	119	-490	(Atkinson & Arey, 2003)
β-pinene	251	0	(Atkinson & Arey, 2003)
∑(Limonene, Carene)	1065 ^c	0	(Atkinson & Arey, 2003)
Camphene	66	0	(Atkinson & Arey, 2003)
DMS	19	-520	(Atkinson & Arey, 2003)
MBO	4.6	400	(Atkinson & Arey, 2003)
Alcohols			
Methanol	94	2650	(Atkinson & Arey, 2003)
Ethanol	0.2	0	(Atkinson & Arey, 2003)
Ketones			
Acetone	0.003	0	(Atkinson & Arey, 2003)
MEK	0	0	
Aldehydes			
Acetaldehyde	140	1860	(Atkinson & Arey, 2003)
Propanal	0.65	0	(Atkinson & Arey, 2003)
Acrolein	17.2	1190	(Atkinson & Arey, 2003)
Butanal	170	1500	(Atkinson & Arey, 2003)
Formaldehyde	0.056	0	(Atkinson & Arey, 2003)
Other			
CO	0.00004	0	(Hjorth et al., 1986)
HO ₂	400	0	(IUPAC, 2008a)

^aCalculated as 1-butene, ^bAverage A Factor of Ethylbenzene and m,p-Xylene, ^cAverage A Factor of d-limonene and carene

Table 2.5. Measured k_{VOC} by flight. All units are in s^{-1} .

k_{VOC} ^a	RF01	RF03	RF04	RF05	RF08
Average	2.5×10^{-4}	1.4×10^{-4}	4.6×10^{-4}	1.4×10^{-4}	1.3×10^{-4}
Median	1.8×10^{-4}	1.3×10^{-4}	2.1×10^{-4}	1.3×10^{-4}	1.3×10^{-4}
Minimum	3×10^{-5}	1×10^{-4}	1.2×10^{-4}	6×10^{-5}	3×10^{-5}
Maximum	1.03×10^{-3}	2.7×10^{-4}	4.62×10^{-3}	3.1×10^{-4}	4.9×10^{-4}

^aIncludes CH₄ and CO contributions

For WINTER flights without TOGA and/or PICARRO measurements, k_{VOC} was calculated from the average contributions from flights with measurements, based on their relative geographic locations (see Table 2.6). For example, the average VOC contribution from RF04 was applied to flights RF07, RF09, and RF10 due to RF04 being the only continental night flight with available TOGA measurements. This method of estimation was necessary for the box model calculations but reduces the spatial and temporal variability of k_{VOC} and introduces uncertainty into the box model analyses for these flights.

Table 2.6. Estimation method of k_{VOC} for WINTER flights without TOGA and/or PICARRO measurements

Flight	VOC contribution to k_{VOC}	CO and CH ₄ contribution to k_{VOC}
RF06	Measured by TOGA	Single value, campaign average ($5.7 \times 10^{-5} s^{-1}$)
RF07	Single value, RF04 average ($4.6 \times 10^{-4} s^{-1}$)	Measured by PICARRO
RF09	Single value, RF04 average ($4.6 \times 10^{-4} s^{-1}$)	Measured by PICARRO
RF10	Single value, RF04 average ($4.6 \times 10^{-4} s^{-1}$)	Measured by PICARRO
RF11	Single value, RF05 average ($1.4 \times 10^{-4} s^{-1}$)	Measured by PICARRO

Due to a lack of radical measurements during WINTER, the first-order NO₃ loss rate constant for the NO_x recycling reaction with HO₂ ($k_{HO_2} = k_{2.8} [s^{-1}]$) (R2.8) was estimated from the second order NO₃ + HO₂ reaction rate constant (IUPAC, 2008b) and HO₂ concentrations from 2011 over the UK (Stone et al., 2014), which are the most recently reported aircraft observations of HO₂ in the wintertime RL, over a populated region in the Northern Hemisphere. Reported HO₂ measurements suffered from a small RO₂ interference and were defined as $1.15 \cdot HO_2 + 2 \times 10^5$ molec/cm³ (Stone et al., 2014). As calculated here, k_{HO_2} accounted for 19-50% (36% average) of

the modeled NO_3 loss rate constant ($k_{\text{NO}_3} = k_{\text{HO}_2} + k_{\text{VOC}}$), though the overall modeled loss through NO_3 was a relatively small fraction of the total combined loss from N_2O_5 and NO_3 (11.5% average, see Section 2.4.2.7.10). Calculated rate constants for both R2.7 and R2.8 were treated as constants throughout each simulation duration, which has the potential to add variability to the $\gamma(\text{N}_2\text{O}_5)$ and $\phi(\text{ClNO}_2)$ results since VOC reactivity is likely to decrease with time via depletion of reactive VOCs. NO_3 reactions with RO_2 were not explicitly included in this mechanism due to a lack of wintertime RO_2 aircraft field measurements. If this treatment were to result in k_{NO_3} values greater than the upper bound of the uncertainty already considered (discussed in Chapters 4 and 5), derived $\gamma(\text{N}_2\text{O}_5)$ values would be reduced and $\phi(\text{ClNO}_2)$ values increased.

Direct NO_3 uptake was also excluded from the mechanism since reported NO_3 uptake coefficients are generally small on inorganic aerosol ($\gamma(\text{NO}_3) \sim 10^{-3}$ (reviewed in Brown & Stutz, 2012)), which dominated the WINTER aerosol composition (Figure 4.11). Some analyses however, have suggested larger values of uptake onto organic surfaces (Mao et al., 2013; Ng et al., 2017). Previous observation, laboratory, and modeling-based studies have suggested that NO_3 uptake only accounts for 0.4-17% of the total NO_3 loss budget (Aldener et al., 2006; Moise et al., 2002; Sommariva et al., 2009; Wong & Stutz, 2010) and based on typical WINTER conditions, an NO_3 uptake coefficient of 0.1 would double the typical k_{NO_3} , which would decrease the median derived $\gamma(\text{N}_2\text{O}_5)$ by 10% and increase $\phi(\text{ClNO}_2)$ values by < 30%, based on the k_{NO_3} sensitivity test (Section 2.4.2.7.10). As a result of the multiple sources of uncertainty, k_{NO_3} calculated here is likely a lower limit. The box model, however, displayed a small sensitivity to k_{NO_3} (Table 3.4). Therefore, more explicit treatment of NO_3 chemistry was not required for this mechanism to accurately simulate nocturnal N_2O_5 chemistry during WINTER in the RL.

Due to a lack of aircraft and ground-based VOC measurements during the UWFPS study, a constant k_{VOC} value of $2 \times 10^{-4} \text{ s}^{-1}$ was used for UWFPS simulations. This value is based on average WINTER k_{VOC} values and previous measurements of k_{VOC} during the winter season in Colorado (Wagner et al., 2013). The same assumptions as WINTER simulations were made for reactions of NO_3 with HO_2 and RO_2 during UWFPS.

Additional N_2O_5 loss through direct homogeneous (i.e. gas phase) hydrolysis with water vapor (Mentel et al., 1996; Wahner et al., 1998a) was not included in the mechanism. Results from environmental simulation chamber experiments have proposed an additional N_2O_5 loss process through homogeneous hydrolysis with water vapor (Mentel et al., 1996; Wahner et al., 1998a) as parameterized by the first order loss rate constant k_{Homo} in E2.8 - E2.10. The equations were derived from laboratory / chamber data at a single temperature and may not be applicable to the colder temperatures encountered during WINTER and UWFPS. Estimates of k_{Homo} for the WINTER campaign are shown in comparison to derived total $k_{\text{N}_2\text{O}_5}$ rate constants in Figure 2.18. Low absolute water vapor at colder temperatures leads to values of $k_{Homo} \sim 10 \times$ lower than total $k_{\text{N}_2\text{O}_5}$ during WINTER, suggesting this reaction pathway is a minor contributor to N_2O_5 loss relative to heterogeneous uptake. Previous field studies have also shown that E2.8 - E2.10 likely over-predicts k_{Homo} (e.g. Brown et al., 2009) at temperatures near 290 K. Over-prediction of the lowest derived WINTER $k_{\text{N}_2\text{O}_5}$ values may also suggest that current parameterizations of k_{Homo} are over-predictions of the $\text{N}_2\text{O}_5 + \text{H}_2\text{O}$ rate constant. This result is consistent with parameterized values exceeding the smallest WINTER loss rate constants (Figure 2.18), and also suggests that homogeneous loss is a minor contributor to total N_2O_5 loss, derived from the box model.

$$k_{Homo} = k_I[\text{H}_2\text{O}] + k_{II}[\text{H}_2\text{O}]^2 \quad (2.8)$$

$$k_I = 2.5 \times 10^{-22} \text{ cm}^3 \text{ molecule}^{-1} \text{ s}^{-1} \quad (2.9)$$

$$k_{II} = 1.8 \times 10^{-39} \text{ cm}^6 \text{ molecule}^{-2} \text{ s}^{-1} \quad (2.10)$$

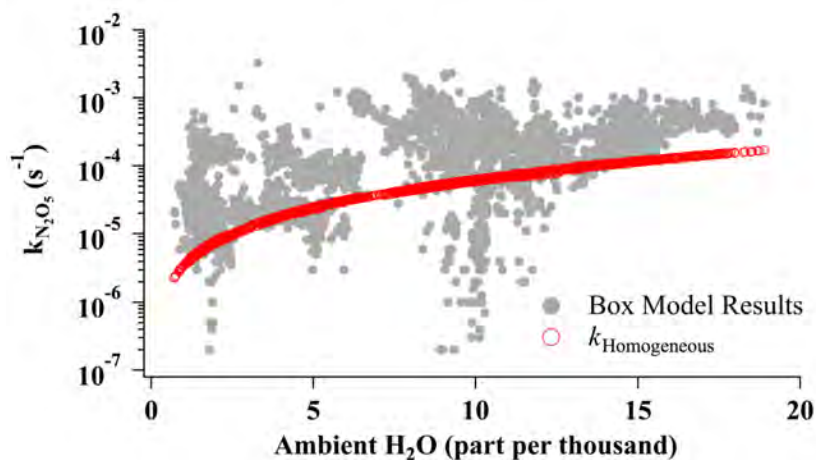


Figure 2.18. Comparison of box-model derived $k_{N_2O_5}$ and calculated k_{Homo} as a function of ambient water vapor for WINTER.

Though box model simulations primarily focused on nocturnal chemical reactions, photolysis reactions were included for NO_2 , O_3 , NO_3 , N_2O_5 , and $ClNO_2$ in the 1.3 hours prior to sunset (discussed in the next section) in order to account for photochemical reactions. During this time, the model integration period was split into three steps and photolysis rates were calculated as a function of time before sunset, using exponential fits to averaged WINTER observations of photolysis frequencies (Figure 2.19, red lines). Averages were used for consistency amongst flights without photolysis data. Photolysis rates for $j(NO_2)$, $j(O^1D)$, $j(N_2O_5)$ and $j(ClNO_2)$ were calculated from actinic flux measurements from the NCAR HARP-AF. For the $\gamma(N_2O_5)$ analysis presented in Chapter 4, $j(NO_3)$ was derived from a multivariate fit of $j(NO_3)$ to $j(NO_2)$ and SZA measured aboard the NOAA P-3 aircraft during the 2010 CalNEX campaign (Ryerson et al., 2013) (Figure 2.20). The multivariate fit of $j(NO_3)$ was limited to SZAs between 75 and 100° to capture the photolysis profile shape within two hours of sunset and reproduces measured CalNEX $j(NO_3)$ frequencies within 4%. For the $\phi(ClNO_2)$ analysis presented in Chapter 5, the model was updated to run with 30-40% reductions in $j(ClNO_2)$ values (based on an update to the JPL recommendation)

and $j(\text{NO}_3)$ values calculated from a re-analysis of WINTER actinic flux measurements (Figure 2.21). Similar to the updated k_{VOC} calculation, the model had minimal sensitivity to changes in $j(\text{NO}_3)$ values ($< 0.3\%$ in median $\gamma(\text{N}_2\text{O}_5)$). Yields of ClNO_2 , however, were slightly more sensitive to the reduction in the $j(\text{ClNO}_2)$ values, with a reduction in median $\phi(\text{ClNO}_2)$ of 3% in the updated simulations.

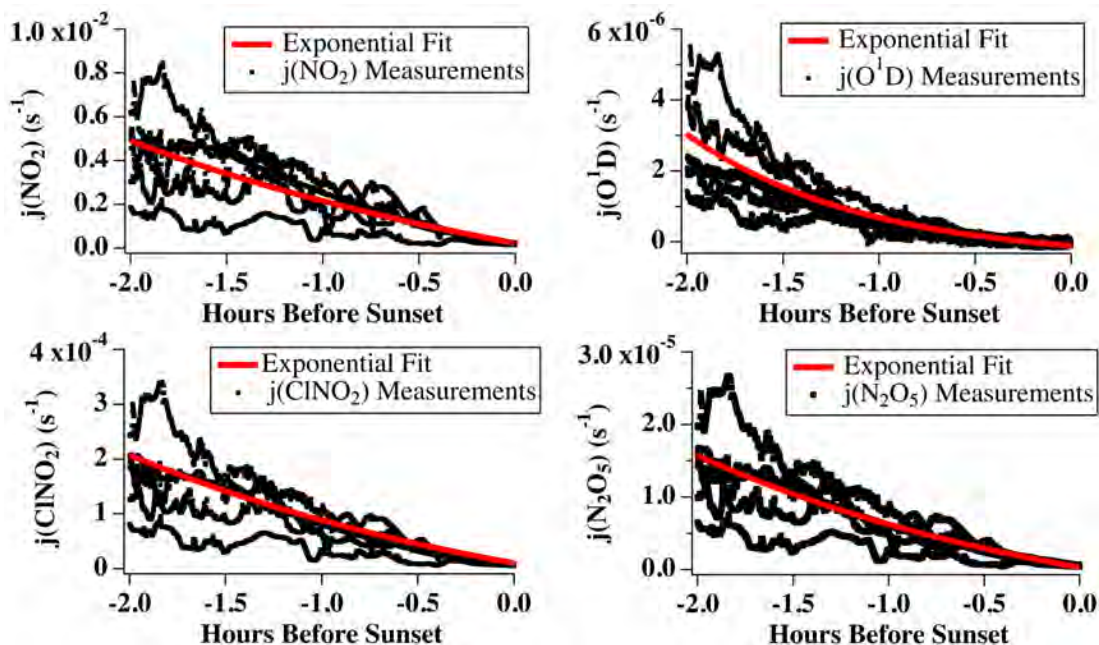


Figure 2.19. Measured photolysis rates for all day-into-night WINTER flights. Red lines: Exponential fits used to calculate photolysis rates for the iterative box model.

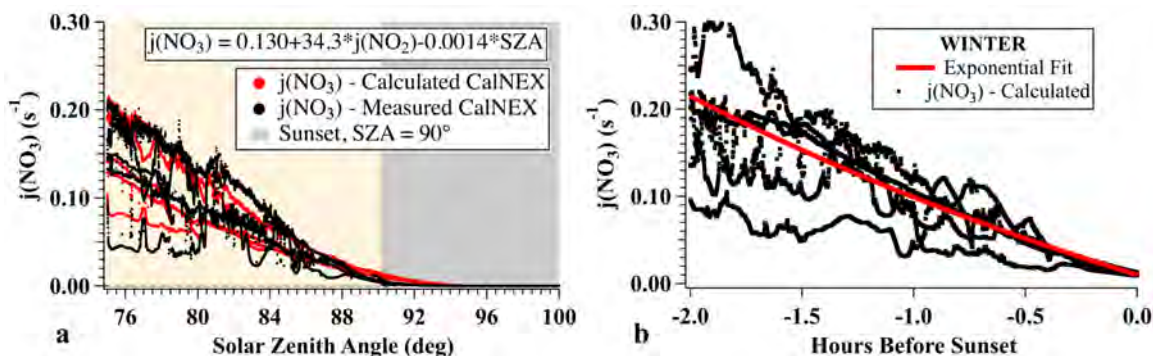


Figure 2.20. Photolysis profiles of $j(\text{NO}_3)$ of the $\gamma(\text{N}_2\text{O}_5)$ analysis in Chapter 4. (a) Measured and calculated $j(\text{NO}_3)$ for the CalNEX Campaign. (b) WINTER photolysis rates calculated with CalNEX multivariate fit to $j(\text{NO}_2)$ and SZA . Red line: Exponential fit used to determine the photolysis rates for the iterative box model.

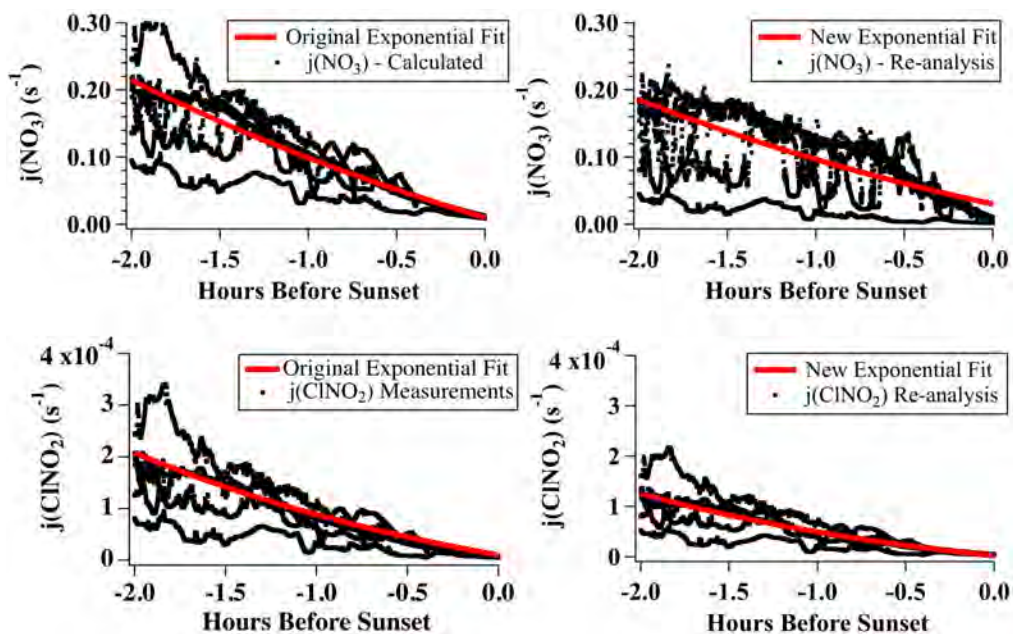


Figure 2.21. Comparison of $j(\text{NO}_3)$ and $j(\text{ClNO}_2)$ values used in the $\gamma(\text{N}_2\text{O}_5)$ (Chapter 4) and $\phi(\text{ClNO}_2)$ (Chapter 5) analyses. The left column shows the $j(\text{NO}_3)$ values derived from CalNEX measurements and original $j(\text{ClNO}_2)$ values. The right column shows the $j(\text{NO}_3)$ values calculated from a re-analysis of WINTER measurements and updated $j(\text{ClNO}_2)$.

2.4.2.3 Simulation Duration and Start Time Determination

Each simulation was initialized at the onset of nocturnal N_2O_5 production and forward integrated, assuming constant reaction rate coefficients and SA, until the time of aircraft measurement. As defined by Wagner et al. (2013), the simulation start time was set as the time of sunset ($\text{SZA} = 90^\circ$), while duration was the time elapsed between sunset and measurement. These definitions make two additional assumptions: 1) nocturnally-dominant N_2O_5 chemistry began exactly at sunset and 2) air measured from the aircraft in the RL has been decoupled from the surface since sunset (i.e. not influenced by surface NO_x emissions).

Regarding the first assumption, cold wintertime temperatures and low actinic flux allow nocturnal species such as N_2O_5 and NO_3 to build up prior to sunset (i.e. $\text{SZA} > 90^\circ$). To account for non-zero concentrations at sunset, each simulation began at a time prior to sunset, determined by the average time when N_2O_5 observations significantly deviated from those predicted by the

N_2O_5 - NO_3 daytime steady state (Day-SS). Expressions shown in Equation E2.11 and E2.12 are derived from Reactions R2.4, R2.1r, R2.1f, R2.3, and R2.11 in Table 2.3 and represent the daytime NO_3 - N_2O_5 steady state established by a balance between production and rapid photolytic and thermal destruction and/or reaction with NO (e.g. Brown et al., 2005; Brown et al., 2016; Osthoff et al., 2006). These expressions do not account for an increase in N_2O_5 heterogeneous loss associated with declining temperatures near sunset, resulting in an exceedance of calculated day-SS concentrations relative to N_2O_5 measurements near sunset when nocturnal heterogeneous chemistry becomes dominant over thermal loss. This divergence was observed in time series of calculated and observed N_2O_5 mixing ratios during 4 day-into-night WINTER flights (Figure 2.22), and was used to determine the pre-sunset simulation start time. Divergence was defined as the time when day-SS mixing ratios exceeded N_2O_5 observations by a factor of 1.4, to account for combined uncertainties in the day-SS calculation and N_2O_5 measurements. Considering both CRDS and I TOF-CIMS N_2O_5 measurements, divergence between measured and calculated mixing ratios ranged from 0.8-1.75 hours, with an average of 1.3 hrs.

$$[\text{NO}_3]_{\text{daytime ss}} = \frac{k_{2.4}[\text{O}_3][\text{NO}_2]}{k_{2.3}[\text{NO}] + j(\text{NO}_3)} \quad (2.11)$$

$$[\text{N}_2\text{O}_5]_{\text{daytime ss}} = \frac{k_{2.1f}}{k_{2.1r}} [\text{NO}_2][\text{NO}_3]_{\text{daytime ss}} \quad (2.12)$$

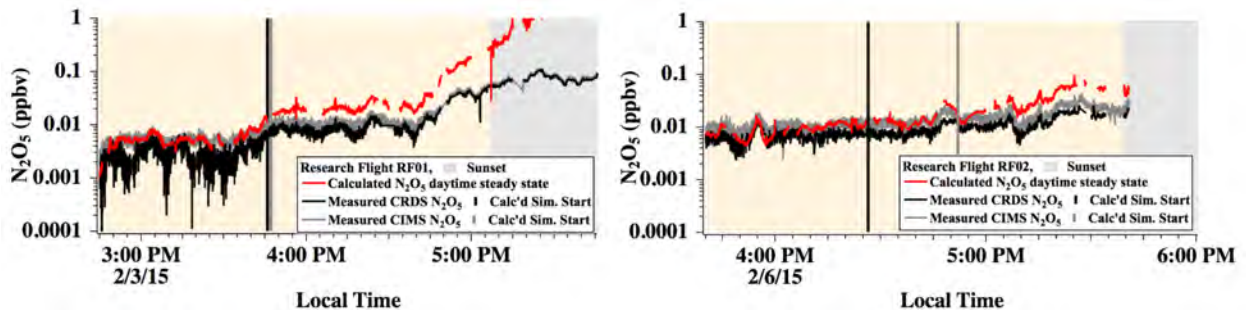


Figure 2.22. Time series of daytime steady state N_2O_5 mixing ratios (red) and CRDS (black) and I TOF-CIMS (gray) observations for two example WINTER flights. Vertical lines represent the time of divergence as calculated from CRDS (black) and I TOF-CIMS (gray) observations.

To address the second assumption made by Wagner et al. (2013), estimates of air age were calculated for every 10 second period using measured aircraft ratios of NO_2/NO_y to determine whether the air had been influenced by NO_x emissions during the simulation duration. While WINTER flights were mainly conducted in the nocturnal RL, where decoupling from the surface layer leads to minimal influence from surface- NO_x emissions, decoupling may not occur immediately at sunset and assuming this as a simulation start time (as in Wagner et al. (2013)) could result in a too-long simulation duration, which would serve to increase and decrease the derived $\gamma(\text{N}_2\text{O}_5)$ and $\phi(\text{ClNO}_2)$ values, respectively.

Air age, calculated from the ratio of measured NO_2/NO_y in E2.13 was used to provide an estimate of when sampled air was last influenced by surface emissions, relative to the calculated time of sunset. Equation E2.13 represents the nocturnal oxidation of NO_2 in excess O_3 (rate limiting oxidation process) where $k_{2,4}$ is the rate constant for this reaction (Table 2.3) and s^* is the stoichiometric factor. The stoichiometric factor varies between 0 and 2 and represents the number of NO_2 molecules lost to NO_3 and/or N_2O_5 production, calculated every 10-seconds for each flight during WINTER. If the age in E2.13 was determined to be greater than the time elapsed since sunset, the simulation start time was set to 1.3 hours prior to sunset and NO_x was initialized in the model as NO_2 . If the calculated age was less than the time elapsed since sunset, the simulation start time was set to the time of most recent NO_x influence (i.e. measurement time – air age) and NO_x was initialized in the model as NO .

$$\text{Age [s]} = \frac{\ln ([\text{NO}_2]/[\text{NO}_y])}{-s^* * k_{2,4} * [\text{O}_3]} \quad (2.13)$$

Although this method allows individual start times to be calculated independent of sunset, it does require an additional assumption that NO_y is conserved overnight (i.e. $[\text{NO}_y]_{\text{t}_{\text{initial}}} = [\text{NO}_y]_{\text{t}_{\text{final}}}$). Loss of NO_y through surface deposition of HNO_3 has been accounted for by correcting

the HNO_3 fraction of NO_y by assuming a 1 cm s^{-1} deposition velocity (winter in the eastern U.S. (Sickles & Shadwick, 2007)) and nocturnal boundary layer (NBL) height estimated from vertical profiles of potential temperature. Additional uncertainties in NO_y measurements arise from sampling an unknown fraction of aerosol nitrate by both the CRDS and CL NO_y instruments, though both agreed within 4% during the WINTER campaign (10-second avg. data, Figure 2.28).

Due to a lack of photolysis rate data and uncertainties in the NH_4NO_3 fraction sampled by the NO_y channel, a simulation start time was not calculated for flights during the UWFPS study. Therefore, base case simulations were run with the same start time for aged air (1.3 hours) derived from WINTER. The UWFPS simulations also used the same photolysis rates for the 1.3 hours prior to sunset as during WINTER, as shown in Figure 2.19 and Figure 2.21.

2.4.2.4 Model Fit Parameters for WINTER Flights

Specific instruments that were used as model fit parameters varied by flight (Table 2.7). Specifically, the model was iteratively fit to reproduce TD-LIF measurements of NO_2 instead of CRDS measurements for simulations of WINTER flights RF01, RF03, and RF04, due to a known problem with the CRDS inlet that resulted in incorrect zeroing for NO , NO_2 , and O_3 on these flights. For this same reason, the model was fit to reproduce NCAR CL measurements of O_3 for these same flights. NCAR CL O_3 observations were additionally used for flights RF05 and RF06 due to a data quality issue with CRDS O_3 for those flights. For N_2O_5 , the model was fit to CRDS measurements for all flights. Gas-phase NO_y and aerosol nitrate were used to calculate the air age and used CRDS NO_y and AMS aerosol nitrate for all flights except RF05, where AMS data were unavailable and substituted with PILS-IC particle nitrate measurements.

Table 2.7. Instrument Measurement used as Fit Parameters for each WINTER flight

Flight Number	Type ^a	NO ₂	O ₃	N ₂ O ₅	CINO ₂	NO _y	Aerosol Nitrate
RF01: 2015-02-03	D2N	TD-LIF	CL	CRDS	I- TOF-CIMS	CRDS	AMS
RF03: 2015-02-07	D2N	TD-LIF	CL	CRDS	I- TOF-CIMS	CRDS	AMS
RF04: 2015-02-11	D2N	TD-LIF	CL	CRDS	I- TOF-CIMS	CRDS	AMS
RF05: 2015-02-20	N	CRDS	CL	CRDS	I- TOF-CIMS	CRDS	PILS-IC
RF06: 2015-02-23	N	CRDS	CL	CRDS	I- TOF-CIMS	CRDS	AMS
RF07: 2015-02-24	N	CRDS	CRDS	CRDS	I- TOF-CIMS	CRDS	AMS
RF08: 2015-03-01	N2D	CRDS	CRDS	CRDS	I- TOF-CIMS	CRDS	AMS
RF09: 2015-03-03	N	CRDS	CRDS	CRDS	I- TOF-CIMS	CRDS	AMS
RF10: 2015-03-07	N	CRDS	CRDS	CRDS	I- TOF-CIMS	CRDS	AMS
RF11: 2015-03-09 ^b	D2N	CRDS	CRDS	I- TOF-CIMS	I- TOF-CIMS	CRDS	AMS

^aFlight Type refers to the time of day at which the flight occurred. D2N = Day-into-Night flight that started prior to sunset and landed after dark, N = entire flight occurred at night after sunset and before sunrise, N2D= Night-into-Day flight that started after sunset and observed a sunrise.

^bRF11 only used to calculate photolysis frequencies and not $\gamma(\text{N}_2\text{O}_5)$ values, as explained in Section 2.4.2.7.8.

2.4.2.5 Limitations and Filters for WINTER Simulations

To focus on nocturnal air that had been in contact with surface emissions the previous day but not during the night, simulations were limited to aircraft measurements within the RL (SZA > 90°), at altitudes below the free troposphere (typically ~1000 mAGL) and above the nocturnal boundary layer (estimated to be ~100 mAGL) (Stull, 1988). The depth of the RL was time and location dependent and determined throughout each flight using the altitude of inversions (i.e. steeper increases in potential temperature with height) observed during vertical profiles. Data were additionally filtered to exclude periods with overlapping gas-phase measurements and reported relative humidity > 95% (1.7% of derived values), due to uncertainty in the aerosol hygroscopic growth curve at high RH (Chapter 4).

One limitation of this box model is that non-convergence occurs as $k_{\text{N}_2\text{O}_5}$ approaches zero (minimum $2 \times 10^{-7} \text{ s}^{-1}$) and k_{CINO_2} approaches $k_{\text{N}_2\text{O}_5}$ (i.e. $\phi(\text{CINO}_2) = 1$), likely as a result of an increased sensitivity to uncertainties in chemical fit parameters. Absence of data close to this limit biases the WINTER median $\gamma(\text{N}_2\text{O}_5)$ high and $\phi(\text{CINO}_2)$ low. Of the total number of derived $k_{\text{N}_2\text{O}_5}$ values for WINTER, 245 or 8% did not converge. Model non-convergence for $\gamma(\text{N}_2\text{O}_5)$ occurred

on 5 of 9 flights, with the majority occurring on RF10. A total of 12.6% of $\phi(\text{ClNO}_2)$ points did not converge, the majority of which (389 of 486 total points) occurred during RF03, in a plume of urban outflow off the coast of New York. Model non-convergence for these and simulations of other flights could arise from multiple sources of box model uncertainties including air age, simulation start time, and disagreement between the N_2O_5 and ClNO_2 measurements, used as model fit parameters. The maximum biases introduced from these non-convergent points are relatively small and do not change the main conclusions presented in either Chapters 4 or 5. For example, assuming a value of 0 for all non-converging points decreases the campaign median $\gamma(\text{N}_2\text{O}_5)$ by less than 12%. Assuming a $\phi(\text{ClNO}_2)$ value of 1 for all non-converging points only increases the median $\phi(\text{ClNO}_2)$ by 22.8% from 0.138 to a value of 0.169. Due to these small biases compared to the large range in model-predicted values, these points are not further considered.

A second limitation is that the model cannot account for time-varying changes in SA or reaction rate constants. For example, assuming a constant value for NO_3 -VOC reactivity, which may decrease over time, could lead to an over-prediction in $\gamma(\text{N}_2\text{O}_5)$ and under-prediction in $\phi(\text{ClNO}_2)$ at longer simulation durations, with the opposite trends at shorter times. In addition, aerosol SA could increase over time from N_2O_5 uptake, although simulation duration during WINTER did not show a statistically significant ($p > 0.05$) correlation with aerosol size and showed a weak correlation ($r^2 = 0.20$) with other contributing factors such as aerosol nitrate. The possible increase in SA over time (impacting $\gamma(\text{N}_2\text{O}_5)$ only) was estimated for each point in the WINTER campaign by assuming that all nitrate formed in the model from N_2O_5 uptake resulted in aerosol-phase nitrate. This method provides an upper limit to the potential change in SA from N_2O_5 uptake as aerosol thermodynamics are expected to partition some fraction of this nitrate to gas-phase nitric acid. The average SA increase from nitrate accumulation was 5.0% for all

WINTER flights with a maximum of 24.5%. These upper limit percent changes are well within the uncertainty of the SA measurement ($\sim 40\%$) included in the total error analysis for $\gamma(\text{N}_2\text{O}_5)$ (Chapter 4) and are therefore not considered further. At least one of these factors, however, likely contributes to the negative correlation observed between WINTER $\gamma(\text{N}_2\text{O}_5)$ values and simulation duration but cannot be confirmed with available aircraft data and may serve to increase the variability in the $\gamma(\text{N}_2\text{O}_5)$ results presented in Chapter 4.

2.4.2.6 Limitations for UWFPS Campaign

As described above, the box model was run in a similar manner for the UWFPS campaign and, therefore, has many of the same limitations. In addition, more limited instrumentation during UWFPS required a larger number of model assumptions, including the use of WINTER photolysis rates and NO_3 reactivity constants as described above. Further discussion of these and other model assumptions, as they pertain to the UWFPS results, are presented in Section 6.2.2 of Chapter 6.

2.4.2.7 Sensitivity Study Results for WINTER Simulations

To test the sensitivity of box model results for $\gamma(\text{N}_2\text{O}_5)$ and $\phi(\text{ClNO}_2)$ to uncertainties in the model parameters described above, a series of 21 additional simulations were conducted for each WINTER flight (210 additional simulations). The results were filtered to remove points where the model did not converge for $k_{\text{N}_2\text{O}_5}$ (i.e. $\gamma(\text{N}_2\text{O}_5) = 0$) or k_{ClNO_2} (i.e. $\phi(\text{ClNO}_2) > 1$) and are summarized in Table 2.8. While $\gamma(\text{N}_2\text{O}_5)$ sensitivities are a direct result of changes in $k_{\text{N}_2\text{O}_5}$ (except for aerosol SA tests), relative $\phi(\text{ClNO}_2)$ sensitivities are typically larger as they are impacted by changes in both $k_{\text{N}_2\text{O}_5}$ and k_{ClNO_2} . Sensitivities are expected to be similar in magnitude for the UWFPS results as both campaigns were conducted in the wintertime nocturnal residual layer above urban regions. Details about each sensitivity study, specific to the WINTER campaign, are presented in the following sections below.

Table 2.8. Sensitivity study results for box model derived median WINTER $\gamma(\text{N}_2\text{O}_5)$ and $\phi(\text{ClNO}_2)$ values.

Parameter	Base Case Value or Instrument		Value Adjustment	Δ Median		Section
	Instrument			$\gamma(\text{N}_2\text{O}_5)$ % ^a	$\phi(\text{ClNO}_2)$ % ^a	
All Data						
Dry Aerosol SA	Measured		-SA uncertainty, +SA uncertainty	+51.0, -25.1	2876	n/a
N_2O_5	CRDS observations		IToF-CIMS observations	-29.1	2639	2806
NO_2	CRDS or TD-LIF		-10%, +10%	-19.6, +18.0	2740	3043
O_3	CRDS or CL		-5%, +5%	-10.9, +10.0	2822	2806
ClNO_2	IToF-CIMS obs.		-30%, +30%	n/a	n/a	3296
Pre-Sunset Time	1.3 hours		0 hours, 1.75 hours	-6.4, +3.7	2003	2089
Age	Calculated		Youngest, Oldest	-7.1, +2.9	2724	2740
SA Growth Factor	Calculated from AMS		Calculated with E-AIM	-5.6	2876	n/a
Photolysis Frequencies	Measured		-40%, +40%	+2.2, -0.1	2003	2182
NO_3 Reactivity (k_{NO_3})	Calculated		-10%, +10% in k_{HO_2} and k_{VOC}	+1.2, -1.0	2854	3390
Ocean Data Only						
N_2O_5 Deposition	n/a		$k_{\text{N}_2\text{O}_5} = k_{\text{Total N}_2\text{O}_5} - k_{\text{N}_2\text{O}_5 \text{ Depos.}}$ ($k_{\text{N}_2\text{O}_5 \text{ Depos.}} = -1.66/\text{BLH s}^{-1}$)	-14.0	1390	1398
$\text{N}_2\text{O}_5 + \text{ClNO}_2$ Deposition	n/a		$k_{\text{N}_2\text{O}_5} = k_{\text{Total N}_2\text{O}_5} - k_{\text{N}_2\text{O}_5 \text{ Depos.}}$ $k_{\text{ClNO}_2} = k_{\text{ClNO}_2 \text{ Het.}} - k_{\text{ClNO}_2 \text{ Depos.}}$	n/a	n/a	1398
Dilution with O_3 Entrainment	n/a		$k_{\text{N}_2\text{O}_5} = k_{\text{Total N}_2\text{O}_5} - k_{\text{Dilution}}$ ($k_{\text{Dilution}} = 3.1 \times 10^{-5} \text{ s}^{-1}$)	-5.7	1658	1785

^aPercent change defined as 100* (sensitivity study median – base case median)/ base case median). N = number of converging points in each comparison. n/a indicates that either $\gamma(\text{N}_2\text{O}_5)$ or $\phi(\text{ClNO}_2)$ are not dependent on the given parameter.

2.4.2.7.1 Aerosol Surface Area

The calculation of $\gamma(\text{N}_2\text{O}_5)$ is directly dependent on the total wet aerosol SA density. Uncertainty in total wet aerosol SA density arises from uncertainties in: 1) the measured dry SA density and 2) the relative-humidity dependent aerosol SA hygroscopic growth factor.

As described in Section 2.3.2.2, uncertainty in measured dry aerosol SA density was 34% for the UHSAS particle counter, and 41% ($<1\mu\text{m}$) and 34% ($>1\mu\text{m}$) for the PCASP. The campaign median $\gamma(\text{N}_2\text{O}_5)$ was most sensitive to these uncertainties (+51.0%/-25.1%, Figure 2.23a) after adjusting dry SA density observations by $\pm 34\%$ (41% for $<1\mu\text{m}$ PCASP) and re-applying the original SA growth factor (described in Chapter 4). Despite the large sensitivity, uncertainties of 34% and 41% are no larger than those used to calculate $\gamma(\text{N}_2\text{O}_5)$ in past field studies (Brown et al., 2009; Morgan et al., 2015; Phillips et al., 2016; Wagner et al., 2013; Wang, X. et al., 2017).

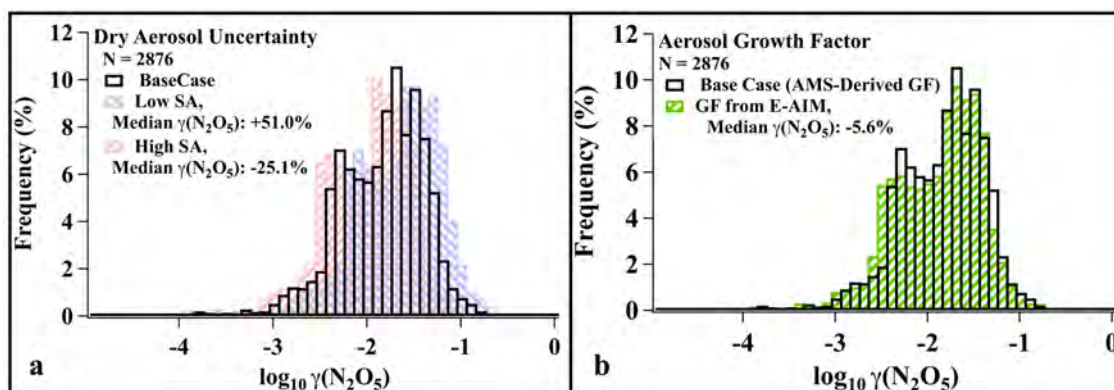


Figure 2.23. Histogram of box model $\gamma(\text{N}_2\text{O}_5)$ sensitivities to (a) uncertainties in dry aerosol surface area density as described in text and (b) wet aerosol SA density calculated from the E-AIM derived growth factor, assuming pure NH_4NO_3 aerosol.

To test the sensitivity of $\gamma(\text{N}_2\text{O}_5)$ to uncertainties in the aerosol hygroscopic growth factor, primarily associated with aerosol composition, $\gamma(\text{N}_2\text{O}_5)$ was recalculated after applying a growth factor calculated by Viral Shah from the Extend-AIM aerosol thermodynamics model (Wexler & Clegg, 2002), which assumed a purely inorganic aerosol composition. Application of this growth factor only decreased the median $\gamma(\text{N}_2\text{O}_5)$ by 5.6%, with the distribution change in Figure 2.23b.

2.4.2.7.2 CRDS vs TD-LIF NO₂ Observations

For flights with overlapping NO_x measurements (RF05-RF11), the slope of the two-sided correlation between TD-LIF and CRDS NO₂ measurements was 0.97 with a correlation coefficient of 0.99 (Figure 2.24a). Changing NO₂ measurements by ±10% (reported accuracy of TD-LIF measurement) changed the median $\gamma(\text{N}_2\text{O}_5)$ by +18.0/-19.6 and median $\phi(\text{ClNO}_2)$ by -18.0/+34.5, with distribution changes shown in Figure 2.24b-c. Despite the large sensitivity to NO₂ concentrations, the CRDS measurements reported an accuracy of 3%, suggesting a 10% uncertainty in NO₂ is an upper limit for RF05-RF11 when CRDS NO₂ measurements were used as model fit parameters.

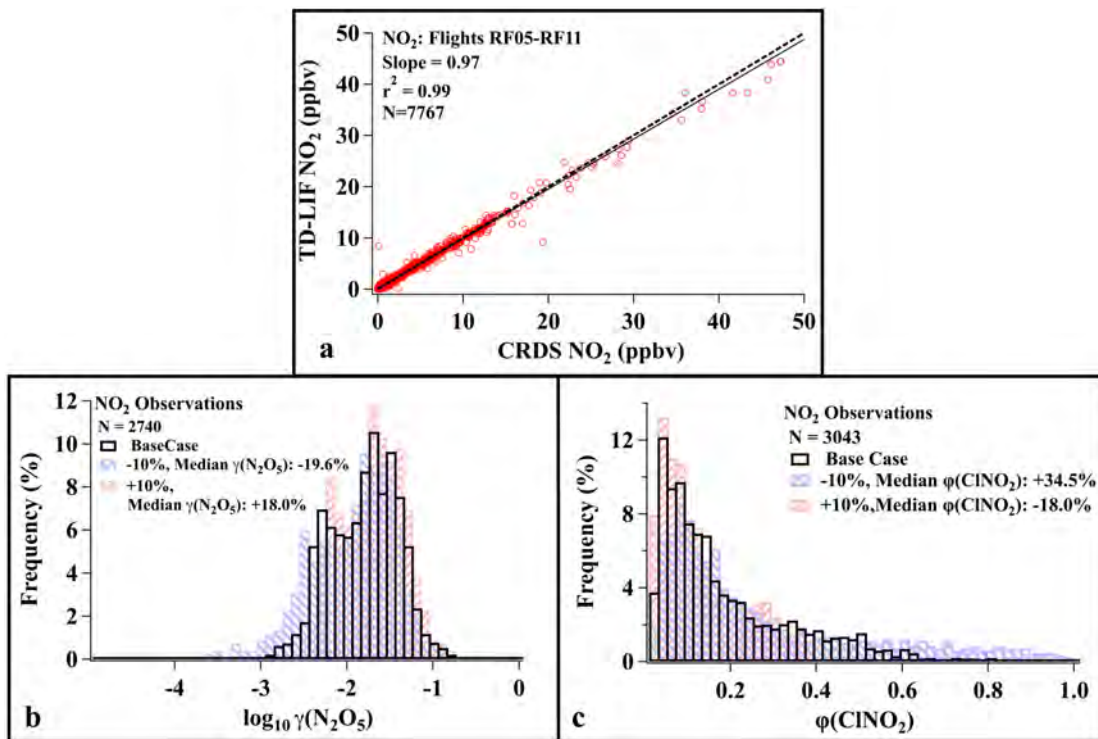


Figure 2.24. (a) Correlation between TD-LIF and CRDS NO₂ Observations (10-second average). Data were filtered to include nocturnal measurements below 1500 mAGL. Dashed line represents the 1:1 correlation. Solid black line is the 2-sided regression fit. Histogram of base case box model (b) $\gamma(\text{N}_2\text{O}_5)$ and (c) $\phi(\text{ClNO}_2)$ results and those calculated with ±10% changes in NO₂.

2.4.2.7.3 CRDS vs CL O₃ Observations

For flights with overlapping O₃ measurements (RF05-06, RF08-09), the slope of the 2-sided correlation between CL and CRDS O₃ was 1.04 with a correlation coefficient of 0.97 (Figure 2.25a). Adjusting O₃ measurements in each simulation by $\pm 5\%$ (reported uncertainties measurements) changed the median $\gamma(\text{N}_2\text{O}_5)$ by $-10.9/+10.0\%$ and median $\phi(\text{ClNO}_2)$ by $+21.4/-13.8\%$, with distribution changes shown in Figure 2.25b-c.

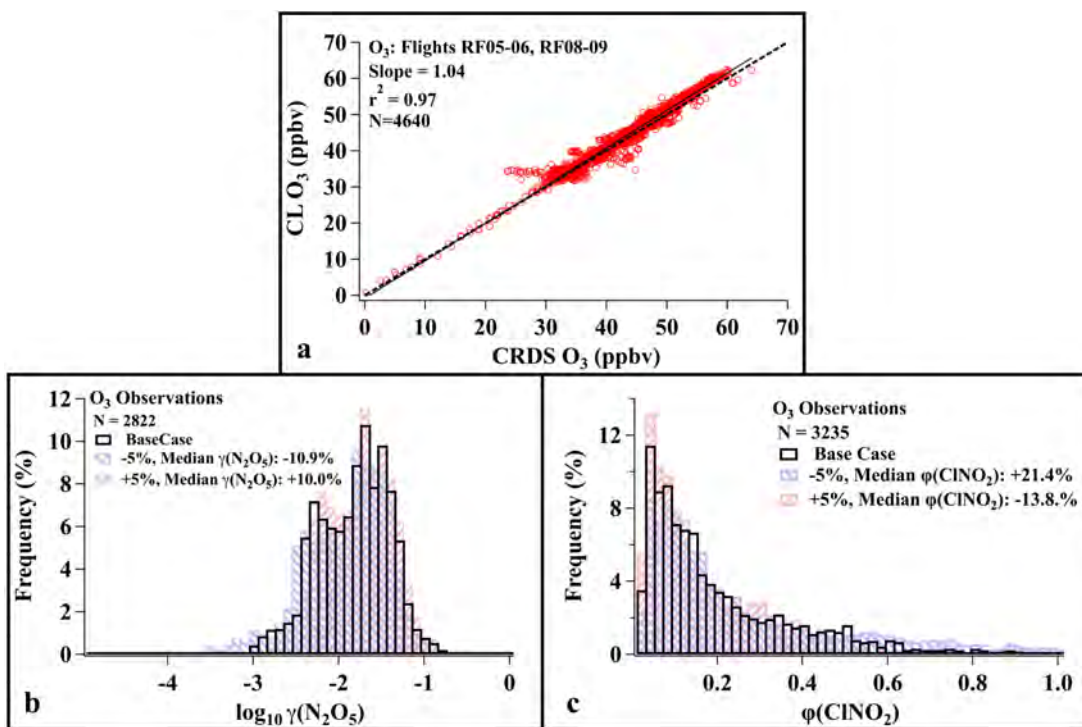


Figure 2.25. (a) Correlation between CL and CRDS O₃ Observations (10-second averages). Data were filtered to include nocturnal measurements below 1500 mAGL. Dashed line represents the 1:1 correlation. Solid black line is the 2-sided regression fit. Histogram of base case box model (b) $\gamma(\text{N}_2\text{O}_5)$ and (c) $\phi(\text{ClNO}_2)$ results and those calculated with $\pm 5\%$ changes in O₃.

2.4.2.7.4 CRDS vs CIMS N₂O₅ Measurements

The slope of the 2-sided correlation between the I- TOF-CIMS and CRDS N₂O₅ measurements was 1.12, with a correlation coefficient of 0.98 (Figure 2.26a). Fitting the box model to CIMS measurements for each flight decreased the median $\gamma(\text{N}_2\text{O}_5)$ by -29.1% and increased the median $\phi(\text{ClNO}_2)$ by 21.8% with distribution changes shown in Figure 2.26b-c.

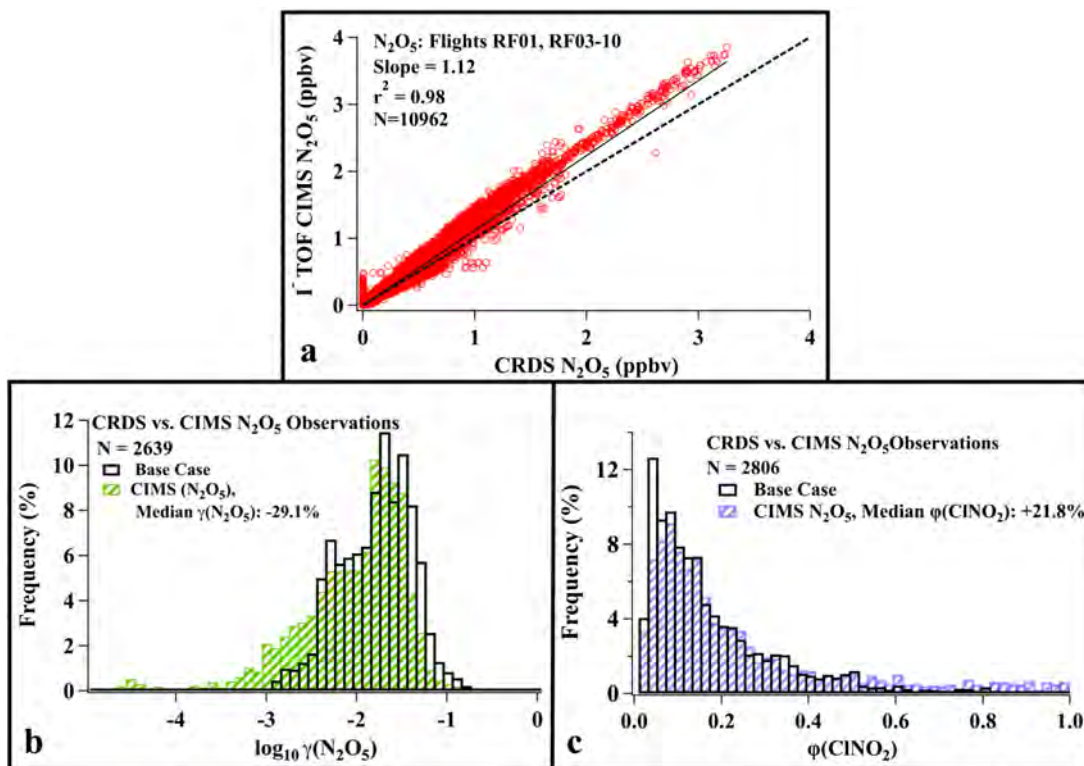


Figure 2.26. (a) Correlation between I-TOF CIMS and CRDS N_2O_5 Observations (10-second averages). Data were filtered to include nocturnal measurements below 1500 m AGL. Dashed line: 1:1 correlation. Solid black line: 2-sided regression fit. Histogram of base case box model (b) $\gamma(N_2O_5)$ and (c) $\phi(CINO_2)$ results and those calculated with I-TOF CIMS N_2O_5 observations.

2.4.2.7.5 CIMS $CINO_2$ Measurements

$CINO_2$ was measured by the University of Washington I-TOF-CIMS with a specified 30% accuracy and limit of detection less than 4 pptv. Values of $\phi(CINO_2)$ are directly dependent on $CINO_2$ and scaling observations by $\pm 30\%$ resulted in $\pm 29.8\%$ changes in the median value. The resulting distributions are shown in Figure 2.27.

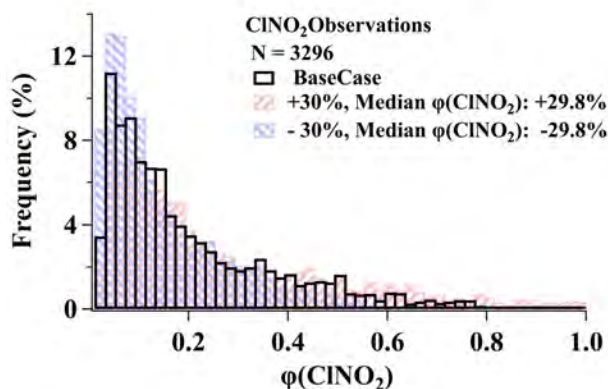


Figure 2.27. Histogram of base case $\phi(CINO_2)$ results and those calculated with $\pm 30\%$ $CINO_2$.

2.4.2.7.6 CRDS vs CL NO_y

For flights with overlapping measurements (RF01, RF03-06, RF08-09), the slope of the two-sided correlation between CL and CRDS NO_y is 1.04 with a correlation coefficient of 0.99 (Figure 2.28). The NO_y measurement was not used directly as a model fit parameter but in combination with aerosol nitrate to provide an estimated air age, used to determine the simulation start time and duration. Box model sensitivities to air age are discussed below in Section 2.4.2.7.8.

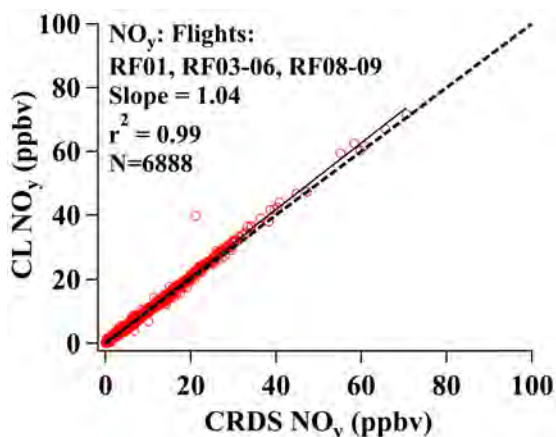


Figure 2.28. Correlation between CL and CRDS NO_y Observations (10-second averages). Data were filtered to include nocturnal measurements below 1500 m AGL. Dashed line represents the 1:1 correlation. Solid black line is the 2-sided regression fit.

2.4.2.7.7 AMS vs PILS-IC Nitrate

As described in Section 2.4.2.3, measurements of submicron aerosol phase nitrate were used in combination with gas-phase NO_y measurements to estimate air age, the sensitivity of which is discussed in a following section. After averaging the 1-Hz AMS measurements to the PILS-IC measurement frequency (~90s), the slope of the two-sided correlation between PILS-IC and AMS nitrate for overlapping flights (RF01, RF03-04, RF06-11) is 0.65 with a correlation coefficient of 0.85 (Figure 2.29). As discussed in Guo et al. (2016) and (Schroder et al., submitted, 2018), the AMS may report larger values for nitrate than the PILS-IC, due to the fact that the PILS-IC only measures inorganic nitrate and the AMS cannot distinguish between the inorganic and organic versions, as well as nitrite that was also present during this study (Guo et al., 2016). Due to the 1-

Hz time resolution of the AMS and the high precision of its measurements, the AMS was used to calculate air age for simulations of all flights except RF05, where AMS data was unavailable. Using PILS-IC nitrate could serve to underestimate the air age and simulation duration on RF05 (less nitrate corresponds to younger air), however increasing the simulation duration to the longest possible time (i.e. start 1.3 hours prior to sunset), only increased the $\gamma(\text{N}_2\text{O}_5)$ values on RF05 by < 10%. Values of $\phi(\text{ClNO}_2)$ were most sensitive to air age and increasing the simulation duration to the longest possible time resulted in a much larger, 61% decrease in median $\phi(\text{ClNO}_2)$ on this flight from a value of 0.159 to 0.061.

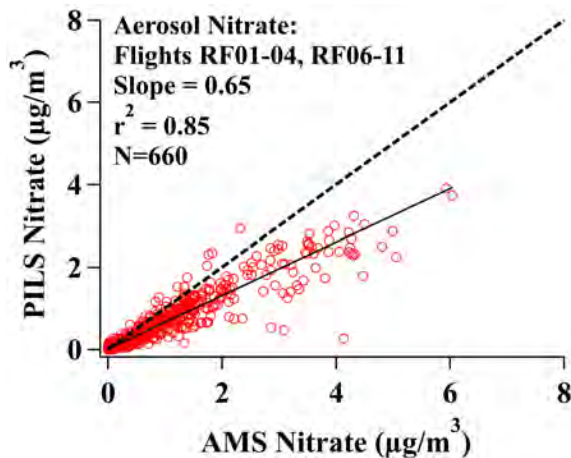


Figure 2.29. Correlation between PILS-IC and AMS Particle Nitrate Observations. AMS measurements were averaged to the PILS collection time (~1.5 minutes) for this comparison only. Data were filtered to include nocturnal measurements below 1500 mAGL. Dashed line represents the 1:1 correlation. Solid black line is the 2-sided regression fit.

2.4.2.7.8 Simulation Duration & Start Time

The duration of each simulation was derived as described in Section 2.4.2.3 using an estimate of air age based on the NO_2/NO_y ratio. For points influenced by surface NO_x emissions after sunset, the simulation duration was set to the calculated air age. For points older than the time elapsed since sunset, the start time was set to 1.3 hours prior to sunset, based on the deviation of measured N_2O_5 from mixing ratios predicted by daytime steady state. Uncertainties and model sensitivities associated with both calculations are discussed here.

Based on both ITOF-CIMS and CRDS measurements from 4 day-into-night flights, N_2O_5 observations deviated from the predicted daytime steady state concentrations between 0.8 and 1.75 hours prior to sunset ($SZA = 90^\circ$), with an average of 1.3 hours. Uncertainties in this pre-sunset start time arise from N_2O_5 measurement uncertainties as well as uncertainties in $j(NO_3)$ photolysis frequencies, O_3 , and NO_2 concentrations used in the calculation of N_2O_5 daytime steady state. To test the model sensitivities to these uncertainties, additional simulations were run for points that had an air age older than sunset, adjusting the pre-sunset start time from 0 to 1.75 hours. Over this range, the median value of $\gamma(N_2O_5)$ changed by $-6.4/+3.7\%$ and median $\phi(CINO_2)$ by $+6.9/-0.7\%$ with distribution changes shown in Figure 2.30.

Despite the small sensitivity of the campaign median $\gamma(N_2O_5)$ and $\phi(CINO_2)$ to this parameter, the model has an increased sensitivity to start time close to sunset. For most flights, this sensitivity was small ($< 10\%$), except for flight RF11. RF11 showed a small sensitivity in $k_{N_2O_5}$ to changes in pre-sunset start times, but a reduction in $\gamma(N_2O_5)$ of 7 orders of magnitude when the simulation was set to start 0.25 hours *after* sunset (time of daytime steady state deviation). As a result of the extreme sensitivity of RF11 to simulation start time, along with missing CRDS measurements to corroborate CIMS measurements, RF11 was eliminated from the analyses presented in the main text.

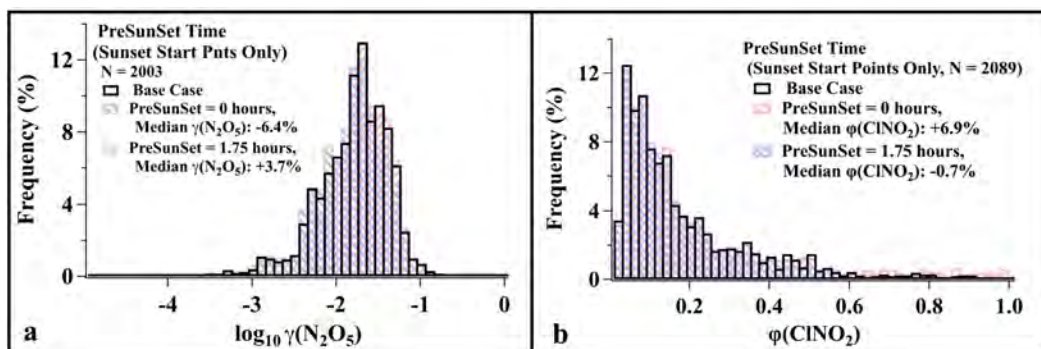


Figure 2.30. Histogram of base case box model (a) $\gamma(N_2O_5)$ and (b) $\phi(CINO_2)$ results and those calculated with a pre-sunset start time of 0 and 1.75 hours.

Uncertainties in the air age calculation arise from uncertainties in the rate of NO_y deposition, stoichiometric factor, and fraction of aerosol nitrate measured by both CL and CRDS instruments. To test these uncertainties, the sensitivity of $\gamma(\text{N}_2\text{O}_5)$ to two extreme cases was explored. The first scenario assumed that all sampled air was last impacted by surface NO_x emissions at, or prior to, sunset. This assumption sets the simulation start time to 1.3 hours prior to sunset for all points, which results in the longest possible simulation duration and largest amount of time to chemically produce N_2O_5 , HNO_3 , and ClNO_2 . Under this assumption, the median $\gamma(\text{N}_2\text{O}_5)$ value increased by 2.9% and median $\phi(\text{ClNO}_2)$ decreased by 25.3% shown in Figure 2.31.

The second scenario attempts to calculate the youngest reasonable air age, providing the model with the least amount of time to chemically produce N_2O_5 , HNO_3 , and ClNO_2 . In this scenario, age was calculated by assuming: 1) no depositional NO_y loss to the surface, 2) a stoichiometric factor of 2, and 3) total NO_y equal to gas-phase NO_y measurement only. These assumptions served to reduce the amount of nitrate, NO_x/NO_y ratio, and subsequent plume age calculated with E2.13. Under this scenario, the median $\gamma(\text{N}_2\text{O}_5)$ was reduced by 7.1% and $\phi(\text{ClNO}_2)$ increased by 43.7%, shown in Figure 2.31. Median $\phi(\text{ClNO}_2)$ was the second most sensitive to air age behind the model sensitivity to the sum of N_2O_5 and ClNO_2 deposition (Section 2.4.2.7.11). Despite this large sensitivity, the median value for $\phi(\text{ClNO}_2)$ remained less than 0.19, within 0.06 of the base case median and lower than values predicted by the parameterization of $\phi(\text{ClNO}_2)$ based on the measured aerosol composition (see Chapter 5).

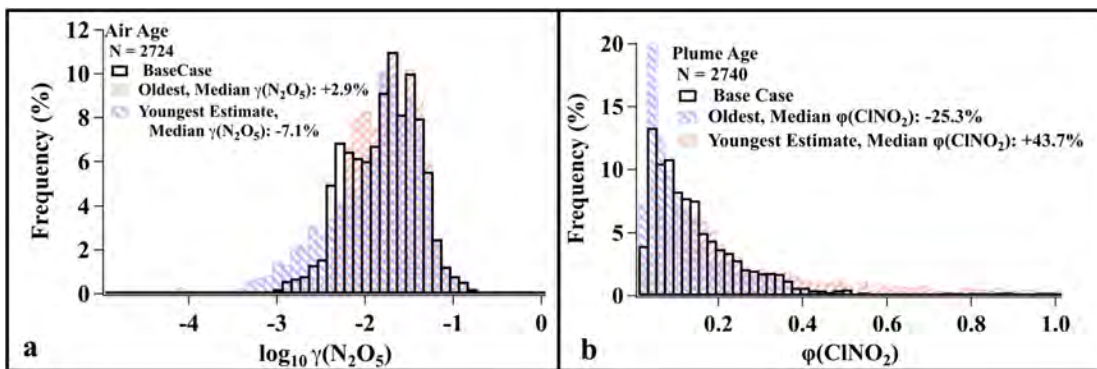


Figure 2.31. Histogram of base case box model (a) $\gamma(\text{N}_2\text{O}_5)$ and (b) $\phi(\text{ClNO}_2)$ results and those calculated with the oldest possible and youngest reasonable air ages.

2.4.2.7.9 Photolysis Frequencies

Uncertainties in photolysis frequency at high sun are driven by a combination of instrument and molecular uncertainties in the cross-section and quantum yields for each molecule. These uncertainties, however, increase to as much as $\pm 40\%$ at low sun angles due to increased optical angular response biases. Due to the small fraction of pre-sunset time (maximum 1.3 hours) relative the total simulation duration, scaling the time-dependent photolysis rates for $j(\text{NO}_2)$, $j(\text{O}_3)$, $j(\text{N}_2\text{O}_5)$, $j(\text{ClNO}_2)$, and $j(\text{NO}_3)$ by $\pm 40\%$ resulted in small changes (Figure 2.32) in both $\gamma(\text{N}_2\text{O}_5)$ ($+2.2/-0.1\%$) and $\phi(\text{ClNO}_2)$ ($+1.3/-3.5\%$). The $\phi(\text{ClNO}_2)$ model results here include the $j(\text{NO}_3)$ and $j(\text{ClNO}_2)$ updates previously described in Section 2.4.2.2.

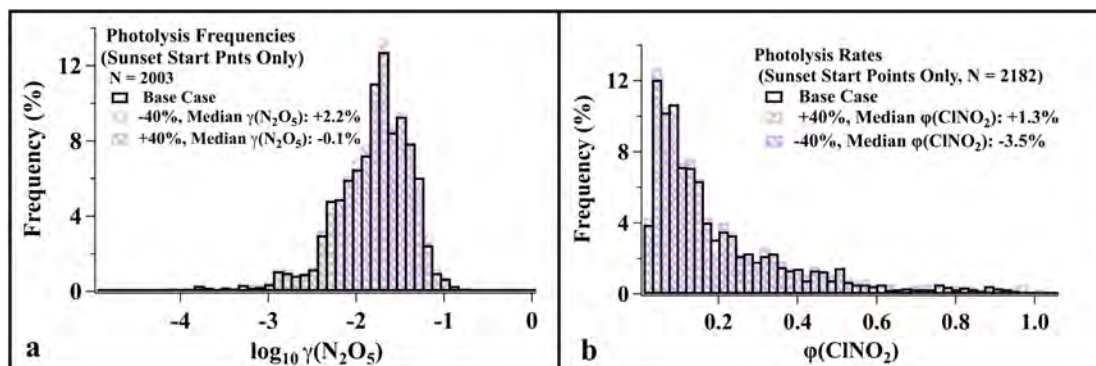


Figure 2.32. Histogram of base case box model (a) $\gamma(\text{N}_2\text{O}_5)$ and (b) $\phi(\text{ClNO}_2)$ values and those calculated with $\pm 40\%$ changes in photolysis frequencies.

2.4.2.7.10 NO₃ Reactivity

As shown in Figure 2.33, modeled median $\gamma(\text{N}_2\text{O}_5)$ and $\phi(\text{ClNO}_2)$ has a small sensitivity (-1.0/+1.2 and +2.7/-2.7%) to 10% changes in the total NO₃ loss rate for WINTER data. Despite the overall small sensitivity, uncertainties associated with individual NO₃ loss processes (directly through reaction and uptake, or indirectly through N₂O₅ loss) were poorly constrained are discussed in this section for completeness.

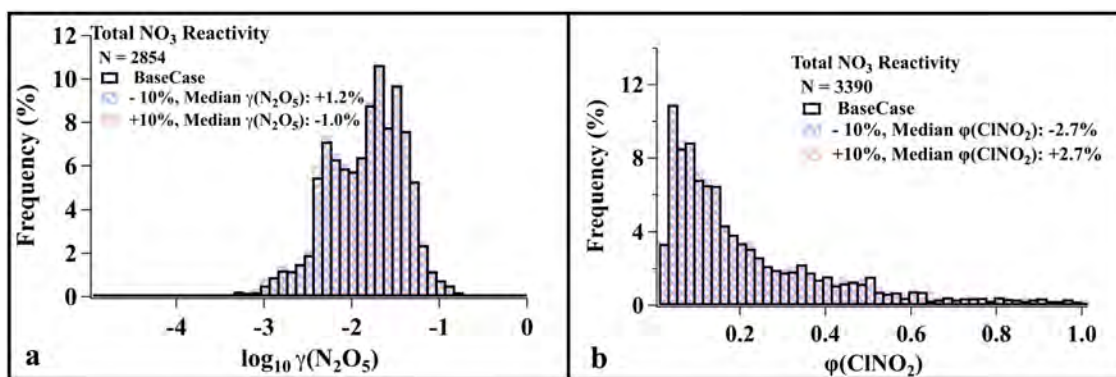


Figure 2.33. Histogram of base case box model (a) $\gamma(\text{N}_2\text{O}_5)$ and (b) $\phi(\text{ClNO}_2)$ results and those calculated with $\pm 10\%$ changes in k_{NO_3} .

In addition to k_{VOC} uncertainties arising from flights without TOGA VOC measurements, there is a potential for missing NO₃ reactivity from VOCs not measured by TOGA. For example, a previous box-modeling analysis of wintertime aircraft observations from the 2011 RONOCO campaign over the United Kingdom (Stone et al., 2014) attributed ~40% of total k_{VOC} to unsaturated hydrocarbons, such as *trans*-2-butene and propene, that were not reported by TOGA. Estimation of propene and ethene from measured wintertime ratios to $\sum(\text{iso}, 1\text{-Butene})$ across the eastern U.S. (Hagerman et al., 1997) suggest that these compounds would increase measured k_{VOC} by < 10%, within the range tested by this sensitivity study. Such missing VOC reactivity in the WINTER data would bias the $\gamma(\text{N}_2\text{O}_5)$ results high and $\phi(\text{ClNO}_2)$ results low, but this study shows nearly the smallest model sensitivity to changes in total k_{NO_3} ($=k_{\text{VOC}} + k_{\text{HO}_2}$) relative to all parameters tested (Table 2.8).

In addition to reaction with VOCs, NO_3 is lost through reactions with HO_2 , RO_2 , and through direct heterogeneous aerosol uptake. As previously noted, reactions with HO_2 and RO_2 radicals serve to regenerate NO_2 (Vaughan et al., 2006), which is represented in this analysis by a single pseudo-first order reaction (Table 2.3, Reaction R2.8). The first order rate constant k_{HO_2} (s^{-1}) was estimated using the rate constant from the $\text{NO}_3 + \text{HO}_2$ reaction ($4 \times 10^{-12} \text{ cm}^3 \text{ molec}^{-1} \text{ s}^{-1}$) (IUPAC, 2008a), multiplied by average observed wintertime HO_2 concentrations ($3 \times 10^7 \text{ molec. cm}^{-3}$) from flights over the UK in 2011 (Stone et al., 2014). Reaction of NO_3 with RO_2 was not explicitly included in this mechanism due to uncertainty in nocturnal wintertime RO_2 concentrations, as well as the efficiency of NO_2 recycling from this reaction. Loss of NO_3 through heterogeneous uptake was also not explicitly included in this mechanism due to the relatively small uptake coefficients ($\gamma(\text{NO}_3) \sim 10^{-3}$) measured on various types of laboratory-derived aerosol (Brown & Stutz, 2012). Based on typical WINTER conditions, an NO_3 uptake coefficient of 0.1 would double the typical k_{NO_3} during WINTER, which would decrease the median derived $\gamma(\text{N}_2\text{O}_5)$ by $\sim 10\%$ and increase the median derived $\phi(\text{ClNO}_2)$ by $\sim 30\%$, based on the k_{NO_3} sensitivity test.

Despite the large number of uncertainties associated with direct NO_3 loss, 10% changes in total k_{NO_3} had a small impact on campaign median values of $\gamma(\text{N}_2\text{O}_5)$ and $\phi(\text{ClNO}_2)$ derived here. This small sensitivity, relative to previous field studies (e.g. Phillips et al., 2016), can be explained by small NO_3 concentrations and low calculated NO_3 reactivity, both driven by low winter temperatures that shift the NO_3 - N_2O_5 equilibrium to favor N_2O_5 . Biogenic emissions, which often constitute the largest loss of NO_3 (e.g. Aldener et al., 2006; Brown & Stutz, 2012), are also greatly reduced in winter due to total lack of isoprene emissions and the strong temperature dependence of monoterpene emissions. Under WINTER conditions the predicted equilibrium concentrations

of NO_3 were typically more than 100 times lower than N_2O_5 ($[\text{N}_2\text{O}_5]/[\text{NO}_3] = K_{eq} * [\text{NO}_2] \geq 100$) and small fractional contributions of NO_3 to the total loss of $\text{NO}_3 + \text{N}_2\text{O}_5$ were predicted by the model ($k_{\text{NO}_3} * [\text{NO}_3] / (k_{\text{NO}_3} * [\text{NO}_3] + k_{\text{N}_2\text{O}_5} * [\text{N}_2\text{O}_5]) = 11.5\%$ average). This WINTER NO_3 loss contribution (also proportional to the degree of model sensitivity) is much lower than previous summertime field studies which have reported NO_3 contributions as large as 85% over rural Texas (Brown et al., 2011). Other wintertime studies have observed a 2.5 - 10% NO_3 contribution in a Utah oil and gas producing basin (Wild et al., 2016) and 26% from aircraft observations over the UK (Stone et al., 2014). The only exception to this trend was research flight 10 to Atlanta, Georgia where warmer temperatures and larger VOC concentrations resulted in reduced $[\text{N}_2\text{O}_5]/[\text{NO}_3]$ ratios between 40 and 100 and the largest fractional contribution (47.3%) of NO_3 to the total loss of N_2O_5 and NO_3 . As a result, the sensitivities of $\gamma(\text{N}_2\text{O}_5)$ and $\phi(\text{ClNO}_2)$ to k_{NO_3} were largest on this flight (-25.2/+3.5% and +10.3/-20.4%, respectively to $\pm 10\%$ changes) and highlights the point that the iterative box model works best under wintertime conditions with low NO_3 reactivity. Application of this model under warmer conditions would require better constraints on NO_3 reactivity. While the increased k_{NO_3} sensitivity did result in relatively larger errors for flight 10 (discussed further in Chapter 4 and Chapter 5), k_{NO_3} may be under-predicted during WINTER (due to missing VOC reactivity, NO_3 uptake, and/or reaction with HO_2 or RO_2 described above). The $\gamma(\text{N}_2\text{O}_5)$ values on flight 10 were some of the lowest of the campaign and increasing k_{NO_3} would therefore serve to decrease these values further below the original magnitude of $< 1 \times 10^{-3}$. The derived $\phi(\text{ClNO}_2)$ values, however, were similar on this flight relative to others and while the sensitivity to k_{NO_3} did increase ($\sim 10 - 20\%$) on RF10, these changes do not impact the results presented in Chapter 5.

2.4.2.7.11 Ocean Surface Deposition

Deposition of N_2O_5 , like NO_y , is expected to be low in RL air that is not in contact with the surface. Shallow nocturnal boundary layers (NBL ~ 100 mAGL) were observed during missed approaches over continental airfields, though higher minimum altitudes did not allow the aircraft to probe these same altitudes over the ocean. The mixed surface layer is expected to deepen over the ocean and previous sondes and 3D model results have indicated marine boundary layer heights of 500 mASL or greater during wintertime off the eastern U.S. coast, independent of the time of day (Seidel et al., 2012). If air sampled over the ocean during WINTER was in contact with the surface, deposition should be included in the model mechanism for these time periods. Due to uncertainties in the ocean deposition velocity of multiple species, as well as the extent of convective mixing over the ocean, deposition was not included in the base case simulations. Instead, model sensitivities to deposition were tested by correcting model-derived $k_{N_2O_5}$ values over the ocean for N_2O_5 deposition, represented as a first order loss term ($k_{N_2O_5\text{Depos.}}$ [s^{-1}]) shown in Equation E2.14. The deposition rate constant was calculated from the ocean exchange velocity of N_2O_5 (-1.66 cm s^{-1}), measured from an ocean pier in California in February 2013 (Kim et al., 2014), and WINTER boundary layer heights (cm) over the ocean determined from the vertical profiles of potential temperature. After subtracting $k_{N_2O_5\text{Depos.}}$ from model results, $k_{Het. Uptake}$ (s^{-1}) is used to calculate the corrected $\gamma(N_2O_5)$ and $\phi(CINO_2)$.

$$Total\ k_{N_2O_5\text{model}} = k_{Het. Uptake} + k_{N_2O_5\text{Depos.}} \quad (2.14)$$

Results in Figure 2.34 show that applying this constant depositional loss can significantly change the $\gamma(N_2O_5)$ and $\phi(CINO_2)$ values over the ocean. There are even some points ($N = 267$) where $k_{N_2O_5\text{Depos.}}$ exceeds the total $k_{N_2O_5\text{model}}$ (percent change $< -100\%$), suggesting that the N_2O_5 deposition velocity is variable and/or the literature value is too large for all WINTER

conditions. For points where $k_{N_2O_5_{Depos.}}$ did not exceed the total $k_{N_2O_5_{model}}$, the median $\gamma(N_2O_5)$ values decreased by 14.0% and median $\phi(ClNO_2)$ was increased by 27.9%.

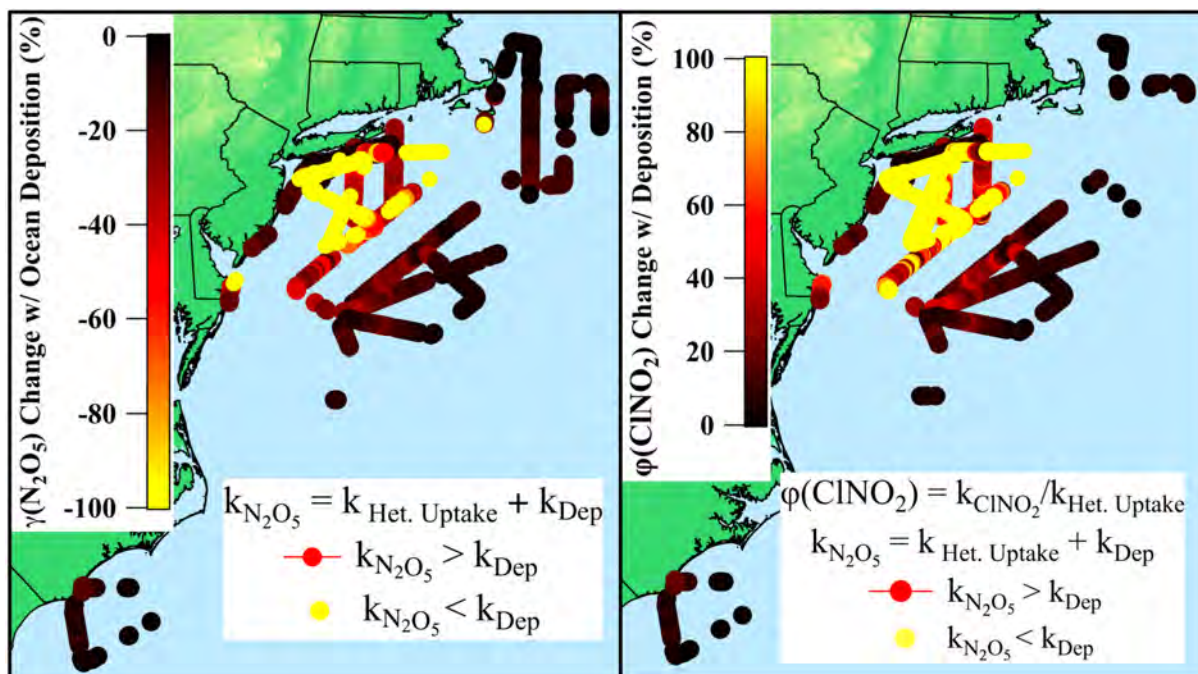


Figure 2.34. Percent change in $\gamma(N_2O_5)$ and $\phi(ClNO_2)$ when accounting for N_2O_5 ocean surface deposition. Yellow points highlight values where the deposition rate constant, calculated from the exchange flux in Kim et al. (2014), was larger than the loss derived from the iterative box model.

In addition to N_2O_5 deposition, observations of $ClNO_2$ by Kim et al. (2014) also suggested a depositional flux of $ClNO_2$ to the ocean, opposite the expected direction based on the expected efficiency of ocean $ClNO_2$ production. To probe the observed differences between WINTER box model results and laboratory-based parameterizations of $\phi(ClNO_2)$ (e.g. Bertram & Thornton, 2009) (discussed extensively in Chapter 5), the model was further tested for sensitivities to both N_2O_5 and possible $ClNO_2$ ocean deposition. In this test, the original k_{ClNO_2} values were recalculated to account for a depositional rate of $ClNO_2$ with an exchange velocity $\sim 1/3$ that of N_2O_5 from Kim et al. (2014), following E2.15 - E2.16. This test increased the median $\phi(ClNO_2)$ value of ocean-only points by 72.9% from 0.145 to 0.251. Results from this and the N_2O_5 -only deposition test are shown in Figure 2.35 plotted against the parameterized $\phi(ClNO_2)$ values from

WINTER, calculated using Bertram and Thornton (2009). Figure 2.35 suggests that while the model is sensitive to assumptions in surface exchange, the sum of N_2O_5 and $ClNO_2$ deposition cannot entirely account for the differences between the box model and parameterized $\phi(ClNO_2)$ values (discussed further in Chapter 5).

$$k_{ClNO_2 Model} = k_{ClNO_2 Het. Production} - k_{ClNO_2 Depos.} \quad (2.15)$$

$$\phi(ClNO_2) = \frac{k_{ClNO_2 Het. Production}}{k_{N_2O_5 Het. Uptake}} \quad (2.16)$$

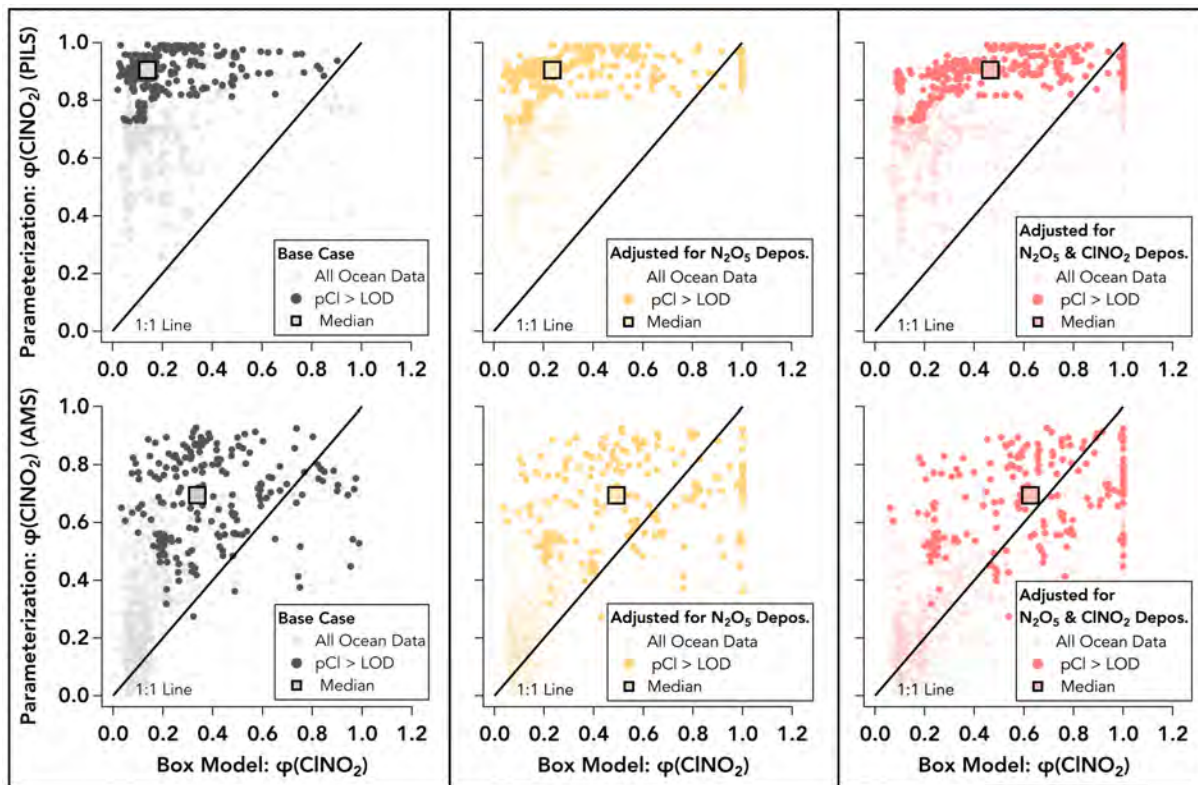


Figure 2.35. Parameterized values of $\phi(ClNO_2)$ calculated from Bertram and Thornton (2009) with PILS (top row) and AMS (bottom row) particle chloride (pCl) measurements vs. box model results. (left) original results; (middle) box model results re-calculated with N_2O_5 surface deposition (-1.66 m s^{-1} exchange velocity); (right) box model results re-calculated with N_2O_5 and $ClNO_2$ (-0.55 m s^{-1} exchange velocity) deposition. Data with pCl > instrument LODs are in bold. Medians (pCl > LOD points) of each comparison are shown by the square points in each panel.

In these tests, constant exchange velocities were applied to both N_2O_5 and $ClNO_2$. As the exchange velocity is wind speed dependent (calculated at a wind speed $\sim 9 \text{ m/s}$ in Kim et al. (2014)), an over-prediction of the velocity during times of low vertical wind speed ($< 9 \text{ m/s}$) could

account for some values of $\phi(\text{ClNO}_2)$ reaching 1 in Figure 2.35. In addition, higher actual wind speeds would increase the exchange velocity and further increase $\phi(\text{ClNO}_2)$ values above those in Figure 2.35. The average wind speed for points in Figure 2.35, however, was 9.3 m/s, suggesting that the applied exchange velocity was appropriate, in an average sense, for the WINTER data.

2.4.2.7.12 Dilution over the Ocean

Convective nocturnal marine boundary layers not only lead to ocean surface deposition but can contribute to air parcel dilution. Due to large flight-by-flight uncertainties in dilution rates and background mixing ratios, dilution was not included in the base case scenarios. Instead, additional simulations were run where dilution was represented as an additional first-order loss process for all chemical species in the mechanism (Table 2.3). The dilution rate constant was set to $3.1 \times 10^{-5} \text{ s}^{-1}$ as calculated from changes in NO_y mixing ratios measured in a single air parcel sampled at multiple times during RF03. This method was also applied to RF08 where a much smaller rate constant of $5 \times 10^{-6} \text{ s}^{-1}$ was determined, suggesting that $3.1 \times 10^{-5} \text{ s}^{-1}$ may be an upper limit. To additionally account for dilution and entrainment of background air over the ocean, background levels of O_3 were entrained at the same rate of dilution. Background levels of O_3 were calculated on a flight-by-flight basis as the intercept of O_3/NO_y correlation plots. As described, dilution and entrainment decreased the median $\gamma(\text{N}_2\text{O}_5)$ (ocean data only) by 5.7% and increased the median $\phi(\text{ClNO}_2)$ by 21.3%. Figure 2.36 shows the percent changes of (left) $\gamma(\text{N}_2\text{O}_5)$ and (right) $\phi(\text{ClNO}_2)$ relative to the base case, with histograms showing the distributions.

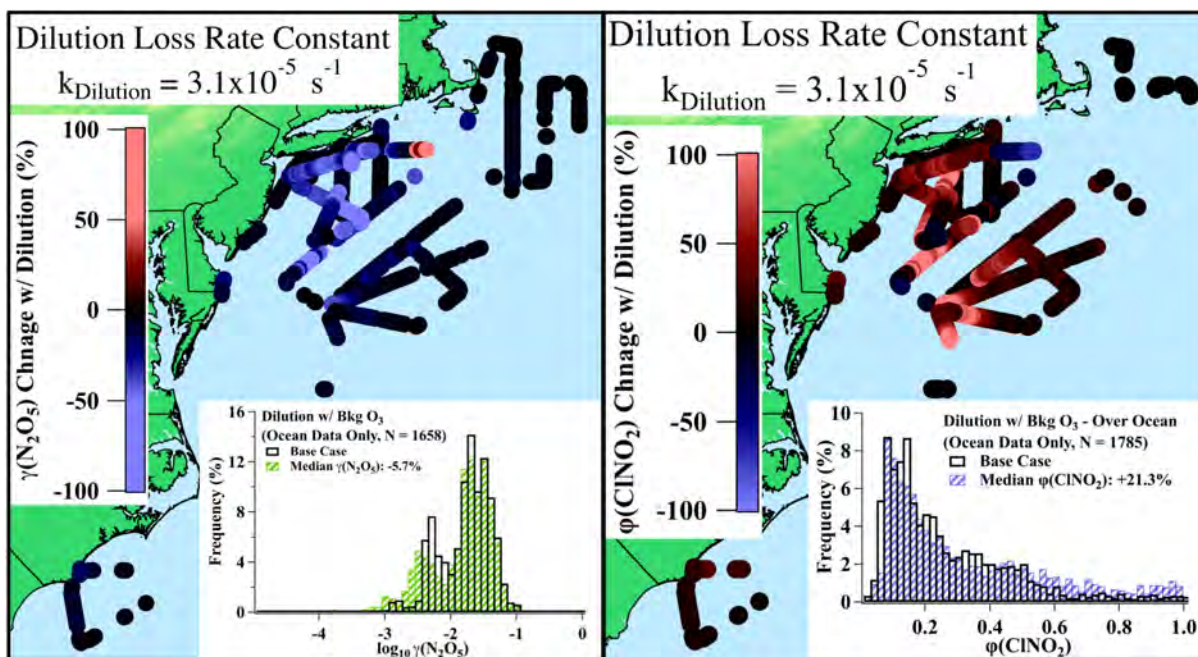


Figure 2.36. Model sensitivity to dilution over the ocean. Map shows the percent change in $\gamma(N_2O_5)$ and $\phi(CINO_2)$ relative to base case. Histograms show the $\gamma(N_2O_5)$ and $\phi(CINO_2)$ distributions in the base case scenarios (black bars) and sensitivity studies (colored bars).

2.5 Conclusions

In this Chapter, I have described the operating principles and calibration procedures for two instruments that utilize cavity ring down spectroscopy to simultaneously provide in situ measurements of NO, NO₂, O₃, NO_y (NOxCARD and ARNOLD), and NO₃ and N₂O₅ (ARNOLD). These instruments have been deployed in three recent field studies including the 2014 summer FRAPPÉ campaign at the BAO tower, the 2015 WINTER aircraft campaign based out of Langley, VA, and the 2017 UWFPS aircraft campaign based out of Salt Lake City, Utah. CRDS instrument accuracies during these campaigns were typically better than 5% for NO, NO₂, and O₃ and 12% for NO_y and N₂O₅ with compound-dependent detection limits for 1Hz measurements of ≤ 95 pptv for NO, NO₂, O₃, 90-200 pptv for NO_y, and ≤ 4.5 pptv for N₂O₅. These characteristics make these instruments useful tools to probe seasonal, temporal, and spatial variabilities in reactive nitrogen oxides and ozone in the ambient atmosphere.

In the last sections of this chapter, I described the model set-up and operation details of two chemical box models that have been developed and adapted from past studies for the analyses presented in Chapters 3 – 6. The DSMACC model utilized more than 15,000 chemical reactions from the Master Chemical Mechanism and was constrained to diel-averaged FRAPPÉ and SONNE observations to simulate average 24-hour photochemical O₃ production at the BAO tower. A dilution rate constant was also included in the model mechanism to represent dilution and O₃ entrainment and was fit through a comparison of observations and model output for 10 secondary compounds. Additional simulations were conducted to test the model sensitivity to model parameters and measurement uncertainties, the results of which are discussed in Section 3.3.4.5, in context of the Chapter 3 results.

A second model has been developed based on the original version presented in Wagner et al. (2013). This model has been designed to simulate the inorganic nocturnal chemistry of reactive nitrogen oxides in the wintertime residual layer. This model iteratively fits to observations of NO₂, O₃, N₂O₅, and ClNO₂ to derive initial (sunset) concentrations of O₃ and NO₂ and heterogeneous loss and production rate constants of N₂O₅ and ClNO₂, respectively. The fit rate constants are subsequently used to derive N₂O₅ uptake coefficients ($\gamma(\text{N}_2\text{O}_5)$) and ClNO₂ yields ($\phi(\text{ClNO}_2)$) throughout each flight. Details of model set-up and operation procedures, limitations, and assumptions have been presented in this chapter along with $\gamma(\text{N}_2\text{O}_5)$ and $\phi(\text{ClNO}_2)$ sensitivities to uncertainties in measurements and model assumptions, such as start time, air age, dilution and deposition. This model has been fit to observations from both the WINTER and UWFPS aircraft campaigns, with results presented in Chapters 4 - 6.

Deployment of the two CRDS instruments, along with additional gas- and aerosol-phase instruments in the FRAPPÉ, WINTER, and UWFPS campaigns, has provided a rich, seasonal data

set that, when combined with chemical box models, has allowed for the targeted investigation of mechanistic and emission-driven uncertainties in the tropospheric transformations of reactive nitrogen oxides and reaction products. These analyses are described in the remaining chapters.

Chapter 3: Influence of oil and gas emissions on summertime ozone in the Colorado Northern Front Range

Abstract

Tropospheric O₃, a photochemical product of nitrogen dioxide, has been decreasing across much of the eastern U.S. but has remained steady or even increased in some western regions. Recent increases in VOC and NO_x emissions associated with the production of oil and natural gas (O&NG) may contribute to this trend in some areas. The Northern Front Range of Colorado has regularly exceeded O₃ air quality standards during summertime in recent years. This region has VOC emissions from a rapidly developing O&NG basin and low concentrations of biogenic VOC in close proximity to urban-Denver NO_x emissions. In this Chapter, VOC OH reactivity (OHR), O₃ production efficiency (OPE), and the observationally constrained DSMACC box model are used to quantify the influence of O&NG emissions on regional summertime O₃ production. Analyses are based on measurements acquired over two summers during the FRAPPÉ and SONNE field studies at the Boulder Atmospheric Observatory (BAO), which is centrally located between major regional O&NG and urban emission sectors. Observational analyses suggest that mixing obscures any OPE differences in air primarily influenced by O&NG or urban emissions sectors. The box model confirms relatively modest OPE differences that are within the uncertainties of the field observations. Box model results also indicate that maximum O₃ at BAO is sensitive to changes in NO_x mixing ratio but also responsive to O&NG VOC reductions. Combined, these analyses show that O&NG alkanes contribute over 80% to the observed carbon mixing ratio,

roughly 50% to the regional VOC OHR, and approximately 20% to regional photochemical O₃ production.

The majority of content in this chapter has been published in McDuffie et al. (2016): Influence of oil and gas emissions on summertime ozone in the Colorado Northern Front Range. *Journal of Geophysical Research: Atmospheres*, 121(14), 8712-8729. The box model results presented in this chapter are an update to the results presented in McDuffie et al., (2016), as described in Section 2.4.1.6. This chapter additionally contains simulation results relevant to assessing the ozone sensitivity to changes in regional biogenic emissions, important when considering potential ozone impacts of drought-sensitive emission sources. Lastly, a model mechanism inter-comparison is presented that has been published as part of a chapter in Ramboll Environ (2017): Science Synthesis Report: Atmospheric Impacts of Oil and Gas Development, reported to the Texas Commission on Environmental Quality.

3.1 Introduction

Tropospheric ozone (O₃) is a secondary pollutant that contributes to the degradation of regional air quality. The only known sources of tropospheric O₃ are through the intrusion of O₃-rich stratospheric air (Roelofs & Lelieveld, 1995) and the oxidation of volatile organic compounds (VOCs) in the presence of nitrogen oxides (NO_x = NO + NO₂) (Chameides, 1978; Crutzen, 1970). In the past two decades, summertime maximum O₃ at rural (receptor) sites across much of the U.S. has exhibited a strongly decreasing trend (Cooper et al., 2012), likely in response to concurrent, declining NO_x emissions (e.g. Butler et al., 2011; Cooper et al., 2012; Environmental Protection Agency (US EPA), 2016). Decreasing O₃ trends have been most pronounced in the eastern U.S., but generally more moderate, or even increasing, at high-elevation western sites (Cooper et al., 2012). Proposed explanations for upward trends include increases in summer temperatures,

contributions from stratospheric intrusions, long range transport of emissions from Asia, western wildfire activity, and/or regional oil and natural gas (O&NG) emissions (Cooper et al., 2012; 2015). Here we focus on summertime O₃ production impacted by O&NG activity in the Colorado Northern Front Range (NFR) (Figure 3.1), a region out of compliance with National Ambient Air Quality Standards (NAAQS) of 75 ppbv for O₃ since 2007 and expected to remain so under recently revised 2015 standards of 70 ppbv (Colorado Department of Public Health and Environment (CDPHE), 2018).

The NFR (Figure 3.1) has urban O₃ precursor emissions in close proximity to those from other sectors, principally agriculture (e.g. animal feedlots) and O&NG production. The NFR's Wattenberg Gas Field of the greater Denver-Julesburg Basin has seen significant recent increases in O&NG production, with the number of active wells nearly doubling in Weld County between January 2008 and July 2015 to over 27,000 (Colorado Oil and Gas Conservation Commission (COGCC), 2/2016). Though O&NG production has increased in multiple U.S. basins, a relatively small number of these basins lie in close proximity to large urban areas, as is the case with the Denver-Julesburg. Biogenic VOC mixing ratios (e.g. isoprene) are relatively low in the NFR compared to other U.S. O&NG producing regions, such as Texas and Pennsylvania (Rutter et al., 2015; Swarthout et al., 2015). Lower biogenic mixing ratios may magnify the influence of O&NG emissions on regional O₃ production. Multiple studies have extensively characterized NFR VOC emissions, including those from O&NG activity (Brantley et al., 2015; Gilman et al., 2013; Pétron et al., 2012; 2014; Swarthout et al., 2013), but remain limited in terms of characterizing their influence on summertime O₃ production.

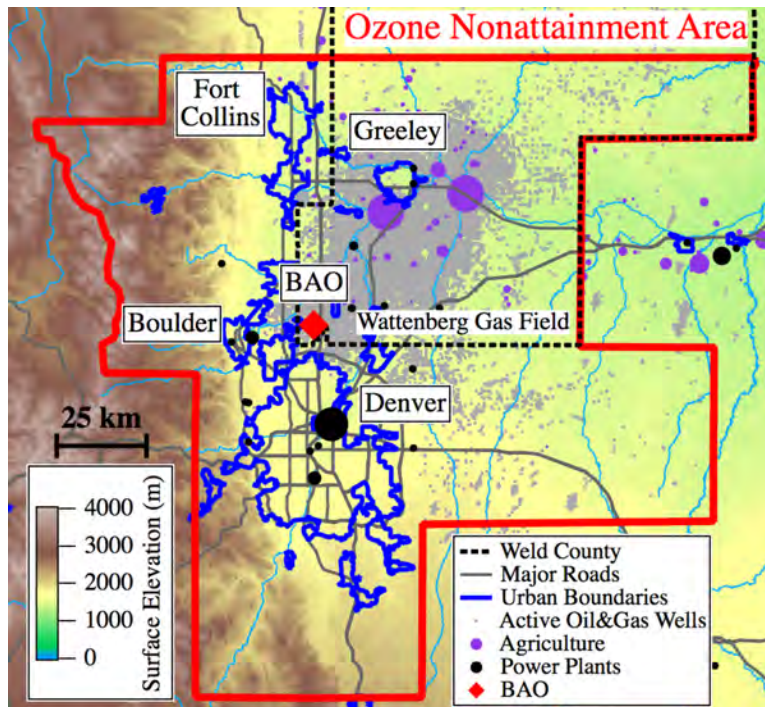


Figure 3.1. Elevation map of the Northern Front Range (NFR) region of Colorado showing the O₃ nonattainment area, Weld County (dashed lines), major roads, rivers, urban regions, power plants (scaled by relative NO_x emissions), large agricultural facilities (feedlots sized by animal capacity), and active O&NG wells ((Colorado Oil and Gas Conservation Commission (COGCC), 1/2016)). The red diamond indicates the location of the BAO measurement site.

Relatively few studies have specifically assessed the influence of emissions associated with O&NG activity on regional summertime O₃ production. Several papers have focused on wintertime O₃ in O&NG producing regions in both the Upper Green River Basin of Wyoming (Field et al., 2015; Oltmans et al., 2014; Rappenglück et al., 2014; Schnell et al., 2009) and the Uintah Basin in Utah (Ahmadov et al., 2015; Carter & Seinfeld, 2012; Edwards et al., 2014; 2013; Helmig et al., 2014; Oltmans et al., 2014). Winter O₃, however, is distinct from summertime urban-influenced O₃ and has so far only occurred in remote areas with low population densities and urban emissions. Winter O₃ is also specific to highly stable inversion conditions that cause an accumulation of VOC emissions from O&NG activity. The influence of O&NG emissions on summer O₃ near urban areas is not well characterized and is a complex issue arising from the interaction of a variety of emissions.

Previous summertime O₃ analyses include two initial studies that used regional models to determine that O₃ production was positively influenced by emissions associated with O&NG activity in the Haynesville region in Texas (Kemball-Cook et al., 2010) and across multiple western U.S. locations (Rodriguez et al., 2009). More recent work has suggested that O&NG-associated NO_x emissions, relative to those of VOCs, contribute disproportionately to summertime O₃ production. For example, O&NG-associated VOC emissions only contribute 8% to O₃ precursors in California's San Joaquin Valley (Gentner et al., 2014) and less than 20% and 7%, respectively, to the O₃ forming potential in the Barnett Basin near Fort Worth, Texas (Rutter et al., 2015) and Pennsylvania's Marcellus Basin (Swarthout et al., 2015). Similarly, regional modeling of the Eagle Ford Basin in Texas showed that changes in regional summertime O₃ concentrations were not driven by O&NG-associated VOCs but rather by emissions of NO_x (Pacsi et al., 2015). As observed from space, NO_x levels associated with O&NG activity (e.g. flaring and combustion from O&NG extraction machinery and transport vehicles) have recently increased over three O&NG producing regions in the central U.S. (Duncan et al., 2016). In other states such as Pennsylvania, the influence of O&NG activity on O₃ may be underestimated or obscured due to: 1) NO_x trends masked by surrounding urban emission reductions (Duncan et al., 2016); and/or 2) gaps in the monitoring network for EPA criteria pollutants such as NO₂ (Carlton et al., 2014). Since publication of this work, at least two additional studies have used observational and modeling-based analyses to assess the impact of O&NG emissions on ozone in the Colorado Front Range (Cheadle et al., 2017; Pfister et al., 2017a), and are discussed in the results section below.

In this analysis, we apply three methods to characterize the influence of VOC and/or NO_x emissions on O₃ production in the NFR. These include VOC OH Reactivity (OHR), O₃ Production Efficiency (OPE), and photochemical box modeling. The VOC OH Reactivity (OHR) (e.g. Gilman

et al., 2013) is a measure of the kinetic oxidation of VOCs by the OH radical and is often the rate limiting step in photochemical O₃ production. A number of O&NG-focused studies have used this metric to highlight the potential contribution of O&NG VOCs to O₃ production in both summer and winter months (Field et al., 2015; Gilman et al., 2013; Rutter et al., 2015; Swarthout et al., 2013; 2015). Although VOC OHR provides a simple assessment of the relative contribution of different VOCs to potential O₃ production, it does not incorporate information about radical propagation or its NO_x dependence, both of which are important for predicting the efficiency of O₃ production. Ozone Production Efficiency (OPE) (e.g. Trainer et al., 1993) is a measure of the number of O₃ molecules produced, or number of NO_x inter-conversion cycles completed, before NO_x is lost through termination reactions (e.g. nitric acid (HNO₃) or organic nitrate production). The OPE is defined as the slope of odd oxygen (O_x = NO₂ + O₃) against NO_z (NO_z = NO_y - NO_x; where NO_y is total oxidized reactive nitrogen). OPE analyses have been used to characterize urban and rural regions across the U.S. as documented in Table 1 of Griffin et al. (2004), but to our knowledge, have not been applied specifically to O₃ production in an O&NG basin. The principle advantage to OPE is that it is an observable quantity that should differentiate between air parcels of different VOC composition and NO_x mixing ratios, for example those influenced by O&NG vs. urban emissions. However, OPE derived from field observations is an upper limit as it suffers from artifacts such as depositional NO_y loss.

Box model analyses are a common tool used to assess the sensitivity of O₃ production to NO_x and VOC emissions within air parcels of known composition. They have been used recently to model O₃ production in western U.S. O&NG basins during winter months (Carter & Seinfeld, 2012; Edwards et al., 2014; 2013). To our knowledge, a box model analysis has not been previously reported for summertime O₃ production in an O&NG basin. Box models have the

advantage of a fully explicit chemical mechanism, but they parameterize transport as a highly simplified, single dilution term. They therefore do not represent heterogeneity in the spatial distribution of emissions. They also do not rely on emission inventories, which can be an important source of uncertainty in three dimensional chemical transport models (e.g. Ahmadov et al., 2015), but parameterize emissions so as to match observations or constrain primary species to observed values. Box model analyses are useful in assessing the NO_x and VOC sensitivities of O₃ and other secondary products (e.g. acetone, MEK, RONO₂) for averaged data, in which chemical and meteorological variability average to typical values (Edwards et al., 2013), or in simulations of air parcel evolution along a known trajectory (Washenfelder et al., 2011b). In these cases, box models provide a simple alternative to 3D chemical transport models.

We present a combination of VOC OHR and OPE analyses along with an observationally constrained box model to: 1) quantify the impacts of O&NG emissions on summertime maximum O₃ and its production efficiency at a specific location within the NFR; and 2) evaluate the O₃ sensitivity to NO_x and VOC emissions. This analysis indicates that the influence of O&NG VOCs on regionally produced O₃ is small relative to their contribution to total VOC mass and OHR, but not negligible on the scale relevant to attainment of regional air quality standards.

3.2 Experimental Analysis Methods

3.2.1 Measurements and Field Campaigns

As described in Chapter 2, measurements at BAO were made in July-August 2012 and July-August 2014, months when the NFR experiences O₃ levels in exceedance of the EPA 8-hour O₃ standard (Colorado Department of Public Health and Environment (CDPHE), 2015). During these two summers, the NFR was studied by three major field campaigns (FRAPPÉ, DISCOVER-

AQ, and SONNE) that contributed data to this analysis. Measurement descriptions can be found in Sections 2.3.1.3 and 2.3.4 and as a complete list in Table 3.1.

Table 3.1 Summary of BAO chemical and physical observations used in this analysis

Compound	Observation Technique/ Instrument	Uncertainty	Limit of Detection or (Precision)	Measurement Frequency	Obs. Year
NO ₂ /NO _x	CRD	< 5%	< 30 pptv	1 s	2012
NO/NO ₂ /O ₃	CRD	< 5%	< 50 pptv	1 s	2014
NO _y	CRD	12%	200 pptv	1 s	2014
NH ₃	QC-TILDAS	90%	< 0.5 ppbv	1 s	2014
CH ₄	Picarro CRD	2 ppbv	(0.23 ppbv)	1 s	2012
CH ₄	Picarro CRD	6%	(0.20 ppbv)	1 s	2014
CO	Picarro CRD	12%	(10 ppbv)	1 s	2014
CO	V-UV Fluorescence	5%	1 ppbv	60 s	2010/2012
O ₃	TECO	2%	1 ppbv	60 s	2012
O ₃ (Background)	TOPAZ LIDAR	< 5 ppbv	(2-6 ppbv)	5 min	2014
Speciated VOCs	GC-MS	< 25%	10 pptv	5 min (30 min freq.)	2012
HCHO ^a	Trace Organic Gas Analyzer (TOGA)	40%	40 pptv	35 s (2 min freq.)	2014
CH ₃ CHO ^a	TOGA	20%	10 pptv	35 s (2 min freq.)	2014
j(NO ₂) - downwelling	Filter Radiometer	< 25%	1×10 ⁻⁵ s ⁻¹	60 s	2014
j(NO ₂) - total	Filter Radiometer	12%	3.7×10 ⁻⁶ s ⁻¹	60 s	2007
j(O ¹ D) - total	Filter Radiometer	26%	1.1×10 ⁻⁷ s ⁻¹	60 s	2007
Albedo	Multi-Filter Rotating Shadowband Radiometer	2%	8×10 ⁻⁴ W m ⁻² nm ⁻¹	60 s	2014

^aMeasurements from NSF/NCAR C-130 aircraft, deployed as part of the 2014 FRAPPE campaign

3.2.2 Ozone Production Efficiency

Ozone production efficiencies were only derived from 2014 data due to the lack of NO_y measurements in 2012. Chemical observations were averaged to a 1-minute time resolution and filtered to include data after noon (12 - 6 pm Mountain Daylight Time (MDT)) during peak O₃ production and sampling altitudes > 25 mAGL to reduce the influence of deposition to the surface. The slope of the O_x to NO_z correlation at individual, 15-minute intervals was used to isolate and derive the OPE of individual air parcels. In contrast to the O₃/NO_z slope defined in previous studies

(e.g. Hirsch et al., 1996; Olszyna et al., 1994; Trainer et al., 1993; 1995), the use of O_x accounts for local O_3 titration through reaction of NO with O_3 near NO_x emission sources. Additionally, NO_z , instead of NO_y , normalizes age across different air parcels (Trainer et al., 1993). However, by not additionally accounting for NO_y removal processes, such as surface deposition of individual NO_y species (e.g. HNO_3), the OPEs derived here are upper limits. Further details of the OPE derivation method are described in the following sections.

3.2.2.1 OPE Derivation – Data Coverage

During the data collection period of 16 July - 15 August 2014, there were 381 individual time intervals with at least 11, 1-minute data points from which individual OPEs were derived. The number of OPEs was reduced to 305 by applying an intercept filter (described in Section 3.2.2.3) and further reduced to a subset of 80 by filtering for correlation coefficients (r^2) > 0.5. We interpret the highly correlated 80 OPEs to represent periods with the greatest photochemical O_3 production.

Numerous instrument carriage maintenance periods reduced data coverage in 2014. Despite time periods without chemical measurements, Figure 3.2 shows that both OPE populations (305 and 80 subsets) are representative of afternoon O_3 production in 2014. Figure 3.2 shows a time series of the 2014 data collection period (16 July through 15 August, 2014) with the complete time-series of O_3 measured at the surface (independent of carriage operation) and with the CRDS instrument (from the instrument carriage) for the 305 and 80-OPE subsets. The population of 305 OPEs covers at least 15-minutes of 27 (87%) of the possible 31 campaign afternoons (12 pm – 6 pm MDT). The smaller subset of 80 OPEs covers at least 15-minutes of 22 (71%) campaign afternoons. Figure 3.2 shows that both populations are representative of the majority of days during which O_3 concentrations (1-hour average) exceeded 75 ppbv (305 OPEs: 6/8 days, 80 OPEs: 5/8

days) and 70 ppbv (305 OPEs: 9/12 days, 80 OPEs: 8/12 days). Despite representative data coverage, standard errors and deviations for both subsets were large. More data coverage would reduce the standard error and provide a higher precision for observed OPEs in the NFR.

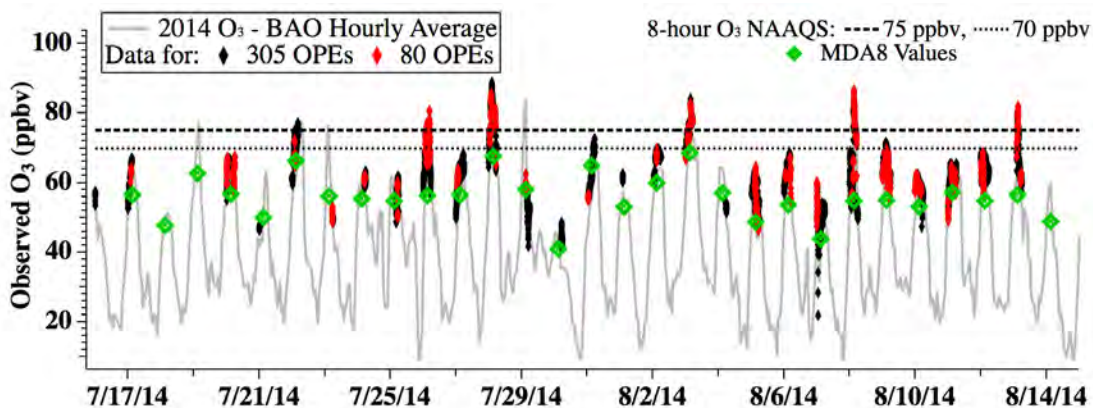


Figure 3.2. O₃ time series, 16 July – 15 August 2014. (Grey) Surface O₃ measured at BAO; (Black) O₃ data coverage for 305 OPEs as measured by CRDS; (Red) O₃ data coverage for 80 OPEs as measured by CRDS; Dashed) EPA 2008 (75 ppbv) and 2015 (70 ppbv) 8-hour O₃ air quality standards (NAAQS); (Green) Maximum Daily 8-hr Average (MDA8).

3.2.2.2 OPE Derivation - Time Interval

Intervals of 15-minutes were used to isolate individual air parcels by reducing the probability of concurrently sampling multiple air parcels with distinct background O₃ concentrations. An example of the utility of this method is given in Figure 3.3. Figure 3.3 shows the 12-6 pm chemical time-series (top) and corresponding O_x/NO_z (bottom) correlation plot for 8 August 2014. The correlation plot clearly shows two air parcels with different chemical histories (i.e. different CH₄/CO ratios) and background O_x levels (i.e. intercepts) sampled at the site. When individually fit, these air parcels have similar slopes (5.4 ± 0.1 and $4.7 \pm < 0.1$ ppbv/ppbv). However, when one fit is applied, the regression produces a slope of $9.7 \pm < 0.1$ ppbv/ppbv, an OPE over 80% larger than the fits of individual populations. This could occur any time air parcels with distinct backgrounds are sampled at the site, indicating the need to derive individual OPEs over shorter time intervals as is done here.

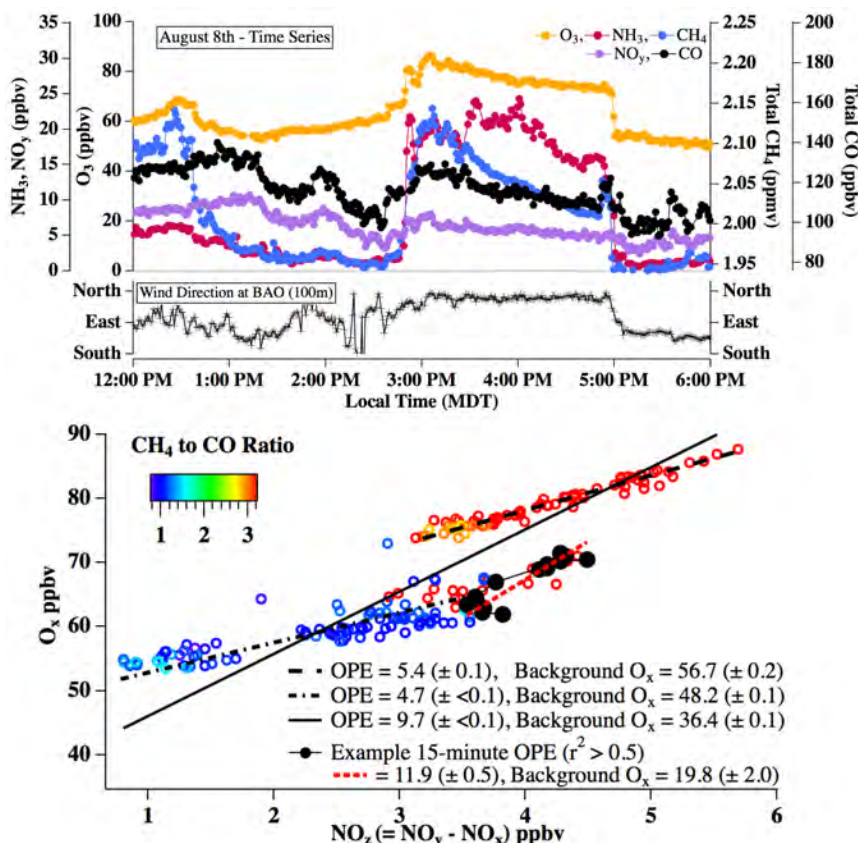


Figure 3.3. (Top) Time series for 8 August 2014 (12 pm - 6 pm MDT); (bottom) O_x/NO_z correlation for 1-minute averaged data on 8 August 2014, colored by observed CH_4/CO ratio; (black points) example 15-minute period used to derive individual OPEs.

3.2.2.3 OPE Derivation - Fit Intercept Filter

Ideally, O_x/NO_z fit intercepts provide a measure of background O_x prior to photochemical production (i.e. zero NO_z). A Gaussian fit (Figure 3.4) applied to the intercepts of 381 OPEs (after point number filter, before r^2 filter) produced a mean O_x background of 56.7 ± 9.3 (2σ) ppbv (average NO_2 : 1.6 ppbv), very similar to the background O_3 of 58 ± 6 ppbv estimated from LIDAR measurements (see Section 2.4.1.4). In some cases, O_x/NO_z fits produce an $r^2 > 0.5$ but with intercepts far from the estimated background O_3 , due to mixing of air parcels within a single 15-minute fit interval. The black points in the lower correlation plot of Figure 3.3 show an example of this type of event during the transition period between the two distinct air parcels (red and blue points) measured on 8 August 2014. In this example, an intercept < 47.4 ppbv (i.e. 56.7 ppbv - 2σ)

indicates two different air parcels are being sampled during a single interval. Thus, all individual OPEs with intercepts $\pm 2\sigma$ from the mean background were filtered from the analysis. The intercept filter reduced the number of OPEs from 381 to 305.

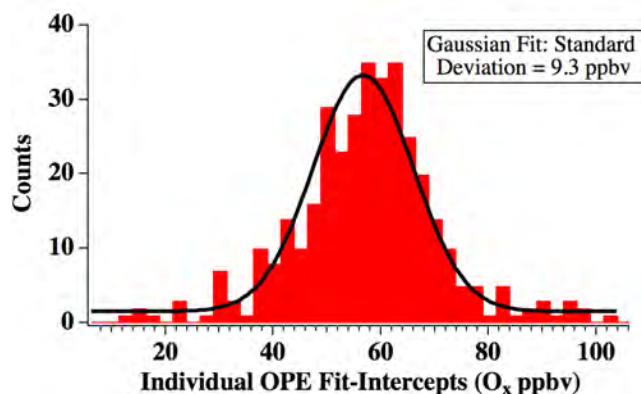


Figure 3.4. Histogram and Gaussian fit of 381 OPEs (point filter applied).

3.2.3 Box Model - Overview and Set-Up

As described in Chapter 2, model simulations were performed with DSMACC (Emmerson & Evans, 2009), a zero dimension box model that uses the Master Chemical Mechanism (MCM v3.3.1) for its chemistry scheme and the NCAR Tropospheric Ultraviolet and Visible Radiation Model (TUV v5.2) (Madronich et al., 1998) for photolysis rates. The subset of chemistry used here includes a complete inorganic mechanism and degradation scheme for 50 primary VOCs, with a total of 4002 species and 15555 reactions.

Briefly, to represent the NFR as a photochemical box, all DSMACC simulations were initialized at 8 am MDT, integrated forward for 24-hours with a 10 minute time step, while initialized with, and constrained every 30 minutes to, SONNE (Section 2.3.4.1) diel average observations of temperature, pressure, and mixing ratios of CO, CH₄, 42 non-methane VOCs, and water vapor (derived from 10 m relative humidity measurements). Section 2.4.1 provides further information on DSMACC constraints, which force the model to accurately represent primary

species whose average concentrations are governed by processes not represented in the box model, such as emissions and horizontal transport.

An additional dilution rate constant was applied to all 4002 model compounds to simulate average vertical transport and loss from the box (as described in Section 2.4.1.4). A dilution rate constant of $1.11 \times 10^{-4} \text{ s}^{-1}$ was derived from a fit of the model output to the diel average observations of 10 secondary products, including O_3 , 6 oxygenated VOCs, and 3 alkyl nitrates. These compounds were initialized to their average observed values (8 am MDT) but not otherwise constrained (Figure 2.16). To account for entrainment and mixing with the residual layer during morning boundary layer growth, background mixing ratios (Table 2.2) were added to the model at the same rate of dilution. At the fit dilution rate, the average model-to-observation difference for all 10 compounds was -12.6% (for individual compounds, Table 2.2). Table 2.1 summarizes the model treatment of all chemical observations and Figure 3.5 illustrates the observed non-methane VOCs in terms of their diel average OHR.

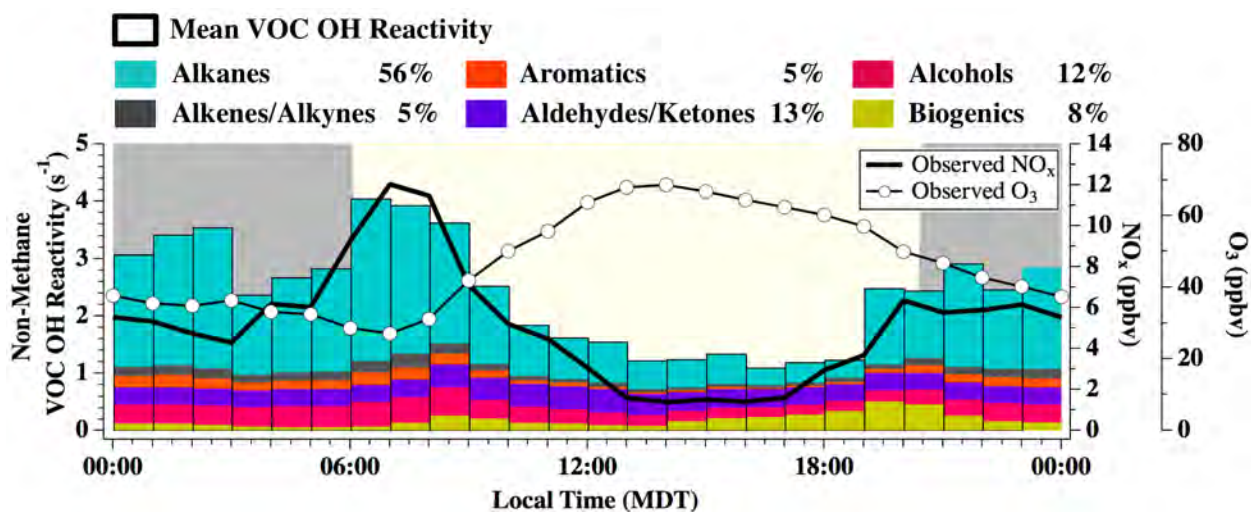


Figure 3.5. Diel average of non-methane VOC and NO_x model constraints (SONNE measurements). VOCs (left axis) are given in VOC OH reactivity, NO_x and O_3 (right axes) are given in mixing ratio. Bar height is the average VOC OHR colored by the fractional VOC class contribution every 60-minutes. Average VOC class contributions are calculated from the sum of averaged (24-hour) individual VOCs. VOC OHR does not include contributions from HCHO , CO , or CH_4 . Aldehydes and ketones shown here were not used as model constraints but instead used to derive the dilution rate constant.

In order to quantify the impact of primary O&NG VOCs on maximum photochemical O₃ production in the NFR, three VOC scenarios were developed. Simulations run with the base (Case 1) VOC scenario were constrained to diel average chemical and physical observations at BAO to represent O₃ production under average conditions. Cases 2 and 3 removed and doubled the VOC contributions from O&NG activities as described in Section 2.4.1.2 to further quantify the influence of O&NG VOCs on average O₃ production in this region. Differences between these VOC cases in terms of the carbon mixing ratio (ppbC) and OHR are summarized in Table 3.2. For NO_x, no contribution from O&NG activity was assumed. County level NO_x emissions based on the U.S. EPA NEI-2011 version 1 inventory (further details in Appendix A) suggest an O&NG contribution of 5.5% to NO_x emissions in the NFR nonattainment area (Figure 3.1). Past work in a Utah O&NG basin has shown that NO_x emissions from O&NG production can be overestimated by a factor of 4 (Ahmadov et al., 2015), indicating that the 5.5% contribution of O&NG activity to NO_x emissions may be an upper limit.

Table 3.2. VOC Scenario Statistics by non-methane VOC class^a.

	Alkanes	Alkenes & Alkynes	Aromatics	Aldehydes & Ketones	Alcohols	Biogenic	Alkyl Nitrates
<i>Case 1 - Observed VOCs</i>							
<i>Total Average VOC OHR = 2.41 (s⁻¹), Total Average ppbC = 162.75</i>							
OHR	1.36	0.12	0.12	0.32	0.29	0.20	<0.01
ppbC	132.16	1.91	4.50	10.66	12.50	0.95	0.06
<i>Case 2 - O&NG VOCs Removed</i>							
<i>Total Average VOC OHR = 1.13, (s⁻¹) Total Average ppbC = 46.76</i>							
OHR	0.18	0.11	0.10	0.27	0.29	0.20	<0.01
ppbC	18.72	1.85	3.37	9.32	12.50	0.95	0.04
<i>Case 3 - O&NG VOCs Doubled</i>							
<i>Total Average VOC OHR = 3.67 (s⁻¹), Total Average ppbC = 278.31</i>							
OHR	2.55	0.12	0.14	0.37	0.29	0.20	<0.01
ppbC	245.60	1.97	5.63	11.59	12.50	0.95	0.07

^aVOC OHR in units of s⁻¹, mixing ratio of carbon in parts per billion of carbon (ppbC). Derived from box model results (24-hour average) at NO_x scaling factor =1

3.3 Results and Discussion

3.3.1 Observed chemical composition and wind patterns

Air composition at BAO during the summers of 2012 and 2014 contained chemical tracers from all regional emission sectors (e.g. O&NG, urban, and agriculture), irrespective of wind direction. The histogram in Figure 3.6b plots simple chemical tracers for all major emission sectors (O&NG: CH₄; agriculture: NH₃; urban: CO and NO_x), averaged between 2012 and 2014 observation years, binned by wind direction, and normalized to westerly mixing ratios. Data have been binned by four wind directions and filtered to include wind speeds > 2.5 m/s to minimize the influence of nearby emission sources and to be consistent with the threshold used by Pétron et al. (2012). Figure 3.6b shows that air at the site has a substantial contribution from all regional emission sources irrespective of local north, east, or southerly wind directions. In addition, enhancements of tracers in the direction of each major emission source (e.g. NO_x is slightly enhanced in southerly winds) are smaller than those observed in wintertime (Figure 7: Brown et al., 2013). These observations suggest significant mixing and recirculation that causes regional air on average to have characteristics of all surrounding emission sectors.

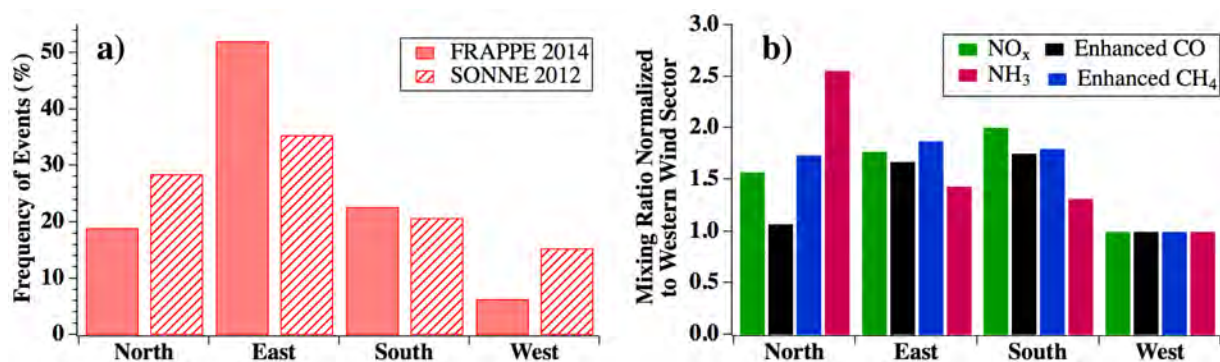


Figure 3.6. (a) Histogram of July-August 2012 and 2014 wind direction measured at BAO (100 m); (b) Median mixing ratios of chemical tracers averaged between 2012 and 2014 campaign years, normalized to mixing ratios in the western wind sector to illustrate relative sector-to-sector differences on the same scale for all species. CO and CH₄ plotted as normalized enhancements above observed 2012 and 2014 backgrounds. All data filtered for wind speeds > 2.5 m/s. Binned wind directions are north: 315°-45°, east: 45°-135°, south: 135°-225°, and west: 225°-315°.

Several mechanisms serve to mix emissions from different sources within the NFR. During summer, winds follow a typical mountain-valley diel pattern. During the day, thermally driven upslope winds predominately flow from the east, with a slight southerly component (Toth & Johnson, 1985). Beginning in late afternoon, flow patterns turn around and a westerly downslope occurs along the South Platte River Basin, often accompanied by afternoon regional thunderstorm activity (Toth & Johnson, 1985). Figure 3.6a provides a histogram of 30-minute averaged winds measured at BAO during July and August 2012 and 2014 (100 m winds, speed > 2.5 m/s, 11am – 3pm MDT), which illustrate this dominant afternoon easterly flow prior to the downslope switch. A terrain-forced mesoscale vortex circulation pattern, termed the Denver Cyclone, is also a common occurrence during summer months (Crook et al., 1990; Szoke et al., 1984; Szoke, 1991; Wilczak & Glendening, 1988). These complex circulation patterns combine to mix air parcels, making it difficult to model the daily evolution of emissions from spatially distinct regional emission source sectors.

3.3.2 VOC OH Reactivity – 2012

The campaign average ($\pm 1\sigma$ standard deviation) OHR for non-methane VOCs (excluding HCHO) observed during SONNE was $2.4 \pm 0.9 \text{ s}^{-1}$. This compares to a previous determination at BAO of $3 \pm 3 \text{ s}^{-1}$ based on an analysis of data from same instrument in winter 2011 (Gilman et al., 2013) and summertime measurements near O&NG operations in Pennsylvania of $2.4 \pm 1.4 \text{ s}^{-1}$ (includes CH_4 , excludes HCHO) (Swarthout et al., 2015). More recent VOC measurements from 2015 at BAO have reported the same average summertime value of 2.4 s^{-1} (excluding CH_4) (Abeleira et al., 2017). On average, alkanes were the dominant contributing class to VOC OHR (56%, Figure 3.5), of which the majority can be attributed to primary O&NG emissions (87%: VOC OHR, 86%: ppbC, Figure 2.14). Previous studies in Texas have estimated a similar

contribution from light alkanes (i.e. O&NG emissions) in the Eagle Ford Shale area (~70%, Schade & Roest, 2016), but also a much smaller contribution from fugitive O&NG production emissions in the Barnett Shale region (~13%, Rutter et al., 2015). Abeleira et al. (2017) reported an average 46-58% contribution from O&NG VOCs (determined using positive matrix factorization analysis) during morning hours in summer 2015 at BAO.

Biogenic VOCs are highly reactive with OH (Table 2.1) and have been shown to dominate VOC OHR in O&NG regions in Pennsylvania ($47 \pm 22\%$, Swarthout et al., 2015) and Texas (70%, Rutter et al., 2015), but only contributed on average, 8% to VOC OHR at BAO in 2012. This result highlights the importance of O&NG emissions relative to biogenic emissions on O₃ production in the NFR, making this location unique compared to two east/southeastern U.S. O&NG basins. It has also been shown, however, that there was widespread regional drought in the NFR during July and August 2012 (Abeleira et al., 2017; National Oceanic and Atmospheric Administration (NOAA), 2012). Drought conditions have been shown to suppress biogenic emissions, such as isoprene (e.g. Guenther et al., 2006), and thus could cause an underrepresentation of the biogenic influence on VOC OHR and O₃ in this study. For example, measurements from BAO in 2015, a non-drought year, showed a much larger contribution of biogenic VOCs, up to 49%, to VOC OHR (Abeleira et al., 2017). The magnitude of biogenic emissions in the NFR, however, is still lower than many other U.S. locations (as well as NFR anthropogenic emissions, Figure 2.13), making O₃ in the NFR potentially less sensitive to drought-induced changes in emissions of biogenic VOCs. This result is confirmed through additional model simulations presented in Section 3.3.4.3.

3.3.3 Ozone Production Efficiency – 2014

During the 2014 campaign, afternoon O_x was correlated with NO_z (Figure 3.7), typical of summertime relationships between O₃ and oxidized reactive nitrogen observed in other U.S.

regions (e.g. Trainer et al., 1993). Individual OPEs were derived from a 2-sided regression fit of O_x to NO_z every 15-minutes between 12 and 6 pm MDT after removing time intervals with fewer than 11, 1-minute data points. This time period was chosen to minimize the effects of non-photochemical factors such as morning O_3 entrainment (see Section 3.3.3.2) and to compare the products of photochemistry (i.e. NO_z , O_3) in distinct air parcels. Increasing the time period to 9 am - 6 pm MDT introduces additional scatter in the data from the OPE analyses but does not change the main conclusions presented below. Further, fits with intercepts more than $\pm 2\sigma$ from the mean intercept were also removed, as described further below and in Section 3.2.2.3. There were 305 OPE fits that met these criteria, which represent at least 15-minutes of 27 (87%) afternoons in 2014 (see Figure 3.2). The average ($\pm 1\sigma$) of these 305 OPEs was 2.9 ± 4.4 ppbv/ppbv.

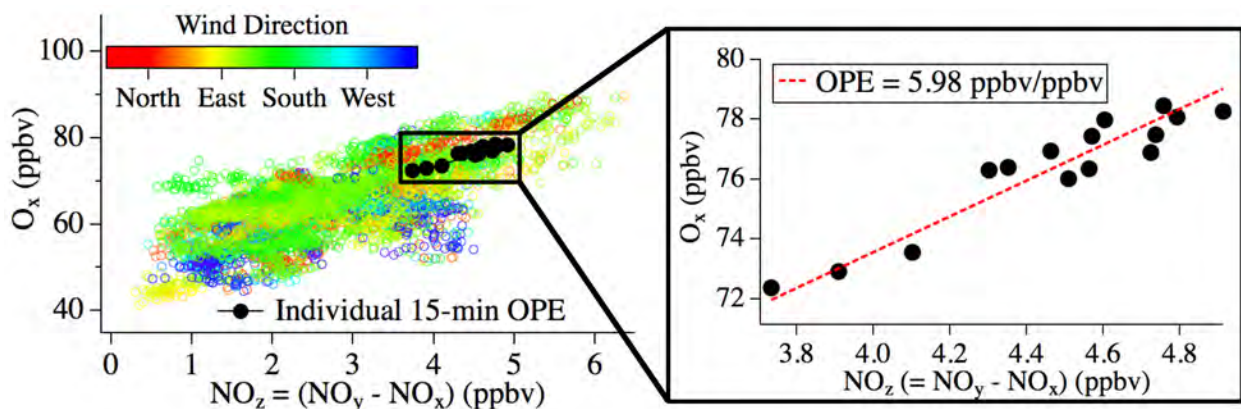


Figure 3.7. (left) Observed O_x/NO_z correlation for 16 July – 15 August 2014 (12 pm – 6 pm MDT, $N = 8268$), colored by observed wind direction; (right) Example O_x/NO_z correlation during one, 15-minute time interval. This OPE meets the point number (> 11), intercept (56.7 ± 9.3 ppbv), and $r^2 (> 0.5)$ filter requirements discussed in text.

To ensure at least a 98.4% (i.e. significant) probability of correlation, a subset of these OPEs with correlation coefficients (r^2) > 0.5 was also selected. There were 80 OPEs that met the r^2 threshold, which represent at least 15-minutes of 22 (71%) afternoons in 2014 (see Figure 3.2). The average ($\pm 1\sigma$) of this 80-OPE subset was 5.3 ± 3.6 ppbv/ppbv. Selection of this subset reduced scatter in the data but also introduced a high bias by eliminating data scattered close to zero (e.g.

with small changes in O_x and/or NO_z). We take this smaller 80-OPE subset to represent time periods with the greatest photochemical O_3 production but compare both 305 and 80-OPE populations below. Both populations are representative of the majority of high (> 70 ppbv) O_3 days observed at BAO in 2014.

Average OPEs ($\pm 1\sigma$) derived here are similar to those from analyses in other regions of the U.S.. However, many previous studies have defined OPE as the slope of O_3/NO_z or O_3/NO_y , making it difficult to directly compare values here to much of the past ~20 years of OPE literature. Nevertheless, the averages of 2.9 (305-OPEs) and 5.3 (80-OPEs) ppbv/ppbv fall within the range of 2-8 ppbv/ppbv for O_x/NO_z previously reported for urban regions across the U.S. (Kleinman et al., 2002; Nunnermacker et al., 1998; St. John et al., 1998; Zaveri et al., 2003).

3.3.3.1 NFR Emission Sector OPEs

To distinguish the influence of different emission sectors on OPE, individual OPEs were sorted according to two markers of air transport history: 1) wind direction; and 2) simple chemical tracers. Sorting the data according to these markers contrasts the O_3 production associated with the relatively different VOC composition and NO_x mixing ratios of O&NG and urban emission sectors. As this section describes, however, any dependence of OPE on these parameters is considerably smaller than the variability and/or uncertainty in the observed OPE data.

3.3.3.1.1 OPE as a Function of Wind Direction

Air arriving at BAO from the northeast is expected to have traveled over regional O&NG operations, while that from the southeast to have been relatively more urban influenced (Figure 3.1). However, the OPE measured at BAO does not vary strongly with wind direction. The overall O_x/NO_z correlation in 2014, colored by wind direction (Figure 3.7, left), does not show a clear difference in air arriving from south or north of the site. Analysis of individual OPEs against wind

direction reveals similar results. Figure 3.8 provides a wind rose of the 80-OPE subset ($r^2 > 0.5$) colored by northeast (NE: 0-90°), southeast (SE: 90-180°), and western (W: 180-360°) wind directions (15-minute average). Box and whisker plots for NE and SE wind sectors show no statistically significant (i.e. $p > \alpha$, $\alpha = 0.05$) difference in their average (difference = 0.6 ppbv/ppbv, $p = 0.43$) or median (difference = 0.1 ppbv/ppbv, $p = 0.88$) values. In addition, there is no significant difference between average NE and SE OPEs (difference = 0.5 ppbv/ppbv, $p = 0.39$) when calculated from the larger population of 305 without the r^2 selection. Due to the large observed variability in OPE, 95% confidence intervals for differences in mean NE and SE OPEs are 0.6 ± 1.4 ppbv/ppbv and 0.5 ± 1.1 ppbv/ppbv for the 80 and 305-OPE populations, respectively. This wind direction analysis suggests a 95% probability that the OPE influence of O&NG emissions is less than 1.8 ppbv/ppbv. During times of high photochemical activity in 2014 (e.g. highest NO_z mixing ratios, Figure 3.7), an OPE less than 1.8 ppbv/ppbv suggests that the O&NG sector contributes at most 11 ppbv to total O_3 . The actual O&NG influence determined from the box model analysis is likely considerably smaller (see Section 3.3.4.2).

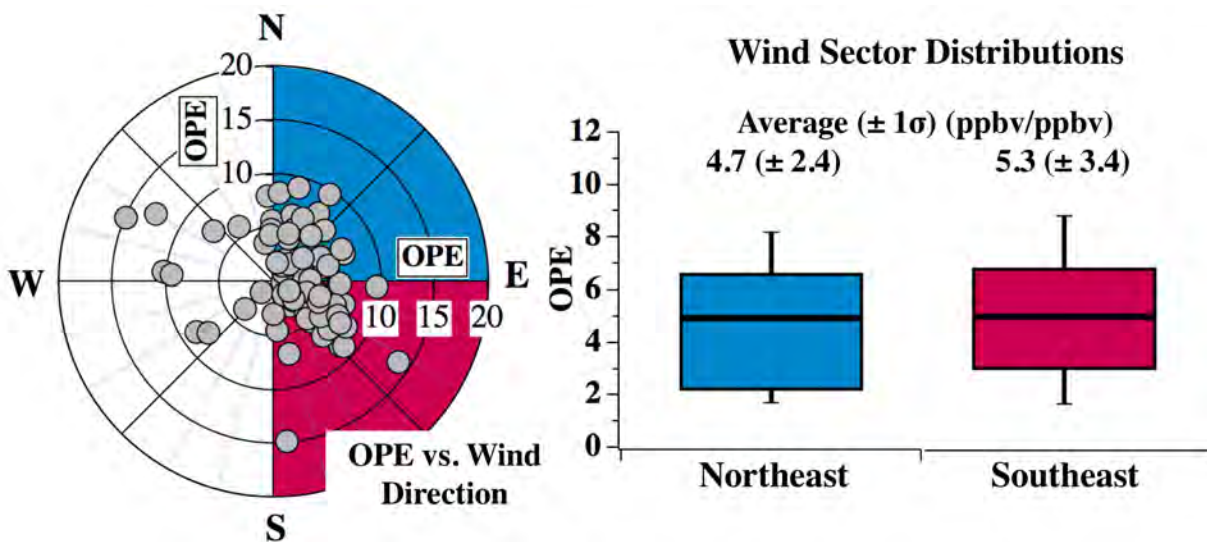


Figure 3.8. 80 individual OPEs with high ($r^2 > 0.5$) O_x/NO_z correlation plotted radially as a function of wind direction, colored by NE (0-90°, blue) and SE (90-180°, red) wind sectors. Box and whisker plots show median OPE for each wind sector (SE: 5.1 ppbv/ppbv, NE: 4.9 ppbv/ppbv) and range between the 10th and 90th percentiles.

Due to the complexity of local air trajectories, including diel flow patterns that mix urban and O&NG emissions (Section 3.3.1), it is difficult to accurately determine air transport and mixing histories using observed wind directions alone. A back-trajectory model has the potential to track air transport history more accurately than local wind direction. As with observed wind direction, wind sectors for the 80-OPE subset as defined by a back-trajectory model (described in Appendix A), show no statistically significant difference between average OPEs from the NE and SE wind sectors (difference = 0.6 ppbv/ppbv, $p = 0.55$, Figure 3.9).

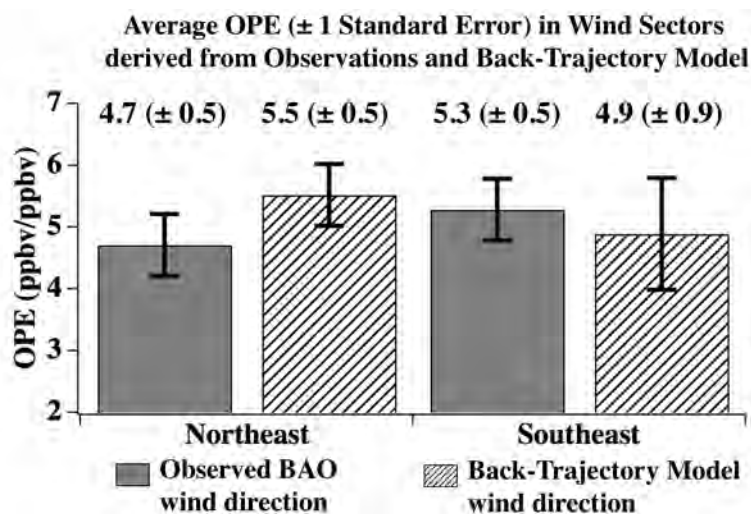


Figure 3.9. Average ($\pm 1\sigma^*$) observational OPEs in northeast and southeast wind sectors as derived from winds observed at BAO (solid) and FLEXPART model simulations (dashed).

The lack of statistically significant difference in observed OPE with observed or modeled wind direction is evidence for mixing between air parcels that obscures quantifiable differences between urban and O&NG sectors and/or an OPE effect from O&NG emissions that has a 95% probability of being less than 1.8 ppbv/ppbv. We interpret these results to mean either: 1) observed OPEs are the product of both urban and O&NG emissions that were well-mixed prior to measurement at BAO; or 2) an OPE influence of urban and O&NG emissions that are similar enough (i.e. < 1.8 ppbv/ppbv) to be obscured by mixing when air is transported to BAO. The box

modeling results discussed in Section 3.3.4.4 are consistent with the second scenario and suggest an O&NG influence on regional average OPE of 1.3 ppbv/ppbv.

3.3.3.1.2 OPE as a function of Chemical Tracers

Chemical tracers provide an additional method to determine air transport history. In the NFR, CH₄ is emitted primarily by O&NG (Table 2.1), NH₃ by agriculture, and CO and NO_x by urban activity. Background mixing ratios (minimum observed campaign values) of CO (76 ppbv) and CH₄ (1916 ppbv) were subtracted prior to analysis. Figure 3.10 shows correlations of the 80-OPE subset with NO_x, NO_y, NH₃, CH₄, and CO. Correlations visually indicate a slight decrease in OPE with increasing tracer mixing ratios, however, correlation coefficients indicate no statistically significant trend at the 95% confidence level ($p > 0.05$). Correlations between chemical tracers and the 305 OPE-population are also insignificant ($p > 0.22$). These results indicate relatively well-mixed air, also suggested by the dominant easterly flow and non-directionally enhanced tracer mixing ratios shown in Figure 3.6.

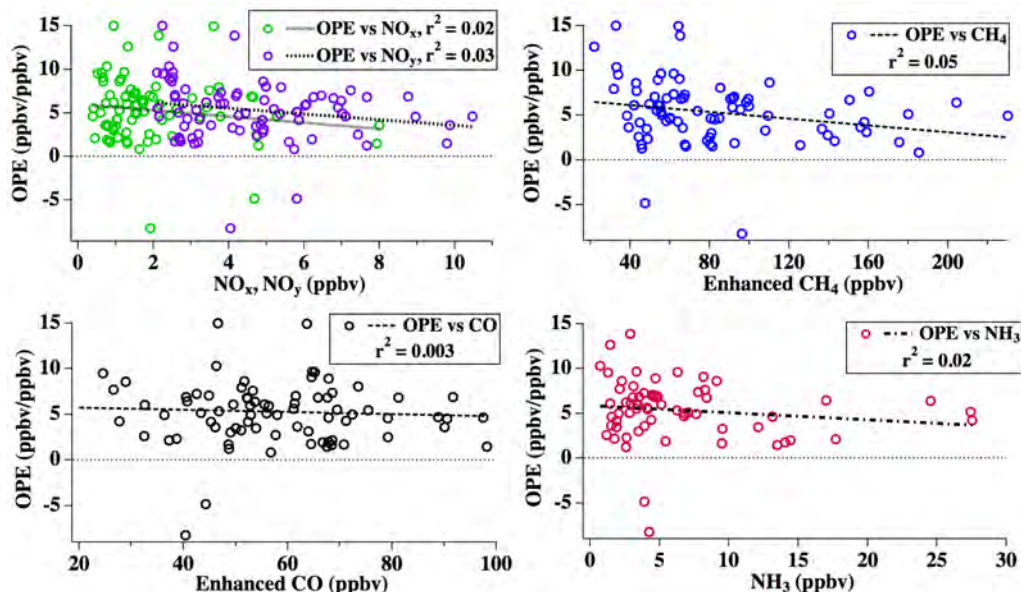


Figure 3.10. 80 individual OPEs with high ($r^2 > 0.5$) O_x/NO_z correlation as a function of simple chemical tracers. CH₄ and CO mixing ratios are the enhancements above background. Correlation coefficients (r^2) for all species suggest no statistically significant trend (95% confidence level) in OPE with tracers.

A second possibility is that these tracers are not specific enough to their assigned emission sectors. As previously discussed in Pétron et al. (2012; 2014), approximately 25% of CH₄ emissions are not associated with O&NG operations, including three landfills located approximately 3 km to the south-southwest of BAO. In addition, NEI-2011 inventories attribute 27% of NO_x emissions in Weld County (Figure 3.1) to O&NG operations (Appendix A). Ideally, this analysis would be conducted with more specific chemical tracers not available in 2014 (e.g. O&NG: propane, urban: acetylene) but suggests that simple tracers used here do not uniquely distinguish the influence of different emission sectors on observed OPE at BAO.

3.3.3.2 Uncertainty in OPE Analysis

Interpretation of the O_x/NO_z relationship is subject to several limitations (Ryerson et al., 1998; Trainer et al., 1993) that are presented below in terms of their relation to deriving an average OPE under NFR conditions.

First, variability in background O₃ may complicate the OPE analysis (e.g. Neuman et al., 2009). Backgrounds are represented by the intercept of the O_x/NO_z correlation and will artificially change the derived OPE if one fit is applied to air parcels with different backgrounds (see example, Figure 3.3). Therefore, OPE was derived from short time intervals (15 minutes) and filtered for intercepts greater than 2σ from the mean O_x background (further details, Section 3.2.2.3) in order to isolate air parcels with similar O₃ backgrounds.

Second, O_x is not always positively correlated with NO_z. This is likely the result: of 1) environmental conditions that do not promote photochemical activity; and/or 2) transport processes that mix air parcels with differences in background O₃ mixing ratios similar to their photochemical O₃ enhancements. Summer 2014 in the NFR was unseasonably cool with high thunderstorm activity (Figure 2.15), which can enhance the downwind transport of O₃ but also

inhibit the stagnation and accumulation of pollution that contributes to OH radical generation and efficient O₃ production. These environmental conditions can lead to periods of time with moderate photochemical activity and O₃ production of only a few ppbv, similar to the variability observed in 2014 background O₃ (O_x background: 56.7 ± 9.3 (2σ) ppbv). Mixing and/or sampling of these air parcels remove any observable O_x/NO_z correlation. The r² filter is applied to remove these events but by doing so, biases the 80-OPE average high.

Third, OPE is highly sensitive to HNO₃ deposition (e.g. Neuman et al., 2009; Sillman et al., 1998; Trainer et al., 1993). Preferential loss of HNO₃ relative to O₃ will artificially raise the O_x/NO_z slope since HNO₃ is frequently the largest NO_z component in summer. Assuming a HNO₃ deposition velocity of 1-5 cm/s (see Section 2.4.1.4) and a boundary layer of 2 km, the estimated loss to dry deposition occurs with a rate constant of $0.5 - 2.5 \times 10^{-5} \text{ s}^{-1}$. An upper limit range for HNO₃ loss can be estimated by assuming: 1) 100% of measured NO_z is HNO₃ (2014 PAN measurements confirm NO_z is not 100% HNO₃); and 2) the maximum duration for transport and O₃ production is 6 hours. The average daytime value of NO_z in 2014 was 2.7 ppbv, which equates to an average of 0.3-1.4 ppbv (11-52%) lost over 6 hours using the rate constants above. Recalculating individual OPEs with NO_z values corrected for this loss produces an average OPE ($\pm 1\sigma$) of $3.3 (\pm 2.2)$ and $4.7 (\pm 3.2)$ ppbv/ppbv for the smaller subset of 80 highly correlated fits. This value is lower than the original average of 5.3 ppbv/ppbv but within the standard deviation of 3.6 ppbv/ppbv.

Fourth, unintended conversion of NH₃ to NO may also occur in the presence of ambient levels of O₃ at temperatures of 650° C in the CRDS instruments' NO_y quartz oven (Womack et al., 2016). This conversion does not occur in the NO_x channel and would result in an artificially large value for NO_z after subtraction of NO_x from the NO_y measurement channel. A constant fractional

conversion of 6.4%, irrespective of the ambient NH₃ mixing ratio at 2014 observed O₃ mixing ratios, is an upper limit to the interference. Adjusting NO_z measurements of the 80-OPE subset with concurrent NH₃ and O₃ measurements increases the average OPE to 5.9 ppbv/ppbv. Combination of HNO₃ and NH₃ artifacts suggest the true average OPE is between 3.3 and 5.9 (-2.0/+0.6) ppbv/ppbv, a range encompassed by the standard deviation ($1\sigma = 3.6$ ppbv/ppbv) of the originally derived average.

Lastly, OPE is also sensitive to non-photochemical sources of O₃ such as stratospheric intrusions, or entrainment from elevated levels above the boundary layer. Previous work in rural Georgia has highlighted the influence of O₃ and NO_z entrainment on O₃ production (Kleinman et al., 1994) but has also noted that these events do not always occur and are typically confined to morning hours when the boundary layer undergoes vertical expansion. No filter was applied specifically for O₃ or NO_z entrainment, but is minimized by deriving OPEs after local noon (after the majority of entrainment from the residual layer). Morning entrainment (before local noon) would manifest itself as an increase in background O₃ (shifted intercept) and would not influence the slope of the O_x/NO_z regression. In the event entrainment were to continue after noon, the longer atmospheric lifetime of O₃ relative to HNO₃ (due to deposition rate differences) would artificially raise observed OPEs.

Overall, analysis of 2014 data provides an average and expected distribution of observed OPEs at BAO, but does not distinguish the influence of urban emissions from the O&NG sector. This result does not change with the selection of highly correlated OPEs. These observations lead to three possible conclusions: 1) based on observational and modeled-wind direction analyses, the OPE difference between O&NG and urban emission sectors has a 95% probability of being within 1.8 ppbv/ppbv; 2) OPE differences are obscured by regional air mixing; and/or 3) small OPE

differences cannot be distinguished using simple chemical tracers with multiple emission sources. Although OPE does not statistically vary with either wind direction or chemical tracer analyses, the similarity provides a point of comparison between the observations and box model simulations described below.

3.3.4 Box Model Simulations – Maximum Photochemical O₃

Model simulations were constrained to SONNE diel average observations as described above. With the dilution rate constant derived from a fit to 10 secondary species, the Case 1 VOC scenario simulates maximum O₃ to within -0.3% (-0.2 ppbv) of the SONNE diel average. The average relative deviation between the model output and observations for O₃ is -0.05% (11 am - 3 pm MDT, ± 2 hours from solar noon). Figure 3.11 illustrates the observed diel average and model output for O₃, which suggests an accurate base case simulation of maximum O₃ produced at BAO. Deviation between simulated and observed O₃ profiles after 4 pm MDT is the result of the constant dilution/background-O₃ entrainment rate that is applied to the entire 24-hour simulation, as described in Section 2.4.1.4.

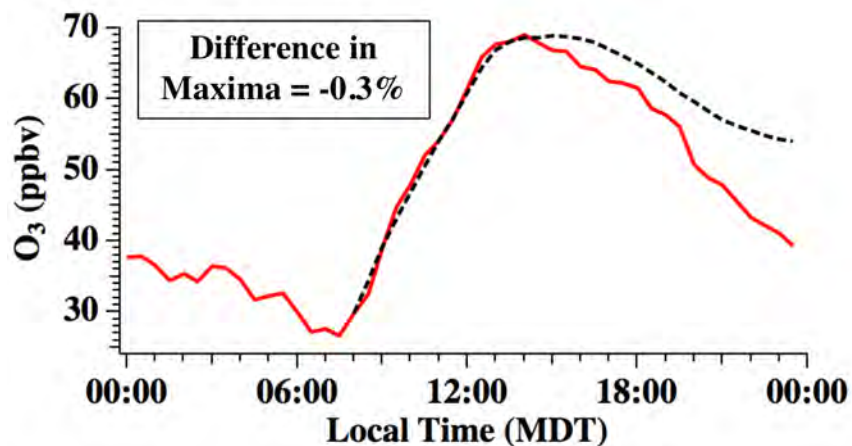


Figure 3.11. Base Case Simulated O₃. Observed diel average (red) and base-case simulated (black dashed) mixing ratios. Difference between observed and modeled maxima is -0.3%.

3.3.4.1 NO_x Sensitivity

Case 1 simulations were run while constrained to SONNE observed mixing ratios of VOCs, NO_x, and temperature (as described in Section 2.4.1.2.1). To test the sensitivity of maximum photochemical O₃ to NO_x, 11 simulations were run with the Case 1 VOC scenario, scaling observed NO_x mixing ratios (displayed in Figure 3.5) by a factor of 0 to 5. As shown in Figure 3.12 and Table 3.3, observed SONNE NO_x mixing ratios (NO_x scaling factor = 1) produce a maximum of 16.3 ppbv of photochemical O₃, while doubling observed NO_x increases photochemical O₃ to 18.9 ppbv. Here photochemical O₃ is defined as the difference between simulated O₃ and the simultaneous mixing ratio of O₃ in the zero-NO_x simulation. Photochemical O₃ production does not occur without NO_x, however O₃ is introduced to the model to simulate entrainment of background O₃ into the boundary layer (see Section 2.4.1.4). O₃ entrainment occurs at the same rate in each simulation and is therefore represented by the zero-NO_x simulation. Subtracting these mixing ratios from each nonzero-NO_x simulation provides the photochemically produced O₃ for the given amount of NO_x.

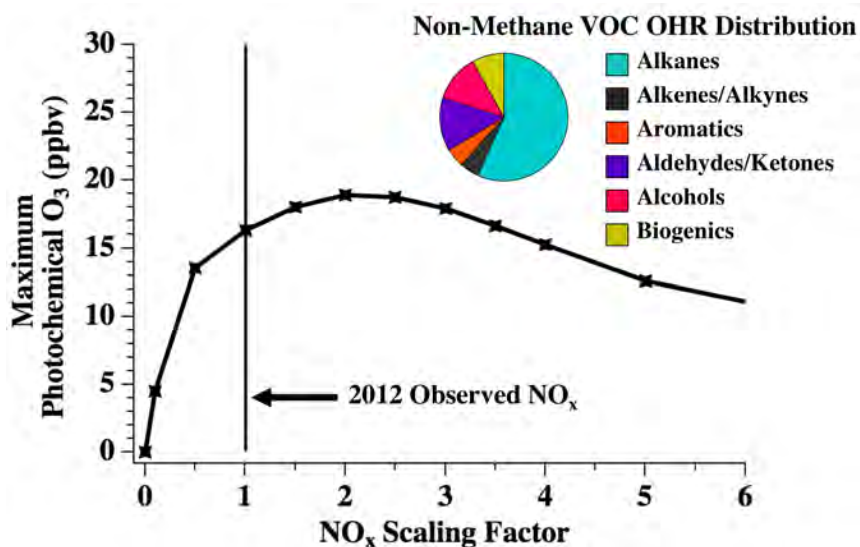


Figure 3.12. NO_x sensitivity of maximum photochemical O₃ in the base case simulation. 11 simulations are shown with SONNE (2012) observed NO_x mixing ratios, represented by a scaling factor of 1, scaled from 0 to 5. Pie chart insert represents the 24-hour average fractional contribution of non-methane VOCs to OH Reactivity.

Figure 3.12 suggests that photochemical O₃ production in the region surrounding BAO is NO_x limited. An increase or decrease in NO_x by a factor of 2 leads to a 16-17% (± 2.6-2.8 ppbv) change in maximum photochemical O₃. However, NO_x increases above a factor of 2 move O₃ production into the NO_x saturated (VOC sensitive) photochemical regime, such that further increases will reduce maximum O₃. These results are consistent with NO_x sensitivities derived from previous 3D modeling of NFR O₃ with a 2010 emission scenario (Colorado Department of Public Health and Environment (CDPHE), 2008).

3.3.4.2 O&NG Influence

To determine the average influence of O&NG emissions on maximum photochemical O₃, the fraction of VOCs attributed to primary O&NG emissions were removed (Case 2) and doubled (Case 3) as described in Section 2.4.1.2. Twenty-two additional simulations were run with these two VOC scenarios while scaling SONNE observed NO_x mixing ratios between 0 and 5. Results of these simulations in comparison to Case 1 from Figure 3.12 are listed in Table 3.3 and shown in Figure 3.13. Pie chart inserts represent the 24-hour average, non-methane VOC-class fractional contribution to VOC OHR and carbon mixing ratio (ppbC) for each VOC scenario. At observed NO_x mixing ratios, the difference in maximum photochemical O₃ between Cases 1 and 2 (no O&NG VOC emission contribution) is 17.8%, or a 2.9 ppbv decrease. Similar to maximum O₃, the O&NG VOC influence on photochemical MDA8 (Maximum Daily 8-hour Average) is a decrease of 18.3%, or 2.4 ppbv. Doubling the mixing ratio of O&NG VOCs increases simulated maximum photochemical O₃ by 13.5% or 2.2 ppbv, indicating a non-linear change in O₃ with O&NG VOCs. These three VOC scenarios suggest that while O₃ production is sensitive to NO_x, maximum and MDA8 O₃ mixing ratios will also respond to reductions in O&NG VOCs, again

consistent with previous 3D model results (Colorado Department of Public Health and Environment (CDPHE), 2008).

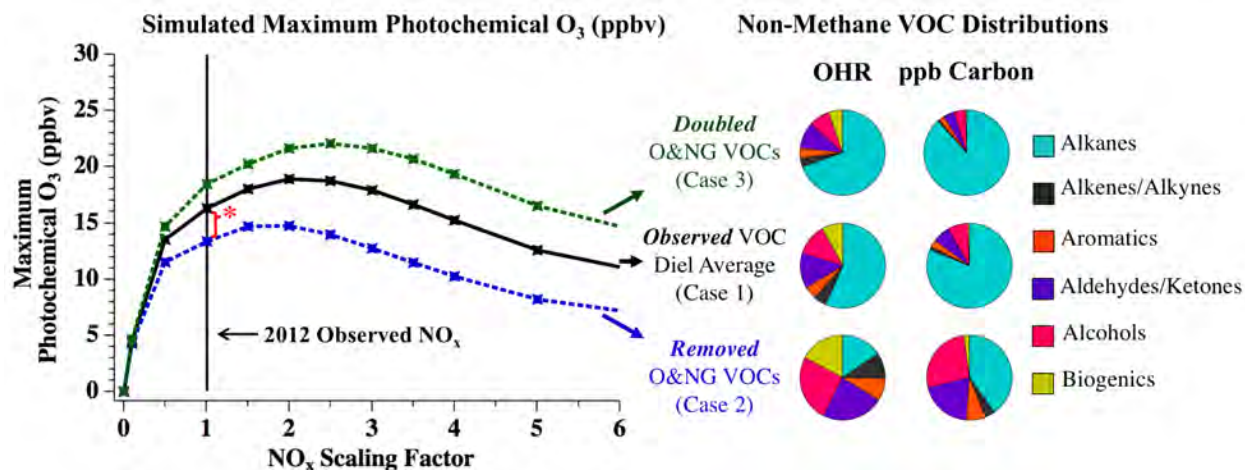


Figure 3.13. NO_x sensitivity of simulated maximum photochemical O_3 mixing ratios for three VOC scenarios. Asterisk indicates a difference of 17.4% between observed VOC base case (Case 1) and VOC scenario with O&NG VOCs removed (Case 2) at SONNE (2012) observed NO_x mixing ratios. Pie chart inserts illustrate the 24-hour average non-methane VOC OHR (s^{-1}) and carbon mixing ratio (ppbC) of each VOC scenario (VOC scenarios derived from work by Jessica Gilman). Distributions do not include CH_4 , CO, or HCHO.

Since publication of this work, regional modeling efforts with the Community Multiscale Air Quality (CMAQ) model have suggested that both NO_x and VOC emissions from O&NG activities (defined from an adjusted *a priori* emissions inventory) contributed an average of 6 - 8 ppbv to MDA8 O_3 during FRAPPÉ (Pfister et al., 2017a). While this absolute amount is larger than the average contribution predicted by the box model (even when considering O&NG NO_x , discussed below), the regional model results are consistent as they also show a sensitivity of O_3 in the NFR to changes in both O&NG and ‘mobile’ (i.e. NO_x) emission sources (Pfister et al., 2017a). An additional analysis of discrete flask samples and O_3 measurements near Greeley, CO (Figure 3.1) on 13 August 2014, attributed the formation of all O_3 above median background levels to local O&NG emissions (Cheadle et al., 2017). This localized contribution of O&NG activity to O_3 was estimated to be 10 times higher than the average predicted by the box model (20-30 ppbv vs 3 ppbv). Additional analyses are required to confirm an O&NG O_3 contribution of this magnitude.

Table 3.3. Maximum Simulated Photochemical O₃ for three VOC scenarios.

SONNE NO _x Scaling Factor	Maximum Photochemical O ₃ (ppbv)	Change Relative to Case 1 (ppbv) (%)	
<i>Case 1 - Observed VOC Distribution</i>			
0.0	0	-	-
0.1	4.5	-	-
0.5	13.5	-	-
1.0	16.3	-	-
1.5	18.0	-	-
2.0	18.9	-	-
2.5	18.8	-	-
3.0	17.9	-	-
3.5	16.6	-	-
4.0	15.2	-	-
5.0	12.6	-	-
<i>Case 2 - O&NG VOCs Removed</i>			
0.0	0	0	0
0.1	4.3	- 0.2	- 4.3
0.5	11.6	- 1.9	- 14.1
1.0	13.4	- 2.9	- 17.8
1.5	14.7	- 3.3	- 18.3
2.0	14.8	- 4.1	- 21.7
2.5	14.0	- 4.8	- 25.5
3.0	12.8	- 5.1	- 28.5
3.5	11.5	- 5.1	- 30.7
4.0	10.3	- 4.9	- 32.2
5.0	8.2	- 4.4	- 34.9
<i>Case 3 - O&NG VOCs Doubled</i>			
0.0	0	0	0
0.1	4.6	+ 0.1	+ 2.2
0.5	14.7	+ 1.2	+ 8.9
1.0	18.5	+ 2.2	+ 13.5
1.5	20.2	+ 2.2	+ 12.2
2.0	21.7	+ 2.8	+ 14.8
2.5	22.1	+ 3.3	+ 17.6
3.0	21.6	+ 3.7	+ 20.7
3.5	20.7	+ 4.1	+ 24.7
4.0	19.4	+ 4.2	+ 27.6
5.0	16.5	+ 3.9	+ 30.9

The 16.3 ppbv of photochemical O₃ produced in Case 1 represents the maximum O₃ enhancement under average conditions. Observed O₃ mixing ratios in 2014, however, (Figure 3.7) show that O₃ enhancements above background can be approximately 30 ppbv on days with high photochemical activity (e.g. high O₃ and NO_z mixing ratios). As described below in Section 3.3.4.5, model sensitivity studies show that photochemical O₃ is highly sensitive to photolysis

rates, potentially explaining the large enhancements on days with photolysis rates larger than average values. In contrast, the O&NG VOC contribution to O₃ (~20%) is not highly sensitive to photolysis rates (Section 3.3.4.5). Therefore, assuming mixing ratios of VOCs and NO_x similar to their observed diel average values, the absolute contribution from O&NG VOCs could be ~ 6 ppbv on photochemically active days with ~30 ppbv of regional photochemical O₃ production.

The total contribution of O&NG activity to photochemical O₃ will depend on emissions of NO_x as well as VOCs. The difference of 17.8% highlighted in Figure 3.13 assumes no change in NO_x from observed mixing ratios. Applying NO_x reductions of 5.5% based on EPA NEI -2011 inventories (see Section 3.2.3), Cases 1 and 2 suggest that O&NG activity contributes 19.0% (3.1 ppbv) to maximum photochemical O₃, in comparison to 17.8% (2.9 ppbv) from VOC emissions alone. However, NEI inventory estimates of O&NG NO_x emissions may be overestimated (e.g. Ahmadov et al., 2015). Thus, the total O&NG contribution to modeled maximum photochemical O₃ at diel average mixing ratios of NO_x and VOCs is between 17.8 and 19.0%, or 2.9 and 3.1 ppbv.

As shown in Figure 3.13, alkanes contributed 82% to the average SONNE non-methane carbon mixing ratio measured at BAO (Figure 3.13 pie chart), of which 86% are attributed to O&NG emissions (Figure 2.14). Despite this dominant fraction, the alkane contribution to average non-methane VOC OHR was 56% and less than 18% to maximum photochemical O₃. This result is consistent with previous literature showing that alkanes are not efficient at producing O₃ (e.g. Russell et al., 1995) and demonstrates the difficulty in using either carbon mixing ratio or VOC OHR for attribution of photochemically produced O₃ to O&NG VOC emissions.

Despite evidence for reasonably well mixed urban and O&NG emissions, Figure 3.1 suggests spatial heterogeneity in emissions from these sources, which can result in different photochemical regimes for O₃ production (also shown by CMAQ simulations in Pfister et al.

(2017a)) For example, NO_x and urban VOCs are expected in larger concentrations ~30 km south of BAO near urban-Denver (Brown et al., 2013; Swarthout et al., 2013), while O&NG VOCs may be larger ~50 km north of BAO centered in the Wattenberg Gas Field near Greeley (Swarthout et al., 2013). However, O_3 levels in exceedance of NAAQS occur across these same distances (Colorado Department of Public Health and Environment (CDPHE), 2015), with observations suggesting a level of similarity in O_3 enhancements across the NFR (Abeleira & Farmer, 2017). Buffering effects in the VOC- NO_x sensitivity curves (Figure 3.14) can explain regional O_3 enhancements despite different photochemical regimes. Figure 3.14 shows that if, for example, the absolute mixing ratios of non-O&NG VOCs remained the same but O&NG VOCs were doubled and NO_x reduced by 30% (Figure 3.14: red diamond), the model predicts the same maximum O_3 produced as that at BAO. This implies that north of BAO, with a potentially larger abundance of O&NG VOCs, this region would be more sensitive to NO_x emission reductions. In contrast, if the non-O&NG VOCs remained the same but O&NG VOCs were reduced by 50% at two southern locations, the model predicts nearly the same maximum O_3 produced for NO_x emissions 1.4 to 2.7 \times higher than those at BAO (Figure 3.14: red box and triangle). O_3 production at the second of these points (red triangle) is in the NO_x -saturated regime but still produces the same photochemical O_3 as at the NO_x -limited BAO. These scenarios suggest that O_3 enhancements in the NFR can be regional, while effective control strategies should still be informed by finer scale VOC/ NO_x observations.

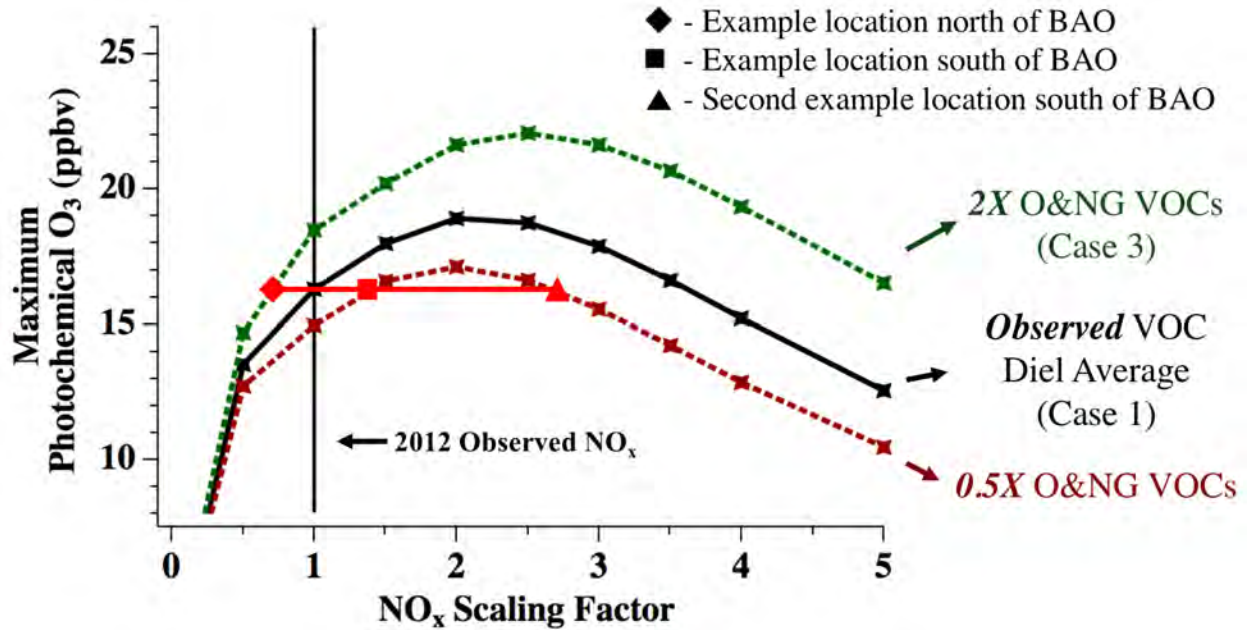


Figure 3.14. NO_x sensitivity curves for three VOC scenarios. In contrast to Figure 3.13, the third VOC scenario has O&NG VOCs reduced by half instead of completely removed. The red line and symbols provide example locations to the north and south of BAO with different O&NG and NO_x mixing ratios that experience the same photochemical O_3 enhancement as that at BAO.

3.3.4.3 Biogenic Influence

As discussed in Section 3.3.2, summer 2012 experienced drought conditions with suppressed biogenic emissions relative to a non-drought year in summer 2015 (Abeleira et al., 2017). As biogenic VOCs, such as isoprene, are efficient ozone producers (e.g. high OH reactivity), an increase in their concentrations could shift the curves in Figures 3.13 and 3.14 to an even more NO_x sensitive regime. There remain, however, large uncertainties surrounding the potential impact of biogenic emissions on the magnitude of local O_3 production in regions like Colorado that have a limited number of local biogenic sources and frequent upslope winds that keep the emissions from the western mountain forests largely isolated from the NFR (Section 3.3.1). To test the sensitivity of modeled local O_3 production to changes in drought-impacted emissions of biogenic VOCs, DSMACC simulations were run with the base (case 1) VOC scenario with isoprene concentrations increased by a factor of three. A factor of three was chosen as the

average isoprene mixing ratios in 2015 (0.18 ppbv, Abeleira et al., 2017) were three time larger than in 2012 (0.06 ppbv, Figure 2.13). Results for all three VOC scenarios are shown in Figure 3.15 with pie charts representing the updated fraction of each VOC class to OHR and ppbC. The base case shows that increasing isoprene constraints by a factor of three increases maximum daily photochemical O₃ (at observed NO_x levels) from 16.3 ppbv to 16.7 ppbv (2.5%) and slightly increases the NO_x sensitivity of O₃ production. As expected, the fractional influence of less reactive O&NG VOCs on photochemical O₃ decreases from 17.8% to 16.1% under the high-isoprene scenario. These results suggest that overall, the presence of drought conditions in the NFR can impact average photochemical O₃ production, but that the impact remains small relative to other VOC sources, including O&NG VOCs with larger magnitudes of emissions.

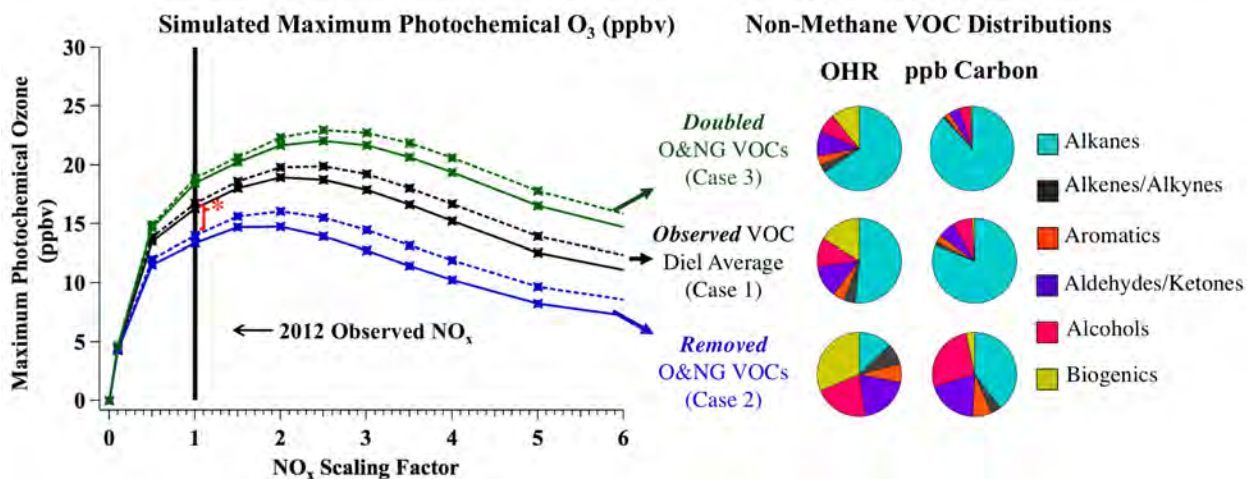


Figure 3.15. Same format as Figure 3.13 but instead showing three additional simulations where isoprene constraints have been multiplied by 3 (dashed lines).

3.3.4.4 Model Ozone Production Efficiency

Case 1 and 2 simulations were additionally used to calculate the influence of O&NG VOC emissions on modeled OPEs. The OPE of each model simulation was calculated from the average $\Delta O_x / \Delta NO_z$ ratio between 11 am - 3 pm MDT, the same time period during which the model was fit to best reproduce 10 secondary products (see Section 2.4.1.4). Here ΔO_x and ΔNO_z are used to

capture photochemical O₃ production and NO_x oxidation. Delta O_x and ΔNO_z are defined as the difference between the O_x and NO_z mixing ratios in a given simulation and the simultaneous values in the zero-NO_x simulation (as described in Section 3.3.4.1). The HNO₃ dilution rate constant was the same as all other 4002 species ($k = 1.11 \times 10^{-4} \text{ s}^{-1}$), but its deposition rate was set to 0 s⁻¹ to remove the influence of HNO₃ loss on NO_z. Eliminating HNO₃ deposition does not impact simulated maximum photochemical O₃ but does decrease Case 1 OPE by 7.5% (see Table 3.4). Simulated OPE was also found to decrease with increasing NO_x mixing ratios, consistent with previous OPE model simulation results (e.g. Lin et al., 1988).

At a NO_x scaling factor of 1, OPEs derived from the Case 1 and 2 VOC scenarios are 6.5 (± 0.5) ppbv/ppbv and 5.2 (± 0.5) ppbv/ppbv, respectively. Errors are derived from the quadrature addition of OPE uncertainties associated with model parameters listed in Table 3.4 (not including HNO₃ deposition). These results suggest that O&NG VOC emissions increase the efficiency of O₃ production at BAO by 1.3 ppbv/ppbv (20%). To account for NEI-estimated O&NG NO_x emissions (see Section 3.2.3), the OPE for Case 2 (no O&NG VOCs) was calculated at a NO_x scaling factor of 0.945 (-5.5%). The OPE influence of O&NG emissions did not change, as this small NO_x reduction did not influence the simulated OPE by > 0.1 ppbv/ppbv. The similarity between Cases 1 and 2 suggests that the OPE influence of O&NG emissions is small enough to be obscured in observations at BAO due to air transport and mixing, as discussed previously in Section 3.3.3.1.

3.3.4.5 Model Sensitivity Studies

As described above, simulations for all three VOC scenarios were constrained every 30-minutes to chemical species and physical parameters. The only tunable model parameter was the dilution rate constant, which was derived by minimizing the deviation between observations and model output for 10 select secondary products, including O₃. A ±10% change in the dilution rate

constant changes simulated maximum photochemical O₃ in Case 1 by + 1.3/- 1.1 ppbv (+ 7.8/- 6.6%) and average model-to-observation relative deviation of all 10 compounds by + 1.6/- 1.2 %.

Table 3.4. Box-Model Sensitivity Study Results^a

Parameter	Base Case Value	Value Adjustment	Δ Max Photochemical O ₃		Δ OPE (%) ^b
			(ppbv)	(%) ^b	
Photolysis rates	8 A.M. MDT values: j(NO ₂) = 3.6 × 10 ⁻³ s ⁻¹ j(O ¹ D) = 4.0 × 10 ⁻⁶ s ⁻¹	±25%	+6.0/-5.4	+35.9/-32.3	+4.6/-3.1
Dilution	k = 1.05 × 10 ⁻⁴ s ⁻¹	±10%	±2.3	±13.8	±1.5
Temperature	SONNE observations	±10%	+1.3/-1.1	+7.8/-7.1	-
Background O ₃	58 ppbv	±10%	±0.8	±4.8	+7.7/-6.2
Enhanced CH ₄	SONNE observations-background	±10%	±0.1	±0.6	±3.1
O ₃ deposition	k = 3.5 × 10 ⁻⁶ s ⁻¹	±10%	±<0.1	-	-
Albedo	0.067	±10%	±<0.1	-	-
HNO ₃ deposition	k = 2.2 × 10 ⁻⁵ s ⁻¹	-100%	-<0.1	-	+7.7 ^c

^aCalculated for Case 1 VOC scenario at NO_x scaling factor = 1.

^bValues not provided if change is <0.1 ppbv (max photochemical O₃) or <0.1 ppbv/ppbv (OPE).

^cHNO₃ deposition artificially increases modeled OPE by 7.7%; all OPE simulations were run without HNO₃ deposition as this does not change photochemical O₃ and is necessary to accurately model OPE.

Case 1 (at observed NO_x mixing ratios) was additionally tested for sensitivities to ±10% changes in other model constraints including photolysis rates, albedo, temperature, background O₃, enhanced CH₄, and O₃/HNO₃ deposition rates (see Table 3.4). Sensitivity differences between maximum photochemical O₃ and OPE can be explained by the additional dependence of OPE on photochemical NO_x oxidation. Of the parameters tested, OPE is most sensitive to changes in temperature while maximum photochemical O₃ is most sensitive to changes in photolysis rates (more than the dilution rate constant). To test the sensitivity of the main box model results to photolysis rates, initial 8 am j(O¹D) and j(NO₂) values were adjusted by ± 10 and ± 25%. Results of ± 25% adjustments are further analyzed here as this is the maximum uncertainty of 2014 j(NO₂) downwelling photolysis frequencies (see Table 3.1). Twenty-two additional Case 1 (observed VOC) simulations and four additional Case 2 (no O&NG VOC) simulations were run with photolysis rates adjusted by ± 25%, to test the sensitivity of BAO photochemical O₃ to NO_x and O&NG VOC under this range of photolysis rates. The NO_x sensitivity results are shown in Figure 3.16 and reveal that photochemical O₃ at BAO remains NO_x sensitive at observed SONNE NO_x mixing ratios, regardless of photolysis rate. In addition, simulations run at observed NO_x mixing

ratios with Cases 1 and 2 suggest that O&NG VOCs contribute 15.1 - 19.4% to photochemical O₃ at BAO, in comparison to 17.8% derived with original photolysis rates (Figure 3.17). The difference in maximum photochemical O₃ between Cases 1 and 2 is therefore not as sensitive to changes in photolysis as is the absolute maximum simulated O₃. In other words, regardless of 25% changes in photolysis rates, BAO photochemical O₃ remains sensitive to NO_x (Figure 3.16) and the O&NG VOC influence ranges from 15.1 to 19.4% (Figure 3.17), within 2.7 percent of 17.8% derived under original photolysis conditions.

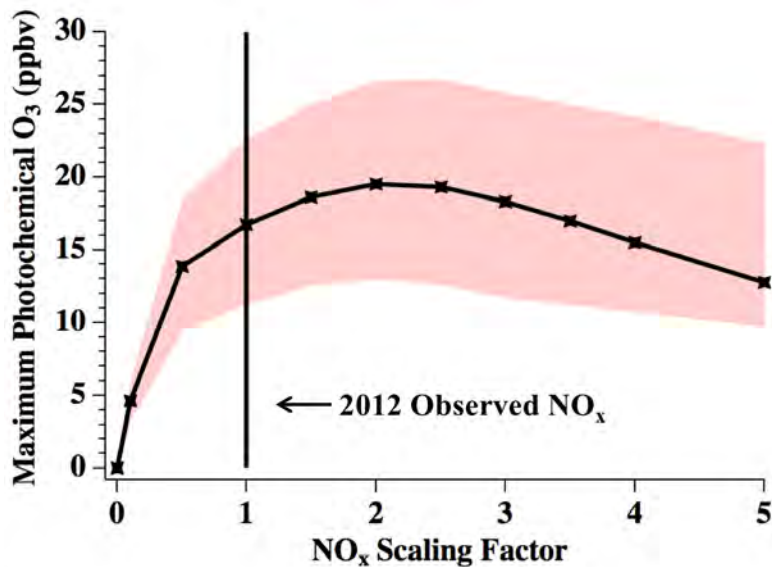


Figure 3.16. NO_x sensitivity of maximum photochemical O₃ with ± 25% adjusted photolysis rates. (Black) Original case 1 NO_x sensitivity curve; (red shading) Photochemical O₃ at each NO_x scaling factor with ± 25% original photolysis rates.

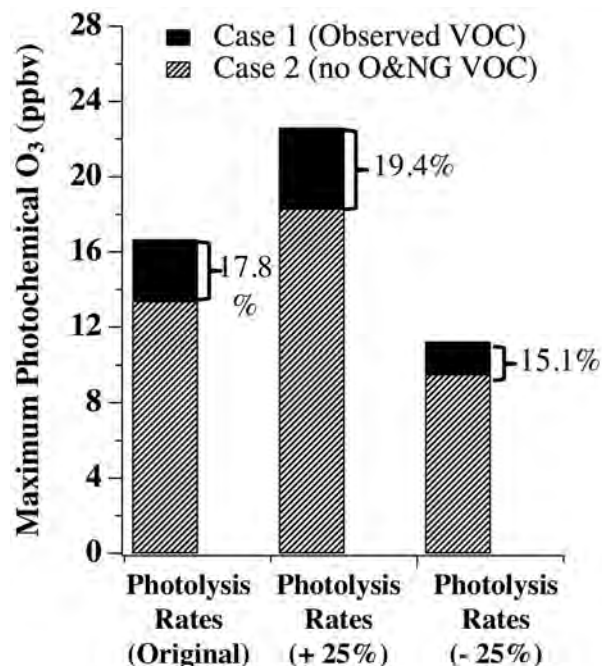


Figure 3.17. Maximum O₃ sensitivity to O&NG VOCs with photolysis rates scaled by $\pm 25\%$. (Solid Bars) case 1 maximum photochemical O₃ (at observed SONNE NO_x mixing ratios); (dashed bars) case 2 maximum photochemical O₃ (at observed SONNE NO_x mixing ratios).

3.3.4.6 Model Chemical Mechanism Comparison

To investigate the choice of model chemical mechanism on these results, DSMACC box model simulations, as described above, were repeated with the MCM replaced with the Carbon Bond 6r3 chemical mechanism. The CB6r3 mechanism is implemented in the EPA’s regional CMAQ model and is used in the development process of Colorado’s State Implementation Plan (SIP), required by the EPA due to the NFR nonattainment status. The SIP is developed through collaborations between state and local officials and planning agencies and must demonstrate, typically through air quality modeling, that proposed emissions reduction strategies will reduce O₃ levels below the current NAAQS. The CB6r3 VOC degradation scheme is simplified relative to the MCM by “lumping” VOC species rather than treating them explicitly. Relative to the 4002 chemical species and 15555 chemical reactions in the MCM, the lumped CB6r3 mechanism had a total of 94 species and 323 reactions (including depositional loss). These lumped chemical

schemes are necessary to increase model computational efficiency, but have largely been developed for simulations of urban VOC photochemistry. Comparison to the MCM is therefore useful as there remain uncertainties in the ability of these lumped chemical schemes to accurately simulate photochemical O₃ production in areas influenced by O&NG emissions.

First, the VOC OHR is compared between the two mechanism. The CB6r3 mechanism predicts an OHR of 2.5 s⁻¹, which is within one standard deviation of the original determination presented in 3.3.2, suggesting minimal difference between VOC schemes for this metric. Second, base case simulations in DSMACC were re-run with the lumped mechanism. To accurately constrain DSMACC simulations to observed VOCs with the CB6r3 mechanism, Greg Yarwood at Ramboll Environ provided “mapping” information for the contribution of explicit VOCs to each of the CB6r3 lumped species. For example, n-butane is represented in CB6r3 by 4 paraffin or “PAR” species whereas 1-butene is represented by 1 OLE (terminal alkene species) and 2 “PAR” species.

The resulting observed and simulated (MCM and CB6r3) diel profiles of total O₃ are shown in Figure 3.18. Both model mechanisms closely track the observed O₃ profile during the period of photochemical production (~8 am - 2 pm). The maximum O₃ predicted is 68.8 ppb at 3 pm and 69.5 ppb at 3:30 pm with the MCM and CB6r3 mechanisms, respectively, within 0.7% of the maximum observed O₃ of 69.0 ppb at 2 pm. Predicted O₃ from both mechanisms is nearly in exact agreement, with the MCM being 0.7 ppbv lower than the CB6r3. Both models are also slightly late in the timing of the maximum observed O₃, but the MCM is closer to the observed value than the CB6r3. Finally, the Case 2 and 3 VOC scenarios (Section 2.4.1.2) were re-simulated with the lumped mechanism, with results shown in Figure 3.19 relative to the original MCM simulations. The NO_x sensitivity profiles are similar between the MCM and CB6r3 mechanisms, however, the

CB6r3 mechanism predicts a more rapid increase and then decrease of O_3 with increasing NO_x . Similar to the original MCM results, the CB6r3 mechanism also predicts that O_3 production at BAO is NO_x sensitive at observed values (NO_x scaling factor =1). Comparing Case 1 and 2 scenarios also suggests that O&NG VOC emissions contribute 17.8% to locally produced, photochemical O_3 , the same fractional amount as predicted by the MCM.

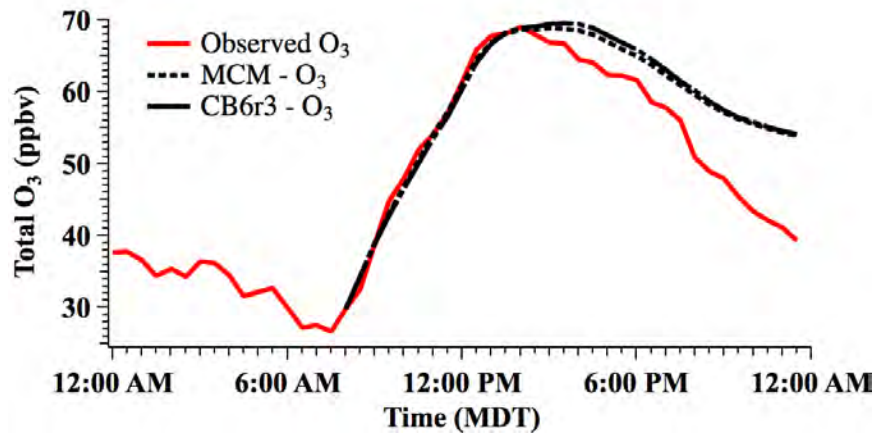


Figure 3.18. Diel average ozone observed (red line) compared to simulated with explicit (dotted black line) and lumped (dash-dot black line) VOC mechanisms.

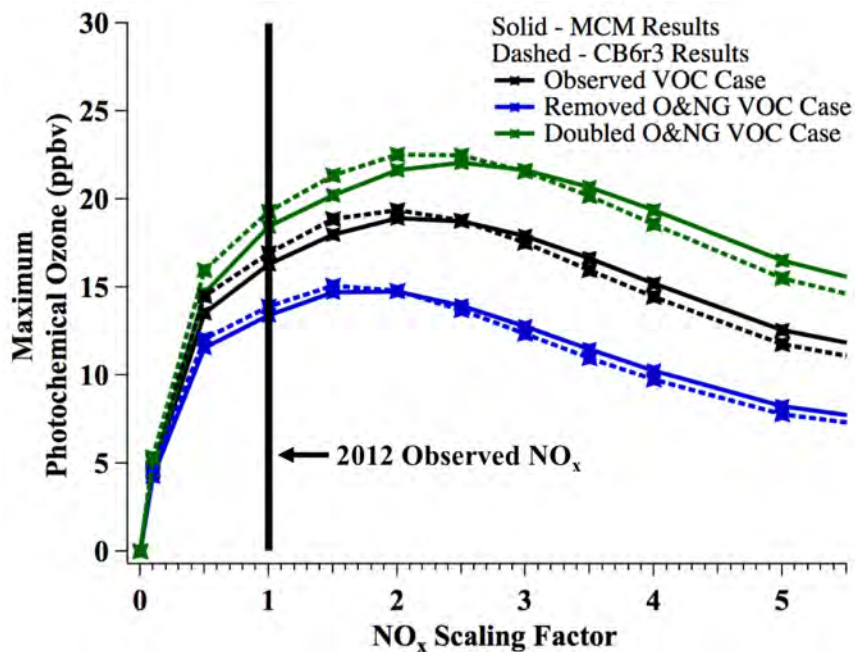


Figure 3.19. NO_x sensitivity of simulated maximum photochemical ozone mixing ratios for three VOC scenarios. As in Figure 3.13, colors represent the VOC scenarios (black – observed VOCs, green – doubled O&G VOCs, blue – zero O&G OVCs). Solid lines are the updated MCM results, and the dotted lines are the CB6r3 results.

Overall, this comparison suggests excellent agreement between chemically “lumped” and explicit mechanisms in terms of the absolute amount of O₃ predicted as well as the predicted sensitivity to changes in NO_x. Though promising, this result is specific to only one location at one time. Further comparisons, extending to multiple locations and over multiple time scales will be required to fully evaluate the accuracy of lumped chemically schemes, used in regional/ state O₃ assessments, relative to mechanisms with more explicit VOC chemistry.

3.4 Conclusions and Future Work

The Northern Front Range of Colorado has been in nonattainment with the NAAQS for O₃ since 2007. Summertime photochemical O₃ in the NFR is influenced by regional NO_x emissions, concentrated around urban-Denver, and large VOC emissions from a rapidly developing O&NG basin. The BAO site lies between these major regional emission sectors and exhibits influence from each (O&NG, urban, and agriculture). Data from this site were used to quantify the influence of O&NG emissions on O₃ production using an observationally constrained box model and metrics of VOC OHR and OPE.

OPEs derived from 2014 O_x/NO_z correlations at 15-minute time intervals during 27 afternoons have an average of 2.9 ± 4.4 (1 σ) ppbv/ppbv for all determinations and 5.3 ± 3.6 (-2.0/+0.6) ppbv/ppbv for a smaller subset with high correlation between O_x and NO_z. A difference in average OPE could not be statistically distinguished for air primarily influenced by O&NG and urban emissions using observed wind direction, modeled back-trajectories or simple chemical tracers. These results suggest the OPE influence of O&NG and urban emissions at BAO is obscured by air mixing and/or do not differ to within 1.8 ppbv/ppbv. The simulated OPE difference of 1.3 ppbv/ppbv with and without O&NG primary VOCs falls within the uncertainty of the 2014 observational analyses.

Box model simulations constrained to diel average chemical and physical observations indicate that maximum photochemical O₃ at BAO is NO_x sensitive. Simulations with removed and doubled primary O&NG VOC contributions showed that O&NG VOC emissions contribute on average 17.8% (2.9 ppbv) to maximum photochemical O₃ and scale non-linearly with changes in O&NG VOCs. This result was unchanged when simulated with a “lumped” chemical mechanism that only had 2% the number of chemical reactions as the MCM. NEI reported emissions of O&NG NO_x are estimated to contribute up to an additional 1.2% (0.20 ppbv) to the total contribution of O&NG activity to maximum O₃ photochemically produced at BAO. Increasing model constraints of isoprene by a factor of three resulted in an increase of maximum photochemical O₃ of 2.5% relative to the base case. Observed alkanes contributed on average 82% to the observed carbon mixing ratio, of which 86% could be attributed to O&NG emissions. However, alkanes only contributed 56% to VOC OHR and less than 18% to modeled maximum photochemical O₃.

Future work in the NFR is required to address several key uncertainties. First, detailed multi-year studies are required to assess the influence of rapid changes in O&NG and urban activities on ambient levels of VOCs and NO_x and the sensitivity of photochemical O₃ production. Between 2012 and 2014, the number of active wells in Weld County increased by ~2000, oil production more than doubled, and natural gas production increased by a factor of ~1.6 (Colorado Oil and Gas Conservation Commission (COGCC), 2/2016). Since early 2015, O&NG drilling activity has declined nationwide. In addition, the NFR population increased by 12% to over 3 million people between 2010 and 2016 (United States Department of Agriculture (USDA), 2016) and continues to grow, influencing the absolute emissions of NO_x and distribution across the region. Such rapid changes in O&NG activity and urban development suggest the potential for year-to-year changes in photochemical O₃ sensitivities and emissions of VOC and NO_x.

Second, spatially distributed studies from across the region are required to understand the differences in O₃ sensitivities and the impact of air parcel transport in the more VOC impacted areas to the north and NO_x impacted areas to the south. Recent analyses have suggested that regions north of BAO may be more NO_x sensitive with areas closer to metro Denver more sensitive to changes in VOC emissions (Pfister et al., 2017a). The magnitude of O₃ production, however, is also highly dependent on the extent of emission mixing and air transport (Evans & Helmig, 2017; Pfister et al., 2017b). Continued analysis of 2014 and 2015 field studies should be informative. Future studies incorporating the type of detailed measurements and models presented here at ground sites that span the NFR would serve to improve the understanding of regional O₃ production sensitivities to VOCs and NO_x, as well address recent trends in emissions of both urban and O&NG NO_x and VOCs.

Lastly, it will be important to quantify the primary sources of O₃ on days when levels exceed the NAAQS, not just under average summertime conditions. As area non-attainment designation and classification is based on the yearly 4th highest observed MDA8 O₃ value, future compliance of the NFR is dependent on mitigating O₃ on these highest days. Additional field work and modeling based analyses will be required quantify the gradient of VOC/NO_x sensitivity across the NFR, necessary for the development of these effective local O₃ mitigation strategies.

Chapter 4: Heterogeneous N₂O₅ uptake during winter: Aircraft measurements during the 2015 WINTER campaign and critical evaluation of current parameterizations

Abstract

Nocturnal dinitrogen pentoxide (N₂O₅) heterogeneous chemistry impacts regional air quality and the distribution and lifetime of tropospheric oxidants. Formed from the oxidation of nitrogen oxides, N₂O₅ is heterogeneously lost to aerosol with a highly-variable reaction probability, $\gamma(\text{N}_2\text{O}_5)$, dependent on aerosol composition and ambient conditions. Reaction products include soluble nitrate (HNO₃ or NO₃⁻) and nitryl chloride (ClNO₂). We report the first-ever derivations of $\gamma(\text{N}_2\text{O}_5)$ from ambient wintertime aircraft measurements in the critically important nocturnal residual boundary layer. Box modeling of the 2015 Wintertime INvestigation of Transport, Emissions, and Reactivity (WINTER) campaign over the eastern U.S. derived 2876 individual $\gamma(\text{N}_2\text{O}_5)$ values with a median value of 0.0143 and range of 2×10^{-5} to 0.1751. WINTER $\gamma(\text{N}_2\text{O}_5)$ values exhibited the strongest correlation with aerosol water content, but weak correlations with other variables, such as aerosol nitrate and organics, suggesting a complex, non-linear dependence on multiple factors, or an additional dependence on a non-observed factor. This factor may be related to aerosol phase, morphology (i.e. core-shell), or mixing state, none of which are commonly measured during aircraft field studies. Despite general agreement with previous laboratory observations, comparison of WINTER data with 14 literature parameterizations (used

to predict $\gamma(\text{N}_2\text{O}_5)$ in chemical transport models) confirms that none of the current methods reproduce the full range of $\gamma(\text{N}_2\text{O}_5)$ values. Nine reproduce the WINTER median within a factor of two. Presented here is the first field-based, empirical parameterization of $\gamma(\text{N}_2\text{O}_5)$, fit to WINTER data, based on the functional form of previous parameterizations.

The work in this chapter has been adapted from McDuffie et al., (2018): Heterogeneous N_2O_5 uptake during winter: Aircraft measurements during the 2015 WINTER campaign and critical evaluation of current parameterizations. *Journal of Geophysical Research: Atmospheres*. <https://doi.org/10.1002/2018JD028336>.

4.1 Introduction

The chemical formation and nocturnal fate of tropospheric N_2O_5 strongly influences the availability and distribution of tropospheric oxidants, such as ozone (O_3), the hydroxyl radical (OH), and nitrogen oxides ($\text{NO}_x = \text{NO} + \text{NO}_2$) (Dentener & Crutzen, 1993; Macintyre & Evans, 2010; Tie et al., 2001). This chemistry is also vitally important to ammonium nitrate particle formation under cold conditions or in regions of large NH_3 emissions (Baasandorj et al., 2017; Pusede et al., 2016; Riemer et al., 2003) and has implications for regional air quality control strategies due to negative health impacts of $\text{PM}_{2.5}$ (Dockery et al., 1993). Formed from the oxidation of NO_x , N_2O_5 exists in thermochemical equilibrium with the nitrate radical (NO_3), as shown by the scheme Figure 4.1.

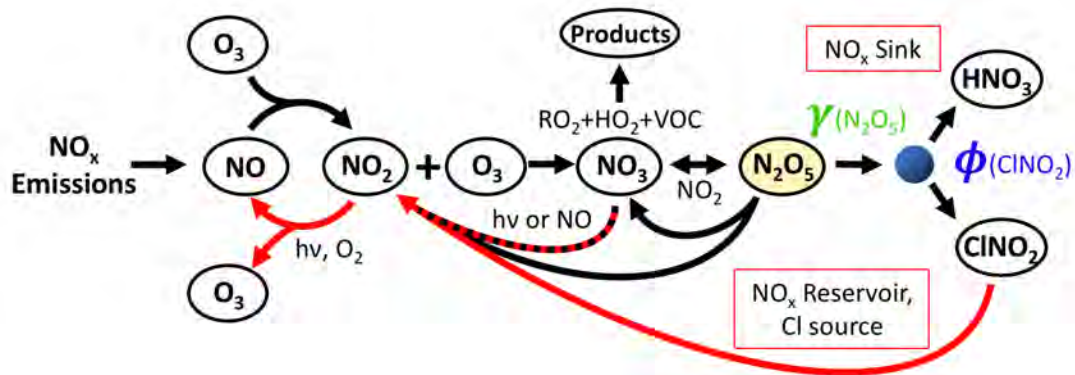


Figure 4.1. Schematic of the N_2O_5 chemical system. Black arrows indicate reactions that do not require sunlight, red arrows show photochemical reactions.

The short lifetime of NO_3 against photolysis and reaction with photochemically-generated NO prevents buildup of appreciable N_2O_5 mixing ratios (> 10 pptv) during the day (e.g. Brown et al., 2005). Reaction of NO_3 with NO near NO_x emission sources will also suppress N_2O_5 production at night near the surface. As a result of boundary layer dynamics that decouple the nocturnal boundary layer (NBL) from the residual layer (RL) (Stull, 1988), N_2O_5 formed at night near urban areas in the RL will therefore either persist (in equilibrium with NO_3 and NO_2) until sunrise, or be lost heterogeneously through uptake onto aerosol. The uptake coefficient, $\gamma(\text{N}_2\text{O}_5)$, is defined as the net probability N_2O_5 will be irreversibly taken up onto an aerosol surface upon collision. Collision and successful surface accommodation are followed by diffusion and aqueous reaction with particle water or chloride to form soluble nitrate ($\text{HNO}_3 + \text{NO}_3^-$) and/or nitryl chloride (ClNO_2), the mechanism of which (Figure 4.2) has been the topic of many previous studies (e.g. Bertram & Thornton, 2009) and is discussed in later sections. Upon sunrise, unreacted N_2O_5 will irreversibly, thermally dissociate back to NO_2 and NO_3 , where NO_3 will rapidly photolyze to form a second NO_2 molecule that can contribute to O_3 and the formation of NO_x the following day (Figure 4.1). The product branching ratio between HNO_3 and photolabile ClNO_2 , represented by $\phi(\text{ClNO}_2)$, also has implications for global distributions of oxidants and chlorine radicals (Osthoff

et al., 2008; Sarwar et al., 2014; Thornton et al., 2010), discussed in Chapter 5. Overall, the pathways in Figure 4.1 illustrate the potential role of N_2O_5 and its uptake efficiency in the regional transport and distribution of NO_x and tropospheric oxidants.

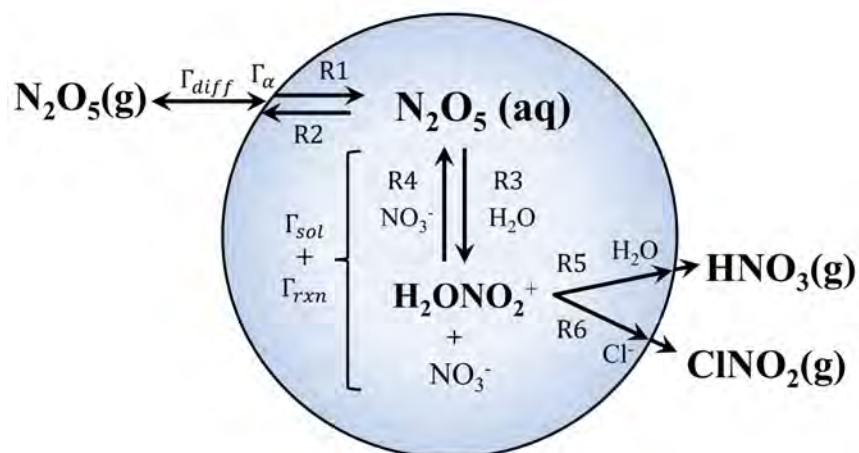


Figure 4.2. Uptake schematic highlighting the relation between the chemical mechanism and resistor model framework in terms of each mechanistic step (R4.1-R4.6) and its associated conductance (Γ).

The chemical mechanism and aerosol uptake efficiency of N_2O_5 have been primarily studied during northern mid-latitude, summertime field campaigns (see references below), despite the greater importance of N_2O_5 uptake in governing NO_x abundance during winter (e.g. Dentener & Crutzen, 1993). As discussed in Wagner et al. (2013), there are three key differences during winter that can impact N_2O_5 chemistry including: 1) longer nights that allow more time for N_2O_5 production/loss, 2) colder temperatures that favor N_2O_5 in its equilibrium with NO_3 , and 3) differences in aerosol composition (Zhang et al., 2007) that could lead to changes in uptake efficiency. Despite these important differences, only three field studies have reported determinations of N_2O_5 uptake efficiencies during the winter season (Brown et al., 2016; Wagner et al., 2013; Wild et al., 2016), and none from aircraft, limiting the altitude and spatial diversity of previous observations.

The majority of previous field studies have derived $\gamma(\text{N}_2\text{O}_5)$ values using the steady state approximation (Brown et al., 2003), which must infer $\gamma(\text{N}_2\text{O}_5)$ from measurements of aerosol surface area, nitrogen oxides, and O_3 , and may not be well suited to the cold temperatures and high NO_x concentrations encountered during winter in urban areas that keep N_2O_5 and NO_3 from achieving steady state concentrations (Brown et al., 2003). While previous flow tube reactor experiments in ambient air have provided direct measurements of N_2O_5 -aerosol loss rates (e.g. Bertram et al., 2009a), uptake coefficients in these studies must also be calculated from additional aerosol surface area measurements. Additionally challenging is that heterogeneous reactions are complex and driven by many physiochemical, thermodynamic, and kinetic factors that change with ambient conditions and aerosol surface/bulk composition (e.g. Kolb et al., 2002; Pöschl et al., 2007). Previous experiments investigating the mechanism and kinetics of $\gamma(\text{N}_2\text{O}_5)$ on laboratory-derived aerosol (Anttila et al., 2006; Bertram & Thornton, 2009; Folkers et al., 2003; Mentel et al., 1999; Mozurkewich & Calvert, 1988; Thornton et al., 2003), show a dependence on several key factors including aerosol surface water availability and composition.

Both laboratory and previous field studies have reported values of $\gamma(\text{N}_2\text{O}_5)$ between $\sim 10^{-4}$ and 0.1, a range which Macintyre and Evans (2010) showed can either minimally (<3%) or significantly (>15%) impact the annually-averaged, global budgets of O_3 and the hydroxyl radical (OH). This large oxidant sensitivity has led to the development of multiple laboratory-based parameterizations (Anttila et al., 2006; Davis et al., 2008; Evans & Jacob, 2005; Gaston et al., 2014; Riemer et al., 2003), some in combination with a proposed chemical mechanism (Bertram & Thornton, 2009; Griffiths et al., 2009; Riemer et al., 2009), to describe $\gamma(\text{N}_2\text{O}_5)$ as a function of key factors. While one parameterization has successfully predicted field-derived $\gamma(\text{N}_2\text{O}_5)$ values under certain ambient conditions (Bertram et al., 2009b), disagreements largely persist between

parameterized and field-derived values (Brown et al., 2009; Chang et al., 2016; Morgan et al., 2015; Phillips et al., 2016; Riedel et al., 2012a). Due to the limited number of field studies that have quantified $\gamma(\text{N}_2\text{O}_5)$, particularly in winter, these parameterization-field discrepancies could result from comparisons to a relatively small number of data sets, incorrect identification of the factors controlling $\gamma(\text{N}_2\text{O}_5)$, or an inaccurate functional dependence on factors already incorporated. The importance of $\gamma(\text{N}_2\text{O}_5)$ in regulating global concentrations of tropospheric oxidants (O_3 , OH), combined with its observed orders of magnitude range, highlights the need for a larger database of field derived $\gamma(\text{N}_2\text{O}_5)$ values and determination of their dependence on physical and chemical variables.

We present a box model analysis to quantitatively derive $\gamma(\text{N}_2\text{O}_5)$ under the cold, high- NO_x conditions encountered during the Wintertime INvestigation of Transport, Emissions, and Reactivity (WINTER) aircraft campaign over the eastern U.S. in February – March 2015. Box model results are compared to $\gamma(\text{N}_2\text{O}_5)$ values derived using the steady state approximation to assess this methods applicability to conditions encountered during the WINTER campaign. Observed correlations between box model $\gamma(\text{N}_2\text{O}_5)$ results and multiple factors of aerosol composition, relative humidity, and temperature are then used in combination with results from a critical evaluation of 14 literature parameterizations to inform the first empirical, field-based parameterization of $\gamma(\text{N}_2\text{O}_5)$.

4.2 Methods

4.2.1 WINTER Campaign and Measurements

As described in Chapter 2, the WINTER campaign conducted 13 research flights with the NSF/NCAR C-130 aircraft over the eastern United States between 3 February and 13 March 2015. Flight tracks in Figure 4.4a show the geographical distribution of flights conducted during various

times of day and night (night defined as solar zenith angle (SZA) > 90°) over both continental and marine environments. Aircraft instrumentation included measurements of many species, including reactive nitrogen oxides, O₃, and aerosol composition. Several species were measured by duplicate techniques. Instrument details, including accuracy and measurement frequency, are given in Table 4.1 and described in detail in Section 2.3.2.2.

Table 4.1. Summary of WINTER observations used in the Box Model analysis

Compound	Method/ Instrument	Accuracy	Meas. Frequency	Reference
<u>Gas-Phase Species</u>				
NO	CRDS ^{a,b}	4%	1s	(Fuchs et al., 2009)
	CL ^c	10%	1s	(Weinheimer et al., 1994)
NO ₂	CRDS ^a	3%	1s	(Fuchs et al., 2009)
	TD-LIF ^d	10%	1s	(Day et al., 2002)
O ₃	CRDS ^a	4%	1s	(Washenfelder et al., 2011a)
	CL	5%	1s	(Weinheimer et al., 1994)
NO _y	CRDS	12%	1s	(Wild et al., 2014)
	CL	50%	1s	(Weinheimer et al., 1994)
N ₂ O ₅	CRDS	12%	1s	(Dubé et al., 2006)
	I-CIMS ^e	30%	1s	(Lee et al., 2014)
CINO ₂	I-CIMS	30%	1s	(Lee et al., 2014)
Speciated VOCs	TOGA ^f	< 50%	35s, 2 min	(Apel et al., 2015)
<u>Aerosol Measurements</u>				
Nitrate (<1µm)	AMS ^g	35%	1s,	(DeCarlo et al., 2006)
	PILS-IC ^h	20%	3 min	(Guo et al., 2016)
Chloride (<1µm)	AMS	35%	1s	(DeCarlo et al., 2006)
	PILS-IC	20%	3 min	(Guo et al., 2016)
Sulfate (<1µm)	AMS	35%	1s	(DeCarlo et al., 2006)
Organic (<1µm)	AMS	35%	1s	(DeCarlo et al., 2006)
Dry Surface Area	UHSAS ⁱ	34%	1s	(Cai et al., 2008)
Density (<1µm)				
Dry Surface Area	PCASP ^j	41%	1s	(Strapp et al., 1992)
	PCASP	34%	1s	(Strapp et al., 1992)
Density (1-3µm)				
<u>Radiative Measurements</u>				
J-values	HARP-AF ^k	<25-40% ^k	10s	(Shetter & Müller, 1999)

^aExcludes Research Flights 01-04 due know problem in the sampling inlet line

^bNOAA, Cavity Ringdown Spectrometer

^cNCAR, Chemiluminescence Detector

^dUniversity of California Berkeley, Thermal Dissociation – Laser Induced Fluorescence Detector

^eUniversity of Washington, High Resolution, Time of Flight, Iodide Chemical Ionization Mass Spectrometer

^fNCAR, Trace Organic Gas Analyzer

^gUniversity of Colorado Boulder, Aerosol Mass Spectrometer

^hGeorgia Institute of Technology, Particle Into Liquid Sampler – Ion Chromatography

ⁱNCAR, Ultra-High Sensitivity Aerosol Spectrometer

^jNCAR, Passive Cavity Aerosol Spectrometer Probe

^kHIAPER Airborne Radiation Package - Actinic Flux. For uncertainty description, see Section 2.4.2.7.9.

Total wet aerosol surface area (used in E4.5) was estimated by applying separate relative humidity-dependent surface area growth factors to the measured dry surface area density of <1 μm and 1-3 μm particles. Growth factors were derived from the Extended-AIM Aerosol Thermodynamics Model (Wexler & Clegg, 2002) for 1-3 μm particles, assuming pure NaCl particles and no solid formation (metastable). For <1 μm particles, surface area growth factors (red circles, Figure 4.3) were calculated for every 10 second period following E4.1- E4.4, with total dry mass and density (M_{Dry} , ρ_{dry}) reported by the AMS and aerosol liquid water (M_{Wet}) calculated as described below. Growth factors for <1 μm aerosol were additionally calculated using the E-AIM Model, assuming pure NH₄NO₃ aerosol and no solid formation (red dashed line, Figure 4.3). For comparison, Figure 4.3 also shows growth factors used in previous field studies during winter in Colorado (Wagner et al., 2013) and fall in Texas (Brown et al., 2009). Differences in growth factors may be due to differences in aerosol composition, in particular the presence of aerosol organics, which can decrease the aerosol hygroscopicity and alter the deliquescence point (Attwood et al., 2014). For this study, data have been filtered to exclude RH values > 95% (arbitrarily chosen) due to the increased uncertainty in growth factors (large divergence between different parameterizations) at high RH. Sensitivity of $\gamma(\text{N}_2\text{O}_5)$ to the chosen hygroscopic growth factor curve is presented in Chapter 2, Section 2.4.2.7.1.

$$\text{Aerosol SA Growth Factor} = \left(\frac{V_{Total}}{M_{Dry} * \rho_{dry}} \right)^{\frac{2}{3}} \quad (4.1)$$

$$V_{Total} = M_{Wet} * \rho_{water} + M_{Dry} * \rho_{dry} \quad (4.2)$$

$$M_{Wet} = M_{Inorg. water} + M_{Org. water} \quad (4.3)$$

$$M_{Org. water} = \left(\frac{a_w}{1-a_w} \right) * \kappa_{Org} * \left(\frac{M_{org}}{\rho_{org}} \right) * \rho_{water} \quad (4.4)$$

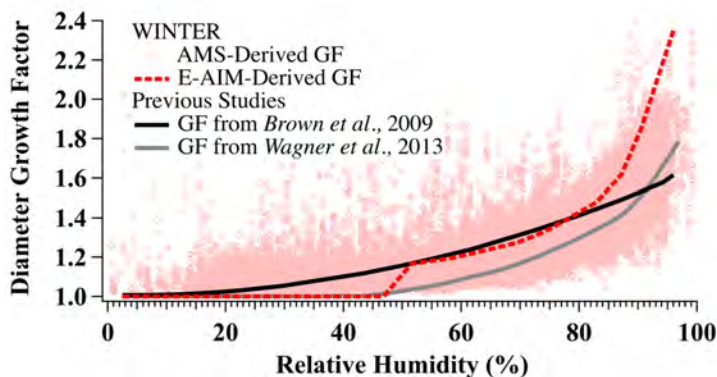


Figure 4.3. Hygroscopic Diameter Growth Factors for $<1\mu\text{m}$ diameter aerosol. (Red circles) derived for WINTER, used for base case calculations; (red dashed line) derived for WINTER, assuming pure NH_4NO_3 aerosol (calculated from E-AIM by Viral Shah); (black, gray lines) reported in Brown et al. (2009) and Wagner et al. (2013), respectively. Surface area growth factors are the square of diameter growth factors.

Aerosol liquid water mass (M_{Wet}) (used in Section 4.4 and Chapter 5) was calculated in E4.3 as the sum of inorganic-associated water (calculated from ISORROPIA by Hongyu Guo, as described in Guo et al. (2016)) and the organic-associated water, estimated in E4.4 by the measured dry organic aerosol mass (M_{org}) and density (ρ_{org}), water activity (a_w), water density (ρ_{water}), and the organic hygroscopicity constant (κ_{org}). Here, equilibrium is assumed and a_w is taken as ambient relative humidity/100. A single value of 0.1 is used for κ_{org} . While previous studies have found a dependence of κ_{org} on factors such as O:C ratio, organic aerosol mass, and organic volatility (Cerully et al., 2015; Jimenez et al., 2009; Mei et al., 2013), multiple parameterizations (e.g. Chang et al., 2010; Mei et al., 2013) and field studies have generally found that κ_{org} ranges from 0-0.4 for aged, organic-containing aerosol (Petters & Kreidenweis, 2007; Rickards et al., 2013; Suda et al., 2012), with values ~ 0.1 for aerosol in the southeastern U.S. (Brock et al., 2016; Shingler et al., 2016). The liquid water content (LWC), is calculated as the mass fraction of aerosol water, taken as M_{Wet} divided by the total aerosol mass ($M_{Wet} + M_{Dry}$).

4.2.2 Iterative Box Model

The iterative box model used in this analysis is based on the description in Wagner et al. (2013), developed to simulate the nocturnal evolution of air sampled at a tall tower in Colorado. As described in detail in Chapter 2 (Section 2.4.2) and briefly here, key aspects of the model have been updated for use with WINTER aircraft data.

4.2.2.1 Model Description

The first-order loss rate coefficient of N_2O_5 ($k_{\text{N}_2\text{O}_5}$ [s^{-1}]) and production rate coefficient of ClNO_2 (k_{ClNO_2} [s^{-1}]) were derived for every 10-second period of all WINTER night flights using a zero-dimensional box model, developed to simulate the nocturnal chemical evolution of an air parcel in the RL (assuming constant temperature and RH), from the onset of N_2O_5 production (1.3 hours prior to sunset or time of NO_x emission, Section 2.4.2.3) until the time of aircraft measurement. The model used three main steps (Figure 2.17) to derive $k_{\text{N}_2\text{O}_5}$ and k_{ClNO_2} by iteratively fitting final simulated mixing ratios to aircraft observations of NO_2 , O_3 , N_2O_5 , and ClNO_2 . The instrument-specific observations used as fit parameters varied by flight and are listed in Table 2.7. Correlation plots of all overlapping measurements in 2.4.2.7 indicate agreement to within 12% for all species. An additional 45 model simulations suggest a small sensitivity (< 20%) in $\gamma(\text{N}_2\text{O}_5)$ to measurement accuracies and instrument choice, except for CRDS vs CIMS N_2O_5 , as discussed in Section 2.4.2.7.4.

Model-derived values for $k_{\text{N}_2\text{O}_5}$ and k_{ClNO_2} were then used in E4.5 and E4.6, with aircraft observations of aerosol surface area density (SA) and the mean molecular speed of N_2O_5 (c) to calculate $\gamma(\text{N}_2\text{O}_5)$ and $\phi(\text{ClNO}_2)$ for every 10 second period. The 10 second interval was chosen to increase the model computation efficiency while maintaining the spatial resolution (~1-10 km) of

the data products. The remainder of this Chapter will focus on $\gamma(\text{N}_2\text{O}_5)$ with an analysis of $\phi(\text{ClNO}_2)$ results presented in Chapter 5.

$$\gamma(\text{N}_2\text{O}_5) = \frac{4 * k_{\text{N}_2\text{O}_5}}{c * SA} \quad (4.5)$$

$$\phi(\text{ClNO}_2) = \frac{k_{\text{ClNO}_2}}{k_{\text{N}_2\text{O}_5}} \quad (4.6)$$

In this work, SA is assumed constant over each simulation duration and represents the total wet aerosol SA density for particles $< 3 \mu\text{m}$ in diameter. Though previous field studies have limited the calculation of $\gamma(\text{N}_2\text{O}_5)$ to particles $< 1 \mu\text{m}$ (Bertram et al., 2009b; Riedel et al., 2012a; Wagner et al., 2013), the small contribution of 1-3 μm particles (0.5-4%) to total dry SA density will only slightly decrease the WINTER $\gamma(\text{N}_2\text{O}_5)$ results relative to past studies. Measurements of 3-10 μm particles were excluded from this analysis due to their small contribution (0-2%) to the total dry SA density. Variations over the simulation duration of SA are not considered here, but could lead to an increased variability in derived $\gamma(\text{N}_2\text{O}_5)$ values. Further discussion of this limitation is presented in Section 2.4.2.5.

The expression for $\gamma(\text{N}_2\text{O}_5)$ in E4.5 is simplified from that discussed in Fuchs and Sutugin (1970) for conditions where $\gamma(\text{N}_2\text{O}_5)$ is not limited by gas-phase diffusion to the aerosol surface. According to previous studies (e.g. Dentener & Crutzen, 1993; Pöschl et al., 2007), this approximation is valid for small particles with diameters less than the N_2O_5 mean free path ($\sim 0.1 \mu\text{m}$) or small uptake coefficients (< 0.1). Despite some particle diameters $> 0.1 \mu\text{m}$ measured during WINTER (max $dN/d\log D_p$ occurred at $\leq 0.15 \mu\text{m}$ dry diameter), previous field studies have suggested that correction for diffusion increases derived $\gamma(\text{N}_2\text{O}_5)$ values by $< 5\%$ (Aldener et al., 2006).

The box model chemical mechanism and associated uncertainties are discussed in Chapter 2 (Section 2.4.2) and described briefly here. The model mechanism included 14 reactions and 15 compounds (see Table 2.3), chosen as the simplest set of reactions to accurately describe the nocturnal inorganic chemistry of N_2O_5 . As noted in previous studies, large uncertainties in mechanisms of nocturnal chemistry arise from uncertainties in NO_3 loss reactions (e.g. Phillips et al., 2016; Wagner et al., 2011). In the absence of photochemical radical production, NO_3 serves as one of the primary nocturnal tropospheric oxidants for volatile organic compounds (VOCs). NO_3 also reacts with RO_2 and HO_2 radicals, which can contribute to nocturnal NO_x recycling (Vaughan et al., 2006). In this analysis, NO_3 -VOC oxidation reactions were lumped and treated as a net NO_x sink (R2.7) with a rate constant (k_{VOC} [s^{-1}]) calculated from TOGA WINTER VOC measurements (described in Section 2.4.2.2). Due to a lack of radical measurements during WINTER, the first-order NO_3 loss rate constant for the NO_x recycling reaction with HO_2 (k_{HO_2} [s^{-1}]) (R2.8) was estimated from the second order $\text{NO}_3 + \text{HO}_2$ reaction rate constant (IUPAC, 2008b) and HO_2 concentrations from 2011 over the UK (Stone et al., 2014). These are the most recently reported aircraft observations of HO_2 in the wintertime RL, over a populated region in the Northern Hemisphere. Calculated rate constants for both R2.7 and R2.8 were treated as constants throughout each simulation duration, which has the potential to add variability to the $\gamma(\text{N}_2\text{O}_5)$ results since VOC reactivity is likely to decrease with time via depletion of reactive VOCs. NO_3 reactions with RO_2 were not explicitly included in this mechanism due to a lack of wintertime RO_2 aircraft field measurements. If this treatment were to result in k_{NO_3} values outside the bounds of uncertainty already considered (described below), derived $\gamma(\text{N}_2\text{O}_5)$ values would be reduced. Direct NO_3 uptake was also excluded from the mechanism since reported NO_3 uptake coefficients are generally small on inorganic aerosol ($\gamma(\text{NO}_3) \sim 10^{-3}$ (Brown & Stutz, 2012)), which dominated the

WINTER aerosol composition (Figure 4.11). While some analyses have suggested larger values of NO_3 uptake onto organic surfaces (Mao et al., 2013; Ng et al., 2017), NO_3 uptake coefficients of ≤ 0.1 would decrease the median $\gamma(\text{N}_2\text{O}_5)$ by $< 10\%$ (Section 2.4.2.7.10).

Due to the multiple sources of uncertainty in k_{NO_3} (including VOC measurements, HO_2/RO_2 reactions, and NO_3 uptake), values calculated here are likely lower limits. The box model, however, displayed the smallest sensitivity of all parameters tested to k_{NO_3} (Table 2.8), with the campaign median changing by $-1.0/+1.2\%$ in response to $\pm 10\%$ changes in both k_{VOC} and k_{HO_2} . For one WINTER flight, however, relatively warmer temperatures did increase the sensitivity of modeled $\gamma(\text{N}_2\text{O}_5)$ to k_{NO_3} ($-25.2\%/+3.5\%$ to $\pm 10\%$ changes, discussed in Section 2.4.2.7.10). As k_{NO_3} values here are likely lower limits, an increase in NO_3 reactivity on this flight would serve to decrease $\gamma(\text{N}_2\text{O}_5)$ below the original values of $< 1 \times 10^{-3}$. This flight highlights the fact that this particular model is most appropriate (has the lowest uncertainties) under cold, wintertime conditions with low NO_3 reactivity. As a result of the small k_{NO_3} sensitivity on all other flights, more explicit treatment of NO_3 chemistry was not required for this mechanism to accurately simulate nocturnal N_2O_5 chemistry during WINTER.

4.2.2.2 Model Filter, Limitations, and Sensitivity Studies

As described further in Section 2.4.2.5, simulations were limited to aircraft measurements within the RL ($\text{SZA} > 90^\circ$), at altitudes below the free troposphere (typically ~ 1000 mAGL) and above the nocturnal boundary layer (estimated to be ~ 100 mAGL) (Stull, 1988) and were additionally filtered to remove points with reported relative humidity $> 95\%$ (1.7% of derived values). One limitation of this box model is that non-convergence occurs as $k_{\text{N}_2\text{O}_5}$ approaches zero (minimum $2 \times 10^{-7} \text{ s}^{-1}$). The maximum bias introduced from this non-convergence is relatively small ($< 12\%$) and does not change the main conclusions presented in later sections. A second limitation

is that the model cannot account for time-varying changes in SA or reaction rate constants. For example, assuming a constant value for NO_3 -VOC reactivity, which may decrease overtime, could lead to an over-prediction in $\gamma(\text{N}_2\text{O}_5)$ at longer simulation durations and under-prediction at shorter times. In addition, $\gamma(\text{N}_2\text{O}_5)$ itself and/or aerosol SA could change with time. An average 5% increase in SA was estimated assuming all N_2O_5 uptake in the model led to nitrate aerosol, which is an upper limit as some fraction will partition to the gas-phase. These factors are not further considered but may serve to increase the variability in the literature parameterization comparisons presented in Section 4.4.3.2.

To test the robustness of the box model to uncertainties in model parameters and assumptions described above, a series of 18 sensitivity studies were additionally conducted for each WINTER flight (162 additional simulations). A summary of resulting changes in campaign-median $\gamma(\text{N}_2\text{O}_5)$ values are provided in Table 2.8. Resulting median $\gamma(\text{N}_2\text{O}_5)$ values showed small (< 11%) sensitivities to uncertainties in air age (duration), simulation start time, aerosol hygroscopic growth factor, NO_3 reactivity, photolysis frequencies, and O_3 measurements, but larger sensitivities (> 20%) to uncertainties in measured dry aerosol SA density, NO_2 , and N_2O_5 . Data collected over the ocean (defined by the GPS coordinates of the eastern U.S. shoreline) were additionally tested for sensitivities to N_2O_5 ocean surface deposition (rate calculated from Kim et al. (2014)) and dilution and showed -14% and -5.7% changes, respectively. Extensive details for all sensitivity studies are in Section 2.4.2.7.

4.3 Results

4.3.1 Box Model Results

Figure 4.4b shows WINTER flight tracks colored by model-derived $\gamma(\text{N}_2\text{O}_5)$, with a histogram illustrating the campaign-wide distribution in Figure 4.4c. As described, the box model

derived 2876, 10-second averaged, individual $\gamma(\text{N}_2\text{O}_5)$ determinations over the course of 9 WINTER flights, providing the first regional scale determinations of $\gamma(\text{N}_2\text{O}_5)$ during a single winter season, as well as over 50 times more individual $\gamma(\text{N}_2\text{O}_5)$ determinations than all previous aircraft studies combined (see Figure 4.9) (Brown, S. S. et al., 2006; Brown et al., 2009; Morgan et al., 2015). In addition, the model accounted for 35% of all nocturnal RL data collected during WINTER, compared to 7% from 25 days of continuous sampling in 2011 at a Colorado ground site (Wagner et al., 2013).

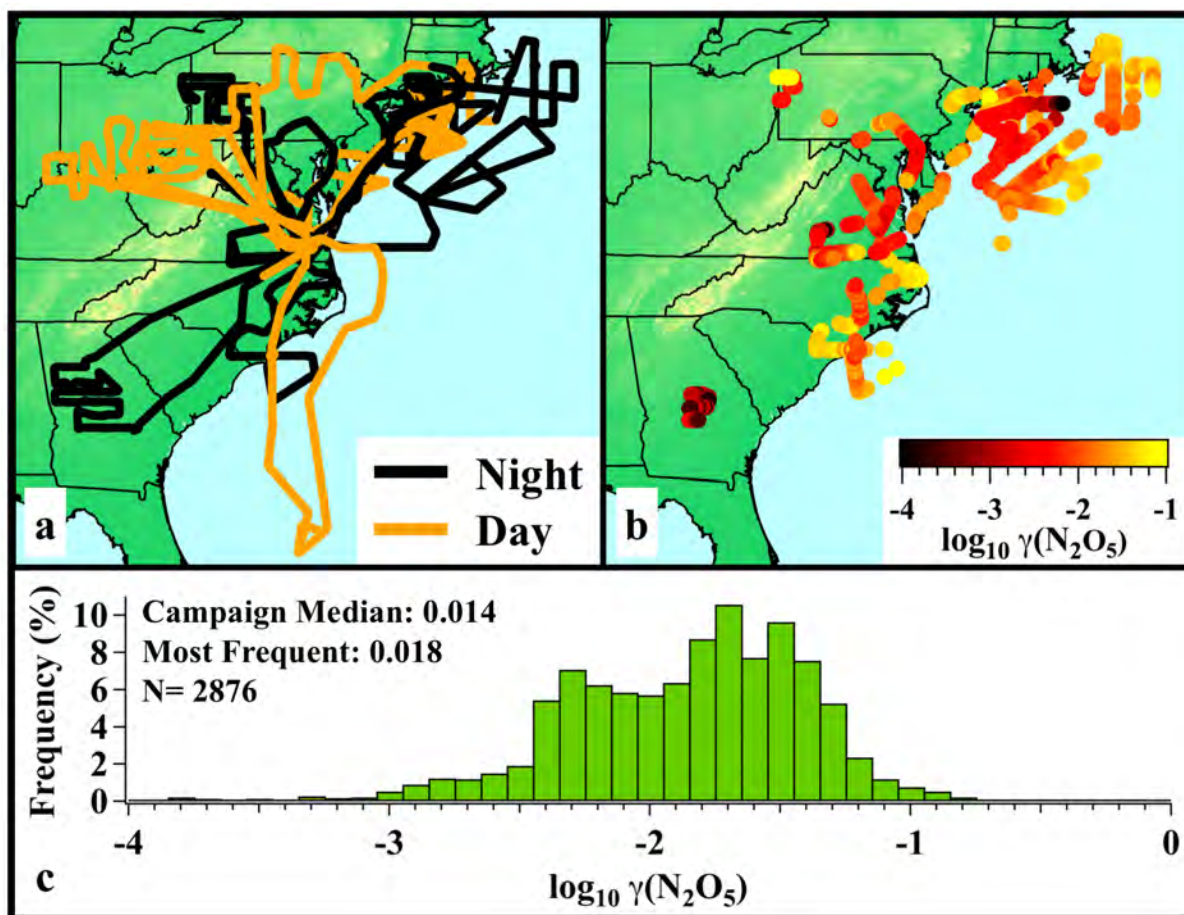


Figure 4.4. (a) Map of WINTER flight tracks of the NSF/NCAR C-130 in the Eastern U.S., colored to show day and night (as defined by $\text{SZA} > 90^\circ$) flight periods, which represented 42 and 58% of the data, respectively. The aircraft was based at NASA Langley in coastal Virginia and executed 13 flights of approximately 8 hours duration between 3 February – 13 March 2015. (b) Flight tracks colored by $\gamma(\text{N}_2\text{O}_5)$, derived from the box model analysis. (c) Histogram of box model results.

Over this single, 5-week period, $\gamma(\text{N}_2\text{O}_5)$ ranged four orders of magnitude from 2×10^{-5} to 0.1751 with median value of 0.0143 ($1\sigma: \pm 0.007$ or $\pm 52\%$), which is within 43% of where GEOS-Chem estimates of O_3 and OH are most sensitive to $\gamma(\text{N}_2\text{O}_5)$ (Macintyre & Evans, 2010). The histogram in Figure 4.4c shows the most frequent value occurred at 0.018 and a secondary peak at a lower value of 0.004. Figure 4.4b does not show a strong geographical dependence in $\gamma(\text{N}_2\text{O}_5)$, with continental and marine flights encompassing the same range (Figure 4.5). Marine flights, however, could have been largely influenced by continental emission sources due to persistent off-shore winds during WINTER.

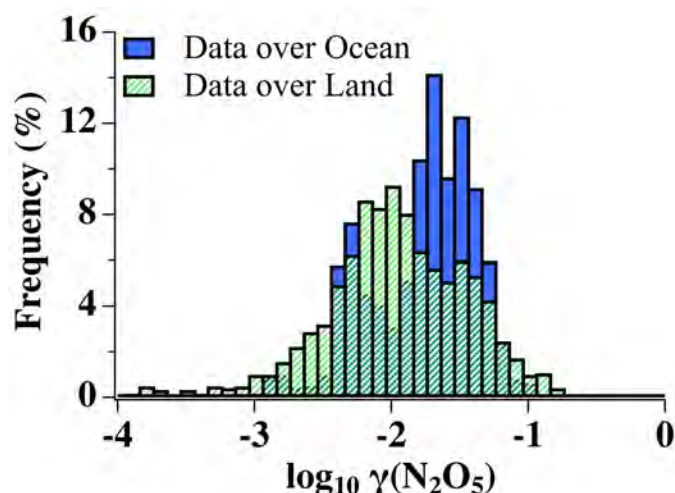


Figure 4.5. Histogram of base case results comparing the distributions of $\gamma(\text{N}_2\text{O}_5)$ values derived over the U.S. main land (green) and Atlantic ocean (blue).

Errors for each individual point during WINTER are shown by flight in Figure 4.6, calculated from the quadrature addition of measurement uncertainties (NO_2 , O_3 , N_2O_5 , and dry SA density, Table 4.1) and model sensitivities to the aerosol hygroscopic growth factor, 50% changes in k_{NO_3} (50% in k_{VOC} and k_{HO_2}), air age, and start time (Table 2.8). In addition to Figure 4.6, times-series from three different flights (continental and marine) in Figure 4.7 illustrate the observed variability in $\gamma(\text{N}_2\text{O}_5)$ and some associated variables within and between different parcels of air.

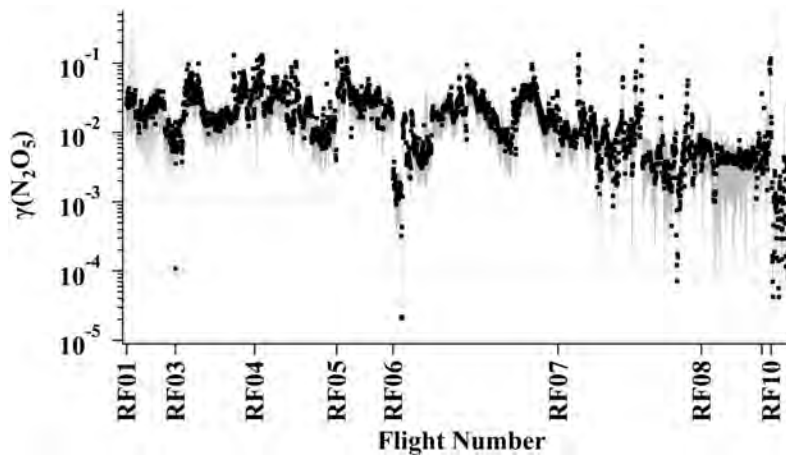


Figure 4.6. WINTER $\gamma(\text{N}_2\text{O}_5)$ results listed by flight, with shaded regions indicating error estimates for each determination.

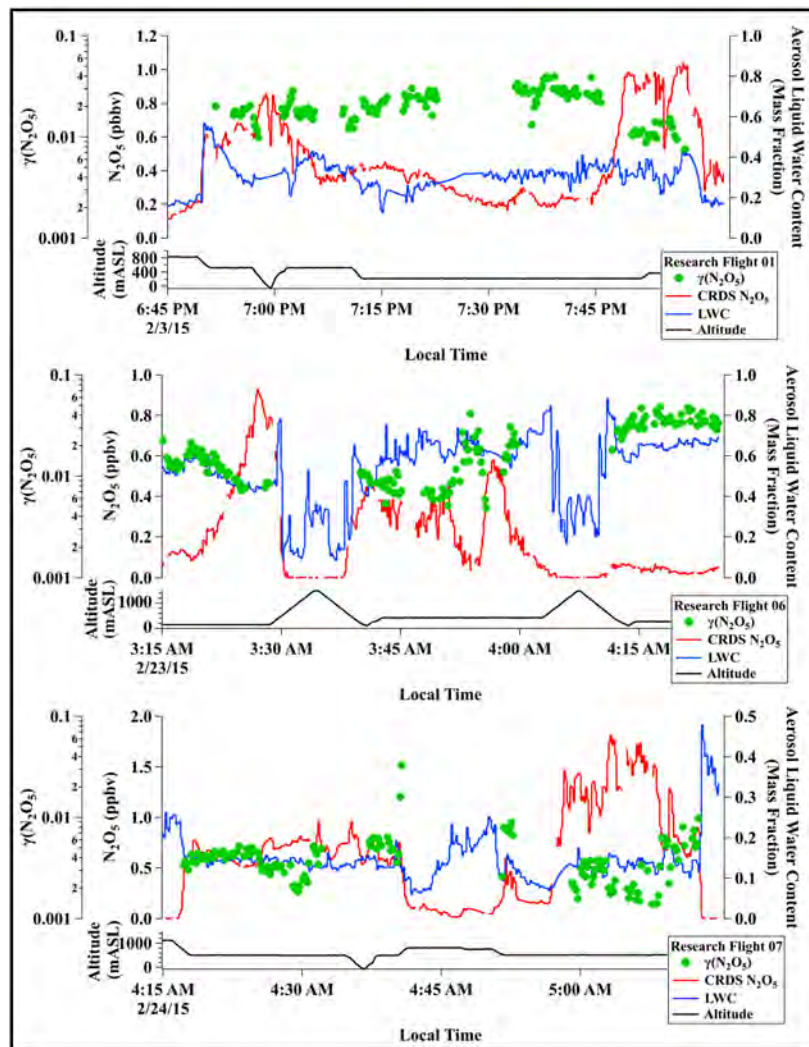


Figure 4.7. Example time-series from three different WINTER research flights illustrating the variability of $\gamma(\text{N}_2\text{O}_5)$, N_2O_5 , and aerosol liquid water content (LWC) (calculated by Hongyu Guo from ISORROPIA) within and between different air parcels sampled.

The majority of smallest $\gamma(\text{N}_2\text{O}_5)$ values ($< 10^{-3}$, discussed further in Sections 4.4.3.2) were derived on research flight 10. These are lower than many values previously reported by field and laboratory-studies, and are most sensitive to changes in k_{NO_3} . Despite a small sensitivity of the campaign median to k_{NO_3} ($\sim 5\%$ change in $\gamma(\text{N}_2\text{O}_5)$ for a 50% change in k_{NO_3}), these particular points are reduced from values $\sim 1 \times 10^{-3}$ to as low as 2×10^{-5} if total NO_3 reactivity ($k_{\text{VOC}} + k_{\text{HO}_2}$) is increased by 50% (to account for possible sources of missing k_{NO_3} , Section 2.4.2.7.10). All additional sources of error, including measurement uncertainties, were small for these values as they were derived when fitting the model to the largest concentrations of N_2O_5 (Figure 4.11). Despite the increased uncertainty in k_{NO_3} , it remains important to derive and distinguish $\gamma(\text{N}_2\text{O}_5)$ values in this range as GEOS-Chem results (lower panel in Figure 4.9) show that oxidants and NO_x remain sensitive to $\gamma(\text{N}_2\text{O}_5)$ down to values of 1×10^{-5} . It is additionally important to identify the physical cause of these lowest values as $\gamma(\text{N}_2\text{O}_5)$ values in this range are not typically predicted by $\gamma(\text{N}_2\text{O}_5)$ parameterizations based on the current mechanistic understanding of N_2O_5 uptake (Section 4.4.3).

An additional comparison of box model results to $\gamma(\text{N}_2\text{O}_5)$ values calculated from WINTER GEOS-Chem simulations (described in Appendix B) is shown in Figure 4.8 and indicates: 1) no spatial, systematic trend in the percent differences between the two determinations, 2) a smaller range in GEOS-Chem-derived $\gamma(\text{N}_2\text{O}_5)$ values relative to the box model, and 3) a 25.3% lower median value in GEOS-Chem. While a discussion of differences between GEOS-Chem and box model results (sources include deposition, dilution, aerosol composition, and surface area) are outside the scope of this Chapter, a $\gamma(\text{N}_2\text{O}_5)$ parameterization similar to that used in GEOS-Chem (Appendix B) is discussed with other literature parameterizations in Section 4.4.3.2.

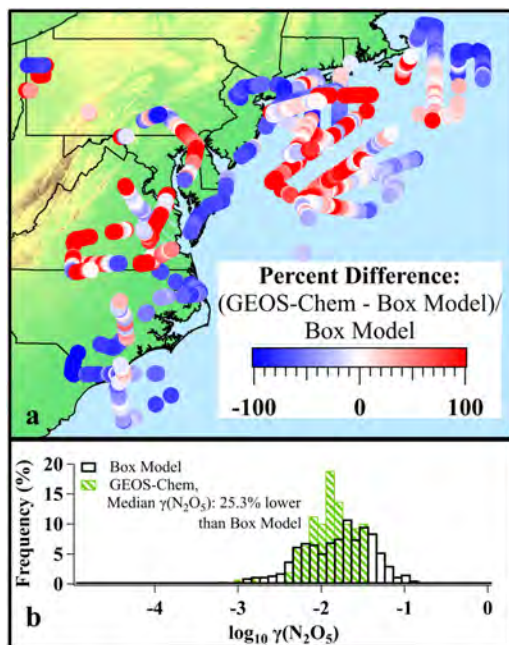


Figure 4.8. Comparison of WINTER $\gamma(\text{N}_2\text{O}_5)$ values derived from the box model and GEOS-Chem simulations (60 second averages). Map shows the WINTER flight tracks, colored by the percent difference in box model and GEOS-Chem results (from Viral Shah). Percent difference = $(\text{GEOS-Chem} - \text{box model}) / \text{box model} * 100$. Histogram insert shows the distributions of both.

WINTER $\gamma(\text{N}_2\text{O}_5)$ values are shown in comparison to all previous field determinations of $\gamma(\text{N}_2\text{O}_5)$ in the upper panel of Figure 4.9 (and Table B.1). The 4 order-of-magnitude range in WINTER values encompasses all values previously reported, despite a large variability in previous sample locations, platforms, and seasons. Using the nocturnal steady-state approximation, previous aircraft studies have reported $\gamma(\text{N}_2\text{O}_5)$ values ranging from 0.001 - 0.02 over the Northeast U.S. in August 2004 (Brown, S. S. et al., 2006), 4×10^{-4} - 0.019 over Texas in October 2006 (Brown et al., 2009), 0.001 - 0.01 over California in May and June 2010 (Chang et al., 2016), and 0.0076 - 0.03 over Northwestern Europe/UK in July 2010 (Morgan et al., 2015). These values largely fall within the lower population of WINTER $\gamma(\text{N}_2\text{O}_5)$ values (Figure 4.4c). Multiple studies have also derived $\gamma(\text{N}_2\text{O}_5)$ values ranging from 3×10^{-5} to 0.11 (see Table B.1) using flow reactors and the steady state approximation during both summer and fall seasons from a ship (Aldener et al., 2006) and multiple ground sites in the U.S. (Bertram et al., 2009b; Riedel et al., 2012a), Europe (Phillips

et al., 2016), and China (Tham et al., 2016; Wang, X. et al., 2017; Wang, H. et al., 2017; Wang, Z. et al., 2017).

Few studies, and none from aircraft, have reported $\gamma(\text{N}_2\text{O}_5)$ values during the winter season, where colder temperatures and low NO_3 reactivities are expected to increase nocturnal N_2O_5 production and lifetime relative to warmer seasons. Using a box-model approach, Wagner et al. (2013) derived $\gamma(\text{N}_2\text{O}_5)$ values between 0.002 and 0.1 in Weld County, Colorado in February-March 2011, Wild et al. (2016) fit an average $k_{\text{N}_2\text{O}_5}$ (in E4.5) value to that predicted by the steady state approximation to derive single value of 0.026 for January-February 2012 in rural Utah, and Brown et al. (2016) used the steady state approximations to derive values between 0.004 and 0.029 in Hong Kong, China during December 2013. An additional analysis of the N_2O_5 lifetime ($(k_{\text{N}_2\text{O}_5})^{-1}$) near Fairbanks, Alaska, showed that N_2O_5 loss may be enhanced by the presence of ice surfaces at high latitudes during winter (Apodaca et al., 2008). Comparison between all past field studies in Figure 4.9 does not indicate a strong seasonal dependence of $\gamma(\text{N}_2\text{O}_5)$, nor bias from sampling platform type (i.e. aircraft, ship, or ground) or analysis method.

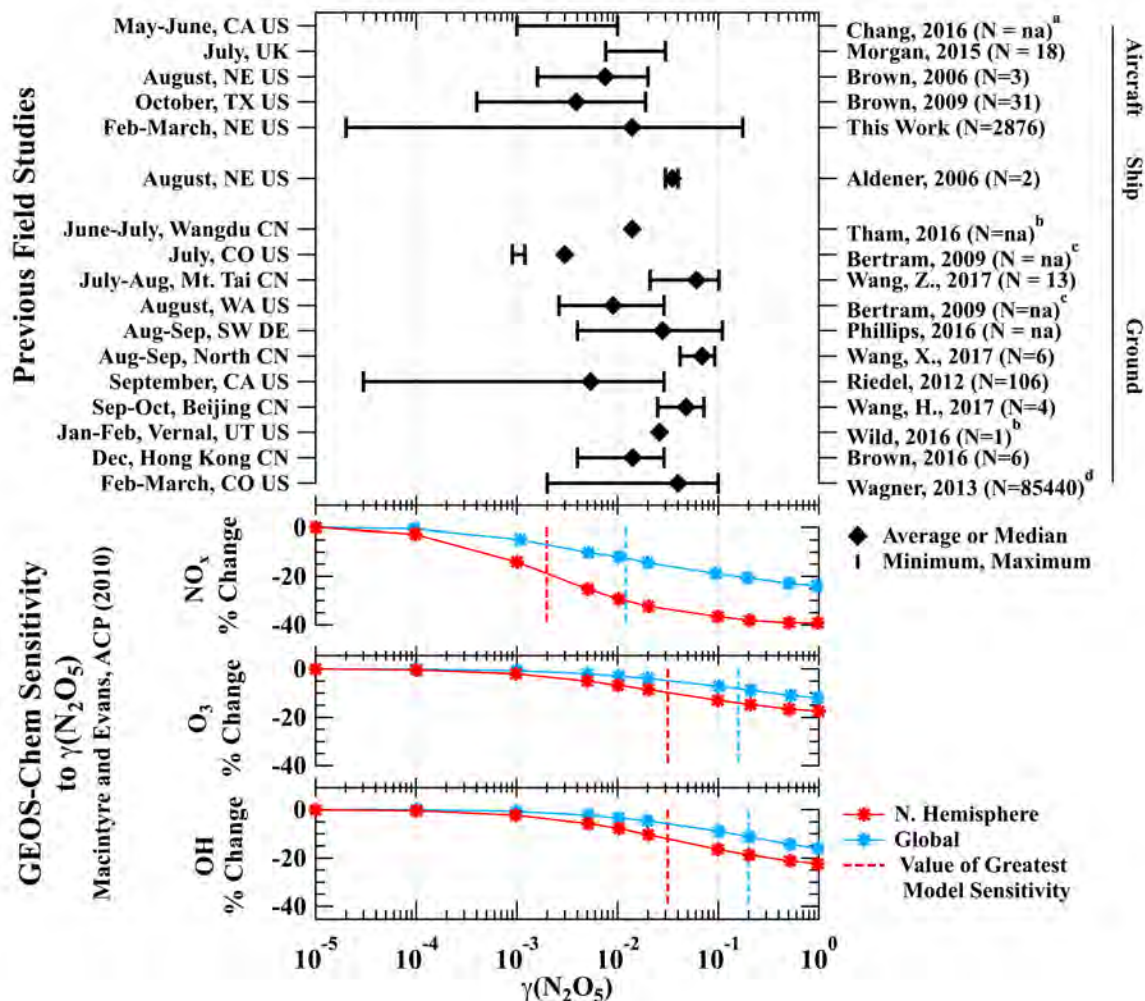


Figure 4.9. Previous field determinations of $\gamma(N_2O_5)$ in comparison to OH, O₃, and NO_x sensitivities in GEOS-Chem, data courtesy of Mat Evans (Macintyre & Evans, 2010). N represents the number of points in each study, if reported. ^aApproximate range, exact values not reported. ^bRange not reported. ^cAverage not reported, diamond represents the median, Minimum and maximum values not reported, 25th and 75th percentiles shown instead. ^dAverage and median not reported, diamond represents the most frequent value. Vertical lines in the lower panels show the value of $\gamma(N_2O_5)$, NO_x, O₃, and OH are most sensitive to in the northern hemisphere (red) and globally (blue).

To provide a broader context for all field-determinations of $\gamma(N_2O_5)$, the lower panel of Figure 4.9 shows the GEOS-Chem-predicted sensitivity (from Macintyre and Evans (2010)) of annual averages of tropospheric oxidants (O₃, OH) and NO_x to changes in $\gamma(N_2O_5)$, both globally (blue) and in the Northern Hemisphere (red). These results show that N₂O₅ uptake can lead to > 15% reductions in OH and O₃ and 40% reductions in NO_x over the $\gamma(N_2O_5)$ range of 1×10^{-5} to 1,

with vertical lines corresponding to the values of greatest model sensitivity (greatest $\Delta\text{oxidant}/\Delta\gamma(\text{N}_2\text{O}_5)$). Nearly all previous field determinations, and 95% of WINTER values, fall between 0.002 to 0.2, encompassing the range where global and regional annual burdens of NO_x , OH and O_3 display a maximum sensitivity to $\gamma(\text{N}_2\text{O}_5)$ (Macintyre & Evans, 2010), highlighting the importance of developing and incorporating an accurate and robust $\gamma(\text{N}_2\text{O}_5)$ parameterization into 3D chemical transport models.

4.3.2 Comparison to the Steady State Approximation

The nocturnal steady state approximation has been the most common method for deriving $\gamma(\text{N}_2\text{O}_5)$ from ambient observations of O_3 , NO_2 , and N_2O_5 (Table B.1). Despite its successful application to previous field data (Aldener et al., 2006; Brown et al., 2016; Brown, S. S. et al., 2006; Brown et al., 2009; Chang et al., 2016; Morgan et al., 2015; Phillips et al., 2016; Tham et al., 2016; Wang, X. et al., 2017; Wang, Z. et al., 2017; Wang, H. et al., 2017) and relative simplicity relative to the iterative box model, this approach can fail under cold temperatures, high NO_2 concentrations, and small sinks for both N_2O_5 and NO_3 (Brown et al., 2003). To evaluate the applicability of this method to WINTER data, this section compares model-derived $\gamma(\text{N}_2\text{O}_5)$ values to those estimated assuming steady state concentrations of N_2O_5 .

The nocturnal steady state lifetime of N_2O_5 ($\tau_{ss}(\text{N}_2\text{O}_5)$) is shown in E4.7. The equilibrium rate constant for Reactions R2.1f and R2.1r (Table 2.3) is given by K_{eq} , k_{VOC} is the first order loss rate constant of NO_3 (R2.7), and $k_{\text{N}_2\text{O}_5}$ is the total loss rate constant of N_2O_5 (R2.5+R2.6). Substituting the expression relating $k_{\text{N}_2\text{O}_5}$ and $\gamma(\text{N}_2\text{O}_5)$ from E4.5, E4.7 can be rearranged to E4.8 to solve for the steady state approximation of N_2O_5 uptake ($\gamma_{ss}(\text{N}_2\text{O}_5)$) using ambient measurements of total wet aerosol SA density, N_2O_5 , NO_2 , and O_3 .

$$\tau_{ss}(N_2O_5)^{-1} = \frac{k_{2.4}[NO_2][O_3]}{[N_2O_5]} \approx (k_{N_2O_5}) + \frac{k_{VOC}}{K_{eq}[NO_2]} \quad (4.7)$$

$$\gamma_{ss}(N_2O_5)0.25cSA = \frac{k_{2.4}[NO_2][O_3]}{[N_2O_5]} - \frac{k_{VOC}}{K_{eq}[NO_2]} \quad (4.8)$$

Results in Figure 4.10a show that the steady state approximation generally over predicts $\gamma(N_2O_5)$ with a slope of 1.13, relative to the box model, which does not make assumptions about steady state. Figure 4.10c shows the distributions of the two derivation methods, with a 20% larger median predicted by the steady state approximation than the original box model. The color scale in Figure 4.10a shows that agreement between the model and the steady state approximation is generally better for older air (i.e. longer simulation duration). Disagreement at the lowest $\gamma(N_2O_5)$ values may be driven by high measured NO_x that keeps the system from reaching equilibrium despite long simulation times (not shown).

Figure 4.10b shows the steady state N_2O_5 lifetime ($(k_{N_2O_5})^{-1}$) calculated from E4.7 against the box model-predicted lifetime. Under steady state, these lifetimes should be equivalent to within 30% due to combined instrument sampling uncertainties for N_2O_5 , O_3 , and NO_2 (Table 4.1). Despite the wintertime, high- NO_x conditions, Figure 4.10b indicates that the steady state approximation was valid (i.e. $(k_{N_2O_5})^{-1}$ within 30% of the box model) for 65% of the model-derived points. During these times, the percent difference between the box model and steady state calculated $\gamma(N_2O_5)$ values was largely less than 40% (Figure 4.10b, color scale). The box model analysis, however, is applicable to a wider range of conditions and includes additional NO_2 recycling reactions (R2.8) and is therefore a more accurate representation of the WINTER data.

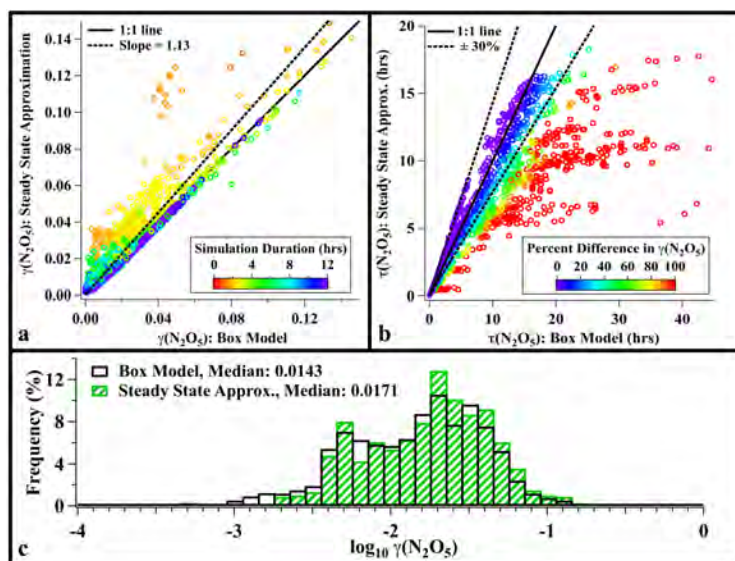


Figure 4.10. Comparison of iterative box model and steady state approximation. (a) Comparison of WINTER $\gamma(\text{N}_2\text{O}_5)$ values, colored by simulation duration; (b) comparison of WINTER N_2O_5 lifetimes, colored by percent difference between box model and steady state predicted $\gamma(\text{N}_2\text{O}_5)$ values; (c) histogram comparing box model results to those derived by the steady state approximation.

4.4 Discussion

4.4.1 Model Mechanism Background

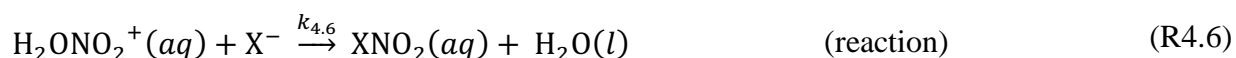
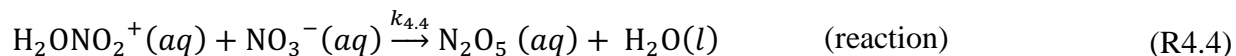
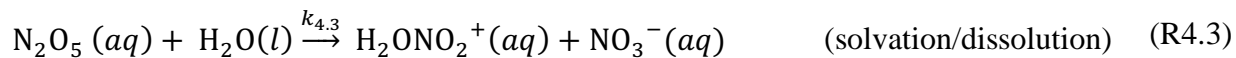
The expression for $\gamma(\text{N}_2\text{O}_5)$ in E4.5 does not provide any information about the mechanistic factors controlling uptake, required for the development of a predictive parameterization for regional/global 3D models. As briefly described here, and in further detail elsewhere (Davidovits et al., 2006; Kolb et al., 2002; Pöschl et al., 2007 and references therein), $\gamma(\text{N}_2\text{O}_5)$ has been described using a resistor model framework with decoupled, individual processes represented in terms of their resistance to uptake ($1/\Gamma$). Using this approach, the net uptake coefficient is represented in E4.9 by adding, in series, the conductance terms (Γ) for the processes of (1) gas-phase diffusion (Γ_{diff}), (2) surface mass accommodation (α), and the parallel processes of (3) bulk-phase solubility (Γ_{sol}) and (4) reaction (Γ_{rxn}). In accordance with this model framework, net

$\gamma(\text{N}_2\text{O}_5)$ increases with decreasing resistance but is ultimately controlled by the individual process that has the largest resistance (smallest Γ) to uptake.

$$\frac{1}{\gamma(\text{N}_2\text{O}_5)} = \frac{1}{\Gamma_{diff}} + \frac{1}{\alpha} + \frac{1}{\Gamma_{sol} + \Gamma_{rxn}} \quad (4.9)$$

Previous studies have proposed that both α and Γ_{sol} or Γ_{rxn} can act as the limiting process under certain conditions, which may change as a function of aerosol composition and availability of liquid water (e.g. Badger et al., 2006; Bertram & Thornton, 2009; Folkers et al., 2003; Griffiths & Cox, 2009; Hallquist et al., 2000; Thornton & Abbatt, 2005). The probability of surface accommodation may be impacted by surface-specific conditions such as surfactant organic coatings (e.g. Thornton & Abbatt, 2005) and temperature (e.g. Griffiths & Cox, 2009; Hallquist et al., 2000). Specific factors controlling Γ_{sol} and/or Γ_{rxn} can be further analyzed through the chemical mechanism provided by mechanistic reactions R4.1 - R4.6, discussed in detail by Bertram and Thornton (2009) and reviewed by Chang et al. (2011). The chemical mechanism, shown diagrammatically in relation to the resistor model in Figure 4.2, indicates that Γ_{sol} and Γ_{rxn} (R4.3 - R4.6) are dependent on factors such as aerosol water and the availability of bulk-phase nucleophiles.

In order to evaluate the agreement between the laboratory-based mechanism and field-derived results, the following sections analyze the trends in WINTER $\gamma(\text{N}_2\text{O}_5)$ values with each individual factor thought to contribute to uptake resistance. WINTER $\gamma(\text{N}_2\text{O}_5)$ results are then compared to previously derived parameterizations for $\gamma(\text{N}_2\text{O}_5)$ to inform an empirical, field-derived parameterization for $\gamma(\text{N}_2\text{O}_5)$ on ambient aerosol, further used to evaluate the current mechanistic understanding of N_2O_5 uptake.



4.4.2 Dependence of $\gamma(\text{N}_2\text{O}_5)$ on Controlling Variables

The large number of data points and wide spatial domain during WINTER provide the most comprehensive test to date of the ability of lab-based $\gamma(\text{N}_2\text{O}_5)$ parameterizations to reproduce field observations. This comparison has been previously limited to a small number of data points and/or single locations that reduce variability in relevant factors (e.g. aerosol nitrate) (Brown et al., 2009; Morgan et al., 2015; Phillips et al., 2016; Wagner et al., 2013). Figure 4.11 shows the WINTER $\gamma(\text{N}_2\text{O}_5)$ medians and distributions by flight, in comparison to those of factors thought to influence the rate-limiting uptake process, including RH, temperature, pH, and aerosol composition. A dependence of $\gamma(\text{N}_2\text{O}_5)$ on any particular factor is not immediately clear in Figure 4.11. The relationships between $\gamma(\text{N}_2\text{O}_5)$ and each individual factor are therefore individually presented in the following sub-sections to identify dominant factors associated with $\gamma(\text{N}_2\text{O}_5)$ and provide insight into the uptake mechanism.

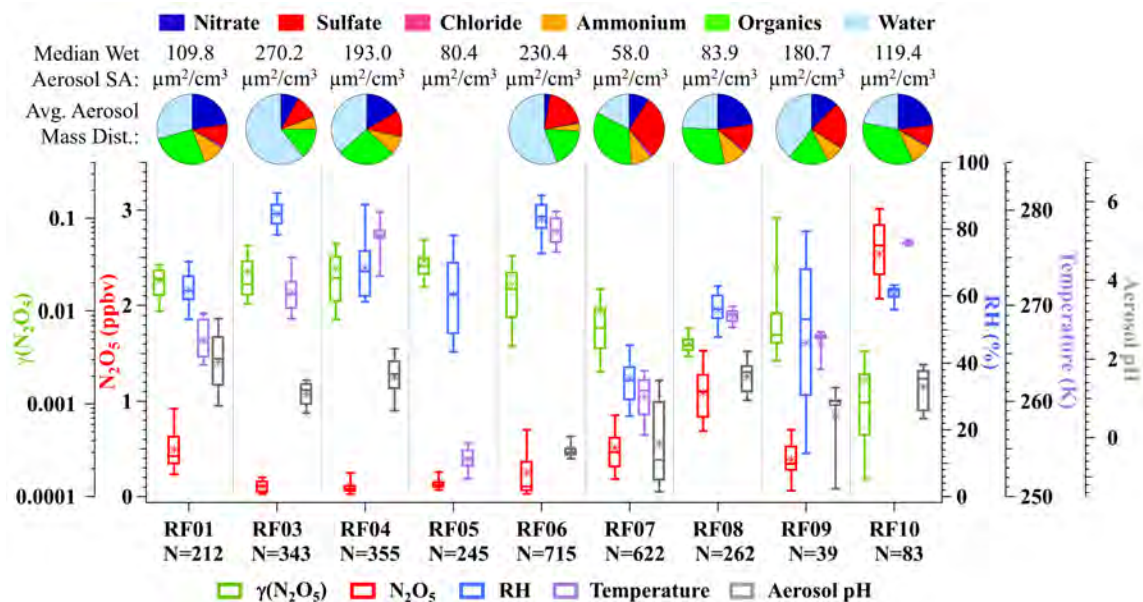


Figure 4.11. Model-derived $\gamma(\text{N}_2\text{O}_5)$ and observed ambient variables listed by flight. Box and whisker plots show 10-90th and 25-75th percentiles, with median (bar) and average (star) values. Pie charts represent the average distribution of submicron aerosol composition as measured by the AMS with corresponding median surface area (including water) listed above. To account for the presence of sea salt, aerosol chloride was measured by the PILS-IC, with an average contribution ranging from 0.1-1.2% for all night flights. AMS measurements were unavailable on RF05 as well as subsequently calculated pH and liquid water. Data shown are only for points with simultaneous $\gamma(\text{N}_2\text{O}_5)$ observations, the number of which are given under each flight label. Inorganic water component and pH were calculated with ISORROPIA by Hongyu Guo, as described in Guo et al. (2016)

4.4.2.1 Ambient Temperature

Early laboratory studies reported a strong negative temperature dependence of $\gamma(\text{N}_2\text{O}_5)$ (i.e. increasing with decreasing temperature) on highly acidic sulfuric acid particles (pH \sim -1) (Hallquist et al., 2000; Robinson et al., 1997). In contrast, smaller and/or inconsistent trends with temperature have been observed on weakly acidic/neutral aerosol including $(\text{NH}_4)_2\text{SO}_4$ and $(\text{NH}_4)\text{HSO}_4$ below 290 K (Griffiths & Cox, 2009; Hallquist et al., 2003; Mozurkewich & Calvert, 1988), nitrate containing aerosol at any temperature (Hallquist et al., 2003), pure water and 1M NaCl from 260-280 K (George et al., 1994; Schweitzer et al., 1998), and a single study of pure organic liquid particles over 268-298 K (Gross et al., 2009). A negative temperature dependence is consistent with uptake limitation by either mass accommodation (R4.1) (α) (a thermodynamic

process governed by Gibb's Free Energy that becomes more favorable as lower temperatures reduce the entropic barrier to uptake, as discussed in Griffiths and Cox (2009)) or the net balance between bulk-phase solubility (R4.3) and re-evaporation (R4.2) (as discussed in Mozurkewich and Calvert (1988)). Clear trends in previous studies however, appear to be complicated by the presence of halides (X^-), water, and the reversible reaction of N_2O_5 through the nitrate effect (Section 4.4.2.3), suggesting uptake is either limited by a different mechanistic step, or that these steps are not dominantly controlled by temperature.

WINTER determinations of $\gamma(N_2O_5)$ do not show a statistically significant ($p > 0.05$) correlation with temperature over the observed range of 247-283 K (Figure 4.12). Despite a lack of trend and a high level of variability, the model-derived $\gamma(N_2O_5)$ values largely fall within the range of previous laboratory determinations discussed above (Figure 4.13). Phillips et al. (2016) is the only previous field study to examine the temperature dependence of $\gamma(N_2O_5)$ and also found no clear trend over the range ~278-292 K for particles containing mixtures of organics, sulfate, ammonium, and nitrate. Similar to past laboratory results, Figure 4.12 suggests that $\gamma(N_2O_5)$ is not dominantly controlled by temperature.

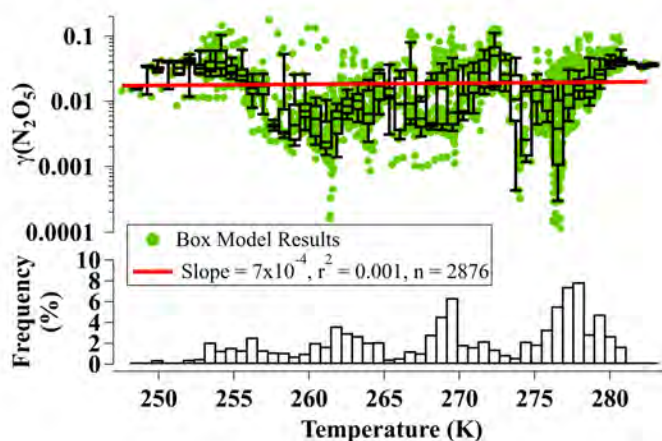


Figure 4.12. Variation of $\gamma(N_2O_5)$ with ambient observed temperature. Box and whisker plots show 10th to 90th (bars), and 25th to 75th (boxes) percentiles, and median values. The histogram shows the distribution of observed temperatures. The red line shows the linear fit to all of the data points (green) with fit results listed in the box.

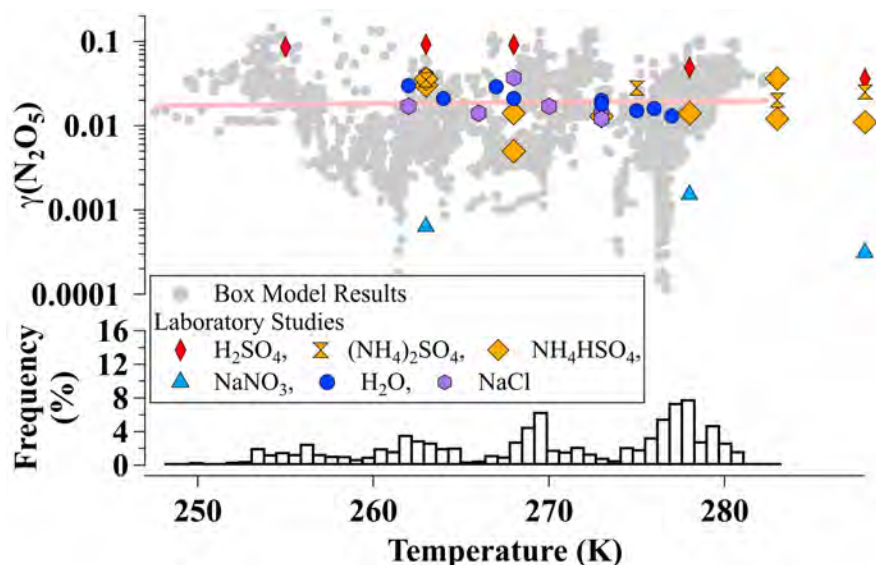


Figure 4.13. Comparison of the temperature dependence of $\gamma(\text{N}_2\text{O}_5)$ with literature laboratory results for inorganic aerosol. Gray dots/red line WINTER results from Figure 4.12. Laboratory measurements for H_2SO_4 (diamonds) (Hallquist et al., 2000), $(\text{NH}_4)_2\text{SO}_4$ (orange circles) and NH_4HSO_4 (triangles) (Griffiths & Cox, 2009), NaNO_3 (squares) (Hallquist et al., 2003), pure water (blue circles) (George et al., 1994; Schweitzer et al., 1998), and 1M NaCl (George et al., 1994).

4.4.2.2 Relative Humidity/Aerosol Liquid Water

Resistance to solubility (R4.3) and/or reaction (R4.5) will decrease with an increased availability of liquid water, consistent with previous laboratory results showing more efficient uptake on aqueous aerosol than on solid inorganic or organic particles (e.g. Gross et al., 2009; Hu & Abbatt, 1997; Mozurkewich & Calvert, 1988; Stewart et al., 2004; Thornton & Abbatt, 2005; Thornton et al., 2003). Aerosol liquid water is largely controlled by ambient RH, but also by aerosol hygroscopicity, making aerosol water molarity a potentially better predictor of $\gamma(\text{N}_2\text{O}_5)$ on ambient aerosol. Two previous laboratory studies found a positive dependence on water molarity (Badger et al., 2006; Thornton et al., 2003), but a larger number have presented $\gamma(\text{N}_2\text{O}_5)$ as a function of RH. These studies show a positive trend in $\gamma(\text{N}_2\text{O}_5)$ with RH on weakly acidic/neutral aerosol, but one that is composition dependent and becomes weaker as RH increases above 50% (Badger et al., 2006; Behnke et al., 1997; Bertram & Thornton, 2009; Folkers et al., 2003; Folkers, 2001; Hallquist et al., 2003; Kane et al., 2001; Mentel et al., 1999; Mozurkewich & Calvert, 1988;

Sohn, 1998; Wahner et al., 1998b). The change in correlation strength with increasing RH suggests that uptake is limited by the term $\Gamma_{sol} + \Gamma_{rxn}$ (R4.3 and/or R4.5) at low RH, but becomes limited by a different process, such as α (R4.1) as water availability increases (e.g. Bertram & Thornton, 2009; Thornton & Abbatt, 2005). The exact RH associated with this sensitivity change is thought to depend on the deliquescence point of each aerosol type and its propensity to form supersaturated liquids (e.g. Kane et al., 2001), which can be impacted by aerosol acidity and organics (e.g. Losey et al., 2016). In addition, several studies have observed the opposite, decreasing trend in $\gamma(\text{N}_2\text{O}_5)$ with RH on highly acidic sulfuric acid particles (Fried et al., 1994; Hallquist et al., 2000; Hu & Abbatt, 1997; Kane et al., 2001; Mozurkewich & Calvert, 1988), which supports an alternative, acid catalyzed mechanism discussed in Section 4.4.2.5.

WINTER $\gamma(\text{N}_2\text{O}_5)$ values show a statistically significant ($p < 0.05$), positive correlation with aerosol water. For completeness, Figure 4.14 shows the correlations with RH (a), aerosol water molarity (b) and aerosol liquid water content (c). In this study aerosol water molarity and liquid water content (aerosol water mass fraction) are calculated using $< 1 \mu\text{m}$ AMS aerosol measurements and estimates of aerosol liquid water and organic hygroscopicity, as described in Section 4.2.1. The higher correlation observed with water molarity ($r^2 = 0.150$) than with RH ($r^2 = 0.075$) is consistent with uptake being limited by the availability of aerosol water, which is not always directly proportional to RH. There is not, however, a clear plateau above 50% RH or $\sim 15 \text{ M} [\text{H}_2\text{O}]$ as observed in previous laboratory studies (e.g. Bertram & Thornton, 2009), which suggests a more constant water dependence under all observed conditions. Despite the large variability in WINTER values in Figure 4.14, data above 20% RH roughly fall within the range of laboratory values for inorganic aerosol discussed above (Figure 4.15). No previous field studies have examined the $\gamma(\text{N}_2\text{O}_5)$ dependence on aerosol water molarity, but several studies have observed a positive,

though generally weak correlation with RH from both ground (Bertram et al., 2009b; Brown et al., 2016; Phillips et al., 2016; Wang, X. et al., 2017) and aircraft (Morgan et al., 2015) campaigns. No correlation with RH was observed over 34-85% for flights over Texas in October 2006 (Brown et al., 2009). High $\gamma(\text{N}_2\text{O}_5)$ values in Beijing, however, were attributed to high aerosol liquid water content (Wang, H. et al., 2017). Previous studies have not quantitatively assessed the trend in $\gamma(\text{N}_2\text{O}_5)$ with liquid water content (water mass fraction), but the high correlation in Figure 4.14 ($r^2 = 0.153$) may suggest this as an even stronger predictor of $\gamma(\text{N}_2\text{O}_5)$ than water molarity.

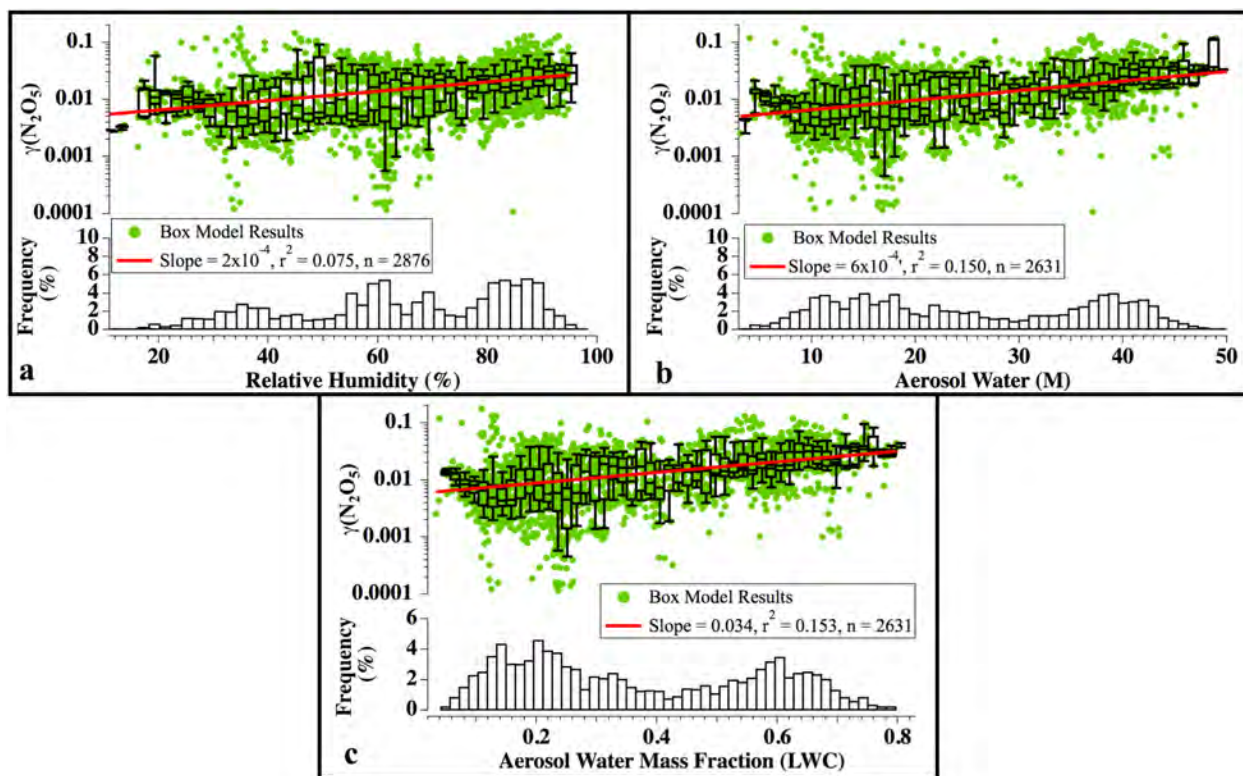


Figure 4.14. (a) WINTER $\gamma(\text{N}_2\text{O}_5)$ with relative humidity, (b) aerosol water molarity (inorganic component calculated from ISORROPIA by Hongyu Guo) (M), and (c) aerosol water liquid content (water mass fraction). Box and whisker plots, histogram, and fit lines as in Figure 4.12.

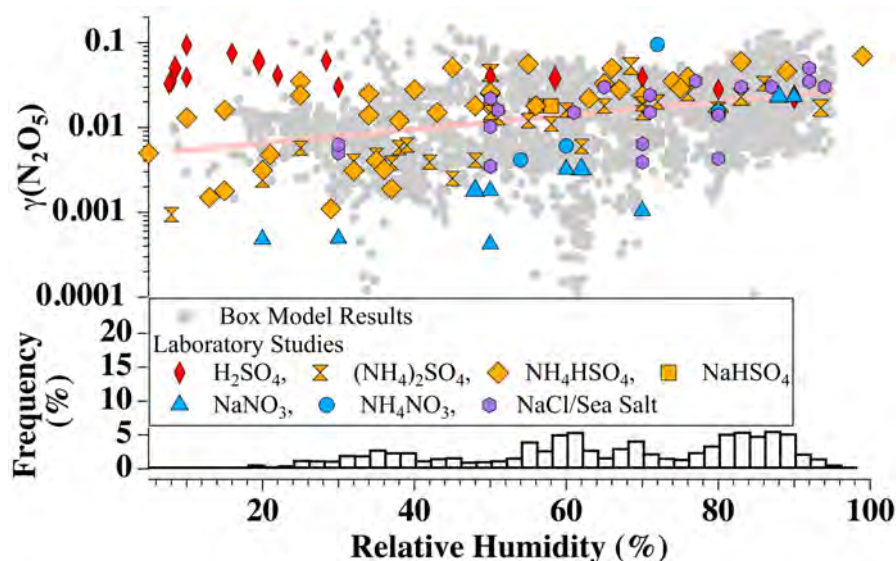


Figure 4.15. Comparison of the $\gamma(\text{N}_2\text{O}_5)$ RH dependence with literature laboratory results for inorganic aerosol. Gray dots/red line are WINTER results from Figure 4.14a. Laboratory measurements for H_2SO_4 (diamonds) (Hallquist et al., 2000; Hu & Abbatt, 1997; Kane et al., 2001; Mozurkewich & Calvert, 1988), $(\text{NH}_4)_2\text{SO}_4$ (hourglasses) (Badger et al., 2006; Hallquist et al., 2003; Hu & Abbatt, 1997; Kane et al., 2001), NH_4HSO_4 (diamonds) (Bertram & Thornton, 2009; Folkers et al., 2003; Griffiths & Cox, 2009; Hallquist et al., 2003; Kane et al., 2001; Sohn, 1998), NaHSO_4 (squares) (Mentel et al., 1999; Mozurkewich & Calvert, 1988), NaNO_3 (triangles) (Hallquist et al., 2003; Wahner et al., 1998b), NH_4NO_3 (circles) (Folkers, 2001), and NaCl and synthetic sea salt (hexagons) (Behnke et al., 1997; Behnke et al., 1991; McNeill et al., 2006; Stewart et al., 2004; Thornton & Abbatt, 2005).

4.4.2.3 The Nitrate Effect

Non-linear suppression of $\gamma(\text{N}_2\text{O}_5)$ by aerosol-phase nitrate, or the “nitrate effect”, has been consistently observed on both laboratory-derived (Bertram & Thornton, 2009; Hallquist et al., 2003; Mentel et al., 1999; Thornton et al., 2003; Wahner et al., 1998b) and ambient-observed nitrate-containing aerosol (Bertram et al., 2009b; Morgan et al., 2015; Riedel et al., 2012a; Wagner et al., 2013). WINTER $\gamma(\text{N}_2\text{O}_5)$ values follow this expected trend and show a statistically significant ($p < 0.05$) negative correlation with aerosol nitrate mass fraction (including water) in Figure 4.16a.

The current mechanism suggests aerosol nitrate may impact the rate limiting step, $\Gamma_{sol} + \Gamma_{rxn}$, but may also serve to reduce net $\gamma(\text{N}_2\text{O}_5)$ in addition to, and independent from, the actual rate

limiting process. For example, suppression in net uptake has been observed in previous laboratory studies in which nitrate has caused additional reductions in $\gamma(\text{N}_2\text{O}_5)$ under low RH where uptake is expected to be rate limited by the presence of aerosol water (R4.3 or R4.5) (Bertram & Thornton, 2009). This observation has been explained with the chemical mechanism in Figure 4.2 as a competition between aerosol-phase nitrate (NO_3^-) and H_2O for the H_2ONO_2^+ intermediate, in which the recombination reaction with NO_3^- (R4.4) has a 20-30 \times larger rate constant than reaction with H_2O (R4.5) (Bertram & Thornton, 2009; Griffiths et al., 2009). Solvated N_2O_5 will therefore reform at sufficiently low $\text{H}_2\text{O}:\text{NO}_3^-$ molar ratios and evaporate back into the gas-phase via R4.2, resulting in apparent suppression of the observed net uptake coefficient, even when the overall process is limited by water availability (e.g. Bertram & Thornton, 2009; Mentel et al., 1999; Thornton et al., 2003; Wahner et al., 1998b). At high $\text{H}_2\text{O}:\text{NO}_3^-$ ratios (dilute nitrate), however, $\gamma(\text{N}_2\text{O}_5)$ can also become nitrate-independent as the rate of R4.5 exceeds that of R4.4. The decrease in $\gamma(\text{N}_2\text{O}_5)$ suppression with increasing $\text{H}_2\text{O}:\text{NO}_3^-$ molar ratios has been observed in both laboratory studies (e.g. Bertram & Thornton, 2009; Griffiths et al., 2009; Mentel et al., 1999; Wahner et al., 1998b) and field observations (Bertram et al., 2009b; Morgan et al., 2015; Riedel et al., 2012a), as well as in WINTER results, shown in Figure 4.16b.

Clear suppression of $\gamma(\text{N}_2\text{O}_5)$ at low $\text{H}_2\text{O}:\text{NO}_3^-$ ratios is obscured to some extent by scatter in the WINTER data. Even when normalized to values at high $\text{H}_2\text{O}:\text{NO}_3^-$ ratios (not shown), persistent scatter in the WINTER data below 100 $\text{H}_2\text{O}:\text{NO}_3^-$ suggests that nitrate suppression is not the only factor controlling uptake. There is agreement, however, in the magnitude of $\gamma(\text{N}_2\text{O}_5)$ at the highest molar ratios (> 100) where WINTER $\gamma(\text{N}_2\text{O}_5)$ values become nitrate-independent and fall within the range of pure water (shaded region of Figure 4.16b) (George et al., 1994; Schweitzer et al., 1998; Van Doren et al., 1990). Bertram and Thornton (2009) observed a similar

plateau in $\gamma(\text{N}_2\text{O}_5)$ to a value of 0.03 at $\text{H}_2\text{O}:\text{NO}_3^-$ ratios > 40 , while Morgan et al. (2015) and Riedel et al. (2012a) observed plateaus in field observations at $\text{H}_2\text{O}:\text{NO}_3^-$ molar ratios > 50 . Phillips et al. (2016) did not observe this trend over the range of ratios 0.5-60 in field data collected from a ground site in Germany. Though a clear plateau in WINTER $\gamma(\text{N}_2\text{O}_5)$ values did not appear until a higher molar ratio (~ 100), qualitative similarities between WINTER results and previous studies suggest that conditions exist on ambient aerosol where $\gamma(\text{N}_2\text{O}_5)$ is not suppressed by nitrate, and falls within a limited range of values consistent with laboratory studies of uptake to liquid water. These data, however, account for a small fraction ($<18\%$) of the total $\gamma(\text{N}_2\text{O}_5)$ determinations during WINTER (two flights, RF03 and RF06, where thermodynamic partitioning and high humidity over the ocean contributed to NO_3^- dilution), suggesting that nitrate suppression must generally be considered for accurate uptake parameterization, even if uptake is rate-limited by a different process.

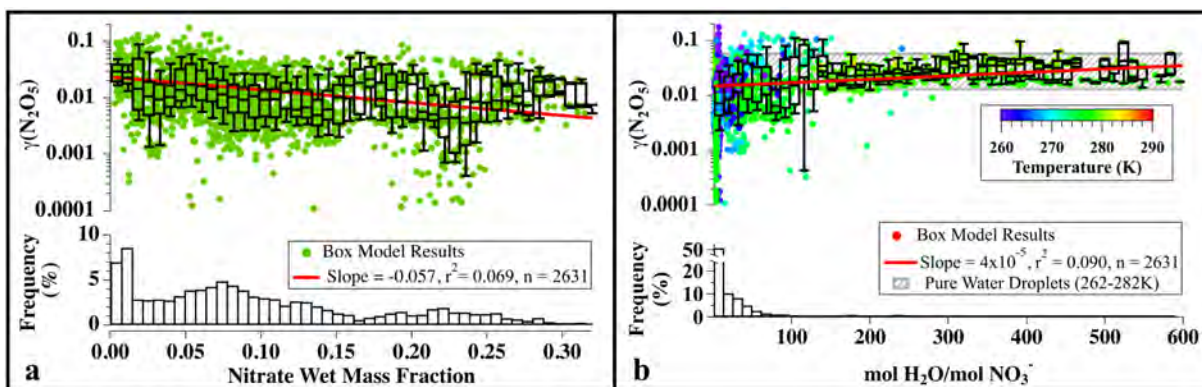


Figure 4.16. (a) WINTER $\gamma(\text{N}_2\text{O}_5)$ with aerosol nitrate mass fraction, including contribution from aerosol water (inorganic component from ISORROPIA simulations by Hongyu Guo); (b) WINTER $\gamma(\text{N}_2\text{O}_5)$ with aerosol $\text{H}_2\text{O}:\text{NO}_3^-$ molar ratio, colored by ambient temperature. The shaded region represents the range of previous laboratory determinations of $\gamma(\text{N}_2\text{O}_5)$ on pure water droplets over the range of 262-277 K (George et al., 1994), 264-275 K (Schweitzer et al., 1998), and 271-282 K (Van Doren et al., 1990). Box and whisker plots, histograms, and fit lines as in preceding figures.

4.4.2.4 Aerosol Nitrate/Chloride

Similar to aerosol-phase NO_3^- , particle chloride (Cl^-) is expected to influence $\gamma(\text{N}_2\text{O}_5)$ without necessarily contributing to the rate limiting step. This occurs through a reduction in nitrate suppression by a competition between NO_3^- and Cl^- for the H_2ONO_2^+ intermediate, in which the reaction rate constant with Cl^- (R4.6) is $\sim 30\times$ greater than the rate constant for NO_3^- (R4.4) (Bertram & Thornton, 2009). Previous laboratory studies have found efficient uptake onto chloride-containing aerosol (Behnke et al., 1997; McNeill et al., 2006; Stewart et al., 2004; Thornton & Abbatt, 2005) with Bertram and Thornton (2009) observing complete elimination of the nitrate effect for mixed aqueous $\text{NaNO}_3/\text{NaCl}$ particles above 2 M aerosol Cl^- ($[\text{Cl}^-]$). Results for WINTER are shown in Figure 4.17 as a function of $[\text{Cl}^-]$ (a) and $\text{Cl}^-:\text{NO}_3^-$ molar ratio (b). WINTER data in Figure 4.17a do not show a positive correlation between $\gamma(\text{N}_2\text{O}_5)$ and $[\text{Cl}^-]$ (as measured by the PILS-IC). As expected, however, Figure 4.17b shows a statistically significant ($p < 0.05$) positive correlation with $\text{Cl}^-:\text{NO}_3^-$ ratio, but with large scatter in the data at the lowest ratios. A plateau in $\gamma(\text{N}_2\text{O}_5)$ values was also observed at the highest molar ratios, similar to the trend observed by Bertram and Thornton (2009), but these high $\text{Cl}^-/\text{NO}_3^-$ ratios were only seen in a small fraction of WINTER data. A previous field study by Morgan et al. (2015) found only a weak dependence of $\gamma(\text{N}_2\text{O}_5)$ on aerosol chloride mass fraction and did not evaluate the trend with $[\text{Cl}^-]$ or $\text{Cl}^-:\text{NO}_3^-$. Overall, WINTER and previous field results suggest that aerosol Cl^- may influence $\gamma(\text{N}_2\text{O}_5)$, but that it is not a dominant predictor. The effects of aerosol Cl^- on various $\gamma(\text{N}_2\text{O}_5)$ parameterizations are discussed in Section 4.4.3.2.

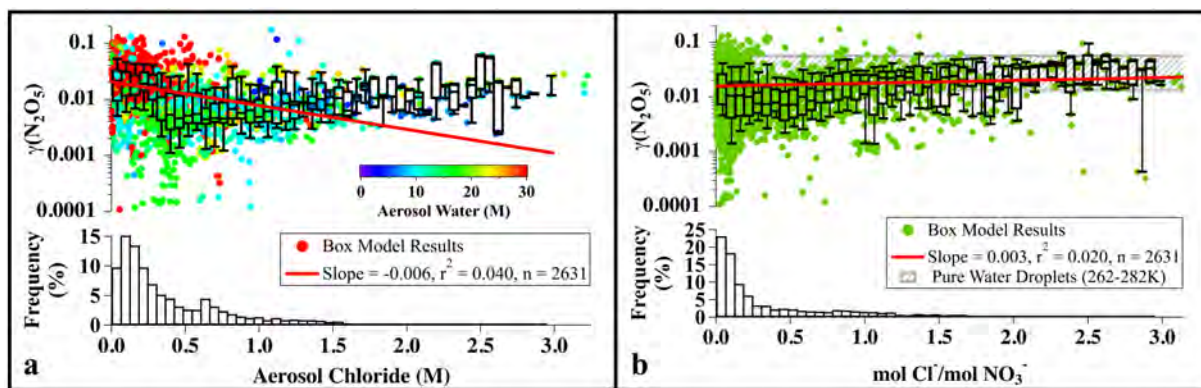
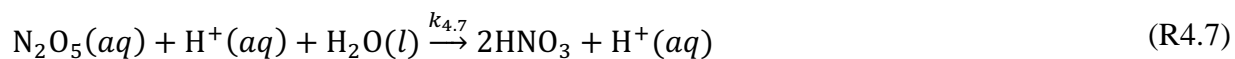


Figure 4.17. (a) WINTER $\gamma(\text{N}_2\text{O}_5)$ with aerosol chloride molarity (derived from PILS-IC measurements), colored by aerosol water molarity (inorganic component calculated by Hongyu Guo from ISORROPIA); (b) WINTER $\gamma(\text{N}_2\text{O}_5)$ with aerosol $\text{Cl}:\text{NO}_3^-$ molar ratio. The gray shaded region represents the range of previous laboratory determinations of $\gamma(\text{N}_2\text{O}_5)$ on pure water droplets. Box and whisker plots, histograms, and fit lines as in preceding figures.

4.4.2.5 Aerosol pH

Previous laboratory studies of N_2O_5 uptake onto highly acidic sulfuric acid surfaces found relatively large $\gamma(\text{N}_2\text{O}_5)$ values with no dependence on RH at low humidity (Fried et al., 1994; Hallquist et al., 2000; Hu & Abbatt, 1997; Kane et al., 2001; Mozurkewich & Calvert, 1988; Robinson et al., 1997). These results led to an alternative mechanism first proposed by Robinson et al. (1997), in which N_2O_5 solvation is catalyzed by the H^+ ion instead of reaction with water. This reaction replaces R4.3 and R4.5 with the process shown in R4.7. Though many of these previous laboratory studies were focused on highly acidic stratospherically-relevant H_2SO_4 concentrations, some studies (e.g. Hallquist et al., 2000) observed enhanced uptake at lower, tropospheric-relevant concentrations (pH \sim 1), within the WINTER observed range (-2 to 5).



This analysis is the first field study to quantitatively examine the correlation between pH (calculated from aerosol thermodynamic modeling by Hongyu Gu, as described in Guo et al. (2016)) and $\gamma(\text{N}_2\text{O}_5)$. WINTER $\gamma(\text{N}_2\text{O}_5)$ values have an overall negative correlation with pH ($p < 0.05$), as would be expected according to R4.7 (Figure 4.18a). Acid-catalyzed hydrolysis,

however, cannot be confirmed from WINTER data due to covariance of pH with aerosol water and NO_3^- . As shown in Figure 4.18b, pH is correlated with aerosol nitrate above pH 1 due to thermodynamic partitioning that leads to an increase in aerosol nitrate with decreasing acidity. One previous field study has suggested this thermodynamic partitioning as a potential explanation for variations in $\gamma(\text{N}_2\text{O}_5)$ over the eastern U.S. (Brown, S. S. et al., 2006). To account for the possibility of nitrate partitioning driving the overall negative trend, data in Figure 4.18a were additionally fit between pH -2 and 1 (dashed line), yielding a statistically significant ($p < 0.05$) positive correlation, opposite of the expected trend. This result suggests that despite the high particle acidity observed during WINTER (Guo et al., 2016), acid catalysis does not dominantly contribute to $\gamma(\text{N}_2\text{O}_5)$.

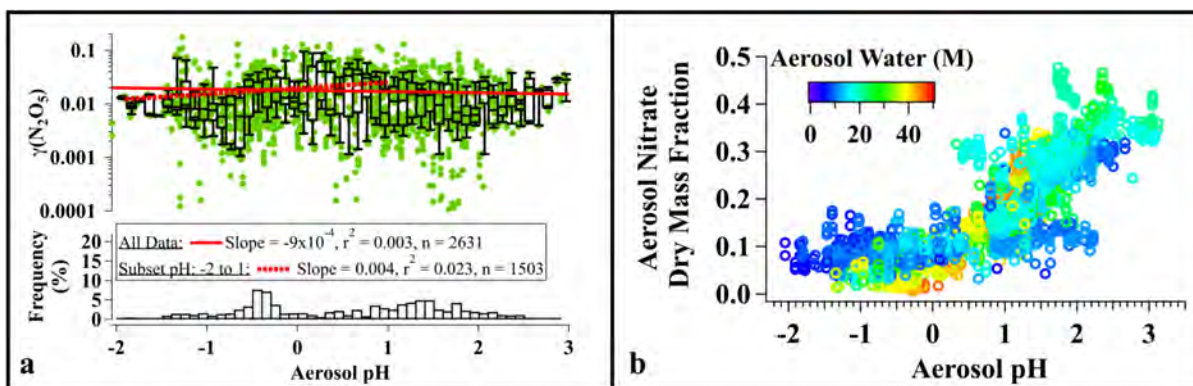


Figure 4.18. (a) WINTER $\gamma(\text{N}_2\text{O}_5)$ with aerosol pH (inorganic component calculated by Hongyu Guo from ISORROPIA). Box and whisker plot, histogram, and fit line as in preceding figures. Dashed line is linear regression fit to data between pH -2 to 1 to separate the influence from nitrate suppression at pH >1. (b) Correlation of measured aerosol nitrate dry mass fraction and pH for points with concurrent $\gamma(\text{N}_2\text{O}_5)$ values, colored by aerosol water molarity.

4.4.2.6 Aerosol Organic Content

While one recent study has shown that cationic surfactants can enhance the rate of N_2O_5 bulk-phase reaction by facilitating surface reactions (Shaloski et al., 2017), the majority of previous laboratory studies have found that the presence of organics suppresses $\gamma(\text{N}_2\text{O}_5)$ relative to pure inorganic salts. The magnitude of suppression, however, is strongly dependent on the organic composition (e.g. Griffiths et al., 2009; Gross et al., 2009), particle phase state (e.g.

Thornton et al., 2003), and the presence of surfactants (e.g. Cosman et al., 2008 and references therein), which are controlled by factors such as RH, temperature, and molecular structure and composition. The mechanism by which organic suppression occurs can be explained as a limitation to either α , Γ_{sol} and/or Γ_{rxn} , which are difficult to de-convolve. For example, insoluble organic surfactants can create monolayers or liquid-liquid phase separations (You et al., 2014 and references therein) that either limit the exchange of N_2O_5 across the air-surface interface (R4.1, α) and/or reduce N_2O_5 bulk-phase solubility and/or diffusion and reaction (R4.3-R4.6: Γ_{sol} and/or Γ_{rxn}) (Badger et al., 2006; Cosman et al., 2008; Folkers et al., 2003; McNeill et al., 2006; Thornton & Abbatt, 2005). Organic-induced phase changes from aqueous to glassy solids (highly viscous) can also occur as a function of T, RH, and molecular composition (Shiraiwa et al., 2017), limiting the amount of available surface water for N_2O_5 solvation and reaction (R4.3, R4.5: Γ_{sol} and/or Γ_{rxn}). Various $\gamma(N_2O_5)$ parameterizations have attempted to account for these suppressive effects by incorporating increased resistance in E4.9 from both reactive and non-reactive organic coatings that impact N_2O_5 solubility and diffusion (e.g. Anttila et al., 2006; Gaston et al., 2014), or by parameterizing α as a function of organic mass fraction and RH (Badger et al., 2006). These and other parameterizations for organics are discussed further in Section 4.4.3.2.

Although aerosol organics are known to suppress $\gamma(N_2O_5)$, composition-driven changes in morphology (i.e. liquid organic coatings) and/or phase state are difficult to predict with available WINTER aerosol observations. Similarly, organic composition and morphology are unknown factors in previous field-studies of $\gamma(N_2O_5)$, though one study, using $\gamma(N_2O_5)$ from Riedel et al. (2012a) and single particle measurements from an aerosol time of flight mass spectrometer (ATOFMS), concluded that molecular composition and physical properties of the aerosol organics were likely the largest controlling factors during that study (Ryder et al., 2014).

Laboratory studies indicate that organic coatings and/or liquid-liquid phase separations should result in a negative correlation of $\gamma(\text{N}_2\text{O}_5)$ with organic dry mass fraction (McNeill et al., 2006) and positive correlation with atomic O:C ratio (e.g. Bertram et al., 2011; Gaston et al., 2014). WINTER data have statistically significant ($p < 0.05$) correlations with these variables with slopes of the predicted sign (Figure 4.19a and d), but with low correlation coefficients ($r^2 < 0.02$) relative to other variables (Table 4.2). A stronger ($r^2 = 0.114$), negative correlation with organic mass fraction is found when aerosol water is included in the total mass (Figure 4.19b). This observation suggests that the magnitude of organic suppression could be impacted by the presence of water, which could have implications for how the organic suppression is treated in parameterizations. This observation also agrees with previous studies that observed reductions in organic suppression at high RH on aqueous organics or partially coated aerosol (e.g. Badger et al., 2006; Thornton et al., 2003). With dry organic mass fraction, previous field results have shown either weak ($r^2 = 0.004$) or no correlation with $\gamma(\text{N}_2\text{O}_5)$ (Brown et al., 2009; Morgan et al., 2015) and have not assessed the relative relationship with wet mass fraction. The only other field study to evaluate $\gamma(\text{N}_2\text{O}_5)$ as a function of the O:C ratio observed no trend over the relatively small range of 0.49 to 0.66 (Morgan et al., 2015). Restricting the fit to WINTER data with O:C between 0.5 and 1 (similar to that in Gaston et al. (2014)) increased the correlation coefficient to 0.063. Two previous summertime field studies have additionally used the Org:SO₄²⁻ ratio as a proxy for the amount of organics relative to surface water (due to SO₄²⁻ hygroscopicity). These studies observed cases in which there was both strong negative (Bertram et al., 2009b) and no observable dependence (Bertram et al., 2009b; Phillips et al., 2016) on this ratio, likely the result of differences in aerosol composition and water content. The weak correlation with this factor in Figure 4.19c suggests that the Org:SO₄²⁻ is not a strong predictor of $\gamma(\text{N}_2\text{O}_5)$ during WINTER compared to other variables,

but may also reflect the generally lower concentrations of aerosol SO_4^{2-} relative to NO_3^- during the winter season.

Overall, many of the $\gamma(\text{N}_2\text{O}_5)$ WINTER values were lower than those predicted for uptake onto pure inorganic salts, especially at high humidity (e.g. Figure 4.15), suggesting some level of organic suppression. WINTER data, however, cannot confirm the magnitude nor the mechanism of this effect without knowledge or measurement of aerosol morphology (i.e. coatings) or phase due to concurrent impacts on $\gamma(\text{N}_2\text{O}_5)$ from co-varying factors, such as aerosol water and anions.

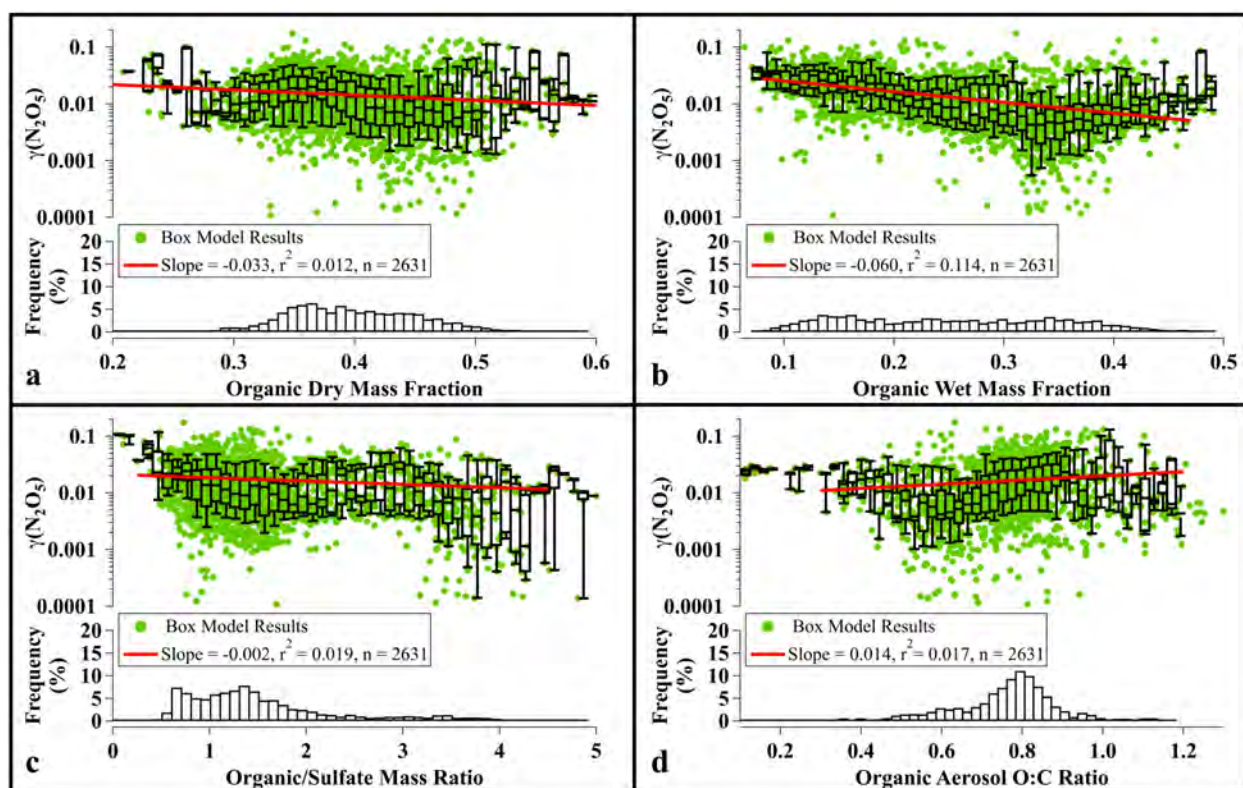


Figure 4.19. WINTER $\gamma(\text{N}_2\text{O}_5)$ with (a) aerosol organic dry mass fraction, (b), organic wet mass fraction (including water, inorganic component calculated by Hongyu Guo from ISORROPIA), (c) aerosol Org: SO_4^{2-} mass ratio, and (d) O:C ratio. All aerosol data were collected by the AMS. Box and whisker plots, histograms, and fit lines as in preceding figures.

4.4.2.7 Aerosol Size

Assuming dependence on a rate limiting step, current theory suggests that $\gamma(\text{N}_2\text{O}_5)$ will be dependent on aerosol size if reaction of the intermediate H_2ONO_2^+ (R4.4-R4.6) occurs within the

entire aerosol volume, but size-independent if reaction occurs within the surface layer. These cases will have different implications for the parameterization of $\gamma(\text{N}_2\text{O}_5)$ as the former suggests an aerosol size dependence, while the latter suggests a dependence on aerosol surface composition and morphology. Volume or surface layer reaction can be estimated by the reacto-diffusion length (diffusion distance of N_2O_5 prior to bulk-phase reaction, q (m)), which has been shown by one study to vary enough that uptake can be volume-limited on sulfate aerosol, while surface-limited on sodium chloride (Gaston & Thornton, 2016). Other laboratory studies on both inorganic and organic aerosol have been inconclusive, showing evidence for both surface and volume-limited reactions (e.g. Mozurkewich & Calvert, 1988). As discussed by Thornton et al. (2003) and Gaston and Thornton (2016), volume-limited reactions should yield a linear, positive correlation between $\gamma(\text{N}_2\text{O}_5)$ and aerosol size (SA-weighted particle radius or volume to SA concentration ratio) with a slope indicative of the reaction rate between N_2O_5 and water, anions, or halides (R4.4 - R4.6). WINTER $\gamma(\text{N}_2\text{O}_5)$ results (not shown) are consistent with this positive trend over the observed range (30 – 300nm) of median SA-weighted particle radii (defined in Section 4.4.3.2) but have a low correlation coefficient ($r^2 = 0.025$), suggesting that aerosol size is an overall weak predictor of $\gamma(\text{N}_2\text{O}_5)$ relative to other factors, such as aerosol water. These results add to the inconclusiveness of prior studies, but likely represent the varying, overlapping size dependences (or independences) of different aerosol compositions, indicating that factors other than aerosol size are stronger predictors of $\gamma(\text{N}_2\text{O}_5)$ on ambient aerosol.

4.4.2.8 Trends Summary

Identification of the rate limiting process in E4.9 and its associated factors are important for accurate parameterization of $\gamma(\text{N}_2\text{O}_5)$. Correlations between WINTER $\gamma(\text{N}_2\text{O}_5)$ results and all uptake-relevant variables (summarized in Table 4.2) show some of the strongest correlations with

aerosol water and nitrate, suggesting that uptake (assuming the currently accepted mechanism) is largely controlled by $\Gamma_{sol} + \Gamma_{rxn}$, and more specifically, impacted by the N_2O_5 solvation reaction R4.3 ($N_2O_5 + H_2O$) and/or bulk-phase reactions R4.5 and R4.4 ($H_2ONO_2^+ + H_2O$ or NO_3^-). Uptake suppression from aerosol organics is also likely, due to the third highest correlation with wet organic mass fraction and generally lower $\gamma(N_2O_5)$ values during WINTER than those derived on pure inorganic laboratory aerosol. Correlations, however, between $\gamma(N_2O_5)$ and aerosol organic mass fraction, O:C ratio, and Org:SO₄²⁻ cannot discriminate as to whether an organic suppression occurs by impacting α and/or $\Gamma_{sol} + \Gamma_{rxn}$. In addition, the observed positive correlation between $\gamma(N_2O_5)$ and the most highly acidic aerosols (pH -2 to 1) does not support the importance of an acid catalyzed mechanism.

The results presented here are generally consistent with those observed in previous laboratory and field studies (when trends have been reported). Despite this general agreement, low correlation ($r^2 = 0.153$) of the most highly correlated variable (liquid water content) suggests that uptake is either sensitive to non-measured variables (such as aerosol morphology (i.e. liquid organic coating) or phase) or to a large number of inter-related variables (Table B.2), highlighting the difficulty in identifying the dominant controlling factors required to develop a robust parameterization. The final section uses these results in combination with several parameterizations previously/currently implemented in 3D models to evaluate their applicability to WINTER values and provide insight for improving the predictive capabilities of $\gamma(N_2O_5)$ during winter over the eastern U.S., where $\gamma(N_2O_5)$ is seasonally important.

Table 4.2. Summary of $\gamma(\text{N}_2\text{O}_5)$ Trend Analyses

	Variable	Correlation Coefficient (r^2)	Correlation Sign	N
1	Aerosol, Liquid Water Content (Mass Fraction)	0.153	+	2631
2	Aerosol, Water Molarity	0.150	+	2631
3	Aerosol Organics, Wet Mass Fraction	0.114	-	2631
4	Aerosol $\text{H}_2\text{O}/\text{NO}_3^-$ Molar Ratio	0.090	+	2631
5	Ambient Relative Humidity	0.075	+	2876
6	Aerosol Nitrate, Wet Mass Fraction	0.069	-	2631
7	Aerosol Organics, O:C Ratio (0.5-1)	0.063	+	2372
8	Aerosol Chloride, Wet Mass Fraction	0.039	-	2631
9	Aerosol Nitrate, Dry Mass Fraction	0.032	-	2631
10	Surface Area Weighted Aerosol Radius	0.025	+	2876
11	Aerosol pH (-2 to 1)	0.023	+	1503
12	Aerosol $\text{Cl}^-/\text{NO}_3^-$ Molar Ratio	0.020	+	2631
13	Aerosol Organic/Sulfate Mass Ratio	0.019	-	2631
14	Aerosol Organics, O:C Ratio	0.017	+	2631
15	Aerosol Chloride, Dry Mass Fraction	0.013	-	2631
16	Aerosol Organics, Dry Mass Fraction	0.012	-	2631
17	Aerosol pH (full range)	0.003	-	2631
18	Ambient Temperature	0.001 ^a	+	2876

^aNot a statistically significant result ($p > 0.05$)

4.4.3 Parameterization of $\gamma(\text{N}_2\text{O}_5)$

4.4.3.1 Previous $\gamma(\text{N}_2\text{O}_5)$ Parameterizations

When first incorporated into 3D chemical transport models, $\gamma(\text{N}_2\text{O}_5)$ was set to a constant value of 0.1 for sulfate-containing aerosol, broadly considered at that time as a proxy for tropospheric aerosol, based on early laboratory measurements of uptake onto water, ammonium bisulfate, and sulfuric acid particles (Dentener & Crutzen, 1993). As reviewed by Chang et al. (2011), later laboratory studies suggested that uptake onto tropospheric-relevant aerosol was composition dependent and much less efficient, leading Evans and Jacob (2005) to develop a parameterization (hereafter referred to as EJ05) based on the work of Kane et al. (2001), Hallquist et al. (2003), and Thornton et al. (2003) to capture the temperature and RH dependence of $\gamma(\text{N}_2\text{O}_5)$ onto externally-mixed inorganic salts and suppression by pure organic liquids. At the time, incorporation of EJ05 into GEOS-Chem improved model predictions of climatological observations (Evans & Jacob, 2005). Since then, the inorganic component of EJ05 has been largely

replaced by a parameterization by Bertram and Thornton (2009) (hereafter BT09) expanded from earlier work (Mentel et al., 1999; Wahner et al., 1998b), that accounts for the water, nitrate, and chloride effects on internally-mixed aerosol through the dependence of $\gamma(\text{N}_2\text{O}_5)$ on aerosol water, size, and molar ratios of $\text{H}_2\text{O}:\text{NO}_3^-$ and $\text{Cl}^-\text{:NO}_3^-$. Davis et al. (2008) (Dav08) additionally used a statistical analysis of early laboratory studies (similar to those used by Evans and Jacob (2005)) to develop a parameterization for internally-mixed inorganic aerosol as a function of RH and temperature for different sulfate and nitrate containing particles. Neither Dav08 nor BT09 directly includes a dependence on aerosol organics, though BT09 can account for organic-associated changes in aerosol water. Both require combination with additional organic parameterizations, such as those described in Anttila et al. (2006), to calculate total N_2O_5 loss rates impacted by surface-organic impedance. These current organic parameterizations, however, have large uncertainties in their mechanistic treatment and have generally under-predicted $\gamma(\text{N}_2\text{O}_5)$ in comparison to field studies (Brown et al., 2009; Morgan et al., 2015; Phillips et al., 2016). This uncertainty has led some models, such as the U.S. EPA's CMAQ model, to exclude all organic dependencies in their parameterizations and simply note that $\gamma(\text{N}_2\text{O}_5)$ may be over-predicted under high organic aerosol concentrations (Sarwar et al., 2014). To date, a single parametrization to account for the combined influence of all inorganic and organic aerosol components has not been developed. In the remaining sections, 14 previous and current versions of proposed and implemented parameterizations are compared to WINTER data to evaluate their applicability and provide insight for the development of the first field-based empirical $\gamma(\text{N}_2\text{O}_5)$ parameterization.

4.4.3.2 Comparison of Box Model Results to Laboratory-Derived Parameterizations

Nearly all laboratory-derived parameterizations for $\gamma(\text{N}_2\text{O}_5)$ (except for IUPAC speciated recommendations and those for surface and volume confined uptake in Mentel et al. (1999) and

Wahner et al. (1998b)) are shown in comparison to WINTER box model results in Figures 4.20 - 4.22. Details of each parameterization are given in Table B.3 in Appendix B. Agreement between parameterized $\gamma(\text{N}_2\text{O}_5)$ and box model results are assessed here according to the root-mean-square-error (RMSE: standard deviation of the residuals) and by the median percent difference of each comparison (shown in Figure 4.22). The correlation coefficient (r^2) and point number of each comparison are provided for reference in Figure 4.20 and Table B.3. Black squares in Figures 4.20 and 4.21 represent the median value of each parameterization relative to the WINTER median. Dashed lines represent agreement within factors of ± 2 and ± 10 and are included as an additional evaluation method.

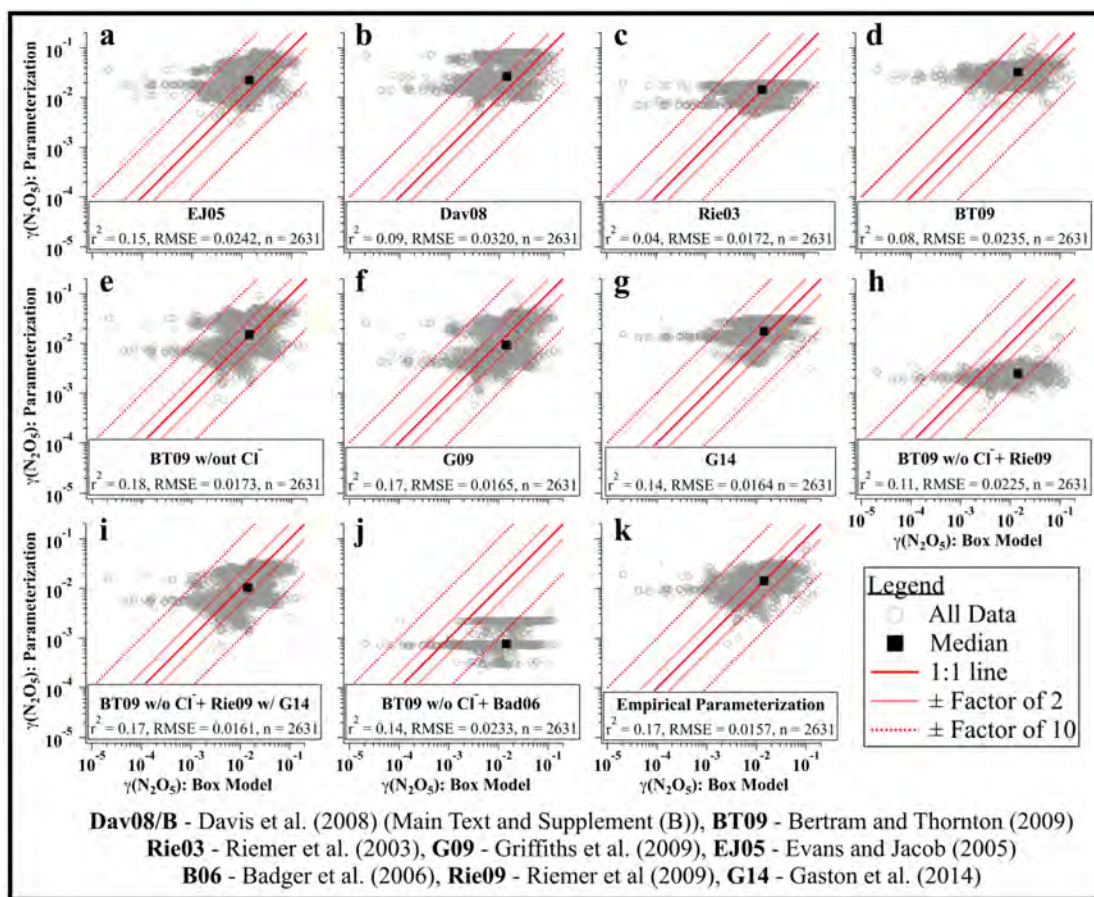


Figure 4.20. Comparisons between parameterized and model-derived $\gamma(\text{N}_2\text{O}_5)$ values. Correlation coefficient, RMSE (root-mean-square-error), and point number are provided on each plot. Red lines indicate the 1:1 line. Black squares represent median values. Dashed lines represent the range of values within factors of ± 2 and ± 10 .

The original parameterization proposed by EJ05 generally over-predicts $\gamma(\text{N}_2\text{O}_5)$ relative to the WINTER box model (Figure 4.20a), with a median percent difference of +120% (Figure 4.22). This result is consistent with two other field studies that found EJ05 to over-predict $\gamma(\text{N}_2\text{O}_5)$ relative to values derived from the steady state approximation (Brown et al., 2009) and flow tube experiments (Bertram et al., 2009b). EJ05 includes an RH and T-dependence for $\gamma(\text{N}_2\text{O}_5)$ onto sulfate aerosol as well as an RH dependence for organics, but may under-predict any organic suppression since it is based on laboratory data of water soluble organics (Thornton et al., 2003).

Three parameterizations shown in Figure 4.20b-d consider uptake onto inorganic aerosol only. These parameterizations include the previously described Dav08 (Figure 4.20b) and BT09 (Figure 4.20d), as well as Rie03 (Figure 4.20c), developed by Riemer et al. (2003) to account for the increase in aerosol hygroscopicity associated with aerosol sulfate. All three parameterizations generally over-predicted WINTER results (Figure 4.22) with Rie03 producing the lowest RMSE (0.0172) and best median agreement (+9%), while BT09 had a slightly higher correlation coefficient ($r^2 = 0.08$ vs 0.04). The under-prediction of largest values by Rie03 is likely due to an imposed maximum value of 0.02 (value of pure water), smaller than the top 34% of WINTER values. Over-prediction of smallest $\gamma(\text{N}_2\text{O}_5)$ values by all three parameterizations is likely due to a missing organic suppression effect. Previous flights over the UK found that Rie03 under-predicted $\gamma(\text{N}_2\text{O}_5)$ (Morgan et al., 2015), while flights over Texas found a general over-prediction (Brown et al., 2009). The only three studies to compare Dav08 to field-derived data have also found large over-predictions by this parameterization (Bertram et al., 2009b; Brown et al., 2009; Chang et al., 2016), but also a slight under-prediction at low (< 30%) ambient RH (Chang et al., 2016). An additional version of Dav08, (Dav08B presented in the appendix of Davis et al. (2008)), produced a lower RMSE than the original version (0.0243 vs. 0.0320) when compared to WINTER

data (Figure 4.21a), but one that remained higher than that for both BT09 (0.0235) and Rie03. For BT09, previous field studies have found both good agreement (Bertram & Thornton, 2009; Phillips et al., 2016) as well as over-predictions (Chang et al., 2016; Morgan et al., 2015; Riedel et al., 2012a) of $\gamma(\text{N}_2\text{O}_5)$. Similar to results presented in Riedel et al. (2012a) and Morgan et al. (2015), agreement with BT09 improved (higher r^2 and lower RMSE) when the chloride contribution was removed from the parameterization (Figure 4.20e). A fourth parameterization (G09) in the same form as BT09 w/o Cl, but with different reaction rate constants (Griffiths et al., 2009), resulted in the lowest RMSE and median percent difference of all tested inorganic-only parameterizations (Figure 4.20, Figure 4.22). These results suggest that 1) the reversal of the nitrate effect by chloride is not as large on ambient aerosol as on laboratory particles (i.e. $k_{4.6}$ is too large, $k_{4.4}$ too small, and/or aerosol chloride is unavailable for reaction with H_2ONO_2^+) and/or 2) the suppressive effects of organics, which are not included in BT09, are better captured without an enhancement from chloride. All parameterizations, however, largely over-predict the smallest WINTER values, suggesting a missing suppressive effect.

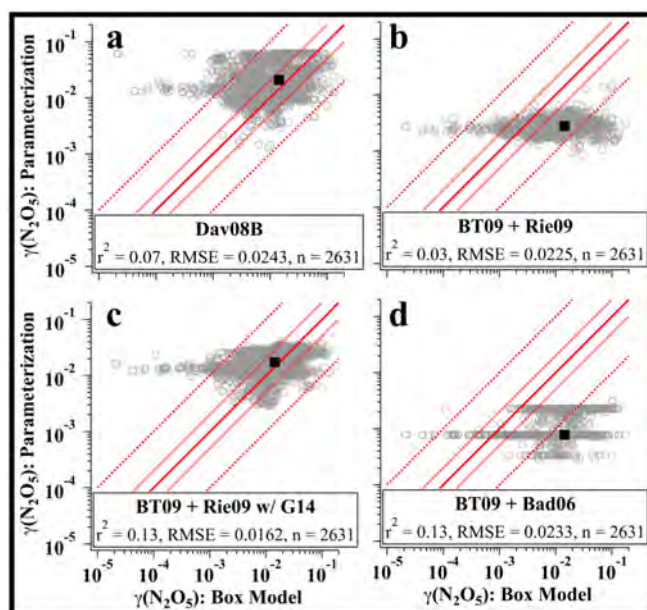


Figure 4.21. Supplemental comparisons between $\gamma(\text{N}_2\text{O}_5)$ parameterizations and box-model results. Same format as Figure 4.20.

Four additional parameterizations shown in Figure 4.20g-j account for both the inorganic and organic aerosol components. The first (Figure 4.20g), follows the work of Anttila et al. (2006) and Gaston et al. (2014). To account for the suppressive effects of organics, Anttila et al. (2006) adapted the $\Gamma_{sol} + \Gamma_{rxn}$ term in the traditional resistor model in E4.9 to account for added resistance to uptake from an organic coating of an aqueous core, reactive toward N_2O_5 (E4.10 - E4.15). Implementation of this parameterization requires knowledge of the N_2O_5 reaction (k_{org}) and bulk-phase diffusion (D_{org}) rate constants within the organic layer, which were adopted here as a function of O:C ratio and ambient RH (Table B.3: G14) from Gaston et al. (2014). Uptake limits from diffusion (Γ_{diff}) and accommodation (α) were not included in the comparisons here as the estimated limit of pure water, $\alpha \sim 0.04$ (Anttila et al., 2006), is smaller than the top 10% of WINTER values.

$$\frac{1}{\gamma} = \frac{1}{\Gamma_{diff}} + \frac{1}{\alpha} + \frac{cR_p}{4RTH_{org}D_{org}(q_{org}F - 1)} \quad (4.10)$$

$$q_{org} = R_p \sqrt{\frac{k_{org}}{D_{org}}}, \text{ organic layer reacto-diffusion parameter} \quad (4.11)$$

$$q_{aq} = R_c \sqrt{\frac{k_{aq}}{D_{org}}}, \text{ aqueous phase reacto-diffusion parameter} \quad (4.12)$$

$$q_{org}^* = \frac{R_c}{R_p} q_{org} \quad (4.13)$$

$$F = \frac{\coth(q_{org}) + h(q_{aq}, q_{org}^*)}{1 + \coth(q_{org}) * h(q_{aq}, q_{org}^*)} \quad (4.14)$$

$$h(q_{aq}, q_{org}^*) = -\tanh(q_{aq}) * \frac{\frac{H_{aq}D_{aq}}{H_{org}D_{org}}(q_{aq} \coth(q_{aq}) - 1) - (q_{org}^* \coth(q_{org}^*) - 1)}{\frac{H_{aq}D_{aq}}{H_{org}D_{org}}(q_{aq} \coth(q_{aq}) - 1) - (q_{org}^* \tanh(q_{org}^*) - 1)} \quad (4.15)$$

The second and third parameterizations follow the work of Riemer et al. (2009) and implement a simplified resistor framework that models uptake through a thin, non-reactive organic

coating (E4.16). In this framework, the $\Gamma_{sol} + \Gamma_{rxn}$ term has been split into two that separately account for uptake resistance from an aqueous inorganic core of radius R_c and an organic coating of thickness ℓ . Similar to the full resistor model, uptake is modeled by a two-layer system with varying N_2O_5 solubility (H_{org} vs. H_{aq}) and diffusion (D_{org} vs. D_{aq}) coefficients between the organic and aqueous layers, but does not require knowledge of k_{org} .

$$\frac{1}{\gamma(N_2O_5)} = \frac{1}{\Gamma_{diff}} + \frac{1}{\alpha} + \frac{1}{\Gamma_{aq. core}} + \frac{1}{\Gamma_{org. coat}} \quad (4.16)$$

$$\frac{1}{\Gamma_{aq. core}} = \frac{1}{\frac{V}{SA} K_H k_{R3} \left(1 - \frac{1}{\left(\frac{k_{4.5}[H_2O(l)]}{k_{4.4}[NO_3^-]} \right) + 1 + \left(\frac{k_{4.6}[Cl^-]}{k_{4.4}[NO_3^-]} \right)} \right)} \quad (4.17)$$

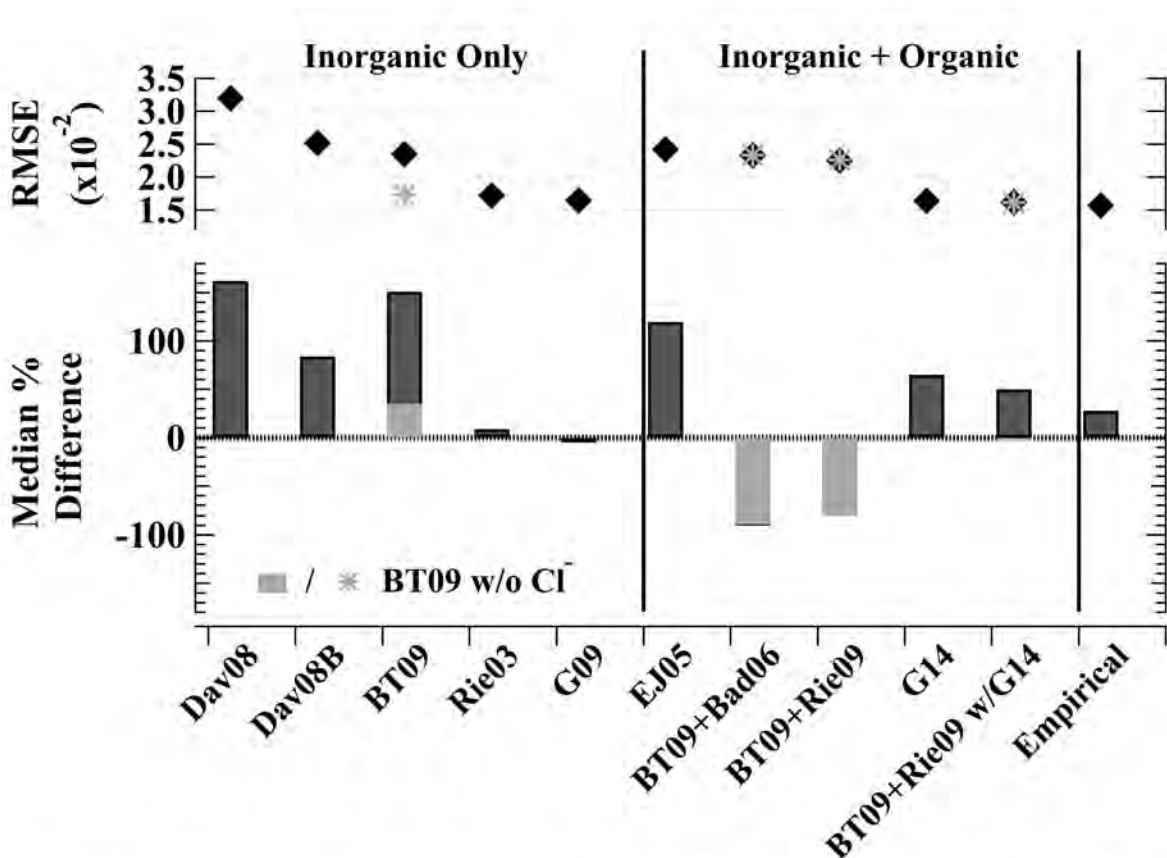
$$\frac{1}{\Gamma_{org. coat}} = \frac{c\ell R_p}{4RTH_{org}D_{org}R_c} \quad (4.18)$$

For comparison here, we take the approach of Riemer et al. (2009) who used BT09 to determine $\Gamma_{aq. core}$ (E4.17) and E4.18 for the organic coating. As in Riemer et al. (2009), the total particle radius (R_p) and volume ratio of the inorganic aerosol material (β) are used to calculate an organic layer thickness ℓ . The radius of the aqueous core (R_c) is defined as R_p minus ℓ . Here, R_p is defined for every 10 second period as the median radius with respect to the measured WINTER surface area distribution. In the first of these two comparisons (Figure 4.20h), bulk-phase solubility and diffusion coefficients were estimated by scaling the product $H_{aq} * D_{aq}$ by a constant factor of $\varepsilon = 0.03$, derived by Anttila et al. (2006) from a fit of E4.10 to experimental data of N_2O_5 uptake onto SOA produced from monoterpene ozonolysis. In the second comparison (Figure 4.20i) ε was calculated as a function of RH and O:C ratio following the work of Gaston et al. (2014) who parameterized ε based on experiments of N_2O_5 uptake onto ammonium sulfates coated with insoluble organics ranging from low (< 0.5) to high (> 0.7) O:C ratios (see Table B.3 for details).

The final comparison (Figure 4.20j) does not assume an organic coating, but rather applies a reduction to the mass accommodation coefficient (α). By fitting a modified resistance model (assuming uptake is limited by reaction R4.3 and aerosol volume) to experimental uptake data for humic acid/ammonium sulfate particles, Badger et al. (2006) determined a range of α values from 1×10^{-4} to 0.01 as a function of RH and dry humic acid mass fraction.

Of these four approaches, parameterizing α largely under-predicts $\gamma(\text{N}_2\text{O}_5)$, with a median percent difference of (-89%) and the highest RMSE (Figure 4.22). Treating organics as a coating with the other three parameterizations improves the median percent difference but cannot reproduce the full range in WINTER values. Both under- and over-prediction could result from a number of factors including incorrect estimation of the coating thickness, bulk-phase diffusion and solubility rates, or an enhancement from organics by facilitating surface reactions (Shaloski et al., 2017). Similar to WINTER, results from three previous field studies found that the simplified resistor framework generally under-predicted $\gamma(\text{N}_2\text{O}_5)$, likely due to an over-prediction of the organic suppression effect (Morgan et al., 2015; Phillips et al., 2016), but improved agreement relative to the inorganic-only parameterizations (Chang et al., 2016). No previous field studies have implemented the full resistor framework, but in this comparison, it was found to have worse agreement with WINTER results (higher median difference, higher RMSE, lower r^2) relative to the modified framework, when excluding chloride and including a dependence on O:C and RH. Agreement between the box model results and each organic parameterization remained the same or was slightly degraded (higher RMSE/lower r^2) when particle Cl^- was included in the BT09 parameterization (Figure 4.21b-d and Figure 4.22), suggesting that the magnitude of Cl^- enhancement may not apply to ambient aerosol. Overall, of the combined inorganic and organic

parameterizations tested, the modified resistor method, mediated by the O:C ratio and relative humidity, without a chloride enhancement, best reproduced the WINTER $\gamma(\text{N}_2\text{O}_5)$ values.



Dav08/B - Davis et al. (2008) (Main Text and Supplement (B)), BT09 - Bertram and Thornton (2009)
 Rie03 - Riemer et al. (2003), G09 - Griffiths et al. (2009), EJ05 - Evans and Jacob (2005)
 B06 - Badger et al. (2006), Rie09 - Riemer et al (2009), G14 - Gaston et al. (2014)

Figure 4.22. Comparison of 14 literature and empirical parameterizations relative to WINTER $\gamma(\text{N}_2\text{O}_5)$ results. Comparisons are given in terms of their root-mean-square-error (upper panel) and median percent difference (lower panel). Comparisons are listed in order of decreasing RMSE within each group of parameterization type (inorganic only, combined inorganic and organic, and empirical). Parameterizations that incorporated BT09 are shown with (dark gray) and without (light gray) the contribution from chloride.

Considering all 14 parameterizations tested here, nine reproduced the median WINTER $\gamma(\text{N}_2\text{O}_5)$, within a factor of two. Parameterizations with the worst agreement (largest RMSE and median percent difference) were the inorganic-only parameterizations most frequently used in chemical transport models, EJ05, Dav08, and BT09. Those with the best agreement either excluded the chloride enhancement in BT09 or accounted for an organic suppression of $\gamma(\text{N}_2\text{O}_5)$, mediated

by the aerosol O:C ratio and ambient RH. None of the 14 parameterizations, however, were able to reproduce the 4-orders of magnitude range observed during WINTER, with an under-prediction of the highest values and a roughly 1-2 orders of magnitude over-prediction of WINTER values $<1 \times 10^{-3}$. Over-prediction of low values suggests an additional suppressive effect not accounted for by the current treatments of organics, possibly due to changes in uptake resistance (i.e. bulk-phase solubility, diffusion, or accommodation) associated with a change in aerosol morphology (i.e. liquid organic coating) or phase.

As previously shown, uptake is largely controlled by the availability of liquid water relative to nitrate and the aerosol phase state, both of which can be impacted by the presence of organics in the form of hydrophobic coatings or induced phase changes. Values $<1 \times 10^{-3}$ have only been observed in previous laboratory studies as the result of strong nitrate suppression (Hallquist et al., 2003) or uptake onto solid aerosol (Kane et al., 2001), pure organic liquids (Gross et al., 2009; McNeill et al., 2006), and pure secondary organic aerosol (SOA)/coated seed aerosol, formed from the products of monoterpene ozonolysis (Anttila et al., 2006; Escorcia et al., 2010; Folkers et al., 2003). WINTER data in Figures 4.16 and 4.19 show many of the lowest $\gamma(\text{N}_2\text{O}_5)$ values (nearly exclusive to flight RF10, Figure 4.4) were clustered around the highest aerosol nitrate and organic mass fractions, though many values $< 1 \times 10^{-3}$ occurred throughout each individual distribution, including O:C ratio. This result may be due to the lack of direct ambient observations of aerosol morphology, molecular composition, and/or mixing state, which could lead to additional suppression, independent of the factors listed above.

Despite a lack of direct ambient phase state measurements, previous studies reviewed by You et al. (2014) suggest that the formation of aerosol organic coatings through liquid-liquid phase separation can occur as a function of RH and O:C ratio within the Org:SO₄²⁻ ratio range of 0.1-15

(observed during WINTER). Parameterization of the separation relative humidity (SRH) (as described by Bertram et al. (2011)) applied to WINTER data (Figure 4.23) shows that phase separations could have been present on some WINTER aerosol (below SRH line). There is no clear correlation however, between the smallest derived $\gamma(\text{N}_2\text{O}_5)$ values and the aerosol parameterized below the SRH line. An additional parameterization has been proposed by Shiraiwa et al. (2017) for the temperature at which aerosol transition from aqueous to glassy (highly viscous) solids, as a function of temperature, O:C ratio, and molecular composition. This transition temperature could not be estimated for WINTER data due to a lack of organic aerosol molecular composition data. The potential glassiness was instead assessed by comparing the aerosol liquid water content on RF10 ($\text{LWC} = \text{liquid water total}/(\text{liquid water total} + \text{AMS total mass})$) to other WINTER flights. The median LWC was not the lowest on RF10 ($\text{RF07} < \text{RF08} < \text{RF10}$) and Figure 4.15 confirms that LWC cannot explain the low $\gamma(\text{N}_2\text{O}_5)$ values as aerosol with the lowest LWCs (< 0.25) correspond to both the highest and lowest WINTER $\gamma(\text{N}_2\text{O}_5)$ values. Combined, these results cannot provide a clear indication of differences in aerosol morphology on RF10 relative to other flights during WINTER.

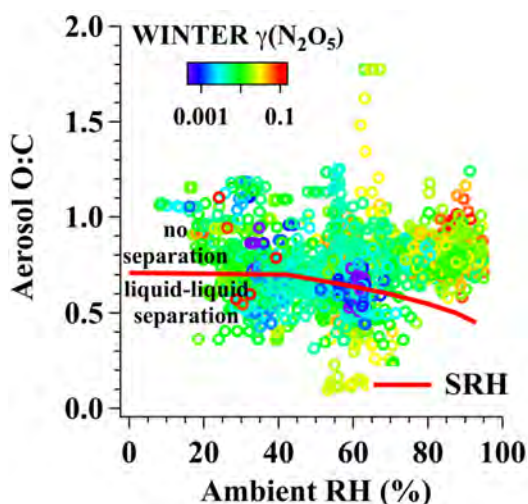


Figure 4.23. WINTER Aerosol O:C vs. Relative humidity. Liquid phase separations are expected to occur below the separation relative humidity line (SRH: red line) as parameterized by Bertram et al. (2011). Graph is colored by model-derived $\gamma(\text{N}_2\text{O}_5)$ values.

Three additional factors were used to assess the influence of biogenic sources on aerosol during RF10 since laboratory studies of biogenic SOA have consistently produced low $\gamma(\text{N}_2\text{O}_5)$ values on the order of 6×10^{-4} (Anttila et al., 2006; Escorcia et al., 2010; Folkers et al., 2003). Though biogenic VOCs are expected to contribute to SOA formation in the southeastern U.S. (e.g. Xu et al., 2015), TOGA measurements were unavailable to confirm the presence of isoprene, α -, or β -pinene on RF10. Previous studies have observed average levels of 0.45 and 0.59 ppbC for α - and β -pinene, respectively, during wintertime in rural GA (Hagerman et al., 1997). These values are larger than averages (> 0.2 ppbC) observed by TOGA over North Carolina during WINTER, potentially suggesting a larger presence of biogenic VOCs further south with a larger monoterpene SOA influence. Shown in Figure 4.24a, the ratio of AMS mass factors f_{44} to f_{43} (i.e. f_{43} = fraction m/z 43 relative to the total mass spectrum signal), is a marker of SOA oxidation and may be suggestive of the dominant aerosol source (biogenic or anthropogenic) (Ng et al., 2010). Additionally, the $f_{\text{CO}_2^+}$ to $f_{\text{C}_5\text{H}_6\text{O}^+}$ ratio (Figure 4.24b) can provide a marker of monoterpene influence when isoprene is low (Hu et al., 2015), as previously observed during winter in rural GA (Hagerman et al., 1997). Based on these mass factors, all aerosol from RF10 (lowest $\gamma(\text{N}_2\text{O}_5)$ values) appear to have a similar source and are similarly aged (Figure 4.24a), but do not have a distinctly enhanced biogenic influence relative to other flights (Figure 4.24b).

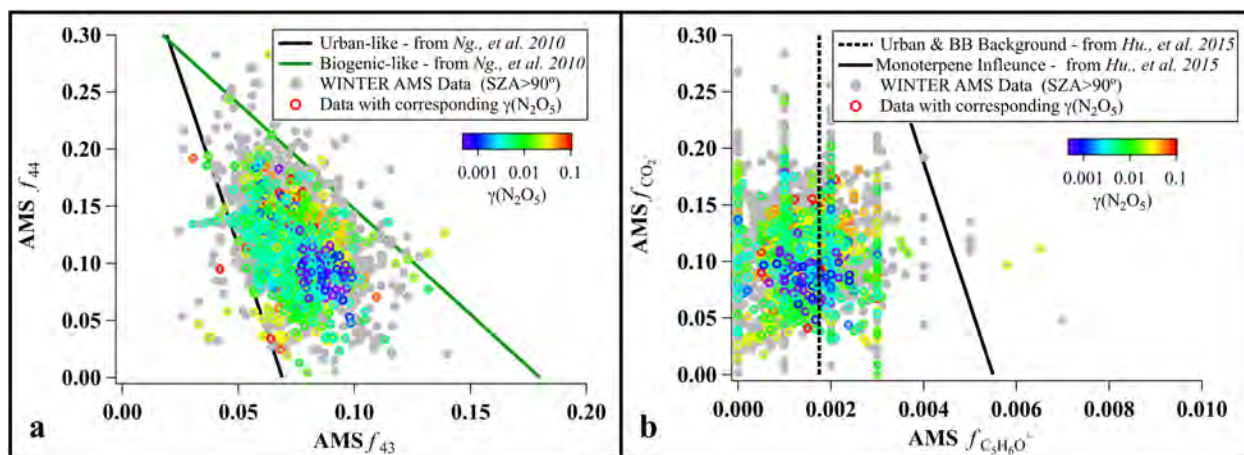


Figure 4.24. (a) AMS mass factor ratio: f_{44} to f_{43} . The black and green lines represent the boundaries defined in Ng et al. (2010). Gray points show all AMS nighttime data ($SZA > 90^\circ$). Points with corresponding derived $\gamma(N_2O_5)$ values are overlaid on top and colored by $\gamma(N_2O_5)$. (b) AMS mass factor ratio: f_{CO_2+} to $f_{C_5H_6O+}$. Dashed line represents the urban background and biomass burning (BB) ratio and black line represents the ratio for monoterpene-influenced SOA as presented in Hu et al. (2015). Gray points show all AMS nighttime data ($SZA > 90^\circ$). Points with corresponding derived $\gamma(N_2O_5)$ values are overlaid on top and colored by $\gamma(N_2O_5)$.

Overall, the underlying cause of low WINTER $\gamma(N_2O_5)$ values cannot be determined. In addition, only one flight was conducted over the continental southeastern U.S., making it impossible to assess the reproducibility of these low $\gamma(N_2O_5)$ results. The median $\gamma(N_2O_5)$ value of 1×10^{-3} (minimum 4×10^{-4}) from this flight, however, was lower than nearly all other determinations from WINTER, as well as the minimum values reported from all but four previous field studies (Figure 4.8). These low values were not reproducible with the steady state approximation, but were not an artifact of the box model since they corresponded to the largest observed N_2O_5 mixing ratios during WINTER (Figure 4.12; indicating slow N_2O_5 loss), were not driven by high aerosol SA though E4.5, and would only decrease further if k_{NO_3} were underestimated (Section 4.2.2.1). Despite studies that suggest nitrate aerosol and biogenic SOA are particularly efficient at suppressing $\gamma(N_2O_5)$ in laboratory settings, this flight did not show a particularly low LWC, large nitrate mass fraction, or large biogenic influence. Additional information regarding the organic

aerosol molecular composition and its influence on particle morphology could possibly elucidate the reason for low $\gamma(\text{N}_2\text{O}_5) \leq 1 \times 10^{-3}$ and should be considered as an area of future research.

4.4.3.3 Empirical Parameterization

In addition to comparison of literature parameterizations, we derive the first field-based, empirical parametrization for $\gamma(\text{N}_2\text{O}_5)$ that uses the same variables as the laboratory parameterizations, but that fits the proportionality constants to obtain the best representation of WINTER observations. This parameterization (E4.19, Figure 4.20k) implements the simplified resistor model approach that best reproduced the WINTER results in Section 4.4.3.2, and produces the lowest RMSE (0.0157) of any literature parameterizations tested.

$$\frac{1}{\gamma} = \frac{1}{\frac{4}{c} \frac{V}{SA} K_H * 2.14 \times 10^5 * [\text{H}_2\text{O}(l)] \left(1 - \frac{1}{\left(\frac{0.04[\text{H}_2\text{O}(l)]}{[\text{NO}_3^-]} \right) + 1} \right)} + \frac{1}{\frac{4RT(0.15 * \text{O:C} + 0.0016 * \text{RH})H_{aq}D_{aq}R_c}{c\ell R_p}} \quad (4.19)$$

Briefly, this method fits the ratio of $k_{4.5}/k_{4.4}$ ($=0.04$), $k_{4.3}$ as a linear function of water ($=2.14 \times 10^5 * [\text{H}_2\text{O}]$), and ε as a linear combination of RH and O:C ratio ($=0.15 * \text{O:C} + 0.0016 * \text{RH}$) (details in Table B.3). Following the approach of Bertram and Thornton (2009), c is the mean molecular speed of N_2O_5 (m s^{-1}), V ($\text{m}^3 \text{m}^{-3}$) and SA ($\text{m}^2 \text{m}^{-3}$) are the aerosol volume and surface area densities, respectively, and the N_2O_5 Henry's law coefficient (K_H) is taken to be 51 (Fried et al., 1994). Following Riemer et al. (2009), R is the ideal gas constant ($\text{m}^3 \text{atm K}^{-1} \text{mol}^{-1}$), T is temperature (K), R_p (m), R_c (m), and ℓ (m) represent the total particle radius, aqueous core radius, and organic coating thickness, respectively (described above). The solubility and diffusion of N_2O_5 through the organic coating are represented by the aqueous Henry's law ($5000 \text{ mol m}^{-3} \text{atm}^{-1}$) (Anttila et al., 2006) and liquid diffusion ($1 \times 10^{-9} \text{ m}^2 \text{ s}^{-1}$) (Riemer et al., 2009) coefficients, scaled by ε ($=0.15 * \text{O:C} + 0.0016 * \text{RH}$). The fit of this parameterization to WINTER data produced a

$k_{4.5}/k_{4.4}$ ratio within a factor of two to those presented in Griffiths et al. (2009) (0.03) and Bertram and Thornton (2009) (0.06), and a value of k_3 (for the average WINTER aerosol water molarity of 20 M) within a factor of 1.2 of Griffiths et al. (2009) ($5 \times 10^6 \text{ s}^{-1}$) and 4 of Bertram and Thornton (2009) ($1.1 \times 10^6 \text{ s}^{-1}$). Restricting the fit to O:C ratios within 0.5 and 1 (range of higher correlation in Figure 4.19), resulted in worse agreement.

Parameterization of $\gamma(\text{N}_2\text{O}_5)$ as a function of temperature, relative humidity and aerosol water and composition, using a mechanistically-accurate empirical fit has the advantage of reproducing the median value from WINTER, but like other literature parameterizations, cannot reproduce the large-scale variability. The failure of this parameterization suggests that there may be other factors that determine $\gamma(\text{N}_2\text{O}_5)$, such as aerosol morphology (i.e. liquid organic coatings), mixing state, and/or phase. Measurements of these properties should be included in future measurements of NO_x , O_3 , and N_2O_5 to test their relevance to understanding N_2O_5 uptake in ambient air.

4.5 Summary, Conclusions, and Future Directions

A box model analysis of nocturnal reactive nitrogen chemistry derived 2876 individual $\gamma(\text{N}_2\text{O}_5)$ values with a median of 0.0143 during periods of darkness on 9 flights over the eastern U.S. during the 6-week WINTER campaign. In comparison to all previous field determinations of $\gamma(\text{N}_2\text{O}_5)$, this analysis produced the largest observed range (2×10^{-5} to 0.1751) in $\gamma(\text{N}_2\text{O}_5)$ with nearly 50 times more data points than all previous aircraft campaigns combined. Comparison to the steady state approximation and 18 sensitivity studies of model parameter uncertainties provided an assessment of the box model robustness. The campaign median $\gamma(\text{N}_2\text{O}_5)$ value was most sensitive to uncertainties in the measured aerosol SA density, similar to all previous field-derived results. The box model results generally agreed with the steady state approximation for

$\gamma(\text{N}_2\text{O}_5)$ at long simulation durations. Compared to a previous modeling sensitivity study, all but the lowest 5% of WINTER $\gamma(\text{N}_2\text{O}_5)$ occurred within the range of values where global burdens of tropospheric oxidants and NO_x are most sensitive to this parameter, highlighting the need for an accurate parameterization of $\gamma(\text{N}_2\text{O}_5)$ for 3D chemical transport models.

Further analysis of correlations between WINTER $\gamma(\text{N}_2\text{O}_5)$ values and RH, temperature, and aerosol composition generally followed trends previously observed in laboratory studies and field campaigns (when trends were observed). These results support the current proposed mechanism for uptake and suggest aerosol water is the dominant controlling factor of ambient $\gamma(\text{N}_2\text{O}_5)$, out of all those proposed and measured. Despite general agreement with past studies, low correlation coefficients with all observed variables suggest that $\gamma(\text{N}_2\text{O}_5)$ is either simultaneously dependent on multiple factors or is at least partly dependent on variables not captured in the ambient WINTER observations. Infrequently measured parameters known to influence $\gamma(\text{N}_2\text{O}_5)$ include aerosol organic coatings and/or phase state. This analysis was also the first to quantitatively assess the dependence of field-derived $\gamma(\text{N}_2\text{O}_5)$ on aerosol pH, but found no evidence in the WINTER data that an acid catalyzed mechanism is an important factor in N_2O_5 uptake efficiency.

Finally, application of 14 literature parameterizations to WINTER data showed that predictions of $\gamma(\text{N}_2\text{O}_5)$ based on pure inorganic and mixed aerosol components (assuming an organic suppression by either reactively thin or thick coatings or by reduction in mass accommodation) generally reproduced the WINTER median but with a 1-2 orders of magnitude under-prediction in the observed range. In four parameterizations, agreement improved when the effect of chloride enhancement was excluded. Best agreement was observed with the simplified resistor model framework, which was further fit to WINTER observations to derive the first field-based, empirical parameterization of $\gamma(\text{N}_2\text{O}_5)$. Gross over-prediction by all parameterizations,

however, of lowest WINTER values $< 1 \times 10^{-3}$ suggests an additional suppressive effect not captured by observed variables or parameterization framework. In the absence of measured organic composition data, the cause of low WINTER values could not be confirmed, but comparisons to previous laboratory studies suggest that aerosol morphology or phase-relevant variables may be stronger predictors of $\gamma(\text{N}_2\text{O}_5)$ than those measured during WINTER and currently included in $\gamma(\text{N}_2\text{O}_5)$ parameterizations. While factors such as aerosol water and nitrate appear to be important predictors of $\gamma(\text{N}_2\text{O}_5)$, measurements of aerosol organic composition and phase should, therefore, be considered in future field-campaigns aimed at understanding the mechanism of heterogeneous N_2O_5 uptake and its impacts on tropospheric oxidant distributions.

Chapter 5: ClNO₂ yields from aircraft measurements during the 2015 WINTER campaign and critical evaluation of current parameterizations

Abstract

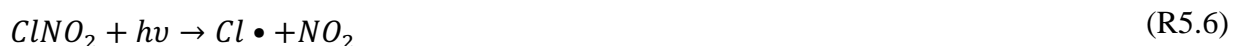
Nitryl chloride (ClNO₂) plays an important role in the budget and distribution of tropospheric oxidants, halogens, and reactive nitrogen species. Formed as a reaction product from the heterogeneous uptake of dinitrogen pentoxide (N₂O₅), the amount of ClNO₂ relative to its nitric acid (HNO₃) co-product is defined as the ClNO₂ production yield, $\phi(\text{ClNO}_2)$. $\phi(\text{ClNO}_2)$ has been increasingly incorporated in 3D chemical models where it is parameterized based on laboratory-derived kinetics and accepted aqueous-phase formation mechanism. Current parameterizations indicate that $\phi(\text{ClNO}_2)$ is only dependent on the aerosol molar ratio of chloride/water. Box model simulations of 9 night flights during the 2015 Wintertime INvestigation of Transport, Emissions, and Reactivity aircraft campaign derived 3425 individual $\phi(\text{ClNO}_2)$ values with a median of 0.138 and range of 0.003 to 1. Comparison of the box model median with those predicted by two other $\phi(\text{ClNO}_2)$ derivation methods agreed within a factor of 1.3, within the uncertainties of each method. In contrast, these values were factors of 2 to 4.3 lower than predictions based on aerosol composition and current parameterizations. An evaluation of factors influencing this observed difference reveals a positive dependence of $\phi(\text{ClNO}_2)$ on aerosol water, opposite of the currently parameterized trend. Additional sources of box model- parameterization differences may include aqueous-phase competition reactions and direct ClNO₂ loss mechanisms. Further laboratory studies of ClNO₂ formation yields and the impacts of aerosol components such as water, sulfate,

and organics are required to elucidate and quantify these processes on ambient aerosol, critical for the development of a robust $\phi(\text{ClNO}_2)$ parameterization.

This Chapter is in preparation for an upcoming peer-reviewed publication to be submitted to *The Journal of Geophysical Research: Atmospheres*, entitled: ClNO_2 yields from aircraft measurements during the 2015 WINTER campaign and critical evaluation of current parameterizations.

5.1 Introduction

Atmospheric reactions of nitryl chloride (ClNO_2) contribute to tropospheric halogen activation and impact the distribution of oxidants and reactive nitrogen species in polluted regions (Simpson et al., 2015 and references therein). ClNO_2 is formed in up to a 1:1 stoichiometric ratio with nitric acid (HNO_3) from the heterogeneous uptake and subsequent reaction of dinitrogen pentoxide (N_2O_5) (R5.1-R5.5). ClNO_2 will photolyze upon sunrise (R5.6) but can build-up at night in the residual layer (RL) where the O_3 oxidation of NO_x ($\text{NO}_2 + \text{NO}$) emissions forms persistent levels of N_2O_5 (e.g. Brown et al., 2007b; Riedel et al., 2013). The production of ClNO_2 is therefore expected to be largest under wintertime conditions where longer nights and cold temperatures stabilize and favor the formation of N_2O_5 in its equilibrium with NO_3 (R5.3) and minimize direct NO_3 loss reactions with volatile organic compounds (VOCs).



While the absolute production of ClNO_2 will depend on the rate of N_2O_5 formation, (R5.1 - R5.3), the uptake efficiency of N_2O_5 (defined as $\gamma(\text{N}_2\text{O}_5)$) (R5.4), and the presence of aerosol phase chloride (expected to vary with geographical differences in chlorine emission sources) (R5.5), the ClNO_2 production yield relative to HNO_3 (defined as $\phi(\text{ClNO}_2)$), is thought to depend only on aerosol-phase chloride and water. A parameterization for $\phi(\text{ClNO}_2)$ based on these expected dependences has been derived in previous laboratory-based studies (Behnke et al., 1997; Bertram & Thornton, 2009; Roberts et al., 2009; Ryder et al., 2015) and is discussed further below. This parameterized production yield has been increasingly incorporated into 3D chemical transport models in order to simulate ClNO_2 formation and evaluate its tropospheric implications (e.g. Sarwar et al., 2014; Sherwen et al., 2017). In contrast to HNO_3 which acts as a net NO_x sink, photodissociation of ClNO_2 upon sunrise will release NO_2 and atomic chlorine that can lead to O_3 formation the following day. For example, a previous study with the Community Multiscale Air Quality Model (CMAQ) found up to 10% increases in 8hr-averaged tropospheric O_3 in January over the United States when including reaction R5.5 in addition to R5.4 in the chemical mechanism. The production yield between HNO_3 and ClNO_2 is therefore important to parameterize accurately and evaluate against field-derived results as it has direct implications for the predicted distributions of tropospheric oxidants and NO_x .

Ambient ClNO_2 was first observed off the coast of Texas in 2006 (Osthoff et al., 2008) and has since been measured from ship, ground, and aircraft-based platforms in both continental and coastal/marine environments throughout North America (Edwards et al., 2013; Faxon et al., 2015; Kercher et al., 2009; Kim et al., 2014; Mielke et al., 2011; Mielke et al., 2016; Osthoff et al., 2008; Riedel et al., 2013; Riedel et al., 2012b; Thornton et al., 2010; Wild et al., 2016; Young et al., 2012), Europe/UK (Bannan et al., 2015; Bannan et al., 2017; Phillips et al., 2016; Phillips et al.,

2012), and Asia (Liu et al., 2017; Tham et al., 2016; Tham et al., 2014; Wang et al., 2016; Wang, X. et al., 2017; Wang et al., 2014; Wang, Z. et al., 2017). Reported mixing ratios range from a few parts per trillion (pptv) to a maximum of 4700 pptv (1-minute average), measured in December 2013 in Southern China (Wang et al., 2016). Many fewer studies, and none from aircraft, have reported the ClNO₂ yield ($\phi(\text{ClNO}_2)$), which requires additional measurements of N₂O₅ and/or total (particle + gas-phase) nitrate. Existing ground-based determinations of $\phi(\text{ClNO}_2)$ show no strong seasonal or geographical dependences and report values that vary within the entire possible range of 0-1 (Mielke et al., 2016; Osthoff et al., 2008; Phillips et al., 2016; Riedel et al., 2013; Tham et al., 2016; Thornton et al., 2010; Wagner et al., 2013; Wagner et al., 2012; Wang, X. et al., 2017). In addition, these field-derived ClNO₂ yields are lower than those predicted by laboratory-derived parameterizations, based on aerosol chloride and water. This disagreement is found in every study to make the comparison (Riedel et al., 2013; Ryder et al., 2015; Thornton et al., 2010; Wagner et al., 2013; Wang, Z. et al., 2017; Wang, X. et al., 2017), which suggests that the current mechanistic understanding of ClNO₂ production may be complicated by the presence of additional aerosol-phase components or an undefined loss processes that consumes ClNO₂ (e.g. Roberts et al., 2008). As ClNO₂ formation continues to be incorporated into 3D models for evaluations of tropospheric halogen (e.g. Sherwen et al., 2017), further investigation into the sources of field – parameterization discrepancies are required to better understand and improve the predictive capabilities of ClNO₂ formation in the wintertime RL.

Here we present the first aircraft determinations of $\phi(\text{ClNO}_2)$, derived from a box model analysis of data from the Wintertime INvestigation of Transport, Emissions, Reactivity (WINTER) campaign, conducted over the eastern U.S. during 3 February – 13 March, 2015. Box model $\phi(\text{ClNO}_2)$ results are compared to other observation-based derivation methods, including the ratio

of ClNO_2 to total soluble nitrate and laboratory-based parameterizations, in order to evaluate similarities and differences between methods used in previous studies. The large data set and regional coverage of WINTER flights, combined with measurements of aerosol composition and multiple gas-phase species, allows for further discussion and evaluation of the observed discrepancy between parameterized $\phi(\text{ClNO}_2)$ values and WINTER box model results. These results can help direct future laboratory studies aimed at developing a robust $\phi(\text{ClNO}_2)$ parameterization for ambient aerosol.

5.2 Methods

5.2.1 Measurement Campaign and Box Model

As described in Chapter 2, the WINTER campaign conducted 9 research flights at various times of night with the NSF/NCAR C-130 aircraft over the eastern United States between 3 February and 13 March 2015. Flight tracks from all 13 research flights (day and night) are shown in Figure 5.1a, colored by times of day and night (defined as solar zenith angle $> 90^\circ$). A box model analysis, previously described in Chapters 2 and 4, was used to simultaneously derive the production rate constant of ClNO_2 (k_{ClNO_2} [s^{-1}] = $k_{5.5}$) with the total heterogeneous loss rate constant of N_2O_5 ($k_{\text{N}_2\text{O}_5}$ [s^{-1}] = $k_{5.4} + k_{5.5}$) to calculate $\phi(\text{ClNO}_2)$ following the middle term of equation E5.1. Assuming ClNO_2 is exclusively formed from reaction on aerosol particles, this definition is equivalent to the rightmost term of E5.1 where the $\phi(\text{ClNO}_2)$ is defined as the amount of ClNO_2 formed relative to the integrated amount of N_2O_5 lost to aerosol uptake.

$$\phi(\text{ClNO}_2) = \frac{k_{\text{ClNO}_2}}{k_{\text{N}_2\text{O}_5}} = \frac{k_{5.5}}{k_{5.4} + k_{5.5}} = \frac{[\text{ClNO}_2]}{\int_{\text{Sunset}}^t (k_{5.4} + k_{5.5})[\text{N}_2\text{O}_5] dt} \quad (5.1)$$

Extensive model details have been presented in Sections 2.4.2 and 4.2.2, and are only briefly described here. Initialized at sunset, the 14-reaction chemical mechanism is integrated forward in time to simulate the nocturnal evolution of an air parcel from sunset until the time of aircraft measurement, assuming constant temperature and relative humidity. Values of $k_{N_2O_5}$ and k_{ClNO_2} are then derived by iteratively fitting the model output of each simulation to 10 s averaged observations of NO_2 , O_3 , N_2O_5 , and $ClNO_2$ by adjusting initial concentrations of O_3 and NO_2 and values of $k_{N_2O_5}$ and k_{ClNO_2} . Finally, values of $\phi(ClNO_2)$ ($\gamma(N_2O_5)$ values in Chapter 4) are derived using the middle term of E5.1. This entire process was repeated throughout each research flight during times when the aircraft was within the RL (defined by flight based on aircraft vertical profiles of potential temperature) and the SZA was $> 90^\circ$. The data were averaged to 10-seconds to reduce variability in the data products, while maintaining the spatial resolution of 1-10 km.

Aircraft measurements used as model fit parameters have been described previously in Section 2.3.2.2 and are summarized in Table 4.1. In addition to these particle and gas-phase measurements, particulate chloride was also measured by both the AMS and PILS. The AMS does not efficiently sample refractory species such as NaCl (Hayes et al., 2013), and the reported chloride values may therefore be lower limits. While the PILS can efficiently collect chloride from refractory and water-soluble species, the majority of PILS-IC chloride measurements during WINTER were below the reported detection limit of $0.12 \mu\text{g sm}^{-3}$. Similarly, many of the AMS chloride measurements were also below the AMS instrument detection limit, reported at 1Hz, typically $\leq 0.06 \mu\text{g sm}^{-3}$ and up to $0.15 \mu\text{g sm}^{-3}$ for data points with derived $\phi(ClNO_2)$ values. The box model calculation of $\phi(ClNO_2)$ is independent of particulate phase chloride and is, therefore, not subject to increased uncertainty associated with these low values. The $\phi(ClNO_2)$

parameterizations, however, are sensitive to uncertainties in particulate chloride and the calculation of aerosol water, which are addressed further below (Section 5.4).

5.2.2 Box Model Limitations, Uncertainties, and Sensitivity Studies

Box model results for $\phi(\text{ClNO}_2)$ are dependent on $k_{\text{N}_2\text{O}_5}$, and therefore subject to many of the same model limitations discussed previously in Section 2.4.2, including the assumption of constant RH and temperature during the course of a trajectory, and uncertainties in NO_3 reactivity (k_{NO_3}) (e.g. VOC measurements, NO_3 aerosol uptake, and reaction with radicals). These uncertainties can increase variability in $k_{\text{N}_2\text{O}_5}$ and therefore k_{ClNO_2} . In addition, model non-convergence occurs as k_{ClNO_2} approaches $k_{\text{N}_2\text{O}_5}$ ($\phi(\text{ClNO}_2) = 1$). The maximum bias introduced from this non-convergence, however, is relatively small (< 23% increase) (Section 2.4.2.5) and these points are not further considered as they do not change the main conclusions presented here.

Additional sources of uncertainty specific to $\phi(\text{ClNO}_2)$ include the model assumptions regarding air-surface interactions. As discussed in Section 2.4.2.7.11, base case simulations were run assuming no interaction with the surface through dry deposition and/or surface emission. While this is a reasonable assumption for isolated air in the continental RL, a well-mixed marine boundary layer is expected at depths of at least 500m during wintertime off the U.S. east coast (Seidel et al., 2012). To test the model for sensitivities to dry deposition, the depositional flux for N_2O_5 was first estimated using the exchange velocity derived from an observational analysis by Kim et al. (2014). Including N_2O_5 deposition increased the median $\phi(\text{ClNO}_2)$ value over the ocean by 27.9%, from a value of 0.145 to 0.186 (Figures 2.34 and 2.35). The second test included estimates for both N_2O_5 and ClNO_2 deposition rates (Section 2.4.2.7.11). While N_2O_5 uptake to chloride-rich seawater is expected to result in a positive ClNO_2 flux from the ocean surface (provided ClNO_2 re-volatilizes to the gas phase), Kim et al. (2014) observed a slight negative

ClNO₂ flux from eddy co-variance measurements at night at a coastal location in Southern California. Including a ClNO₂ dry deposition velocity ~1/3 the magnitude of that for N₂O₅ (based on Kim et al. (2014)), further increased the median box model $\phi(\text{ClNO}_2)$ value over the ocean by 35% to a value of 0.251. Both values, however, remained lower than those predicted by current laboratory-based parameterization (discussed in Section 5.4, shown in Figure 2.35), indicating that the model assumptions of ocean exchange do not change the main conclusions presented here.

Finally, to test the overall model sensitivity to uncertainties in model fit parameters and assumptions, a series of 18 sensitivity studies were conducted for each flight, with the results presented in Section 2.4.2.7 and summarized in Table 2.8. Of the parameters tested, $\phi(\text{ClNO}_2)$ was most sensitive to uncertainties in ClNO₂ and N₂O₅ deposition with increases in the median $\phi(\text{ClNO}_2)$ value over the ocean by 72.9%, to a value of 0.251 (discussed above). Median $\phi(\text{ClNO}_2)$ was the second most sensitive to assumptions in air age with up to 43.7% increases. Uncertainties in chemical measurements used as model fit parameters resulted in a range of -29.8% to +34.5% for changes in median $\phi(\text{ClNO}_2)$ (absolute values of 0.092 to 0.164). The median $\phi(\text{ClNO}_2)$ had less than 7% sensitivities to uncertainties in the time elapsed before sunset, NO₃ reactivity, and photolysis rates. In addition to the previously described deposition tests, data over the ocean were tested for sensitivities to air parcel dilution with simultaneous entrainment of background O₃. The dilution rate was estimated from multiple encounters of the same air parcel on research flight 3. Including dilution and entrainment in data over the ocean increased the median of these points by 21.3% from a value of 0.188 to 0.228. Despite the relatively large percent changes associated with some of these sensitivity tests, the median $\phi(\text{ClNO}_2)$ values for all tests remained less than 0.251, within 0.113 of the base case median and lower than the median predicted by laboratory-based

parameterizations, discussed in Section 5.4.2. Further discussion of the total model error and parameterization comparisons are also discussed below in Section 5.4.2.

5.3 Results

5.3.1 Box Model Analysis

Box model simulations resulted in 3425 individual determinations of $\phi(\text{ClNO}_2)$, encompassing nearly the entire possible range, with values from 0.003 to 1. The number of $\phi(\text{ClNO}_2)$ determinations reported here ($N = 3425$) is larger than the number of $\gamma(\text{N}_2\text{O}_5)$ determinations reported in Chapter 4 ($N=2876$) due to the dependence of $\gamma(\text{N}_2\text{O}_5)$ on aerosol surface area measurements, which were not required for $\phi(\text{ClNO}_2)$ and not always available during WINTER flights. WINTER flight tracks are colored by $\phi(\text{ClNO}_2)$ determinations in Figure 5.1b, with the campaign distribution shown Figure 5.1c. The $\phi(\text{ClNO}_2)$ distribution had a median and most frequent value of 0.138 ($1\sigma: +0.050/-0.045$) and 0.03, respectively.

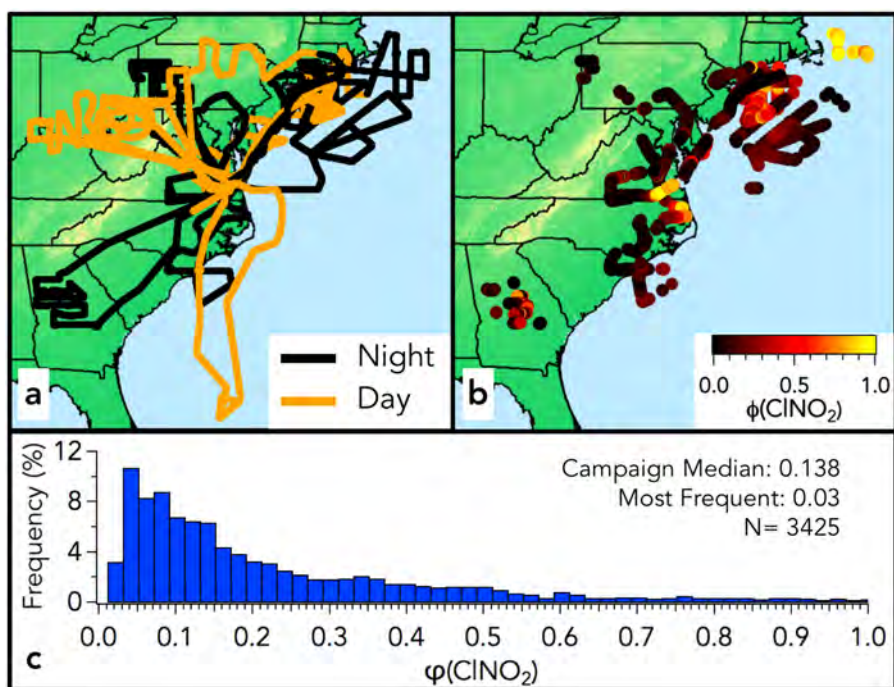


Figure 5.1. WINTER $\phi(\text{ClNO}_2)$ box model results. (a) flight tracks colored by night ($\text{SZA} > 90^\circ$) and daytime ($\text{SZA} < 90^\circ$) flights; (b) flight tracks colored by box-model derived $\phi(\text{ClNO}_2)$ values; (c) histogram of box model $\phi(\text{ClNO}_2)$ results.

Data in Figure 5.1b show several areas of larger $\phi(\text{ClNO}_2)$ associated with specific flights and generally higher values downwind of New York City, the largest regional NO_x source. The $\phi(\text{ClNO}_2)$ values otherwise do not show a strong geographical distribution. Data sampled over both ocean ($N = 1896$) and land ($N = 1529$) encompassed the same range in $\phi(\text{ClNO}_2)$ (Figure 5.2), but with different medians of 0.203 and 0.075, respectively. While larger yields are expected over the ocean, the two populations may encompass a similar range as many WINTER flights over the ocean sampled continental urban outflow.

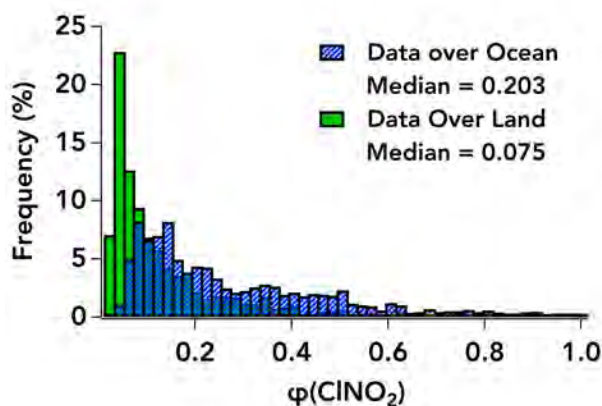


Figure 5.2. Histogram of ClNO_2 yields for data sampled over the ocean (blue) and over land (green). The ocean-land boundary was defined as the geographic boundary of the U.S. east coast.

Box model uncertainties were calculated for each individual $\phi(\text{ClNO}_2)$ value and shown as a time series in Figure 5.3. Error estimates (gray shading) were calculated from the quadrature addition of measurement accuracies (NO_2 : 10% RF01-RF04, 3% RF05-RF10, O_3 : 5%, RF01-RF06, 4% RF07-RF10, N_2O_5 : 12%, ClNO_2 : 30%), and the percent change in each point from model sensitivity tests to air age, start time, photolysis rates, and 50% changes in k_{NO_3} . Some of these sensitivity tests resulted in model non-convergence (i.e. $k_{\text{ClNO}_2} > k_{\text{N}_2\text{O}_5}$) for a fraction of $\phi(\text{ClNO}_2)$ values. In Figure 5.3, the upper limit value for these points was conservatively set to 1. These non-convergence values are not included in the sensitivity studies presented in Sections 2.4.2.7 and 5.2.2, but are used in the comparison to parameterized $\phi(\text{ClNO}_2)$ values presented in

Section 5.4.2. Additionally, uncertainties associated with dilution and deposition are not included in Figure 5.3, but are further discussed in context of the parameterization-box model comparison in Section 5.4.3.3. The contribution of box model uncertainty to differences between parameterized and box model derived $\phi(\text{ClNO}_2)$ values is discussed in Section 5.4.2.

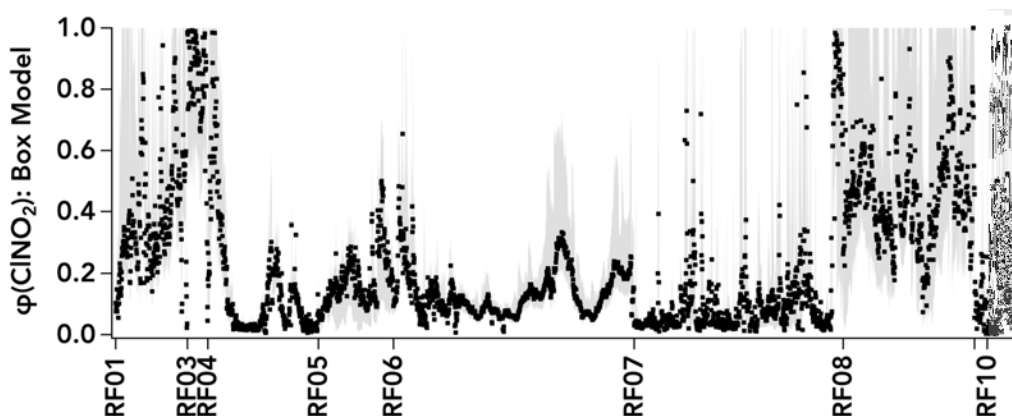


Figure 5.3. Times series of box model $\phi(\text{ClNO}_2)$ values (black dots) and associated errors (gray shading).

WINTER values are qualitatively compared in Figure 5.4 (and Table C.1) to all previously reported field-determinations of $\phi(\text{ClNO}_2)$. Figure 5.4 shows that $\phi(\text{ClNO}_2)$ values are variable and do not show a consistent dependence on geographical location, although the current database may be too sparse to illustrate such differences on continental or seasonal scales. The WINTER distribution and median appear similar to those reported from both continental and coastal locations across North America (Mielke et al., 2016; Mielke et al., 2011; Mielke et al., 2013; Osthoff et al., 2008; Riedel et al., 2013; Thornton et al., 2010; Wagner et al., 2012; Wagner et al., 2013). The reported median (or average) values, however, are consistently larger in Europe (Phillips et al., 2016) and China (Tham et al., 2016; Wang, X. et al., 2017; Wang, Z. et al., 2017) than during WINTER.

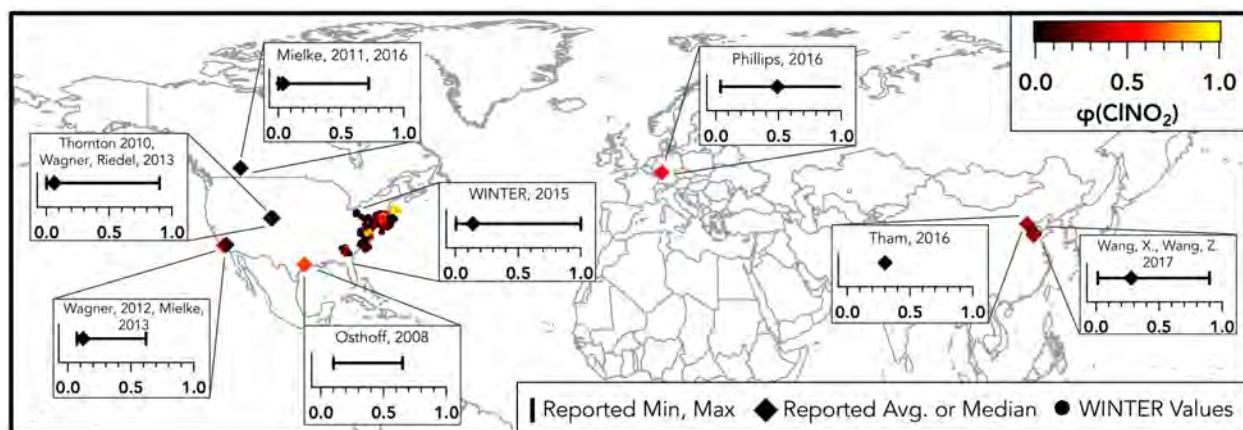


Figure 5.4. Map of all reported field-derived $\phi(\text{ClNO}_2)$ values. The geographic location of each study is shown by a diamond, colored by reported (or calculated) average or median $\phi(\text{ClNO}_2)$. All 3425 values from Figure 5.1 are shown. Graph inserts show the reported range and median or average of each study, if reported. Data from Mielke et al. (2013); Mielke et al. (2016); Osthoff et al. (2008); Phillips et al. (2016); Riedel et al. (2013); Tham et al. (2016); Thornton et al. (2010); Wagner et al. (2013); Wagner et al. (2012); Wang, X. et al. (2017); Wang, Z. et al. (2017).

Additional, real geographical differences in $\phi(\text{ClNO}_2)$ may be obscured by varying $\phi(\text{ClNO}_2)$ derivation methods used in past literature. For example, Mielke et al. (2016), Mielke et al. (2013), and Osthoff et al. (2008) define $\phi(\text{ClNO}_2)$ as the amount of ClNO_2 produced relative to the integrated amount of NO_3 radical formed, not N_2O_5 lost, which may be a lower limit to $\phi(\text{ClNO}_2)$ (discussed in Section 5.3.2). Methods relating the amount of observed ClNO_2 to total nitrate, as employed by Riedel et al. (2013), Wagner et al. (2012), and Phillips et al. (2016) have additional uncertainties described in the following section. Studies by Tham et al. (2014), Wang, X. et al. (2017), and Wang, Z. et al. (2017) defined $\phi(\text{ClNO}_2)$ following the right hand side of E5.3, equivalent to the box model calculation for WINTER, but calculated $k_{\text{N}_2\text{O}_5}$ from the steady state approximation, which may lead to an over-prediction of $k_{\text{N}_2\text{O}_5}$ (under-prediction of $\phi(\text{ClNO}_2)$) in high- NO_x environments (Brown et al., 2003). The study most directly comparable to WINTER is by Wagner et al. (2013), who deployed an earlier version of the WINTER box model and used the right side of E5.1 to derive $\phi(\text{ClNO}_2)$. Further comparisons of these methods are presented next.

5.3.2 Comparison to Multiple Definitions of $\phi(\text{ClNO}_2)$

ClNO_2 yields reported from field data have been calculated using a variety of definitions and methods, making direct, quantitative comparisons between past studies difficult. In this section, four methods are applied to WINTER data in an attempt to provide a direct comparison and evaluation of commonly used methods. In the left panel of Figure 5.5, the average, 10th, 25th, 50th, 75th, and 90th percentiles are shown for each method described below. The right panel of Figure 5.5 shows the median and 1 σ error of each method (described below). Figure 5.5 is not representative of the entire WINTER campaign distribution. Data have been filtered to only include points with simultaneous $\phi(\text{ClNO}_2)$ determinations for all four methods, which reduces the total number from 3425 to 320, mostly as a result of Method 3 (described below). All methods assume that heterogeneous production is the only source of ClNO_2 . Due to the difference in aircraft and ground-based data, derivation of $\phi(\text{ClNO}_2)$ using steady-state derived $k_{\text{N}_2\text{O}_5}$ in E5.1 (used by Tham et al., 2016; Wang, X. et al., 2017; Wang, Z. et al., 2017) could not be compared here.

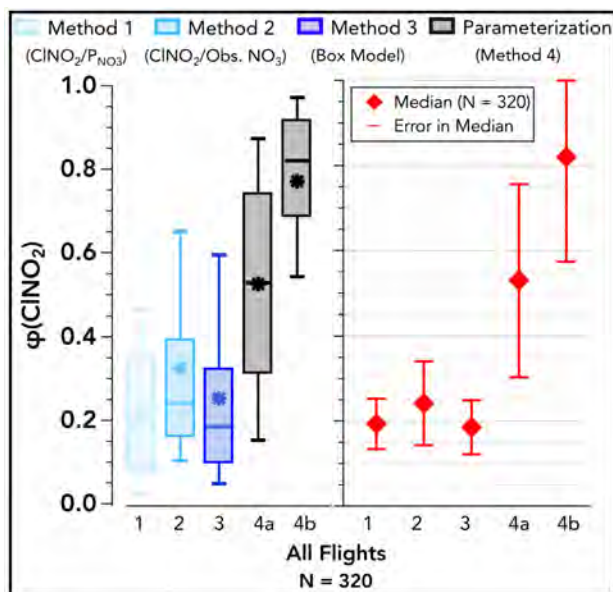


Figure 5.5. (left) Box and whisker plots comparing four derivation methods for $\phi(\text{ClNO}_2)$. Bars: 10th, 50th, and 90th percentiles; boxes: 25th to 75th percentiles; stars: average. Parameterized $\phi(\text{ClNO}_2)$ calculated with (4a) AMS particle chloride and (4b) PILS particle chloride. (Right) Median values of each method (diamond) and absolute errors in medians (whiskers).

In Method 1, $\phi(\text{ClNO}_2)$ was calculated using 10-second averages in E5.2, defined as the amount of ClNO_2 observed per amount of NO_3 radical produced. In E5.2, P_{NO_3} is defined in E5.3 as the instantaneous rate of nitrate radical production from the oxidation of NO_2 with O_3 (R5.2). The term dt_{sunset} is the amount of time elapsed between the onset of nocturnal chemistry (described above) and the time of aircraft measurement. Previously used by Osthoff et al. (2008), Mielke et al. (2013), and Mielke et al. (2016), this definition of $\phi(\text{ClNO}_2)$ may be a lower limit for $\phi(\text{ClNO}_2)$ as NO_3 production does not always lead to N_2O_5 and subsequent $\text{HNO}_3/\text{ClNO}_2$ formation. Instantaneous P_{NO_3} , however, decreases overnight as NO_2 and O_3 are consumed, which could lead to an over-prediction by this method that increases with simulation duration. Results in Figure 5.5a show that for the 320 points compared, Method 1 predicts the lowest average and percentile values (except for the 50th) for $\phi(\text{ClNO}_2)$ of the four methods tested. The median (0.19 ± 0.06), however, is within the uncertainties of the medians calculated using both Methods 2 (0.24 ± 0.10) and 3 (0.19 ± 0.06) (Figure 5.5b). Here, the error in Method 1 is calculated from the quadrature addition of I-TOF-CIMS ClNO_2 measurements (30%) and CRDS measurements of O_3 (4%) and NO_2 (3%). Method 3 (i.e. box model) error was described in the previous results section and the error associated with Method 2 is described below.

$$\phi(\text{ClNO}_2) = \frac{[\text{ClNO}_2]}{P_{\text{NO}_3} * dt_{\text{sunset}}} \quad (5.2)$$

$$P_{\text{NO}_3} = k_{5.2}[\text{O}_3][\text{NO}_2] \quad (5.3)$$

Method 2 defines $\phi(\text{ClNO}_2)$ in E5.4, calculated from the slope of the linear correlation between observed ClNO_2 and total nitrate. This method has been used by Riedel et al. (2013) and Wagner et al. (2012). Here, ClNO_2 yields were calculated every 10 seconds from linear fits of 1Hz ClNO_2 observations against the sum of HNO_3 and submicron particulate NO_3^- (i.e. total soluble

nitrate), as measured with the ITOF-CIMS and AMS, respectively. In these fits, the intercept was not forced to zero and were additionally filtered for times of at least 8 data points and statistically significant ($p < 0.05$) correlation coefficients. Due to the possibility of low correlations during periods of low ClNO_2 production, the r^2 filter may bias the results high relative to the overall WINTER distribution. Filtering all 4 methods for the same points however, provides a direct comparison of derivation methods for this subset of points. Example individual correlations for five flights are highlighted in Figure 5.6. Particle NO_3^- from super micron aerosol (1-4 μm) was not included in this calculation due to the low measurement frequency (~7 minutes between sample), which may bias these ratios high if these large particles serve as a reservoir for nitrate formed overnight. This method also assumes no NO_3^- contribution from reaction of NO_3 with hydrocarbons, though these reactions are expected to be small during winter due to low total NO_3 reactivity. In comparison, the box model is largely independent of observed total NO_3^- and is not highly sensitive to assumptions about NO_3^- loss or previous day production.

$$\phi(\text{ClNO}_2) = \frac{2m}{m+1}, \quad m = \frac{\Delta\text{ClNO}_2}{\Delta\text{NO}_3 \text{ Total}} \quad (5.4)$$

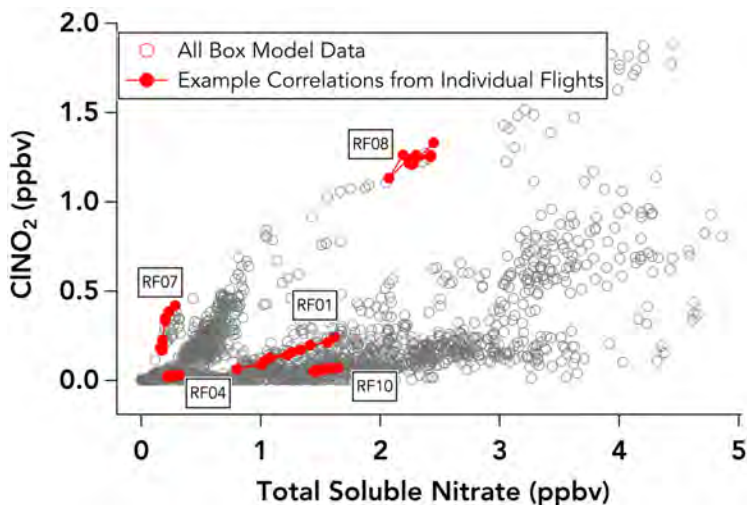


Figure 5.6. Correlation of observed ClNO_2 against total soluble nitrate ($\text{HNO}_3(\text{g}) + \text{NO}_3^-(\text{p})$). Gray points correspond to all WINTER data where the box model derived values for $\phi(\text{ClNO}_2)$. Red points represent example correlations ($r^2 > 0.5$) derived using Method 2.

Applied to WINTER data, Method 2 resulted in 320, 10-second determinations of $\phi(\text{ClNO}_2)$, shown in Figure 5.5. For these points, Method 2 derived larger values for $\phi(\text{ClNO}_2)$ than Methods 1 and 3, but a median (0.24 ± 0.10) within their calculated uncertainties (0.19 ± 0.06 for both) (Figure 5.5b). The total error associated with Method 2 was calculated from the quadrature addition of error in the ClNO_2 measurements (30%) and relative error associated with total nitrate calculated from I-TOF-CIMS HNO_3 (30%) and AMS particulate nitrate (35%) measurements. A previous methods comparison during winter 2013 in Colorado also showed similarity between Methods 2 and 3 with an average $\phi(\text{ClNO}_2)$ value of 0.05 ± 0.15 using Method 2 (Riedel et al., 2013) and a most frequent value of ~ 0.06 from a box model similar to the one used here (Wagner et al., 2013). An additional comparison of Method 2 and the right hand-side of equation E5.1, calculated from the steady state approach and observed ClNO_2 production rate from a ground site in China, found agreement within 0.03 for the campaign average (Wang, Z. et al., 2017).

The parameterization results in Figure 5.5 (Method 4) were calculated using aerosol water and chloride content and the laboratory-based parameterization in E5.5 with rate coefficient ratios from Bertram and Thornton (2009). Additional rate constant ratios are discussed in the following section. Here, parameterized $\phi(\text{ClNO}_2)$ values are calculated separately using measurements of particle-phase chloride from both the PILS (total soluble chloride) and AMS (non-refractory chloride only), discussed further below. All previous field studies to make the comparison between parameterized and field-derived values reported that the parameterized values exceeded those derived from field observation (Riedel et al., 2013; Thornton et al., 2010; Wagner et al., 2013; Wang, X. et al., 2017; Wang, Z. et al., 2017). Reported ClNO_2 yields derived from ambient sea water samples also resulted in values lower than the parameterized equivalents (Ryder et al., 2015).

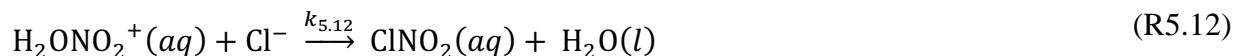
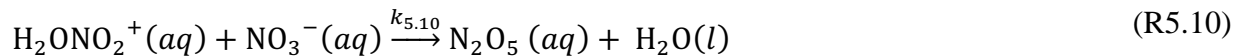
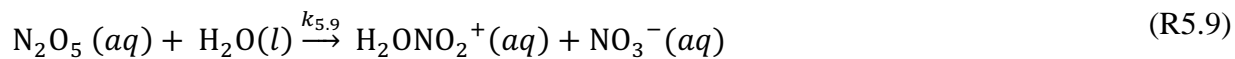
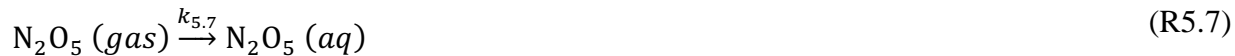
Qualitatively consistent with past results, parameterized values here, using both AMS (a) and PILS (b) particle chloride measurements, were generally larger than those predicted by other methods, with medians of 0.52 and 0.82, respectively. Larger values calculated from the PILS data are consistent with the PILS sampling refractory chloride species. Regardless of particle chloride differences, both predicted median values were factors of 2 to 4.3 larger than all other methods, and outside the range of uncertainties associated with Methods 2 and 3 (Figure 5.5b). The total error associated with the parameterization includes uncertainties in the calculation of aerosol chloride (35% or 20%) and water (~25%), calculated from the error propagation of uncertainties associated with the calculation of aerosol water (e.g. inorganic and organic-associated aerosol water mass). Factors associated with the differences between field-derived and parameterized $\phi(\text{ClNO}_2)$ values are discussed in the following section.

5.4 Discussion – Evaluation of Current $\phi(\text{ClNO}_2)$ Parameterizations

5.4.1 Parameterization Background

Presented in reactions R5.7 - R5.13 is the chemical mechanism first proposed by Behnke et al. (1997) and later evaluated by Bertram and Thornton (2009), Roberts et al. (2009), and Ryder et al. (2015) for the bulk-phase reaction of aqueous N_2O_5 and subsequent formation and evaporation of ClNO_2 (also discussed in Chapter 4). Based on the relative rates of reactions R5.10 - R5.12 ($k_{5.12} > k_{5.10} > k_{5.11}$) and assuming a steady state for the hydrated nitronium ion intermediate (H_2ONO_2^+), an expression can be derived for $\phi(\text{ClNO}_2)$ in E5.5 (derivation shown in section Appendix C1). This expression describes the ClNO_2 yield as a competition reaction between Cl^- and H_2O for the H_2ONO_2^+ intermediate. Based on laboratory studies of ClNO_2 formation from N_2O_5 uptake onto aqueous NaCl particles in wetted flow tube experiments, Behnke et al. (1997) derived a value of 836 ± 32 for the term $k_{5.12}/k_{5.11}$, while more recent studies

laboratory studies on chloride-containing aerosol have derived values in the range of 450 to 505 (Bertram & Thornton, 2009; Roberts et al., 2009; Ryder et al., 2015).



$$\phi(\text{ClNO}_2) = \frac{\Delta[\text{ClNO}_2]}{-\Delta[\text{N}_2\text{O}_5]} = \frac{1}{\left(1 + \frac{k_{5.11}[\text{H}_2\text{O}]}{k_{5.12}[\text{Cl}^-]}\right)} \quad (5.5)$$

5.4.2 Box Model – Parameterization Comparison

Parameterized predictions of WINTER $\phi(\text{ClNO}_2)$ values are plotted in Figure 5.7 (black/gray points) as a function of the aerosol $\text{Cl}^-:\text{H}_2\text{O}$ molar ratio, calculated with both AMS (a) and PILS (b) particle chloride measurements. Aerosol water concentrations were calculated as described previously in Chapter 4, Section 4.2.1. Briefly, inorganic-associated aerosol water (<1 μm diameter) was calculated using the ISORROPIA thermodynamic model by Hongyu Guo, as described in Guo et al. (2016), while the organic-associated water was estimated using relative humidity, a constant hygroscopicity factor of 0.1, and organic mass measured by the AMS. Upper and lower limit values of the Bertram and Thornton (2009) parameterization are shown by the red lines in Figure 5.7, calculated in each panel from the uncertainty in aerosol water calculation (~25%) and measurement uncertainties of each chloride instrument (35% AMS, 20% PILS).

Aerosol chloride from 1-4 μm particles was not included in Figure 5.7 due to the small fractional contribution of this size range to aerosol surface area (0-2%) (required for N_2O_5 uptake), relative to the total surface area contribution from smaller particles ($<1 \mu\text{m}$). The presence of chloride in these larger particles more likely contributes to the formation of gas-phase HCl through acid displacement, which can serve as a pool of chloride that equilibrates with submicron particles (Osthoff et al., 2008).

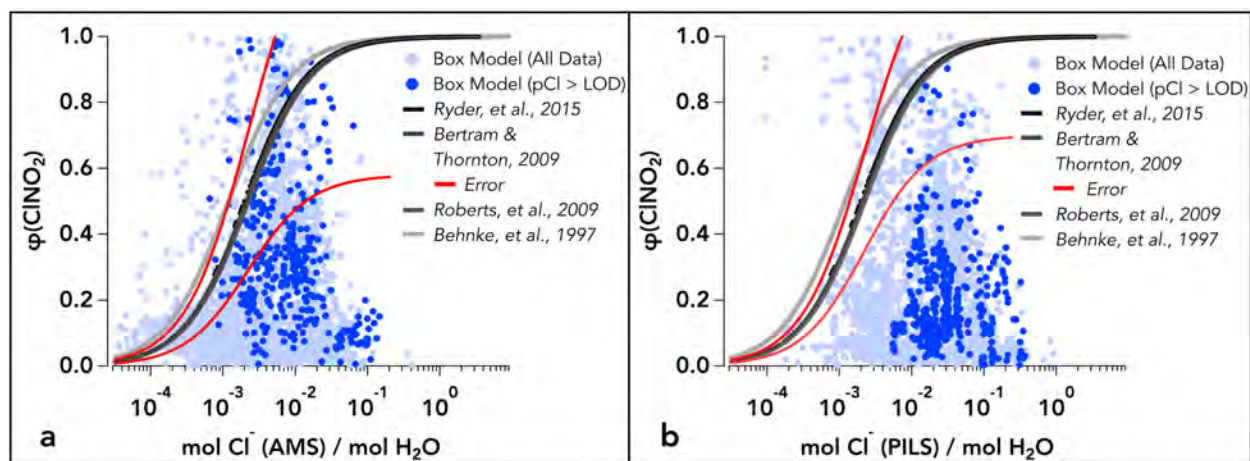


Figure 5.7. $\phi(\text{ClONO}_2)$ as a function of WINTER aerosol chloride to water molar ratio, calculated from (a) AMS and (b) PILS particle chloride measurements. Laboratory-based parameterizations are shown by gray lines and WINTER box model results shown by blue markers. Data with particle chloride measurements above reported detection limits for AMS and PILS instruments are shown by dark blue markers in the respective panels. Red lines represent the total absolute upper and lower error limits of the Bertram and Thornton parameterization.

WINTER box model values are also included in Figure 5.7 (blue), demonstrating the parameterization over-prediction shown for a subset of WINTER data in the previous section. Both sets of chloride measurements were included in Figure 5.7 to assess the role of aerosol chloride uncertainty in the differences between parameterized and model-derived $\phi(\text{ClONO}_2)$ values. Less than 13% of measured chloride concentrations for both instruments were above the reported instrument detection limits (PILS: $0.12 \mu\text{g sm}^{-3}$, AMS: median of $0.05 \mu\text{g sm}^{-3}$) (Figure 5.7, dark blue points). Despite the majority of data corresponding to concentrations below

detection limits (light blue points), both subsets of data consistently show an over-prediction in $\phi(\text{ClNO}_2)$ by each parameterization, even when accounting for uncertainties associated with water and chloride (red lines) in the parameterizations. In addition, the over-prediction trend is largely consistent between both AMS (non-refractory only) and PILS (total water soluble, including NaCl) chloride measurements with 75% and 86% of the box model values (above instrument LODs), respectively, falling below the lower limit error estimate of the Bertram and Thornton (2009) parameterization (lower red line). These results suggest that the uncertainties in aerosol chloride measurements and water calculation are not responsible for the majority of observed over-prediction by current $\phi(\text{ClNO}_2)$ parameterizations.

To assess the contribution of box model error to the observed parameterization-model differences, upper- and lower-limit box model values (calculated from the analysis of total model error) are plotted against parameterized values from Bertram and Thornton (2009) in Figure 5.8. As discussed in Section 5.3.1, errors in box model-derived $\phi(\text{ClNO}_2)$ values were individually calculated from the quadrature addition of measurement uncertainties (O_3 , NO_2 , N_2O_5 , ClNO_2) and model sensitivities to air age, simulation start time, photolysis rates, and 50% changes in total k_{NO_3} . In the evaluation in Figure 5.8, points of model non-convergence during sensitivity studies (i.e. $k_{\text{ClNO}_2} > k_{\text{N}_2\text{O}_5}$) were conservatively set to $\phi(\text{ClNO}_2)$ values of 1. Results show that the median box model values (calculated from data with particle chloride $>$ LOD, black squares in Figure 5.8) remain lower than their parameterized equivalents in all comparisons, regardless of chloride measurement. Only when comparing the upper limit box model value with the lower limit AMS-calculated parameterization (Figure 5.8, bottom right), does the median model value exceed the parameterization. Even when considering these extreme limits, however, 30% of the box model values ($\text{pCl} >$ LOD) remain lower the parameterized lower limit. This comparison indicates that

while the WINTER $\phi(\text{ClNO}_2)$ values are sensitive to model assumptions (air age in particular), model uncertainties are not the main source of parameterization-model discrepancies.

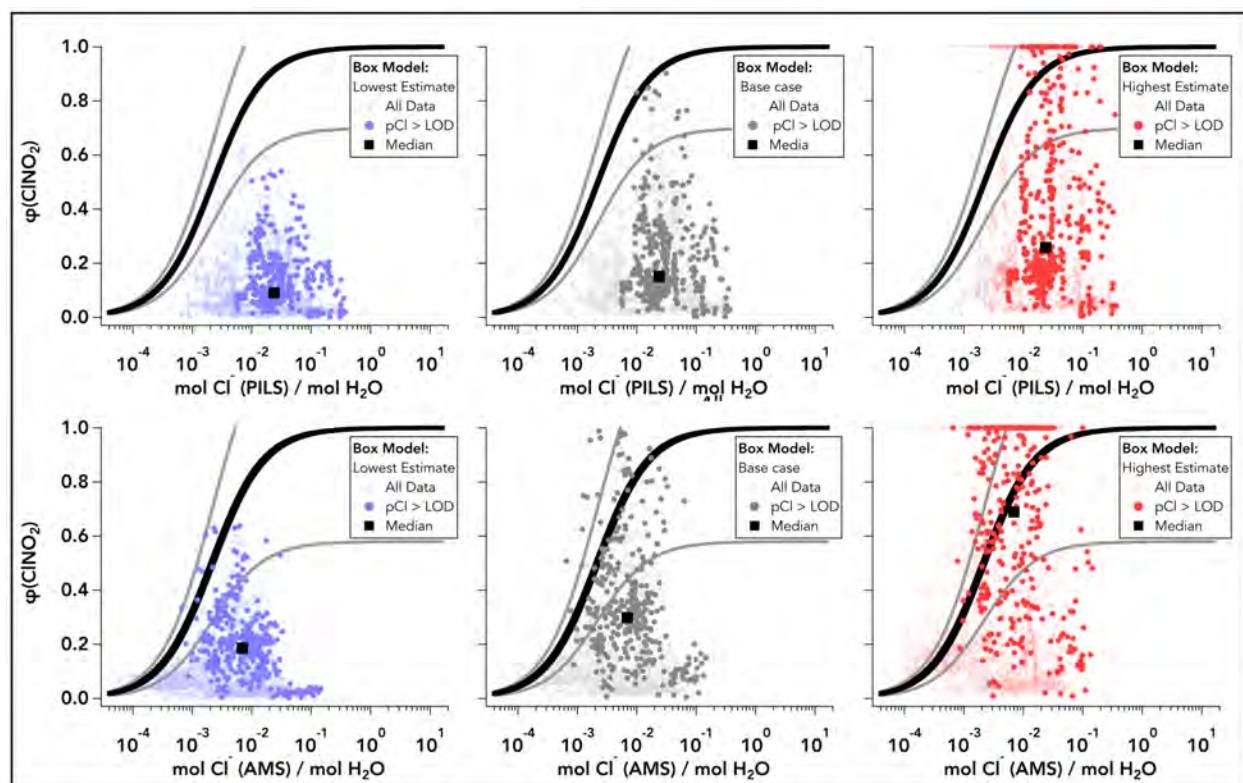


Figure 5.8. Base case (gray) and highest (red) and lowest (blue) estimated box model $\phi(\text{ClNO}_2)$ values, plotted against WINTER $\text{Cl}:\text{H}_2\text{O}$ molar ratio. Black curve represented the $\phi(\text{ClNO}_2)$ values predicted by the Bertram and Thornton (2009) parameterization. Grady curve are the parameterization error upper and lower limits. Squares represent the median $\phi(\text{ClNO}_2)$ value of each set of modeled WINTER $\phi(\text{ClNO}_2)$ values ($p\text{Cl} > \text{LOD}$ points only), plotted at the median $\text{Cl}:\text{H}_2\text{O}$ molar ratio (inorganic water component calculated by Hongyu Guo from ISORROPIA).

Combined, results in Figures 5.7 and 5.8 suggests a large suppression of the field-derived $\phi(\text{ClNO}_2)$ values relative to predictions from laboratory-based parameterizations. Calculated with both PILS and AMS chloride, the Bertram and Thornton (2009) parameterization over-predicted more than 90% of the WINTER base case values, which was only reduced to 75% when considering the lower-limit parameterized values relative to base case simulations. These results are qualitatively consistent with all other reported field-parameterization comparisons (Riedel et al., 2013; Ryder et al., 2015; Thornton et al., 2010; Wagner et al., 2013; Wang, Z. et al., 2017;

Wang, X. et al., 2017), suggesting the presence of a at least one physiochemical process suppressing $\phi(\text{ClNO}_2)$ relative to production yields predicted on pure NaCl/inorganic aqueous solutions. In the following sections we use box model $\phi(\text{ClNO}_2)$ results and observed WINTER variables to examine possible sources of the parameterization – box model difference. In the first section we discuss observed trends in parameterization – box model differences with measured aerosol composition, particularly aerosol water. The last two sections assess two possible mechanistic sources of $\phi(\text{ClNO}_2)$ suppression that have been discussed previously in field (Mielke et al., 2013; Phillips et al., 2016; Wang, Z. et al., 2017) and laboratory-based (e.g. Roberts et al., 2008; Ryder et al., 2015) studies of ClNO_2 yield. These include: 1) the presence of additional competition reactions for the H_2ONO_2^+ intermediate, and 2) direct loss of gas- or aqueous-phase ClNO_2 via surface deposition/aerosol uptake and aqueous-phase reaction.

5.4.3 Sources of Parametrization-Box Model Differences

5.4.3.1 Observed Trends/Water Dependence

Of the aerosol components calculated or measured during WINTER, differences in parameterized and box model-derived $\phi(\text{ClNO}_2)$ were most strongly correlated with aerosol water (calculation described in Section 4.2.1). Table 5.1 shows that the largest correlation coefficients between parameterization-model differences and aerosol composition (for both PILS and AMS calculated parameterizations) were associated with aerosol water molarity ($r^2 = 0.54$ (AMS), 0.22 (PILS)), ambient RH ($r^2 = 0.53$ (AMS), 0.27 (PILS)), and aerosol liquid water content (water mass fraction) ($r^2 = 0.51$ (AMS), 0.21 (PILS)) (stronger correlations than $\gamma(\text{N}_2\text{O}_5)$ trends in Table 4.2). The only other parameters with correlation coefficients above 0.1 were with wet (including aerosol water) mass fractions of aerosol organics, sulfate, and ammonium. When eliminating the role of water, the dry (excluding water) mass fractions produced lower correlation coefficients ($r^2 \leq 0.05$)

for each of these species. Two previous field studies observed a negative correlation between absolute $\phi(\text{ClNO}_2)$ values (derived using the steady state of N_2O_5) and aerosol-phase nitrate mass (Wang, Z. et al., 2017), as well as reduced $\text{ClNO}_2/\text{N}_2\text{O}_5$ gas-phase ratios corresponding to aerosol with low Cl/organic mass ratios (Mielke et al., 2013). Neither of these studies quantitatively evaluated role of aerosol composition in the difference between parameterized and field-derived values. For comparison, WINTER box model $\phi(\text{ClNO}_2)$ values were only weakly correlated with Cl/organic mass ratio ($r^2 \leq 0.027$ for both chloride measurements) and showed an even weaker, positive correlation with aerosol phase nitrate mass ($r^2 = 0.024$).

Table 5.1. Correlations between $\phi(\text{ClNO}_2)$ parameterization-box model differences and aerosol composition factors. Correlation coefficients and trend signs are provided for parameterized values calculated with AMS (a) and PILS (b) particle chloride measurements. Data are for all box model results. N = 2884 for AMS parameterization, N = 3141 for PILS parameterization. All results are statistically significant.

Variable	(a)		(b)	
	Correlation Coefficient (r^2)	Correlation Sign	Correlation Coefficient (r^2)	Correlation Sign
1 Water Molarity	0.540	-	0.224	-
2 Ambient Relative Humidity	0.537	-	0.273	-
3 Liquid Water Content (Mass Fraction)	0.513	-	0.208	-
4 Organics Wet Mass Fraction	0.427	+	0.195	+
5 Ammonium Wet Mass Fraction	0.304	+	0.017	+
6 Sulfate Wet Mass Fraction	0.164	+	0.247	+
8 Ammonium Dry Mass Fraction	0.055	+	0.067	+
9 Sulfate Dry Mass Fraction	0.045	-	0.023	+
10 Nitrate, Wet Mass Fraction	0.045	+	0.010	-
11 Cl/NO ₃ ⁻ Molar Ratio (PILS)	0.033	-	0.087	+
12 Organics, Dry Mass Fraction	0.032	+	0.028	+
13 Cl/NO ₃ ⁻ Molar Ratio (AMS)	0.027	+	0.006	+
14 Organic/Sulfate Mass Ratio	0.015	+	0.001	-
15 Nitrate, Dry Mass Fraction	0.006	+	0.067	-
16 pH (full range)	0.002	+	0.085	-
17 Organics, O:C Ratio	0.002	-	0.004	-

The differences between parameterized and box model-derived $\phi(\text{ClNO}_2)$ are plotted against aerosol water molarity in Figure 5.9, for parameterized values calculated with both AMS (a) and PILS (b) chloride measurements. Trends in Figure 5.9 show negative correlations with aerosol water for points with aerosol chloride both above and below the instrument detection limits

(black and gray points, respectively). While quantitatively different slopes are derived from each fit, all trends (with AMS and PILS chloride, above and below detection limits) are qualitatively consistent, suggesting either aerosol water or an associated factor is an important predictor of the observed $\phi(\text{ClNO}_2)$ differences.

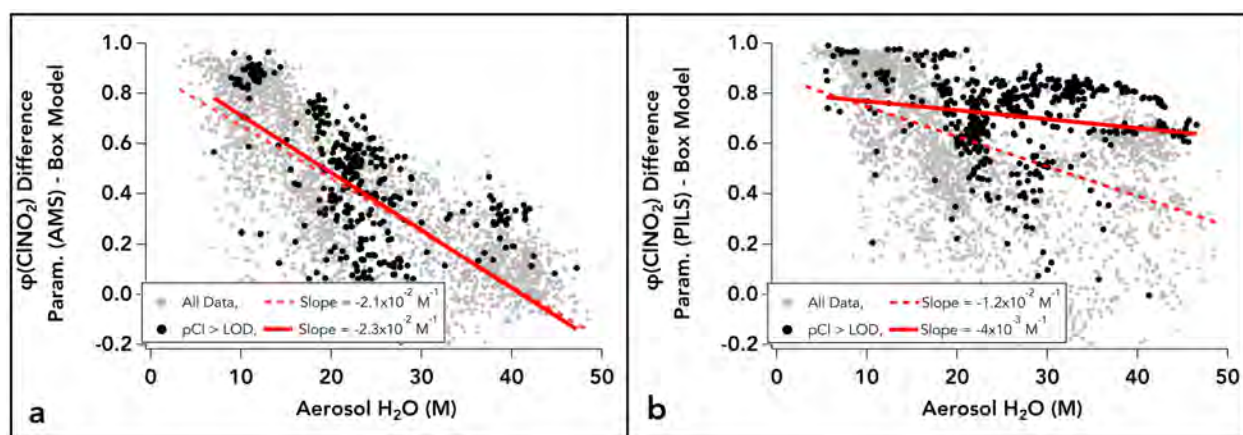


Figure 5.9. Difference between $\phi(\text{ClNO}_2)$ parameterization and box model results for WINTER, calculated using AMS (a) and PILS (b) particle chloride against aerosol water (inorganic component calculated by Hongyu Guo from ISORROPIA). Data above chloride detection limits shown in black points with the fit line slopes by solid lines. All data are shown in gray points with fit line slopes by dashed lines.

Based on the aqueous formation mechanism in R5.7 - R5.13, the role of water in the yield of ClNO_2 is to act in competition with aqueous-phase chloride for the H_2ONO_2^+ intermediate. This competition results in a decrease in parameterized $\phi(\text{ClNO}_2)$ values as water increases (Figure 5.10a and b). The opposite trend is observed for WINTER box model results, which show a positive correlation with water (Figure 5.10c), except for two research flights with the largest water concentrations (exceeding 40 [M]). Combined, these opposite trends with water lead to the negative slopes in Figure 5.9.

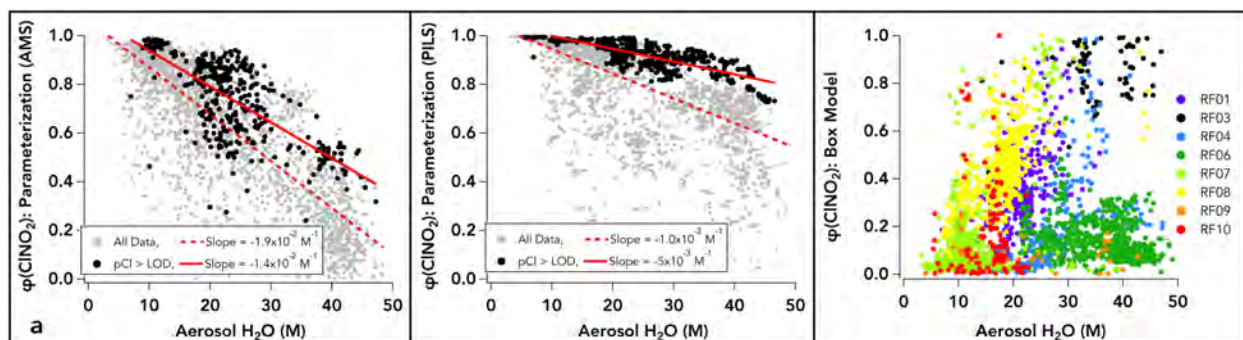


Figure 5.10. (a) Parameterized WINTER $\phi(\text{ClNO}_2)$ values (with AMS chloride) against aerosol water (inorganic component from ISORROPIA calculated by Hongyu Guo); (b) Parameterized WINTER $\phi(\text{ClNO}_2)$ values (with PILS chloride) against aerosol water. In both a and b, points above instrument LODs in black, all data in gray. Correlation fits in solid and dashed lines, respectively. (c) Box model derived WINTER $\phi(\text{ClNO}_2)$ values with aerosol water. Points colored by flight number according to legend.

The trend in Figure 5.9 is not the result of uncertainty in the water molarity calculation. For example, points below 20 M H_2O in Figure 5.9 would require H_2O concentrations in E5.5 more than 100 times larger, on average, to bring the parameterization into agreement with the box model results, well outside the $\sim 25\%$ uncertainty in $[\text{H}_2\text{O}]$. Disagreement with the box model at low aerosol water (and RH) may, therefore, suggest that laboratory-based parameterizations are not applicable to environments with limited aerosol water since they have largely been derived from studies conducted at either high relative humidity ($> 55\%$) or on aqueous solutions (Behnke et al., 1997; Bertram & Thornton, 2009; Roberts et al., 2009; Ryder et al., 2015). Correlations between aerosol water and box model $\phi(\text{ClNO}_2)$ values in Figure 5.10c, however, also show quantitatively different trends for each flight, suggesting that multiple factors may be contributing to the discrepancy. The only other field study to examine the $\phi(\text{ClNO}_2)$ relationship with water showed no trend between RH values of ~ 65 and 90% (Phillips et al., 2016) (corresponding to WINTER water concentrations of ~ 20 - 45 M). As WINTER is the first study to report a positive water dependence in $\phi(\text{ClNO}_2)$, further studies of ClNO_2 production under a range of aerosol water conditions will be required to confirm this result.

The physical mechanism for the observed box model trend with water is uncertain, but may be related to the availability of chloride, as discussed previously as a possible cause of $\phi(\text{ClNO}_2)$ suppression in field-derived results (e.g. Mielke et al., 2013). Current $\phi(\text{ClNO}_2)$ parameterizations assume internally-mixed aerosol where all Cl^- is readily available for reaction, which may not be the case for ambient aerosol. For example, measured particle chloride may not be present equally throughout the particle size distribution, an effect that would increase the parametrized $\phi(\text{ClNO}_2)$ values if the largest chloride concentrations were present in a different size range than the particles contributing the most to surface area density (i.e. participating in N_2O_5 uptake). Based on the measured aerosol size distributions by the UHSAS (0.06-1 μm) and PCASP (1-3 μm) during WINTER, the median of the aerosol surface area distribution ($dS/d\log D_p$) corresponded to particle diameters between 0.12 and 0.3 μm , for the data shown in Figure 5.7. The size distribution of total particle chloride, however, was not reported during WINTER and cannot be further evaluated as a possible source of observed parameterization – box model discrepancy.

Additionally, even if particle chloride is distributed evenly throughout the size distribution, it may not be accessible within the aerosol itself. For example, previous studies have found that aqueous Cl^- has a propensity to partition away from the surface (e.g. Cummings & Wick, 2013) and that submicron sea salt aerosol may form organic coatings (Ault et al., 2013), especially when aged (Laskin et al., 2012). Limited amounts of absolute aerosol water could also reduce the mobility of aqueous-phase Cl^- through RH- and composition-dependent changes in aerosol phase or viscosity (e.g. Shiraiwa et al., 2017) and/or aerosol liquid-liquid phase separations (e.g. Bertram et al., 2011). Each of these processes would serve to limit the availability of Cl^- at the aerosol surface. This may reduce field-derived $\phi(\text{ClNO}_2)$ values relative to parameterizations if N_2O_5 dissociation and reaction occurs near the surface, physically removed from Cl^- residing in the bulk.

Changes in aerosol phase and morphology (i.e. core-shell) were not measured during WINTER, and as a result, parameterizations for each are attempted here. Shiraiwa et al. (2017) have recently proposed a parameterization for the aerosol glass transition temperature, which can be used to predict the temperature at which aerosol transition from an aqueous to highly viscous (i.e. glassy) phase. This parameterization, however, requires knowledge of aerosol organic molecular composition, which was not measured during WINTER. Alternatively, Bertram et al. (2011) proposed a parameterization to predict the humidity at which an aerosol liquid-liquid phase separation would occur, based on ambient relative humidity and aerosol O:C ratio. Applied to WINTER data, this parameterization is shown by the black line in Figure 5.11, below which, phase separation is predicted. WINTER data are also shown in Figure 5.11 for comparison, colored by the parameterization-box model $\phi(\text{ClNO}_2)$ difference. Results in Figure 5.11 shows that, while some WINTER data are predicted to be phase-separated (below the SRH line), these data do not consistently correspond to largest parameterization-box model differences (red points). Therefore, while chloride availability has been discussed in previous field studies as a possible cause of model-parameterization discrepancies (Mielke et al., 2013; Phillips et al., 2016; Wang, Z. et al., 2017), field-based evidence, including from this study, remain inconclusive.

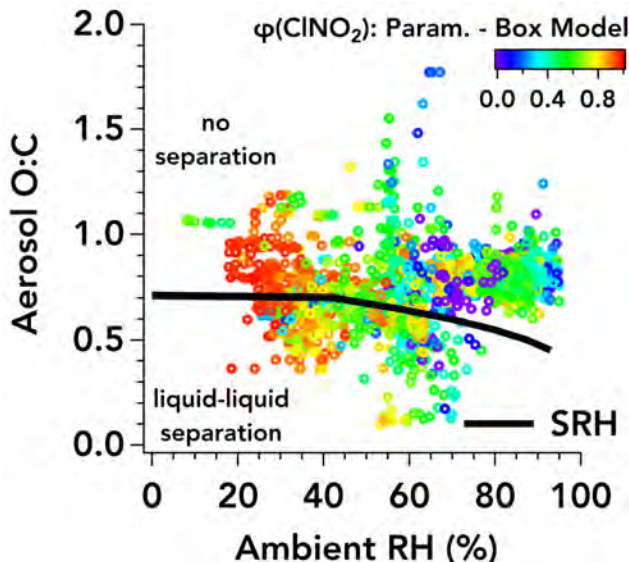
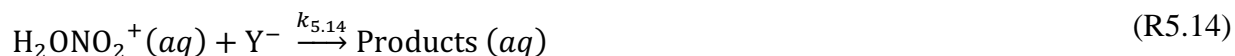


Figure 5.11. Aerosol O:C ratio (from the AMS) vs. the ambient relative humidity. Black line is the parameterized RH where liquid-liquid organic coatings are predicted (separation relative humidity (SRH)) following Bertram et al. (2011). Data below the SRH are predicted to have liquid-liquid separations. Data are colored by difference between parameterized $\phi(\text{ClNO}_2)$ values (Bertram & Thornton, 2009) and those predicted by the box model.

5.4.3.2 Additional Aqueous Competition Reactions

Reaction between the H_2ONO_2^+ intermediate and species other than Cl^- and H_2O could additionally contribute to the observed suppression of $\phi(\text{ClNO}_2)$ on ambient aerosol. Such a process would add an additional competition reaction in the form of R5.14 to the mechanism in R5.7- R5.13. In order for a reaction of this form to compete with aqueous Cl^- and cause a reduction in ClNO_2 production relative to N_2O_5 uptake, the product of $k_{5.14}$ and the concentration of additional reactive compound(s) would have to be comparable to $k_{5.12}[\text{Cl}^-]$. In addition, agreement between the box model $\phi(\text{ClNO}_2)$ and two nitrate-dependent observational methods in Section 5.3.2, suggest that this reaction would also have to produce particle-phase nitrate or gas-phase HNO_3 to maintain consistency between the observational methods.



Previous studies have reported evidence of a competition between particle-phase chloride and halogens. For example, enhanced Br_2 formation relative to ClNO_2 has been observed on ice at $\text{Cl}^-:\text{Br}^-$ ratios < 30 (Lopez-Hilfiker et al., 2012). In addition, reaction of N_2O_5 with dilute NaI and NaBr solutions has shown production of BrNO_2 , Br_2 , and I_2 (Behnke et al., 1994; Schweitzer et al., 1998). While the latter studies do not show direct competition with Cl^- , the stronger nucleophilic character of Br^- and I^- relative to Cl^- may allow for efficient competition. Ambient Br^- and I^- concentrations in sea water (expected $\text{Cl}^-:\text{Br}^-:\text{I}^-$ ratios of $\sim 1:1 \times 10^{-3}:1 \times 10^{-6}$), however, may be too small to compete with Cl^- via R5.14 and these species may alternatively reduce $\phi(\text{ClNO}_2)$ via direct reaction with ClNO_2 , further discussed in the following section. In addition, these reactions may not lead to the production of NO_3^- or HNO_3 (e.g. BrNO_2 formation), making their presence potentially inconsistent with the previous observationally-based methods (Figure 5.5), which incorporate nitrate mass balance between N_2O_5 , particulate nitrate, HNO_3 , and ClNO_2 .

Additional studies have also found efficient reaction between the nitronium ion and aqueous-phase aromatics (Hoggett et al., 1971; Lüttke et al., 1997; Schofield, 1980; Taylor, 1990). Experiments focused specifically on reactions with a subset of phenols (Heal et al., 2007) derived $k_{5.14}/k'_{5.11}$ ratios (between 278 and 293 K and 6 and 10 pH) that correspond to $k_{5.14}/k_{5.11}$ ratios (for average WINTER aerosol water concentrations (Chapter 4)) over an order of magnitude larger than the reported ratios of $k_{5.12}/k_{5.11}$ (Behnke et al., 1997; Bertram & Thornton, 2009; Roberts et al., 2009; Ryder et al., 2015) (further details Appendix C2). Additionally, flow tube reactions of N_2O_5 uptake onto sea-water mimics (Ryder et al., 2015) showed that both phenol and humic acid at low concentrations (< 10 mM) could cause significant reductions in $\phi(\text{ClNO}_2)$ relative to pure NaCl solutions, which may result from both a large $k_{5.14}$ reaction rate constant and enhanced surface concentration of organics relative to chloride (Ryder et al., 2015). Combined, these past

results suggest that even at low organic concentrations, additional competition reactions, generalized by R5.14, could effectively compete with R5.12 and decrease the ClNO₂ production yield relative to that expected from Cl⁻ and water alone. These reactions may also lead to aerosol-phase NO₃⁻, organic nitrates, or HNO₃, maintaining consistency with observational derivations. While AMS measurements of total nitrate during WINTER did show evidence for the presence of organic nitrates, the calculated ‘inorganic-only’ nitrate (scaled to PILS-IC measurements; see (Schroder et al., submitted, 2018)) was consistently the largest fraction of total nitrate measured.

To examine whether there is evidence in the WINTER data to support competition reactions, an additional expression for $\phi(\text{ClNO}_2)$ was derived from R5.9 - R5.12 and R5.14, shown in E5.6, assuming the H₂ONO₂⁺ intermediate is in steady state (see derivation in Appendix C1). Rearranging this expression, a plot of $(\phi(\text{ClNO}_2)^{-1} - 1) * [\text{Cl}^-]/[\text{H}_2\text{O}]$ against $[\text{Y}^-]:[\text{H}_2\text{O}]$ should yield a linear correlation with slope of $k_{5.14}/k_{5.12}$ and intercept of $k_{5.11}/k_{5.12}$. The identity of Y⁻ is unknown, but it could include aqueous-phase species such as organics, halogens, and/or additional anions such as SO₄²⁻, though previous studies on dilute (NH₄)₂SO₄ and (NH₄)HSO₄, chloride containing solutions did not show a suppression in $\phi(\text{ClNO}_2)$ relative to the parameterization (Roberts et al., 2009). To maintain consistency between the box model and other observational methods, these reactions would also need to produce either particle or gas-phase nitrate.

$$\phi(\text{ClNO}_2) = \frac{1}{\left(1 + \frac{k_{5.11}[\text{H}_2\text{O}]}{k_{5.12}[\text{Cl}^-]} + \frac{k_{5.14}[\text{Y}^-]}{k_{5.12}[\text{Cl}^-]}\right)} \quad (5.6)$$

Figure 5.12 shows the correlation between $(\phi(\text{ClNO}_2)^{-1} - 1) * [\text{Cl}^-]/[\text{H}_2\text{O}]$ and molar ratios of (a) SO₄²⁻:H₂O and (b) Org:H₂O (assuming a constant molecular weight of 120 g mol⁻¹). Additional correlations with Br⁻ reaction product, Br₂ (e.g. Behnke et al., 1994; Schweitzer et al., 1998) (BrNO₂ not present above instrument LOD), measured by the I-TOF-CIMS, was not statistically

significant (not shown). The fit results in Figure 5.12 provide mixed evidence for the presence of their competition with Cl^- via R5.14 during WINTER. The positive correlations are consistent with competition with Cl^- , with a rate constant ($k_{5.14}$) 3-25 \times larger than $k_{5.12}$ (Figure 5.12). The negative fit intercepts, however, also indicate that this model for $\phi(\text{ClNO}_2)$ is incorrect when using SO_4^{2-} and total aerosol organics as Y^- . It is possible, however, that the negative intercepts could result from multiple competition reactions of different rates (i.e. with various organic components) and/or additional processes that cause suppression.

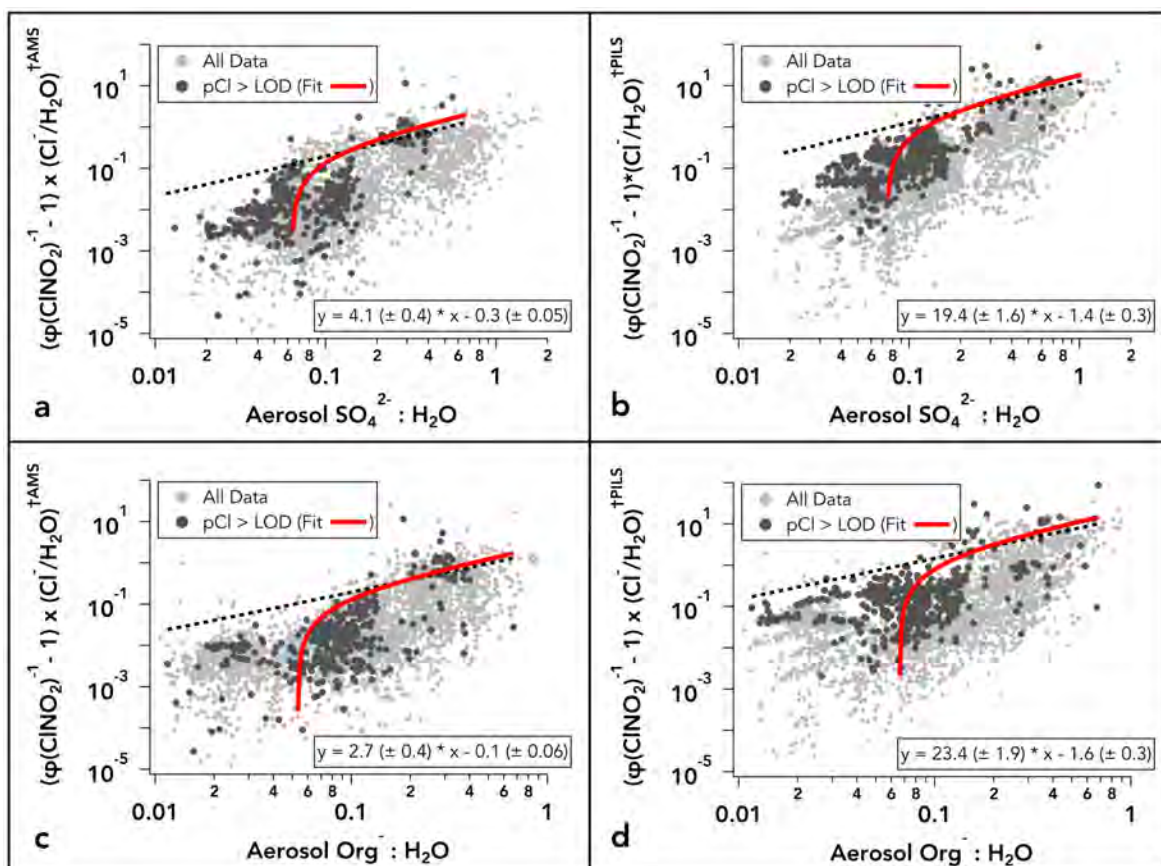


Figure 5.12. Correlation of $(\phi(\text{ClNO}_2)^{-1} - 1) * [\text{Cl}^-]/[\text{H}_2\text{O}]$ product from E5.6 against aerosol $\text{SO}_4^{2-}:\text{H}_2\text{O}$ molar ratio in (a) and (b) and $\text{Org}:\text{H}_2\text{O}$ molar ratio in (c) and (d), calculated using AMS and PILS chloride measurements. Points with $p\text{Cl} > \text{LOD}$ are in dark gray. Red lines are the linear fits with fit equations provided in each figure. From E5.6, slopes are the $k_{5.14}/k_{5.12}$ ratio and intercepts are the $k_{5.11}/k_{5.12}$ ratio. Dashed lines represent the same fits, holding the intercept constant at 0.002 (from Bertram & Thornton, 2009). Organic molarity calculated by applying a constant molecular weight of 120 g mol^{-1} to AMS organic mass concentration measurements. Larger y -values correspond to smaller values of box model $\phi(\text{ClNO}_2)$.

Alternatively, the hypothesis of a competition reaction can be tested by fitting the $[Y^-]:[Cl^-]$ ratio in E5.6 to WINTER box model $\phi(ClNO_2)$ values. This method does not require knowledge of Y^- and estimates the $[Y^-]:[Cl^-]$ ratio that would be required to explain the observed $\phi(ClNO_2)$ values via R5.14 by using the $k_{5.11}/k_{5.12}$ ratio of 0.002 from Bertram and Thornton (2009) and a $k_{5.14}/k_{5.12}$ ratio of 1. This method largely follows the work of Ryder et al. (2015) who required a molar ratio of at least 2 to explain their observed $\phi(ClNO_2)$ values on ambient sea water samples, assuming $k_{5.14}/k_{5.12} = 1$. The ratio required here to reproduce WINTER data ranged from 0 to > 100, with a median of 6.0 and 4.2 for calculations with PILS and AMS chloride, respectively. For comparison, the median molar ratios of $SO_4^{2-}:Cl^-$ and $Org^-:Cl^-$ during WINTER were between 7-25 and 5-23, respectively, but also with values in exceedance of 100.

This analysis provides mixed evidence for the presence of a competition reaction between Cl^- and an additional reactive aqueous-phase compound. The positive correlations between $(\phi(ClNO_2)^{-1} - 1) * [Cl^-]/[H_2O]$ and molar ratios of $SO_4^{2-}:H_2O$ and $Org^-:H_2O$ are consistent with such reactions, but the intercepts that do not reproduce $k_{5.11}/k_{5.12}$ in E5.6 suggest that the model is either: 1) incorrect for sulfate and organics or 2) that there are multiple reactions and/or additional processes contributing to the observed $\phi(ClNO_2)$ suppression. Taking the $k_{5.14}/k_{5.12}$ ratio in E5.6 as 1, the compound in question would require molar ratios in excess of 100 relative to Cl^- to explain the lowest $\phi(ClNO_2)$ values. Many of the box model $\phi(ClNO_2)$ values, however, could be reproduced with much more moderate molar ratios of ~ 6 . Further laboratory studies focused on the aqueous kinetics of $H_2ONO_2^+$ will be required to assess the extent to which a process such as a competition reaction can explain the difference between observed and parameterized $\phi(ClNO_2)$.

5.4.3.3 Direct ClNO₂ loss

Lastly, direct loss of aqueous or gas-phase ClNO₂ could additionally reduce modeled $\phi(\text{ClNO}_2)$ values relative to parameterizations. In the box model calculation of $\phi(\text{ClNO}_2)$, values were derived by iteratively fitting the model output to gas-phase observations of N₂O₅ and ClNO₂. This method is based on the assumption that aqueous-phase ClNO₂ from reaction R5.12 does not react further and efficiently evaporates to the gas-phase based on the low solubility of ClNO₂ ($K_H = 4 \times 10^{-2} \text{ M atm}^{-1}$ (e.g. Frenzel et al., 1998; Roberts et al., 2008)), where it is stable throughout the night. Additional direct loss mechanisms of ClNO₂, independent from N₂O₅, would therefore serve to reduce the net $\phi(\text{ClNO}_2)$ derived by the model. Possible direct loss mechanisms could include: 1) gas-phase ClNO₂ loss through surface deposition and/or aerosol uptake, and 2) direct aqueous-phase reaction prior to evaporation.

Surface deposition and/or aerosol uptake of ClNO₂ would serve to reduce the box-model calculated $\phi(\text{ClNO}_2)$ by reducing ambient gas-phase ClNO₂ and the subsequently-derived ClNO₂ production rate constant (k_{ClNO_2}). The effect of ClNO₂ loss from aerosol uptake is expected to be small as uptake coefficients ($\gamma(\text{ClNO}_2)$) have been measured on the order of 1×10^{-5} (e.g. Schweitzer et al., 1998). Adjusting the box model-derived k_{ClNO_2} in E5.1 for loss associated with an uptake coefficient of this magnitude increased the median box model $\phi(\text{ClNO}_2)$ value by 1%. The potential loss of ClNO₂ through ocean surface deposition has been discussed previously in Sections 5.2.2 and 2.4.2.7.11. Though box model simulations were limited to the RL, increased mixed-layer depths over the ocean allow for possible air-sea exchange of N₂O₅ and ClNO₂ on WINTER flights over marine environments (Figure 5.1). While ocean emission of ClNO₂ may be expected based on the positive water dependence of N₂O₅ uptake (Section 4.4.2.3) and typical ocean salinity ($\sim 0.55 \text{ M } [\text{Cl}^-]$), previous observations of N₂O₅ and ClNO₂ from the Scripps

Institution of Oceanography (SIO) pier by Kim et al. (2014) found a net depositional flux of both N_2O_5 and ClNO_2 to the ocean surface. As previously discussed in Section 5.2.2, adjusting the box model ($k_{\text{N}_2\text{O}_5}$ and k_{ClNO_2}) results for deposition of both N_2O_5 and ClNO_2 could reduce, but not entirely eliminate the parameterization-box model differences (Figure 2.35). Combined, these results suggest that possible gas-phase ClNO_2 loss through aerosol uptake and/or ocean surface deposition may contribute to the low box model $\phi(\text{ClNO}_2)$ values, but are not the only cause.

Direct loss of aqueous-phase ClNO_2 could also reduce the modeled $\phi(\text{ClNO}_2)$ values relative to parameterizations. This could occur through direct aqueous-phase reaction with species X^- , as generalized in reaction R5.15. Though difficult to directly probe with WINTER field data, the possibility of direct ClNO_2 reaction can be evaluated using the potential reaction products from R5.15 and associated variables. For example, previous laboratory studies have identified reaction mechanisms for R5.15 that form halogenated products such as Br_2 , BrNO_2 (Fickert et al., 1998; Frenzel et al., 1998; Schweitzer et al., 1998; Schweitzer et al., 1999), or Cl_2 , the latter of which is facilitated by particle acidity (Roberts et al., 2008). ITOF CIMS observations of BrNO_2 did not exceed the instrument detection limit during WINTER (1s, 1σ of 1 pptv) and no statistically significant correlations were found between WINTER $\phi(\text{ClNO}_2)$ observations (or box model – parameterization differences) and ITOF-CIMS observations of Br_2 or Cl_2 (above their 1s, 1σ detection limits of 0.5 pptv and 0.4 pptv, respectively). In addition, a negative correlation ($p < 0.05$) was observed between particle acidity and Cl_2 , opposite of the expected trend from Roberts et al. (2008), despite high acidity calculated for aerosol during WINTER ($\text{pH} \sim -2$ to 3 (Guo et al., 2016)).



Without further knowledge of the identity of species X^- and/or possible reaction products, the possibility of R5.15 can be evaluated using the $\phi(\text{ClNO}_2)$ expression in E5.7, derived from aqueous-phase reactions R5.9 - R5.12 and R5.15, assuming H_2ONO_2^+ is in steady state, and that aqueous-phase ClNO_2 is lost via R5.15 before it can partition to the gas-phase via R5.13 (derivation in Appendix C1). Using E5.7, the $k_{5.15}[X^-]$ (s^{-1}) product required to reproduce box model values was calculated for each point using values of $\frac{k_{5.11}}{k_{5.12}}$ (0.002), $\frac{k_{5.12}}{k_{5.10}}$ (29), and $k'_{5.9}$ expression from Bertram and Thornton (2009), along with estimates of aqueous-phase concentrations of N_2O_5 and ClNO_2 from measured gas-phase mixing ratios and Henry's Law constants of 51 (unitless) (Fried et al., 1994) and $4 \times 10^{-2} \text{ M atm}^{-1}$ (Frenzel et al., 1998; Roberts et al., 2008), respectively. Derived $k_{5.15}[X^-]$ values suggest that reproduction of the box model values by invoking direct ClNO_2 loss in E5.7 would require $k_{5.15}[X^-]$ products between 1×10^5 and $8 \times 10^9 \text{ s}^{-1}$ for both AMS and PILS chloride. Assuming a larger solubility for N_2O_5 of 5 M atm^{-1} (e.g. Griffiths et al., 2009; Mentel et al., 1999) would require even larger values of $k_{5.15}[X^-]$. Based on these results, the largest parameterization-box model differences (requiring the largest $k_{5.15}[X^-]$ values) would, therefore, require reaction rate constants near the diffusion controlled limit ($\sim 1 \times 10^9 \text{ M}^{-1} \text{ s}^{-1}$), or aqueous concentrations of $[X^-]$ greater than 1 M. Median differences, however, could be reproduced with more moderate $k_{5.15}[X^-]$ values of 9×10^7 and $1 \times 10^8 \text{ s}^{-1}$ for calculations with AMS and PILS chloride, respectively.

$$\phi(\text{ClNO}_2) = \frac{1}{\left(1 + \frac{k_{5.11}[\text{H}_2\text{O}]}{k_{5.12}[\text{Cl}^-]}\right)} - \frac{k_{5.15}[X^-][\text{ClNO}_2]_{aq}}{k'_{5.9}[\text{N}_2\text{O}_5]_{aq} \left(1 - \frac{1}{\frac{k_{5.11}[\text{H}_2\text{O}]}{k_{5.10}[\text{NO}_3^-]} + 1 + \frac{k_{5.12}[\text{Cl}^-]}{k_{5.10}[\text{NO}_3^-]}}\right)} \quad (5.7)$$

Results in this section are consistent with the possibility that direct loss of gas- and/or aqueous-phase ClNO₂ could contribute to some of the smaller parameterization – box model differences found in WINTER data. Agreement between box model and parameterized $\phi(\text{ClNO}_2)$ values improved when considering the possibility of surface deposition of both gas-phase ClNO₂ and N₂O₅ (Figure 2.35), though box model median values remained lower than the parameterized equivalents. The addition of gas-phase loss through ClNO₂ aerosol uptake only increased median $\phi(\text{ClNO}_2)$ by 1% when considering an uptake coefficient of 1×10^{-5} . The possible identify of species X⁻ in R5.15 remains unknown. Low di-halogen concentrations do not provide evidence of direct loss through reactions with halogens, despite the highly-acidic WINTER aerosol. Results from calculating $k_{R4.9}[\text{X}^-]$ in E5.7 suggest that direct aqueous loss of ClNO₂ vis R5.15 would require concentrations of species $[\text{X}^-] > 1 \text{ M}$ and/or reaction rate constants near the diffusion-limited rate to reproduce the lowest box model $\phi(\text{ClNO}_2)$ values. Without additional information about WINTER aerosol composition or other possible aqueous-phase ClNO₂ reactions, the possibility of direct aqueous-phase ClNO₂ loss during WINTER cannot be further evaluated.

5.5 Conclusions and Future Work

A box model analysis of 9 night flights during the 2015 WINTER aircraft campaign derived 3425, individual determinations of $\phi(\text{ClNO}_2)$ with a median value of 0.138 (1 σ : +0.050/-0.045) and a range from 0.003 to 1. While the yield of ClNO₂ production is thought to depend on the presence of aqueous-phase chloride and thus the proximity to chloride emission sources, WINTER $\phi(\text{ClNO}_2)$ values over the ocean showed a similar range to those derived from continental flights, likely due to sampling continental outflow over the ocean. Comparison of a subset of WINTER box model $\phi(\text{ClNO}_2)$ values to those calculated with two other commonly used methods, showed agreement between their predicted median values, within the uncertainty of each

method. In contrast, parameterization of WINTER $\phi(\text{ClNO}_2)$ values predicted a median value over a factor of two larger than all other methods and outside the bounds of the combined uncertainties for two. Expanding the comparison to all box model values confirms that parameterized values, calculated with both AMS and PILS particle chloride, are upper limits to $\phi(\text{ClNO}_2)$ on ambient aerosol. Parameterized $\phi(\text{ClNO}_2)$ values over-predicted $\geq 90\%$ of the box model derived values for points both above and below particle chloride instrument detection limits and over 75% when additionally considering the lower parameterization limit, accounting for particle chloride and water uncertainties. This result is qualitatively consistent with all previous studies that have compared field-derived and parameterization-predicted $\phi(\text{ClNO}_2)$ values. When considering total box model error, upper limit estimates of median $\phi(\text{ClNO}_2)$ values remained lower than their parameterized equivalents (considering both chloride measurements), suggesting the presence of at least one physiochemical process causing $\phi(\text{ClNO}_2)$ suppression on ambient aerosol relative laboratory-tested chloride-containing solutions.

Processes related to the observed parameterization – box model differences were assessed using ambient observations of aerosol composition and mechanistic processes that have been discussed in previous laboratory and field-based literature. The observed difference between parameterized and modeled $\phi(\text{ClNO}_2)$ values was most strongly correlated with calculated aerosol water, with differences decreasing with increases in aerosol water molarity, liquid water content, and relative humidity. This trend is caused by the opposite water dependences predicted by parameterizations (decreasing with water due to a competition between R5.11 and R5.12) and box model results (increasing with water) and is not driven by uncertainties in the aerosol water calculation. The positive dependence observed in box model results may be related to the physical availability of chloride, though a parameterization of aerosol phase-separations did not

consistently predict core shell morphology at the lowest water concentrations. The only other study to compare field-derived $\phi(\text{ClNO}_2)$ values to relative humidity observed no trend over the limited range of 65 – 90% RH. As WINTER results are the first to show a positive water dependence in $\phi(\text{ClNO}_2)$ and the mechanism remains unclear, further laboratory studies of ClNO_2 formation conducted over a wide range of aerosol water concentrations are required to confirm the observed water dependence. In addition, the relatively low correlation coefficients between $\phi(\text{ClNO}_2)$ differences and aerosol water (≤ 0.53), indicate that multiple factors may lead to suppression relative to parameterized results.

The presence of additional aqueous-phase competition reactions (R5.14) and/or direct ClNO_2 loss through deposition/uptake or direct aqueous-phase reaction (R5.15) could also suppress $\phi(\text{ClNO}_2)$ relative to laboratory parameterizations. Both processes have been observed in previous laboratory studies and are discussed in previous literature as possible causes of the low field-derived $\phi(\text{ClNO}_2)$ values. Competition reactions and direct aqueous-phase loss were evaluated by appending additional reactions to the original aqueous-phase ClNO_2 formation mechanism and deriving updated expressions for $\phi(\text{ClNO}_2)$ (E5.6 - E5.7). By invoking an additional competition reaction between Cl^- and an aqueous-phase compound $[\text{Y}^-]$, the Y^-/Cl^- molar ratio would need to be >100 to explain the greatest differences between parameterized and box model derived $\phi(\text{ClNO}_2)$ values. Previous laboratory studies have shown $\phi(\text{ClNO}_2)$ suppression and efficient competition reactions with halogens and aromatics, but observed no suppression on dilute SO_4^{2-} containing solutions. Assessing the role of SO_4^{2-} and organics as the potential compound Y^- produced mixed results that suggest these species are not in competition with Cl^- via R5.14 or that there are multiple, overlapping processes leading to the observed suppression. Low halogen concentrations did not yield statistically significant results. Similarly,

incorporation of direct aqueous-phase ClNO_2 loss (through direct reaction with species X^- in R5.15) into the reaction mechanism suggested that the largest parameterization – model differences would either require reaction rate constants near the diffusion limit, or concentrations of X^- greater than 1 M. Past laboratory studies have found efficient ClNO_2 reaction on dilute halogen containing solutions and acidic aerosol, though a lack of correlation between $\phi(\text{ClNO}_2)$ and expected reaction products during WINTER do not support these results. Additional evaluation of depositional losses by surface deposition or aerosol uptake indicated that these gas-phase loss processes could not explain the largest parameterization – box model differences.

WINTER box model results here are consistent with an additional process, such as direct gas/aqueous-phase ClNO_2 loss and/or competition reactions with additional reactive aerosol components, contributing to the observed differences with values predicted by current parameterizations. The greatest differences, however, occurred at the lowest concentrations of aerosol water, suggesting a dependence of $\phi(\text{ClNO}_2)$ on aerosol water that is not currently captured in $\phi(\text{ClNO}_2)$ parameterizations. Mechanistic identification of this and other possible factors leading to $\phi(\text{ClNO}_2)$ suppression will be required to develop a robust parameterization that can help improve model predictions of ClNO_2 formation from N_2O_5 heterogeneous uptake, and lead to a better understanding of the halogen influence on tropospheric chemistry.

Chapter 6: Evaluating the contribution of nocturnal heterogeneous reactive nitrogen chemistry to particulate matter formation during winter pollution events in Northern Utah

Abstract

This analysis presents aircraft and ground-based observations from the 2017 Utah Winter Fine Particulate Study, based out of Salt Lake City, Utah. Mountain basins in Northern Utah, including Salt Lake Valley (SLV), suffer from wintertime air pollution events associated with stagnant atmospheric conditions that cause total particulate matter concentrations ($PM < 2.5 \mu m$ in diameter) to exceed national ambient air quality standards. Effective PM mitigation requires identification of ambient aerosol composition and the sources and chemistry of its precursors. Previous studies in SLV have found that $PM_{2.5}$ is primarily composed of ammonium nitrate (NH_4NO_3), and while nocturnal heterogeneous chemistry has been suggested as a dominant wintertime source in other western U.S. basins, the role of this chemistry in Utah has not been quantified. Vertically resolved measurements confirm that $PM_{2.5}$ is principally composed of NH_4NO_3 during wintertime pollution events in SLV and that formation is largely limited by available HNO_3 , though periods of NH_3 -limitation were also observed near the surface. Additional observation and box-model analyses quantify the factors controlling the nitrate contribution from heterogeneous chemistry, including the NO_3 production rate, N_2O_5 heterogeneous uptake coefficient ($\gamma(N_2O_5)$), and production yield of $ClNO_2$ relative to HNO_3 ($\phi(ClNO_2)$), with medians during pollution events of $0.37 \text{ ppbv hr}^{-1}$, 0.071, and 0.220, respectively. Finally, observationally-

constrained simulations suggest that heterogeneous chemistry produce an average of $13 \mu\text{g m}^{-3}$ of nitrate per night (67% of projected total morning nitrate) during pollution events, which is the best estimate to-date of the contribution of heterogeneous chemistry to PM formation in the SLV non-attainment region.

This Chapter is in preparation for an upcoming peer-reviewed publication to be submitted to *Atmospheric Chemistry and Physics*, entitled: Evaluating the contribution of nocturnal heterogeneous reactive nitrogen chemistry to particulate matter formation during wintertime pollution events in Northern Utah.

6.1 Introduction

Over 80% of Utah's population lives in counties that experience periods of elevated fine particulate matter ($\text{PM}_{2.5} < 2.5 \mu\text{m}$ in diameter) during the winter season (U.S. Census Bureau, 2018; Whiteman et al., 2014). During Utah winters, highest observed $\text{PM}_{2.5}$ levels are limited to three northern valleys along the western side of the Wasatch Mountains (Wasatch Front), shown in Figure 6.1 (north to south: Cache Valley (Logan Non-attainment area (NAA)), Salt Lake Valley (Salt Lake NAA), and Utah Valley (Provo NAA)). These valleys were designated by the U.S. EPA as "Moderate" non-attainment areas in December 2009, with the Salt Lake and Provo areas reclassified from moderate to "Serious" in May 2017 (Utah Department of Environmental Quality). Elevated $\text{PM}_{2.5}$ concentrations in these regions impact public health and are associated with increases in emergency room visits for asthma (Beard et al., 2012). Short-term exposure has also been shown to increase the chance of triggering acute ischemic heart disease events by 4.5%-6% per $10 \mu\text{g m}^{-3}$ of $\text{PM}_{2.5}$ in sensitive populations living in the Wasatch Front (Pope et al., 2006; Pope et al., 2015)

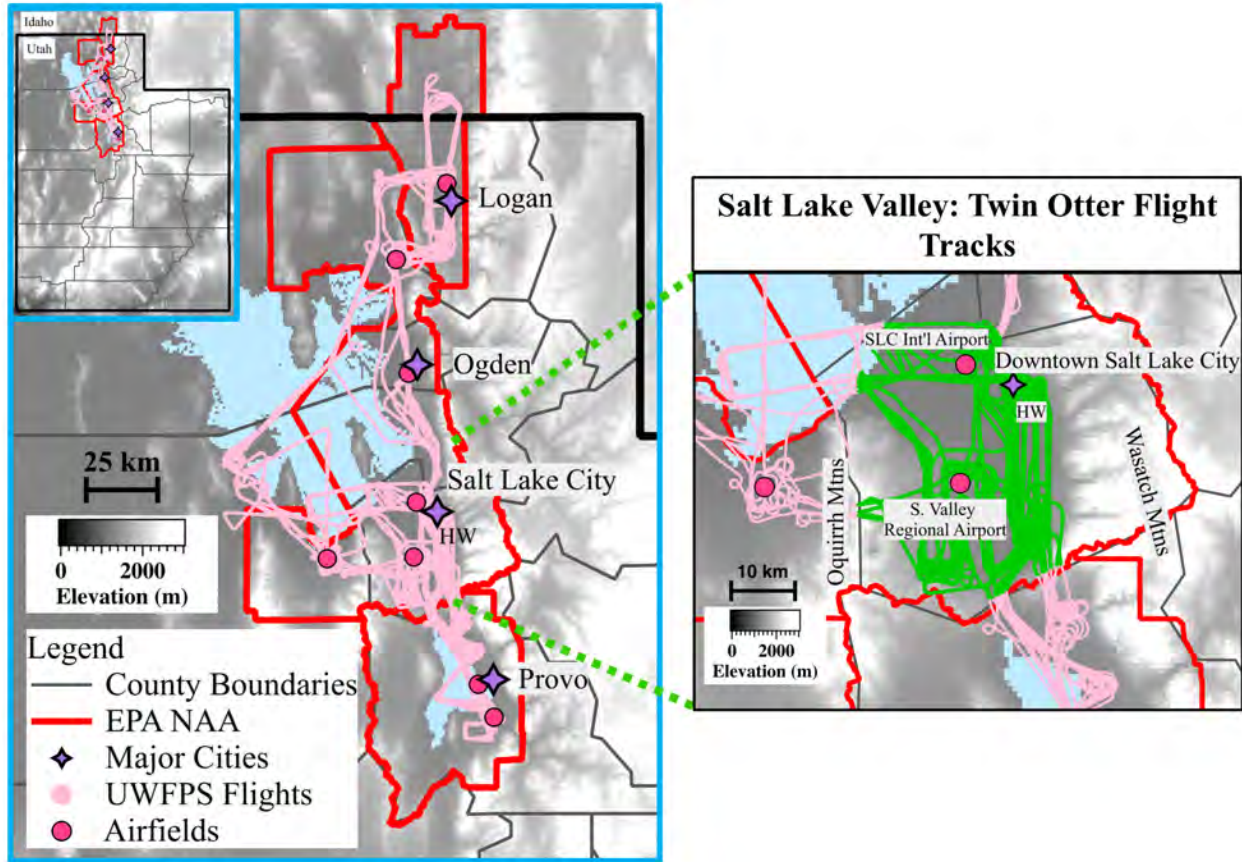


Figure 6.1. Left) Elevation Map of Utah’s Wasatch Front Range (Utah State in insert), with the Great Salt Lake (north) and Utah Lake (south) shown in blue, and county borders in black. U.S. EPA designated non-attainment areas (NAA) for $PM_{2.5}$ are shown in red. From north to south these include the Logan NAA: “Moderate” status, Salt Lake City NAA: “Serious” status, and Provo NAA: “Serious” status. UWFPS flight tracks are shown in pink. Purple markers indicate the locations of major cities, including Logan in Cache Valley, Salt Lake City in Salt Lake Valley, and Provo in Utah Valley. The location of missed approaches conducted with the TO are shown in dark pink circles. The Hawthorne measurement site in Salt Lake Valley is labeled as HW. Right) Zoomed in view of Salt Lake Valley with flight data for this analysis highlighted in green.

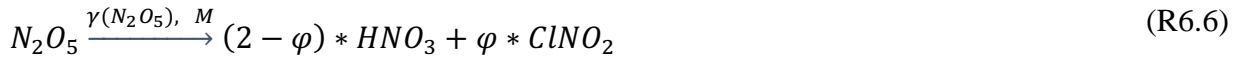
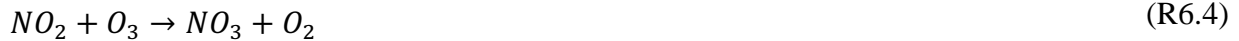
Elevated wintertime $PM_{2.5}$ concentrations in these valleys typically correspond to multi-day events of high atmospheric stability (e.g. Baasandorj et al., 2017; Gillies et al., 2010; Green et al., 2015; Silcox et al., 2012; Silva et al., 2007; Wang et al., 2012; Whiteman et al., 2014), associated with large, synoptic-scale high-pressure systems that transit from west to east, simultaneously impacting multiple basins across the Intermountain western U.S. (e.g. Reeves & Stensrud, 2009). Warm temperatures aloft cause boundary layer stratification that reduce mixing and trap cold air and emissions near the surface (Figure 1.3). These events, termed persistent cold

air pools (PCAPs), typically mix-out after 1-5 days but have been observed to persist as long as 18 days (Whiteman et al., 2014). Similar meteorological patterns have been linked to wintertime $PM_{2.5}$ accumulation in basins across the western U.S. (e.g. Chen et al., 2012; Green et al., 2015). During past PCAP and pollution events in Utah, data reported from ground-based measurements in Salt Lake Valley (SLV) have reported day to day build-up rates of total $PM_{2.5}$ mass in the range of $\sim 6\text{-}10 \mu\text{g m}^{-3} \text{ day}^{-1}$ (Baasandorj et al., 2017; Silcox et al., 2012; Whiteman et al., 2014) before plateauing after ~ 6 days into an event (Baasandorj et al., 2017). Average 24-hour concentrations reported during PCAP events between 2001 and 2016 have been as large as $40\text{-}80 \mu\text{g m}^{-3}$ in Salt Lake (Baasandorj et al., 2017; Silcox et al., 2012) and Utah Valleys (Malek et al., 2006), and up to $132.5 \mu\text{g m}^{-3}$ in Logan, Utah (Cache Valley) (Malek et al., 2006).

Previous ground-based studies have identified ammonium nitrate aerosol (NH_4NO_3) as the main component of $PM_{2.5}$ (70 - 80% by mass) in all three Northern Utah Valleys (Baasandorj et al., 2017; Hansen et al., 2010; Kelly et al., 2013; Kuprov et al., 2014; Long et al., 2003; Long et al., 2005a; Long et al., 2005b; Silva et al., 2007). Ammonium nitrate formation is thermodynamically favorable under cold wintertime conditions from the equilibrium with gas-phase ammonia (NH_3) and nitric acid (HNO_3), shown in R6.1 (e.g. Kuprov et al., 2014; Mozurkewich, 1993; Nowak et al., 2012). Mitigation will therefore require control of these gas-phase species and will be most effective if the reagent with more limited concentrations is identified and targeted. Both model and observation-informed ground-based analyses have suggested that NH_4NO_3 formation in Cache and Salt Lake Valleys is HNO_3 -limited (Kuprov et al., 2014; Mangelson et al., 1997; Martin, 2006; Utah Division of Air Quality, 2014c, 2014b, 2014a), though uncertainties remain in the temporal and spatial variation of this limitation.



While NH_3 is directly emitted from agricultural sources, industrial processes, waste disposal, and automobile emissions (Behera et al., 2013; Livingston et al., 2009), HNO_3 forms chemically in the atmosphere from the oxidation of NO_x ($= \text{NO} + \text{NO}_2$), which in turn arises from combustion emissions. There are two mechanism by which this formation occurs. The first is through daytime NO_2 oxidation by the hydroxyl radical (R6.2) and the second is through the nocturnal heterogeneous hydrolysis of dinitrogen pentoxide (N_2O_5) (R6.6), which itself is a product of nocturnal NO_x oxidation (R6.3 - R6.5). The former is relatively more important during the summer whereas the latter, the focus of this study, may be relatively more important in winter due to reduced OH concentrations, colder temperatures, and longer nights.



The role of nocturnal reactive nitrogen chemistry in the formation of $\text{PM}_{2.5}$ has been considered previously in multiple wintertime studies. These studies have identified this heterogeneous chemistry and subsequent morning transport from aloft as a major source of surface-level NH_4NO_3 in other basins, such as California's San Joaquin Valley (e.g. Brown, S. G. et al., 2006; Prabhakar et al., 2017; Pusede et al., 2016; Watson & Chow, 2002). It has also been considered recently in northern Utah (Baasandorj et al., 2017; Kuprov et al., 2014). In an analysis of ground-based HNO_3 and $\text{PM}_{2.5}$ observations in SLV, Kuprov et al. (2014) suggested that daytime HNO_3 formation was dominant over the contribution from nocturnal heterogeneous

chemistry. Baasandorj et al. (2017), however, note that ground-based measurements may not capture the extent of heterogeneous chemistry aloft in the residual layer (RL), which is expected to be distinct from the surface composition (e.g. Brown et al., 2007a; Brown & Stutz, 2012; Stutz et al., 2004). For example, reduced mixing at night leads to the build-up of surface NO_x emissions that cause oxidant depletion (e.g. Baasandorj et al., 2017), which, in addition to efficient destruction of NO_3 with NO (R6.7), limit the formation of N_2O_5 and HNO_3 at the surface relative to the upper NBL and RL. Therefore, vertical gradients in NO_x and oxidants could promote efficient HNO_3 and NH_4NO_3 formation aloft, which could contribute to enhanced surface-level $\text{PM}_{2.5}$ concentrations the following day.

Confirmation and quantification of this contribution to NH_4NO_3 formation during pollution events will require vertically resolved observations of relevant chemical compounds at night, not previously collected during past studies. Analyses in the San Joaquin Valley have estimated nocturnal heterogeneous contributions from aircraft vertical profiles during the mid-morning (Prabhakar et al., 2017) and vertically resolved measurements in SLV have been limited to ground-based observations at different elevations along the Wasatch Front (e.g. Baasandorj et al., 2017). Based on these observations, Baasandorj et al. (2017) estimated a large amount of HNO_3 production associated with heterogeneous chemistry in SLV. This was determined using nitrate radical production rates (P_{NO_3}), calculated from late afternoon observations, which they considered representative of nocturnal RL composition in the absence of direct measurements. In the event that particle formation in the RL is HNO_3 -limited, the absolute contribution from nocturnal heterogeneous chemistry in this altitude range will depend not only on P_{NO_3} , but the efficiency of N_2O_5 uptake onto aerosol ($\gamma(\text{N}_2\text{O}_5)$), and product yield of HNO_3 relative to nitryl chloride (ClNO_2) ($2-\phi(\text{ClNO}_2)$), which is known to form from N_2O_5 uptake onto chloride-containing aerosol

(Behnke et al., 1997; Osthoff et al., 2008). Only by quantifying these processes in the RL at night, can the role of heterogeneous chemistry to Utah air pollution be determined and aid in the development of effective mitigation strategies.

In this study we present results from the Utah Winter Fine Particulate Study (UWFPS), which collected aircraft and ground-based observations throughout Cache, Salt Lake, and Utah Valleys during January and February 2017. This analysis will focus on data from 16 aircraft flights during two pollution events between 16 January and 1 February 2017 in SLV, the most populated of the three Utah non-attainment areas. An overview of $PM_{2.5}$ during winter 2016-2017 is presented in the first section. Second, ambient mixing ratios of total (gas and particle-phase) oxidized and reduced nitrogen are used to assess the limiting reagent to NH_4NO_3 aerosol, as well as spatial and temporal trends. These results are further evaluated against model-predicted changes in aerosol mass and gas-particle partitioning associated with reductions in total oxidized and reduced nitrogen. The final section presents upper-limit $PM_{2.5}$ production rates from aircraft P_{NO_3} values, in addition to results from an observationally-informed chemical box model, used to calculate $\gamma(N_2O_5)$, $\phi(ClNO_2)$, and the combined contribution of nocturnal heterogeneous chemistry to NH_4NO_3 formation in SLV.

6.2 Methods

6.2.1 UWFPS Campaign Overview and Instrumentation

As described in Chapter 2, the Utah Winter Fine Particulate Study (UWFPS) conducted 23 research flights during both day and night during January and February 2017 with the NOAA Twin Otter (TO) aircraft. The TO was equipped with aerosol and gas-phase instrumentation, summarized in Table 6.1. While flights were conducted over Salt Lake, Cache, and Utah Valleys, the focus of this analysis will be on the more densely populated, Salt Lake Valley, with flight tracks highlighted in the right panel of Figure 6.1.

Additional ground-based measurements used in this analysis include hourly PM_{2.5}, NO₂, O₃, and temperature measurements from the Utah Department of Air Quality (UDAQ) instrumentation at the Hawthorne monitoring site (Figure 6.1). Total PM_{2.5} mass was measured with a Thermo Scientific 1405-DF Dichotomous Ambient Air Monitor, NO₂ with a Teledyne API T200U Chemiluminescence detector, and O₃ with a Teledyne API T400 UV absorption spectrometer, all in accordance with EPA guidelines.

Table 6.1. Aircraft measurements used in this analysis

Compound	Method/ Instrument	Accuracy	Meas. Frequency	Reference
<i>Gas-Phase Species</i>				
NO	CRDS ^a	5%	1s	(Fuchs et al., 2009; Wild et al., 2014)
NO ₂	CRDS	5%	1s	(Fuchs et al., 2009; Wild et al., 2014)
O ₃	CRDS	5%	1s	(Washenfelder et al., 2011a; Wild et al., 2014)
NO _y	CRDS	12%	1s	(Wild et al., 2014)
N ₂ O ₅	ICIMS ^c	30%	1s	(Lee et al., 2014)
ClNO ₂	ICIMS	30%	1s	(Lee et al., 2014)
NH ₃	QC-TILDAS ^d		1s	(Ellis et al., 2010)
<i>Aerosol Measurements</i>				
Aerosol (<1 μm) Composition	AMS ^e	20%	10s	(Bahreini et al., 2009; Middlebrook et al., 2012)
Dry Surface Area Density (<1 μm)	UHSAS ^f	34% ^g	3s	(Brock et al., 2011)

^aNOAA, Cavity Ring down Spectrometer (NOxCARD)

^bHawthorne

^cUniversity of Washington I-Time of Flight Chemical Ionization Mass Spectrometer

^dUniversity of Toronto, Quantum Cascade Tunable Infrared Laser Differential Absorption Spectrometer

^eNOAA, Aerosol Mass Spectrometer

^fDroplet Measurement Techniques, Ultra-High Sensitivity Aerosol Spectrometer

^gEstimated according to the performance of a different UHSAS in the WINTER campaign

6.2.2 Box Model

A zero-dimension chemical box model has been developed to simulate the nocturnal chemical evolution of an air parcel from sunset until the time of aircraft measurement. Extensive model details have been previously discussed in Section 2.4.2. Briefly, the model forward-integrates the chemical mechanism (Table 2.3, in Chapter 2) while iteratively adjusting the total

heterogeneous loss rate constant of N_2O_5 ($k_{\text{N}_2\text{O}_5}$) and production rate constant of ClNO_2 (k_{ClNO_2}) until the model output simultaneously reproduces ambient observations of O_3 , NO_2 , N_2O_5 , and ClNO_2 within 1% (0.5% for NO_2 and O_3). The N_2O_5 uptake coefficients ($\gamma(\text{N}_2\text{O}_5)$) and ClNO_2 production yields ($\phi(\text{ClNO}_2)$) are then calculated following equations E4.5 - E4.6. The model repeats this process every 10 seconds for flights conducted between sunset and sunrise, as calculated by time, GPS altitude, and location. Reaction R6.6 is the only source of nitrate in the model. The model output of total nitrate (gas + particle-phase, hereafter referred to as nocturnal nitrate), therefore, represents the absolute amount produced from nocturnal heterogeneous processes during the simulation duration.

For the UWFPS campaign, the box model was run in a similar manner to that described previously for the WINTER campaign (Chapter 2). More limited instrumentation during the UWFPS campaign, however, required a larger number of model assumptions that are summarized here. First, loss of nitrate radical from its reaction with volatile organic compounds (VOC) was assumed constant. Due to a lack of VOC measurements during the UWFPS campaign (besides select species measured at a ground site at the University of Utah) the rate coefficient for this reaction (k_{NO_3}) was set to $2 \times 10^{-4} \text{ s}^{-1}$, based on average values measured during the WINTER campaign (1.3×10^{-4} to $4.6 \times 10^{-4} \text{ s}^{-1}$) (Table 2.5) and those previously reported (3×10^{-5} to $1 \times 10^{-2} \text{ s}^{-1}$) during winter 2012 in Colorado (Wagner et al., 2013). While uncertainties in k_{NO_3} can lead to large model uncertainties under summertime conditions (e.g. Phillips et al., 2016), NO_3 -VOC reactivity is largely reduced during the winter season as a result of lower biogenic emissions and colder temperatures that favor N_2O_5 in its equilibrium with NO_3 . While the UWFPS model results are expected to be sensitive to this parameter, previous WINTER simulations showed a small sensitivity to k_{NO_3} relative to other uncertainties, with median $\gamma(\text{N}_2\text{O}_5)$ and $\phi(\text{ClNO}_2)$ values

changing by < 6% and 14%, respectively, for 50% changes in k_{NO_3} (Figure 2.33). Additional NO_x -regeneration from reactions of NO_3 with HO_2 and RO_2 radicals were not included here due to a lack of relevant measurements. Based on previous model sensitivity studies, an under-prediction in k_{NO_3} would cause an over-prediction in both the loss rate of N_2O_5 and subsequent production of nitrate (Section 2.4.2.7.10). In addition to the potential under-prediction of VOC-reactivity, VOC reactivity may also decrease overnight. Time varying rate constants are not currently captured in this model (see Section 2.4.2.5) and may lead to increased variability in the results presented below in Section 6.3.3.

Second, all simulations were initialized at 1.3 hours prior to sunset, assuming no initial concentrations of N_2O_5 and $ClNO_2$. The pre-sunset time of 1.3 hours was derived for the WINTER campaign based on the time when predicted-daytime N_2O_5 concentrations (Brown et al., 2005) diverged from ambient observations near sunset. This value was not recalculated for UWFPS simulations as daytime N_2O_5 calculations require measurements of $j(NO_3)$ photolysis rates, not measured during UWFPS. Photolysis rates from WINTER were used to simulate the 1.3 hours prior to sunset. While WINTER photolysis rates may be larger than those during PCAP events, the WINTER simulation showed a small sensitivity (< 3.5%) to 40% changes in these values (Figure 2.32). Additional uncertainties in air age (i.e. simulation start time and duration) may serve to over-predict N_2O_5 loss rates and nocturnal nitrate based on previous sensitivity studies to changes in air age (Section 2.4.2.7.8). A combination of these assumptions will lead to a greater uncertainty in model results near sunset, as discussed in Section 6.3.3.2.

Lastly, deposition and dilution were excluded in model simulations presented here. Similar to continental flights during WINTER, deposition from the residual layer, which is decoupled from the surface (Stull, 1988), should be negligible. Additional contributions from mixing and dilution

were excluded here due to uncertainties in dilution loss rate constants and the presence of stagnant conditions that are typical of PCAP events. Based on previous model sensitivity studies, both N_2O_5 loss and absolute nocturnal nitrate production would decrease by up to 14% with the inclusion of these processes, assuming the same loss rates as during WINTER (Table 2.8).

Application of the described box model to UWFPS observations is used in Section 6.3.3.3 to evaluate the potential contribution of heterogeneous reactive nitrogen chemistry to NH_4NO_3 aerosol formation in SLV. Due, however, to the model assumptions and associated uncertainties, additional observation and modeling-based analyses with additional measurements (including VOC and photolysis rates), will be required to provide determinations of N_2O_5 uptake coefficients and ClNO_2 yields with smaller uncertainties.

6.3 Results and Discussions

6.3.1 $\text{PM}_{2.5}$ in Salt Lake Valley – Winter 2017

Figure 6.2 provides an overview of pollution events during the 2016-2017 winter in SLV and shows a time series of total $\text{PM}_{2.5}$ mass (1-hour and 24-hour averages) measured at the UDAQ Hawthorne site (Figure 6.1). These data show the presence of multiple pollution events that exceeded the NAAQS during the 2016-2017 winter. The four largest events in December 2016 and January 2017 had daily $\text{PM}_{2.5}$ growth rates of 4.6-10.4 $\mu\text{g m}^{-3} \text{day}^{-1}$, similar to those reported from previous years in the same valley (Baasandorj et al., 2017; Silcox et al., 2012; Whiteman et al., 2014). The final two pollution events (10 - 22 January and 25 January - 5 February) overlapped with the TO flights during UWFPS, shown by the gray shading in Figure 6.2. Average non-refractory (NR) PM_1 aerosol mass fractions measured by the AMS (Figure 6.2 pie charts) during these periods show that $\text{PM}_{2.5}$ is primarily composed of NH_4NO_3 , with total mass fractions of 76.6% and 74.0% for the sum of nitrate and ammonium during the first two pollution episodes.

These mass fractions are in agreement with previous observations (e.g. Baasandorj et al., 2017). During the relatively clean period sampled between 8 and 12 February, the $\text{NH}_4 + \text{NO}_3$ fraction decreased to an average of 57%, with a larger relative contribution from organic aerosol. The remaining sections will focus on TO flights during the two late January pollution events and use multiple methods to evaluate the potential contribution of heterogeneous reactive nitrogen chemistry to the observed $\text{PM}_{2.5}$ (NH_4NO_3) mass.

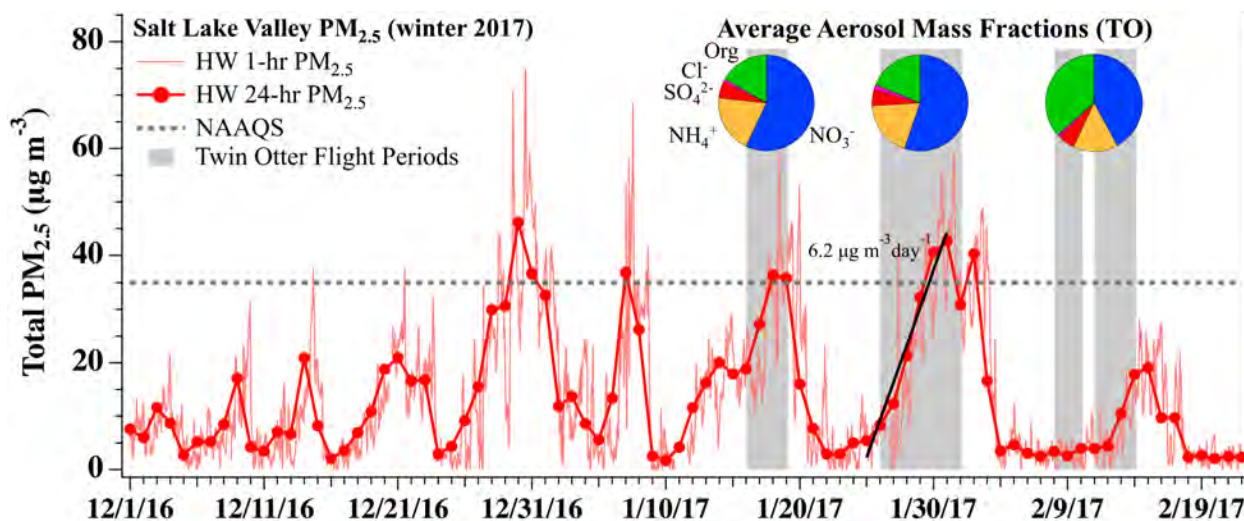


Figure 6.2. Time series of total $\text{PM}_{2.5}$ mass ($\mu\text{g m}^{-3}$) (1-hr and 24-hr averages) for the 2016-2017 winter, measured at the Hawthorne (HW) UDAQ site in Salt Lake Valley. The 24-hour EPA national ambient air quality standard for $\text{PM}_{2.5}$ ($35 \mu\text{g m}^{-3}$) is shown by the dashed gray line. Gray shading indicates days when the TO aircraft was flying as part of the UWFPS campaign. Average aerosol mass fractions, measured by the AMS aboard the TO are given in pie charts for each measurement period. Aerosol components by color are nitrate (blue), ammonium (gold), sulfate (red), non-refractory chloride (pink), and organics (green).

6.3.2 Limiting and Excess Reagents for NH_4NO_3 Aerosol

As NH_4NO_3 was the principal component of $\text{PM}_{2.5}$ during pollution events in SLV (Figure 6.2), the contribution from heterogeneous reactive nitrogen processes will depend on whether NH_4NO_3 formation is limited by available gas-phase NH_3 or HNO_3 . For example, absolute NH_4NO_3 formation in an NH_3 -limited system will be sensitive to changes in NH_3 emissions (up to a certain extent) and not HNO_3 formation processes. In contrast, a HNO_3 -limited system will be

sensitive to changes in both day and nighttime NO_x oxidation processes that lead to HNO_3 formation. Daytime NO_x oxidation rates during winter depend on specific conditions but are generally slower, such that nighttime oxidation may play a dominant role (e.g. Kenagy et al., 2018; Wood et al., 2005). The following sections present two methods for identifying the limiting reagent to NH_4NO_3 formation in SLV in winter 2017.

6.3.2.1 Method #1: Molar Ratios of Oxidized to Reduced Nitrogen

Under ambient conditions, gas-phase NH_3 and HNO_3 are in a thermodynamic equilibrium with their particulate equivalents ($\text{NO}_3^-(p)$ and $\text{NH}_4^+(p)$). The limiting reagent can therefore be inferred from observations of the ratio of total oxidized ($\text{HNO}_3(g) + \text{NO}_3^-(p)$) to total reduced nitrogen ($\text{NH}_x = \text{NH}_3(g) + \text{NH}_4^+(p)$), shown in E6.1. This ratio does not account for other contributing aerosol components such as $(\text{NH}_4)_2\text{SO}_4$, NH_4HSO_4 , and NH_4Cl , but should generally represent the NH_4NO_3 aerosol system when particulate concentrations of sulfate and inorganic chloride are low, as was observed during UWFPS 2017 (Figure 6.2). Under these conditions, a nitrogen ratio greater than 1 indicates that oxidized nitrogen is in excess and NH_4NO_3 particle formation is limited by the presence of NH_3 . Conversely, a ratio smaller than 1 indicates that formation is limited by the presence of HNO_3 , which itself is limited by the oxidation rate of NO_x .

$$N\text{Ratio} = \frac{\text{HNO}_3(g) + \text{NO}_3^-(p)}{\text{NH}_3(g) + \text{NH}_4^+(p)} \quad (6.1)$$

A time series of nitrogen ratios in SLV between 17 and 31 January is shown in Figure 6.3, calculated from 10s averaged (AMS frequency) measurements of gas and particle-phase compounds. Figure 6.3 shows that NH_4NO_3 particle formation in SLV during pollution episodes is largely limited by HNO_3 (median ratio 0.74), but variable (0.29 -1.03, 10th - 90th percentile range), and altitude dependent (color scale in Figure 6.3), with periods of NH_3 limitation at the

lowest altitudes. These results are in contrast to all previous ground-based observations that show exclusive $\text{HNO}_3(\text{g})$ limitation in SLV (Kelly et al., 2013; Utah Division of Air Quality, 2014c). The increased frequency of NH_3 -limitation with episode duration (Figure 6.3) is also opposite the trend predicted by Baasandorj et al. (2017), who suggested that observed ground-site oxidant depletion should lead to more HNO_3 -limited conditions over time. Despite these discrepancies with previous surface observations, particle formation aloft (≥ 400 mAGL) was nearly always limited by HNO_3 in 2017 (Figure 6.3). Removed from surface NO emissions that limit N_2O_5 formation, this altitude range is where the HNO_3 contribution from nocturnal heterogeneous nitrogen chemistry is expected to be greatest.

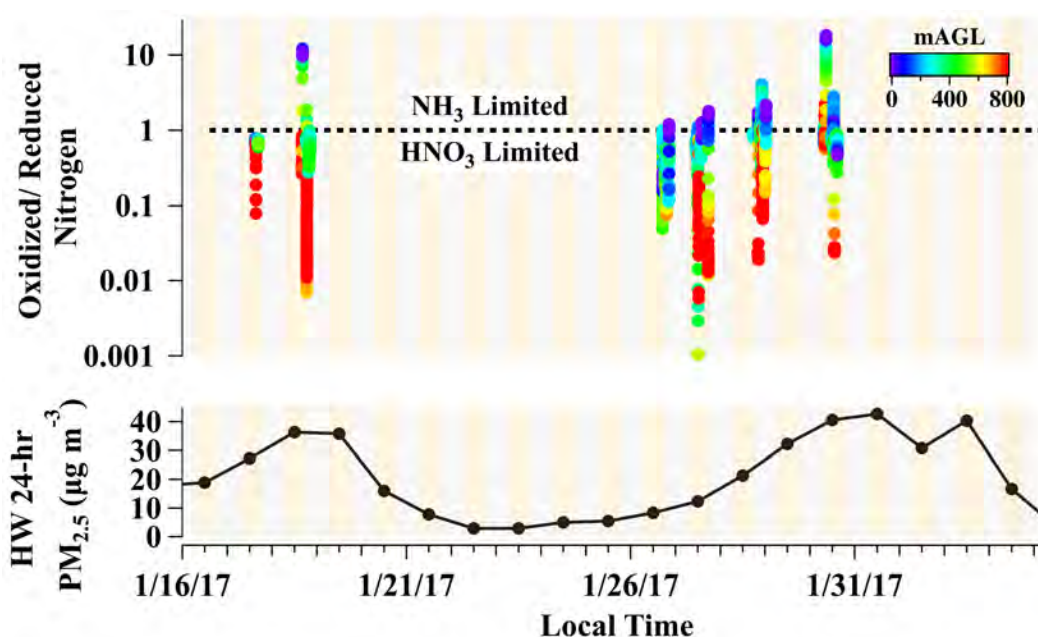


Figure 6.3. Time series of calculated nitrogen ratios (10s average) for pollution events in SLV (top) and concurrent $\text{PM}_{2.5}$ mass (24-hour average) measured at the HW ground-site (bottom). Individual nitrogen ratios are colored by the aircraft altitude (mAGL), yellow and gray shading indicate times of day and night.

6.3.2.2 Method #2 - ISORROPIA Model Sensitivity Studies

The ISORROPIA (v2.1) inorganic aerosol thermodynamic equilibrium model (Nenes et al., 1998) was used to test the sensitivity of particle formation in SLV to changes in total oxidized

and reduced nitrogen. All model simulations were run by Alessandro Franchin (CIRES/NOAA). Results included in Franchin et al. (In Prep). Figures 6.4 - 6.6 were also prepared in part by Alessandro Franchin.

The ISORROPIA model is used to predict the aerosol-gas phase partitioning of inorganic aerosol components, assuming thermodynamic equilibrium, provided user inputs of total nitrate ($\text{HNO}_3 + \text{NO}_3^-$), ammonium (NH_x), chloride ($\text{HCl (g)} + \text{Cl}^- \text{(p)}$), sulfate ($\text{SO}_4^{2-} \text{(p)}$, assuming $\text{H}_2\text{SO}_4 \text{(g)}$ was negligible), ambient temperature, and relative humidity. The aerosol particles are assumed to be internally mixed, such that all particles have the same composition (Fountoukis & Nenes, 2007; Nenes et al., 1998). Here, ISORROPIA was run in “forward mode” to predict the particle-gas partitioning of each component from the starting total concentrations. Model inputs were restricted to AMS PM_{10} measurements, which do not include coarse mode aerosol composition or refractory salts such as sodium chloride, nitrate, or sulfate. As a result, the sodium input was set to zero. As the total contribution from refractory salts (Na^+ , Mg^+ , K^+ , Ca^+) was typically less than 5% of the total aerosol mass (measured with an Ambient Ion Monitoring System coupled to ion chromatography at the University of Utah campus), the presence of these species is assumed to not affect the partitioning of other acid gases.

The ISORROPIA model output consists of the concentrations of the gas-phase (HNO_3 , NH_3 , and HCl) and aerosol-phase components (NO_3^- , NH_4^+ , Cl^-), further divided into solid and liquid phases. In this analysis, the focus is on the partitioning between the gas and aerosol phase, disregarding whether the aerosol components are solid or liquid.

Base case partitioning simulations are first evaluated in Figure 6.4 (y-axis) by comparing results to measurements (x-axis) from all UWFPS flights (Salt Lake, Cache, and Utah Valleys). The left column shows the total input mass of each species and therefore returns exact agreement

between the model and observations along the 1:1 line. The middle and right columns show the model-predicted vs. observed concentrations of gas-phase and particle-phase species, respectively. This comparison shows agreement for gas and particle phase ammonium (top row), and particulate nitrate (center right). Gas phase nitric acid (center) has periods of both model over- and under-prediction, which likely results from measurement uncertainty in the relatively small fraction of HNO_3 that is present in the gas-phase relative to particle-phase. There is a less than satisfactory agreement for the chloride species, with a model under-prediction of HCl and over-prediction of particle Cl^- (bottom right two panels, Figure 6.4). This discrepancy is likely related to the model itself, as ISORROPIA has previously been shown to overestimate aerosol chloride by up to 40%, while still behaving well for ammonium and nitrate species (e.g. Nenes et al., 1998). This chloride-partitioning trend has also been observed in the Extended-AIM aerosol thermodynamics partitioning model. It should still be noted however, that the subsequent nitrate and ammonium sensitivity studies are also sensitive to the model chloride partitioning, especially in the case of total nitrate (gas + particle) reduction, leading to an increased uncertainty in those results.

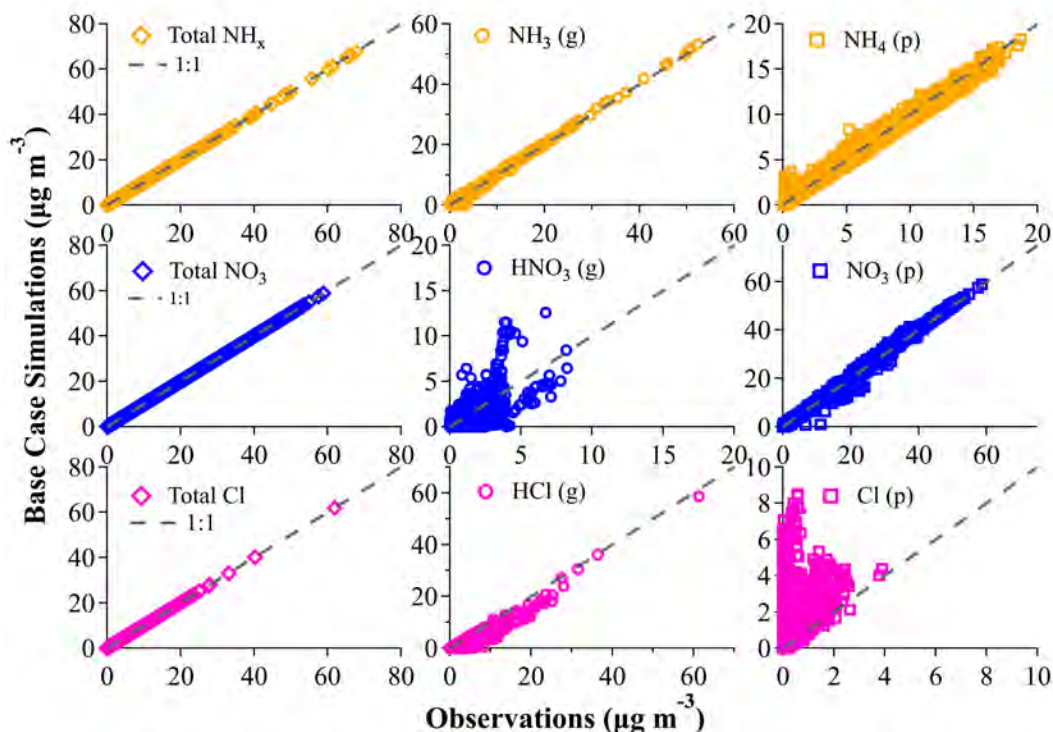


Figure 6.4. Reproduced from UWFPS Report (UWFPS Science Team, 2018). Comparison between measurements (x-axis) and model results (y-axis) of the phase partitioning of ammonium (yellow), nitrates (blue) and chloride (pink) for all TO flights. left column) Input total ammonium, nitrate, and chloride (gas + aerosol). Center column) model-observation comparison of gas-phase concentrations, right column) model-observation comparison of particle-phase concentrations.

The second part of this analysis, two tests were conducted to assess the sensitivity of the system to reductions in total ammonium and nitrate, carried out by decreasing the inputs of each by a factor of two. Results for the nitrate-reduction case for total PM_{10} mass and individual component partitioning are shown in Figure 6.5 for SLV data. The modeled HNO_3 and NO_3^- decreased as expected, relative to base case results (Figure 6.5b). The Cl^- slightly increased, pointing towards replacement of some of the NH_4NO_3 with particle-phase NH_4Cl . The NH_3 increased, reflecting the evaporation of part of the NH_4NO_3 in the aerosol phase. Particulate NH_4^+ appeared to have multiple responses to total nitrate reduction, one where it decreased and one where it did not. Under HNO_3 -limited conditions, a reduction in available nitrate is expected to reduce particulate NH_4^+ . Combined with the ~50% reduction in total PM_{10} mass in Figure 6.5a,

these results suggest that NH_4NO_3 formation in the SLV is largely HNO_3 -limited, but also experiences periods of NH_3 -limitation, consistent with observed nitrogen ratio results (Section 6.3.2.1).

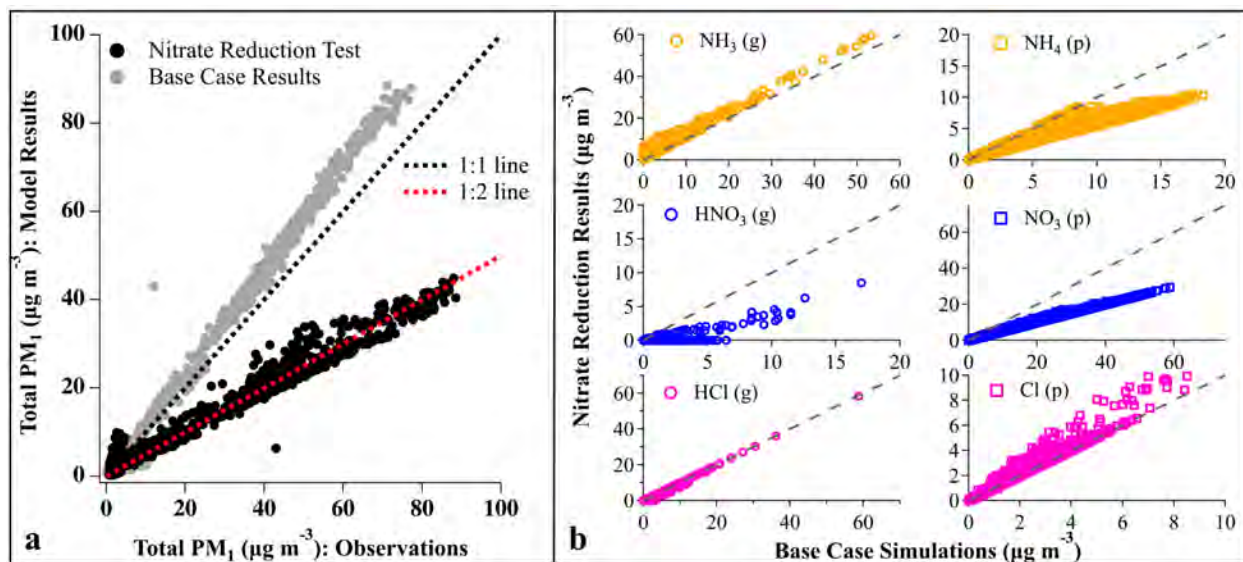


Figure 6.5. Comparison between base case model results (x-axis) and simulations with a 50% reduction in total nitrate (y-axis), for SLV only (run by Alessandro Franchin). (a) Total aerosol mass from the base case and sensitivity test simulations compared to observed total aerosol mass; (b) Changes in gas-phase (left column) and particle phase (right column) for ammonium, nitrate, and chloride relative to base case simulations.

Results from the ammonium-reduction test are shown in Figure 6.6. The modeled NH_3 decreased as expected, while HNO_3 and HCl increased, reflecting the partial evaporation NH_4NO_3 and NH_4Cl . Both particle-phase nitrate and ammonium showed two responses to reductions in total ammonium (Figure 6.6, right column). The partial sensitivities to ammonium, combined with proportional reductions in total PM_{10} mass (Figure 6.6a), suggest that NH_4NO_3 formation in SLV is either NH_3 -limited and/or close to the transition regime where a 50% reduction in total ammonium causes the system to transition from the HNO_3 -limited to NH_3 -limited regime.

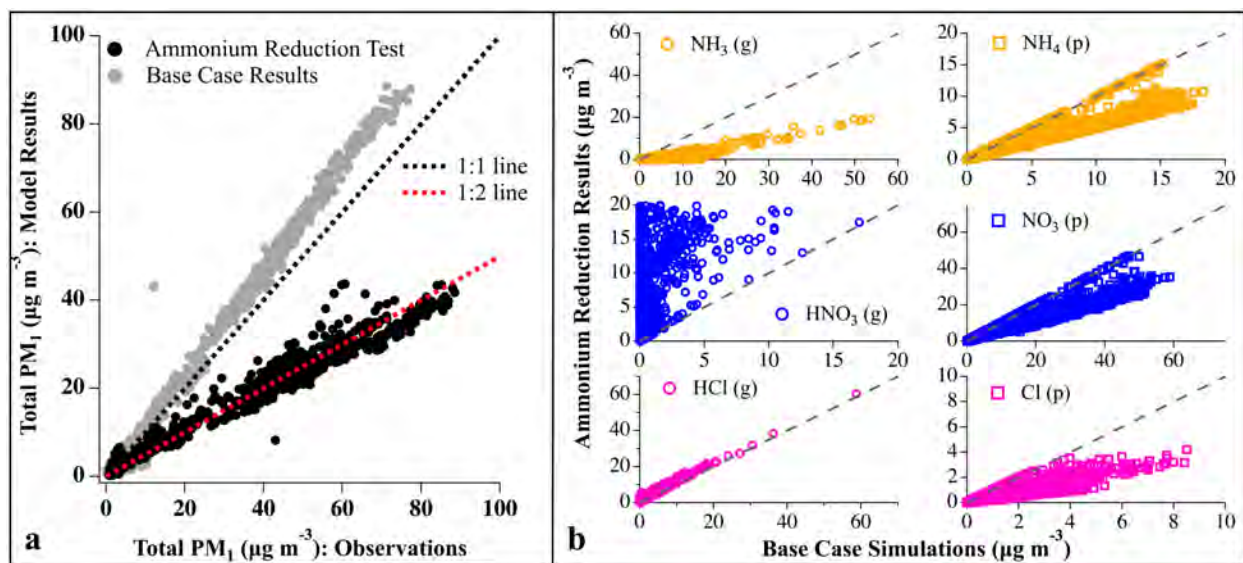


Figure 6.6. Comparison between base case model results (x-axis) and simulations with a 50% reduction in total ammonium (y-axis), for SLV only (run by Alessandro Franchin). Panels a and b are in the same format as Figure 6.5.

The ISORROPIA-predicted aerosol mass reductions presented here support the observation-based nitrogen ratio results from Section 6.3.2.1. These analyses show that NH_3NO_3 formation in SLV is at times NH_3 -limited, or near the transition regime, but is largely HNO_3 -limited under conditions sampled in 2017. Therefore, the rate of HNO_3 formation from nocturnal heterogeneous reactive nitrogen chemistry is a critical process for the development of a process level understanding of total $\text{PM}_{2.5}$ mass production during pollution events in SLV. Quantification of this contribution during winter 2017 is assessed in the final section using observation and model-based methods.

6.3.3 Nitrate Production via Heterogeneous Reactive Nitrogen Chemistry

Under HNO_3 -limited conditions, the absolute amount of nitrate produced from heterogeneous chemistry will depend on the production rate of the nitrate radical (Section 6.3.3.1), the N_2O_5 uptake efficiency (Section 6.3.3.2), and the yields of ClNO_2 and HNO_3 (Section 6.3.3.2). This section provides observational and box-model based analyses of each of these factors. The

final section (Section 6.3.3.3) provides model-calculated estimates of the fractional contribution of heterogeneous chemistry to PM_{2.5} mass during winter 2017.

6.3.3.1 Nitrate Radical Production Rates

An upper limit estimate for the contribution of heterogeneous HNO₃ production to total PM_{2.5} mass can be calculated as two times the nitrate radical production rate P_{NO_3} , as defined in E6.2 - E6.3. This method assumes: 1) N₂O₅ is produced quantitatively from NO₃ (i.e. no competing reaction of NO₃ + VOC), 2) N₂O₅ is efficiently taken up onto aerosol, 3) aqueous-phase reactions form two molecules of HNO₃ for every molecule of N₂O₅ ($\phi(\text{ClNO}_2) = 0$), and 4) there is no loss of any species to deposition or dilution. The value of P_{NO_3} is also expected to vary with altitude due to surface NO_x emissions that can deplete O₃ during pollution events, as described previously by Baasandorj et al. (2017).

$$P_{NO_3} = k_4[O_3][NO_2] \quad [\text{ppbv hr}^{-1}] \quad (6.2)$$

$$k_4 = 1.4 \times 10^{-13} e^{(-2470/\text{Temp})} \quad [\text{cm}^3 \text{ molecule}^{-1} \text{ s}^{-1}] \quad (6.3)$$

UWFPS results provide the first vertically-resolved calculations of P_{NO_3} in SLV. Median, 25th, and 75th percentile data from nighttime vertical profiles conducted in SLV during pollution events are plotted in Figure 6.7 (right) along with the AMS-measured PM₁ profiles (left) and ground-based PM and P_{NO_3} values from HW. Data from vertical profiles in Figure 6.7 show that the CRDS-calculated P_{NO_3} values are elevated throughout the polluted layer (below ~ 700 mAGL). Median values in Figure 6.7 are lower than those between 0.5 and 2 ppbv hr⁻¹ calculated during late afternoon periods (representative of residual layer) in winter 2016 (Baasandorj et al., 2017). Figure 6.7 also shows a more well-mixed pollution layer than expected, with aircraft P_{NO_3} values similar to the median calculated at HW for the same nights (light blue square). The vertical homogeneity in P_{NO_3} may be a result of vertical profile location (e.g. profiles at air fields, removed

from the highest concentrations of urban emissions), or time within the pollution episode. For example, the dark square in Figure 6.7 and the P_{NO_3} times series from HW in Figure 6.8, both show that surface level P_{NO_3} approached 0 ppbv hr⁻¹ as the late January- early February pollution event progressed, consistent with trends previously observed (Baasandorj et al., 2017). As the TO was not flying at night after the peak of this pollution episode, the vertical P_{NO_3} structure during that time cannot be assessed. Measured P_{NO_3} values, however, can be compared to the observed PM_{2.5} build-up rates in Figure 6.2 (discussed below), as these periods were concurrent with TO night flights.

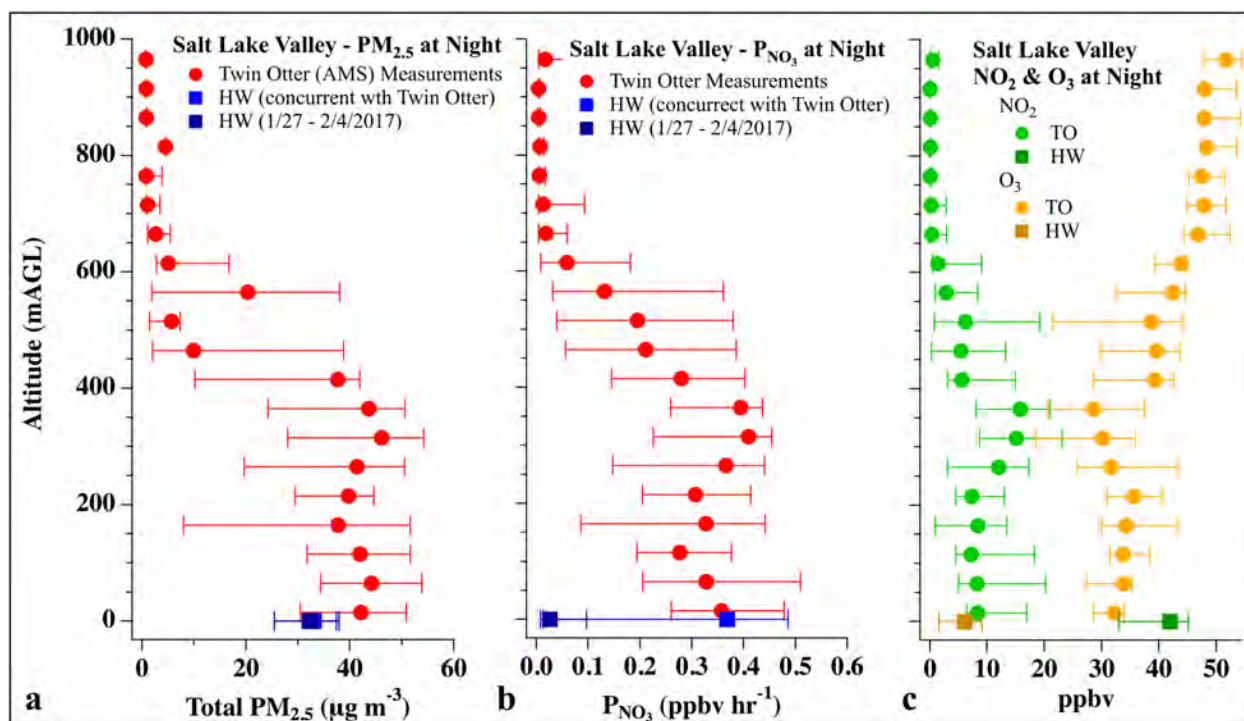


Figure 6.7. Twin Otter vertical profiles (mAGL) of total PM_{2.5} (measured by the AMS), P_{NO_3} (calculated from ambient temperature and NOxCaRD measurements of NO₂ and O₃ (1Hz)), NO₂, and O₃ (measured by NOxCaRD) during pollution events in SLV. Circles are the median at each altitude bin and bars represent the 25th-75th percentile range. Light blue squares in (a) and (b) and squares in (c) are the median values measured and calculated (from 1 hour averages of PM_{2.5}, NO₂, O₃, and temperature (reported by Munkh Bassandorj)) at the HW ground site during concurrent nights with TO flights. Dark blue squares in (a) and (b) are the average nighttime values (8 pm – 7 am local time) from 27 January – 4 February. Bars for each represent the 25th-75th percentile range.

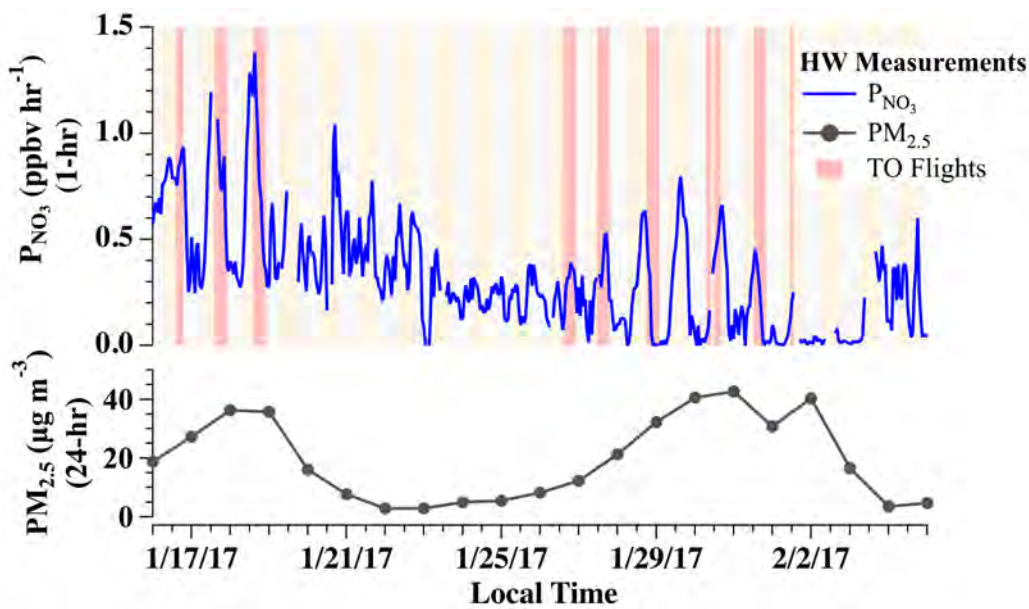


Figure 6.8. Time series $PM_{2.5}$ (24-hour average) (bottom) and P_{NO_3} (top) calculated from hourly NO_2 , O_3 , and temperature measurements (reported by Munkh Bassandroj) at the Hawthorne ground-site. Day and night are shown by the yellow and gray shading. TO flight periods are shown by the red shading.

The average P_{NO_3} for all TO night flights in SLV between 16 January and 1 February 2017 was 0.37 ± 0.19 (1σ), ppbv h⁻¹. Provided the assumptions above, this instantaneous production rate corresponds to $24.0 \mu\text{g m}^{-3}$ of nitrate aerosol produced in a typical 14-hour night, larger than the $PM_{2.5}$ accumulation rate of $4\text{--}10 \mu\text{g m}^{-3} \text{ day}^{-1}$ observed at HW (Figure 6.2). These elevated P_{NO_3} values indicate the potential for a large fraction of $PM_{2.5}$ in SLV to be produced from nocturnal heterogeneous reactive nitrogen chemistry. Because the instantaneous rate exceeds their daily accumulation rate, however, additional processes must reduce the absolute amount of nitrate heterogeneously produced. These processes can include N_2O_5 uptake, $ClNO_2$ formation and dilution/deposition, which are discussed below.

6.3.3.2 Modeled Uptake Coefficients and Production Yields

In addition to P_{NO_3} , both the aerosol uptake efficiency of N_2O_5 ($\gamma(N_2O_5)$) and production yield of HNO_3 ($2\text{-}\phi(ClNO_2)$), will impact the absolute amount of HNO_3 formed from nocturnal

heterogeneous reactive nitrogen chemistry. A previously-developed box model was used to quantify these two parameters during pollution events in SLV, by fitting to observations of N_2O_5 and ClNO_2 , as described above in Section 6.2.2. For all TO flights during pollution events between 16 January and 1 February 2017, the median model-derived $\gamma(\text{N}_2\text{O}_5)$ and $\phi(\text{ClNO}_2)$ values ($N = 2487$) were 0.055 and 0.220, respectively. For SLV alone, medians were similar with values of 0.071 and 0.220 for $\gamma(\text{N}_2\text{O}_5)$ and $\phi(\text{ClNO}_2)$, respectively, for these same flights. The distributions of $\gamma(\text{N}_2\text{O}_5)$ and $\phi(\text{ClNO}_2)$ results for SLV ($N = 1245$) are shown by the histograms in Figure 6.9. Campaign results from the recent 2015 WINTER campaign over the U.S. east coast (Chapter 4 and Chapter 5) are shown for comparison. Results in Figure 6.9 show that N_2O_5 uptake was more efficient during UWFPS ($5\times$ larger median than WINTER) despite large nitrate aerosol fractions, which have been shown to suppress uptake in other environments (e.g. Bertram & Thornton, 2009; McDuffie et al., 2018; Wagner et al., 2013) (Section 4.4.2.3). In contrast, the ClNO_2 production yields were similar between the two campaigns with most values falling below 40%, despite the potentially large source of refractory aerosol chloride from the Great Salt Lake.

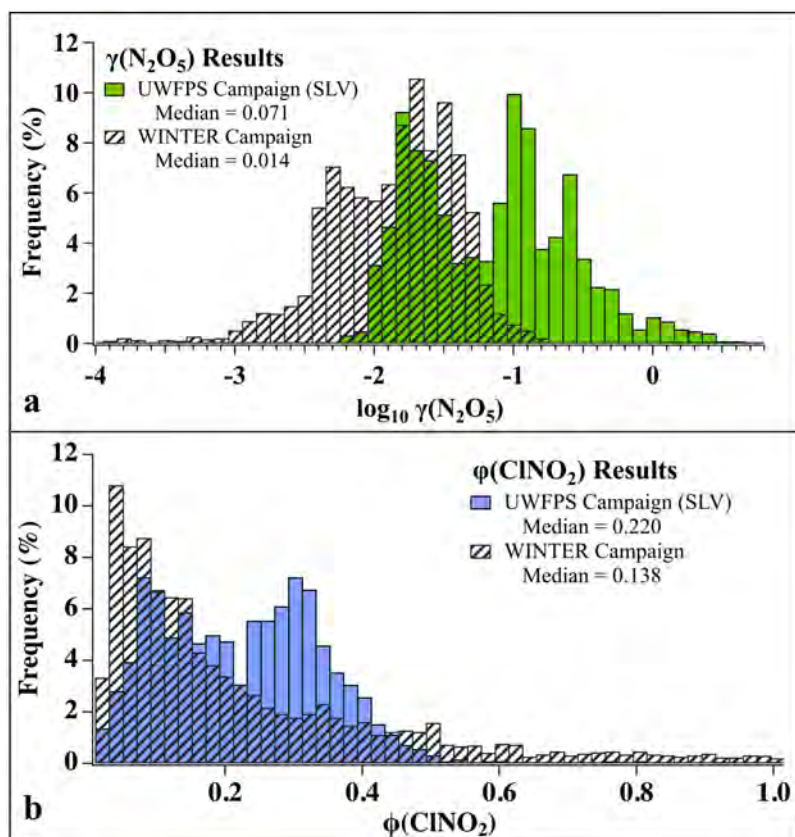


Figure 6.9. (a) Histograms of $\gamma(\text{N}_2\text{O}_5)$ determinations from SLV during pollution events (green) and WINTER campaign results (dashed bars); (b) histograms of $\phi(\text{ClNO}_2)$ determinations from SLV during pollution events (blue) and WINTER campaign results (dashed bars). Medians are provided in each plot.

While large uptake coefficients and small ClNO_2 yields suggest efficient production of HNO_3 in SLV, the $\gamma(\text{N}_2\text{O}_5)$ and $\phi(\text{ClNO}_2)$ values presented here may be upper and lower limits respectively. As discussed in Section 6.2.2, limited observations of VOC and photolysis rates, and uncertainties in air age, dilution, and deposition, may cause the $\gamma(\text{N}_2\text{O}_5)$ values to be over-predicted and $\phi(\text{ClNO}_2)$ values to be under-predicted. These biases are also more likely near sunset where the model is more sensitive to assumptions in simulation start time. While the largest 22% of UWFPs $\gamma(\text{N}_2\text{O}_5)$ values exceed the largest field-derived value (Figure 4.9), general agreement with WINTER results provide confidence in the median values.

To further evaluate the box model-derived $\gamma(\text{N}_2\text{O}_5)$ values, determinations are compared to two other derivation methods in Figure 6.10. The first method calculates $\gamma(\text{N}_2\text{O}_5)$ based on the steady state approximation ($\gamma(\text{N}_2\text{O}_5)_{\text{ss}}$) as described previously in Section 4.3.2 and defined in E4.7 and E4.8 (Brown et al., 2003). While this method shows excellent agreement (2-sides slope of 1.07 ± 0.01) with box model results, it likely over-predicts $\gamma(\text{N}_2\text{O}_5)$ values under cold, high NO_x conditions where it takes longer for the $\text{N}_2\text{O}_5\text{-NO}_3$ system to achieve a steady state (Brown et al., 2003). The color scale in Figure 6.10 shows that the largest $\gamma(\text{N}_2\text{O}_5)$ values (≥ 0.1) were exclusively derived for air sampled within 3 hours of sunset (4.3 hour simulation time), where the steady state is likely not applicable. Agreement with the box model during these times provides further evidence of box-model over-prediction of $\gamma(\text{N}_2\text{O}_5)$ values within at least three hours of sunset.

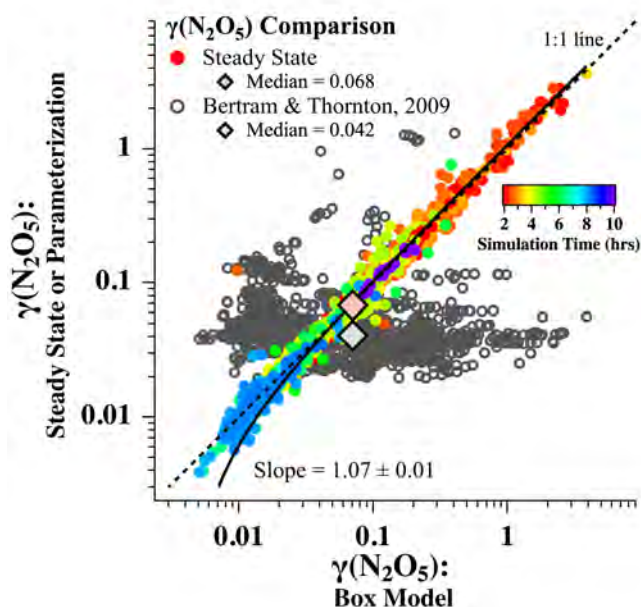


Figure 6.10. Methods comparison for $\gamma(\text{N}_2\text{O}_5)$ values during SLV pollution events. Solid circles show the comparison between steady state (y-axis) and box model (x-axis) derived values, colored by model simulation duration (i.e. time since sunset+1.3 hrs). The 2-sided fit has a slope of 1.07 ± 0.01 (black line). Open circles show the comparison between parametrized values (from Bertram and Thornton (2009)) (y-axis) and box model (x-axis) results. Dashed line is the 1:1 correlation.

The second method derives $\gamma(\text{N}_2\text{O}_5)$ from a laboratory-based parameterization by Bertram and Thornton (2009), based on aerosol volume to surface area ratio and aerosol molarities of water

(described below), nitrate, and chloride. This parameterization has had mixed success in reproducing field-derived results (e.g. Bertram et al., 2009b; McDuffie et al., 2018; Riedel et al., 2012a), but is currently used to predict N_2O_5 uptake onto internally-mixed inorganic aerosol in many global models. Here, wet aerosol volume was calculated using the UHSAS-measured dry aerosol volume density and the inorganic-associated aerosol water mass, calculated from the base case ISORROPIA results derived by Alessandro Franchin, discussed in Section 6.3.2.2. This estimate does not include organic-associated aerosol water, which is expected to be small due to the small observed aerosol organic mass fractions (Figure 6.2). The empirically-based parameterization derived by McDuffie et al. (2018) in Chapter 4 could not be applied to this data as there were no available measurements of aerosol O:C ratio. Parameterized $\gamma(\text{N}_2\text{O}_5)$ values in Figure 6.10 show agreement with the box model median value (within 42%, diamonds in Figure 6.10), but not with the modeled variability. This trend was also observed in comparisons of box model and parameterized $\gamma(\text{N}_2\text{O}_5)$ values from the WINTER campaign (Chapter 4, Section 4.4.3.2). The Bertram and Thornton (2009) parameterization was also used with aerosol water and chloride to predict $\phi(\text{ClNO}_2)$ values for UWFPS. Consistent with results presented in Chapter 5, these parameterized values were larger than box model values with a median of 0.65 relative to the box model predicted median of 0.22.

Despite disagreement in the predicted distributions, overall agreement between median $\gamma(\text{N}_2\text{O}_5)$ values suggests that the median N_2O_5 uptake coefficient in SLV during pollution events is typically between 0.042 and 0.071. These values (in contrast to the WINTER median) fall in the range where global model predictions of NO_x become insensitive to changes in uptake efficiency (Macintyre and Evans (2010); lower panel of Figure 4.9), and depend more strongly on changes in the gas-phase nocturnal oxidation rate of NO_3 (i.e. P_{NO_3}). The limited sensitivity of NO_x to large

$\gamma(\text{N}_2\text{O}_5)$ values, therefore provides confidence in this model's ability to predict the magnitude of NO_x conversion to HNO_3 and ClNO_2 in SLV, despite uncertainties in exact $\gamma(\text{N}_2\text{O}_5)$ values. The final section below presents forward-integrated simulation results to quantify the magnitude of nocturnal nitrate produced during pollution events in SLV.

6.3.3.3 Modeled Nitrate Production Rates and Fractional Contribution of Heterogeneous Chemistry to Total NH_4NO_3 Aerosol

In base case model simulations, the model iteratively derives values for $\gamma(\text{N}_2\text{O}_5)$ and $\phi(\text{ClNO}_2)$ by integrating the chemical mechanism forward in time from sunset until the time of aircraft measurement. Holding these fit results constant, the model can be further integrated until the time of sunrise, as shown for a representative SLV point in Figure 6.11. As total nitrate ($\text{HNO}_3 + \text{NO}_3^-$) is initialized in the model with a concentration of $0 \mu\text{g m}^{-3}$, the model output for nitrate at sunrise represents the absolute amount of total nitrate produced from nocturnal chemistry over the course of a single night.

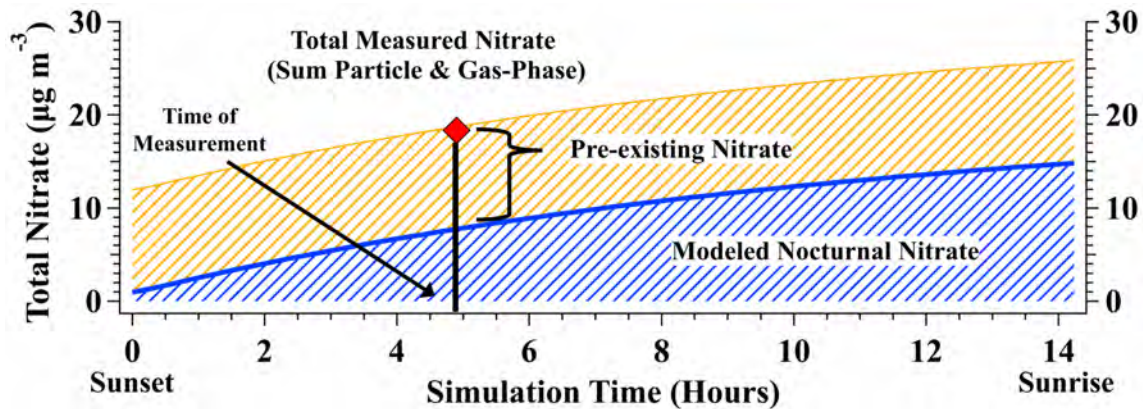


Figure 6.11. Simulation of nocturnal chemistry from sunset to sunrise of a representative air parcel sampled over SLV on 28 January 2017. Model derived $\gamma(\text{N}_2\text{O}_5)$ and $\phi(\text{ClNO}_2)$ values for this point were 0.05 and 0.21, respectively. Modeled nocturnal nitrate (blue) is the absolute amount calculated by the model from nocturnal chemistry. Pre-existing nitrate (yellow) represents the nitrate present at sunset from the previous day and is calculated as the difference between total measured nitrate from the aircraft (red diamond) and the model calculated value at the time of aircraft measurement (vertical black line). Assuming pre-existing nitrate is constant overnight (i.e. no deposition or dilution), the fractional contribution of nocturnal nitrate is calculated as the ratio of modeled nitrate to total nitrate (pre-existing + modeled) at sunrise (simulation hour 14).

Given that $\text{PM}_{2.5}$ during pollution events in SLV is mainly composed of NH_4NO_3 (Section 6.3.1), which is largely formation-limited by HNO_3 (Section 6.3.2), the production rate of nitrate can be taken as the approximate production rate of $\text{PM}_{2.5}$ (though aerosol organics did contribute to ~20% of total $\text{PM}_{2.5}$ mass (Figure 6.2)). Forward integrated simulations for all TO flights during pollution events in SLV predict total nitrate production rates ranging from 0.012 to $34 \mu\text{g m}^{-3} \text{night}^{-1}$. The average value during this period in SLV was $13 \mu\text{g m}^{-3} \text{night}^{-1}$ ($15 \mu\text{g m}^{-3} \text{night}^{-1}$ for the example simulation in Figure 6.11), which is slightly larger than the total daily production rates of $4.6 - 10.4 \mu\text{g m}^{-3} \text{day}^{-1}$ observed on the ground during the same time (Figure 6.2). Dilution or depositional loss of total nitrate, N_2O_5 , or ClNO_2 (not included in base case simulations) may account for the difference between instantaneous residual layer nitrate production rates and daily buildup rates during PCAPs. In addition, incomplete mixing with the surface could lead to higher $\text{PM}_{2.5}$ concentrations aloft than at the surface (Franchin et al., In Prep).

Regardless of these uncertainties, modeled production rates do suggest that nocturnal heterogeneous processes could account for a large fraction of nitrate and $\text{PM}_{2.5}$ accumulation during pollution events in SLV. Comparing modeled nitrate to the total nitrate predicted at sunrise (as described in Figure 6.11 caption), box model simulations estimate that nocturnal chemistry over the course of one night accounts for an average of 67 ± 23 (1σ) % of total nitrate aloft, present at sunrise. The total contribution from nocturnal chemistry may be even larger if previous day nitrate (Figure 6.11, yellow shading) is primarily from nocturnal chemistry the previous night. These results suggest that nocturnal heterogeneous production aloft may be the primary source of $\text{PM}_{2.5}$ during pollution events in SLV. Further quantification and evaluation of these results, however, will require additional observations and more sophisticated box- and 3D- chemical transport modeling efforts.

6.4 Conclusions and Future Work

Aerosol and gas-phase measurements collected during the 2017 UWFPS campaign showed multiple pollution events that exceeded $PM_{2.5}$ standards in Salt Lake Valley, the most populated region in Utah State. During these events, aerosol particles were largely composed of NH_4NO_3 , which forms from the reaction between gas-phase NH_3 and HNO_3 . While NH_3 is emitted from surface sources, HNO_3 is chemically formed from the oxidation of NO_x emissions. This oxidation can occur through daytime reactions with photochemical OH radicals, or nocturnal heterogeneous reactions involving NO_3 and N_2O_5 . The contribution of nocturnal chemistry to $PM_{2.5}$ formation in SLV is dependent on whether NH_4NO_3 formation is NH_3 or HNO_3 -limited, as well as the NO_3 production rate, N_2O_5 uptake efficiency, and HNO_3 production yield.

In contrast to previous ground-based analyses, the first vertically resolved measurements of aerosol composition and gas-phase precursors in SLV showed that NH_4NO_3 formation transitioned from HNO_3 -limited to more frequent periods of NH_3 -limitation as pollution events progressed. This was confirmed by aerosol thermodynamic modeling, which predicted an aerosol mass sensitivity to reductions in total reduced nitrogen mass. Both observation and modeling-based analyses, however, agreed that NH_4NO_3 formation in 2017 was largely HNO_3 -limited aloft during pollution events, providing the possibility of a large contribution from nocturnal heterogeneous chemistry to HNO_3 and $PM_{2.5}$ formation.

Analysis of vertically-resolved nitrate radical production rates (upper-limit estimate to heterogeneous HNO_3 formation) and results from an observationally-informed chemical box model, suggest that nocturnal chemistry is the primary mechanism for $PM_{2.5}$ production in SLV during pollution events. While the box model has uncertainties associated with limited available measurements and model assumptions, modeled nitrate is largely insensitive to specific values of

derived N_2O_5 uptake coefficients (used to predict total modeled nitrate) and will be more sensitive to changes in nocturnal gas-phase NO_3 production rates. The model design limits its ability to fully quantify the contribution of nocturnal oxidation to NH_4NO_3 relative to daytime processes. Confirmation and further evaluation of these results will require additional vertically resolved measurements of aerosol composition, gas-phase precursors, VOCs, radicals, and physical parameters, as well as more sophisticated modeling of these multi-day pollution accumulation events with box- and 3D-chemical transport models. The observation and modeling-based results presented here however, highlight the importance of nocturnal chemistry to the formation of $\text{PM}_{2.5}$ in SLV, which will provide constraints for regulatory models of $\text{PM}_{2.5}$ used to assess control strategies in this populated non-attainment area.

Chapter 7: Summary and Conclusions

In this thesis, I have described four analyses that used a combination of field observations and chemical box modeling to: 1) address key questions regarding the sensitivity of local O₃ production to specific emission sources in the Colorado Front Range, 2) provide critical, regional determinations of N₂O₅ uptake coefficients and ClNO₂ production yields during the winter season, and 3) evaluate the contribution of nocturnal heterogeneous N₂O₅ reactions to air pollution in Salt Lake Valley, Utah.

Field observations used in this thesis were primarily collected during three field campaigns with two custom-built cavity ring down spectrometers. As described in Chapter 2, these sensitive instruments have the advantage of collecting precise, simultaneous measurements of NO, NO₂, O₃, N₂O₅, NO₃, and the sum of reactive nitrogen oxides, NO_y. Deployment in both aircraft and ground-based campaigns in polluted regions across the U.S., concurrent with additional gas-phase and aerosol composition measurements, provided an important observational database that has and will continue to be used to address scientific questions with relevance to air quality, climate, and fundamental atmospheric chemical processes.

In this thesis, these field-observations informed two chemical box models, which, as described in Chapter 2, have advantages of computational simplicity and explicit chemical representation, relative to 3D chemical transport models. These two models were customized to investigate photochemical O₃ production in the Colorado Front Range and inorganic nocturnal reactive nitrogen chemistry in the wintertime residual layer.

In Chapter 3, I presented results from the summer 2014 FRAPPÉ campaign, based at the Boulder Atmospheric Observatory in Colorado. These data were combined with additional chemical and meteorological data collected at the same site in summer 2012 to constrain a chemically-explicit box model, used to investigate the influence of oil and natural gas (O&NG) VOCs, NO_x, and biogenic emissions on local photochemical O₃ production. Observational analysis of 2012 VOC data showed that alkanes, of which 86% were attributed to regional O&NG activities, contributed to 82% of the observed total VOC mixing ratio and 56% of the calculated OH reactivity. Additional analyses of summer 2014 observations could not statistically distinguish an influence of O&NG activity on local O₃ production using metrics of wind direction, simple chemical tracers, or ozone production efficiencies. In contrast, model simulations conducted with and without O&NG VOCs derived a 17.8% (2.9 ppbv) contribution of these VOCs to diel averaged maximum photochemical O₃ under 2012 conditions. This contribution did not include O&NG NO_x emissions, which may have contributed an additional 1.2% to maximum O₃ concentrations. Additional NO_x sensitivity simulations concluded that O₃ production under these conditions was NO_x limited at BAO, but may have been VOC limited south, toward Denver and even more NO_x sensitive north, toward Fort Collins. Additional sensitivity studies showed that tripling isoprene chemical constraints increased maximum photochemical O₃ by 2.5 %, indicating that drought conditions in 2012 did not significantly alter the original results.

Finally, model sensitivity studies were tested in Chapter 3 with a “lumped” chemical mechanism, with only 2% the number of reactions as the original simulations. Uncertainties remain regarding the applicability of such mechanisms to O&NG-influenced regions, as they have largely been developed for the chemistry expected in urban mixtures of VOCs. Here, both lumped and explicit mechanisms were able to reproduce the maximum observed diel averaged O₃ to within

0.7%. Additional observations and analyses are required to: 1) confirm the results presented here, 2) identify how the O₃ NO_x-VOC sensitivity regimes change across the Northern Front Range, and 3) determine how changes in the number of active O&NG sites and industry regulations since 2014 have and will continue to alter the influence of these emissions on local O₃ pollution.

In Chapters 4 and 5, I presented results from a box model analysis of data collected during the 2015 WINTER aircraft campaign over the eastern United States. Iteratively fit to WINTER observations of NO₂, O₃, N₂O₅, and ClNO₂, simulations of inorganic reactive nitrogen chemistry derived 2876 and 3425 individual values of $\gamma(\text{N}_2\text{O}_5)$ and $\phi(\text{ClNO}_2)$, respectively. The median $\gamma(\text{N}_2\text{O}_5)$ was 0.0143 with a range of 2×10^{-5} to 0.1751, encompassing the range of values reported from all previous field-studies. The derived $\phi(\text{ClNO}_2)$ values had a median of 0.138 and nearly encompassed the full possible range with a minimum and maximum of 0.003 and 1, respectively. Box model-derived values for $\gamma(\text{N}_2\text{O}_5)$ were within 13% of those predicted by the steady state approximation, while additional observation-based derivation methods for $\phi(\text{ClNO}_2)$ all agreed with the box model median to within the combined uncertainties of each method.

Both $\gamma(\text{N}_2\text{O}_5)$ and $\phi(\text{ClNO}_2)$ values were additionally evaluated in Chapters 4 and 5 against ambient observations of temperature, relative humidity, and aerosol composition, in order to critically evaluate parameterizations currently used in chemical transport models. Of the 14 $\gamma(\text{N}_2\text{O}_5)$ parameterizations tested, nine reproduced the median within a factor of 2, but none could reproduce the observed variability in the box model results. The worst agreement was found with the three parameterizations most frequently implemented in GEOS-Chem and CMAQ models. The form of the parameterization that best reproduced the box model results was finally used in Chapter 4 to derived the first field-based parameterization of $\gamma(\text{N}_2\text{O}_5)$. Fit to WINTER observations of aerosol nitrate, water, O:C ratio, relative humidity, particle radius, surface area, and volume, this

parameterization reproduced the median within a factor of 2 but was unable to reproduce the box model variability. These results suggest the possibility of an incorrectly parameterized $\gamma(\text{N}_2\text{O}_5)$ dependence, or an additional dependence on a non-measured variable such as aerosol phase or organic coating.

Results in Chapter 5 also showed that the laboratory based-parameterizations of $\phi(\text{ClNO}_2)$ were unable to reproduce WINTER box model results. In these comparisons, over 75% of the box model $\phi(\text{ClNO}_2)$ values were over-predicted parameterizations, even when accounting for parameterization uncertainties. Consistent with past field studies, the parametrization over-prediction suggested the presence of at least one additional process suppressing ClNO_2 formation on ambient aerosol, relative to the chloride-containing solutions that were used to derive current parameterizations. Correlations of the parameterization-box model difference with WINTER aerosol composition showed a strong negative dependence on calculated aerosol water. This trend was the result of positive correlation between box model $\phi(\text{ClNO}_2)$ and aerosol water, opposite of the parameterized trend, which is based on the currently-accepted aqueous-phase ClNO_2 formation mechanism. The mechanism by which low aerosol water concentrations may suppress ClNO_2 formation remains unclear.

Adjusting model $\phi(\text{ClNO}_2)$ values for direct loss of gas-phase ClNO_2 through surface deposition and aerosol uptake could improve parameterization – box model differences. In each test however, the median box model value remained lower than its parameterized equivalent. Lastly, two additional $\phi(\text{ClNO}_2)$ parameterizations were evaluated, which were altered to incorporate additional competition and aqueous-phase loss reactions. WINTER data provided mixed evidence in support of a competition reaction between aqueous-phase chloride and an additional reactive compound, and showed that direct aqueous-phase ClNO_2 loss would have had

to occur through reaction with a compound in excess of 1M concentrations or with a reaction rate constant $> 1 \times 10^9 \text{ s}^{-1}$. These results highlight the need for further laboratory and field-based studies to evaluate the mechanisms of ClNO₂ formation suppression on ambient aerosol under a wide range of environmental conditions. Such studies are required for the development of a robust $\phi(\text{ClNO}_2)$ parameterization that will help to improve the accuracy of simulations involving tropospheric halogens and reactive nitrogen chemistry.

In Chapter 6, I presented results from the recent UWFPS aircraft campaign in Northern Utah, during January and February 2017. This campaign provided the first vertically resolved chemical observations in Salt Lake Valley, collected during two wintertime pollution events. These observations are vital to investigating nocturnal chemistry in the residual layer and assessing the contribution of HNO₃ formation from N₂O₅ heterogeneous chemistry to total PM_{2.5} mass during regional pollution events. UWFPS observations showed that ~75% of the PM₁ mass sampled during pollution events in 2017 was attributable to NH₄NO₃, which was formation-limited aloft by the availability of HNO₃ relative to gas-phase NH₃. These results were confirmed by aerosol mass and partitioning simulations with the ISORROPIA model. Calculations of P_{NO_3} provided an upper limit estimate of 24.0 $\mu\text{g m}^{-3}$ for the contribution of nocturnal chemistry to NH₄NO₃ mass. This accumulation from a single night was large enough to explain the build-up of all PM_{2.5} observed at the ground.

The same winter box model was then fit to UWFPS aircraft observations to derive $\gamma(\text{N}_2\text{O}_5)$ and $\phi(\text{ClNO}_2)$ values. The $\gamma(\text{N}_2\text{O}_5)$ values had a median 5× larger than during WINTER, while median $\phi(\text{ClNO}_2)$ values were within 0.08. Similar to results in Chapter 4, a laboratory-based parameterization of $\gamma(\text{N}_2\text{O}_5)$ could not capture the variability in box model derived values, which agreed with the steady state approximation to within 7%. Values of $\phi(\text{ClNO}_2)$ were also over-

predicted by the parameterization, consistent with results from Chapter 5. While there was uncertainty in model results due to required assumptions, including start time, NO_3 -VOC reactivity, and deposition, the $\gamma(\text{N}_2\text{O}_5)$ values were large enough that HNO_3 formation was likely more sensitive to changes in the gas-phase formation rate of NO_3 than to N_2O_5 aerosol uptake. Additional forward-integrations with the model, using the fit $\gamma(\text{N}_2\text{O}_5)$ and $\phi(\text{ClNO}_2)$ values, predicted that nocturnal chemistry during a single night contributed an average of 67% to total (gas and particle phase) nitrate present at sunrise. The total contribution over the course of multiple days could be larger, assuming the majority of nitrate present at sunset forms the previous night. Additional observations of chemical and physical parameters are required to reduce the uncertainty in these results. In addition, photochemical box and 3D modeling is needed to further quantify the contribution of photochemical NO_x oxidation relative to nocturnal heterogenous chemistry to $\text{PM}_{2.5}$ formation in this region.

Reactive nitrogen oxides and their tropospheric transformations are integral to controlling the oxidizing capacity of the atmosphere and to air quality near Earth's surface. While uncertainties remain, the research tools and analysis methods developed for this thesis have allowed for the targeted investigation of fundamental heterogenous processes in the ambient environment, the evaluation of the emission sensitivities of nitrogen oxide chemistry, and its contribution to the production of atmospheric pollutants during both summer and winter seasons. Results in this thesis have not only advanced the collective knowledge of atmospheric reactive nitrogen chemistry, but have contributed to the literature that forms the scientific basis for air quality decision making, vital to ensuring healthy air for years to come.

Bibliography

Abeleira, A., Pollack, I., Sive, B., Zhou, Y., V. Fischer, E., & K. Farmer, D. (2017). Source Characterization of Volatile Organic Compounds in the Colorado Northern Front Range Metropolitan Area during Spring and Summer 2015: Sources of VOCs in the Colorado NFRMA. *122*. <https://doi.org/10.1002/2016JD026227>

Abeleira, A. J., & Farmer, D. K. (2017). Summer ozone in the northern Front Range metropolitan area: weekend–weekday effects, temperature dependences, and the impact of drought. *Atmospheric Chemistry and Physics*, *17*(11), 6517-6529. <https://doi.org/10.5194/acp-17-6517-2017>

Ahmadov, R., McKeen, S., Trainer, M., Banta, R., Brewer, A., Brown, S., et al. (2015). Understanding high wintertime ozone pollution events in an oil- and natural gas-producing region of the western US. *Atmospheric Chemistry and Physics*, *15*(1), 411-429. <https://doi.org/10.5194/acp-15-411-2015>

Aldener, M., Brown, S. S., Stark, H., Williams, E. J., Lerner, B. M., Kuster, W. C., et al. (2006). Reactivity and loss mechanisms of NO₃ and N₂O₅ in a polluted marine environment: Results from in situ measurements during New England Air Quality Study 2002. *Journal of Geophysical Research: Atmospheres*, *111*(D23). <https://doi.org/10.1029/2006JD007252>

Altshuller, A. P. (1993). Production of aldehydes as primary emissions and from secondary atmospheric reactions of alkenes and alkanes during the night and early morning hours. *Atmospheric Environment. Part A. General Topics*, *27*(1), 21-32. [https://doi.org/10.1016/0960-1686\(93\)90067-9](https://doi.org/10.1016/0960-1686(93)90067-9)

Alvarez, R. J., Senff, C. J., Langford, A. O., Weickmann, A. M., Law, D. C., Machol, J. L., et al. (2011). Development and Application of a Compact, Tunable, Solid-State Airborne Ozone Lidar System for Boundary Layer Profiling. *Journal of Atmospheric and Oceanic Technology*, *28*(10), 1258-1272. <https://doi.org/10.1175/JTECH-D-10-05044.1>

Anderson, L. G., Lanning, J. A., Barrell, R., Miyagishima, J., Jones, R. H., & Wolfe, P. (1996). Sources and sinks of formaldehyde and acetaldehyde: An analysis of Denver's ambient concentration data. *Atmospheric Environment*, *30*(12), 2113-2123. [https://doi.org/10.1016/1352-2310\(95\)00175-1](https://doi.org/10.1016/1352-2310(95)00175-1)

- Anttila, T., Kiendler-Scharr, A., Tillmann, R., & Mentel, T. F. (2006). On the reactive uptake of gaseous compounds by organic-coated aqueous aerosols: Theoretical analysis and application to the heterogeneous hydrolysis of N₂O₅. *The Journal of Physical Chemistry A*, *110*(35), 10435-10443. <https://doi.org/10.1021/jp062403c>
- Apel, E. C., Hornbrook, R. S., Hills, A. J., Blake, N. J., Barth, M. C., Weinheimer, A., et al. (2015). Upper tropospheric ozone production from lightning NO_x-impacted convection: Smoke ingestion case study from the DC3 campaign. *Journal of Geophysical Research: Atmospheres*, *120*(6), 2505–2523. <https://doi.org/10.1002/2014JD022121>
- Apodaca, R. L., Huff, D. M., & Simpson, W. R. (2008). The role of ice in N₂O₅ heterogeneous hydrolysis at high latitudes. *Atmospheric Chemistry and Physics*, *8*(24), 7451-7463. <https://doi.org/10.5194/acp-8-7451-2008>
- Atkinson, R. (1987). A structure-activity relationship for the estimation of rate constants for the gas-phase reactions of OH radicals with organic compounds. *International Journal of Chemical Kinetics*, *19*(9), 799-828. <https://doi.org/10.1002/kin.550190903>
- Atkinson, R. (2003). Kinetics of the gas-phase reactions of OH radicals with alkanes and cycloalkanes. *Atmospheric Chemistry and Physics*, *3*(6), 2233-2307. <https://doi.org/10.5194/acp-3-2233-2003>
- Atkinson, R., & Aschmann, S. M. (1984). Rate constants for the reactions of O₃ and OH radicals with a series of alkynes. *International Journal of Chemical Kinetics*, *16*(3), 259-268. <https://doi.org/10.1002/kin.550160308>
- Atkinson, R., & Arey, J. (2003). Atmospheric degradation of volatile organic compounds. *Chemical Reviews*, *103*(12), 4605-4638. <https://doi.org/10.1021/cr0206420>
- Attwood, A. R., Washenfelder, R. A., Brock, C. A., Hu, W., Baumann, K., Campuzano-Jost, P., et al. (2014). Trends in sulfate and organic aerosol mass in the Southeast U.S.: Impact on aerosol optical depth and radiative forcing. *Geophysical Research Letters*, *41*(21), 7701-7709. <https://doi.org/10.1002/2014GL061669>
- Augustine, J. A., DeLuisi, J. J., & Long, C. N. (2000). SURFRAD—A national Surface Radiation Budget Network for Atmospheric Research. *Bulletin of the American Meteorological Society*, *81*(10), 2341-2357. [https://doi.org/10.1175/1520-0477\(2000\)081<2341:SANSRB>2.3.CO;2](https://doi.org/10.1175/1520-0477(2000)081<2341:SANSRB>2.3.CO;2)
- Ault, A. P., Moffet, R. C., Baltrusaitis, J., Collins, D. B., Ruppel, M. J., Cuadra-Rodriguez, L. A., et al. (2013). Size-Dependent Changes in Sea Spray Aerosol Composition and Properties with Different Seawater Conditions. *Environmental Science & Technology*, *47*(11), 5603-5612. <https://doi.org/10.1021/es400416g>
- Avnery, S., Mauzerall, D. L., Liu, J., & Horowitz, L. W. (2011). Global crop yield reductions due to surface ozone exposure: 1. Year 2000 crop production losses and economic damage. *Atmospheric Environment*, *45*(13), 2284-2296. <https://doi.org/https://doi.org/10.1016/j.atmosenv.2010.11.045>

Baasandorj, M., Hoch, S. W., Bares, R., Lin, J. C., Brown, S. S., Millet, D. B., et al. (2017). Coupling between chemical and meteorological processes under persistent cold-air pool conditions: Evolution of wintertime PM_{2.5} pollution events and N₂O₅ observations in Utah's Salt Lake Valley. *Environmental Science & Technology*, 51(11), 5941-5950. <https://doi.org/10.1021/acs.est.6b06603>

Badger, C. L., Griffiths, P. T., George, I., Abbatt, J. P. D., & Cox, R. A. (2006). Reactive uptake of N₂O₅ by aerosol particles containing mixtures of humic acid and ammonium sulfate. *The Journal of Physical Chemistry A*, 110(21), 6986-6994. <https://doi.org/10.1021/jp0562678>

Bahreini, R., Ervens, B., Middlebrook, A. M., Warneke, C., de Gouw, J. A., DeCarlo, P. F., et al. (2009). Organic aerosol formation in urban and industrial plumes near Houston and Dallas, Texas. *Journal of Geophysical Research: Atmospheres*, 114(D7). <https://doi.org/10.1029/2008JD011493>

Bannan, T. J., Bacak, A., Le Breton, M., Flynn, M., Ouyang, B., McLeod, M., et al. (2017). Ground and Airborne U.K. Measurements of Nitryl Chloride: An Investigation of the Role of Cl Atom Oxidation at Weybourne Atmospheric Observatory. *Journal of Geophysical Research: Atmospheres*, 122(20), 11,154-11,165. <https://doi.org/10.1002/2017JD026624>

Bannan, T. J., Booth, A. M., Bacak, A., Muller, J. B. A., Leather, K. E., Le Breton, M., et al. (2015). The first UK measurements of nitryl chloride using a chemical ionization mass spectrometer in central London in the summer of 2012, and an investigation of the role of Cl atom oxidation. *Journal of Geophysical Research: Atmospheres*, 120(11), 5638-5657. <https://doi.org/10.1002/2014JD022629>

Beard, J. D., Beck, C., Graham, R., Packham, S. C., Traphagan, M., Giles, R. T., & Morgan, J. G. (2012). Winter temperature inversions and emergency department visits for asthma in Salt Lake County, Utah, 2003-2008. *Environmental Health Perspectives*, 120(10), 1385-1390. <https://doi.org/10.1289/ehp.1104349>

Behera, S. N., Sharma, M., Aneja, V. P., & Balasubramanian, R. (2013). Ammonia in the atmosphere: a review on emission sources, atmospheric chemistry and deposition on terrestrial bodies. *Environmental Science and Pollution Research*, 20(11), 8092-8131. <https://doi.org/10.1007/s11356-013-2051-9>

Behnke, W., Scheer, V., & Zetzsch, C. (1994). 18.P.01 Production of BrNO₂, BrNO₂ and ClNO₂ from the reaction between SEA SPRAY aerosol and N₂O₅. *Journal of Aerosol Science*, 25, 277-278. [https://doi.org/10.1016/0021-8502\(94\)90369-7](https://doi.org/10.1016/0021-8502(94)90369-7)

Behnke, W., Krüger, H. U., Scheer, V., & Zetzsch, C. (1991). Formation of atomic Cl from sea spray via photolysis of nitryl chloride: Determination of the sticking coefficient of N₂O₅ on NaCl aerosol. *Journal of Aerosol Science*, 22, S609-S612. [https://doi.org/10.1016/S0021-8502\(05\)80175-2](https://doi.org/10.1016/S0021-8502(05)80175-2)

Behnke, W., George, C., Scheer, V., & Zetzsch, C. (1997). Production and decay of ClNO₂ from the reaction of gaseous N₂O₅ with NaCl solution: Bulk and aerosol experiments. *Journal of Geophysical Research: Atmospheres*, 102(D3), 3795-3804. <https://doi.org/10.1029/96JD03057>

- Bell, M. L., Peng, R. D., & Dominici, F. (2006). The Exposure–Response Curve for Ozone and Risk of Mortality and the Adequacy of Current Ozone Regulations. *Environmental Health Perspectives*, *114*(4), 532-536. <https://doi.org/10.1289/ehp.8816>
- Bertram, A. K., Martin, S. T., Hanna, S. J., Smith, M. L., Bodsworth, A., Chen, Q., et al. (2011). Predicting the relative humidities of liquid-liquid phase separation, efflorescence, and deliquescence of mixed particles of ammonium sulfate, organic material, and water using the organic-to-sulfate mass ratio of the particle and the oxygen-to-carbon elemental ratio of the organic component. *Atmospheric Chemistry and Physics*, *11*(21), 10995-11006. <https://doi.org/10.5194/acp-11-10995-2011>
- Bertram, T. H., & Thornton, J. A. (2009). Toward a general parameterization of N₂O₅ reactivity on aqueous particles: the competing effects of particle liquid water, nitrate and chloride. *Atmospheric Chemistry and Physics*, *9*(21), 8351-8363. <https://doi.org/10.5194/acp-9-8351-2009>
- Bertram, T. H., Thornton, J. A., & Riedel, T. P. (2009a). An experimental technique for the direct measurement of N₂O₅ reactivity on ambient particles. *Atmospheric Measurement Techniques*, *2*(1), 231-242. <https://doi.org/10.5194/amt-2-231-2009>
- Bertram, T. H., Thornton, J. A., Riedel, T. P., Middlebrook, A. M., Bahreini, R., Bates, T. S., et al. (2009b). Direct observations of N₂O₅ reactivity on ambient aerosol particles. *Geophysical Research Letters*, *36*(19), L19803 <https://doi.org/10.1029/2009GL040248>
- Borbon, A., Gilman, J. B., Kuster, W. C., Grand, N., Chevaillier, S., Colomb, A., et al. (2013). Emission ratios of anthropogenic volatile organic compounds in northern mid-latitude megacities: Observations versus emission inventories in Los Angeles and Paris. *Journal of Geophysical Research: Atmospheres*, *118*(4), 2041-2057. <https://doi.org/10.1002/jgrd.50059>
- Brantley, H. L., Thoma, E. D., & Eisele, A. P. (2015). Assessment of volatile organic compound and hazardous air pollutant emissions from oil and natural gas well pads using mobile remote and on-site direct measurements. *Journal of the Air & Waste Management Association*, *65*(9), 1072-82. <https://doi.org/10.1080/10962247.2015.1056888>
- Brioude, J., Arnold, D., Stohl, A., Cassiani, M., Morton, D., Seibert, P., et al. (2013). The Lagrangian particle dispersion model FLEXPART-WRF version 3.1. *Geosci. Model Dev.*, *6*(6), 1889-1904. <https://doi.org/10.5194/gmd-6-1889-2013>
- Brock, C. A., Wagner, N. L., Anderson, B. E., Attwood, A. R., Beyersdorf, A., Campuzano-Jost, P., et al. (2016). Aerosol optical properties in the southeastern United States in summer – Part 1: Hygroscopic growth. *Atmospheric Chemistry and Physics*, *16*(8), 4987-5007. <https://doi.org/10.5194/acp-16-4987-2016>
- Brock, C. A., Cozic, J., Bahreini, R., Froyd, K. D., Middlebrook, A. M., McComiskey, A., et al. (2011). Characteristics, sources, and transport of aerosols measured in spring 2008 during the aerosol, radiation, and cloud processes affecting Arctic Climate (ARCPAC) Project. *Atmos. Chem. Phys.*, *11*(6), 2423-2453. <https://doi.org/10.5194/acp-11-2423-2011>

Brown, S. G., Hyslop, N. P., Roberts, P. T., McCarthy, M. C., & Lurmann, F. W. (2006). Wintertime Vertical Variations in Particulate Matter (PM) and Precursor Concentrations in the San Joaquin Valley during the California Regional Coarse PM/Fine PM Air Quality Study. *Journal of the Air & Waste Management Association*, 56(9), 1267-1277. <https://doi.org/10.1080/10473289.2006.10464583>

Brown, S. S. (2003). Absorption spectroscopy in high-finesse cavities for atmospheric studies. *Chemical Reviews*, 103(12), 5219-38. <https://doi.org/10.1021/cr020645c>

Brown, S. S., & Stutz, J. (2012). Nighttime radical observations and chemistry. *Chemical Society Reviews*, 41(19), 6405-47. <https://doi.org/10.1039/c2cs35181a>

Brown, S. S., Stark, H., & Ravishankara, A. R. (2003). Applicability of the steady state approximation to the interpretation of atmospheric observations of NO₃ and N₂O₅. *Journal of Geophysical Research*, 108(D17). <https://doi.org/10.1029/2003jd003407>

Brown, S. S., Dubé, W. P., Osthoff, H. D., Wolfe, D. E., Angevine, W. M., & Ravishankara, A. R. (2007a). High resolution vertical distributions of NO₃ and N₂O₅ through the nocturnal boundary layer. *Atmospheric Chemistry and Physics*, 7(1), 139-149. <https://doi.org/10.5194/acp-7-139-2007>

Brown, S. S., Osthoff, H. D., Stark, H., Dubé, W. P., Ryerson, T. B., Warneke, C., et al. (2005). Aircraft observations of daytime NO₃ and N₂O₅ and their implications for tropospheric chemistry. *Journal of Photochemistry and Photobiology A: Chemistry*, 176(1-3), 270-278. <https://doi.org/10.1016/j.jphotochem.2005.10.004>

Brown, S. S., Dubé, W. P., Tham, Y. J., Zha, Q., Xue, L., Poon, S., et al. (2016). Nighttime chemistry at a high altitude site above Hong Kong. *Journal of Geophysical Research: Atmospheres*, 121(5), 2457-2475. <https://doi.org/10.1002/2015JD024566>

Brown, S. S., Ryerson, T. B., Wollny, A. G., Brock, C. A., Peltier, R., Sullivan, A. P., et al. (2006). Variability in nocturnal nitrogen oxide processing and its role in regional air quality. *Science*, 311(5757), 67-70. <https://doi.org/10.1126/science.1120120>

Brown, S. S., Dubé, W. P., Peischl, J., Ryerson, T. B., Atlas, E., Warneke, C., et al. (2011). Budgets for nocturnal VOC oxidation by nitrate radicals aloft during the 2006 Texas Air Quality Study. *Journal of Geophysical Research: Atmospheres*, 116(D24), D24305 <https://doi.org/10.1029/2011JD016544>

Brown, S. S., Dubé, W. P., Fuchs, H., Ryerson, T. B., Wollny, A. G., Brock, C. A., et al. (2009). Reactive uptake coefficients for N₂O₅ determined from aircraft measurements during the Second Texas Air Quality Study: Comparison to current model parameterizations. *Journal of Geophysical Research: Atmospheres*, 114(D7), D00F10. <https://doi.org/10.1029/2008JD011679>

Brown, S. S., Thornton, J. A., Keene, W. C., Pszenny, A. A. P., Sive, B. C., Dubé, W. P., et al. (2013). Nitrogen, Aerosol Composition, and Halogens on a Tall Tower (NACHTT): Overview of a wintertime air chemistry field study in the front range urban corridor of Colorado. *Journal of Geophysical Research: Atmospheres*, 118(14), 8067-8085. <https://doi.org/10.1002/jgrd.50537>

Brown, S. S., Dubé, W. P., Osthoff, H. D., Stutz, J., Ryerson, T. B., Wollny, A. G., et al. (2007b). Vertical profiles in NO₃ and N₂O₅ measured from an aircraft: Results from the NOAA P-3 and surface platforms during the New England Air Quality Study 2004. *Journal of Geophysical Research*, 112(D22). <https://doi.org/10.1029/2007jd008883>

Burkholder, J. B., & Talukdar, R. K. (2012). Temperature dependence of the ozone absorption spectrum over the wavelength range 410 to 760 nm. *Geophysical Research Letters*, 21(7), 581-584. <https://doi.org/10.1029/93GL02311>

Butler, T. J., Vermeylen, F. M., Rury, M., Likens, G. E., Lee, B., Bowker, G. E., & McCluney, L. (2011). Response of ozone and nitrate to stationary source NO_x emission reductions in the eastern USA. *Atmospheric Environment*, 45(5), 1084-1094. <https://doi.org/10.1016/j.atmosenv.2010.11.040>

Cai, Y., Montague, D. C., Mooiweer-Bryan, W., & Deshler, T. (2008). Performance characteristics of the ultra high sensitivity aerosol spectrometer for particles between 55 and 800nm: Laboratory and field studies. *Journal of Aerosol Science*, 39(9), 759-769. <https://doi.org/10.1016/j.jaerosci.2008.04.007>

Carlton, A. G., Little, E., Moeller, M., Odoyo, S., & Shepson, P. B. (2014). The data gap: Can a lack of monitors obscure loss of clean air act benefits in fracking areas? *Environmental Science & Technology*, 48(2), 893-894. <https://doi.org/10.1021/es405672t>

Carter, W. P. L., & Seinfeld, J. H. (2012). Winter ozone formation and VOC incremental reactivities in the Upper Green River Basin of Wyoming. *Atmospheric Environment*, 50, 255-266. <https://doi.org/10.1016/j.atmosenv.2011.12.025>

Cerully, K. M., Bougiatioti, A., Hite Jr, J. R., Guo, H., Xu, L., Ng, N. L., et al. (2015). On the link between hygroscopicity, volatility, and oxidation state of ambient and water-soluble aerosols in the southeastern United States. *Atmospheric Chemistry and Physics*, 15(15), 8679-8694. <https://doi.org/10.5194/acp-15-8679-2015>

Chameides, W. L. (1978). The photochemical role of tropospheric nitrogen oxides. *Geophysical Research Letters*, 5(1), 17-20. <https://doi.org/10.1029/GL005i001p00017>

Chang, R. Y. W., Slowik, J. G., Shantz, N. C., Vlasenko, A., Liggio, J., Sjostedt, S. J., et al. (2010). The hygroscopicity parameter (κ) of ambient organic aerosol at a field site subject to biogenic and anthropogenic influences: relationship to degree of aerosol oxidation. *Atmospheric Chemistry and Physics*, 10(11), 5047-5064. <https://doi.org/10.5194/acp-10-5047-2010>

Chang, W. L., Bhave, P. V., Brown, S. S., Riemer, N., Stutz, J., & Dabdub, D. (2011). Heterogeneous atmospheric chemistry, ambient measurements, and model calculations of N₂O₅: A review. *Aerosol Science and Technology*, 45(6), 665-695. <https://doi.org/10.1080/02786826.2010.551672>

Chang, W. L., Brown, S. S., Stutz, J., Middlebrook, A. M., Bahreini, R., Wagner, N. L., et al. (2016). Evaluating N₂O₅ heterogeneous hydrolysis parameterizations for CalNex 2010. *Journal of Geophysical Research: Atmospheres*, 121(9), 5051-5070. <https://doi.org/10.1002/2015JD024737>

Cheadle, L. C., Oltmans, S., G., P., Schnell, R. C., Mattson, E. J., Herndon, S. C., et al. (2017). Surface ozone in the Colorado northern Front Range and the influence of oil and gas development during FRAPPE/DISCOVER-AQ in summer 2014. *Elementa Science of the Anthropocene*, 5(61). <https://doi.org/10.1525/elementa.254>

Chen, H., Karion, A., Rella, C. W., Winderlich, J., Gerbig, C., Filges, A., et al. (2013). Accurate measurements of carbon monoxide in humid air using the cavity ring-down spectroscopy (CRDS) technique. *Atmospheric Measurement Techniques*, 6(4), 1031-1040. <https://doi.org/10.5194/amt-6-1031-2013>

Chen, L. W. A., Watson, J. G., Chow, J. C., Green, M. C., Inouye, D., & Dick, K. (2012). Wintertime particulate pollution episodes in an urban valley of the Western US: a case study. *Atmospheric Chemistry and Physics*, 12(21), 10051-10064. <https://doi.org/10.5194/acp-12-10051-2012>

Colorado Department of Public Health and Environment (CDPHE). (2008). Denver Metro Area & North Front Range 8-Hour Ozone State Implementation Plan (SIP) Technical Support Documents (TSD), Appendix E, Executive Summary. [Available at <http://www.colorado.gov/airquality/documents/deno308/>].

Colorado Department of Public Health and Environment (CDPHE). (2015, 9/30/2015). Ozone Standard Exceedance Summary Table [Available at http://www.colorado.gov/airquality/html_resources/ozone_summary_table.pdf].

Colorado Department of Public Health and Environment (CDPHE). (2018). History of Ozone in Colorado. [Available at <https://www.colorado.gov/pacific/cdphe/ozone-planning-chronology>].

Colorado Oil and Gas Conservation Commission (COGCC). (1/2016). Oil and natural gas wells data available in the "Downloads" section. [Available at <http://cogcc.state.co.us/data2.html#/downloads>].

Colorado Oil and Gas Conservation Commission (COGCC). (2/2016). County level production available in the "DataBase" section. [Available at <http://cogcc.state.co.us/>].

Cooper, O. R., Langford, A. O., Parrish, D. D., & Fahey, D. W. (2015). Challenges of a lowered U.S. ozone standard. *Science*, 348(6239), 1096-1097. <https://doi.org/10.1126/science.aaa5748>

Cooper, O. R., Gao, R.-S., Tarasick, D., Leblanc, T., & Sweeney, C. (2012). Long-term ozone trends at rural ozone monitoring sites across the United States, 1990-2010. *Journal of Geophysical Research: Atmospheres*, 117(D22), D22307 <https://doi.org/10.1029/2012jd018261>

Cosman, L. M., Knopf, D. A., & Bertram, A. K. (2008). N₂O₅ reactive uptake on aqueous sulfuric acid solutions coated with branched and straight-chain insoluble organic surfactants. *Journal of Physical Chemistry A*, 112(11), 2386-2396. <https://doi.org/10.1021/jp710685r>

Crook, N. A., Clark, T. L., & Moncrieff, M. W. (1990). The Denver cyclone. Part I: Generation in low froude number flow. *Journal of the Atmospheric Sciences*, 47(23), 2725-2742. [https://doi.org/10.1175/1520-0469\(1990\)047<2725:TDCPIG>2.0.CO;2](https://doi.org/10.1175/1520-0469(1990)047<2725:TDCPIG>2.0.CO;2)

Crosson, E. R. (2008). A cavity ring-down analyzer for measuring atmospheric levels of methane, carbon dioxide, and water vapor. *Applied Physics B*, 92(3), 403-408. <https://doi.org/10.1007/s00340-008-3135-y>

Crutzen, P. J. (1970). The influence of nitrogen oxides on the atmospheric ozone content. *Quarterly Journal of the Royal Meteorological Society*, 96(408), 320-325. <https://doi.org/10.1002/qj.49709640815>

Cummings, O. T., & Wick, C. D. (2013). Interfacial behavior of simple inorganic salts at the air-water interface investigated with a polarizable model with electrostatic damping. *The Journal of Chemical Physics*, 139(6), 064708. <https://doi.org/10.1063/1.4817775>

Davidovits, P., Kolb, C. E., Williams, L. R., Jayne, J. T., & Worsnop, D. R. (2006). Mass accommodation and chemical reactions at gas-liquid interfaces. *Chemical Reviews*, 106(4), 1323-1354. <https://doi.org/10.1021/cr040366k>

Davidson, J. A., Viggiano, A. A., Howard, C. J., Dotan, I., Fehsenfeld, F. C., Albritton, D. L., & Ferguson, E. E. (1978). Rate constants for the reactions of O₂⁺, NO₂⁺, NO⁺, H₃O⁺, CO₃⁻, NO₂⁻, and halide ions with N₂O₅ at 300 K. *The Journal of Chemical Physics*, 68(5), 2085-2087. <https://doi.org/10.1063/1.436032>

Davis, J. M., Bhave, P. V., & Foley, K. M. (2008). Parameterization of N₂O₅ reaction probabilities on the surface of particles containing ammonium, sulfate, and nitrate. *Atmospheric Chemistry and Physics*, 8(17), 5295-5311. <https://doi.org/10.5194/acp-8-5295-2008>

Day, D. A., Wooldridge, P. J., Dillon, M. B., Thornton, J. A., & Cohen, R. C. (2002). A thermal dissociation laser-induced fluorescence instrument for in situ detection of NO₂, peroxy nitrates, alkyl nitrates, and HNO₃. *Journal of Geophysical Research: Atmospheres*, 107(D6), ACH 4-1-ACH 4-14. <https://doi.org/10.1029/2001JD000779>

DeCarlo, P. F., Kimmel, J. R., Trimborn, A., Northway, M. J., Jayne, J. T., Aiken, A. C., et al. (2006). Field-deployable, high-resolution, time-of-flight aerosol mass spectrometer. *Analytical Chemistry*, 78(24), 8281-8289. <https://doi.org/10.1021/ac061249n>

Dentener, F. J., & Crutzen, P. J. (1993). Reaction of N₂O₅ on tropospheric aerosols: Impact on the global distributions of NO_x, O₃, and OH. *Journal of Geophysical Research*, 98(D4), 7149. <https://doi.org/10.1029/92jd02979>

Dibb, J. E., Talbot, R. W., & Scheuer, E. M. (2000). Composition and distribution of aerosols over the North Atlantic during the Subsonic Assessment Ozone and Nitrogen Oxide Experiment (SONEX). *Journal of Geophysical Research: Atmospheres*, 105(D3), 3709-3717. <https://doi.org/10.1029/1999JD900424>

Dibb, J. E., Talbot, R. W., Scheuer, E. M., Blake, D. R., Blake, N. J., Gregory, G. L., et al. (1999). Aerosol chemical composition and distribution during the Pacific Exploratory Mission (PEM) Tropics. *Journal of Geophysical Research: Atmospheres*, 104(D5), 5785-5800. <https://doi.org/10.1029/1998JD100001>

Dockery, D. W., Pope, C. A., Xu, X., Spengler, J. D., Ware, J. H., Fay, M. E., et al. (1993). An association between air pollution and mortality in six U.S. cities. *New England Journal of Medicine*, 329(24), 1753-1759. <https://doi.org/10.1056/NEJM199312093292401>

Dorn, H. P., Apodaca, R. L., Ball, S. M., Brauers, T., Brown, S. S., Crowley, J. N., et al. (2013). Intercomparison of NO₃ radical detection instruments in the atmosphere simulation chamber SAPHIR. *Atmospheric Measurement Techniques*, 6(5), 1111-1140. <https://doi.org/10.5194/amt-6-1111-2013>

Dubé, W. P., Brown, S. S., Osthoff, H. D., Nunley, M. R., Ciciora, S. J., Paris, M. W., et al. (2006). Aircraft instrument for simultaneous, in situ measurement of NO₃ and N₂O₅ via pulsed cavity ring-down spectroscopy. *Review of Scientific Instruments*, 77(3), 034101. <https://doi.org/10.1063/1.2176058>

Duncan, B. N., Lamsal, L. N., Thompson, A. M., Yoshida, Y., Lu, Z., Streets, D. G., et al. (2016). A space-based, high-resolution view of notable changes in urban NO_x pollution around the world (2005–2014). *Journal of Geophysical Research: Atmospheres*, 121(2), 2015JD024121. <https://doi.org/10.1002/2015JD024121>

Edwards, P. M., Young, C. J., Aikin, K., deGouw, J., Dubé, W. P., Geiger, F., et al. (2013). Ozone photochemistry in an oil and natural gas extraction region during winter: simulations of a snow-free season in the Uintah Basin, Utah. *Atmospheric Chemistry and Physics*, 13(17), 8955-8971. <https://doi.org/10.5194/acp-13-8955-2013>

Edwards, P. M., Brown, S. S., Roberts, J. M., Ahmadov, R., Banta, R. M., deGouw, J. A., et al. (2014). High winter ozone pollution from carbonyl photolysis in an oil and gas basin. *Nature*, 514(7522), 351-4. <https://doi.org/10.1038/nature13767>

Ellis, R. A., Murphy, J. G., Pattey, E., van Haarlem, R., O'Brien, J. M., & Herndon, S. C. (2010). Characterizing a Quantum Cascade Tunable Infrared Laser Differential Absorption Spectrometer (QC-TILDAS) for measurements of atmospheric ammonia. *Atmos. Meas. Tech.*, 3(2), 397-406. <https://doi.org/10.5194/amt-3-397-2010>

Emmerson, K. M., & Evans, M. J. (2009). Comparison of tropospheric gas-phase chemistry schemes for use within global models. *Atmospheric Chemistry and Physics*, 9(5), 1831-1845. <https://doi.org/10.5194/acp-9-1831-2009>

Environmental Protection Agency (US EPA). (2016). National Emissions Inventory (NEI) air pollutant emissions trends data. [Available at: <https://www.epa.gov/air-emissions-inventories/air-pollutant-emissions-trends-data>].

Escorcía, E. N., Sjøstedt, S. J., & Abbatt, J. P. D. (2010). Kinetics of N₂O₅ hydrolysis on secondary organic aerosol and mixed ammonium bisulfate–secondary organic aerosol particles. *Journal of Physical Chemistry A*, 114(50), 13113-13121. <https://doi.org/10.1021/jp107721v>

Evans, J. M., & Helmig, D. (2017). Investigation of the influence of transport from oil and natural gas regions on elevated ozone levels in the northern Colorado front range. *Journal of the Air & Waste Management Association*, 67(2), 196-211. <https://doi.org/10.1080/10962247.2016.1226989>

- Evans, M. J., & Jacob, D. J. (2005). Impact of new laboratory studies of N₂O₅ hydrolysis on global model budgets of tropospheric nitrogen oxides, ozone, and OH. *Geophysical Research Letters*, 32(9), L09813. <https://doi.org/10.1029/2005GL022469>
- Faxon, C. B., Bean, J. K., & Ruiz, L. H. (2015). Inland concentrations of Cl₂ and ClNO₂ in southeast Texas suggest chlorine chemistry significantly contributes to atmospheric reactivity. *Atmosphere*, 6(10), 1487-1506. <https://doi.org/10.3390/atmos6101487>
- Feister, U., & Grewe, R. (1995). Spectral albedo measurements in the UV and visible region over different types of surfaces. *Photochemistry and Photobiology*, 62(4), 736-744. <https://doi.org/10.1111/j.1751-1097.1995.tb08723.x>
- Fickert, S., Helleis, F., Adams, J. W., Moortgat, G. K., & Crowley, J. N. (1998). Reactive uptake of ClNO₂ on aqueous bromide solutions. *Journal of Physical Chemistry A*, 102(52), 10689-10696. <https://doi.org/10.1021/jp983004n>
- Field, R. A., Soltis, J., McCarthy, M. C., Murphy, S., & Montague, D. C. (2015). Influence of oil and gas field operations on spatial and temporal distributions of atmospheric non-methane hydrocarbons and their effect on ozone formation in winter. *Atmos. Chem. Phys.*, 15(6), 3527-3542. <https://doi.org/10.5194/acp-15-3527-2015>
- Finlayson-Pitts, B. J., & Pitts, J. N. (2000). In B. J. F.-P. N. Pitts (Ed.), *Chemistry of the Upper and Lower Atmosphere* (pp. 15-42). San Diego: Academic Press.
- Folkers, M. (2001). Bestimmung der Reaktionswahrscheinlichkeit von N₂O₅ an troposphärisch relevanten Aerosolen, Ph.D. Thesis, Universität Köln.
- Folkers, M., Mentel, T. F., & Wahner, A. (2003). Influence of an organic coating on the reactivity of aqueous aerosols probed by the heterogeneous hydrolysis of N₂O₅. *Geophysical Research Letters*, 30(12), 1644. <https://doi.org/10.1029/2003GL017168>
- Fountoukis, C., & Nenes, A. (2007). ISORROPIA II: a computationally efficient thermodynamic equilibrium model for K⁺ -Ca²⁺ -Mg²⁺ -NH₄⁺ -Na⁺ -SO₄²⁻ -NO₃⁻ -Cl⁻ -H₂O aerosols. *Atmospheric Chemistry and Physics*, 7(17), 4639-4659. <https://doi.org/10.5194/acp-7-4639-2007>
- Franchin, A., Middlebrook, A. M., Crosman, E. T., Docherty, K. S., Fibiger, D. L., Goldberger, L., et al. Aircraft study of the chemical and physical properties of aerosols during intense winter pollution episodes in the Great Salt Lake Basin. *In Preparation*.
- Franchin, A., Crosman, E. T., Docherty, K. S., Fibiger, D. L., Goldberger, L., Hoch, S. W., et al. (In Prep). Airborne and ground based observations of aerosol chemical and physical properties during intense winter pollution episodes in the Great Salt Lake Basin. *In Preparation*.
- Frenzel, A., Scheer, V., Sikorski, R., George, C., Behnke, W., & Zetzsch, C. (1998). Heterogeneous Interconversion Reactions of BrNO₂, ClNO₂, Br₂, and Cl₂. *The Journal of Physical Chemistry A*, 102(8), 1329-1337. <https://doi.org/10.1021/jp973044b>

Fried, A., Henry, B. E., Calvert, J. G., & Mozurkewich, M. (1994). The reaction probability of N_2O_5 with sulfuric acid aerosols at stratospheric temperatures and compositions. *Journal of Geophysical Research: Atmospheres*, 99(D2), 3517-3532. <https://doi.org/10.1029/93JD01907>

Fried, A., Wang, Y., Cantrell, C., Wert, B., Walega, J., Ridley, B., et al. (2003). Tunable diode laser measurements of formaldehyde during the TOPSE 2000 study: Distributions, trends, and model comparisons. *Journal of Geophysical Research: Atmospheres*, 108(D4), 8365. <https://doi.org/10.1029/2002JD002208>

Fuchs, & Sutugin, A. G. (1970). *Highly Dispersed Aerosols*: Ann Arbor Science Publishers, Ann Arbor MI, 1970.

Fuchs, H., Dube, W. P., Cicciola, S. J., & Brown, S. S. (2008). Determination of inlet transmission and conversion efficiencies for in situ measurements of the nocturnal nitrogen oxides, NO_3 , N_2O_5 and NO_2 , via pulsed cavity ring-down spectroscopy. *Analytical Chemistry*, 80(15), 6010-6017. <https://doi.org/10.1021/Ac8007253>

Fuchs, H., Dube, W. P., Lerner, B. M., Wagner, N. L., Williams, E. J., & Brown, S. S. (2009). A sensitive and versatile detector for atmospheric NO_2 and NO_x based on blue diode laser cavity ring-down spectroscopy. *Environmental Science & Technology*, 43(20), 7831-6. <https://doi.org/10.1021/es902067h>

Gaston, C. J., & Thornton, J. A. (2016). Reacto-diffusive length of N_2O_5 in aqueous sulfate- and chloride-containing aerosol particles. *Journal of Physical Chemistry A*, 120(7), 1039-1045. <https://doi.org/10.1021/acs.jpca.5b11914>

Gaston, C. J., Thornton, J. A., & Ng, N. L. (2014). Reactive uptake of N_2O_5 to internally mixed inorganic and organic particles: the role of organic carbon oxidation state and inferred organic phase separations. *Atmospheric Chemistry and Physics*, 14(11), 5693-5707. <https://doi.org/10.5194/acp-14-5693-2014>

Gentner, D. R., Ford, T. B., Guha, A., Boulanger, K., Brioude, J., Angevine, W. M., et al. (2014). Emissions of organic carbon and methane from petroleum and dairy operations in California's San Joaquin Valley. *Atmospheric Chemistry and Physics*, 14(10), 4955-4978. <https://doi.org/10.5194/acp-14-4955-2014>

George, C., Ponche, J. L., Mirabel, P., Behnke, W., Scheer, V., & Zetzsch, C. (1994). Study of the uptake of N_2O_5 by water and NaCl solutions. *The Journal of Physical Chemistry*, 98(35), 8780-8784. <https://doi.org/10.1021/j100086a031>

Gerbig, C., Schmitgen, S., Kley, D., Volz-Thomas, A., Dewey, K., & Haaks, D. (1999). An improved fast-response vacuum-UV resonance fluorescence CO instrument. *Journal of Geophysical Research: Atmospheres*, 104(D1), 1699-1704. <https://doi.org/10.1029/1998JD100031>

Gillies, R. R., Wang, S.-Y., & Booth, M. R. (2010). Atmospheric Scale Interaction on Wintertime Intermountain West Low-Level Inversions. *Weather and Forecasting*, 25(4), 1196-1210. <https://doi.org/10.1175/2010WAF2222380.1>

- Gilman, J. B., Lerner, B. M., Kuster, W. C., & de Gouw, J. A. (2013). Source signature of volatile organic compounds from oil and natural gas operations in northeastern Colorado. *Environmental Science & Technology*, 47(3), 1297-305. <https://doi.org/10.1021/es304119a>
- Gilman, J. B., Burkhardt, J. F., Lerner, B. M., Williams, E. J., & Kuster, W. C. (2010). Ozone variability and halogen oxidation within the Arctic and sub-Arctic springtime boundary layer. *Atmospheric Chemistry and Physics*, 10(21), 10223-10236. <https://doi.org/10.5194/acp-10-10223-2010>
- Green, M. C., Chow, J. C., Watson, J. G., Dick, K., & Inouye, D. (2015). Effects of Snow Cover and Atmospheric Stability on Winter PM_{2.5} Concentrations in Western U.S. Valleys. *Journal of Applied Meteorology and Climatology*, 54(6), 1191-1201. <https://doi.org/10.1175/JAMC-D-14-0191.1>
- Griffin, R. J., Johnson, C. A., Talbot, R. W., Mao, H., Russo, R. S., Zhou, Y., & Sive, B. C. (2004). Quantification of ozone formation metrics at Thompson Farm during the New England Air Quality Study (NEAQS) 2002. *Journal of Geophysical Research: Atmospheres*, 109(D24), D24302. <https://doi.org/10.1029/2004JD005344>
- Griffiths, P. T., & Cox, A. R. (2009). Temperature dependence of heterogeneous uptake of N₂O₅ by ammonium sulfate aerosol. *Atmospheric Science Letters*, 10(3), 159-163. <https://doi.org/10.1002/asl.225>
- Griffiths, P. T., Badger, C. L., Cox, R. A., Folkers, M., Henk, H. H., & Mentel, T. F. (2009). Reactive uptake of N₂O₅ by aerosols containing dicarboxylic acids. Effect of particle phase, composition, and nitrate content. *The Journal of Physical Chemistry A*, 113(17), 5082-5090. <https://doi.org/10.1021/jp8096814>
- Gross, S., Iannone, R., Xiao, S., & Bertram, A. K. (2009). Reactive uptake studies of NO₃ and N₂O₅ on alkenoic acid, alkanolate, and polyalcohol substrates to probe nighttime aerosol chemistry. *Physical Chemistry Chemical Physics*, 11(36), 7792-7803. <https://doi.org/10.1039/B904741G>
- Guenther, A., Karl, T., Harley, P., Wiedinmyer, C., Palmer, P. I., & Geron, C. (2006). Estimates of global terrestrial isoprene emissions using MEGAN (Model of Emissions of Gases and Aerosols from Nature). *Atmospheric Chemistry and Physics*, 6(11), 3181-3210. <https://doi.org/10.5194/acp-6-3181-2006>
- Guo, H., Sullivan, A. P., Campuzano-Jost, P., Schroder, J. C., Lopez-Hilfiker, F. D., Dibb, J. E., et al. (2016). Fine particle pH and the partitioning of nitric acid during winter in the northeastern United States. *Journal of Geophysical Research: Atmospheres*, 121(17), 10,355-10,376. <https://doi.org/10.1002/2016JD025311>
- Hagerman, L. M., Aneja, V. P., & Lonneman, W. A. (1997). Characterization of non-methane hydrocarbons in the rural southeast United States. *Atmospheric Environment*, 31(23), 4017-4038. [https://doi.org/10.1016/S1352-2310\(97\)00223-9](https://doi.org/10.1016/S1352-2310(97)00223-9)

Hallquist, M., Stewart, D. J., Baker, J., & Cox, A. R. (2000). Hydrolysis of N₂O₅ on submicron sulfuric acid aerosols. *The Journal of Physical Chemistry A*, 104(17), 3984-3990. <https://doi.org/10.1021/jp9939625>

Hallquist, M., Stewart, D. J., Stephenson, S. K., & Cox, A. R. (2003). Hydrolysis of N₂O₅ on submicron sulfate aerosols. *Physical Chemistry Chemical Physics*, 5(16), 3453-3463. <https://doi.org/10.1039/B301827J>

Hansen, J. C., Woolwine Iii, W. R., Bates, B. L., Clark, J. M., Kuprov, R. Y., Mukherjee, P., et al. (2010). Semicontinuous PM_{2.5} and PM₁₀ Mass and Composition Measurements in Lindon, Utah, during Winter 2007. *Journal of the Air & Waste Management Association*, 60(3), 346-355. <https://doi.org/10.3155/1047-3289.60.3.346>

Harrison, L. L., Michalsky, J., & Berndt, J. (1994). Automated multifilter rotating shadow-band radiometer: an instrument for optical depth and radiation measurements. *Applied Optics*, 33(22), 5118-5125. <https://doi.org/10.1364/AO.33.005118>

Hayes, P. L., Ortega, A. M., Cubison, M. J., Froyd, K. D., Zhao, Y., Cliff, S. S., et al. (2013). Organic aerosol composition and sources in Pasadena, California, during the 2010 CalNex campaign. *Journal of Geophysical Research: Atmospheres*, 118(16), 9233-9257. <https://doi.org/10.1002/jgrd.50530>

Heal, M. R., Harrison, M. A. J., & Neil Cape, J. (2007). Aqueous-phase nitration of phenol by N₂O₅ and ClNO₂. *Atmospheric Environment*, 41(17), 3515-3520. <https://doi.org/https://doi.org/10.1016/j.atmosenv.2007.02.003>

Helmig, D., Thompson, C. R., Evans, J., Boylan, P., Hueber, J., & Park, J. H. (2014). Highly elevated atmospheric levels of volatile organic compounds in the Uintah Basin, Utah. *Environmental Science & Technology*, 48(9), 4707-4715. <https://doi.org/10.1021/es405046r>

Henderson, B. H., Pinder, R. W., Crooks, J., Cohen, R. C., Hutzell, W. T., Sarwar, G., et al. (2011). Evaluation of simulated photochemical partitioning of oxidized nitrogen in the upper troposphere. *Atmospheric Chemistry and Physics*, 11(1), 275-291. <https://doi.org/10.5194/acp-11-275-2011>

Hirsch, A. I., Munger, J. W., Jacob, D. J., Horowitz, L. W., & Goldstein, A. H. (1996). Seasonal variation of the ozone production efficiency per unit NO_x at Harvard Forest, Massachusetts. *Journal of Geophysical Research: Atmospheres*, 101(D7), 12659-12666. <https://doi.org/10.1029/96JD00557>

Hjorth, J., Ottobriini, G., & Restelli, G. (1986). Reaction of the NO₃ radical with CO: Determination of an upper limit for the rate constant using FTIR spectroscopy. *International Journal of Chemical Kinetics*, 18(8), 819-827. <https://doi.org/10.1002/kin.550180802>

Hodzic, A., & Jimenez, J. L. (2011). Modeling anthropogenically controlled secondary organic aerosols in a megacity: a simplified framework for global and climate models. *Geoscientific Model Development*, 4(4), 901-917. <https://doi.org/10.5194/gmd-4-901-2011>

Hoggett, J. G., Moodie, R. B., Penton, J. R., & Schofield, K. (1971). *Nitration and Aromatic Reactivity*: University Press: Great Britain.

Hu, J. H., & Abbatt, J. P. D. (1997). Reaction probabilities for N₂O₅ hydrolysis on sulfuric acid and ammonium sulfate aerosols at room temperature. *The Journal of Physical Chemistry A*, 101(5), 871-878. <https://doi.org/10.1021/jp9627436>

Hu, W. W., Campuzano-Jost, P., Palm, B. B., Day, D. A., Ortega, A. M., Hayes, P. L., et al. (2015). Characterization of a real-time tracer for isoprene epoxydiols-derived secondary organic aerosol (IEPOX-SOA) from aerosol mass spectrometer measurements. *Atmospheric Chemistry and Physics*, 15(20), 11807-11833. <https://doi.org/10.5194/acp-15-11807-2015>

IPCC. (2014). Summary for Policymakers. In C. B. Field, V. R. Barros, D. J. Dokken, K. J. Mach, M. D. Mastrandrea, T. E. Bilir, M. Chatterjee, K. L. Ebi, Y. O. Estrada, R. C. Genova, B. Girma, E. S. Kissel, A. N. Levy, S. MacCracken, P. R. Mastrandrea, & L. L. White (Eds.), *Climate Change 2014: Impacts, Adaptation, and Vulnerability. Part A: Global and Sectoral Aspects. Contribution of Working Group II to the Fifth Assessment Report of the Intergovernmental Panel on Climate Change* (pp. 1-32). Cambridge, United Kingdom, and New York, NY, USA: Cambridge University Press.

IUPAC. (2008a). IUPAC Task Group on Atmospheric Chemical Kinetic Data Evaluation – Data Sheet NO_x18 [Available at http://iupac.pole-ether.fr/htdocs/datasheets/pdf/NOx18_HO2_NO3.pdf].

IUPAC. (2008b). Data Sheet NO_x18. [Available at: <http://iupac.pole-ether.fr>].

Jenkin, M. E., Young, J. C., & Rickard, A. R. (2015). The MCM v3.3.1 degradation scheme for isoprene. *Atmospheric Chemistry and Physics*, 15(20), 11433-11459. <https://doi.org/10.5194/acp-15-11433-2015>

Jimenez, J. L., Canagaratna, M. R., Donahue, N. M., Prevot, A. S. H., Zhang, Q., Kroll, J. H., et al. (2009). Evolution of organic aerosols in the atmosphere. *Science*, 326(5959), 1525. <https://doi.org/10.1126/science.1180353>

Kaimal, J. C., & Gaynor, J. E. (1983). The Boulder Atmospheric Observatory. *Journal of Climate and Applied Meteorology*, 22(5), 863-880. [https://doi.org/10.1175/1520-0450\(1983\)022<0863:TBAO>2.0.CO;2](https://doi.org/10.1175/1520-0450(1983)022<0863:TBAO>2.0.CO;2)

Kane, S. M., Caloz, F., & Leu, M.-T. (2001). Heterogeneous uptake of gaseous N₂O₅ by (NH₄)₂SO₄, NH₄HSO₄, and H₂SO₄ aerosols. *The Journal of Physical Chemistry A*, 105(26), 6465-6470. <https://doi.org/10.1021/jp010490x>

Kelly, K. E., Kotchenruther, R., Kuprov, R., & Silcox, G. D. (2013). Receptor model source attributions for Utah's Salt Lake City airshed and the impacts of wintertime secondary ammonium nitrate and ammonium chloride aerosol. *Journal of the Air & Waste Management Association*, 63(5), 575-590. <https://doi.org/10.1080/10962247.2013.774819>

- Kemball-Cook, S., Bar-Ilan, A., Grant, J., Parker, L., Jung, J., Santamaria, W., et al. (2010). Ozone impacts of natural gas development in the Haynesville Shale. *Environmental Science & Technology*, 44(24), 9357-9363. <https://doi.org/10.1021/es1021137>
- Kenagy, H. S., Sparks, T. L., Ebben, C. J., Wooldridge, P. J., Lopez-Hilfiker, F. D., Lee, B. H., et al. (2018). NO_x Lifetime and NO_y Partitioning During WINTER. *Journal of Geophysical Research: Atmospheres* - Submitted.
- Kercher, J. P., Riedel, T. P., & Thornton, J. A. (2009). Chlorine activation by N₂O₅: Simultaneous, in situ detection of ClNO₂ and N₂O₅ by chemical ionization mass spectrometry. *Atmospheric Measurement Techniques*, 2(1), 193-204. <https://doi.org/10.5194/amt-2-193-2009>
- Kim, M. J., Farmer, D. K., & Bertram, T. H. (2014). A controlling role for the air-sea interface in the chemical processing of reactive nitrogen in the coastal marine boundary layer. *Proceedings of the National Academy of Sciences of the United States of America*, 111(11), 3943-3948. <https://doi.org/10.1073/pnas.1318694111>
- Kim, P. S., Jacob, D. J., Fisher, J. A., Travis, K., Yu, K., Zhu, L., et al. (2015). Sources, seasonality, and trends of southeast US aerosol: an integrated analysis of surface, aircraft, and satellite observations with the GEOS-Chem chemical transport model. *Atmospheric Chemistry and Physics*, 15(18), 10411-10433. <https://doi.org/10.5194/acp-15-10411-2015>
- Kleinman, L., Daum, P. H., Lee, Y.-N., Nunnermacker, L. J., Springston, S. R., Weinstein-Lloyd, J., & Rudolph, J. (2002). Ozone production efficiency in an urban area. *Journal of Geophysical Research: Atmospheres*, 107(D23), 4733. <https://doi.org/10.1029/2002JD002529>
- Kleinman, L. I., Lee, Y.-N., Springston, S. R., Nunnermacker, L., Zhou, X., Brown, R., et al. (1994). Ozone formation at a rural site in the southeastern United States. *Journal of Geophysical Research: Atmospheres*, 99(D2), 3469-3482. <https://doi.org/10.1029/93JD02991>
- Kolb, C. E., Davidovits, P., Jayne, J. T., Shi, Q., & Worsnop, D. R. (2002). Kinetics of trace gas uptake by liquid surfaces. *Progress in Reaction Kinetics and Mechanism*, 27(1), 1-46. <https://doi.org/10.3184/007967402103165324>
- Kuprov, R., Eatough, D. J., Cruickshank, T., Olson, N., Cropper, P. M., & Hansen, J. C. (2014). Composition and secondary formation of fine particulate matter in the Salt Lake Valley: Winter 2009. *Journal of the Air & Waste Management Association*, 64(8), 957-969. <https://doi.org/10.1080/10962247.2014.903878>
- Langford, A. O., Senff, C. J., Alvarez, R. J., Brioude, J., Cooper, O. R., Holloway, J. S., et al. (2015). An overview of the 2013 Las Vegas Ozone Study (LVOS): Impact of stratospheric intrusions and long-range transport on surface air quality. *Atmospheric Environment*, 109, 305-322. <https://doi.org/10.1016/J.Atmosenv.2014.08.040>
- Laskin, A., Moffet Ryan, C., Gilles Mary, K., Fast Jerome, D., Zaveri Rahul, A., Wang, B., et al. (2012). Tropospheric chemistry of internally mixed sea salt and organic particles: Surprising reactivity of NaCl with weak organic acids. *Journal of Geophysical Research: Atmospheres*, 117(D15). <https://doi.org/10.1029/2012JD017743>

Lee, B. H., Lopez-Hilfiker, F. D., Mohr, C., Kurtén, T., Worsnop, D. R., & Thornton, J. A. (2014). An iodide-adduct high-resolution time-of-flight chemical-ionization mass spectrometer: Application to atmospheric inorganic and organic compounds. *Environmental Science & Technology*, 48(11), 6309-6317. <https://doi.org/10.1021/es500362a>

Lee, B. H., Lopez-Hilfiker, F. D., Veres, P., McDuffie, E. E., Fibiger, D. L., Sparks, T. L., et al. (2018). Flight deployment of a high-resolution time-of-flight chemical ionization mass spectrometer: Observations of reactive halogen and nitrogen oxide species. *Journal of Geophysical Research: Atmospheres*, In Preparation.

Lin, X., Trainer, M., & Liu, S. C. (1988). On the nonlinearity of the tropospheric ozone production. *Journal of Geophysical Research: Atmospheres*, 93(D12), 15879-15888. <https://doi.org/10.1029/JD093iD12p15879>

Liu, X., Qu, H., Huey, L. G., Wang, Y., Sjostedt, S., Zeng, L., et al. (2017). High levels of daytime molecular chlorine and nitryl chloride at a rural site on the North China Plain. *Environmental Science & Technology*, 51(17), 9588-9595. <https://doi.org/10.1021/acs.est.7b03039>

Livingston, C., Rieger, P., & Winer, A. (2009). Ammonia emissions from a representative in-use fleet of light and medium-duty vehicles in the California South Coast Air Basin. *Atmospheric Environment*, 43(21), 3326-3333. <https://doi.org/10.1016/j.atmosenv.2009.04.009>

Long, R. W., Eatough, N. L., Eatough, D. J., Meyer, M. B., & Wilson, W. E. (2005a). Continuous Determination of Fine Particulate Matter Mass in the Salt Lake City Environmental Monitoring Project: A Comparison of Real-Time and Conventional TEOM Monitor Results. *Journal of the Air & Waste Management Association*, 55(12), 1782-1796. <https://doi.org/10.1080/10473289.2005.10464776>

Long, R. W., Eatough, N. L., Mangelson, N. F., Thompson, W., Fiet, K., Smith, S., et al. (2003). The measurement of PM_{2.5}, including semi-volatile components, in the EMPACT program: results from the Salt Lake City Study. *Atmospheric Environment*, 37(31), 4407-4417. [https://doi.org/10.1016/S1352-2310\(03\)00585-5](https://doi.org/10.1016/S1352-2310(03)00585-5)

Long, R. W., Modey, W. K., Smith, P. S., Smith, R., Merrill, C., Pratt, J., et al. (2005b). One- and Three-Hour PM_{2.5} Characterization, Speciation, and Source Apportionment Using Continuous and Integrated Samplers. *Aerosol Science and Technology*, 39(3), 238-248. <https://doi.org/10.1080/027868290925633>

Lopez-Hilfiker, F. D., Constantin, K., Kercher, J. P., & Thornton, J. A. (2012). Temperature dependent halogen activation by N₂O₅ reactions on halide-doped ice surfaces. *Atmos. Chem. Phys.*, 12(11), 5237-5247. <https://doi.org/10.5194/acp-12-5237-2012>

Losey, D. J., Parker, R. G., & Freedman, M. A. (2016). pH dependence of liquid-liquid phase separation in organic aerosol. *The Journal of Physical Chemistry Letters*, 7(19), 3861-3865. <https://doi.org/10.1021/acs.jpcllett.6b01621>

Lüttke, J., Scheer, V., Levsen, K., Wünsch, G., Neil Cape, J., Hargreaves, K. J., et al. (1997). Occurrence and formation of nitrated phenols in and out of cloud. *Atmospheric Environment*, 31(16), 2637-2648. [https://doi.org/10.1016/S1352-2310\(96\)00229-4](https://doi.org/10.1016/S1352-2310(96)00229-4)

Macintyre, H. L., & Evans, M. J. (2010). Sensitivity of a global model to the uptake of N₂O₅ by tropospheric aerosol. *Atmospheric Chemistry and Physics*, 10(15), 7409-7414. <https://doi.org/10.5194/acp-10-7409-2010>

Madronich, S. S., McKenzie, R. L., Bjorn, L. O., & Caldwell, M. M. (1998). Changes in biologically active ultraviolet radiation reaching the Earth's surface. *Journal of Photochemistry and Photobiology B-Biology*, 46(1-3), 5-19. [https://doi.org/doi.org/10.1016/S1011-1344\(98\)00182-1](https://doi.org/doi.org/10.1016/S1011-1344(98)00182-1)

Malek, E., Davis, T., Martin, R. S., & Silva, P. J. (2006). Meteorological and environmental aspects of one of the worst national air pollution episodes (January, 2004) in Logan, Cache Valley, Utah, USA. *Atmospheric Research*, 79(2), 108-122. <https://doi.org/10.1016/j.atmosres.2005.05.003>

Mangelson, N. F., Lewis, L., Joseph, J. M., Cui, W., Machir, J., Eatough, D. J., et al. (1997). The contribution of sulfate and nitrate to atmospheric fine particles during winter inversion fogs in Cache Valley, Utah. *Journal of the Air & Waste Management Association*, 47(2), 167-175. <https://doi.org/10.1080/10473289.1997.10464429>

Mao, J., Paulot, F., Jacob, D. J., Cohen, R. C., Crouse, J. D., Wennberg, P. O., et al. (2013). Ozone and organic nitrates over the eastern United States: Sensitivity to isoprene chemistry. *Journal of Geophysical Research: Atmospheres*, 118(19), 2013JD020231. <https://doi.org/10.1002/jgrd.50817>

Martin, R. (2006). Cache Valley Air Quality Studies [Available at <http://citeseerx.ist.psu.edu/viewdoc/download?doi=10.1.1.127.8179&rep=rep1&type=pdf>].

McDuffie, E. E., Edwards, P. M., Gilman, J. B., Lerner, B. M., Dubé, W. P., Trainer, M., et al. (2016). Influence of oil and gas emissions on summertime ozone in the Colorado Northern Front Range. *Journal of Geophysical Research: Atmospheres*, 121(14), 8712-8729. <https://doi.org/10.1002/2016jd025265>

McDuffie, E. E., Fibiger, D. L., Dubé, W. P., Lopez-Hilfiker, F., Lee, B. H., Thornton, J. A., et al. (2018). Heterogeneous N₂O₅ uptake during winter: Aircraft measurements during the 2015 WINTER campaign and critical evaluation of current parameterizations. *Journal of Geophysical Research: Atmospheres*. <https://doi.org/10.1002/2018JD028336>

McManus, J. B., Shorter, J. H., Nelson, D. D., Zahniser, M. S., Glenn, D. E., & McGovern, R. M. (2008). Pulsed quantum cascade laser instrument with compact design for rapid, high sensitivity measurements of trace gases in air. *Applied Physics B*, 92(3), 387-392. <https://doi.org/10.1007/s00340-008-3129-9>

- McNeill, V. F., Patterson, J., Wolfe, G. M., & Thornton, J. A. (2006). The effect of varying levels of surfactant on the reactive uptake of N_2O_5 to aqueous aerosol. *Atmospheric Chemistry and Physics*, 6(6), 1635-1644. <https://doi.org/10.5194/acp-6-1635-2006>
- Mei, F., Hayes, P. L., Ortega, A., Taylor, J. W., Allan, J. D., Gilman, J., et al. (2013). Droplet activation properties of organic aerosols observed at an urban site during CalNex-LA. *Journal of Geophysical Research: Atmospheres*, 118(7), 2903-2917. <https://doi.org/10.1002/jgrd.50285>
- Mentel, T., F. Bleilbens, D., & Wahner, A. (1996). A study of nighttime nitrogen oxide oxidation in a large reaction chamber—the fate of NO_2 , N_2O_5 , HNO_3 , and O_3 at different humidities. *Atmospheric Environment*, 30(23), 4007-4020. [https://doi.org/10.1016/1352-2310\(96\)00117-3](https://doi.org/10.1016/1352-2310(96)00117-3)
- Mentel, T., F. Sohn, M., & Wahner, A. (1999). Nitrate effect in the heterogeneous hydrolysis of dinitrogen pentoxide on aqueous aerosols. *Physical Chemistry Chemical Physics*, 1(24), 5451-5457. <https://doi.org/10.1039/A905338G>
- Michalsky, J. J., & Hodges, G. B. (2013). Field measured spectral albedo—four years of data from the western U.S. prairie. *Journal of Geophysical Research: Atmospheres*, 118(2), 813-825. <https://doi.org/10.1002/jgrd.50149>
- Middlebrook, A. M., Bahreini, R., Jimenez, J. L., & Canagaratna, M. R. (2012). Evaluation of Composition-Dependent Collection Efficiencies for the Aerodyne Aerosol Mass Spectrometer using Field Data. *Aerosol Science and Technology*, 46(3), 258-271. <https://doi.org/10.1080/02786826.2011.620041>
- Mielke, L. H., Furgeson, A., & Osthoff, H. D. (2011). Observation of ClNO_2 in a Mid-Continental Urban Environment. *Environmental Science & Technology*, 45(20), 8889-8896. <https://doi.org/10.1021/es201955u>
- Mielke, L. H., Furgeson, A., Odame-Ankrah, C. A., & Osthoff, H. D. (2016). Ubiquity of ClNO_2 in the urban boundary layer of Calgary, Alberta, Canada. *Canadian Journal of Chemistry*, 94(4), 414-423. <https://doi.org/10.1139/cjc-2015-0426>
- Mielke, L. H., Stutz, J., Tsai, C., Hurlock, S. C., Roberts, J. M., Veres, P. R., et al. (2013). Heterogeneous formation of nitryl chloride and its role as a nocturnal NO_x reservoir species during CalNex-LA 2010. *Journal of Geophysical Research: Atmospheres*, 118(18), 10,638-10,652. <https://doi.org/10.1002/jgrd.50783>
- Moise, T., Talukdar, R. K., Frost, G. J., Fox, R. W., & Rudich, Y. (2002). Reactive uptake of NO_3 by liquid and frozen organics. *Journal of Geophysical Research: Atmospheres*, 107(D2), AAC 6-1-AAC 6-9. <https://doi.org/10.1029/2001JD000334>
- Morgan, W. T., Ouyang, B., Allan, J. D., Aruffo, E., Di Carlo, P., Kennedy, O. J., et al. (2015). Influence of aerosol chemical composition on N_2O_5 uptake: airborne regional measurements in northwestern Europe. *Atmospheric Chemistry and Physics*, 15(2), 973-990. <https://doi.org/10.5194/acp-15-973-2015>

- Mozurkewich, M. (1993). The dissociation constant of ammonium nitrate and its dependence on temperature, relative humidity and particle size. *Atmospheric Environment. Part A. General Topics*, 27(2), 261-270. [https://doi.org/10.1016/0960-1686\(93\)90356-4](https://doi.org/10.1016/0960-1686(93)90356-4)
- Mozurkewich, M., & Calvert, J. G. (1988). Reaction probability of N₂O₅ on aqueous aerosols. *Journal of Geophysical Research: Atmospheres*, 93(D12), 15889-15896. <https://doi.org/10.1029/JD093iD12p15889>
- National Oceanic and Atmospheric Administration (NOAA). (2012). National centers for environmental information, State of the Climate: Drought for August 2012. [Available at: <https://www.ncdc.noaa.gov/sotc/drought/201208>].
- Nenes, A., Pandis, S. N., & Pilinis, C. (1998). ISORROPIA: A new thermodynamic equilibrium model for multiphase multicomponent inorganic aerosols. *Aquatic Geochemistry*, 4(1), 123-152. <https://doi.org/10.1023/a:1009604003981>
- Neuman, J. A., Nowak, J. B., Zheng, W., Flocke, F., Ryerson, T. B., Trainer, M., et al. (2009). Relationship between photochemical ozone production and NO_x oxidation in Houston, Texas. *Journal of Geophysical Research: Atmospheres*, 114(D7), D00F08. <https://doi.org/10.1029/2008JD011688>
- Ng, N. L., Canagaratna, M. R., Zhang, Q., Jimenez, J. L., Tian, J., Ulbrich, I. M., et al. (2010). Organic aerosol components observed in Northern Hemispheric datasets from Aerosol Mass Spectrometry. *Atmospheric Chemistry and Physics*, 10(10), 4625-4641. <https://doi.org/10.5194/acp-10-4625-2010>
- Ng, N. L., Brown, S. S., Archibald, A. T., Atlas, E., Cohen, R. C., Crowley, J. N., et al. (2017). Nitrate radicals and biogenic volatile organic compounds: oxidation, mechanisms, and organic aerosol. *Atmospheric Chemistry and Physics*, 17(3), 2103-2162. <https://doi.org/10.5194/acp-17-2103-2017>
- Nowak, J. B., Neuman, J. A., Bahreini, R., Middlebrook, A. M., Holloway, J. S., McKeen, S. A., et al. (2012). Ammonia sources in the California South Coast Air Basin and their impact on ammonium nitrate formation. *Geophysical Research Letters*, 39(7), L07804. <https://doi.org/10.1029/2012GL051197>
- Nunnermacker, L. J., Imre, D., Daum, P. H., Kleinman, L., Lee, Y. N., Lee, J. H., et al. (1998). Characterization of the Nashville urban plume on July 3 and July 18, 1995. *Journal of Geophysical Research: Atmospheres*, 103(D21), 28129-28148. <https://doi.org/10.1029/98JD01961>
- Olaguer, E. P., Rappenglück, B., Lefer, B., Stutz, J., Dibb, J., Griffin, R., et al. (2009). Deciphering the role of radical precursors during the second Texas Air Quality Study. *Journal of the Air & Waste Management Association*, 59(11), 1258-1277. <https://doi.org/10.3155/1047-3289.59.11.1258>
- Olszyna, K. J., Bailey, E. M., Simonaitis, R., & Meagher, J. F. (1994). O₃ and NO_y relationships at a rural site. *Journal of Geophysical Research: Atmospheres*, 99(D7), 14557-14563. <https://doi.org/10.1029/94JD00739>

Oltmans, S., Schnell, R., Johnson, B., Petron, G., Mefford, T., & Neely, R. (2014). Anatomy of wintertime ozone associated with oil and natural gas extraction activity in Wyoming and Utah. *Elementa Science of the Anthropocene*, 2(000024). <https://doi.org/10.12952/journal.elementa.000024>

Osthoff, H. D., Pilling, M. J., Ravishankara, A. R., & Brown, S. S. (2007). Temperature dependence of the NO₃ absorption cross-section above 298 K and determination of the equilibrium constant for NO₃ + NO₂ → N₂O₅ at atmospherically relevant conditions. *Physical Chemistry Chemical Physics*, 9(43), 5785-5793. <https://doi.org/10.1039/B709193A>

Osthoff, H. D., Sommariva, R., Baynard, T., Pettersson, A., Williams, E. J., Lerner, B. M., et al. (2006). Observation of daytime N₂O₅ in the marine boundary layer during New England Air Quality Study–Intercontinental Transport and Chemical Transformation 2004. *Journal of Geophysical Research: Atmospheres*, 111(D23), D23S14. <https://doi.org/10.1029/2006JD007593>

Osthoff, H. D., Roberts, J. M., Ravishankara, A. R., Williams, E. J., Lerner, B. M., Sommariva, R., et al. (2008). High levels of nitryl chloride in the polluted subtropical marine boundary layer. *Nature Geoscience*, 1(5), 324-328. <https://doi.org/10.1038/ngeo177>

Pacsi, A. P., Kimura, Y., McGaughey, G., McDonald-Buller, E. C., & Allen, D. T. (2015). Regional ozone impacts of increased natural gas use in the Texas power sector and development in the Eagle Ford Shale. *Environmental Science & Technology*, 49(6), 3966-3973. <https://doi.org/10.1021/es5055012>

Peischl, J., Ryerson, T. B., Holloway, J. S., Trainer, M., Andrews, A. E., Atlas, E. L., et al. (2012). Airborne observations of methane emissions from rice cultivation in the Sacramento Valley of California. *Journal of Geophysical Research: Atmospheres*, 117(D24), D00V25. <https://doi.org/10.1029/2012JD017994>

Pétron, G., Karion, A., Sweeny, C., Miller, B., Montzka, S., Frost, G. J., et al. (2014). A new look at methane and nonmethane hydrocarbon emissions from oil and natural gas operations in the Colorado Denver-Julesburg Basin. *Journal of Geophysical Research: Atmospheres*, 119, 6836-6852. <https://doi.org/10.1002/2013JD021272>

Pétron, G., Frost, G., Miller, B. R., Hirsch, A. I., Montzka, S. A., Karion, A., et al. (2012). Hydrocarbon emissions characterization in the Colorado Front Range: A pilot study. *Journal of Geophysical Research: Atmospheres*, 117(D4), D04304. <https://doi.org/10.1029/2011JD016360>

Petters, M. D., & Kreidenweis, S. M. (2007). A single parameter representation of hygroscopic growth and cloud condensation nucleus activity. *Atmospheric Chemistry and Physics*, 7(8), 1961-1971. <https://doi.org/10.5194/acp-7-1961-2007>

Pfister, G. G., Flocke, F., Hornbrook, R. S., Orlando, J., Lee, S., & Schroder, J. R. (2017a). Process-Based and Regional Source Impact Analysis for FRAPPE and DISCOVER-AQ 2014. Final Report to the Colorado Department of Public Health and Environment. [Available at: https://www.colorado.gov/airquality/tech_doc_repository.aspx?action=open&file=FRAPPE-NCAR_Final_Report_July2017.pdf].

Pfister, G. G., Reddy, P. J., Barth, M. C., Flocke, F. F., Fried, A., Herndon, S. C., et al. (2017b). Using Observations and Source-Specific Model Tracers to Characterize Pollutant Transport During FRAPPÉ and DISCOVER-AQ. *Journal of Geophysical Research: Atmospheres*, 122(19), 10,510-10,538. <https://doi.org/10.1002/2017JD027257>

Phillips, G. J., Tang, M. J., Thieser, J., Brickwedde, B., Schuster, G., Bohn, B., et al. (2012). Significant concentrations of nitryl chloride observed in rural continental Europe associated with the influence of sea salt chloride and anthropogenic emissions. *Geophysical Research Letters*, 39(10), L10811. <https://doi.org/10.1029/2012GL051912>

Phillips, G. J., Thieser, J., Tang, M., Sobanski, N., Schuster, G., Fachinger, J., et al. (2016). Estimating N₂O₅ uptake coefficients using ambient measurements of NO₃, N₂O₅, ClNO₂ and particle-phase nitrate. *Atmospheric Chemistry and Physics*, 16(20), 13231-13249. <https://doi.org/10.5194/acp-16-13231-2016>

Pope, C. A., Muhlestein, J. B., May, H. T., Renlund, D. G., Anderson, J. L., & Horne, B. D. (2006). Ischemic Heart Disease Events Triggered by Short-Term Exposure to Fine Particulate Air Pollution. *Circulation*, 114(23), 2443.

Pope, C. A., Muhlestein, J. B., Anderson, J. L., Cannon, J. B., Hales, N. M., Meredith, K. G., et al. (2015). Short-Term Exposure to Fine Particulate Matter Air Pollution Is Preferentially Associated With the Risk of ST-Segment Elevation Acute Coronary Events. *Journal of the American Heart Association*, 4(12).

Pöschl, U., Rudich, Y., & Ammann, M. (2007). Kinetic model framework for aerosol and cloud surface chemistry and gas-particle interactions; Part 1: General equations, parameters, and terminology. *Atmospheric Chemistry and Physics*, 7(23), 5989-6023. <https://doi.org/10.5194/acp-7-5989-2007>

Prabhakar, G., Parworth, C. L., Zhang, X., Kim, H., Young, D. E., Beyersdorf, A. J., et al. (2017). Observational assessment of the role of nocturnal residual-layer chemistry in determining daytime surface particulate nitrate concentrations. *Atmospheric Chemistry and Physics*, 17(23), 14747-14770. <https://doi.org/10.5194/acp-17-14747-2017>

Pusede, S. E., Duffey, K. C., Shusterman, A. A., Saleh, A., Laughner, J. L., Wooldridge, P. J., et al. (2016). On the effectiveness of nitrogen oxide reductions as a control over ammonium nitrate aerosol. *Atmospheric Chemistry and Physics*, 16(4), 2575-2596. <https://doi.org/10.5194/acp-16-2575-2016>

Pye, H. O. T., Liao, H., Wu, S., Mickley, L. J., Jacob, D. J., Henze, D. K., & Seinfeld, J. H. (2009). Effect of changes in climate and emissions on future sulfate-nitrate-ammonium aerosol levels in the United States. *Journal of Geophysical Research: Atmospheres*, 114(D1), D01205. <https://doi.org/10.1029/2008JD010701>

Ramboll Environ. (2017). Science Synthesis Report: Atmospheric Impacts of Oil and Gas Development in Texas. Final Report to the Texas Commission on Environmental Quality. [Available at:

https://www.tceq.texas.gov/assets/public/implementation/air/am/contracts/reports/oth/582166321516-20170629-environ-oilgas_impact_aq_synthesis.pdf].

Rappenglück, B., Ackermann, L., Alvarez, S., Golovko, J., Buhr, M., Field, R. A., et al. (2014). Strong wintertime ozone events in the Upper Green River basin, Wyoming. *Atmospheric Chemistry and Physics*, *14*(10), 4909-4934. <https://doi.org/10.5194/acp-14-4909-2014>

Reeves, H. D., & Stensrud, D. J. (2009). Synoptic-Scale Flow and Valley Cold Pool Evolution in the Western United States. *Weather and Forecasting*, *24*(6), 1625-1643. <https://doi.org/10.1175/2009WAF2222234.1>

Rickards, A. M. J., Miles, R. E. H., Davies, J. F., Marshall, F. H., & Reid, J. P. (2013). Measurements of the sensitivity of aerosol hygroscopicity and the κ parameter to the O/C ratio. *The Journal of Physical Chemistry A*, *117*(51), 14120-14131. <https://doi.org/10.1021/jp407991n>

Riedel, T. P., Bertram, T. H., Ryder, O. S., Liu, S., Day, D. A., Russell, L. M., et al. (2012a). Direct N₂O₅ reactivity measurements at a polluted coastal site. *Atmospheric Chemistry and Physics*, *12*(6), 2959-2968. <https://doi.org/10.5194/acp-12-2959-2012>

Riedel, T. P., Bertram, T. H., Crisp, T. A., Williams, E. J., Lerner, B. M., Vlasenko, A., et al. (2012b). Nitryl chloride and molecular chlorine in the coastal marine boundary layer. *Environmental Science & Technology*, *46*(19), 10463-10470. <https://doi.org/10.1021/es204632r>

Riedel, T. P., Wagner, N. L., Dubé, W. P., Middlebrook, A. M., Young, C. J., Öztürk, F., et al. (2013). Chlorine activation within urban or power plant plumes: Vertically resolved ClNO₂ and Cl₂ measurements from a tall tower in a polluted continental setting. *Journal of Geophysical Research: Atmospheres*, *118*(15), 8702-8715. <https://doi.org/10.1002/jgrd.50637>

Rierner, N., Vogel, H., Vogel, B., Anttila, T., Kiendler-Scharr, A., & Mentel, T. F. (2009). Relative importance of organic coatings for the heterogeneous hydrolysis of N₂O₅ during summer in Europe. *Journal of Geophysical Research: Atmospheres*, *114*(D17), D17307. <https://doi.org/10.1029/2008JD011369>

Rierner, N., Vogel, H., Vogel, B., Schell, B., Ackermann, I., Kessler, C., & Hass, H. (2003). Impact of the heterogeneous hydrolysis of N₂O₅ on chemistry and nitrate aerosol formation in the lower troposphere under photochemical conditions. *Journal of Geophysical Research: Atmospheres*, *108*(D4), 4144. <https://doi.org/10.1029/2002JD002436>

Roberts, J. M., Osthoff, H. D., Brown, S. S., & Ravishankara, A. R. (2008). N₂O₅ oxidizes chloride to Cl₂ in acidic atmospheric aerosol. *Science*, *321*(5892), 1059. <https://doi.org/10.1126/science.1158777>

Roberts, J. M., Osthoff, H. D., Brown, S. S., Ravishankara, A. R., Coffman, D., Quinn, P., & Bates, T. (2009). Laboratory studies of products of N₂O₅ uptake on Cl⁻ containing substrates. *Geophysical Research Letters*, *36*(20), L20808. <https://doi.org/10.1029/2009GL040448>

- Robinson, G. N., Worsnop, D. R., Jayne, J. T., Kolb, C. E., & Davidovits, P. (1997). Heterogeneous uptake of ClONO₂ and N₂O₅ by sulfuric acid solutions. *Journal of Geophysical Research: Atmospheres*, 102(D3), 3583-3601. <https://doi.org/10.1029/96JD03457>
- Rodriguez, M. A., Barna, M. G., & Moore, T. (2009). Regional impacts of oil and gas development on ozone formation in the western United States. *Journal of the Air & Waste Management Association*, 59(9), 1111-1118. <https://doi.org/10.3155/1047-3289.59.9.1111>
- Roelofs, G.-J., & Lelieveld, J. (1995). Distribution and budget of O₃ in the troposphere calculated with a chemistry general circulation model. *Journal of Geophysical Research: Atmospheres*, 100(D10), 20983-20998. <https://doi.org/10.1029/95JD02326>
- Russell, A., Milford, J., Bergin, M. S., McBride, S., McNair, L., Yang, Y., et al. (1995). Urban ozone control and atmospheric reactivity of organic gases. *Science*, 269(5223), 491-5. <https://doi.org/10.1126/science.269.5223.491>
- Rutter, A. P., Griffin, R. J., Cevik, B. K., Shakya, K. M., Gong, L., Kim, S., et al. (2015). Sources of air pollution in a region of oil and gas exploration downwind of a large city. *Atmospheric Environment*, 120, 89-99. <https://doi.org/10.1016/j.atmosenv.2015.08.073>
- Ryder, O. S., Campbell, N. R., Shaloski, M., Al-Mashat, H., Nathanson, G. M., & Bertram, T. H. (2015). Role of organics in regulating ClNO₂ production at the air-sea interface. *The Journal of Physical Chemistry A*, 119(31), 8519-8526. <https://doi.org/10.1021/jp5129673>
- Ryder, O. S., Ault, A. P., Cahill, J. F., Guasco, T. L., Riedel, T. P., Cuadra-Rodriguez, L. A., et al. (2014). On the role of particle inorganic mixing state in the reactive uptake of N₂O₅ to ambient aerosol particles. *Environmental Science & Technology*, 48(3), 1618-1627. <https://doi.org/10.1021/es4042622>
- Ryerson, T. B., Buhr, M. P., Frost, G. J., Goldan, P. D., Holloway, J. S., Hübler, G., et al. (1998). Emissions lifetimes and ozone formation in power plant plumes. *Journal of Geophysical Research: Atmospheres*, 103(D17), 22569-22583. <https://doi.org/10.1029/98JD01620>
- Ryerson, T. B., Andrews, A. E., Angevine, W. M., Bates, T. S., Brock, C. A., Cairns, B., et al. (2013). The 2010 California Research at the Nexus of Air Quality and Climate Change (CalNex) field study. *Journal of Geophysical Research: Atmospheres*, 118(11), 5830-5866. <https://doi.org/10.1002/jgrd.50331>
- Sandu, A., & Sander, R. (2006). Technical note: Simulating chemical systems in Fortran90 and Matlab with the Kinetic PreProcessor KPP-2.1. *Atmospheric Chemistry and Physics*, 6, 187-195. <https://doi.org/10.5194/acp-6-187-2006>
- Sansonetti, C. J., Salit, M. L., & Reader, J. (1996). Wavelengths of spectral lines in mercury pencil lamps. *Applied Optics*, 35(1), 74-77. <https://doi.org/10.1364/AO.35.000074>
- Sarwar, G., Simon, H., Xing, J., & Mathur, R. (2014). Importance of tropospheric ClNO₂ chemistry across the Northern Hemisphere. *Geophysical Research Letters*, 41(11), 4050-4058. <https://doi.org/10.1002/2014gl059962>

- Schade, G. W., & Roest, G. (2016). Analysis of non-methane hydrocarbon data from a monitoring station affected by oil and gas development in the Eagle Ford shale, Texas. *Elementa Science of the Anthropocene*, 4(96). <https://doi.org/10.12952/journal.elementa.000096>
- Schnell, R. C., Oltmans, S. J., Neely, R. R., Endres, M. S., Molenaar, J. V., & White, A. B. (2009). Rapid photochemical production of ozone at high concentrations in a rural site during winter. *Nature Geoscience*, 2(2), 120-122. <https://doi.org/10.1038/ngeo415>
- Schofield, K. (1980). *Aromatic Nitration*: University Press: Great Britain.
- Schroder, J. C., Campuzano-Jost, P., Day, D. D., Shah, V., Larson, K., Sommers, J. M., et al. (2018). Sources and secondary production of organic aerosols in the Northeastern U.S. during WINTER. *Journal of Geophysical Research: Atmospheres* - Submitted.
- Schweitzer, F., Mirabel, P., & George, C. (1998). Multiphase Chemistry of N₂O₅, ClNO₂, and BrNO₂. *The Journal of Physical Chemistry A*, 102(22), 3942-3952. <https://doi.org/10.1021/jp980748s>
- Schweitzer, F., Mirabel, P., & George, C. (1999). Heterogeneous Chemistry of Nitryl Halides in Relation to Tropospheric Halogen Activation. *Journal of Atmospheric Chemistry*, 34(1), 101-117. <https://doi.org/10.1023/A:1006249921480>
- Seidel, D. J., Zhang, Y., Beljaars, A., Golaz, J.-C., Jacobson, A. R., & Medeiros, B. (2012). Climatology of the planetary boundary layer over the continental United States and Europe. *Journal of Geophysical Research: Atmospheres*, 117(D17), D17106. <https://doi.org/10.1029/2012JD018143>
- Shah, V., Jaegle, L., Thornton, J. A., Lopez-Hilfiker, F. D., Lee, B. H., Schroder, J. C., et al. (2018). Chemical feedbacks weaken the wintertime response of particulate sulfate and nitrate to emissions reductions over the eastern U.S. *Journal of Geophysical Research: Atmospheres*.
- Shaloski, M. A., Gord, J. R., Staudt, S., Quinn, S. L., Bertram, T. H., & Nathanson, G. M. (2017). Reactions of N₂O₅ with salty and surfactant-coated glycerol: Interfacial conversion of Br⁻ to Br₂ mediated by alkylammonium cations. *The Journal of Physical Chemistry A*, 121(19), 3708-3719. <https://doi.org/10.1021/acs.jpca.7b02040>
- Sherwen, T., Evans, M. J., Sommariva, R., Hollis, L. D. J., Ball, S. M., Monks, P. S., et al. (2017). Effects of halogens on European air-quality. *Faraday Discussions*, 200(0), 75-100. <https://doi.org/10.1039/C7FD00026J>
- Shetter, R. E., & Müller, M. (1999). Photolysis frequency measurements using actinic flux spectroradiometry during the PEM-Tropics mission: Instrumentation description and some results. *Journal of Geophysical Research: Atmospheres*, 104(D5), 5647-5661. <https://doi.org/10.1029/98JD01381>
- Shetter, R. E., Junkermann, W., Swartz, W. H., Frost, G. J., Crawford, J. H., Lefer, B. L., et al. (2003). Photolysis frequency of NO₂: Measurement and modeling during the International

Photolysis Frequency Measurement and Modeling Intercomparison (IPMMI). *Journal of Geophysical Research: Atmospheres*, 108(D16), 8544. <https://doi.org/10.1029/2002JD002932>

Shingler, T., Crosbie, E., Ortega, A., Shiraiwa, M., Zuend, A., Beyersdorf, A., et al. (2016). Airborne characterization of subsaturated aerosol hygroscopicity and dry refractive index from the surface to 6.5 km during the SEAC4RS campaign. *Journal of Geophysical Research: Atmospheres*, 121(8), 4188-4210. <https://doi.org/10.1002/2015JD024498>

Shiraiwa, M., Li, Y., Tsimpidi, A. P., Karydis, V. A., Berkemeier, T., Pandis, S. N., et al. (2017). Global distribution of particle phase state in atmospheric secondary organic aerosols. *Nature Communications*, 8, 15002. <https://doi.org/10.1038/ncomms15002>

Sickles, J. E., & Shadwick, D. S. (2007). Changes in air quality and atmospheric deposition in the eastern United States: 1990–2004. *Journal of Geophysical Research: Atmospheres*, 112(D17), D17301. <https://doi.org/10.1029/2006JD007843>

Silcox, G. D., Kelly, K. E., Crosman, E. T., Whiteman, C. D., & Allen, B. L. (2012). Wintertime PM_{2.5} concentrations during persistent, multi-day cold-air pools in a mountain valley. *Atmospheric Environment*, 46, 17-24. <https://doi.org/10.1016/j.atmosenv.2011.10.041>

Sillman, S., He, D., Pippin, M. R., Daum, P. H., Imre, D. G., Kleinman, L. I., et al. (1998). Model correlations for ozone, reactive nitrogen, and peroxides for Nashville in comparison with measurements: Implications for O₃-NO_x-hydrocarbon chemistry. *Journal of Geophysical Research: Atmospheres*, 103(D17), 22629-22644. <https://doi.org/10.1029/98JD00349>

Silva, P. J., Vawdrey, E. L., Corbett, M., & Erupe, M. (2007). Fine particle concentrations and composition during wintertime inversions in Logan, Utah, USA. *Atmospheric Environment*, 41(26), 5410-5422. <https://doi.org/10.1016/j.atmosenv.2007.02.016>

Simpson, W. R., Brown, S. S., Saiz-Lopez, A., Thornton, J. A., & von Glasow, R. (2015). Tropospheric Halogen Chemistry: Sources, Cycling, and Impacts. *Chemical Reviews*, 115(10), 4035-4062. <https://doi.org/10.1021/cr5006638>

Sohn, M. (1998). Heterogene Reaktionen von Stickoxiden an Aerosolpartikeln, Doktorarbeit, Philipps-Universität Marburg.

Sommariva, R., Osthoff, H. D., Brown, S. S., Bates, T. S., Baynard, T., Coffman, D., et al. (2009). Radicals in the marine boundary layer during NEAQS 2004: a model study of day-time and night-time sources and sinks. *Atmospheric Chemistry and Physics*, 9(9), 3075-3093. <https://doi.org/10.5194/acp-9-3075-2009>

St. John, J. C., Chameides, W. L., & Saylor, R. (1998). Role of anthropogenic NO_x and VOC as ozone precursors: A case study from the SOS Nashville/Middle Tennessee Ozone Study. *Journal of Geophysical Research: Atmospheres*, 103(D17), 22415-22423. <https://doi.org/10.1029/98JD00973>

Stark, H., Lerner, B. M., Schmitt, R., Jakoubek, R., Williams, E. J., Ryerson, T. B., et al. (2007). Atmospheric in situ measurement of nitrate radical (NO₃) and other photolysis rates using

spectroradiometry and filter radiometry. *Journal of Geophysical Research: Atmospheres*, 112(D10). <https://doi.org/10.1029/2006JD007578>

Stewart, D. J., Griffiths, P. T., & Cox, R. A. (2004). Reactive uptake coefficients for heterogeneous reaction of N₂O₅ with submicron aerosols of NaCl and natural sea salt. *Atmospheric Chemistry and Physics*, 4(5), 1381-1388. <https://doi.org/10.5194/acp-4-1381-2004>

Stone, D., Evans, M. J., Walker, H., Ingham, T., Vaughan, S., Ouyang, B., et al. (2014). Radical chemistry at night: comparisons between observed and modelled HO_x, NO₃ and N₂O₅ during the RONOCO project. *Atmospheric Chemistry and Physics*, 14(3), 1299-1321. <https://doi.org/10.5194/acp-14-1299-2014>

Strapp, J. W., Leitch, W. R., & Liu, P. S. K. (1992). Hydrated and dried aerosol-size-distribution measurements from the particle measuring systems FSSP-300 probe and the deiced PCASP-100X Probe. *Journal of Atmospheric and Oceanic Technology*, 9(5), 548-555. [https://doi.org/10.1175/1520-0426\(1992\)009<0548:HADASD>2.0.CO;2](https://doi.org/10.1175/1520-0426(1992)009<0548:HADASD>2.0.CO;2)

Stull, R. B. (1988). *An Introduction to Boundary Layer Meteorology*. The Netherlands: Kluwer Academic: Dordrecht.

Stutz, J., Alicke, B., Ackermann, R., Geyer, A., White, A., & Williams, E. (2004). Vertical profiles of NO₃, N₂O₅, O₃, and NO_x in the nocturnal boundary layer: 1. Observations during the Texas Air Quality Study 2000. *Journal of Geophysical Research: Atmospheres*, 109(D12). <https://doi.org/10.1029/2003JD004209>

Suda, S. R., Petters, M. D., Matsunaga, A., Sullivan, R. C., Ziemann, P. J., & Kreidenweis, S. M. (2012). Hygroscopicity frequency distributions of secondary organic aerosols. *Journal of Geophysical Research: Atmospheres*, 117(D4), D04207. <https://doi.org/10.1029/2011JD016823>

Swarthout, R. F., Russo, R. S., Zhou, Y., Hart, A. H., & Sive, B. C. (2013). Volatile organic compound distributions during the NACHTT campaign at the Boulder Atmospheric Observatory: Influence of urban and natural gas sources. *Journal of Geophysical Research: Atmospheres*, 118(18), 10,614-10,637. <https://doi.org/10.1002/jgrd.50722>

Swarthout, R. F., Russo, R. S., Zhou, Y., Miller, B. M., Mitchell, B., Horsman, E., et al. (2015). Impact of Marcellus Shale natural gas development in southwest Pennsylvania on volatile organic compound emissions and regional air quality. *Environmental Science & Technology*, 49(5), 3175-3184. <https://doi.org/10.1021/es504315f>

Szoke, E. J. (1991). Eye of the Denver Cyclone. *Monthly Weather Review*, 119(5), 1283-1292. [https://doi.org/10.1175/1520-0493\(1991\)119<1283:EOTDC>2.0.CO;2](https://doi.org/10.1175/1520-0493(1991)119<1283:EOTDC>2.0.CO;2)

Szoke, E. J., Weisman, M. L., Brown, J. M., Caracena, F., & Schlatter, T. W. (1984). A subsynoptic analysis of the Denver tornadoes of 3 June 1981. *Monthly Weather Review*, 112(4), 790-808. [https://doi.org/10.1175/1520-0493\(1984\)112<0790:ASAOTD>2.0.CO;2](https://doi.org/10.1175/1520-0493(1984)112<0790:ASAOTD>2.0.CO;2)

Taylor, R. (1990). *Electrophillic Aromatic Substitution*: John Wiley, New York.

- Tham, Y. J., Yan, C., Xue, L., Zha, Q., Wang, X., & Wang, T. (2014). Presence of high nitryl chloride in Asian coastal environment and its impact on atmospheric photochemistry. *Chinese Science Bulletin*, 59(4), 356-359. <https://doi.org/10.1007/s11434-013-0063-y>
- Tham, Y. J., Wang, Z., Li, Q., Yun, H., Wang, W., Wang, X., et al. (2016). Significant concentrations of nitryl chloride sustained in the morning: investigations of the causes and impacts on ozone production in a polluted region of northern China. *Atmospheric Chemistry and Physics*, 16(23), 14959-14977. <https://doi.org/10.5194/acp-16-14959-2016>
- Thornton, J. A., & Abbatt, J. P. D. (2005). N₂O₅ reaction on submicron sea salt aerosol: Kinetics, products, and the effect of surface active organics. *The Journal of Physical Chemistry A*, 109(44), 10004-10012. <https://doi.org/10.1021/jp054183t>
- Thornton, J. A., Braban, C. F., & Abbatt, J. P. D. (2003). N₂O₅ hydrolysis on sub-micron organic aerosols: the effect of relative humidity, particle phase, and particle size. *Physical Chemistry Chemical Physics*, 5(20), 4593-4603. <https://doi.org/10.1039/B307498F>
- Thornton, J. A., Kercher, J. P., Riedel, T. P., Wagner, N. L., Cozic, J., Holloway, J. S., et al. (2010). A large atomic chlorine source inferred from mid-continental reactive nitrogen chemistry. *Nature*, 464(7286), 271-4. <https://doi.org/10.1038/nature08905>
- Tie, X., Brasseur, G., Emmons, L., Horowitz, L., & Kinnison, D. (2001). Effects of aerosols on tropospheric oxidants: A global model study. *Journal of Geophysical Research*, 106(D19), 22931. <https://doi.org/10.1029/2001jd900206>
- Tie, X., Emmons, L., Horowitz, L., Brasseur, G., Ridley, B., Atlas, E., et al. (2003). Effect of sulfate aerosol on tropospheric NO_x and ozone budgets: Model simulations and TOPSE evidence. *Journal of Geophysical Research: Atmospheres*, 108(D4). <https://doi.org/10.1029/2001JD001508>
- Toth, J. J., & Johnson, R. H. (1985). Summer surface flow characteristics over northeast Colorado. *Monthly Weather Review*, 113(9), 1458-1469. [https://doi.org/10.1175/1520-0493\(1985\)113<1458:SSFCO>2.0.CO;2](https://doi.org/10.1175/1520-0493(1985)113<1458:SSFCO>2.0.CO;2)
- Trainer, M., Ridley, B. A., Buhr, M. P., Kok, G., Walega, J., Hübler, G., et al. (1995). Regional ozone and urban plumes in the southeastern United States: Birmingham, A case study. *Journal of Geophysical Research: Atmospheres*, 100(D9), 18823-18834. <https://doi.org/10.1029/95JD01641>
- Trainer, M., Parrish, D. D., Buhr, M. P., Norton, R. B., Fehsenfeld, F. C., Anlauf, K. G., et al. (1993). Correlation of ozone with NO_y in photochemically aged air. *Journal of Geophysical Research*, 98(D2), 2917. <https://doi.org/10.1029/92jd01910>
- U.S. Census Bureau. (2018). Quickfacts [Available at: <https://www.census.gov/quickfacts/>].
- United States Department of Agriculture (USDA). (2016). 2012 census of agriculture, County Level Data available from the USDA National Agricultural Statistics Service Quick Stats [Available from <http://quickstats.nass.usda.gov>].

US EPA. (2016). NAAQS Table [Available at: <https://www.epa.gov/criteria-air-pollutants/naaqs-table>].

US EPA. (2017). 2015 National Ambient Air Quality Standards (NAAQS) for Ozone. [Available at <https://www.epa.gov/ozone-pollution/2015-national-ambient-air-quality-standards-naaqs-ozone>]. Retrieved from <http://www3.epa.gov/airquality/ozonepollution/actions.html>

Utah Department of Environmental Quality. Serious Area PM_{2.5} State Implementation Plan Development [Available at: <https://deq.utah.gov/legacy/pollutants/p/particulate-matter/pm25/serious-area-state-implementation-plans/index.htm>].

Utah Division of Air Quality. (2014a). Utah State Implementation: Plan Control Measures for Area and Point Sources, Fine Particulate Matter, PM_{2.5} SIP for the Logan, UT Nonattainment Area

Utah Division of Air Quality. (2014b). Utah State Implementation: Plan Control Measures for Area and Point Sources, Fine Particulate Matter, PM_{2.5} SIP for the Provo, UT Nonattainment Area

Utah Division of Air Quality. (2014c). Utah State Implementation: Plan Control Measures for Area and Point Sources, Fine Particulate Matter, PM_{2.5} SIP for the Salt Lake City, UT Nonattainment Area [Available at: http://www.deq.utah.gov/Laws_Rules/daq/sip/docs/2014/12Dec/SIP%20IX.A.21_SLC_FINAL_Adopted%2012-3-14.pdf].

UWFPS Science Team. (2018). 2017 Utah Winter Fine Particulate Study Final Report [Available at: <https://deq.utah.gov/legacy/programs/air-quality/research/projects/northern-ut-air-pollution/winter-fine-particulate-aircraft-study.htm>].

Van Doren, J. M., Watson, L. R., Davidovits, P., Worsnop, D. R., Zahniser, M. S., & Kolb, C. E. (1990). Temperature dependence of the uptake coefficients of nitric acid, hydrochloric acid and nitrogen oxide (N₂O₅) by water droplets. *The Journal of Physical Chemistry*, 94(8), 3265-3269. <https://doi.org/10.1021/j100371a009>

Vandaele, A. C., Hermans, C., Simon, P. C., Carleer, M., Colin, R., Fally, S., et al. (1998). Measurements of the NO₂ absorption cross-section from 42 000 cm⁻¹ to 10 000 cm⁻¹ (238–1000 nm) at 220 K and 294 K. *Journal of Quantitative Spectroscopy and Radiative Transfer*, 59(3), 171-184. [https://doi.org/10.1016/S0022-4073\(97\)00168-4](https://doi.org/10.1016/S0022-4073(97)00168-4)

Vaughan, S., Canosa-Mas, C. E., Pfrang, C., Shallcross, D. E., Watson, L., & Wayne, R. P. (2006). Kinetic studies of reactions of the nitrate radical (NO₃) with peroxy radicals (RO₂): an indirect source of OH at night? *Physical Chemistry Chemical Physics*, 8(32), 3749-3760. <https://doi.org/10.1039/B605569A>

Wagner, N. L., Dubé, W. P., Washenfelder, R. A., Young, C. J., Pollack, I. B., Ryerson, T. B., & Brown, S. S. (2011). Diode laser-based cavity ring-down instrument for NO₃, N₂O₅, NO, NO₂ and O₃ from aircraft. *Atmospheric Measurement Techniques*, 4(6), 1227-1240. <https://doi.org/10.5194/amt-4-1227-2011>

- Wagner, N. L., Riedel, T. P., Roberts, J. M., Thornton, J. A., Angevine, W. M., Williams, E. J., et al. (2012). The sea breeze/land breeze circulation in Los Angeles and its influence on nitryl chloride production in this region. *Journal of Geophysical Research: Atmospheres*, *117*(D21), D00V24. <https://doi.org/10.1029/2012JD017810>
- Wagner, N. L., Riedel, T. P., Young, C. J., Bahreini, R., Brock, C. A., Dubé, W. P., et al. (2013). N₂O₅ uptake coefficients and nocturnal NO₂ removal rates determined from ambient wintertime measurements. *Journal of Geophysical Research: Atmospheres*, *118*(16), 9331-9350. <https://doi.org/10.1002/jgrd.50653>
- Wahner, A., Mentel, T. F., & Sohn, M. (1998a). Gas-phase reaction of N₂O₅ with water vapor: Importance of heterogeneous hydrolysis of N₂O₅ and surface desorption of HNO₃ in a large teflon chamber. *Geophysical Research Letters*, *25*(12), 2169-2172. <https://doi.org/10.1029/98GL51596>
- Wahner, A., Mentel, T. F., Sohn, M., & Stier, J. (1998b). Heterogeneous reaction of N₂O₅ on sodium nitrate aerosol. *Journal of Geophysical Research: Atmospheres*, *103*(D23), 31103-31112. <https://doi.org/10.1029/1998JD100022>
- Wang, H., Lu, K., Chen, X., Zhu, Q., Chen, Q., Guo, S., et al. (2017). High N₂O₅ concentrations observed in urban Beijing: Implications of a large nitrate formation pathway. *Environmental Science & Technology Letters*, *4*(10), 416-420. <https://doi.org/10.1021/acs.estlett.7b00341>
- Wang, S.-Y., Gillies, R. R., Martin, R., Davies, R. E., & Booth, M. R. (2012). Connecting Subseasonal Movements of the Winter Mean Ridge in Western North America to Inversion Climatology in Cache Valley, Utah. *Journal of Applied Meteorology and Climatology*, *51*(3), 617-627. <https://doi.org/10.1175/JAMC-D-11-0101.1>
- Wang, T., Tham, Y. J., Xue, L., Li, Q., Zha, Q., Wang, Z., et al. (2016). Observations of nitryl chloride and modeling its source and effect on ozone in the planetary boundary layer of southern China. *Journal of Geophysical Research: Atmospheres*, *121*(5), 2476-2489. <https://doi.org/10.1002/2015JD024556>
- Wang, X., Wang, T., Yan, C., Tham, Y. J., Xue, L., Xu, Z., & Zha, Q. (2014). Large daytime signals of N₂O₅ and NO₃ inferred at 62 amu in a TD-CIMS: chemical interference or a real atmospheric phenomenon? *Atmospheric Measurement Techniques*, *7*(1), 1. <https://doi.org/10.5194/amt-7-1-2014>
- Wang, X., Wang, H., Xue, L., Wang, T., Wang, L., Gu, R., et al. (2017). Observations of N₂O₅ and ClNO₂ at a polluted urban surface site in North China: High N₂O₅ uptake coefficients and low ClNO₂ product yields. *Atmospheric Environment*, *156*, 125-134. <https://doi.org/10.1016/j.atmosenv.2017.02.035>
- Wang, Z., Wang, W., Tham, Y. J., Li, Q., Wang, H., Wen, L., et al. (2017). Fast heterogeneous N₂O₅ uptake and ClNO₂ production in power plant and industrial plumes observed in the nocturnal residual layer over the North China Plain. *Atmospheric Chemistry and Physics*, *17*(20), 12361-12378. <https://doi.org/10.5194/acp-17-12361-2017>

- Washenfelder, R. A., Wagner, N. L., Dube, W. P., & Brown, S. S. (2011a). Measurement of atmospheric ozone by cavity ring-down spectroscopy. *Environmental Science & Technology*, 45(7), 2938-44. <https://doi.org/10.1021/es103340u>
- Washenfelder, R. A., Young, C. J., Brown, S. S., Angevine, W. M., Atlas, E. L., Blake, D. R., et al. (2011b). The glyoxal budget and its contribution to organic aerosol for Los Angeles, California, during CalNex 2010. *Journal of Geophysical Research*, 116. <https://doi.org/10.1029/2011jd016314>
- Watson, J. G., & Chow, J. C. (2002). A wintertime PM_{2.5} episode at the Fresno, CA, supersite. *Atmospheric Environment*, 36(3), 465-475. [https://doi.org/https://doi.org/10.1016/S1352-2310\(01\)00309-0](https://doi.org/https://doi.org/10.1016/S1352-2310(01)00309-0)
- Weinheimer, A. J., Walega, J. G., Ridley, B. A., Gary, B. L., Blake, D. R., Blake, N. J., et al. (1994). Meridional distributions of NO_x, NO_y, and other species in the lower stratosphere and upper troposphere during AASE II. *Geophysical Research Letters*, 21(23), 2583-2586. <https://doi.org/10.1029/94GL01897>
- Wexler, A. S., & Clegg, S. L. (2002). Atmospheric aerosol models for systems including the ions H⁺, NH₄⁺, Na⁺, SO₄²⁻, NO₃⁻, Cl⁻, Br⁻, and H₂O. *Journal of Geophysical Research: Atmospheres*, 107(D14), ACH 14-1-ACH 14-14. <https://doi.org/10.1029/2001JD000451>
- Whiteman, C. D., Hoch, S. W., Horel, J. D., & Charland, A. (2014). Relationship between particulate air pollution and meteorological variables in Utah's Salt Lake Valley. *Atmospheric Environment*, 94, 742-753. <https://doi.org/10.1016/j.atmosenv.2014.06.012>
- Wilczak, J. M., & Glendening, J. W. (1988). Observations and mixed-layer modeling of a terrain-induced mesoscale gyre: The Denver Cyclone. *Monthly Weather Review*, 116(12), 2688-2711. [https://doi.org/10.1175/1520-0493\(1988\)116<2688:OAMLMO>2.0.CO;2](https://doi.org/10.1175/1520-0493(1988)116<2688:OAMLMO>2.0.CO;2)
- Wild, R. J., Edwards, P. M., Dube, W. P., Baumann, K., Edgerton, E. S., Quinn, P. K., et al. (2014). A measurement of total reactive nitrogen, NO_y, together with NO₂, NO, and O₃ via cavity ring-down spectroscopy. *Environmental Science & Technology*, 48(16), 9609-15. <https://doi.org/10.1021/es501896w>
- Wild, R. J., Edwards, P. M., Bates, T. S., Cohen, R. C., de Gouw, J. A., Dubé, W. P., et al. (2016). Reactive nitrogen partitioning and its relationship to winter ozone events in Utah. *Atmospheric Chemistry and Physics*, 16(2), 573-583. <https://doi.org/10.5194/acp-16-573-2016>
- Womack, C. C., Neuman, J. A., Veres, P. R., Eilerman, S. J., Brock, C. A., Decker, Z. C. J., et al. (2016). Evaluation of the accuracy of thermal dissociation CRDS and LIF techniques for atmospheric measurement of reactive nitrogen species. *Atmospheric Measurement Techniques*, 2016, 1-30. <https://doi.org/10.5194/amt-2016-398>
- Wong, K. W., & Stutz, J. (2010). Influence of nocturnal vertical stability on daytime chemistry: A one-dimensional model study. *Atmospheric Environment*, 44(31), 3753-3760. <https://doi.org/10.1016/j.atmosenv.2010.06.057>

Wood, E. C., Bertram, T. H., Wooldridge, P. J., & Cohen, R. C. (2005). Measurements of N₂O₅, NO₂, and O₃ east of the San Francisco Bay. *Atmospheric Chemistry and Physics*, 5(2), 483-491. <https://doi.org/10.5194/acp-5-483-2005>

Xu, L., Suresh, S., Guo, H., Weber, R. J., & Ng, N. L. (2015). Aerosol characterization over the southeastern United States using high-resolution aerosol mass spectrometry: Spatial and seasonal variation of aerosol composition and sources with a focus on organic nitrates. *Atmospheric Chemistry and Physics*, 15(13), 7307-7336. <https://doi.org/10.5194/acp-15-7307-2015>

Yokelson, R. J., Burkholder, J. B., Fox, R. W., Talukdar, R. K., & Ravishankara, A. R. (1994). Temperature Dependence of the NO₃ Absorption Spectrum. *The Journal of Physical Chemistry*, 98(50), 13144-13150. <https://doi.org/10.1021/j100101a009>

You, Y., Smith, M. L., Song, M., Martin, S. T., & Bertram, A. K. (2014). Liquid-liquid phase separation in atmospherically relevant particles consisting of organic species and inorganic salts. *International Reviews in Physical Chemistry*, 33(1), 43-77. <https://doi.org/10.1080/0144235X.2014.890786>

Young, A. H., Keene, W. C., Pszenny, A. A. P., Sander, R., Thornton, J. A., Riedel, T. P., & Maben, J. R. (2013). Phase partitioning of soluble trace gases with size-resolved aerosols in near-surface continental air over northern Colorado, USA, during winter. *Journal of Geophysical Research: Atmospheres*, 118(16), 9414-9427. <https://doi.org/10.1002/jgrd.50655>

Young, C. J., Washenfelder, R. A., Roberts, J. M., Mielke, L. H., Osthoff, H. D., Tsai, C., et al. (2012). Vertically Resolved Measurements of Nighttime Radical Reservoirs in Los Angeles and Their Contribution to the Urban Radical Budget. *Environ Sci Technol*, 46(20), 10965-10973. <https://doi.org/10.1021/es302206a>

Zaveri, R. A., Berkowitz, C. M., Kleinman, L. I., Springston, S. R., Doskey, P. V., Lonneman, W. A., & Spicer, C. W. (2003). Ozone production efficiency and NO_x depletion in an urban plume: Interpretation of field observations and implications for evaluating O₃-NO_x-VOC sensitivity. *Journal of Geophysical Research: Atmospheres*, 108(D14), 4436. <https://doi.org/10.1029/2002JD003144>

Zhang, Q., Jimenez, J. L., Canagaratna, M. R., Allan, J. D., Coe, H., Ulbrich, I., et al. (2007). Ubiquity and dominance of oxygenated species in organic aerosols in anthropogenically-influenced Northern Hemisphere midlatitudes. *Geophysical Research Letters*, 34(13), L13801. <https://doi.org/10.1029/2007GL029979>

Glossary of Terms

- AGL – Above Ground Level
- AIM – Ambient Ion Monitor
- AMS – Aerosol Mass Spectrometer
- APN – acyl peroxy nitrates
- ARNOLD – Atmospheric Ring down Nitrogen Oxide Laser Detector
- ARW – Advanced Research version of the Weather research forecast model
- ASL – Above Sea Level
- B06 – Badger et al., 2006
- BAO – Boulder Atmospheric Observatory
- BLH – Boundary Layer Height
- BT09 – Bertram and Thornton, 2009
- CalNEX – California NEXus campaign
- CB6 – Carbon Bond 6 Mechanism
- CL – Chemiluminescence
- CMAQ – Community Multiscale Air Quality model
- CRD/S – Cavity Ring Down Spectroscopy
- CTM – Chemical Transport Model
- CW – Continuous Wave
- Dav08/B – David et al., 2008 (Main Text and Supplement (B))
- DISCOVER-AQ – Deriving Information on Surface Conditions from Column and Vertically Resolved Observations Relevant to Air Quality
- DMT – Droplet Measurement Technologies
- DSMACC – Dynamically Simple Model for Atmospheric Chemical Complexity
- DU – Dobson Unit
- EJ05 – Evans and Jacob, 2005
- EPA – Environmental Protection Agency
- FLEXPART – FLEXible PARTicle dispersion model
- FRAPPÉ – Front Range Air Pollution and Photochemistry Experiment
- G09 – Griffiths, et al., 2009
- G14 – Gaston et al., 2014
- GS-MS – Gas Chromatography – Mass Spectrometry
- HARP-AF – High-performance Instrumented Airborne Platform for Environmental Research (HIAPER) Airborne Radiation Package – Actinic Flux
- HW – Hawthorne measurement site
- ID – Inner Diameter
- I-TOF-CIMS – Iodide Time-of-Flight Chemical Ionization Mass Spectrometer
- LOD – Limit of Detection
- LPM – Liters Per Minute

- MCM – Master Chemical Mechanism
- MDA8 – Maximum Daily 8-hr Average
- MDT – Mountain Daylight Time
- NAA – Non-Attainment Area
- NAAQS – National Ambient Air Quality Standard
- NAM – North American Mesoscale model
- NBL – Nocturnal Boundary Layer
- NCAR – National Center for Atmospheric Research
- NE – NorthEast
- NEI – National Emission Inventory
- NFR – Northern Front Range
- NO_x – NO + NO₂
- NO_xCaRD – Nitrogen Oxides by Cavity Ring Down
- NSF – National Science Foundation
- NUM – N₂O₅ (or NOAA) Uptake Model
- O&NG – Oil and Natural Gas
- OHR – VOC OH Reactivity
- OMI – Ozone Monitoring Instrument
- OPE – Ozone Production Efficiency
- O_x – O₃ + NO₂
- PAN – Peroxy acyl nitrate
- PCASP – Passive Cavity Aerosol Spectrometer Probe
- pCl – particle Chloride
- PILS – Particle Into Liquid Sampler
- ppbC – parts per billion by carbon
- ppbv – parts per billion by volume
- PSS – Photo Stationary State
- QC-TILDAS (or TLDAS) – Tunable Infrared Laser Differential Absorption Spectrometer
- R09 – Riemer et al., 2009
- Rie03 – Riemer et al., 2003
- RL – Residual Layer
- SAR – Structure Activity Relationship
- SCC – Source Classification Code
- SE – SouthEast
- SIP – State Implementation Plan
- SLV – Salt Lake Valley, Utah
- SONNE – Summer Ozone Near Natural gas Emissions
- SRH – Separation Relative Humidity
- SURFRAD – SURface and RADiation budget monitoring mobile laboratory
- SZA – Solar Zenith Angle
- TD-LIF – Thermal Dissociation – Laser Induced Fluorescence instrument
- TO – Twin Otter
- TOGA – Trace Organic Gas Analyzer
- TOLNet – Tropospheric Ozone Lidar Network
- TOPAZ LIDAR – Tunable Optical Profiler for Aerosol and oZone LIDAR (Light Detection And Ranging)

- TUV – Tropospheric Ultraviolet and Visible radiation model
- UDAQ – Utah Department of Air Quality
- UHSAS – Ultra-High Sensitivity Aerosol Spectrometer
- UWFPS – Utah Wintertime Fine Particulate Study
- VOC – Volatile Organic Compound
- WINTER – Wintertime INvestigation of Transport, Emissions, and Reactivity
- WRF – Weather Research Forecast model

Appendix A

Supplemental Information for Chapter 3 – Influence of Oil and Gas Emissions on Local Photochemical Ozone Formation in the Northern Front Range of Colorado

A.1. County-Level NO_x Emission Inventory Description

County level NO_x emissions used in Chapter 3 (provided by Stu McKeen) were also used in Ahmadov et al. (2015), and are based on the U.S. EPA NEI-2011 (version 1) inventory (see documentation at <http://www3.epa.gov/ttnchie1/net/2011inventory.html>). Temporal allocations (monthly and day of week) of emissions from each Source Classification Code (SCC) are prescribed according to the file `amptpro_for_2011_platform_with_carb_mobile_2011CEM_moves_13aug2013_v0` within the auxiliary files supplied by the EPA (ftp://ftp.epa.gov/EmisInventory/2011v6/v1platform/data_common_to_all_years/). July average weekday emissions were used in the analysis presented here. Emissions from the O&NG production sector were treated separately from other sources by windowing the set of SCCs directly associated with O&NG exploration and extraction (2310000000 to 2310199999) as well as SCCs within the point source emission file directly associated with O&NG extraction (31000101-31088811, 40400300-40400340, 30600801-30600999). We note that mobile on-road and non-road emissions that may also be associated with O&NG production activity are not specified within the NEI, and therefore were not included in the window.

Table A.1 provides county level NEI NO_x emissions by sector for nine Colorado counties that are encompassed by the nonattainment area (Figure A.1). Units are in short-tons of NO₂

emitted per day. The relative contribution from O&NG activity to total NO_x emissions in the nonattainment area is 5.5% (Table A.1). In Weld county (Figure A.1), 27% of NO_x emissions are from the O&NG sector. NO_x emissions in Larimer County (Fort Collins) are lower than in counties that encompass the Denver urban boundary (Jefferson, Arapahoe, Adams, and Denver).

Table A.1. NEI-2011 NO_x emission inventory for nine Colorado counties by emission source^a.

County	O&NG Sources	Area Sources (Non O&NG)	Non-Road Sources	On-Road Sources	Point Sources	Sources Sum	O&NG Fraction (%)
Adams	0.75	1.88	8.43	26.36	33.67	71.09	1.1
Arapahoe	0.09	0.87	8.12	23.55	2.58	35.21	0.2
Boulder	0.35	0.59	5.38	11.14	9.12	26.59	1.3
Broomfield	0.10	<0.01	0.76	3.21	0.28	4.35	2.4
Denver	0.06	0.90	8.78	29.81	18.86	58.41	0.1
Douglas	0.00	1.97	5.90	17.40	0.59	25.85	0
Jefferson	0.00	0.86	8.57	25.41	5.51	40.34	0
Larimer	0.16	0.49	5.30	15.52	9.21	30.68	0.5
Weld	18.28	3.16	7.73	17.27	22.35	68.78	26.6
Total	19.78	10.72	58.97	169.67	102.17	361.31	5.5

^aUnits are tones NO₂/day

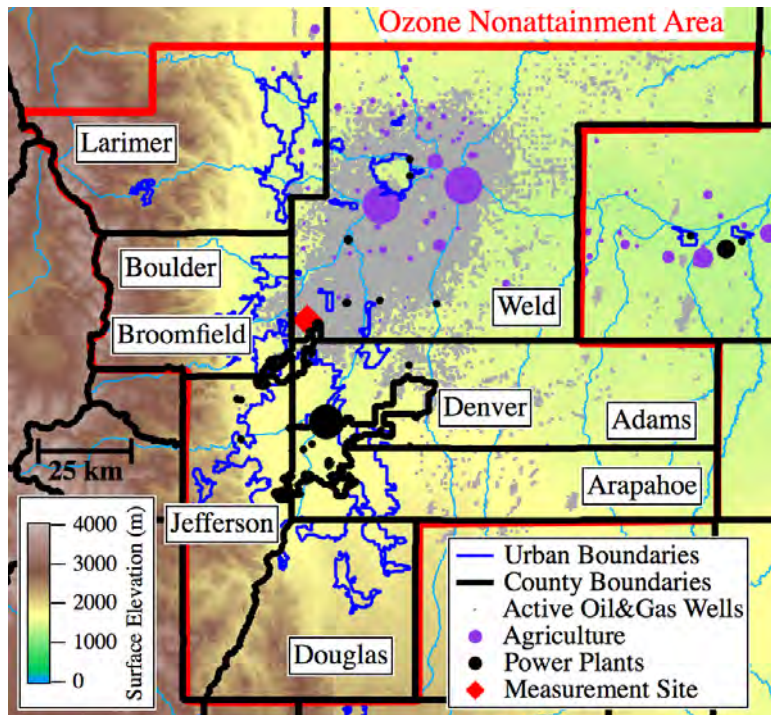


Figure A.1. Northern Front Range O₃ Nonattainment Area with county boundaries.

A.2. Observed OPE Wind Sectors assigned by Back-Trajectory Model

In addition to wind directions observed at BAO, air transport histories were derived with a backward-trajectory transport model for 16 July - 15 August 2014 by Wayne Angevine. For summer 2014 trajectories, meteorological parameters (winds and vertical mixing) were generated by runs of the Advanced Research version of the Weather Research and Forecast model (ARW). Model runs were started at 0 UTC every 24-hours with initial and boundary conditions from North American Mesoscale model (NAM) analyses, and run for 30 hours. Continuous fields were constructed from the 6-30 hour output, allowing 6 hours for spin-up. ARW was run on an outer domain covering the contiguous U.S. with 12-km grid spacing, and an inner domain covering Colorado and portions of surrounding states at 4-km spacing, with two-way nesting. Sixty Vertical levels were used with the lowest level at 16 mAGL. References for all schemes can be found in the WRF User Guide (http://www2.mmm.ucar.edu/wrf/users/docs/user_guide_V3/users_guide_chap5.htm). Time-averaged winds from these simulations were incorporated into a Lagrangian particle transport and dispersion model, FLEXPART/WRF version 3.1 (Brioude et al., 2013). The transport model releases 3000 virtual particles every 30-minutes from BAO and tracks them backwards in time for 48-hours (or until they leave the domain) to derive their geographical origin e.g. footprints ($\text{m}^3 \text{ s kg}^{-1}$). The surface layer is 100 m thick and the output grid has a 4 km spacing. The particles are perfectly passive as no sources, sinks, or transformations are considered. FLEXPART simulations were run with a 30 minute time resolution for the entire 2014 data collection period.

Wind sectors were assigned to the 80-OPEs using the geometrical centroid location in each corresponding simulation footprint. Footprints were filtered for values greater than $20 \text{ m}^3 \text{ s kg}^{-1}$. Centroid latitude and longitude values for each footprint were converted into wind direction sectors

(northeast (NE): 0-90°, southeast (SE): 90-180°, west (W): 180-360°) using their relative location to BAO. Examples of individual OPEs, their corresponding footprints, and assigned wind sector can be found in Figure A.2.

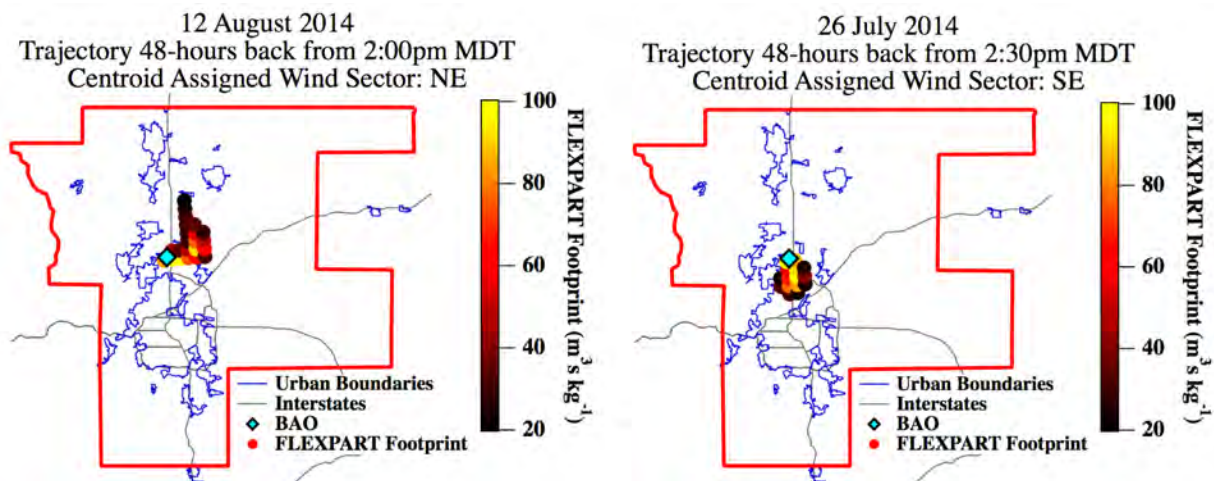


Figure A.2. Two example 48-hour FLEXPART back trajectory footprints. Footprints overlaid onto the NFR O₃ nonattainment area and labeled with centroid assigned wind sector direction.

Appendix B

Supplemental Information for Chapter 4 – Heterogeneous N₂O₅ uptake during winter: Aircraft measurements during the 2015 WINTER campaign and critical evaluation of current parameterizations

B.1. WINTER GEOS-Chem Simulations – Additional Details

The 3D GEOS-Chem Model was run with a 60 second time resolution by the University of Washington (Viral Shah and Lyatt Jaegle) for each flight during the WINTER campaign. The aerosol multi-component system for sulfate-nitrate-ammonium (SNA: SO₄²⁻, NO₃⁻, NH₄⁺), organic aerosol (OA), black carbon, dust and sea-salt was most recently described in Kim et al. (2015). To simulate OA, the simple linear approach of Hodzic and Jimenez (2011) was used, as implemented by Kim et al. (2015) in GEOS-Chem, with updates from (Shah et al., submitted, 2018). The gas-particle partitioning of SO₄²⁻-NO₃⁻-NH₄⁺ aerosol was computed with the ISORROPIA II thermodynamic module (Fountoukis & Nenes, 2007), as implemented by Pye et al. (2009). (Shah et al., submitted, 2018) conducted a detailed evaluation of GEOS-Chem against WINTER observations of aerosol composition, finding that GEOS-Chem reproduces observations to within 20%.

Values of $\gamma(\text{N}_2\text{O}_5)$ were parameterized using Evans and Jacob (2005) for black carbon, dust and sea-salt aerosol. For SNA aerosol, Evans and Jacob (2005) was replaced with the Bertram and Thornton (2009) parameterization. As this version of GEOS-Chem did not include full chlorine chemistry, it was assumed that 10% of Cl⁻ from submicron sea salt was displaced onto SNA aerosol. The ClNO₂ yield, $\phi(\text{ClNO}_2)$, on SNA was also calculated using the Bertram and Thornton

(2009) parameterization as a function of liquid water content and Cl^- concentrations. For all other aerosol $\phi(\text{ClNO}_2) = 0$ was assumed, except for sea salt aerosol with $\phi(\text{ClNO}_2) = 1$. Uptake onto OA was also updated to use the laboratory measurements of Badger et al. (2006) on humic acid, with $\gamma(\text{N}_2\text{O}_5) = 10^{-4}$ for $\text{RH} < 50\%$ and 10^{-3} for $\text{RH} \geq 50\%$. These values are 1-2 orders of magnitude lower than what was previously assumed in GEOS-Chem.

B.2. – Results – Additional Information

Table B.1. $\gamma(\text{N}_2\text{O}_5)$ results from this work and all previous field studies, listed in order of collection date.

Location	Dates	Platform	$\gamma(\text{N}_2\text{O}_5)$			N	Method	Reference
			Min.	Max.	Average			
Northeastern U.S.	Aug., 2002	Ship	0.03, 0.04, 0.035			2	Steady State	(Aldener et al., 2006)
Northeastern U.S.	Aug. 2004	Aircraft	0.0016, 0.02, 0.0075			3	Steady State	(Brown, S. S. et al., 2006)
Texas, U.S.	Oct., 2006	Aircraft	0.0004, 0.019, 0.0039			31	Steady State	(Brown et al., 2009)
Boulder, CO, U.S.	July, 2008	Ground	0.0009, 0.0012 ^a , 0.003 ^b			n/a	Direct Measurement, Flow Reactor	(Bertram et al., 2009b)
Seattle, WA, U.S.	Aug., 2008	Ground	0.0026, 0.029 ^a , 0.009 ^b			n/a	Direct Measurement, Flow Reactor	(Bertram et al., 2009b)
SFO Pier Facility, CA, U.S.	Sept., 2009	Ground	3×10^{-5} , 0.029, 0.0054			106	Direct Measurement, Flow Reactor	(Riedel et al., 2012a)
Southern, CA, U.S.	May-June, 2010	Aircraft	$\sim 1 \times 10^{-3e}$, $\sim 1 \times 10^{-2c}$, n/a			n/a	Steady State	(Chang et al., 2016)
NW Europe/UK	July, 2010	Aircraft	0.0076, 0.030, n/a			18	Steady State	(Morgan et al., 2015)
Weld County, CO, U.S.	Feb.-March, 2011	Ground	0.002, 0.1, 0.04 ^d			85440	Box Model	(Wagner et al., 2013)
SW Germany	Aug.-Sept., 2011	Ground	0.004, 0.11, 0.028			n/a	Multiple Methods, including SS	(Phillips et al., 2016)
Vernal, UT, U.S.	Jan.-Feb., 2012	Ground	0.026			1	Fit to reproduce average $k_{\text{N}_2\text{O}_5}$	(Wild et al., 2016)
Hong Kong, China	Dec., 2013	Ground	0.004, 0.029, 0.0141			10	Steady State	(Brown et al., 2016)
Wangdu, China	Jun.-July, 2014	Ground	n/a, n/a, 0.014			1	Steady State	(Tham et al., 2016)
Mt. Tai, China	July-Aug., 2014	Ground	0.021, 0.102, 0.061			13	Steady State	(Wang, Z. et al., 2017)
Ji'nan, China	Aug.-Sept., 2014	Ground	0.042, 0.092, 0.069			6	Steady State	(Wang, X. et al., 2017)
Northeastern U.S.	Feb.-March, 2015	Aircraft	2×10^{-5} , 0.175, 0.014 ^b			2876	Box Model	<i>This Work</i>
Beijing, China	Sep-Oct. 2016	Ground	0.025, 0.072, 0.048			4	Steady State	(Wang, H. et al., 2017)

^aInterquartile range reported

^bMedian value

^cExact values not reported, presented in manuscript figure only, therefore not included in Figure 4.9

^dMost frequent value

Table B.2. Correlations Between Trend Variables. Correlation coefficients (r) for two-sided regression fits (for data with corresponding $\gamma(\text{N2O5})$ values only). No statistically significant ($p > 0.05$) correlation between variables shown by \times .

Variables	LWC	H ₂ O Molarity	Organic Wet Mass Fraction	H ₂ O/NO ₃ Molar Ratio	RH	Nitrate Wet Mass Fraction	Chloride Wet Mass Fraction	Nitrate Dry Mass Fraction	pH (-2 to 1)	Cl ⁻ /NO ₃ ⁻ Molar Ratio	Org:SO ₄ ²⁻ Ratio	O:C Ratio	Chloride Dry Mass Fraction	Organic Dry Mass Fraction	pH (full range)	Temp	
LWC	1	0.99	-0.89	0.62	0.91	-0.51	-0.46	-0.24	0.30	0.27	-0.31	0.19	-0.23	-0.23	-0.09	0.61	
H ₂ O Molarity		1	-0.90	0.60	0.92	-0.49	-0.45	-0.23	0.31	0.26	-0.32	0.20	-0.21	-0.25	-0.07	0.62	
Organic Wet MF			1	-0.54	-0.76	0.36	0.32	0.11	-0.21	-0.25	0.42	-0.19	0.12	0.63	0.08	-0.45	
H ₂ O/NO ₃ MR				1	0.48	-0.54	-0.19	-0.53	-0.09	0.67	-0.35	0.14	\times	-0.14	-0.38	0.47	
RH					1	-0.30	-0.50	-0.06	0.40	0.13	-0.11	0.13	-0.28	-0.10	0.11	0.62	
Nitrate Wet MF						1	\times	0.93	0.30	-0.53	0.60	-0.28	-0.14	-0.09	0.75	-0.16	
Chloride Dry MF								1	-0.42	0.31	-0.07	-0.13	0.95	-0.05	-0.20	-0.41	
Nitrate Dry MF									1	0.54	0.56	-0.23	-0.25	-0.20	0.82	-0.07	
pH (-2 to 1)										1	0.38	\times	-0.38	0.08	\times	0.19	
Cl ⁻ /NO ₃ ⁻ MR											1	-0.35	0.51	-0.10	-0.51	0.21	
Org:SO ₄ ²⁻ Ratio												1	-0.33	0.34	0.57	\times	
O:C Ratio													1	\times	-0.24	0.18	
Chloride Dry MF														1	-0.24	-0.24	
Organic Dry MF															1	\times 0.07	
pH (full range)																1	\times
Temp																	1

Table B.3 Laboratory Parameterizations discussed in Section 4.4.3.2. Here, $k_{RX} = k_{4,x}$

Parameterization Name	Aerosol Type	Parameterization	Reference	Comparison to WINTER	Median
				r^2 RMSE	
EJ05		$\gamma = \sum_{i=1}^3 F_i * \gamma_i$ where, F_i = dry mass fraction $i = 1, 2, 3$, 1 = Aerosol sulfate, 2 = organic, 3 = chloride $\gamma_1 = \alpha \times 10^{-\beta}$ where, $\alpha = 2.79 \times 10^{-4} + 1.3 \times 10^{-4} * RH - 3.43 \times 10^{-6} * RH^2 + 7.52 \times 10^{-8} * RH^3$ $\beta = 4 \times 10^{-2} * (T - 294)$, for $T \geq 282K$ $\beta = -0.48$, for $T < 282K$ $\gamma_2 = 5.2 \times 10^{-4} * RH$, for $RH < 57\%$ $\gamma_2 = 0.03$, for $RH \geq 57\%$ $\gamma_3 = 0.005$, for $RH < 62\%$ $\gamma_3 = 0.03$, for $RH \geq 62\%$	(Evans & Jacob, 2005)	0.15 0.0242	0.0225
Dav08		$\gamma = \sum_{i=1}^3 x_i * \gamma_i^*$ where, $i = 1, 2, 3$ 1 = NH_4HSO_4 , 2 = $(NH_4)_2SO_4$, 3 = NH_4NO_3 $\lambda_1 = -4.10612 + 0.02386 * RH - 0.23771 * \max((T - 291), 0)$ $\gamma_1 = 1 / (1 + e^{-\lambda_1})$ $\gamma_1^* = \min(\gamma_1, 0.08585)$ $x_1 = 1 - (x_2 + x_3)$ $\lambda_2 = (-4.10612 - 0.80570) + 0.02386 * RH + (-0.23771 + 0.10225) * \max((T - 291), 0)$ $\gamma_1 = 1 / (1 + e^{-\lambda_2})$ $\gamma_2^* = \min(\gamma_2, 0.053)$ $x_2 = \max(0, \min(1 - x_3, \frac{[NH_4^+]}{[NO_3^-] + [SO_4^{2-}] - 1}))$ $\lambda_3 = -8.10774 + 0.04902 * RH$ $\gamma_3 = 1 / (1 + e^{-\lambda_3})$ $\gamma_3^* = \min(\gamma_3, 0.0154)$ $x_3 = \frac{[NO_3^-]}{[NO_3^-] + [SO_4^{2-}]}$	(Davis et al., 2008)	0.09 0.0320	0.0268
	NH_4HSO_4				
	$(NH_4)_2SO_4$				
	NH_4NO_3				

Table B.3 Cont.

Dav08B	NH ₄ HSO ₄ (NH ₄) ₂ SO ₄	Same as Dav08 except. $\lambda_1 = -2.67270 + 0.09553 * \min((RH-46), 0) - 0.20427 * \max((T-291), 0)$ $\lambda_2 = (-2.67270 - 0.97579) + 0.09553 * \min((RH-46), 0)$	(Davis et al., 2008)	0.07	0.0243	0.0211
Rie03	Sulfate and Nitrate	$\gamma = f * \gamma_1 + (1 - f) * \gamma_2$ where, $f = \frac{mSO_4^{2-}}{mSO_4^{2-} + mNO_3^-}$ $\gamma_1 = 0.02$ $\gamma_2 = 0.002$ mSO_4^{2-} [μg/m ³] = mass concentration of aerosol sulfate mNO_3^- [μg/m ³] = mass concentration of aerosol nitrate	(Riemer et al., 2003)	0.04	0.0172	0.0145
BT09	Water, Size, Nitrate, and Chloride	$\gamma = \frac{4V}{cSA} K_H k_{R3} \left(1 - \frac{1}{\left(\frac{k_{R5} [H_2O(L)]}{k_{R4} [NO_3^-]} \right) + 1 + \left(\frac{k_{R6} [Cl^-]}{k_{R4} [NO_3^-]} \right)} \right)$ where, c = mean molecular speed [m s ⁻¹] V = Particle volume [m ³ m ⁻³], calculated from AMS inputs into ISORROPIA SA = particle wet surface area density [m ² m ⁻³] K _H = Henry's Law Coefficient, 5 l from (Fried et al., 1994) $k_{R3} = \beta - \beta e^{(-\delta [H_2O(L)])}$ $\beta = 1.15 \times 10^6$ [s ⁻¹] $\delta = 0.13$ [M ⁻¹] $k_{R5}/k_{R4} = 0.06$ $k_{R6}/k_{R4} = 29$ [H ₂ O(L)] [M], H ₂ O described in Section 4.2.2. [NO ₃ ⁻] [M], derived from AMS measured particle nitrate and Vol. [Cl ⁻] [M], derived from interpolated PILS-IC Cl ⁻ and Vol.	(Bertram & Thornton, 2009)	0.08	0.0235	0.0325
BT09 w/o Cl⁻	Water, Size, Nitrate	$\gamma = \frac{4V}{cSA} K_H k_{R3} \left(1 - \frac{1}{\left(\frac{k_{R5} [H_2O(L)]}{k_{R4} [NO_3^-]} \right) + 1} \right)$ same parameters as above	(Bertram & Thornton, 2009)	0.18	0.0173	0.0151
G09	Water, Nitrate	Same as BT09 w/o Cl ⁻ except, $k_{R3} = 5 \times 10^6$ [s ⁻¹] $k_{R5}/k_{R4} = 1/30$	(Griffiths et al., 2009)	0.17	0.0165	0.0093

Table B.3 Cont.

BT09 + Rie09	Thin Organic Coating, Water, Size Nitrate, and Chloride	$\frac{1}{\gamma} = \frac{1}{\gamma_{core}} + \frac{1}{\gamma_{org. coat}}$ where, $\gamma_{core} = \text{BT09}$ $\gamma_{org. coat} = \frac{4RT H_{org} D_{org} R_c}{c \ell R_p}$	(Anttila et al., 2006)	0.03	0.0225	0.0028
		and, R [$\text{m}^3 \text{atm K}^{-1} \text{mol}^{-1}$], gas constant T [K], temperature $H_{org} D_{org} = \varepsilon H_{aq} D_{aq}$ $H_{aq} = 5000$ [$\text{mol m}^{-3} \text{atm}^{-1}$], Henry's Law Coefficient in aqueous core $D_{aq} = 1 \times 10^{-9}$ [$\text{m}^2 \text{s}^{-1}$], N_2O_5 Liquid Diffusion Coefficient $\varepsilon = 0.03$, scaling coefficient R_c [m], particle core radius, $R_p = R_c + \ell$ [m], total radius, median with respect to aerosol SA distribution $\ell = R_p \left(1 - \beta^{\frac{1}{3}}\right)$ [m], organic coating thickness $\beta = \frac{V_{inorganic}}{V_{inorganic} + V_{organic}}$, inorganic component volume fraction	(Anttila et al., 2006) (Anttila et al., 2006) (Riemer et al., 2009) (Riemer et al., 2009) (Riemer et al., 2009)			
BT09 w/o Cl + Rie09	Thin Organic Coating, Water, Size, and Nitrate	Same as above except, $\gamma_{core} = \text{BT09 w/out Cl}$	(Riemer et al., 2009)	0.11	0.0225	0.0025
BT09 + Rie09 w/ G14	Thin Organic Coating, Water, Size, Nitrate, Chloride, and O:C ratio	Same as Rie09+BT09 except, $\varepsilon = 0.06$ for $\text{RH} < 30\%$, $\text{O:C} > 0.7$ $\varepsilon = 0.008$ for $\text{RH} < 30\%$, $\text{O:C} < 0.7$ $\varepsilon = 0.3$, for $30\% < \text{RH} < 70\%$, $\text{O:C} > 0.7$ $\varepsilon = 0.3$, for $30\% < \text{RH} < 70\%$, $\text{O:C} < 0.7$ $\varepsilon = 0.8$, for $\text{RH} > 70\%$	(Gaston et al., 2014)	0.13	0.0162	0.0172
BT09 w/o Cl + Rie09 w/ G14	Thin Organic Coating, Water, Size, Nitrate, and O:C Ratio	Same as above except using BT09 w/o Cl	(Gaston et al., 2014)	0.17	0.0161	0.0104

Table B.3 Cont.

G14	(Anttila et al., 2006)	0.14	0.0164	0.0176
Thick Organic Coating, Size, Water				
$\frac{1}{\gamma} = \frac{cR_p}{4RTH_{org}D_{org}(q_{org}F - 1)}$				
Same as above except,				
$q_{org} = R_p \sqrt{\frac{k_{org}}{D_{org}}}$, organic layer reacto-diffusion parameter				
$q_{aq} = R_c \sqrt{\frac{k_{aq}}{D_{org}}}$, aqueous phase reacto-diffusion parameter				
$q_{org}^* = \frac{R_c}{R_p} q_{org}$				
$F = \frac{\coth(q_{org}) + h(q_{aq}, q_{org}^*)}{1 + \coth(q_{org}) * h(q_{aq}, q_{org}^*)}$				
$h(q_{aq}, q_{org}^*) = -\tanh(q_{aq})$ $\frac{H_{aq}D_{aq}}{H_{org}D_{org}}(q_{aq} \coth(q_{aq}) - 1) - (q_{org}^* \coth(q_{org}^*) - 1)$ $* \frac{H_{aq}D_{aq}}{H_{org}D_{org}}(q_{aq} \coth(q_{aq}) - 1) - (q_{org}^* \tanh(q_{org}^*) - 1)$				
$H_{org}D_{org} = \varepsilon H_{aq}D_{aq}$				
$k_{aq} = k_{R3}$ from BT09 above				
For RH < 30%, O:C > 0.7				
$\varepsilon = 0.06$, $k_{org} = 7 \times 10^4$ [s ⁻¹], $D_{org} = 6 \times 10^{-11}$ [m ² s ⁻¹]				
For RH < 30%, O:C < 0.7				
$\varepsilon = 0.008$, $k_{org} = 1.23 \times 10^4$ [s ⁻¹], $D_{org} = 8 \times 10^{-12}$ [m ² s ⁻¹]				
For 30% < RH < 70%, O:C > 0.7				
$\varepsilon = 0.3$, $k_{org} = 2 \times 10^5$ [s ⁻¹], $D_{org} = 5 \times 10^{-10}$ [m ² s ⁻¹]				
For 30% < RH < 70%, O:C < 0.7				
$\varepsilon = 0.05$, $k_{org} = 3.5 \times 10^4$ [s ⁻¹], $D_{org} = 5 \times 10^{-11}$ [m ² s ⁻¹]				
For RH > 70%, O:C < 0.7				
$\varepsilon = 0.8$, $k_{org} = 5.6 \times 10^4$ [s ⁻¹], $D_{org} = 1 \times 10^{-9}$ [m ² s ⁻¹]				
For RH > 70%, O:C > 0.7				
$\varepsilon = 1$, $k_{org} = 3.2 \times 10^5$ [s ⁻¹], $D_{org} = 1 \times 10^{-9}$ [m ² s ⁻¹]				

Table B.3 Cont.

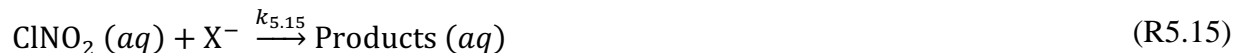
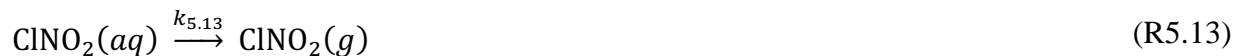
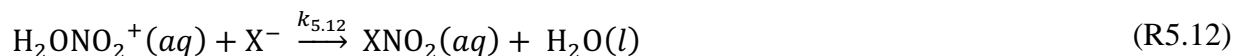
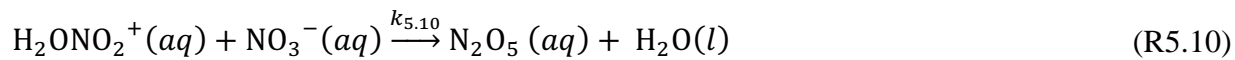
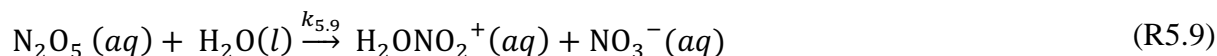
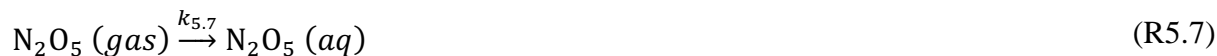
	(Badger et al., 2006)	0.13	0.0233	0.0008
Bad06 + BT09	(Badger et al., 2006)	0.13	0.0233	0.0008
Organics, Water, Size, Nitrate, and Chloride				
	$\frac{1}{\gamma} = \frac{1}{\alpha} + \frac{1}{\gamma_{inorganic}}$			
	where,			
	$\gamma_{inorganic} = \text{BT09}$			
	$f_{org} = \frac{\text{mass}_{inorganic}}{\text{mass}_{inorganic}}$,			
	$\alpha =$			
	For $f_{org} >= 0.67$			
	0.0005 for $\text{RH} \leq 25\%$			
	0.0003 for $25\% < \text{RH} \leq 70\%$			
	0.0014 for $\text{RH} \geq 70\%$			
	For $0.2 \leq f_{org} < 0.67$			
	0.00034 for $\text{RH} \leq 25\%$			
	0.0008 for $25\% < \text{RH} \leq 70\%$			
	0.0024 for $\text{RH} \geq 70\%$			
	For $0.09 \leq f_{org} < 0.2$			
	0.00052 for $\text{RH} \leq 25\%$			
	0.0021 for $25\% < \text{RH} <= 70\%$			
	0.0057 for $\text{RH} \geq 70\%$			
	For $0.06 \leq f_{org} < 0.09$			
	0.0007 for $\text{RH} \leq 25\%$			
	0.0034 for $25\% < \text{RH} \leq 70\%$			
	0.0090 for $\text{RH} \geq 70\%$			
	For $f_{org} \leq 0.06$			
	0.00065 for $\text{RH} \leq 25\%$			
	0.0050 for $25\% < \text{RH} \leq 70\%$			
	0.0099 for $\text{RH} \geq 70\%$			
Bad06 + BT09 w/o Cl⁻	(Badger et al., 2006)	0.14	0.0233	0.0008
Organics, Water, Size, and Nitrate				
	Same as above except with BT09 w/o Cl ⁻			
WINTER (Figure 13k)	This Work	0.17	0.0157	0.0142
Organics, water, Size, Nitrate				
	$\frac{1}{\gamma} = \frac{1}{\gamma_{core}} + \frac{1}{\gamma_{org.coat}}$			
	where,			
	$\gamma_{core} = \frac{4V}{cSA} K_H k_{R3} \left(1 - \frac{1}{\left(\frac{k_{R5}[H_2O(l)]}{k_{R4}[NO_3^-]} \right) + 1} \right)$			
	$\gamma_{org.coat} = \frac{4RT\varepsilon H_{aq} D_{aq} R_c}{c\ell R_p}$			
	All variables same as above except,			
	k_{R3} , fit; = $2.14 \times 10^{3.8} [H_2O(l)] [M^{-1} s^{-1}]$			
	$k_{R5}/k_{R4} = 0.04$			
	ε , fit; = $0.15 * O:C \text{ Ratio} + 0.0016 * RH$			

Appendix C

Supplemental Information for Chapter 5 – Heterogeneous ClNO₂ production during winter: Aircraft measurements during the 2015 WINTER campaign and evaluation of parameterizations

C.1. ClNO₂ Yield Parameterization Derivations

Model Mechanism from Chapter 5



The ClNO₂ yield is defined as:

$$\varphi(\text{ClNO}_2) = \frac{d[\text{ClNO}_2]/dt}{-d[\text{N}_2\text{O}_5]/dt}$$

Also assume [H₂ONO₂⁺] is in steady state.

From R5.9-R5.12

$$[\text{H}_2\text{ONO}_2^+]_{ss} = \frac{k_{5.9}[\text{N}_2\text{O}_5]_{aq}[\text{H}_2\text{O}]}{k_{5.10}[\text{NO}_3^-] + k_{5.11}[\text{H}_2\text{O}] + k_{5.12}[\text{Cl}^-]}$$

1) Original Yield Expression (From R5.3 – 5.6):

Step 1)

$$\begin{aligned} \frac{d[ClNO_2]_{aq}}{dt} &= k_{5.12}[Cl^-][H_2ONO_2^+]_{ss} \\ &= k_{5.9}[N_2O_5]_{aq}[H_2O] \left(\frac{k_{5.12}[Cl^-]}{k_{5.10}[NO_3^-] + k_{5.11}[H_2O] + k_{5.12}[Cl^-]} \right) \end{aligned}$$

Step 2)

$$\begin{aligned} \frac{-d[N_2O_5]_{aq}}{dt} &= k_{5.9}[N_2O_5]_{aq}[H_2O] - k_{5.10}[NO_3^-][H_2ONO_2^+]_{ss} \\ &= k_{5.9}[N_2O_5]_{aq}[H_2O] - \frac{k_{5.10}[NO_3^-]k_{5.9}[N_2O_5]_{aq}[H_2O]}{k_{5.10}[NO_3^-] + k_{5.11}[H_2O] + k_{5.12}[Cl^-]} \\ &= k_{5.9}[N_2O_5]_{aq}[H_2O] \left(1 - \frac{k_{5.10}[NO_3^-]}{k_{5.10}[NO_3^-] + k_{5.11}[H_2O] + k_{5.12}[Cl^-]} \right) \end{aligned}$$

Step 3)

$$\begin{aligned} \frac{d[ClNO_2]_{aq}/dt}{-d[N_2O_5]_{aq}/dt} &= \frac{k_{5.9}[N_2O_5]_{aq}[H_2O] \left(\frac{k_{5.12}[Cl^-]}{k_{5.10}[NO_3^-] + k_{5.11}[H_2O] + k_{5.12}[Cl^-]} \right)}{k_{5.9}[N_2O_5]_{aq}[H_2O] \left(1 - \frac{k_{5.10}[NO_3^-]}{k_{5.10}[NO_3^-] + k_{5.11}[H_2O] + k_{5.12}[Cl^-]} \right)} \\ &= \frac{\left(\frac{k_{5.12}[Cl^-]}{k_{5.10}[NO_3^-] + k_{5.11}[H_2O] + k_{5.12}[Cl^-]} \right)}{\left(\frac{k_{5.10}[NO_3^-] + k_{5.11}[H_2O] + k_{5.12}[Cl^-] - k_{5.10}[NO_3^-]}{k_{5.10}[NO_3^-] + k_{5.11}[H_2O] + k_{5.12}[Cl^-]} \right)} \\ &= \frac{k_{5.12}[Cl^-]}{k_{5.11}[H_2O] + k_{5.12}[Cl^-]} \end{aligned}$$

$$\varphi(ClNO_2) = \frac{1}{\frac{k_{5.11}[H_2O]}{k_{5.12}[Cl^-]} + 1}$$

2) Competition Reaction Expression (from R5.9 – 5.12, 5.14):

Step 1)

$$[\text{H}_2\text{ONO}_2^+]_{ss} = \frac{k_{5.9}[\text{N}_2\text{O}_5]_{aq}[\text{H}_2\text{O}]}{k_{5.10}[\text{NO}_3^-] + k_{5.11}[\text{H}_2\text{O}] + k_{5.12}[\text{Cl}^-] + k_{5.14}[\text{Y}^-]}$$

Step 2)

$$\begin{aligned} \frac{d[\text{ClNO}_2]_{aq}}{dt} &= k_{5.12}[\text{Cl}^-][\text{H}_2\text{ONO}_2^+]_{ss} \\ &= k_{5.9}[\text{N}_2\text{O}_5]_{aq}[\text{H}_2\text{O}] \left(\frac{k_{5.12}[\text{Cl}^-]}{k_{5.10}[\text{NO}_3^-] + k_{5.11}[\text{H}_2\text{O}] + k_{5.12}[\text{Cl}^-] + k_{5.14}[\text{Y}^-]} \right) \end{aligned}$$

Step 3)

$$\begin{aligned} \frac{-d[\text{N}_2\text{O}_5]_{aq}}{dt} &= k_{5.9}[\text{N}_2\text{O}_5]_{aq}[\text{H}_2\text{O}] - k_{5.10}[\text{NO}_3^-][\text{H}_2\text{ONO}_2^+]_{ss} \\ &= k_{5.9}[\text{N}_2\text{O}_5]_{aq}[\text{H}_2\text{O}] - \frac{k_{5.10}[\text{NO}_3^-]k_{5.9}[\text{N}_2\text{O}_5]_{aq}[\text{H}_2\text{O}]}{k_{5.10}[\text{NO}_3^-] + k_{5.11}[\text{H}_2\text{O}] + k_{5.12}[\text{Cl}^-] + k_{5.14}[\text{Y}^-]} \\ &= k_{5.9}[\text{N}_2\text{O}_5]_{aq}[\text{H}_2\text{O}] \left(1 - \frac{k_{5.10}[\text{NO}_3^-]}{k_{5.10}[\text{NO}_3^-] + k_{5.11}[\text{H}_2\text{O}] + k_{5.12}[\text{Cl}^-] + k_{5.14}[\text{Y}^-]} \right) \end{aligned}$$

Step 4)

$$\begin{aligned} \frac{d[\text{ClNO}_2]_{aq}/dt}{-d[\text{N}_2\text{O}_5]_{aq}/dt} &= \frac{k_{5.9}[\text{N}_2\text{O}_5]_{aq}[\text{H}_2\text{O}] \left(\frac{k_{5.12}[\text{Cl}^-]}{k_{5.10}[\text{NO}_3^-] + k_{5.11}[\text{H}_2\text{O}] + k_{5.12}[\text{Cl}^-] + k_{5.14}[\text{Y}^-]} \right)}{k_{5.9}[\text{N}_2\text{O}_5]_{aq}[\text{H}_2\text{O}] \left(1 - \frac{k_{5.10}[\text{NO}_3^-]}{k_{5.10}[\text{NO}_3^-] + k_{5.11}[\text{H}_2\text{O}] + k_{5.12}[\text{Cl}^-] + k_{5.14}[\text{Y}^-]} \right)} \\ &= \frac{\left(\frac{k_{5.12}[\text{Cl}^-]}{k_{5.10}[\text{NO}_3^-] + k_{5.11}[\text{H}_2\text{O}] + k_{5.12}[\text{Cl}^-] + k_{5.14}[\text{Y}^-]} \right)}{\left(\frac{k_{5.10}[\text{NO}_3^-] + k_{5.11}[\text{H}_2\text{O}] + k_{5.12}[\text{Cl}^-] - k_{5.10}[\text{NO}_3^-]}{k_{5.10}[\text{NO}_3^-] + k_{5.11}[\text{H}_2\text{O}] + k_{5.12}[\text{Cl}^-] + k_{5.14}[\text{Y}^-]} \right)} \\ &= \frac{k_{5.12}[\text{Cl}^-]}{k_{5.11}[\text{H}_2\text{O}] + k_{5.12}[\text{Cl}^-] + k_{5.14}[\text{Y}^-]} \end{aligned}$$

$$\varphi(\text{ClNO}_2) = \frac{1}{\frac{k_{5.11}[\text{H}_2\text{O}]}{k_{5.12}[\text{Cl}^-]} + \frac{k_{5.14}[\text{Y}^-]}{k_{5.12}[\text{Cl}^-]} + 1}$$

3) Direct ClNO₂ Loss Expression (from R5.9 – 5.12, 5.15):

Step 1)

$$\begin{aligned} \frac{d[ClNO_2]_{aq}}{dt} &= k_{5.12}[Cl^-][H_2ONO_2^+]_{ss} - k_{5.15}[ClNO_2]_{aq}[X^-] \\ &= k_{5.9}[N_2O_5][H_2O] \left(\frac{k_{5.12}[Cl^-]}{k_{5.10}[NO_3^-] + k_{5.11}[H_2O] + k_{5.12}[Cl^-]} \right) - k_{5.15}[ClNO_2]_{aq}[X^-] \end{aligned}$$

Step 2) same as original derivation

$$\begin{aligned} \frac{-d[N_2O_5]_{aq}}{dt} &= k_{5.9}[N_2O_5]_{aq}[H_2O] \left(1 - \frac{k_{5.10}[NO_3^-]}{k_{5.10}[NO_3^-] + k_{5.11}[H_2O] + k_{5.12}[Cl^-]} \right) \end{aligned}$$

Step 3)

$$\begin{aligned} \frac{d[ClNO_2]_{aq}/dt}{-d[N_2O_5]_{aq}/dt} &= \frac{k_{5.9}[N_2O_5]_{aq}[H_2O] \left(\frac{k_{5.12}[Cl^-]}{k_{5.10}[NO_3^-] + k_{5.11}[H_2O] + k_{5.12}[Cl^-]} \right) - k_{5.15}[ClNO_2]_{aq}[X^-]}{k_{5.9}[N_2O_5]_{aq}[H_2O] \left(1 - \frac{k_{5.10}[NO_3^-]}{k_{5.10}[NO_3^-] + k_{5.11}[H_2O] + k_{5.12}[Cl^-]} \right)} \end{aligned}$$

Term 1

$$\begin{aligned} &= \frac{k_{5.9}[N_2O_5]_{aq}[H_2O] \left(\frac{k_{5.6}[Cl^-]}{k_{5.10}[NO_3^-] + k_{5.11}[H_2O] + k_{5.12}[Cl^-]} \right)}{k_{5.9}[N_2O_5]_{aq}[H_2O] \left(1 - \frac{k_{5.10}[NO_3^-]}{k_{5.10}[NO_3^-] + k_{5.11}[H_2O] + k_{5.12}[Cl^-]} \right)} \end{aligned}$$

Simplifies as in original derivation to:

$$= \frac{1}{\frac{k_{5.11}}{k_{5.12}} \frac{[H_2O]}{[Cl^-]} + 1}$$

Term 2

$$= \frac{k_{5.15}[ClNO_2]_{aq}[X^-]}{k_{5.9}[N_2O_5]_{aq}[H_2O] \left(1 - \frac{k_{5.10}[NO_3^-]}{k_{5.10}[NO_3^-] + k_{5.11}[H_2O] + k_{5.12}[Cl^-]} \right)}$$

$$= \frac{k_{5.15}[\text{ClNO}_2]_{aq}[\text{X}^-]}{k_{5.9}[\text{N}_2\text{O}_5]_{aq}[\text{H}_2\text{O}] \left(1 - \frac{1}{\frac{k_{5.11}[\text{H}_2\text{O}]}{k_{5.10}[\text{NO}_3^-]} + 1 + \frac{k_{5.12}[\text{Cl}^-]}{k_{5.10}[\text{NO}_3^-]}} \right)}$$

Combined expression:

$$\varphi(\text{ClNO}_2) = \frac{1}{\left(1 + \frac{k_{5.11}[\text{H}_2\text{O}]}{k_{5.12}[\text{Cl}^-]} \right)} - \frac{k_{5.15}[\text{ClNO}_2]_{aq}[\text{X}^-]}{k_{5.9}[\text{N}_2\text{O}_5]_{aq}[\text{H}_2\text{O}] \left(1 - \frac{1}{\frac{k_{5.11}[\text{H}_2\text{O}]}{k_{5.10}[\text{NO}_3^-]} + 1 + \frac{k_{5.12}[\text{Cl}^-]}{k_{5.10}[\text{NO}_3^-]}} \right)}$$

C.2. Rate Constant Ratios from Heal et al. (2007)

Reported in Heal et al. (2007):

$$\frac{k_{5.14}}{k_{5.11}[\text{H}_2\text{O}]} = 330 [\text{M}^{-1}] \text{ (pH = 6) and } 1500 [\text{M}^{-1}] \text{ (pH = 10)}$$

Median $[\text{H}_2\text{O}]$ from WINTER is 20 M (McDuffie et al., 2018) (Chapter 4), therefore:

$$\frac{k_{5.14}}{k_{5.11}} = 6600 \text{ (pH = 6) and } 3 \times 10^4 \text{ (pH = 10)}$$

$k_{5.12}/k_{5.11}$ Ratio from Literature:

505 ± 190 (Ryder et al., 2015)

483 ± 175 (Bertram & Thornton, 2009)

450 ± 100 (Roberts et al., 2009)

836 ± 32 (Behnke et al., 1997)

C.3. Results – Additional Information

Table C.1. Previous Field Determinations of $\phi(\text{ClNO}_2)$, listed by campaign date

Date	Location	Platform	Min, Max, Avg (Med)	N	Method	Reference
July-Sept., 2006	Southern TX	Ship	0.1, 0.65, n/a	2	Method #1 ^a , from box model	(Osthoff et al., 2008)
Feb, 2009	Boulder, CO	Ground	n/a, n/a, 0.14	1	Method #3 ^b , from box model	(Thornton et al., 2010)
May-June, 2010	Southern, CA	Ship	0.154, 0.62, n/a	2	Method #2 ^c , total nitrate = $\text{NO}_y\text{-NO}_x$	(Wagner et al., 2012)
May-June, 2010	Southern, CA	Ground	0.07, 0.62, (0.12)	n/a	Method #1	(Mielke et al., 2013)
Apr. 2010-Mar. 2011	Calgary, CA	Ground	n/a, 0.153, (0.01)	n/a	Method #1	(Mielke et al., 2016)
Apr. 2010-Mar. 2011	Calgary, CA	Ground	n/a, 0.704, (0.035)	n/a	Box Model, assumes $\gamma(\text{N}_2\text{O}_5) = 0.02$, constant SA = $250 \mu\text{m}^2 \text{cm}^{-3}$, $k_{\text{VOC}} = 10^{-3} \text{s}^{-1}$	(Mielke et al., 2016; Mielke et al., 2011)
Feb-March, 2011	Weld County, CO	Ground/ Tower	0.24, 1, (0.96)	19	Method #4 ^d , 1 μm particles only	(Young et al., 2013) ^e
Feb-March, 2011	Weld County, CO	Ground/ Tower	0.05, 0.90, 0.065 ^f	85440	Method #3, right term, from box model	(Wagner et al., 2013)
Feb-March, 2011	Weld County, CO	Ground/ Tower	0.05 \pm 0.15 ^g	n/a	Method #2, total nitrate = HNO_3 + particle NO_3	(Riedel et al., 2013)
Aug.-Sept., 2011	SW Germany	Ground	0.035, 1.38, 0.49	33	Various methods including Method #2, total nitrate = Particle NO_3	(Phillips et al., 2016)
20 June – 9 July, 2014	Wangdu, North CN	Ground	n/a, 0.35, 0.30	n/a	Method #3, right term, $k_{\text{N}_2\text{O}_5}$ from steady state approximation	(Tham et al., 2016)
24 July-27 Aug., 2014	Mt. Tai, CN	Ground	0.02, 0.90, 0.28	n/a	Method 3, right term, $k_{\text{N}_2\text{O}_5}$ from steady state approximation	(Wang, Z. et al., 2017)
6 and 20 Sep., 2014	Ji'nan, North CN	Ground	0.014, 0.082, n/a	2	Method #3, right term, $k_{\text{N}_2\text{O}_5}$ from steady state approximation	(Wang, X. et al., 2017)
Feb-March, 2015	Eastern U.S.	Aircraft	0.003, 1, (0.138)	3425	Method #3, left term, from box model	This Work

^aMethod #1: $\phi(\text{ClNO}_2) = \frac{[\text{ClNO}_2]}{P(\text{NO}_3) \cdot dt_{\text{Sunset}}}$, Considered lower limit. ^bMethod #3: $\phi(\text{ClNO}_2) = \frac{k_{\text{ClNO}_2}/dt}{k_{\text{N}_2\text{O}_5} \int_{\text{Sunset}} k_{\text{N}_2\text{O}_5} [\text{N}_2\text{O}_5] dt} = \frac{[\text{ClNO}_2]/dt}{k_{\text{N}_2\text{O}_5} [\text{N}_2\text{O}_5]}$

^cMethod #2: $\phi(\text{ClNO}_2) = \frac{2m}{m+1}$, $m = \frac{\Delta\text{ClNO}_2}{\Delta\text{NO}_3 \text{ Total}}$

^dParameterization (Method #4): $\phi(\text{ClNO}_2) = \frac{1}{(1 + \frac{[\text{H}_2\text{O}]}{485[\text{Cl}^-]})}$

^eResults not included in Figure 5.4, ^fMost frequent value, ^gTypical values for entire campaign, additional individual plume analyses are not included in this table.